Luminescence Spectroscopy of Minerals and Materials

Michael Gaft
Renata Reisfeld
Gérard Panczer

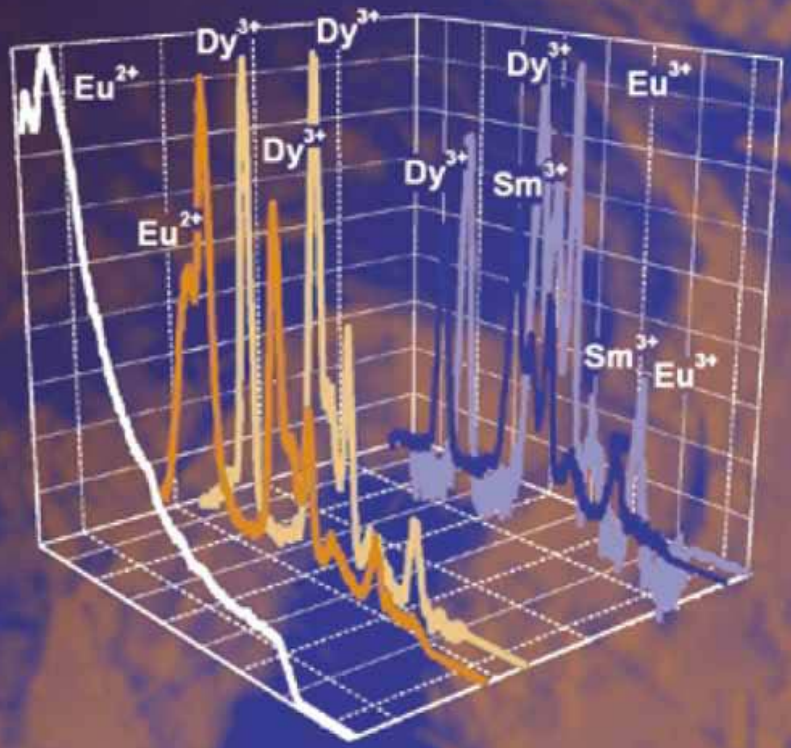

Springer

Michael Gaft
Renata Reisfeld
Gérard Panczer

Modern Luminescence Spectroscopy of Minerals and Materials

with 199 Figures and 31 Tables

Springer

Michael Gaft
ITL, Senior Scientist
12 Hachoma St.
Rishon-Lezion 75140
Israel

The Open University of Israel, Lecturer
108 Ravutski St.
Raanava 43107
Israel

Renata Reisfeld
Dept. of Inorganic and Analytical Chemistry
The Hebrew University
Jerusalem 91904
Israel

Gérard Panczer
Laboratoire de Physico-chimie des Matériaux Luminescents
Université Claude Bernard Lyon 1
43, Bd. du 11 Novembre 1918
Bâtiment Lippmann
69622 Villeurbanne
France

ISBN-10 3-540-21918-8 Springer Berlin Heidelberg New York
ISBN-13 978-3-540-21918-7 Springer Berlin Heidelberg New York

Library of Congress Control Number: 2004107504

Bibliographic information published by Die Deutsche Bibliothek.
Die Deutsche Bibliothek lists this publication in the Deutsche Nationalbibliografie; detailed bibliographic data is available in the Internet at <http://dnb.ddb.de>.

Typesetting: LE-TEX Jelonek, Schmidt & Vöckler GbR, Leipzig
Cover design: E. Kirchner, Heidelberg
Printed on acid-free paper 30/2132/AO 5 4 3 2 1 0

Preface

In the broad sense the subject of our book belongs to the Physics of Minerals field, namely to its spectroscopic part. The main features of our experimental technique are laser excitation of minerals and time-resolved detection of resulting emission and scattering. Laser sources allow the simultaneous study of linear optic events, such as luminescence and breakdown spectroscopies, and non-linear ones, such as Raman spectroscopy and Second Harmonic Generation. The time-resolved technique, namely signal detection only during a certain time gate after a certain delay following the end of the laser pulse, results in drastically improved spectroscopic sensitivity and selectivity. It enables us to receive new data, which contribute greatly to our fundamental knowledge of minerals and may be practically used.

The book is arranged as follows.

The **Introduction** chapter contains the basic definitions of the main scientific terms, such as *spectroscopy, luminescence spectroscopy, luminescent mineral, luminescent center, luminescence lifetime, luminescence spectrum and excitation spectrum.* The state of the art in the *steady-state luminescence* of minerals field is presented. The main advantages of the *laser-induced time resolved technique* in comparison with the steady-state one are shortly described.

The **Theoretical Background** chapter contains description of the main processes involved in luminescence, such as *absorption of the excitation energy*, and *radiative return* to the ground state. The resulting luminescence is considered based on *ligand field theory*, the *configurational diagrams model*, *molecular orbitals theory*, and *band scheme* approximation. The main attention is paid to *luminescence decay*, consisting of radiation decay, non-radiation decay, and special types of decay, such as stepwise energy transfer, cooperative sensitization and cooperative luminescence.

The **Experimental Technique** chapter describes our experimental setup with the following main parts: *laser source* (Ar, excimer, Nd-YAG, nitrogen, dye, OPO), imaging monochromator, *gated detector* (Intensified Charge Coupled Device) and computer with corresponding software. The main features of the experimental devices are described, which enable us to accomplish time-resolved detection.

The **Luminescent Minerals** chapter contains time-resolved luminescence spectra for approximately *50 minerals*. The following information is presented for the each one, comprising literature and original results: short description

of the *crystal structure, optically active color centers, and luminescence centers,* detected by steady state and time-resolved techniques.

The **Interpretation of Luminescence Centers** chapter is devoted to a detailed explanation of the luminescence centers interpretation process, which comprises investigation of spectral and kinetic parameters of excitation and emission at different temperatures from 4.2 to 300 K. In numerous cases the interpretation is confirmed by the study of synthetic minerals analogs artificially activated by potential impurities, which may serve as emission centers. The following luminescence centers have been confidently detected and interpreted:

- *rare-earth elements* (Ce^{3+}, Pr^{3+}, Nd^{3+}, Sm^{3+}, Sm^{2+}, Eu^{3+}, Eu^{2+}, Gd^{3+}, Tb^{3+}, Dy^{3+}, Er^{3+}, Ho^{3+}, Tm^{3+}, Yb^{3+}, Yb^{2+});
- *transition elements* (Mn^{2+}, Mn^{5+}, Cr^{3+}, Fe^{3+}, Ti^{3+});
- s^2 *ions* (Bi^{3+}, Bi^{2+}, Pb^{2+}, Sn^{2+});
- d^{10} *ions* (Ag^{+}, Cu^{+});
- d^0 *complex ions* (WO_4, MoO_4, TiO_4);
- *molecular centers* (UO_2, S_2^-);
- *radiation induced centers*
- *diamond centers* (N3, H3, H4, S2, S3);
- *reabsorption lines* of O_2, H_2O, U^{4+}, Nd^{3+}.

Besides confidently identified centers, the possible participation of Mn^{4+} and V^{2+} is proposed. The centers, such as Mn^{6+}, Cr^{4+},Cr^{5+}, V^{3+} and $V^{4+}$are described, which are not found in minerals yet, but are known in synthetic analogs of minerals, such as apatite, barite, zircon and corundum. Besides that, the centers Ni^{2+} and Ti^{2+} are discussed as possible participants in mineral luminescence. The last part of this chapter is devoted to unidentified emission lines and bands in apatite, barite, calcite and zircon.

The **Applications of Laser-induced Time-resolved Spectroscopic Techniques** chapter starts with a short description of laser-induced spectroscopies, which may be used in combination with laser-induced luminescence, namely Breakdown, Raman and Second Harmonic Generation. The chapter contains several examples of the application of laser-based spectroscopies in remote sensing and radiometric sorting of minerals. The problem of minerals as geomaterials for radioactive waste storage is also considered.

Acknowledgements

Particular thanks mutual for all authors are due to Prof. **Georges Boulon** for his personal involvement in our lives as scientist and friend.

Our special thanks for **Arnold Marfunin**, **Arkadii Tarashchan and Boris Gorobets** for great contribution in minerals luminescence research.

We are very grateful for our colleagues and co-authors for long-time fruitful collaborations: **Philipp Blanc, Alain Baumer, Micheline Boudeulle, Mordechai Brestel, David Carrier, Bernard Champagnon, Noelle Chevarier, Elena Evdokimenko, Victoria Gukova, Patrick Jollivet, Christian Jörgensen, Yoram Kirsh, Svetlana Malinko, Vadim Moroshkin, Lev Nagli, Lutz Nasdalla, Nadege Ollier, Igor Prokofiev, Victor Rassulov, Ina Reiche, Alexander Rogojine, Irina Rudenkova, Anne-Magali Seydoux-Guillaume, Tatiana Shalashilina, Isamu Shinno, Shlomo Shoval, Harry Siegel, Glenn Waychunas.**

Contents

Comrade scientists, you, Newton dears
And precious Einstein, that we love to cry!
In the common earth will sleep our rotten rest;
And Earth swallows everything: the apatite and the dung.

Comrade scientists, Vladimir Vissotski (1938–1980)

Great is the art to penetrate by intelligence in the subterranean deepness where nature forbids the access to our hands and to our eyes; to roam by thought in the Earth womb, to penetrate by reason into the sombre crevasses, to make the things and the activities hidden by the eternal darkness, coming to the day light.

Terrestrian layers, Mikhail Lomonossov (1711–1765)

CHAPTER 1

Introduction

Spectroscopy is the study of the interaction of electromagnetic radiation with matter. There are three aspects to spectroscopic measurement: irradiation of a sample with electromagnetic radiation; measurement of the absorption, spontaneous emission and scattering (Rayleigh elastic scattering, Raman inelastic scattering) from the sample; and analysis and interpretation of these measurements. The main subject of our book is spontaneous luminescence of natural minerals. We have used the term luminescence, which is the general term of the phenomenon. Luminescence may be subdivided into fast fluorescence with spin-allowed transition and slow phosphorescence with spin-forbidden transition. Afterglow may be added, which is related to emission after trapping of an electron elsewhere.

Luminescence spectroscopy measures the energy levels of the luminescence centers. The energy level of a luminescence center is defined as its characteristic state, which is related to the physical nature of the center and to the energetic and dynamic processes that the center undergoes. The ground state is defined as the state with the lowest energy. States of higher energy are called excited states. A center possesses several distinct reservoirs of energy levels, including electronic, vibrational, rotational, transitional, and those associated with nuclear and electron spin. In mineral luminescence, the energy levels of interest are those that are associated with electronic and vibrational transitions.

A *luminescent mineral* is a solid, which converts certain types of energy into electromagnetic radiation over and above thermal radiation. The electromagnetic radiation emitted by a luminescent mineral is usually in the visible range, but can also occur in the ultraviolet (UV) or infrared (IR) range. It is possible to excite the luminescence of minerals by UV and visible radiation (photoluminescence), by a beam of energetic electrons (cathodoluminescence), by X-rays (X-ray excited luminescence) and so on. A special case is so-called thermoluminescence, which is stimulation by the heating of luminescence, preliminary excited in a different way.

The luminescent mineral consists of a host lattice and a *luminescent center*, often called an activator. The determination of the nature of the center responsible for luminescence is not generally a trivial task. Correlation of the observation of the specific luminescence with a particular impurity concentration may give an indication of the source of the emission but it is not proof of the origin, and can sometimes be misleading. Furthermore, it does not give any details about the precise nature of the center. Spectroscopic studies may

provide a number of important parameters, which aid identification of the luminescence center.

Luminescence emission occurs as a result of a radiative electronic transition in which an electron jumps from a higher energy state to a lower one, the difference in energy being released as a photon. Clearly the electron must first be excited into a higher energy state by some means, for example UV or visible light. After excitation the nuclei adjust their positions to the new excited situation, so that the inter-atomic distances equal the equilibrium distances belonging to the excited state. This process is called relaxation. During relaxation there is usually no emission. The system can return to the ground state spontaneously under emission of radiation from the lowest level of the excited state. The emission occurs at a lower energy than the absorption due to the relaxation process. The energy difference between the maximum of the lowest excitation band and that of the emission band is called *Stokes shift*.

The luminescence is usually characterized by its *quantum yield and lifetime*. Luminescence spectroscopy is the measurement and analysis of various features that are related to the luminescence quantum yield and lifetime. The quantum yield is the ratio of the number of photons emitted to the number absorbed. Luminescence centers with the largest quantum yields display the brightest emission. The lifetime is connected to the average time that the luminescence center spends in the excited state prior to its return to the ground state. It is defined as the time required for the luminescence intensity to drop to $1/e$ of its original value. The luminescence quantum yield and lifetime are modified by a number of factors that can increase or decrease the energy losses. The luminescence intensity of the luminescence centers is a function of their concentration, absorbing power at the excitation wavelength, and their quantum yield of the emission wavelength.

A *luminescence emission spectrum* represents the luminescence intensity measured over a range of emission wavelengths at a fixed excitation wavelength. On the other hand, a *luminescence excitation spectrum* is a plot of the luminescence intensity at a particular emission wavelength for a range of excitation wavelengths. A luminescence excitation-emission matrix is a two-dimensional contour plot that displays the luminescence intensities as a function of a range of excitation and emission wavelengths. Each contour represents points of equal luminescence intensity. Measurement of a luminescence lifetime requires excitation by a pulsed source, whose duration is negligible as compared to the lifetime of the emission process. The luminescence intensity is then recorded as a function of time. All spectral and kinetic measurements may be done at room temperature, or at liquid nitrogen or helium temperatures.

In many luminescence centers the intensity is a function of a specific orientation in relation to the crystallographic directions in the mineral. Even if a center consists of one atom or ion, such *luminescence anisotropy* may be produced by a compensating impurity or an intrinsic defect. In the case of cubic crystals this fact does not disrupt optical isotropy since anisotropic centers are oriented statistically uniformly over different crystallographic directions. However, in excitation of luminescence by polarized light the hidden anisotropy may be revealed and the orientation of centers can be determined.

Not every mineral shows luminescence. The reason is that the radiative emission process has a competitor, namely, the *nonradiative return* to the ground state. In that process the energy of the excited state is used to excite the vibrations of the host lattice, i.e. to heat the host lattice.

Many scientists have contributed to an essential part to our current knowledge in this field of mineral physics and its practical applications in Earth sciences. In 1602, an Italian cobbler from Bologna, Vincencio Casiarolo found that by heating a heavy mineral, the so called "Bologna stone", in fact barite $BaSO_4$, it emitted light if it was previously exposed to sun light or heated (Fig. 1.1a). In this way luminescence was discovered. Despite the fact that the Arab alchemist, Alchid Bechil, first isolated phosphorus in the 12th century, the discovery of elementary phosphorus is attributed to Hennig Brand (1669), a German merchant and amateur alchemist who, while concentrating a great quantity of urine, succeeded in extracting it as a solid substance (Fig. 1.1b). The substance glowed in the dark and led to the term *phosphorescence* [from the Greek, *φωσφοροζ (fosforos)*, which carries light]. In 1786, the poet Goethe, a great collector of minerals, showed that, while sending colored lights (through filters) onto a heated barite crystal, blue light only induced luminescence but not the red, yellow or green ones. Georges Stokes in 1852 observed a luminescence phenomenon while studying fluorite and gave this phenomenon the name *fluorescence*. He developed the "Stokes Law of Fluorescence", which dictates that the wavelength of fluorescence emission must be greater than that of the exciting radiation. In 1859, Edmond Becquerel showed that *fluorescence* was in fact

Fig. 1.1. a Cabalistic representation image from the treaty "Il fosforo o vero la Pietra Bolognese" by Marc Antonio Cellio (1680) representing the light emission of heated barite; **b** Painting by Joseph Wright of Derby (18th century) representing the discovery of the phosphorescence of the phosphorus extracted from urine by Hennig Brand in 1669

a *phosphorescence* phenomenon with very short duration, and that uranyl salts had phosphorescence twenty times more intense than calcium (greenockite) or zinc (sphalerite or blende) sulfides. He also emphasized that the red fluorescence of calcite was link to the presence of manganese, thus identifying for the first time the role of activators in fluorescence.

The detailed summary of some key elements in the history of luminescent studies of minerals is well presented in the following books and reviews: Marfunin 1979a; Walker 1985; Waychunas 1989; Goldberg and Weiner 1989; Brittain 1990; Gorobets and Walker 1994; Gorobets et al. 1995; Nasdala et al. 2004. We want to mention specifically the excellent book of Tarashchan (1978), unfortunately not translated into English and remaining practically unknown to anyone except Russian speaking scientists. We think that up to today it remains one of the best books in the field. Gorobets and Rogojine (2001) recently wrote the reference book "Luminescent spectra of minerals". It is the first systematic compilation of the luminescence spectra of minerals together with a contemporary interpretation of the nature of the luminescence centers. This tremendous work summarizes the main achievements in this field up to the year 2000. Many luminescence properties and peculiarities of different minerals have been related to the crystallochemical and structural state of mineral species, varieties and individuals, searching at the same time for possibilities to associate the luminescence behavior with the different conditions of mineral formation and alteration. Different types of luminescent centers have been studied and identified using photo-, cathodo- and X-ray luminescence techniques frequently combined with optical absorption and EPR spectroscopy in minerals such as diamond, apatite, fluorite, scheelite, zircon, calcite etc., which are known as important genetic indicators in many rock- and ore-forming processes. The main minerals, which are luminescent under UV lamp excitation, are summarized in Table 1.1.

At the same time, solid-state physicists intensively dealt with synthetic analogues of luminescent minerals as phosphors and quantum electronic materials, providing the theoretical and experimental background for further applications in high technology material sciences. These achievements are shortly summarized in Table 1.2.

These results were also used in geosciences, remote sensing, exploration, natural dosimetry, mineral processing etc. Starting approximately 20 years ago, UV lasers have been used as luminescence of minerals excitation source. In this way, not only luminescence spectra, but also decay time have been determined. The main motivation was to use laser-induced luminescence for remote sensing of mineral deposits (Kasdan et al. 1981; Seigel and Robbins 1985). Systematic investigations of laser-induced luminescence of minerals started at the same time by one of the authors in the former Soviet Union (Gaft 1989). Luminescence centers established in minerals including decay times are summarized in Table 1.3.

So far presented results are connected with so-called *steady-state spectroscopy*. Conventionally studied steady state or CW (continuous-wave) luminescence is a process where the excitation sources pump the sample at constant intensity over a time necessary to perform the measurement. The end result is

Table 1.1. Minerals luminescent under UV lamp excitation

Native	Diamond
Oxides	Brucite $Mg(OH)_2$, corundum Al_2O_3, ruby Al_2O_3, sapphire Al_2O_3
Halogenides	Fluorite CaF_2, halite NaCl, calomel HgCl
Silica	Agate SiO_2, opal SiO_2, quartz SiO_2
Phyllosilicates	Pyrophyllite $AlSi_2O_5OH$, talc $Mg_3Si_4O_{10}(OH)_2$, serpentine $(Mg,Fe)_3Si_2O_5(OH)_4$
Feldspar	Albite $NaAlSi_3O_8$, microcline $KAlSi_3O_8$
Pyroxenes	Diopside $CaMgSi_2O_6$, spodumene $LiAlSi_2O_6$
Amphiboles	Anthophyllite $(Mg, Fe)_7Si_8O_{22}(OH)_2$, tremolite $Ca_2Mg_5Si_8O_{22}(OH)_2$
Zeolites	Natrolite $Na_2Al_2Si_3O_{10} \times 2H_2O$, laumontite $CaAl_2Si_4O_{12} \times 4H_2O$, analcite $NaAlSi_2O_6 \times H_2O$
Feldspathoids	Sodalite $Na_4Al_3(SiO_4)_3Cl$
Other silicates	Zircon $ZrSiO_4$, datolite $CaBSiO_4(OH)$, danburite $CaB_2Si_2O_8$, eucryptite $LiAlSiO_4$, willemite Zn_2SiO_4, wollastonite $CaSiO_3$, sphene $CaTiSiO_5$, scapolite $Na_4(Al, Si)1_2O_{24}Cl$, axinite $Ca_2(Mn, Fe, Mg)Al_2(BO_3OH)(SiO_3)_4$, benitoite $BaTiSi_3O_9$, thorite $(Th, U)SiO_4$
Carbonates	Aragonite $CaCO_3$, calcite $CaCO_3$, cerussite $PbCO_3$, magnesite $MgCO_3$, strontianite $SrCO_3$, witherite $BaCO_3$
Sulfides	Sphalerite (Zn, Fe)S, wurtzite (Zn, Fe)S
Sulfates	Barite $BaSO_4$, celestine $SrSO_4$, gypsum $CaSO_4 \times 2H_2O$, anhydrite $CaSO_4$, alunite $KAl_3(SO_4)_2(OH)_6$, zippeite $K_4(UO_2)_6(SO_4)_3OH_{10} \times 4H_2O$, ettringite $Ca_6Al_2(SO_4)_3(OH)_{12} \times 26H_2O$, hanksite $Na_{22}K(SO_4)_9(CO_3)_2Cl$
Phosphates	Apatite $Ca_5(PO_4)_3(OH,F,Cl)$, wavellite $Al_3(PO_4)_2(OH)_3 \times 5(H_2O)$, amblygonite (Li, Na)$AlPO_4$(F, OH), pyromorphite $Pb_5(PO_4)_3Cl$, monazite (Ce, La, Th, Nd, Y)PO_4, autunite $Ca(UO_2)_2(PO_4)_2 \times 10H_2O$, xenotime$YPO_4$
Tungstates	Scheelite $CaWO_4$
Molybdates	Powellite $CaMoO_4$, wulfenite $PbMoO_4$
Borates	Colemanite $CaB_3O_4(OH)_3–H_2O$
Organics	Amber $C_{10}H_{16}O$

an emission spectrum, namely the distribution of energy emitted by an excited system in terms of the intensity of emitted optical photons as a function of wavelength or photon energy. Such spectroscopy in many cases is inadequate because the discriminatory power of the normal emission spectra is some-

Table 1.2. Principal luminescent materials and their natural analogies (from Reisfeld and Jörgensen 1977; Moncorge et al. 1994; Boulon 1997)

Material	Synthetic	Natural analogies
Phosphors	(Ce^{3+}, Tb^{3+}): $LaPO_4$	Monazite
	Pr^{3+}: $CaWO_4$	Scheelite
	(Ag^{+}, Al^{3+}): ZnS	Sphalerite
	(Cu^{+}, Al^{3+}): ZnS; Mn^{2+}: ZnS	Sphalerite
	Ce^{3+}:$Y_5(SiO_4)_3F$	Britholite
	Tb^{3+}: $LaSiO_2F$	Wollastonite
	(Ce^{3+}, Tb^{3+}):$Gd_4(Si_2O_7)F_2$	Cuspidine
	Tb^{3+}: $CaYSi_3O_3F_4$	Melilite
Scintillators	Ce^{3+}: $CaWO_4$	Scheelite
	Ce^{3+}: $PbWO_4$	Stolzite
	Ce^{3+}: $YbPO_4$	Xenotime
Dosimeters	U^{6+}: CaF_2 ; REE^{3+}: CaF_2	Fluorite
	(Dy^{3+}, Tb^{3+}): $CaSO_4$	Anhydrite
	(Cr^{3+}, Ti^{3+}): Al_2O_3	Corundum
Laser materials	REE^{3+}: $CaWO_4$	Scheelite
	REE^{3+}: $CaMoO_4$	Molybdenite
	(Er^{3+}, Nd^{3+}): $Y_3Al_5O_{12}$	Garnet
	(Cr^{3+}, Cr^{4+}): $Y_3Al_5O_{12}$	Garnet
	(Yb^{3+}, Nd^{3+}): $Y_3Al_5O_{12}$	Garnet
	(Cr^{3+}, Ti^{3+}): $BeAl_2O_4$	Alexandrite
	REE^{3+}: $ZrSiO_4$	Zircon
	Cr^{4+}: Mg_2SiO_4	Forsterite (olivine)
	Cr^{4+}: $CaMgSiO_4$	Monticellite (olivine)
	Mn^{5+}: $Sr_5(PO_4)_3$(Cl, F)	F, Cl Apatite
	Yb^{3+}: $Sr_5(PO_4)_3$(Cl, F)	Apatite
	Mn^{2+}: $(Ca, Sr, Ba)_2(PO_4, VO_4)Cl$	Spodiosite (apatite)
	Cr^{3+}: $(Ca, Sr)(Y, Gd)_4Si_3O_{13}$	Apatite
	(Nd^{3+}, Ho^{3+}): $Ca_5(PO_4)_3F$	Fluorapatite

what limited. Therefore, most of the previously provided emission spectra of minerals present overlapping features of several types of luminescence centers.

However, *luminescence lifetime*, which is a measure of the transition probability from the emitting level, may be effectively used. It is a characteristic and unique property and it is highly improbable that two different luminescence emissions will have exactly the same decay time. The best way to determine a combination of the spectral and temporal nature of the emission is by using *laser-induced time-resolved spectra.* The time-resolved technique requires relatively complex and expensive instrumentation, but its scientific

Table 1.3. Luminescence centers found in steady-state spectra of minerals

Luminescence center	Transition	Decay time
Rare earth ions (line emission): Nd^{3+}, Sm^{3+}, Sm^{2+}, Eu^{3+}, Gd^{3+}, Tb^{3+}, Dy^{3+}, Yb^{3+}	$4f$–$4f$	The parity does not change and the life time of the excited state is long ($\sim$ 10 µs–1 ms)
Rare earth ions (band emission): Ce^{3+}	$5d$–$4f$	Transition is parity allowed and spin selection is not appropriate $\Rightarrow$ fully allowed (10–100 ns)
Eu^{2+}		Emitting level contains octets and sextets, whereas the ground state level ^8S is an octet, so that the spin selection rule slows down the optical transition rate ($\sim$ 1 µs)
Yb^{2+}, Sm^{2+}		The spin selection rule is more important and decay times are of (100 µs–1 ms)
Transition metal ions:	d–d	Decay time is long
Cr^{3+}	^2E–$^4A_2$ line	The parity selection rule as well as the spin selection rule apply ($\sim$ 1 ms)
	$^4T_2$–$^4A_2$ band	The parity selection rule ($\sim$ 10–100 µs)
Mn^{2+}, Fe^{3+}	$^4T_1$–$^6A_1$ $^4T_2$–$^6A_1$	The parity selection rule as well as the spin selection rule ($\sim$ 1 ms)
d^0 Complex ions: $(VO_4)^{3-}$, $(WO_4)^{2-}$, $(MoO_4)^{2-}$, $(TiO_4)^{4-}$	Charge-transfer	Emitting state is a spin triplet and decay time is long (10–100 µs)
$(UO_2)^{2+}$	Charge-transfer	Considerably long decay time ($\sim$ 0.1–1 ms)

value overweighs such deficiencies. It is important to note that there is simple relationship between steady-state and time-resolved measurements. The steady-statespectrum is an integral of the time-resolved phenomena over intensity decay of the sample, namely:

$$I_{(\text{steady-state})} = \int I_0 \, \mathrm{e}^{-t/\tau} \, \mathrm{d}t = I_0 \, \tau \, , \tag{1.1}$$

where τ is the longest lifetime of the luminescence centers present in a mineral. It turns out that much of the information available from luminescence spectra is lost during the time-averaging process. Time-resolved luminescence can separate overlapping features, which have different origins and therefore different luminescence lifetimes. The method involves recording the intensity in a specific time "window" at a given delay after the excitation pulse with carefully chosen delay time and gate width. The added value of the method is the energetic selectivity of a laser beam, which enables us to combine time-resolved spectroscopy with individual monochromatic excitation.

Time-resolved luminescence spectroscopy may be extremely effective in minerals, many of which contain a large amount of emission centers simultaneously. With the steady state technique only the mostly intensive centers are detected, while the weaker ones remain unnoticed. Fluorescence in minerals is observed over time range of nanoseconds to milliseconds (Table 1.3) and this property was used in our research. Thus our main improvement is laser-induced time-resolved spectroscopy in the wide spectral range from 270 to 1,500 nm, which enables us to reveal new luminescence centers in minerals previously hidden by more intensive centers.

CHAPTER 2

Theoretical Background

The theoretical data essential for understanding luminescence phenomenon may be found in many books, but we believe that for the specific field of mineral luminescence the fundamental books of Marfunin (1979a, 1979b) are the best. Below we tried to present very shortly only the most essential data, especially data connected with kinetic considerations, which are the basis of the time-resolved technique.

2.1 The *s*, *p*, *d*, *f* Atomic Orbitals

According to quantum mechanics laws, electrons in free atoms occupy so-called atomic orbitals. Each orbital is characterized by its energy and is determined by quantum numbers n, l, and m_l; where n is the main quantum number, designated by numbers $1, 2, 3\ldots$, l is the orbital quantum number with $0, 1, 2, \ldots (n-1)$ values and m_l is the magnetic quantum number with $-l, -l+1, \ldots 0, \ldots l-1, l$ values.

For an explanation of luminescence properties of the atomic orbitals, their symmetry and directional properties are most important. The shape of atomic orbitals in space is determined by the l quantum number, designated as s, p, d, f for $l = 0$, 1, 2, 3. The number of possible orientations of the orbitals is given by the number of possible values of the m_l magnetic quantum number and is equal for the s-orbitals to 1, for the p-orbitals to 3, for the d-orbitals to 5 and for the f-orbitals to 7, according to the $(2l + 1)$ rule. In a totally symmetric surrounding all orientations of the orbitals are equivalent and correspond to the same energy value. These orbitals are called degenerate, which means they are characterized by equal energy. Figure 2.1 represents real forms of the p, d and f orbitals.

Each element is characterized by a specific scheme of energy levels. When individual elements are combined forming minerals the energy levels are changed. They now have different energies and form a different system of energy levels typical for the mineral. The process of developing new energy level systems in minerals may be described using different theories of solid state physics, such as ligand field theory, molecular orbitals theory and zone theory, which are especially useful for explanation of absorption and luminescence properties.

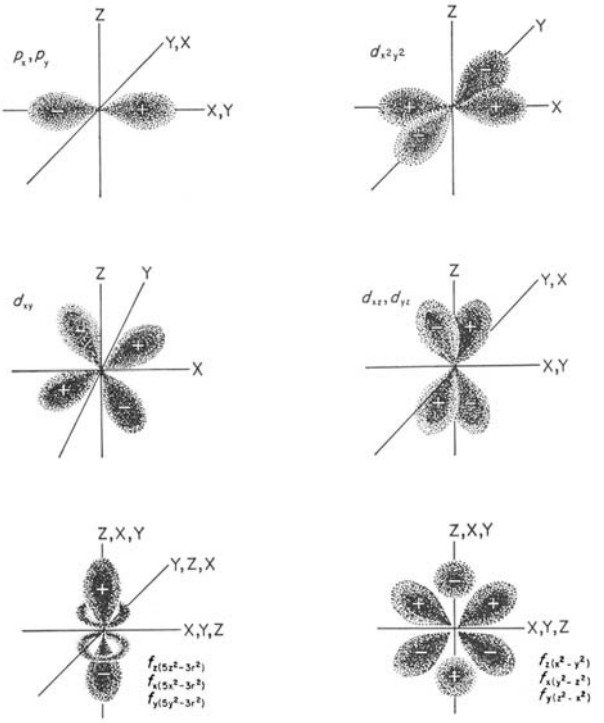

Fig. 2.1. The forms of the angular dependence functions for p, d, and f orbitals (Figgis 1966)

2.2 Point Group Symmetry

As we will demonstrate, luminescent properties, radiative transition characteristics as well as emission under site selective excitation depend on the local environment symmetry of the luminescent center. Therefore it is necessary to take into account and to describe the different local symmetry. There are two systems commonly used in describing symmetry elements of punctual groups:

1. The **Schönflies notation** (1891) used extensively by spectroscopists, and
2. The **Hermann-Mauguin** (1935) or international notation preferred by crystallographers.

Schönflies notation is widely used to describe molecules or assemblages of atoms (polyhedron) such as the local environment of an atom. Thus, it is widely used to describe the symmetry of structural sites. It is a more compact notation but less complete than the Hermann-Mauguin notation. It consists generally of one capital letter, followed by one subscript number and one final letter.

– Symmetry C_n for one rotational axis (cyclic); C_1: identity; C_n: the polyhedron has an n-fold axis of symmetry.

- Symmetry D_n for orthogonal axes (dihedral), n-fold axis of symmetry perpendicular to n 2-fold axes;
- Cubic symmetry: T for 4 axes (tetrahedral), O for 8 axes (octahedral) and I for 20 axes (icosahedra, exists to describe molecules but not crystals);
- Planar symmetry:
  - one subscript letter follows the rotation symmetry (for example C_{3h}); h indicates a planar symmetry (mirror) parallel to the rotation axis (horizontal), v a mirror perpendicular to the rotation axis (vertical) and d a diagonal mirror;
  - S_n, S indicates a mirror symmetry (Spiegel in German) and n invariance by a n-fold rotation around the perpendicular axis to the plane. An added superscript m number indicates sometimes that the symmetry operation is applied m times.

Table 2.1 presents the non-cubic crystallographic point groups with compared notation.

2.3 Absorption of the Excitation Energy

2.3.1 Optical Absorption Spectroscopy

It is a remarkable fact that the contemporary history of absorption and emission spectroscopy began simultaneously, from the simultaneous discoveries that Bunsen and Kirchhoff made in the middle of the 19th century. They observed atomic emission and absorption lines whose wavelengths exactly coincided. Stokes and Kirchhoff applied this discovery to the explanation of the Fraunhofer spectra. Nearly at the same time approximately 150 years ago, Stokes explained the conversion of absorbed ultraviolet light into emitted blue light and introduced the term fluorescence. Apparently, the discovery of the Stokes shift marked the birth of luminescence as a science.

A rule due to Beer and Lambert is that the light absorbed per unit length in a sample depends at any wavelength only on the incident light intensity, i.e.,

$$\frac{\mathrm{d}I(\lambda)}{\mathrm{d}x} = -\alpha I(\lambda)\,, \tag{2.1}$$

where α is a proportionality constant called the absorption coefficient, which also depends on wavelength.

Integrating Eq. 2.1, we find for a non-reflecting sample of thickness t:

$$I_\mathrm{T}(\lambda) = I_\mathrm{o}(\lambda)\exp(-\alpha t)\,, \tag{2.2}$$

where I_T is the transmitted light intensity and I_o the incident light intensity. In these terms, the transmittance spectrum is

$$T(\lambda) = I_\mathrm{T}(\lambda)/I_\mathrm{o}(\lambda) \tag{2.3}$$

Table 2.1. The non-cubic crystallographic point groups. Column pairs give the Schönflies and equivalent Hermann-Mauguin international notation. C indicates cyclic, D indicates dihedral, S represents Spiegel (or "mirror"), with h, v and d meaning respectively horizontal, vertical and diagonal (referring to mirror plane locations.) A minus before a number indicates a horizontal bar above that number. Brackets indicate equivalent alternative. The centrosymmetric point groups are shown in bold. The enantiomorphic point groups are shown in italic. The polar point groups are underlined

	Hexagonal		Tetragonal		Trigonal		Orthorhombic		Monoclinic		Triclinic	
Cyclic	C_6	6	C_4	4	C_3	3			C_2	2	C_1	1
Cyclic+vertical planes	$\underline{C}_{6v}$	6 mm	$\underline{C}_{4v}$	4 mm	$\underline{C}_{3v}$	3m	$\underline{C}_{2v}$	2 mm				
Cyclic+horizontal planes	$\mathbf{C_{6h}}$	6/m	$\mathbf{C_{4h}}$	4/m					$\mathbf{C_{2h}}$	2/m		
	C_{3h}	−6							$\underline{C}_{1h}$ ($\underline{C}_s$)	m (−2)		
Improper rotation			S_4	−4	$\mathbf{S_6}$ ($\mathbf{C_{3i}}$)	−3					$\mathbf{S_2}$ ($\mathbf{C_i}$)	−1
Dihedral	D_6	622	D_4	422	D_3	32	D_2 (V)	222				
Dihedral+horizontal planes	$\mathbf{D_{6h}}$	6/mmm	$\mathbf{D_{4h}}$	4/mmm			$\mathbf{D_{2h}}$ ($\mathbf{V_h}$)	2/mmm (mmm)				
	D_{3h}	−62 m										
Dihedral+planes between axes			D_{2d} (V_d)	−42m	$\mathbf{D_{3d}}$	−32/m (−3m)						

For cubic symmetry, T corresponds to 23, T_h to m3, O to 432, T_d to 4−3 m, O_h to m3m and I to 532 (thus impossible for crystals, but possible for molecules)

so that

$$T(\lambda) = \exp(-\alpha t) \,. \tag{2.4}$$

The absorption spectrum is given by an inversion of Eq. 2.4 i.e.,

$$\alpha(\lambda) = \frac{1}{t} \ln\left(\frac{I_o}{I_T}\right) = \frac{1}{t} \ln\left(T^{-1}\right) \,. \tag{2.5}$$

The absorbance is defined as:

$$\log_{10}\left(\frac{I_c}{I_T}\right) \,. \tag{2.6}$$

In optical spectroscopy a sample is illuminated by monochromatic light with a varying wavelength. The optically active centers rise from the ground to the excited states with the resulting appearance of the absorption band in the optical spectrum. Useful information may be obtained from the absorption spectroscopy, which reveals the excited energy levels. Nevertheless, it has to be noted that the absorption technique is much less sensitive compared to luminescence. The reason is that absorption is a subtractive process. One measures small differences in large numbers (intensity of incident light-intensity of transmitted light). This difference will be very small for very low absorbance from low concentrations. Best sensitivity is $\sim$ 0.0005 OD (optical density), but most spectrophotometers are not nearly this good. On the other hand luminescence measures any detectable light against an essentially zero background. Modern detectors are capable of measuring single photons and thus luminescence can be extremely sensitive.

There are a number of different processes, which may generate optical absorption in the visible and ultraviolet wavelength range. The following transitions are of primary importance for minerals: (Platonov 1979; Rossman 1988):

- *d*–*d* or *f*–*f* electronic transitions between ligand field split spectroscopic states of the free electronic levels of transition metals or rare earth ions. This process involves an ion with a partially filled *d*- or *f*-electron shell being incorporated into a crystalline environment whose symmetry produces a difference in energy between the different orbitals (see Crystal Ligand Theory). Such effects are observed within compounds containing transition metal ions such as Fe^{2+}, Fe^{3+}, Mn^{2+}, Ti^{3+}, Cr^{3+} and associated colors characterize a range of minerals. The intensities of *d*–*d* and *f*–*f* absorption bands can vary over four orders of magnitude: these are governed both by the abundance of the absorbing cation, and by a combination of the symmetry of the cation environment and quantum mechanics selection rules (see Luminescence decay).
- metal to metal charge-transfer between transition metal ions differing in valence state and accommodated in interconnected polyhedra of the mineral structure. This term is used to describe the absorption mechanism by transfer of electrons between transition metal ions in non-metals via an

input of energy in the form of a photon, especially those ions, which are able to adopt multiple valence states in minerals, such as Fe^{2+} and Fe^{3+}, Ti^{3+}, Ti^{4+} and so on. Characteristically, these bands occur in the visible part of the spectrum, and are most intensive in those minerals, which have large quantities of transition metals, and relatively short metal-metal distances.
- ligand to metal charge transfer or an interband transition, which involve the transfer of electron density from the ligand to the metal cation. Charge transfer transitions not only occur between transition metal ions, but also occur in the excitation of electrons between cations and ions. Within oxides, such oxygen-to-metal charge transfer absorption bands typically occur at high energies in the ultraviolet, and are extremely intense: often three to four orders of magnitude more intense than d–d transitions. Effectively, such a charge transfer between anions and cations is often associated with delocalization of an electron, or photoexcitation of an electron into the conduction band of a mineral. Within many minerals, such charge transfer bands appear as an absorption edge, rather than a discrete band: this edge is simply generated because all photons with energy above that of the edge will produce electron delocalization. Absorption generated by such cation–anion charge delocalization processes is common in ore minerals such as sulfides and arsenides.
- radiation induced centers from natural sources in rocks. Such electron-hole centers produced by ionizing radiation are mostly typical for smoky quartz, blue feldspar, green diamonds, and fluorite and calcite samples.

2.3.2 Luminescence Excitation Spectroscopy

A luminescent mineral will only emit radiation when the excitation energy is absorbed. It is possible to categorize luminescence mechanisms into two general classes. In the first the process of excitation is localized near an isolated center and occurs without ionization of any species in the mineral. This type of luminescence is called intra-centric. Excitation and emission occurs due to electronic transitions at the center. In certain luminescent minerals the situation is more complicated, because the activator does not absorb the exciting radiation, but it is absorbed by the other center, which subsequently transfers it to the activator. In this case the absorbing ion is called a sensitizer. The second mechanism occurs when the excitation is light of higher energy than the band gap, or consists of very high-energy radiation or particles. Ionization effects then occur, and the emission is produced by a recombination of electrons or holes at ionized centers. Laser-induced luminescence mainly belongs to the first type direct excitation of centers of emission without their ionization. But during excitation with high-energy photons in semiconductors with a small interband spacing, an electron transfer of impurity ions of the ground substance to the conduction band takes place. In these crystals the energy levels of defects are divided according to their position in the forbidden band into donors (near the conduction band) and acceptors (in the vicinity of the valence band).

Absorption of the excitation energy resulting in luminescence is revealed by excitation spectra. Here the emission results from the transition from the specific electronic level. The excitation spectrum is registered as the intensity of luminescence as a function of the excitation wavelength. The excitation spectrum is measured using two monochromators. One is used to separate the exciting frequency and the other is used for separating a specific region in the luminescence spectrum. The second monochromator is set to a specific frequency, whereas the first one scans the excitation frequency. The appearance of tunable lasers has made it possible to avoid using the first monochromator.

The excitation spectrum demonstrates that for an effective luminescence not only the presence of an emitting level is important, but also the presence of the upper levels with a sufficiently intensive absorption. The excitation spectra enable us to choose the most effective wavelength for luminescence observation. The combination of excitation and optical spectroscopies enable us to determine the full pattern of the center's excited levels, which may be crucial for luminescence center interpretation, energy migration investigation and so on. The main excitation bands and lines of luminescence in minerals are presented in Table 2.2.

2.3.2.1 Selective Spectroscopy

There are a large number of cases where the spectra of luminescence centers remain broad up to helium temperatures. In certain cases, this is explained by a strong electron-phonon interaction, but more often the inhomogeneous broadening, connected with several types of the same center presence, causes this. In such cases it is possible to simplify the spectrum by selective excitation of specific centers.

2.3.2.2 Two-Photon Absorption Spectroscopy

In most luminescence experiments, at least in the mineral luminescence field, excitation is due to absorption of a single photon. However, it is also possible for a luminescence center to absorb two or more long-wavelength photons to reach the excited state. Two-photon excitation occurs by the simultaneous absorption of two lower-energy photons. Such excitation requires special conditions including high local intensities, which can only be obtained from laser sources.

Thus it was not observed until lasers were invented. In principal, one-photon and two-photon excitation follow different selection rules. For example, the inner shell one-photon transitions in transition metal, rare earth, and actinide ions are formally forbidden by the parity selection rule. These ions have d- or f-shells and transitions within them are either even to even ($d \rightarrow d$) or odd to odd ($f \rightarrow f$). The electric dipole transition operator is equal to zero.

Table 2.2. Main luminescence excitation bands and lines in minerals

Center	Electronic transition	$\lambda_{excitation}$ (nm)	$\lambda_{luminescence}$ (nm)
Pr^{3+}	$^3H_4$–$^1S_0$	280	480, 610, 650, IR
	$^3H_4$–$^1I_1$	460	
	$^3H_4$–$^1I_0$	490	
Nd^{3+}	$^4I_{9/2}$–$^4G_{7/2-5/2}$	580	880, 1,060, 1,340
	$^4I_{9/2}$–$^2D_{7/2}$	320	380, 417
	$^4I_{9/2}$–$^2P_{1/2}$	380	535, 600, 670
Sm^{3+}	Charge transfer	230	540, 600, 675
	$^6H_{5/2}$–$^6P_{5/2}$	407	
Sm^{2+}	$4f$–$5d$	450, 580	650, 690, 700, 730, 780, 810
Eu^{3+}	Charge transfer	220	590, 610, 650, 700
	$^7F_0$–$^5H_3$	325	
	$^7F_0$–$^5D_2$	532	
Eu^{2+}	$4f^7$–$4f^6 5d$	250, 310	380–450
Tb^{3+}	$^7F_6$–$^5D_3$	280	380, 417, 440, 550
Dy^{3+}	$^6H_{15/2}$–$^6P_{5/2}$	351	480, 575, 670, 760
Er^{3+}	$^4I_{15/2}$–$^4G_{11/2}$	370	550
Ho^{3+}	$^5I_7$–$^5G_2$	360	550, 640, 760
Tm^{3+}	$^3H_6$–$^3P_0$	360	360, 480, 780, 800
Ce^{3+}	$4f$–$5d$	280, 320–340	350–390
Yb^{2+}	$4f^{14}$–$4f^{13}5d^1$	250, 280, 320,	520–560
Yb^{3+}	$^2F_{7/2}$–$^2F_{5/2}$	920–960	975, 1,014
Gd^{3+}	$^8S_{7/2}$–$^6I_{7/2}$	270	300, 312
Mn^{2+}	$^6A_1(S)$–^4E,$A_1(G)$	380–400	480–700
	$^6A_1(S)$–$^4T_1(G)$	560–575	
Mn^{4+}	$^4A_2$–$^4T_1$	420	650–700
	$^4A_2$–$^4T_2$	530	
Mn^{5+}	$^3A_2$–$^3T_2$	400	1,100–1,500
	$^3A_2$–^1E	590	

Table 2.2. (continued)

Center	Electronic transition	$\lambda_{\text{excitation}}$ (nm)	$\lambda_{\text{luminescence}}$ (nm)
Fe^{3+}	Charge transfer	300	700–750
	$^6A_1(S)$–^4E(D)	380	
	$^6A_1(S)$–$^4T_2$(G)	500	
Cr^{3+}	$^4A_2$–$^4T_1$	410	690–1,000
	$^4A_2$–$^4T_2$	550	
V^{2+}	$^4A_2$–$^4T_1$	410	750–850
	$^4A_2$–$^4T_2$	560	
Pb^{2+}	$^1S_0$–$^3P_1$	220–260	300–400
Bi^{3+}	$^1S_0$–$^3P_1$	280	400–650
Bi^{2+}	$^2P_{1/2}$–$^2S_{1/2}$	270	600–650
Ti^{3+}	$^2T_{2g}$–^2E_g	500	650–950
$(UO_2)^{2+}$	A_{1g}–E_{2u}	400	480–580
S_2^-	$3\sigma_g$–$1\pi_g*$	400	500–700
O_2^-	$3\sigma_g$–$1\pi_g*$	280	400–550
$(MeO_m)^{n-}$	$^1A_1$–$^1T_1$	250–340	480–520

The two-photon transition operator is a tensor whose components may be nonzero. Thus an important reason for doing two-photon spectroscopy is that it allows us to observe the transitions directly as allowed transitions instead of indirectly as forbidden transitions as are all one-photon spectra of transition metal ions.

In single beam two-photon spectroscopy, an intense laser beam having a frequency $h\nu = 1/2(E_2 - E_1)$ is passed through the crystal, and the attenuation of the beam is measured. To measure attenuation directly is extremely difficult and it is better to measure the proportional quantity, while the fluorescence maybe the most useful. Two-photon spectroscopy has not been used so far in the luminescence of minerals field, but many relevant centers have been studied in artificial compounds, such as Cr^{3+}, Mn^{4+}, Cu^+, Ni^{2+}, Eu^{2+} (McClure 1990).

Two-photon excitation results in an apparent violation of Beer's law. In the one-photon technique the amount of light absorbed is proportional to the intensity of the incident light. This results in emission intensity being directly proportional to the intensity of the excitation. The well-known property of two-photon excitation is that emission intensity depends on the square of the incident light intensity.

2.4 Radiative Return to the Ground State – Luminescence

The energy of an electronically excited state may be lost in a variety of ways. A radiative decay is a process in which a molecule discards its excitation energy as a photon. A more common fate is non-radiative decay, in which the excess energy is transferred into the vibration, rotation, and translation of the surrounding molecules. This thermal degradation converts the excitation energy into thermal motion of the environment (i.e., to heat). Two radiative processes are possible: spontaneous emission, just like radioactivity, which is a completely random process where the excited state decays:

$$M^* \rightarrow M + h\,\bar{\nu}\,c\,. \tag{2.7}$$

Rate of spontaneous emission in populating the state

$$f = -N_\mathrm{f} A_\mathrm{fi}\,, \tag{2.8}$$

where A_fi is the Einstein coefficient for spontaneous emission (unit s^{-1}). It obeys 1st order kinetics:

$$\begin{aligned} &\text{Rate} = -\mathrm{d}\left[M^*\right] / \mathrm{d}t \\ &N_\mathrm{f}\left[t\right] = N_\mathrm{f}\left[t = 0\right] \exp(-k\,t)\,, \end{aligned} \tag{2.9}$$

where k = rate constant for spontaneous emission = $A_\mathrm{fi} = 1/\tau$ (τ = natural lifetime of state f, in seconds). Stimulated (or induced) emission can occur in the presence of light of the correct transition energy, incident upon the sample, acting as a stimulant for it to emit a photon of the same energy:

$$M^* + h\,\bar{\nu}\,c \rightarrow M + 2\,\bar{\nu}\,c\,. \tag{2.10}$$

Rate of induced emission in populating the state is:

$$f = -N_\mathrm{f} B_\mathrm{fi}\,\varrho(\bar{\nu})\,, \tag{2.11}$$

where B_fi is the Einstein coefficient of induced emission.

2.4.1 Ligand Field Theory

2.4.1.1 The Concept of the Ligand Field

Most of the electronic spectroscopy in minerals can be interpreted by the well-known ligand field theory. The main luminescence centers in minerals are transition and rare-earth elements. The ground and excited levels in these cases are d and f orbitals, while d–d and d–f emission transitions are subjected to strong influence from nearest neighbors, so called ligands. The basic notion of

a ligand field was first developed many years ago (Bethe 1929). It was supposed that the ions are undeformable spheres and the interactions, which take place between them, are due solely to the electrostatic potentials set by their charges. The charges are taken to be located at the center of the ions coincident with their nuclei. Summing potentials from the individual surrounding ions to give the total potential at any point near the central ion, and then finding the effect of such a potential on the electrons of the central ion solves the problem. The fact that the original considerations were made on the potential developed near an ion, which was part of a lattice, and that such a lattice could occur only in a crystal, led to the term *crystal field* theory. However, later it was found that few of the results of crystal field theory depend on the existence of a lattice, and it is possible to carry most of them over to the model, which is the basis of coordination chemistry – that of the coordination cluster. By *coordination cluster* is meant a central metal ion associated with a number of attached ligands, the whole forming a distinguishable entity and possibly bearing a net electric charge. In the more general model of a coordination compound, the electrons of the central ion are subject to a potential, not necessarily of simple electronic origin, from the ligand atoms. The term *ligand field* theory has been employed to cover all aspects of the manner in which an ion or atom is influenced by its nearest neighbors. Ligand field theory, then, contains crystal field theory as a special case. A great many of the results of ligand field theory depend only on the approximate symmetry of the ligands distribution around the central metal ion rather than on the particular ligands or the details of their locations. Consequently, the results may be obtained in the first place from crystal field theory and then generalized to other models of the bonding. Once the mathematical formalism of the crystal field approach has been developed, calculations within this model are quite straightforward (Figgis 1966).

The splitting of d orbital energies and its consequences are at the heart of crystal field theory. It is possible to examine qualitatively the effect of various distributions of ligand atoms around the central ion upon its d orbitals. The d orbitals in an isolated gaseous metal are degenerate. If a spherically symmetric field of negative charges is placed around the metal, these orbitals remain degenerate, but all of them are raised in energy as a result of the repulsion between the negative charges on the ligands and in the d orbitals. On going from a spherical to an octahedral symmetry, all orbitals are raised in energy, relative to the free ion. However, not all d orbitals will interact to the same extent with the six point charges located on the $+x$, $-x$, $+y$, $-y$, $+z$ and $-z$ axes respectively. The orbitals which lie along these axes (i.e. $x^2 - y^2$, z^2) will be destabilized more than the orbitals which lie in-between the axes (i.e. xy, xz, yz). Δ_o or alternatively $10D_q$ denotes the extent to which these two sets of orbitals are split. The tetrahedral symmetry can be derived from a cubic symmetry where only four of the eight corners are occupied by point charges. In such a situation, it is the xy, yz, xz orbitals that are destabilized as they point towards the incoming point charges, while $x^2 - y^2$ and z^2 are stabilized. The crystal field splitting in a tetrahedral symmetry is intrinsically

smaller than in the octahedral symmetry as there are only four ligands (instead of six ligands in the octahedral symmetry) interacting with the transition metal ion (Fig. 2.2).

The point charge model predicts that

$$\Delta_t = 4/9\Delta_o \tag{2.12}$$

After determination of the qualitative schemes for the term splitting in the crystal fields, it is possible to go to a quantitative estimation of separation between the crystal field levels. All the electronic interaction stages can be represented quantitatively by means of the few parameters:

$$H = H_0 + H_{ee}(B, C) + H_{CF}(D_q) + H_{LS}(\xi) \tag{2.13}$$

where B, C are inter-electronic repulsion (H_{ee}) parameters governing the term separation due to Coulomb repulsion of electrons; D_q is the cubic crystalline field parameter determining the term splitting by a cubic crystalline field (H_{CF}); ξ is the spin–orbit coupling parameter, taking into account further splitting of ion levels in crystals due to an interaction between orbital and spin moments of an ion (H_{LS}).

Interelectron interactions depend on the size, namely the greater the ion size, the more distant the electrons from each other, the less repulsion between them. Hence B and C decrease with a decreasing of oxidation state, from the first transition series to the second and third series and from the first to the last ions within each of the series. For an ion in a crystal the overlapping of transition metal and ligand orbitals leads to a decrease of B and C, namely

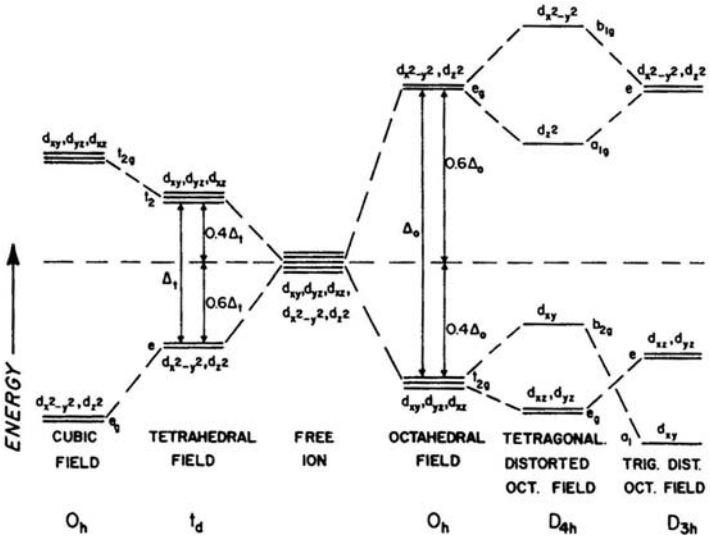

Fig. 2.2. Splitting of the five d-orbitals in various types of ligand fields (Bakhtin and Gorobets 1992)

the more covalent the bonding, the less B and C. For a given transition metal ion the bond covalency depends on the ligand ions, which are arranged in the order of B decreasing in so-called nephelauxetic series:

$$F^- > O^{2-} > Cl^- > Br- > S^{2-} > I^- > Se^{2-} .$$

The crystal field strength D_q is determined by the effective change of the ligands Q, by the average radius r of the d-orbital and by the ligand-metal distance R:

$$\Delta \approx \frac{\langle r^4 \rangle}{R^5} . \tag{2.14}$$

This includes the dependence for D_q on the kind of transition metal ion, on the ligand arrangements in the spectrochemical series in the order of increasing D_q ($I^- < Br^- < Cl^- < F^- < O^{2-} < H_2O$), on the metal-ligand distances and on the coordination ($D_{\mathrm{qoct}} : D_{\mathrm{qcub}} : D_{\mathrm{qtetr}} = 1 : 8/9 : 4/9$).

It appears that the d^1 and d^6, the d^2 and d^7, the d^3 and d^8, and the d^4 and d^9 configurations have great similarity in the splitting of their levels with the crystal field.

After determination of the relative energies of the d orbitals in a transition-metal complex, the distribution of the electrons has to be considered. Degenerate orbitals are filled according to Hunds rules: one electron is added to each of the degenerate orbitals in a subshell before a second electron is added to any orbital in the subshell; electrons are added to a subshell with the same value of the spin quantum number until each orbital in the subshell has at least one electron. But such a filling scheme is valid only for the high spin (or low field) configurations. If there is a large enough energy difference between the five d orbitals, as in the case if the ligand field is very large, Hind's rule of maximum multiplicity no longer applies. As a result, the lower orbitals, for example the three t_{2g} orbitals in an octahedral system, will fill completely before any electrons enter the upper two e_g orbitals. This is a low spin (or high field) configuration. Significant changes could occur in the octahedral $3d^4$ to $3d^7$ cases, and in the tetrahedral $3d^3$ to $3d^6$ cases.

2.4.1.2 Tanabe-Sugano Diagrams

Tanabe and Sugano taking the mutual interactions between the d-electrons as well as the crystal field into account have calculated the energy levels originating from such a configuration (Fig. 2.3). On the utmost left-hand side where the crystal field $\Delta = 0$ we find the energy levels of the free ion. Many of these levels split into two or more levels for $\Delta = 0$. The lowest level, i.e. the ground state, coincides with the x-axis. For the free ion the levels are marked ^{2S+1}L, where S presents the total spin quantum number, and L the total orbital angular momentum. Values of L may be $0(S), 1(P), 2(D), 3(F), 4(D)$, etc. The degeneracy of these levels is $2L + 1$ and maybe lifted by the crystal field. Crystal-field levels

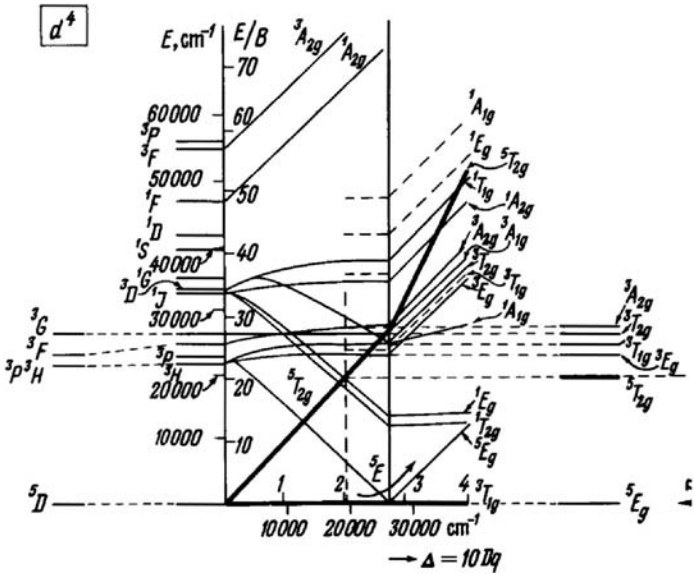

Fig. 2.3. Tanabe-Sugano diagrams for d^4 transition elements (Marfunin 1989a)

are marked ^{2S+1}X, where X may be A (no degeneracy), E (two fold degeneracy) and T (tree fold degeneracy). Subscripts indicate certain symmetry properties. The restrictions of these diagrams are connected to restrictions of the very model of the crystalline field, the fact that the diagrams are calculated only for one B and C value, without stating that the free ion values are taken, which differ considerably from corresponding values in crystals and the fact that splitting by a cubic crystalline field only is shown without spin–orbital splitting.

In order to use the Tanabe-Sugano diagram properly, the transition probabilities have to be taken into consideration. We have a ground state and we have many excited states, but not all transitions from ground to excited state and in the opposite direction are allowed. It is all a question of probability, while some have a high probability of occurrence, namely, allowed and intense transitions and some have a low probability, namely, forbidden and weak or very weak transitions.

The following selection rules are most important:

(i) There must be a change in parity (Laporte Rule) – transitions between states with the same parity are forbidden, thus all d–d transitions are forbidden
(ii) Transitions are allowed between states with the same spin and such transitions are seen only weakly in the 3d transition metal compounds, though more strongly in the 4d and 5d series.

The Laporte selection rule formally forbids all transitions within the d shell among all the energy levels. Nevertheless, the Laporte rule can be relaxed by

two mechanisms. First, if the central ion is at a center of symmetry, there may be coupling of electronic and vibrational wave functions of opposite signs, the vibronic coupling, which lifts the symmetry and produces weakly allowed transitions. Second, in the absence of a center of symmetry, there can be a partial mixing of the 3*d* and 4*p* orbitals, which again results in weak transitions.

2.4.2 Configurational Coordinate Diagram

The energy level diagram of transition metal ions forms a starting point for the analyses of their luminescence properties. The configurational coordinate model is often used to explain optical properties, particularly the effect of lattice vibrations, of a localized center. In this model, a luminescent ion and the ions at its nearest neighbor sites are selected for simplicity. In most cases, one can regard these ions as an isolated molecule by neglecting the effects of other distant ions. In this way, the huge number of actual vibrational modes of the lattice can by approximated by a small number or a combination of specific normal coordinates. These normal coordinates are called the configurational coordinates. The configurational coordinate model explains optical properties of a localized center on the basis of potential curves, each of which represents the total energy of the molecule in its ground or excited state as a function of the configurational coordinate (Fig. 2.4). Here, the total energy means the sum of the electron energy and ion energy. To understand how the configurational coordinate model is built, one is first reminded of the adiabatic potential of a diatomic molecule, in which the variable on the abscissa is simply the inter-atomic distance. In contrast, the adiabatic potential of a platonic molecule requires a multidimensional space, but it is approximated by a single configurational coordinate in the one-dimensional configurational coordinate model. In this model, the totally symmetric vibrational mode or the "breathing mode" is usually employed. Such a simple model can explain a number of facts qualitatively, such as:

- Stokes' law; i.e., the fact that the energy of absorption is higher than that of emission in most cases. The energy difference between the two is called the Stokes' shift;
- Widths of absorption or emission bands and their temperature dependence;
- Thermal quenching of luminescence.

It must be mentioned, however, that the one-dimensional model gives only a qualitative explanation of thermal quenching. A quantitatively valid explanation can by obtained only by a multidimensional model.

Following the path of the optical absorption transition, presume that Hooke's law expresses the bonding force between the luminescent ion and a nearest-neighbor ion. The deviation from the equilibrium position of the ions is taken as the configurational coordinate denoted as Q. The total energies of the ground

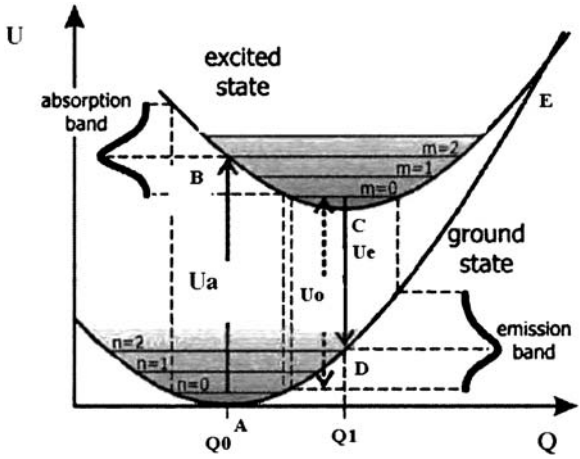

Fig. 2.4. General scheme for explanation of luminescence transition according to the Franck-Condon principle in a configurational coordinate diagram, showing the parameters energy (U) and configurational coordinate (Q). The excitation from the vibrational level $n = 0$ of the ground state to the excited state result in an absorption band with the energy U_a. The relaxation of the system, i.e. from vibrational level $m = 0$ of the excited state to the ground state, causes an emission band with the energy U_e. The energy difference between the lowest possible vibrational levels of the ground and excited state ($n = 0$ and $m = 0$) is U_0, with $U_a > U_0 > U_e$. (After Yacobi and Holt 1990; Nasdala et al. 2004)

state, U_g, and that of the excited state, U_e, are given by the following relations:

$$U_g = K_g \frac{Q^2}{2} \tag{2.15}$$

$$U_e \approx K_e \frac{(Q - Q_0)^2}{2} + U_0 \,, \tag{2.16}$$

where K_g and K_e are the force constants of the chemical bond, Q_o is the interatomic distance at the equilibrium of the ground state, and U_o is the total energy at $Q = Q_o$. The spatial distribution of an electron orbital is different between the ground and excited states, giving rise to a difference in the electron wavefunction overlap with neighboring ions. This difference further induces a change in the equilibrium position and the force constant of the ground and excited states, and is the origin of Stokes' shift. In the excited state, the orbital is more spread out, so that the energy of such an electron orbital depends less on the configuration coordinate; in other words, the potential curve has less curvature. As Fig. 2.4 shows, the nucleus of an emitting ion stays approximately at the same position throughout the optical processes. This is called the Franck-Condon principle. This approximation is quite reasonable since an atomic nucleus is heavier than an electron by 10^3 to 10^5 times. The optical

absorption proceeds from the equilibrium position of the ground state. The probability for an excited electron to lose energy by generating lattice vibration is 10^{12} to 10^{13} s^{-1}, while the probability for light emission is at most 10^{9} s^{-1}. Consequently, state B relaxes to the equilibrium position C before it emits luminescence. This is followed by the emission process C–D and the relaxation process D–A, completing the cycle. At finite temperature, the electron state oscillates around the equilibrium position along the configurational coordinate curve up to the thermal energy of kT. The amplitude of this oscillation causes the spectral width of the absorption transition. When two configurational coordinate curves intersect with each other, an electron in the excited state can cross the intersection E assisted by thermal energy and can reach the ground state nonradiatively. In other words, one can assume a nonradiative relaxation process with the activation energy ΔU, and with the transition probability per unit time N given by:

$$N = s \exp\left(\frac{-\Delta U}{kT}\right), \tag{2.17}$$

where s is a product of the transition probability between the ground and excited states and a frequency, with which the excited state reaches the intersection E. This quantity s can by treated as a constant, since it is only weakly dependent on temperature. It is called the frequency factor and is typically of the order of 10^{13} s^{-1}. The luminescence efficiency η can by expressed as:

$$\eta = \frac{W}{W+N} = \left[1 + \frac{s}{W} \exp \frac{-\Delta U}{kT}\right]^{-1}. \tag{2.18}$$

If the equilibrium position of the excited state C is located outside the configurational coordinate curve of the ground state, the excited state intersects the ground state in relaxing from B to C, leading to a nonradiative process. As described above, the shape of an optical absorption or emission spectrum is decided by the Franck-Condon factor and also by the electronic population in the vibrational levels at thermal equilibrium. For the special case where both ground and excited states have the same angular frequency, the absorption probability can by calculated with harmonic oscillator wavefunctions in a relatively simple form:

$$W_{nm} = \mathrm{e}^{-s}\left[\frac{m!}{n!}\right] S^{n-m}\left[L_m^{n-m}(S)\right]^2. \tag{2.19}$$

Here Laguerre's polynomial functions are used. The quantity S can by expressed as shown below, with K being the force constant of a harmonic oscillator and Q_0 the coordinate of the equilibrium position of the excited state.

$$S = \frac{1}{2}\frac{K}{\hbar\omega}\left(Q - Q_0\right)^2 \tag{2.20}$$

Physically, S is the number of emitted phonons accompanying the optical transition. It is commonly used as a measure of electron-phonon interaction and is called the Huang-Rhys factor. At $m = 0$, the transition probability is given by the simple relation:

$$W_{n_o} = S^n \frac{e^{-s}}{n!} \tag{2.21}$$

If $S < 1$ we are in the weak coupling mode, if $1 < S < 5$, in the intermediate coupling mode, if $S > 5$, in the strong coupling regime.

2.4.3 Molecular Orbital Theory

The further development of the ligand field concept takes place in Molecular Orbitals (MO) Theory. As an atomic orbital is a wave function describing the spatial probability density for a single electron bound to the nucleus of an atom, a molecular orbital is a wave function, which describes the spatial probability density for a single electron bond to the set of nuclei, which constitute the framework of a molecule.

The MO theory treats molecular bonds as a sharing of electrons between nuclei. Unlike the valence bond theory, which treats the electrons as localized balloons of electron density, the MO theory says that the electrons are delocalized. That means that they are spread out over the entire molecule. Now, when two atoms come together, their two atomic orbitals react to form two possible molecular orbitals.

It emerges that the two types restrict all possible types of pair combination for s, p and d orbitals: σ and π molecular orbitals, each of them can be bonding and antibonding. Every pair of atomic orbitals forming the molecular orbital gives not one but always two molecular orbitals: bonding and antibonding. This is reflected in the formation of the two energy levels: a lower level corresponding to bonding and a higher one corresponding to antibonding. In the ground state, the bonding orbitals are usually completely occupied, while the antibonding orbitals are empty or partially occupied by d electrons. The σ-bonding orbitals made from identical atomic orbitals have a center of symmetry and are referred to as even. The σ-antibonding orbitals without a center of symmetry are uneven. On the contrary, π-bonding orbitals are uneven, while π-antibonding orbitals are even. The parity in the MO theory determines some of the selection rules for optical transitions.

The molecule energy level diagrams show the energies of the molecular orbitals made from every possible combination of the atomic orbitals. To achieve this, one constructs the energy levels for each atom and then form from them the molecular orbitals under the following conditions: (1) the atomic orbitals should have a comparable energy, (2) they must overlap appreciably, (3) they must have the same symmetry type, (4) each pair of atomic orbitals forming a bonding molecular orbital must give at the same time an antibonding molecular orbital, (5) each of the atomic orbitals contributes in

a greater or lesser degree to all the molecular orbitals of the same symmetry type. The electronic state of a molecule is represented by a set of all possible molecular orbitals and term symbols are designated: for linear molecules: $^{2S+1}\Lambda$ with $\Lambda = 0, 1, 2$, as Σ, Π, Δ; for nonlinear molecules and complexes: $^{2S+1}\Gamma$ where Γ is the symmetry type (A, B: one-dimensional, non-degenerate type; E: two-dimensional, doubly degenerate; T: three-dimensional, triply degenerate).

2.4.4 Discrete Variational Multi Electron Technique

The main deficiency of the ligand field theory is that its theoretical basis is mainly based on semi-empirical methods. For this reason it is not possible to discuss quantitatively the chemical difference between different ions, since the magnitude of the adjustable parameters may be determined only from experimental data. Recently the general method for the calculation of electronic structures including many-electron interactions from first principles (DV-ME–Discrete Variational MultiElectron) has been developed. With this technique, the multiplet energies are calculated in two steps: in the first step, one electron molecular orbitals (MO) and MO energies are calculated by the DV-X_α molecular orbital method; in the second step, the many-electron Hamiltonian, in which the interactions between two electrons are exactly described, is diagonalized within a subspace spanned by the Slater determinants made up of the obtained one electron data. This method enables us to calculate multiplet structures without any restrictions on the symmetry of the crystal. It was revealed that the DV-ME method not only well reproduced the peak positions in optical spectra from first principles, but was also useful for discussing the effect of covalency and trigonal distortion of impurity-state wave functions on the multiplet structure. It was successfully applied to analyze the multiplet structures of $3d^2$ and $3d^3$ transition metals, f–d transitions of heavy metal ions and rare-earth ions in solids (Ishii et al. 1999; Ishii et al. 2002).

2.4.5 Luminescence Decay

The mechanisms of luminescence decay from an optical center are of critical importance. In particular we have to know if there are any processes internal to the center or external to it, which reduce the luminescence efficiency. It is possible to define two decay times, τ_r, the true radiative decay time which a transition would have in absence of all non-radiative processes, and τ, the actual observed decay time, which may be temperature dependent, as will usually occur when there are internal non-radiative channels, and which may also be specimen dependent, as when there is energy transfer to other impurities in the mineral. The quantum yield may be close to unity if the radiationless decay rate is much smaller than the radiative decay.

2.4.5.1 Radiative Decay

For allowed emission transitions the true lifetime is short, namely $10^{-7} - 10^{-8}$ s, for strongly forbidden transitions in solids it is much longer, a few 10^{-3} s. For the two-level system (excited state and ground state) the population of the excited state decreases according to

$$\mathrm{d}N/\mathrm{d}t = -N_\mathrm{e} P_\mathrm{eg} \,. \tag{2.22}$$

The value of N_e gives the number of luminescent ions in the excited state after an excitation pulse, t the time, and P_eg the probability for spontaneous emission from the excited to the ground state. Integration yields

$$N_\mathrm{e}(t) = N_\mathrm{e}(0)\, \mathrm{e}^{-t/\tau} \,, \tag{2.23}$$

where τ is the radiative decay time.

In the absence of non-radiative decay processes the experimentally observed decay time equals the radiative decay time. When non-radiative processes are present, the experimental value is reduced by a factor equal to the quantum efficiency of the luminescence. There are many factors, which affect the decay time. One is due to competing non-radiative processes, which shorten the measured decay time. We will consider the latter first. The experimentally observed decay time of the luminescence is given by

$$\tau = 1/\left(k_\mathrm{r} + k_\mathrm{i}\right) \tag{2.24}$$

where k_r is the probability of radiative decay and k_I the probability of non-radiative decay processes from the same state. If k_I is much large than k_r not only will decay time be shortened appreciably, but the luminescence intensity will be very weak. Non-radiative deactivation within a center occurs by interaction with the vibrating lattice, which depends on temperature. Thus k_I is temperature dependent.

2.4.5.2 Non-Radiative Decay

Radiative return from the excited state to the ground state is not the only possibility of completing the cycle. The alternative is nonradiative return, i.e. a return without emission of radiation. All the energy absorbed by the mineral, which is not emitted as radiation is dissipated to the lattice (radiationless process). Actually there are many centers, which do not emit at all. Absorption and emission transitions are possible with Stokes shift. The relaxed excited state may, however, reach the crossing point of the two parabolas if the temperature is high enough and return to the ground state in a nonradiative manner. The excitation energy is then completely given up as heat to the lattice. This model accounts for the thermal quenching of luminescence.

Another possibility to return to the ground state is by transfer of the excitation energy from the excited center (S^*) to another center (A). The energy transfer may be followed by emission from A and species S is then said to sensitize species A. However, A^* may also decay nonradiatively and in this case species A is said to be a quencher of the S emission. The most important quenchers in minerals are Fe^{2+}, Co^{2+} and Ni^{2+}, which have intense charge-transfer bands.

Lets consider two centers, S and A, separated in the mineral by distance R, which is so short that the centers S and A have a non-vanishing interaction with each other. If S is in the excited state and A in the ground state, the relaxed excited state of S may transfer its energy to A. Energy transfer can occur only if the energy differences between the ground and excited states of S and A are equal (resonance condition) and if a suitable interaction between both systems exists. The interaction may be either an exchange interaction (if we have wave functions overlapping) or an electric or magnetic multipolar interaction. In such cases, if the excitation spectrum of the A emission is measured, the excitation bands of S will be found as well, since excitation of S yields emission from A via energy transfer. If S is excited selectively, the luminescence of A also presents. Finally, the decay time of the S emission should be shortened by the presence of nonradiative energy transfer, since it shortens the life time of the excited state S^*.

If the spectral overlap consists of a considerable amount of overlap of an emission band and an allowed absorption band, there can be a considerable amount of radiative energy transfer: S^* decays radiatively and the emission band vanishes at the wavelengths where A absorbs strongly.

If we consider now transfer between two identical ions the same considerations can be used. If transfer between S ions occurs at a high rate, in a lattice of S ions there is no reason why the transfer should be restricted to one step. This can bring the excitation energy far from the site where the absorption took place. If in this way, the excitation energy reaches a site where it is lost nonradiatively (quenching site), the luminescence will be quenched. This phenomenon is called concentration quenching.

An additional delay between excitation and emission is often introduced by metastable electron states known as electron traps, which are filled during excitation. Once an electron has become trapped in such a state it requires certain energy to release it but this can be provided thermally. Emission, which follows the emptying of such traps at a fixed temperature, is known as phosphorescence.

2.4.5.3
Special Cases of Decay

The processes involved are stepwise energy transfer, cooperative sensitization of luminescence and cooperative luminescence. As an example of stepwise energy transfer a system containing Er^{3+} and Yb^{3+} may be considered. The latter ion absorbs at 970 nm (10,300 cm^{-1}) and in phonon assisted an Er ion

is excited to its $^4I_{11/2}$ state. Then a second photon is absorbed by another Yb ion and produces $^4I_{11/2}$–$^4F_{7/2}$ in the excited Er by resonance energy transfer. This successive double energy transfer accounts for the fact that the excitation spectrum of such a system agrees with the reflection spectrum of Yb^{3+} and that the intensity of the resulting green emission $^4S_{3/2}$–$^4I_{15/2}$ (after radiationless $^4F_{7/2}$–$^4S_{3/2}$) of erbium is proportional to the square of the flux of infra-red photons. Two excited ($^2F_{5/2}$) Yb ions can cooperatively excite a third ion of another rare-earth element, such as terbium, if the sum of the energies of the donor system corresponds to the excited level of the acceptor system. Cooperative luminescence is the opposite process of cooperative absorption and can be described as two excited ions that simultaneously make transitions downwards, emitting one photon having the sum of the two energy differences. A similar case where an ion emits one photon and simultaneously exciting another ion is also known.

A related phenomenon is the conversion of single visible photons with the result the quantum efficiency can be higher than 100%. If, for example, 0.1% of Pr^{3+} is incorporated in YF_3 and excited with the mercury spectral line at 185 nm, the electron from $4f5d$ states decay non-radiatively to the $^1S_0$ ($4f^2$) state. This system is able to generate two visible photons by $^1S_0$–$^1I_6$, followed by non-radiative decay to the closely adjacent $^3P_0$ and by transition another photon is emitted by transitions to one of the six J-levels of ^3H or ^3F. A condition for this cascade process is that the nephelauxetic effect for inter-shell transitions is sufficiently weakly pronounced for the lowest $4f5d$ state to be above $^1S_0$ (Reisfeld and Jörgensen 1977).

2.4.6 Luminescence in the Band Scheme

Atoms in minerals are very close and influence each other strongly. As a result in certain minerals the energy levels of individual atoms are combined and form the energy zones filled by electrons (Fig. 2.5). The inner atom orbitals of the individual atoms form inner energy zones totally filled by electrons. The outer atom orbitals form the outer energy zones filled by electrons. The last filled zone is called the valence band (VB) because valence electrons take part in its occupation. The higher energy zones, following the valence zone, are empty because they are formed by empty electron orbitals. The lowest of these zones is called the conductivity band (CB). The energy interval between the valence zone and conductivity zone is called the forbidden zone and designated as E_g.

With small dimensions of the forbidden band the electron transfer of the impurity or of the main substance to the conduction band may take place. The most important luminescent minerals of this kind are ZnS and silver bromides. With the interband spacing of 3–4 eV a UV irradiation with a wavelength of less than 300 nm has enough energy to detach electrons and transfer them from the filled valence band into an empty conduction

band. Thus we have a free electron in the conduction band and a free hole in the valence band. The certain defects may catch a free electron, forming an electron center, or a free hole forming a hole center. Upon disappearance of such centers, as a result of recombination with the opposite charge carrier, recombination energy serves as the excitation source for the luminescence center and emission appears (Fig. 2.6). The following processes are possible:

- "Intrinsic" luminescence where an electron is excited from the valence band to the conduction band, so-called interband transition. Recombination of this electron with a hole in the valence band generates a photon, the energy of which corresponds to the energy difference of the band gap (Fig. 2.6a);
- The excited electron may also recombine with an activator, with the following luminescence, or a trap, with the following electron capturing, within the forbidden gap. Traps and activator energy levels are caused by defects in the crystal lattice (Fig. 2.6b).

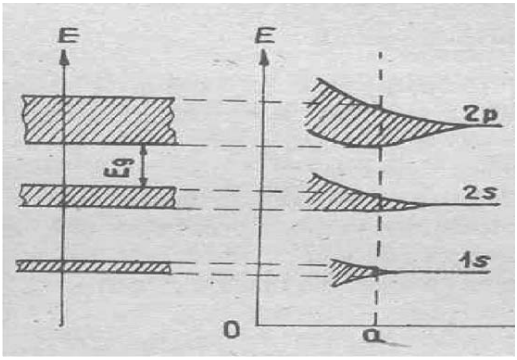

Fig. 2.5. Energy zones formation scheme (Bakhtin and Gorobets 1992)

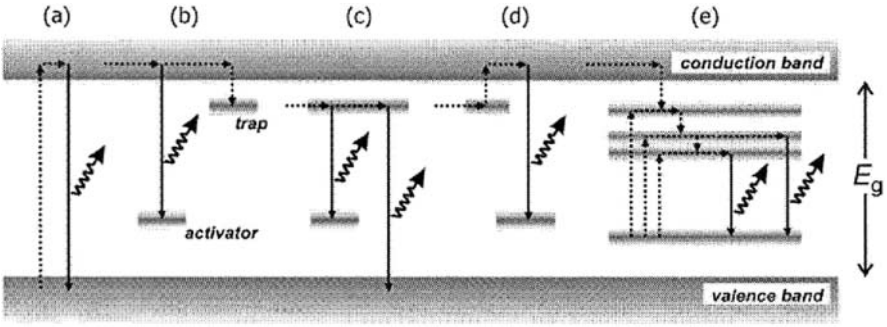

Fig. 2.6. Simplified sketch of electron band structure of a semiconductor mineral, showing the processes of excitation (energy absorption), non-radiative energy transfer and generation of luminescence (after Nasdala et al. 2004)

- Luminescence generation through direct recombination of electrons from a trap with an activator (tunneling) or with a hole in the valence band (Fig. 2.6c);
- Stimulated release from an electron from the trap to the collection band, followed by emissive recombination with an activator. This process is called thermoluminescence (electron release stimulated by heating) and optically stimulated luminescence (electron release stimulated by light) (Fig. 2.6d);
- "Extrinsic" luminescence, where after being excited, electrons of defect ions recombine with the ground state with luminescence emission (Fig. 2.6e);

CHAPTER 3

Experimental Techniques

3.1 Lasers

When lasers first emerged from the laboratory and became commercially available in the late 1960s, they found application in diverse areas. Spectrometric analysis was among the technology's earliest applications. Unlike established continuum sources, the monochromatic, coherent beams from lasers delivered high energy density. The result was a quantum leap in spatial and temporal resolution, sensitivity and speed of acquisition. For more than 40 years, spectrometric techniques implemented sources with narrower wavebands, shorter pulses and tunable emission.

The lasers are used in the luminescence of minerals for the following reasons:

- The concentration of luminescence centers is usually extremely low and we need high-energy sources.
- Several luminescence centers often present simultaneously in one mineral and we need selective monochromatic excitation in a broad spectral range.
- Decay time of many luminescence centers in minerals is extremely short and for time-resolved spectroscopy we need the pulsed source with a very short pulse width.
- For practical applications in remote sensing we need a highly directional, very intense and powerful source.

The only source, which combines all those parameters, is the laser.

3.1.1 The Basic Theory of Laser Action

Einstein's laws of absorption and emission describe the operation of lasers. The luminescence of minerals, considered in this book, is a spontaneous emission where the luminescence is independent of incident radiation. In a stimulated emission the relaxation is accomplished by interaction with a photon of the same energy as the relaxation energy. Thus the quantum state of the excited species and the incident photon are intimately coupled. As a result the incident and the emitted photons will have the same phase and propagation direction. The emitted light of stimulated emission is therefore coherent as opposed to the

random distribution of propagation direction and phase found in spontaneous emission.

The energy level systems used in laser action contain at least three levels. Population inversion is achieved by stimulated absorption through a spin allowed transition from the ground state into a state with high energy, which is then nonradiatively relaxed to a lower state, which has symmetry and spin characteristics that hamper fast spontaneous decay to the ground state. It is from this lower metastable state that the laser action occurs. Lasing is accomplished by placing the laser material between two mirrors. It is initiated either by a spontaneous transition from the metastable level or by an external photon of the right energy. The beam thus created is passed back and forth between the two mirrors, so that it on each pass through the laser media initiates more stimulated emission and increases in power.

3.1.2 Short Description of the Lasers Used for Luminescence of Minerals Excitation

a. **Argon ion CW laser** is one of the earliest types of lasers. We used it in steady-state spectroscopy. It consists of a capillary tube where an electrical discharge generates a high current density plasma of argon. The argon ions created in the discharge are the laser medium. The argon laser is capable of emitting several different wavelengths, one at a time or even simultaneously, such as 514.5, 496.5, 488.0, 476.5 and 457.9 nm.
b. **Excimer lasers** contain an excited complex consisting of two or more different atoms or molecules, which exists only in an excited state, while the ground state is repulsive and after radiative de-excitation it falls apart again. An electric pulsed discharge is used within the laser tube to supply the energy to the laser process. The gas filling consists of three major constituents: rare gas (Ar, Kr, He), a halogen compound (F, Cl, Br) and a buffer gas (He, Ne). Within the discharge the excited complexes are formed, e.g. XeCl. Sometimes it is also possible to use nitrogen as laser gas. The major advantages of the excimer laser are high pulse energies, high repetition rates, and direct generation of the UV light. Selecting the appropriate gas mixture may choose several different wavelengths (ArF – 193 nm, KrCl – 222 nm, KrF – 248 nm, XeCl – 308 nm, N_2 – 337 nm). The main disadvantages are poor beam quality, relatively long pulse durations and toxic gases.
c. **Nd-YAG lasers** (neodymium doped yttrium aluminum garnet) can work in CW mode and in a pulsed version. In a first step electric energy is stored in capacitors. This energy is discharged into flash lamps within approximately 100 µs. The emitted optical energy is subsequently stored in the laser crystal and is opened by means of an electro-optical cell (Q-switch) as a single pulse of 0.1 to 1 J within approximately 6–10 ns. The primary IR radiation is at 1,064 nm, which may be frequency doubled to 532 nm. By additional optically non-linear frequency conversion wavelengths of 355 and 266 nm are attainable.
d. **The dye laser** is the best laser for spectroscopy because it may be tunable over a comparatively large range of wavelengths. The laser media are molecules

of an organic dye dissolved in a suitable solvent. A so-called pump laser, an excimer laser in our case, provides the energy input.

e. **OPO lasers** (Optical Parametric Oscillator) are optical devices pumped by a laser to produce two wavelengths, called the signal and idler, different from those of the pump laser. They are more complicated than laser oscillators due to the nonlinear nature of the gain medium. Within an optically non-linear crystal an incoming photon is broken up into two photons, while the cutting line between the two photon energies can be chosen arbitrarily. OPOs can be used to shift the wavelength of fixed-frequency lasers to a desired wavelength.

3.2 Steady-State Luminescence Spectroscopy

3.2.1 Experimental Apparatus

Firstly we shall consider the various forms of conventionally determined spectra, as distinct from time-resolved spectra, which can be obtained using continuous excitation. The measurement of emission spectra enables parameters such as the spectral position, spectral width, and spectral intensity to be determined. Moreover, the variation of these parameters with temperature is very important in deciding the origin of spectral bands. Sometimes the luminescence from single crystals is polarized and this can also give information as to the nature of the center.

The traditional steady-state experimental setup has a UV lamp as the excitation source. It is equipped with two monochromators to select both the excitation and emission wavelengths. To record an excitation spectrum, the emission monochromator is set at the desired wavelength, generally the emission maximum. The excitation monochromator is then scanned through the excitation bands of the luminescence center. To improve the specificity of the technique is to employ a tunable laser as the active component of the system. In an ideal laser-based spectroscopic system the exciting wavelength would be tunable through the large fraction of the ultraviolet and visible regions of the electromagnetic spectrum. Emission spectra are recorded by choosing an appropriate excitation wavelength and scanning wavelength with the emission monochromator. The luminescence is quantified with the corresponding electronic devices. Band-pass excitation filters have to be used to remove second order diffraction from the excitation source. Polarizers may be added to both the excitation and emission paths. The sample holder usually contains cryostat enabling spectral measurements at low temperatures.

The observed excitation spectrum is distorted because the light intensity of the excitation source is a function of the wavelength and the transmission efficiency of the excitation monochromator is a function of wavelength. The emission spectra are distorted by the wavelength-dependent efficiency of the emission monochromator and the photomultiplier (PMP) tubes. Thus both

spectra have to be corrected for the system response. It is well known that for gratings the maximum efficiency is controlled by the blaze applied during manufacture of the grating. In the same way, PMP are strongly wavelength dependent. Consequently, luminescence of a given apparatus represents biased information about the original luminescence of the sample. The recorded signal differs greatly from that of the original emission. Determination of the system response is essential to correct spectra for discrepancies due to the method of acquisition so that they may be compared among laboratories. The calibration of wavelength and intensity may be achieved with reference lamps whose emission spectra are known.

In our research the steady-state photoluminescence spectra in the UV-visible range were investigated under UV lamps and lasers excitations and analyzed by a grating monochromator equipped with continuous-flow helium cryostat at temperatures from 20 to 300 K. The steady-state luminescence in the range of 200–900 nm was measured by a photomultiplier tube and in the range of 900–1,600 nm was detected by a Ge-detector. The steady-state cathodoluminescence (CL) spectra were recorded with a CL spectrometer on a Jeol JSM-840 scanning electron microscope. The recording system consists of a parabolic mirror, a silica window allowing the passage of UV emission, a Jobin-Yvon H-10 spectrometer and a Hamamatsu R636 photomultiplier, which allows detection from 200 to 900 nm. Steady-state spectroscopy has been combined with lifetime measurements. We used the time-domain technique, where the sample is excited with a pulse of laser light, while the width of pulse is much shorter than the measured decay time. The time-dependent intensity is measured following the excitation pulse, and decay time is calculated from the slope of a plot of log $I(t)$ versus t, or from the time at which the intensity decreases to $1/e$ of a value at $t = 0$. Decay information is extremely important, but if you found several decay components at the same λ, it is not possible to know if they are connected with an individual luminescence center or with several ones.

3.2.2 Spectral Deconvolution

Natural minerals may contain simultaneously up to 20–25 luminescence centers, which are characterized by strongly different emission intensities. Usually one or two centers dominate, while others are not detectable by steady-state spectroscopy. In certain cases deconvolution of the luminescence spectra may be useful, especially in the case of broad emission bands. It was demonstrated that for deconvolution of luminescence bands into individual components, spectra have to be plotted as a function of energy. This conversion needs the transposition of the y-axis by a factor λ^2/hc (Townsend and Rawlands 2000). The intensity is then expressed in arbitrary units. Deconvolution is made with a least squares fitting algorithm that minimizes the difference between the experimental spectrum and the sum of the Gaussian curves. Based on the presumed band numbers and wavelengths, iterative calculations give the band positions that correspond to the best fit between the spectrum and the sum of calculated bands. The usual procedure is to start with one or

two bands and to increase the band numbers until the deconvolution does not significantly improve. Band positions can be constrained or assumed for calculation. Such deconvolution can reveal different activators and establish their relative importance, particularly where others overlap some luminescence centers with broader or more intensive emission bands. Deconvolution must be carried out with care and in any case not all bands present in the steady-state spectrum may be assigned to a specific activator by deconvolution into Gaussian curves. Our experience with deconvolution evidences that it may be effective only when the exact number of the bands and lines and their spectral positions are already known. In such cases the relative intensity of each one may be evaluated. Deconvolution of the broad bands of unknown origin for several components and their physical interpretation may lead to mistakes, as occurred in our attempts with zircon and barite emissions.

3.3 Time-Resolved Luminescence Spectroscopy

The different decay times of luminescence centers in minerals, changing from ns to ms (Table 1.3), make time resolved spectroscopy possible and very effective. Let suppose that we have three different luminescence centers with different decay times emitting on the same spectral range. In traditional spectra, the time-integrated intensity is measured on each wavelength from all three centers, namely the resulting signal will be the sum of the three areas under decay curves. This procedure will be repeated on each wavelength with certain steps and the resulting spectrum will be a complicated mixture of the three overlapped spectral features.

Figure 3.1 schematically represents the time-resolved experimental setup used in our experiments. The excitation sources were pulsed lasers, such as excimer XeCl (308 nm), nitrogen (337 nm), three harmonics of Nd-YAG (266, 355 and 532 nm), and tunable dye and OPO, which deliver pulses of $\approx$ 10 ns duration. The spectra observed at the geometry of 90° are analyzed by intensified CCD matrix. Image intensifiers comprise three main components: a photocathode, microchannel plate (MCP) and phosphor screen. The standard operation of these devices starts when the incident photons become converted into electrons at the photocathode. The electrons then accelerated towards the MCP where they are multiplied to an amount dependant on the gain voltage across the MCP. After MCP multiplication, the electrons are accelerated further toward the phosphor screen where they are converted back into photons ready for the CCD to detect. CCD is a two-dimensional array, which comes in a semiconductor "chip" package. Each pixel is overlaid with a small voltage-carrying element known as an electrode. During illumination of the chip, charge accumulates in the pixel. To collect the data, a sequence of voltages is applied across the electrodes to move the charge row by row down the vertical dimension of the chip and into a shift register at the bottom of the array. This charge is then moved similarly across the shift register to the output node

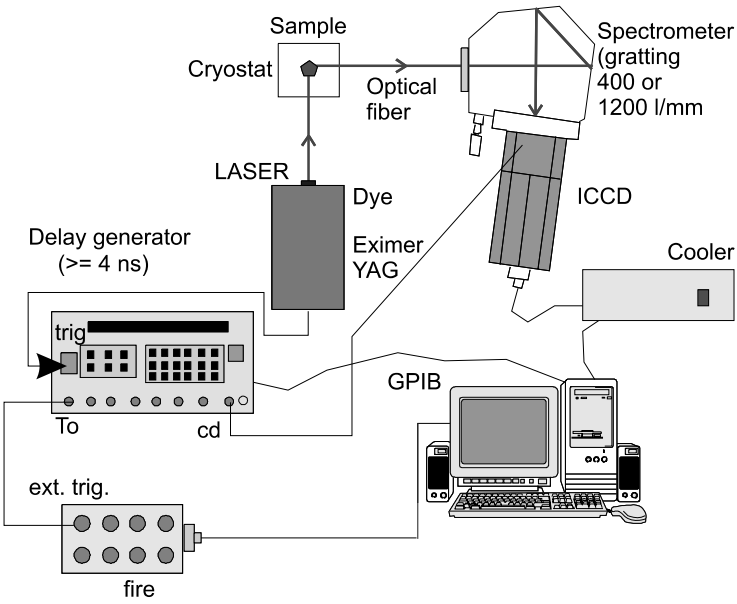

Fig. 3.1. Schematic experimental setup for time-resolved luminescence spectroscopy

where it converted to a digital form processing. The most significant benefit of this readout mode is that the associated readout noise is very low. Typically, CCDs have sensitivity similar to a photomultiplier tube; however, unlike the photomultiplier tube a CCD is not damaged by over-exposure to bright lights. The second purpose of the image intensifier is electronic ultra-short shutter function, which allows a so-called gated mode of operation crucial for time-resolved spectroscopy.

In recent years the use of CMOS (complementary metal oxide semiconductor) technology has received attention for the implementation of image sensors, e.g. for general-purpose imagers and vision systems. CMOS imaging systems have several advantages, which include a lower cost and higher frame rate, which is important for signal/noise ratio when luminescence intensity is very low.

Laser pulses synchronize iStar equipment (ANDOR V). It enables us to accomplish spectral measurements in certain time windows, which are determined by delay time, namely the time between the end of the laser pulse and the beginning of the measurement, and gate width, namely the time between the beginning and the end of the measurement. Simply speaking, the detector is closed during delay time and open during the gate width. After that the system is waiting for other laser pulse and accomplishes the cycle one again. The number of pulses is determined according to the signal/noise ratio and depends on luminescence intensity. Delay time and gate width may be changed from 1 ns to 19 ms. Spectral resolution is determined by the number of measuring pixels

and the monochromator gratings. We use 1,024 channels and gratings from 300 to 1,200 lines/mm. Gratings were of two kinds: ruled where grooves are physically formed into a reflective surface with a diamond on a ruling machine and holographic, produced from laser constructed interference patterns and a photolithographic process.

For delivering the luminescence to the monochromator we used quartz fiber optics, which enables the spectral measurement in the range from 200 to 900 nm. Thanks to the need for fiber optics in the communication technology, low absorption silica fibers have been developed. Similar fibers can be used as measurement fibers to transport light from the sample to the optical bench of the spectrometer. The easy coupling of fibers allows a modular build-up of a system that consists of light source, sampling accessories and fiber optic spectrometer. Advantages of fiber optic spectroscopy are the modularity and flexibility of the system.

The additional improvement used in the system compared to traditional luminescence methods used in luminescence of minerals is the so-called multichannel advantage. Traditionally, spectroscopy has involved using a scanning monochromator and a single element detector, for example a photomultiplier tube, placed at the exit slit. In such a scanning system, a complete spectrum is built up point by point, by moving the grating to select each wavelength. By contrast, in multichannel spectroscopy the grating is fixed and the exit slit and single detector are replaced with an array of detectors, each viewing a different wavelength. In our system 1,024 26-μm detectors are used, so a complete spectrum is recorded in the same time it takes to record one wavelength point with a scanning system. Array based spectrometers also have potential for better stability and reproducibility since they have no moving parts.

Now let suppose that three centers with similar spectral characteristics have different decay times of 10 ns, 1 μs and 1 ms (Fig. 3.2). If we use a delay time of 10 μs and a gate width of 19 ms, two centers with decay times of 10 ns and 1 μs will be already quenched, while the third one with the longest decay time remains. The resulting spectrum will represent only emission of the long-lived center. If we use a delay time of 1 ns and a gate width of 100 ns, only the first center with the shortest decay time will be registered, while the other two are still in the excited state during the measuring time and do not participate in emission. If we use a delay time of 100 ns and a gate width of 10 μs the first center will be already quenched before the beginning of the measuring time, while the third one will be mainly still in the excited state during the measuring time and the resulting spectrum represents only the second center with intermediate decay time. If we use a delay time of 1 ns and a gate width of 50 ns, two long-lived centers will be still in the excited state during the measuring time and the resulting spectrum represents only the first center with the shortest decay time.

One example demonstrates the advantage of the time-resolved technique compared to the steady-state technique. The time-integrated cathodoluminescence spectrum of apatite enables us to detect only two dominant luminescence

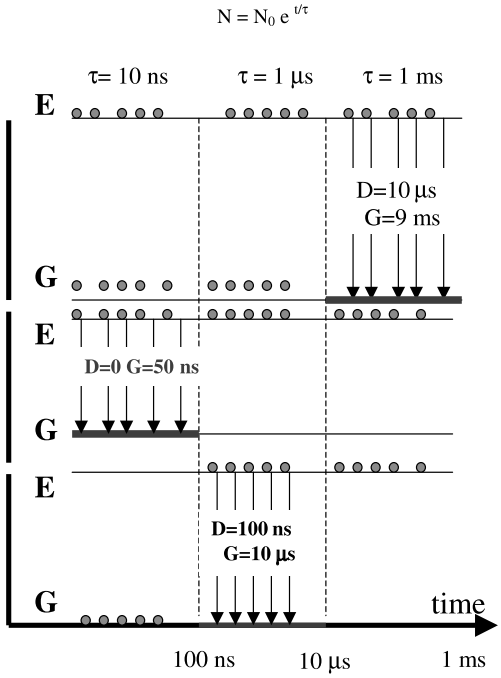

Fig. 3.2. Scheme of simultaneous emission of three luminescence centers in the same spectral range with different decays, which may be resolved by time-resolved spectroscopy

centers, Mn^{2+} and Ce^{3+}. A laser-induced luminescence spectrum with a minimal delay time of several nanoseconds and a maximum gate width of several milliseconds, which is practically steady-state spectroscopy, also demonstrates the same centers, while their relative intensities are different (Figs. 3.3a,b). After a short delay of 100 ns the second Ce^{3+} center is detected, which has a slightly longer decay time compared to the first one (Fig. 3.3c). Using a delay time of 500 ns in order to quench the short-lived Ce^{3+} centers and a narrow gate of 500 ns in order to quench long-lived centers the band of Eu^{2+} dominates the spectrum (Fig. 3.3d). After a delay of 10 µs when luminescence of Eu^{2+} also disappears, the lines of TR^{3+} with very long decay times, such as Tb^{3+}, Dy^{3+} and Eu^{3+} are confidently detected (Fig. 3.3e), while changing excitation from 266 to 337 nm the second type of Eu^{3+} luminescence center appears (Fig. 3.3f). Excitations with 480 and 360 nm enable us to see luminescence lines of Pr^{3+}, Tm^{3+}, Er^{3+} and Sm^{3+} (Figs. 3.3g,h).

The optical setup for time-resolved micro-luminescence measurements is based around an Axiotech 100 HD Zeiss microscope, modified to allow laser injection and fluorescence collection. The sample is observed either under transmission or reflection of polarized white light, or under UV illumination (HBO lamp). A set-up consisting of a dichroic mirror, for the selection of the excitation wavelength, and an objective (Epiplan Neofluar obj. $>$ 350 nm; Ealing/Coherent reflection obj. $<$ 350 nm) is used to focus the laser beam on the sample (spatial resolution over 5 µm with a $\times$50 objective). The lim-

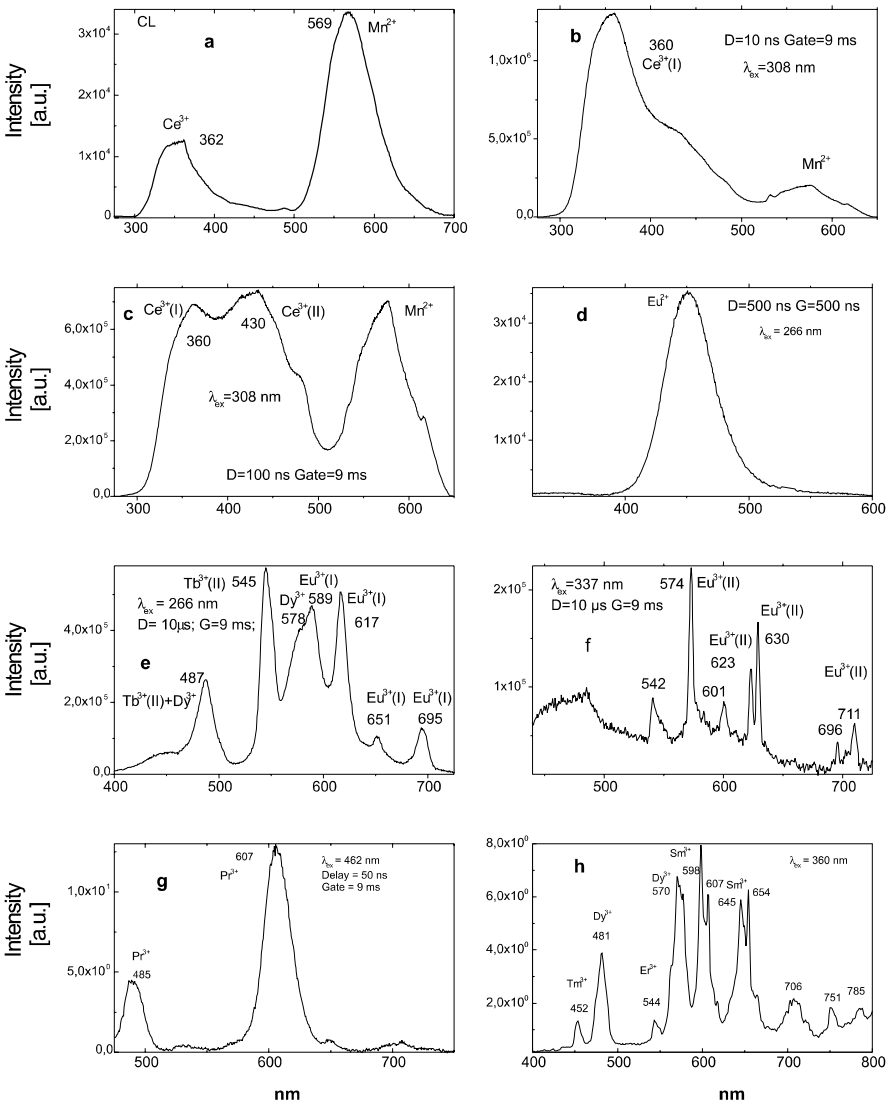

Fig. 3.3. a–h: Cathodoluminescence (**a**) and laser-induced time-resolved luminescence (**b–h**) spectra of the same apatite sample

itation of the spatial resolution is mainly caused by the divergence of the laser beam. The same objective collects emitted fluorescence and feeds it back in a pure silica glass fiber (transparent in the UV, visible and near IR range) (Fig. 3.4).

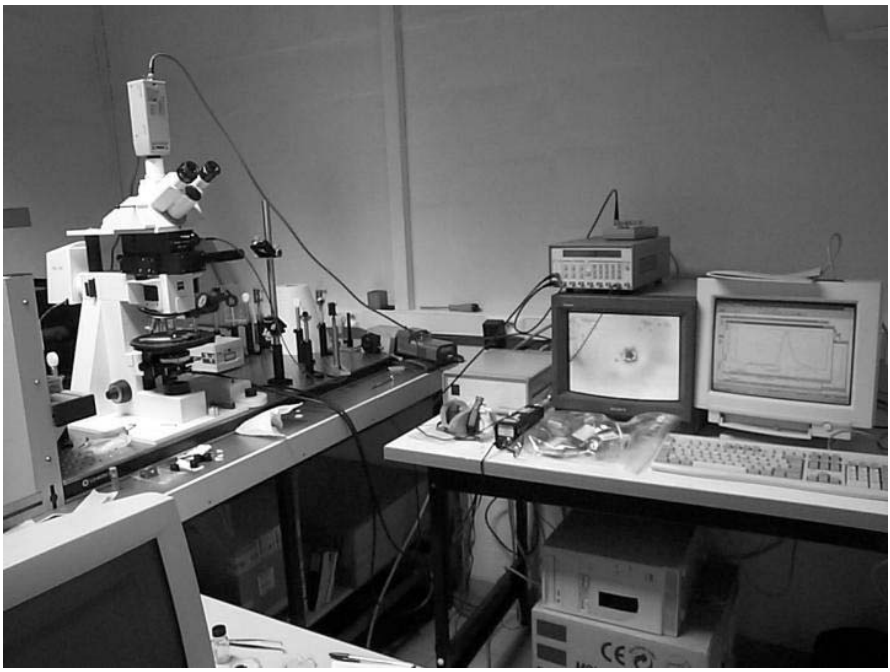

Fig. 3.4. Laser-induced time-resolved micro-luminescence system

3.4 Other Laser Based Spectroscopic Techniques

The experimental setup represented on Fig. 3.1 may be easily transformed for investigation of other spectroscopic properties under laser excitation, such as laser-induced breakdown spectroscopy (LIBS) and Raman spectroscopy. For the LIBS the focusing lens has to be added between the laser and the mineral to create enough power to form plasma. For the Raman investigation a holographic Notch filter has to be added between the mineral and the monochromator. They are fabricated by recording interference patterns formed between two mutually coherent laser beams unlike conventional interference filters, which are made by vacuum evaporation techniques. Since all layers are recorded simultaneously within a thick stack, the optical density of the notch filter is high and its spectral bandwidth can be extremely narrow. Also, since the layering profile is sinusoidal instead of squarewave, holographic notch filters are free from extraneous reflection bands and provide significantly higher laser thresholds.

CHAPTER 4

Luminescent Minerals

Gorobets and Rogojine (2001) gave the general systematization of minerals according to their luminescent properties (Table 4.1). In the case considered, mineral groups comprise phases with similar luminescence properties determined by luminescence and quenching centers. At the first level, all minerals are divided into dielectric, semiconductors, and metals together with intermetallic compounds. From the physical point of view, it means classification by the energy band gap E_g. Minerals with $0 \leq E_g \leq 1$ are incapable of luminescence, because they are opaque to optic photons. Other minerals are principally luminescent if they are not saturated with quenching centers.

At the second level, the type of chemical compounds subdivides luminescent minerals: homoatomic compounds, sulfides, halides and oxygen-bearing compounds. Such level is mainly important for recombination induced luminescence and practically is not considered in our book.

At the third level, the most detailed partition of luminescence minerals is carried out on the basis of metals in the mineral formulae. In rare cases we have minerals with host luminescence, such as uranyl minerals, Mn minerals, scheelite, powellite, cassiterite and chlorargyrite. Much more often luminescent elements are present as impurities substituting intrinsic cations if their radii and charges are close enough. Thus, for example, Mn^{2+} substitutes for Ca^{2+} and Mg^{2+} in many calcium and magnesium minerals, REE^{3+} and REE^{2+} substitutes for Ca^{2+}, Cr^{3+} substitutes for Al^{3+} in oxygen octahedra, Fe^{3+} substitutes for Si^{4+} in tetrahedra and so on. Luminescence centers presently known in solid-state spectroscopy are summarized in Table 4.2 and their potential substitutions in positions of intrinsic cations in minerals in Table 4.3.

Thus, for a mineral to be luminescent the following three conditions must be satisfied at once: (1) a suitable type of crystal lattice favorable to forming emission centers; (2) sufficient content of luminescence centers and (3) a small amount of quenchers. We arrange the luminescent minerals in our book according to the main major element, the substitution of which by luminescence centers determines the emission properties of a mineral.

Besides luminescence properties, we also added the short data on color of corresponding minerals, because, as was already mentioned, such information is often useful for an understanding of luminescence nature. The data on ionic radii of different elements and the main structural data are taken from corresponding Internet sites.

The Figures contains the following symbols: [a.u.] - arbitrary units, D-delay, G-gate.

Table 4.1.

Minerals assemblage according to luminescence properties (Gorobets and Rogojine 2001)

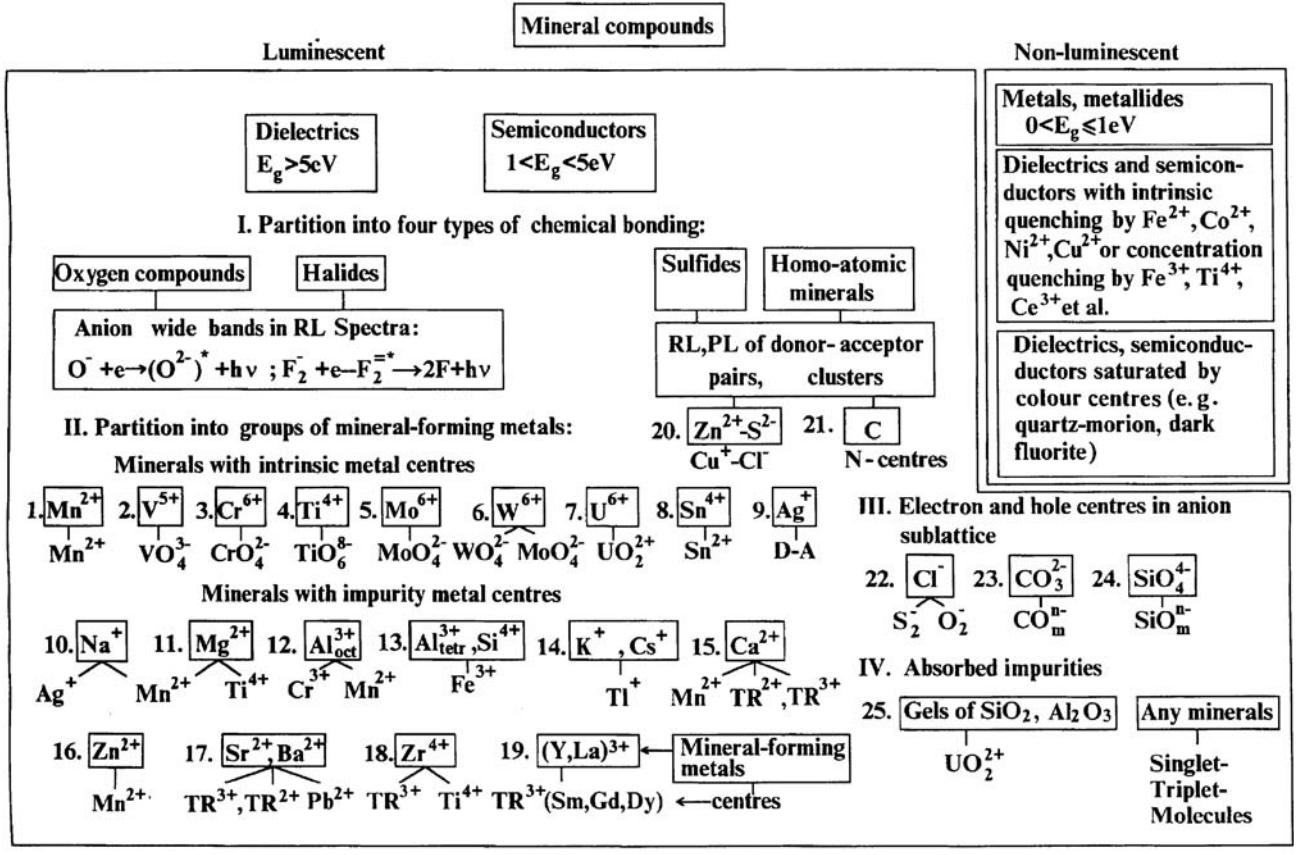

Table 4.2. Luminescent activator ions and valence states ordered to electronic configurations (column numbers correspond to the periodic table columns)

4	5	6	7	8	9	10	11	12	13	14	15	16	17	18
Transitions elements $3d^n$							d^{10}		Heavy ions $4–6s^2$ $4–6sp$					
Ti^{3+}	V^{2+}	Cr^{2+}	Mn^{2+}	Fe^{3+}	Co^{2+}	Ni^{2+}	Cu^{+}		Ga^{+}	Ge^{2+}	As^{3+}			
		Cr^{3+}	Mn^{4+}											
		Cr^{4+}	Mn^{5+}											
		Cr^{5+}												
							Ag^{+}		In^{+}	Sn^{2}	Sb^{3+}			
							Au^{+}		Tl^{+}	Pb^{2+}	Bi^{3+}			
Lanthanides $4f^n–4f^{n-1}\ 5d$														
La	Ce^{3+}	Pr^{3+}	Nd^{3+}	Pm^{3+}	Sm^{3+}	Eu^{3+}	Gd^{3+}	Tb^{3+}	Dy^{3+}	Ho^{3+}	Er^{3+}	Tm^{3+}	Yb^{3+}	Lu
					Sm^{2+}	Eu^{2+}			Dy^{2+}	Ho^{2+}	Er^{2+}	Tm^{2+}	Yb^{2+}	
Actinides $5f^n$														
Ac	Th^{4+}	Pa^{4+}	U^{6+}	Np^{3+}	Pu^{3+}	Am^{3+}	Cm^{3+}	Bk^{3+}	Cf^{3+}	Es^{3+}	Fm^{3+}	Md^{3+}	No^{3+}	Lr

Table 4.3. List of some elements which can be substituted and potential replacement ions with function of charge, ionic radii and coordinence (in brackets) (IR: infrared; R: red; P: pink; Y: yellow; G: green; B: blue; UV: ultraviolet)

Element	Ionic radii	Transition elements	Ionic radii	Absorption (color)	Emission	Rare earths	Ionic radii	Emission
Al^{3+}	0.67 (6)	Cr^{3+}	0.75 (6)	R–G	R	Eu^{3+}	1.09 (6)	R
		Ti^{3+}	0.81 (6)	(B)	R			
		V^{3+}	0.78 (6)	G				
		Fe^{3+}	0.69 (6)	Y	R			
		Mn^{2+}	0.81 (6)	P	G–R			
		Mn^{3+}	0.72 (6)	R–G				
		Mn^{4+}	0.67 (6)					
		V^{2+}	0.93 (6)					
		V^{4+}	0.72 (6)					
Si^{4+}	0.40 (4)	Cr^{4+}	0.55 (4)		IR			
		Fe^{3+}	0.63 (4)	Y	R			
Ca^{2+}	1.14 (6)	Mn^{2+}	0.81 (6)	P	G–R	Eu^{2+}	1.31 (6)	B–UV
		Ni^{2+}	0.83 (6)	G–Y	G–R–IR	Eu^{3+}	1.09 (6)	R
		Cu^{2+}	0.87 (6)	B–G	B	Yb^{2+}	1.06 (6)	
						Sm^{2+}	1.41 (8)	
	1.26 (8)	Mn^{2+}	1.10 (8)	P	G–R	Eu^{2+}	1.39 (8)	B–UV
		Fe^{2+}	0.74 (8)	G		Eu^{3+}	1.21 (8)	R

Table 4.3. (continued)

Element	Ionic radii	Transition elements	Ionic radii	Absorption (color)	Emission	Rare earths	Ionic radii	Emission
Ba^{2+}	1.49 (6)	Ag^{+}	1.29 (6)			Eu^{2+}	1.31 (6)	B–UV
		Cu^{2+}	0.87 (6)			REE^{3+}	1.00–1.17 (6)	
		Bi^{3+}	1.17 (6)					
		Bi^{2+}	0.59 (6)					
P^{5+}	0.31 (4)	Mn^{5+}	0.47 (4)	B	IR			
Zr^{4+}	0.98 (6)	Cr^{5+}	0.71 (8)	G	IR	REE^{3+}	1.00–1.17 (6)	
		Cr^{4+}	0.69 (6)					
		Mn^{2+}	0.81 (6)	P	G–R			
		Fe^{3+}	0.69 (6)	R	R			
Zn^{2+}	0.88 (6)	Mn^{2+}	0.81 (6)	P	G–R			
		Pb^{2+}	1.33 (6)					
Na^{+}	1.16 (6)	Mn^{2+}	0.81 (6)		G–R			
Ti^{4+}	0.74 (6)	Cr^{3+}	0.75 (6)					

4.1 Calcium (Ca^{2+}) Bearing Minerals

The main substituting luminescence centers are Mn^{2+}, TR^{2+} (Sm, Eu, Yb), and TR^{3+} (Ce, Pr, Nd, Sm, Eu, Gd, Tb, Er, Ho, Tm, Yb). Ionic radii of Ca^{2+} are 1.14 Å in 6-coordinated form and 1.26 Å in 8-coordinated form, while the ionic radius of Mn^{2+} is 0.97 Å, ionic radii of Sm^{2+}, Eu^{2+} and Yb^{2+} are 1.36 Å, 1.31 Å and 1.16 Å, respectively, and the ionic radii of TR^{3+} change from 1.00 Å to 1.15 Å for Ce to Yb, respectively.

4.1.1 Apatite $Ca_5(PO_4)_3$(F, Cl, O, OH)

Ninety five percent of the phosphorus on Earth belongs to the minerals of the apatite group. Apatites are inorganic constituents of bones and teeth of vertebrate and man, as well as a basis of many pathologic solid formations. Minerals of the apatite group are the main raw materials in the production of phosphorus fertilizers, fodder and technical phosphates, elementary phosphorus, and phosphor-organic compounds. The mineral is sometimes substantially enriched in rare-earth elements (REE) making their extraction possible (Altshuller 1980).

There are apatites with violet, blue, green, yellow orange and brown colors. The mostly abundant are blue and green and despite numerous investigations the origin of these colors are ambiguous. According to the last investigation, a violet-blue color is connected with the broad absorption band of the SO_3^--radical, which is the result of incorporation of S and U(Th) in the apatite structure. The reason of blue color is Mn^{5+} incorporation substituting for P^{4+}. The green color is mainly connected with the complex defect SO_3–TR(Ce), but the influence of Pr, Nd and also Cr and Fe is also possible (Gilinskaya and Mashkovzev 1994; Gilinskaya and Mashkovzev 1995).

It has been known for a long time that natural apatite is fluorescent. Its luminescent properties have found many applications, such as detection and identification of mineral in rocks, ores, and outcroppings by luminescent Lidar. The synthetic halo-apatite was one of the first phosphors applied for fluorescent lamps. The fluorescence also permits the establishment of genetic relationships between mineral samples and their source (mantle or Earth's crust) and the type of rock. An enrichment of apatite ores by luminescent sorting is possible (Portnov and Gorobets 1969; Gorobets et al. 1997a; Gorobets and Rogojine 2001; Waychunas 2002). Synthetic apatite activated by Yb^{3+} and Mn^{5+} is used as potential laser material (Payne et al. 1994; Moncorge et al. 1994).

Apatite is being considered as a barrier that will prevent the leakage of radioactive nuclei from the radioactive waste storage. Because of the similarity in the chemical and spectral features REE have been chosen as a model of the fission products of the actinides. For this reason it is of importance to recognize whether the elements are incorporated in the bulk of the barrier, or adsorbed on the surface where they can be subjected to leaching out (Martin et al. 1996; Martin et al. 1999a; Martin et al. 1999b).

The composition of the ideal fluor-apatite corresponds to the formula $Ca_{10}(PO_4)_6F_2$. The structure of the apatite is hexagonal, with the symmetry group $P63/m$. There are two different sites for the Ca^{2+} in this structure: 40% of Ca^{2+} ions are associated with the Ca(I) sites and 60% are associated with Ca(II) sites. The point group symmetry of the Ca(I) site is C_3, with each Ca having six oxygen nearest neighbors that form a distorted triangular prism about the Ca^{2+} ion. The Ca(II) site has C_s symmetry with the Ca^{2+} ions sitting at the corners of equilateral triangles with an F^- ion in the center.

Trivalent rare-earth (TR^{3+}) ions that have taken the Ca(II) position are characterized by abnormally high values of Stark splitting. This permits an easy separation of the spectra of these ions from those of TR^{3+} ions in Ca(I) positions (Voronko et al. 1991). The luminescence of RE in synthetic artificially activated apatites may be subdivided into two groups according to activation conditions. A number of RE have been studied after activation in oxidative conditions with the main type always in the low-symmetry Ca(II) site. In nature, REE can easily substitute for Ca, becoming luminescence centers in a crystallographic environment. Luminescence of natural apatites has been the subject of numerous investigations. With steady-state luminescence spectroscopy it was discovered that Eu^{2+}, Ce^{3+}, Mn^{2+}, Dy^{3+}, Nd^{3+}, Sm^{3+} and Sm^{2+} mainly determine apatite luminescence. It was established that TR^{3+} has been detected only in the high symmetry Ca(I) position (Gorobets 1968a; Portnov and Gorobets 1969; Tarashchan and Marfunin 1969; Tarashchan 1978; Gorobets and Rogojine 2001; Waychunas 2002). Laser-induced luminescence of apatite was investigated by nitrogen laser excitation with the main luminescence center being Ce^{3+} with a decay time of $\sim$ 20 ns accompanied by Mn^{2+} with a decay time of $\sim$ 1.5 ms (Gaft 1989).

The natural fluor-apatites in our study consisted of 75 samples from a variety of geologic environments. Concentrations of potential luminescence impurities in several samples are presented in Table 4.4.

For the correct interpretation of the luminescent bands, artificial apatite standards have been investigated, as nominally pure, as activated by different potential luminogen impurities. Natural carbonate-fluor-apatites not containing REE were heated with 1–5 wt. % of oxides of Eu, Pr, Sm and Dy at 900 °C in air and in vacuum. By changing the activation conditions the differentiation between isomorphous substitutions in different Ca-sites has been achieved. Under vacuum the compensation of the excessive positive charge by substitution of F^- by O^{2-} is impossible and the luminescence centers in Ca(II) sites may be less preferential. After heating at this temperature carbonate-fluor-apatite loses its carbonate content and becomes very similar to natural fluor-apatite.

Time-resolved luminescence spectra enable us to detect the following emission centers in natural apatite: Eu–Eu^{2+} in the Ca(II) site, Eu^{3+} in Ca(I) and Ca(II) sites; Sm^{3+} in Ca(I) and Ca(II) sites; Ce^{3+} in Ca(I) and Ca(II) sites; Pr^{3+} – in the Ca(I) site; Nd^{3+}, Dy^{3+}, Tb^{3+}, Er^{3+} and Tm^{3+} in the Ca(I) site;

Yb^{3+} possibly in the Ca(II) site, Mn^{5+} in the P^{5+} site, Mn^{2+} in Ca(I), Ca(II) sites and adsorption on the carbonate-fluor-apatite surface; reabsorption lines of molecular oxygen and water have been found and ascribed (Figs. 4.1–4.6).

Table 4.4. Concentrations of rare-earth elements and manganese (ppm) in several apatites with different colors

	Pr	Sm	Eu	Nd	Dy	Tb
Red	156	134	37	583	72	23
Green	63	50	12	237	41	7
Blue	424	199	28	1,470	59	14
Florida	5	4	1	19	7	1
Ivory	0.03	0.07	0.1	0.18	0.3	0.07

	Er	Tm	Ho	Gd	Ce	Mn
Red	46	4	13	208	1,367	
Green	24	4	9	40	519	
Blue	25	3	11	133	4,052	
Florida	6	1	2	6	45	130
Ivory	1.2	0.4	0.2	1.0	0.3	550

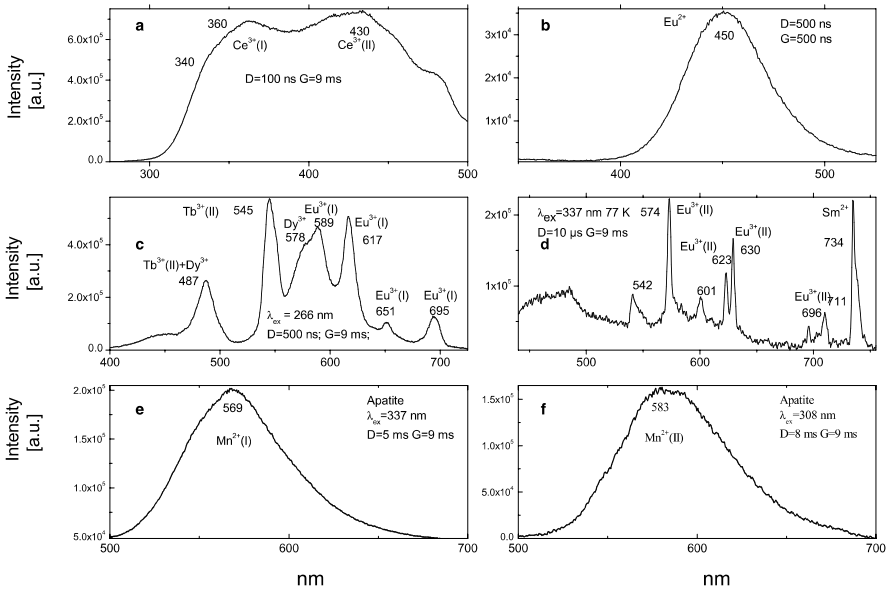

Fig. 4.1. a–f Laser-induced time-resolved luminescence spectra of apatite demonstrating two Ce^{3+}, Tb^{3+}, Eu^{3+} and Mn^{2+} centers in Ca(I) and Ca(II) structural positions. Besides that, Eu^{2+}, Sm^{2+} and Dy^{3+} are detected

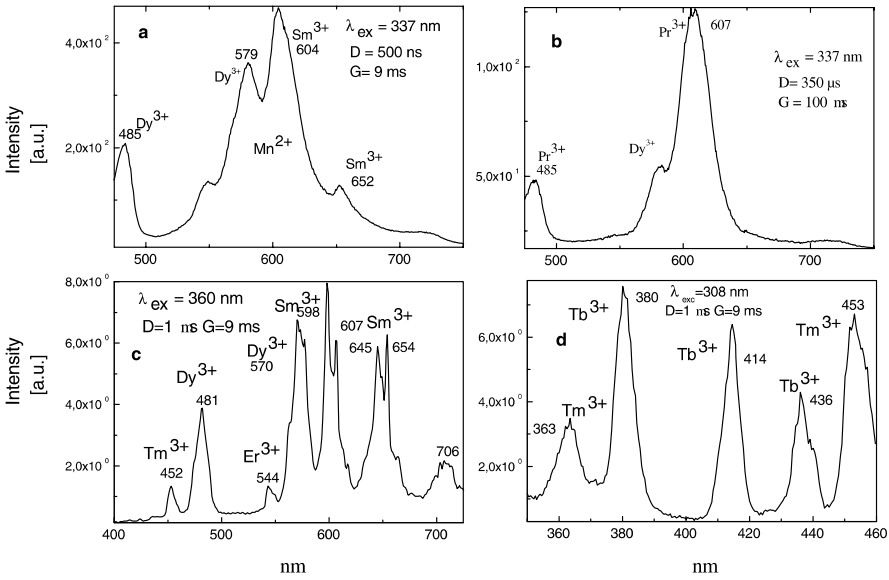

Fig. 4.2. **a–d** Laser-induced time-resolved luminescence spectra of apatite demonstrating Pr^{3+}, Tm^{3+} and two Sm^{3+} centers. Besides that Mn^{2+} and Dy^{3+} are detected

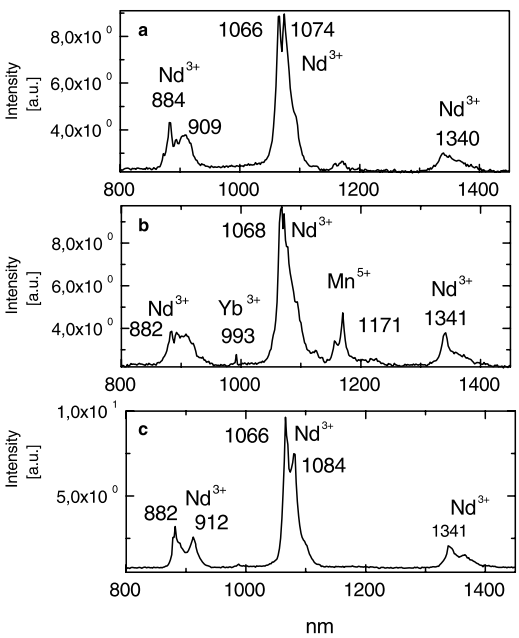

Fig. 4.3. **a–c** Laser-induced time-resolved IR luminescence spectra of apatite demonstrating Nd^{3+}, Yb^{3+} and Mn^{5+} centers

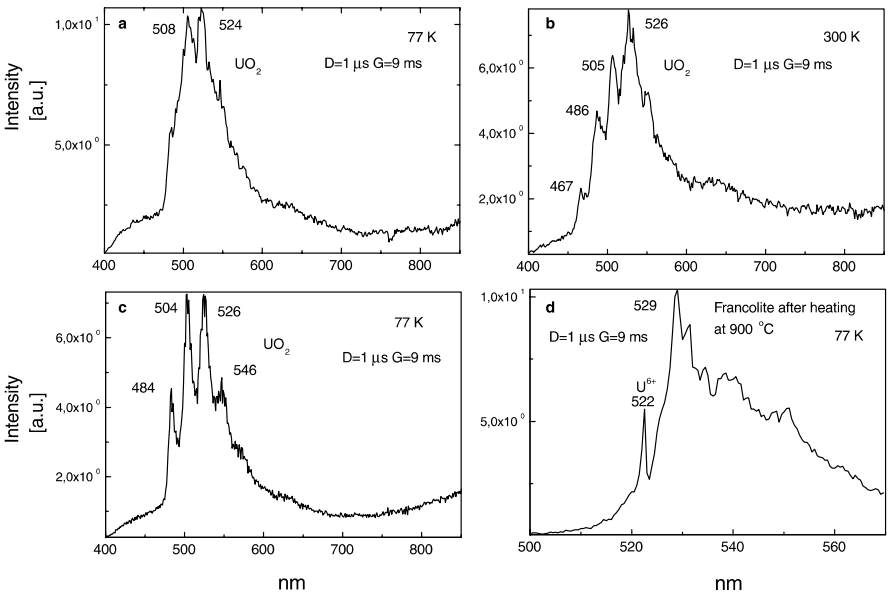

Fig. 4.4. **a–d** Laser-induced time-resolved luminescence spectra of apatite with uranyl (**a–c**) and U^{6+} luminescence (**d**) after oxidizing heating (possibly in fluorite inclusions)

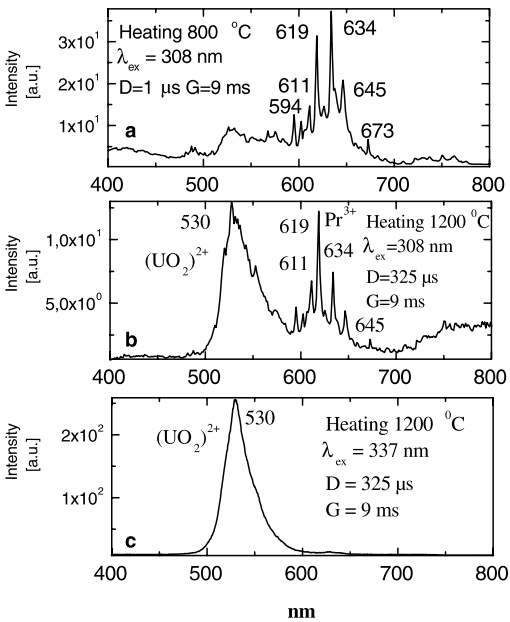

Fig. 4.5. **a–c** Laser-induced time-resolved luminescence spectra of sedimentary apatite (francolite) (**a**) and francolite activated by Pr (**b,c**) after heating demonstrating uranyl and Pr^{3+}, Eu^{3+} and Sm^{3+} centers

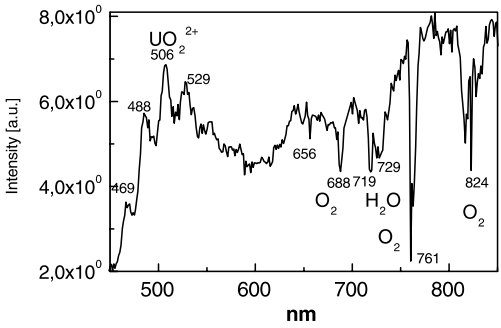

Fig. 4.6. Reabsorption lines of molecular oxygen and water in laser-induced time-resolved luminescence spectra of sedimentary apatite (francolite)

4.1.2 Scheelite $CaWO_4$

Scheelite is a calcium tungstate, $CaWO_4$, with a tetragonal structure ($I4_1/a$) where irregular tetrahedra WO_4 share edges with CaO_8 polyhedra. It is an ore mineral of W and a common accessory mineral in various kinds of rocks and ore deposits. REE geochemistry of scheelite may give information about the source of the ore matter, and about the physico-chemical conditions of ore transport/or precipitation. In nature, REE can easily substitute Ca, and become luminescent centers in such a crystallographic environment.

The method of luminescent spectroscopy is widely used to study the rare-earth elements distribution in natural scheelite (Brugger et al. 2000). Comparisons with synthetic pure and doped phosphors showed that WO_4^{2-} is responsible for the blue emission in scheelite (Tiede and Schleede, quoted in Pringsheim and Vogel 1946). Systematic spectroscopic investigation enabled to detect and interpret trivalent rare-earth element emission (Gorobets and Kudina 1976; Tarashchan 1978). Some regularity appears in the luminescence spectra of scheelite. These regularities are related to the genetic type of mineralisation; in particular, it is possible to recognize a scheelite from a skarn/calcsilicate rock, from a molybdenite-vein, from a metamorphic deposit, from a hydrothermal deposit or from an Au-deposit (Uspensky et al. 1989; Gorobets and Walker 1994). Nevertheless in many cases the possibilities of luminescence spectroscopy are limited because scheelite is characterized by broad luminescent bands of intrinsic (WO_4)-groups and impurity (MoO_4)-groups (Tarashchan 1978; Blasse 1980; Gaft 1989). Such strong bands prevent in many cases the detection of lines of rare-earth elements, especially Tm, Er and Ho, which have weak luminescence in the corresponding spectral range. The thermal X-ray excited luminescence enables to solve this problem in certain cases using the fact that while the intensity of broad band luminescence quickly decreases with increasing temperature, the intensities of the REE lines remains nearly constant (Uspensky and Aleshin 1993). Nevertheless, the lines of certain REE may be hidden by stronger luminescence of others REE. For example, luminescence of Pr^{3+} is difficult to detect because its radiative transitions are hidden by the lines of Sm^{3+}, Dy^{3+} and Nd^{3+}, luminescence of Tm^{3+} is concealed by Tb^{3+} and so on.

The natural scheelite in our study consisted of 90 samples from a variety of geologic environments. Concentrations of potential luminescence impurities in several samples are presented in Table 4.5.

For comparison, steady-state cathodoluminescence spectra (Fig. 4.7) are presented from two scheelite samples with different rare-earth elements concentrations (Table 4.5). It is clearly seen that only broadband emissions are detected, while the narrow lines of several rare-earth elements, mostly Sm^{3+} are extremely weak.

For the correct interpretation of the luminescent bands, artificial standards have been investigated, as nominally pure, as activated by different potential luminogen impurities. Stoichiometric mixtures of $Na_2WO_4.2H_2O$ and $CaCl_2$, together with the REE chloride of interest, were kept for 2 h at 900 °C in open quartz test-tubes filled with molten NaCl, and then where slowly cooled over 20 h. After washing with distilled water, the colorless crystals of scheelite were obtained, 0.01–0.5 mm in size. By using laser-induced time-resolved spectroscopy we were able to detect and ascribe various trivalent rare-earth impurities, such as Sm^{3+}, Dy^{3+}, Eu^{3+}, Pr^{3+}, Er^{3+}, Tm^{3+}, Ho^{3+}, Nd^{3+} and Yb^{3+} (Figs. 4.8–4.9).

Table 4.5. Concentrations of rare-earth elements in several scheelites (ppm)

	Pr	Sm	Eu	Nd	Dy	Tb	Er	Tm	Ho	Gd	Ce	Yb
ZRK	129	134	11	589	41	9	20	2	8	72	832	
FRS	11	10	35	42	13	2	8	1	2	11	100	
BR7	20	120	75	160	120	25	25	2	15	175		8

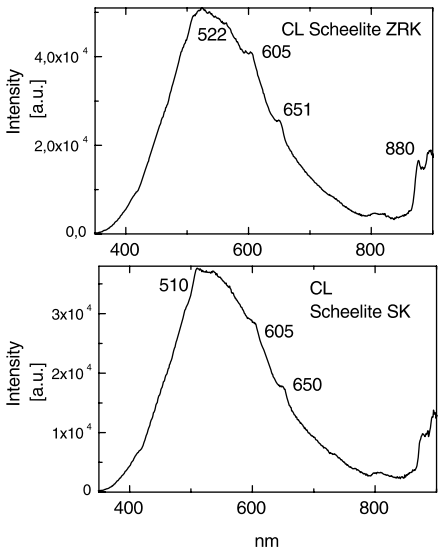

Fig. 4.7. Steady-state cathodoluminescence spectra of scheelite samples

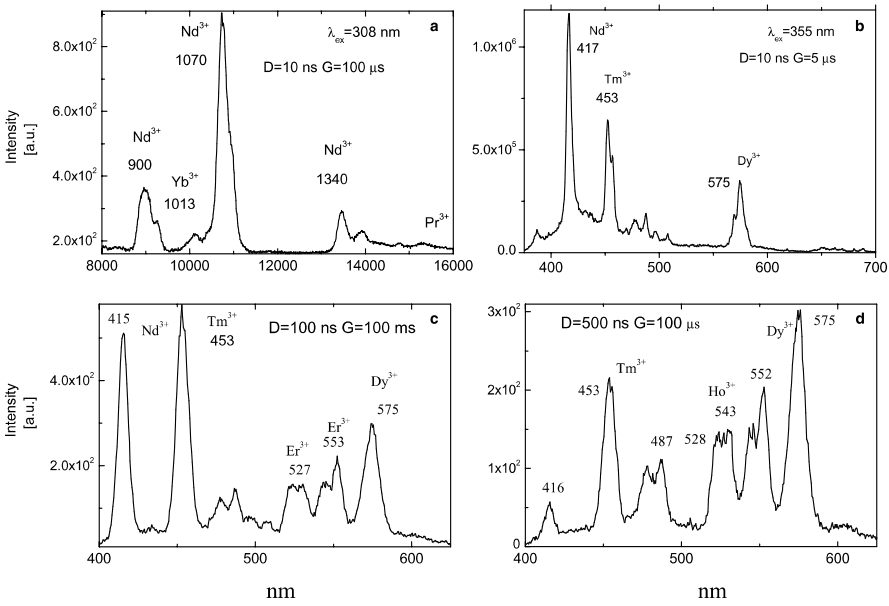

Fig. 4.8. **a–d** Laser-induced time-resolved luminescence spectra of scheelite demonstrating Nd^{3+}, Yb^{3+}, Tm^{3+}, Ho^{3+}, Er^{3+} and Dy^{3+} centers

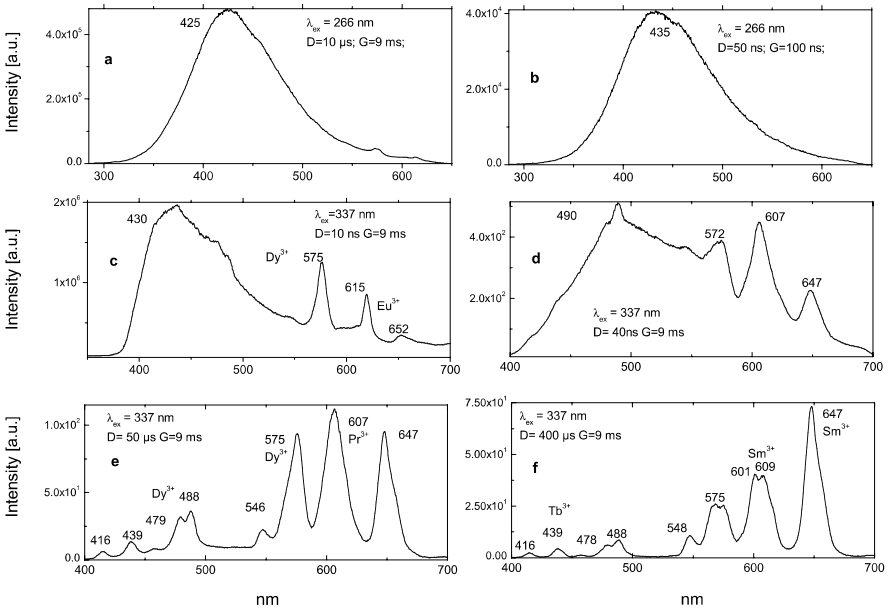

Fig. 4.9. **a–f** Laser-induced time-resolved luminescence spectra of scheelite demonstrating intrinsic, Eu^{3+}, Tb^{3+}, Pr^{3+} and Sm^{3+} centers

4.1.3 Fluorite CaF_2

Fluorite is calcium fluoride, CaF_2, with a cubic face-centered lattice, while each fluorine ion is at the center of one of the smaller cubes obtained by dividing the unit cube into eight parts. Each Ca is coordinated by eight F ions and each F is surrounded by four Ca ions arranged at the corners of a regular tetrahedron.

All varieties of color are mainly connected with two main absorption bands in the violet and yellow parts of the spectrum. The secondary bands are also present – in blue and green diapasons. The main absorption bands are connected with F and M-centers. The first one is anion vacancy, which traps electrons and the second is two neighboring anion vacancies with two trapped electrons. The short-wave band in fluorite is generated by mutual absorption of F and M-centers, while the long-wave band is connected with M-center absorption only. In the green varieties the REE (Sm^{2+}, Yb^{2+} and Dy^{2+}) are also appreciable. Besides that, the centers O_2^-, O_3^- and (Y, TR)O_2 sometimes have influence with resulting yellow and pink colors (Platonov 1979; Krasilschikova et al. 1986).

Fluorite was the first material where Stokes proved that the blue emission excited by UV light had a longer wavelength and was not diffuse light. For this reason he called the blue light fluorescence (quoted in Pringsheim and Vogel 1946). Fluorite is a reservoir for many of the rare earths and their luminescence has been carefully studied (Haberland et al. 1934; Haberland et al. 1939; Tarashchan 1978; Krasilschikova et al. 1986; Kempe et al. 2002). Under UV excitation fluorite usually emits violet fluorescence, which is connected with impurity of Eu^{2+}. Such emission is extremely strong and other centers are not detected. In very rare cases when Eu concentration is unusually low, other centers dominate, for example, Dy^{3+} and emission color becomes yellow (Aierken et al. 2003). Nevertheless, the decay time of Eu^{2+} is 600–800 ns and a delay of 1–5 µs makes it possible to quench it and to see the characteristic lines of other rare-earth elements previously undetected.

The fluorite in our study consisted of 40 samples from different environments. Concentrations of luminescence impurities in several samples are given in Table 4.6. By using laser-induced time-resolved spectroscopy we were able to detect and ascribe the following emission centers: Eu^{2+}, Ce^{3+}, Gd^{3+}, Sm^{3+}, Dy^{3+}, Eu^{3+}, Pr^{3+}, Er^{3+}, Tm^{3+}, Ho^{3+}, Nd^{3+}, Mn^{2+} and the M-center (Figs. 4.10–4.12).

4.1.4 Calcite and Aragonite $CaCO_3$

Calcite is a calcium carbonate, $CaCO_3$, with a rhombohedral cell consisting of the large planar CO_3 groups, which contain a Ca ion at the center of an

Table 4.6. Concentrations of rare-earth elements in several fluorites (ppm)

	Pr	Sm	Eu	Nd	Dy	Tb
Russia	0.3	0.3	0.3	1.0	0.4	0.1
DNT	5.0	12.0	6.5	26.0	27.0	4.0
FLS	57	200	28	370	350	55
UCB	0.1	0.3	–	0.5	0.3	

	Er	Tm	Ho	Gd	Ce	Yb
8	0.2	–	0.1	0.3	2.6	
DNT	14.0	1.7	5.5	22.0	33	
FLS	220	35	70	280	280	260
UCB	0.2	–	0.1	0.3	0.3	0.1

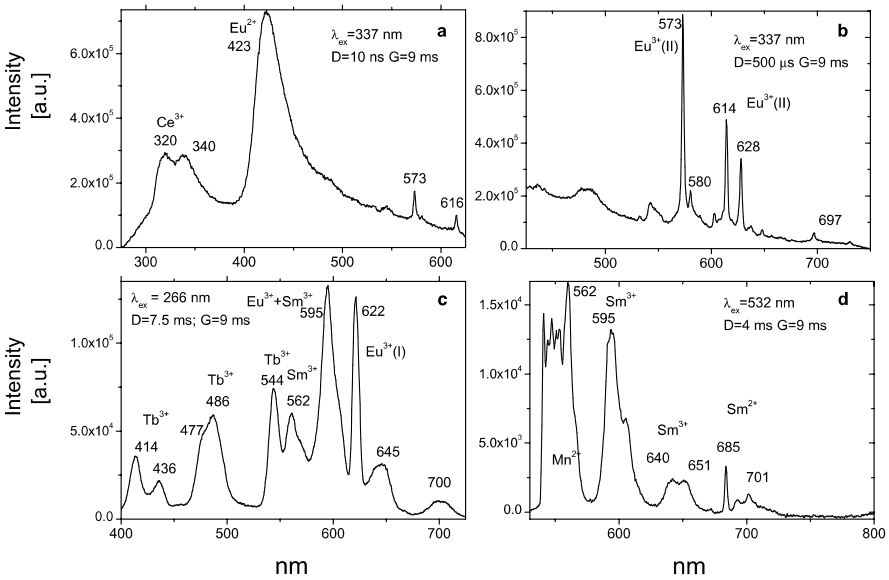

Fig. 4.10. **a–d** Laser-induced time-resolved luminescence spectra of fluorite demonstrating Ce^{3+}, Eu^{2+}, two types of Eu^{3+}, Sm^{3+}, Sm^{2+} and Tb^{3+} centers

equilateral triangle of oxygens (symmetry 3 2/*m*). The structure of calcite is analogous to that of halite NaCl if we consider the unit cube of halite to be shortened along one trigonal axis.

The color of calcite can be due to its iron content, which is present as Fe^{2+}, to Mn^{2+}, to radiation damage centers, which often involve rare earth

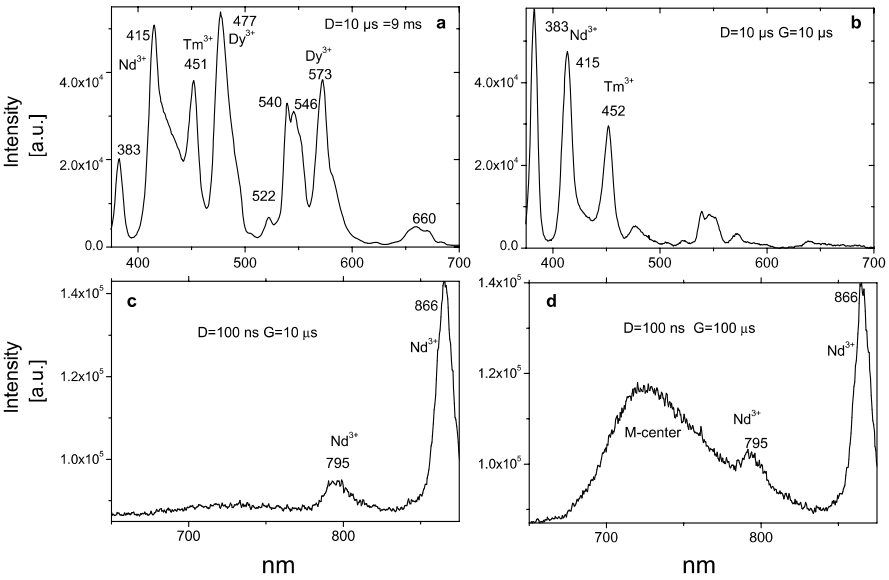

Fig. 4.11. **a–d** Laser-induced time-resolved luminescence spectra of fluorite demonstrating Tm^{3+}, Dy^{3+}, Nd^{3+} and M centers

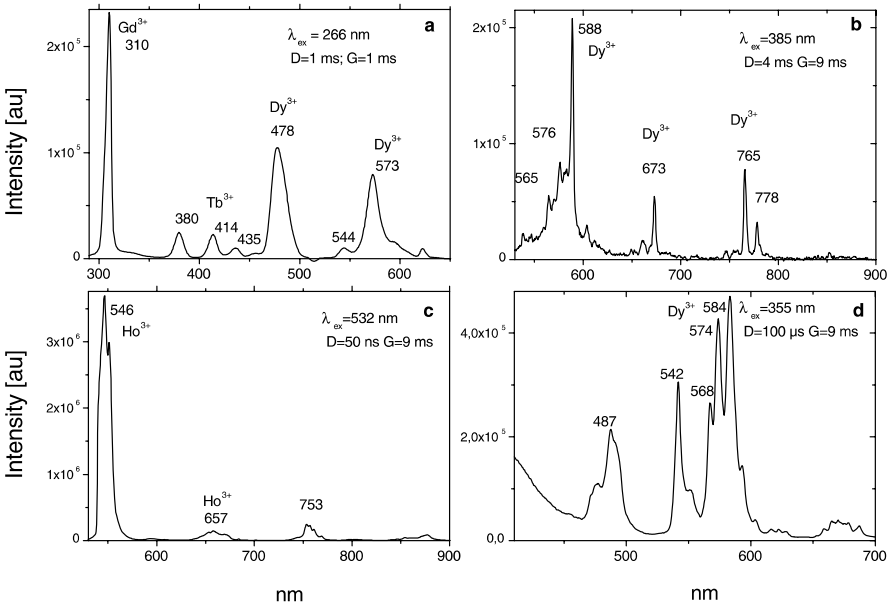

Fig. 4.12. **a–d** Laser-induced time-resolved luminescence spectra of fluorite demonstrating Gd^{3+}, Dy^{3+}, Sm^{3+} and Ho^{3+} centers

or other elements, or occasionally to other elements such as Co^{2+}. The color of rhodochrosite is due to its Mn^{2+} content. Most minerals with Mn^{2+} in six-coordination are pale pink. Because Mn^{2+} does not absorb light strongly, a mineral must have a high Mn^{2+} concentration to be strongly colored by Mn^{2+} (Platonov 1979).

In nature, RE and Mn^{2+} can substitute for Ca, becoming luminescence centers in the crystallographic environment. Most calcite luminescence is attributed to Mn^{2+}, while Mn^{2+} hides rare earth emission, and so far their luminescence in calcite is rather poorly characterized (Blasse and Aguilar 1984; Pedone et al. 1990). Only recently the lines of Sm^{3+} and Dy^{3+} have been confidently established using a hot cathode cathodoluminescence method (Haberman et al. 1996). Besides that, luminescence of Pb^{2+} (Tarashchan 1978) and radiation-induced CO_3^{3-} are known (Kasyanenko and Matveeva 1987). The natural calcite in our study consisted of 30 samples from a variety of geologic environments. Concentrations of potential luminescence impurities in several samples are presented in Table 4.7. By using laser-induced time-resolved spectroscopy we were able to detect the following emission centers: Pb^{2+}, Mn^{2+}, Ce^{3+}, Sm^{3+}, Dy^{3+}, Eu^{3+}, Tb^{3+}, Tm^{3+}, Nd^{3+} and a radiation-induced center (Figs 4.13–4.14).

Table 4.7. Concentrations of rare-earth elements and manganese in calcites (ppm)

	Pr	Sm	Eu	Nd	Dy	Tb	Er
ST1E	5	4	22	18	6	1	2
Franclin	3.3	3.9	0.7	15	7.8	1	
Red	28	17	2.5	92	15	3	9

	Tm	Ho	Gd	Ce	Mn	Pb
ST1E	0.5	1	6	41	6,300	
Franclin	0.7	2	6	22	6,700	450
Red	1.2	3	21	250	113	9.4

Aragonite is a polymorph of calcite, which means that it has the same chemistry as calcite but it has a different structure, and more importantly, different symmetry and crystal shapes. Aragonite's more compact structure is composed of triangular carbonate ion groups (CO_3), with a carbon at the center of the triangle and the three oxygens at each corner. Aragonite has an orthorhombic symmetry (2/*m* 2/*m* 2/*m*) instead of calcite's "higher" trigonal (bar 3 2/*m*) symmetry.

The natural aragonite in our study consisted of 12 samples from a variety of geologic environments. By using laser-induced time-resolved spectroscopy we were able to detect the following emission centers: Mn^{2+}, Sm^{3+} and Dy^{3+}.

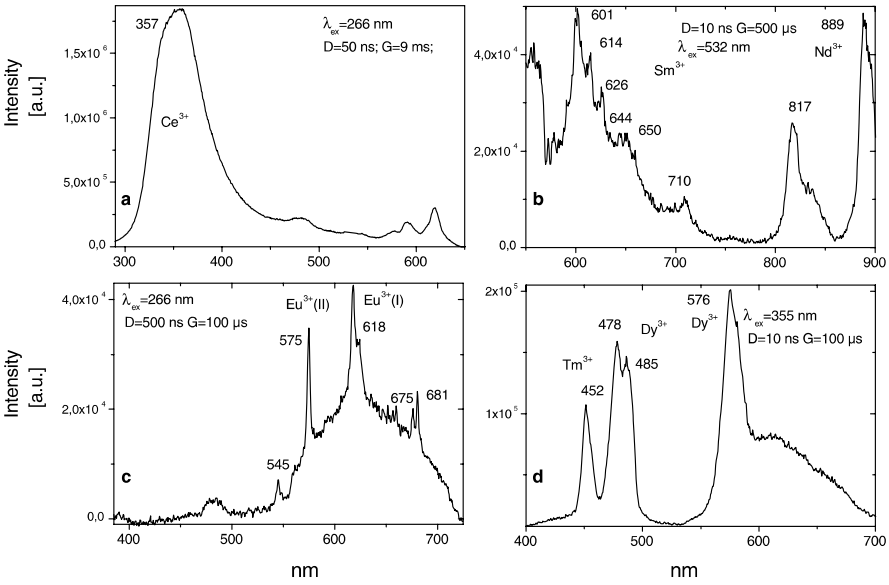

Fig. 4.13. **a–d** Laser-induced time-resolved luminescence spectra of calcite demonstrating Ce^{3+}, Eu^{3+}, Tm^{3+}, Nd^{3+} and Dy^{3+} centers

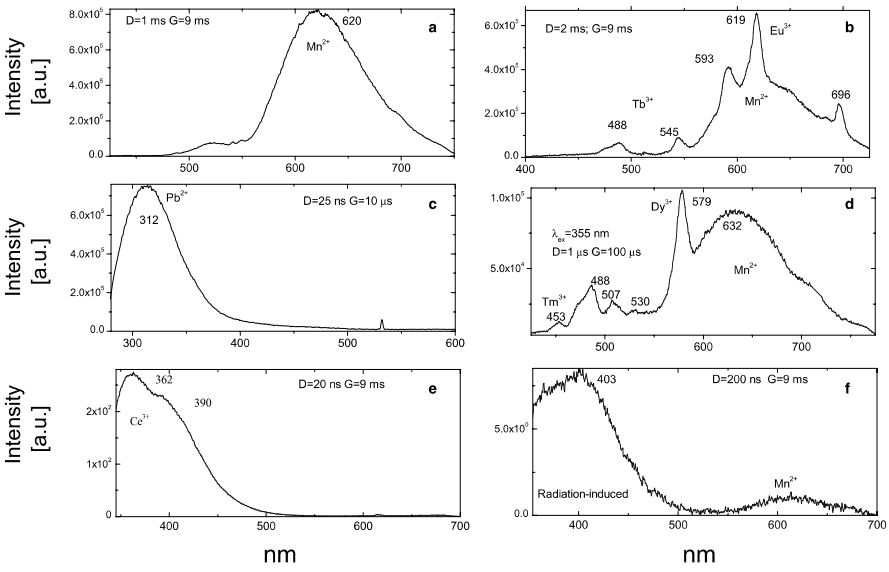

Fig. 4.14. **a–f** Laser-induced time-resolved luminescence spectra of calcite demonstrating Mn^{2+}, Pb^{2+} and radiation-induced centers

4.1.5
Danburite $CaB_2(SiO_4)_2$

Danburite is calcium borosilicate with an orthorhombic structure (2/*m*2/*m*2/*m*) and space group Pnam. The natural danburite in our study consisted of five samples from a variety of geologic environments. Concentrations of potential luminescence impurities in one sample are presented in Table 4.8.

Table 4.8. Concentrations of rare-earth elements in danburite and datolite (ppm)

	Pr	Sm	Eu	Nd	Dy	Tb	Er	Tm	Ho	Gd	Ce
Danburite	0.3	0.2	1.0	1.0	0.1	–	–	–	–	0.1	3
Datolite	3.0	2.0	0.5	11.0	1.0	0.2	0.7	0.1	0.2	1.7	22.0

The luminescence centers Eu^{2+}, Yb^{2+}, Ce^{3+}, Dy^{3+}, and Sm^{3+} characterize the steady-state spectra of danburite (Gaft et al. 1979; Gaft 1989). By using laser-induced time-resolved spectroscopy we were able to detect the following emission centers: Ce^{3+}, Eu^{2+}, Eu^{3+}, Sm^{3+}, Dy^{3+} (Fig. 4.15)

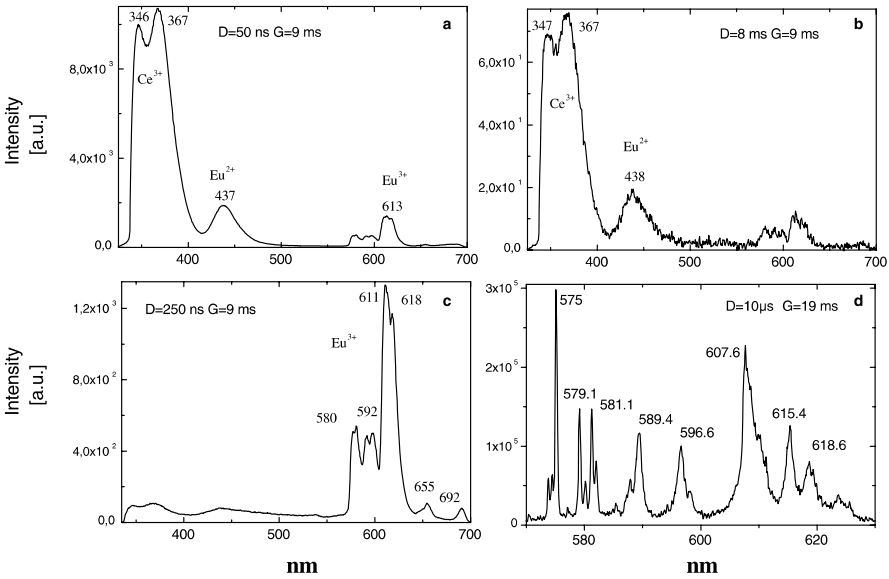

Fig. 4.15. a–d Laser-induced time-resolved luminescence spectra of danburite demonstrating Ce^{3+}, Eu^{2+} and Eu^{3+}

4.1.6
Datolite $CaB(SiO_4)(OH)$

Datolite is calcium borosilicate with a monoclinic structure (2/*m*) and space group $P2_1/c$. It consists of superimposed complex sheets of linked oxygen and O, OH tetrahedra around silicon and boron atoms respectively: the SiO_4 and $B(O,OH)_4$ tetrahedra alternate, forming rings of four and eight tetrahedra. The natural datolite in our study consisted of seven samples from a variety of geologic environments.Concentrations of potential luminescence impurities in one sample are presented in Table 4.8.

Luminescence centers Eu^{2+}, Yb^{2+}, and Mn^{2+}, characterize the steady-state spectra of danburite. By using laser-induced time-resolved spectroscopy we were able to detect the following emission centers: Mn^{2+}, Ce^{3+}, Eu^{2+}, Eu^{3+}, Sm^{3+}, Dy^{3+} (Fig. 4.16).

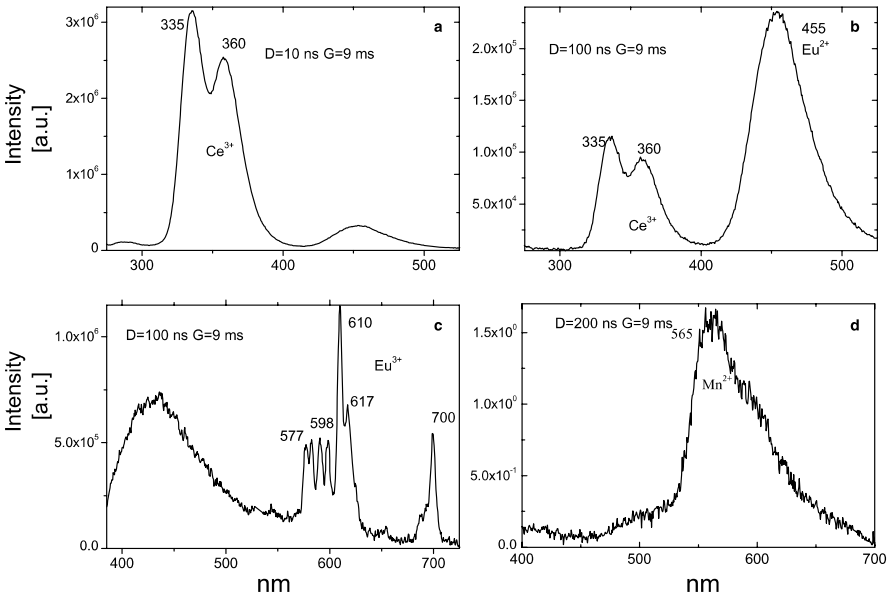

Fig. 4.16. **a–d** Laser-induced time-resolved luminescence spectra of datolite demonstrating Mn^{2+}, Ce^{3+}, $Eu^{2+}$and Eu^{3+} centers

4.1.7
Anhydrite $CaSO_4$

Anhydrite is a calcium sulfate, $CaSO_4$, with an orthorhombic structure (*mmm*) where sulfur atoms, which are at the centers of tetrahedra of oxygens, and calcium atoms lie on the lines of intersection of mirror planes (100) and (010). In nature, REE and Mn can easily substitute for Ca, becoming luminescence

centers in such a crystallographic environment. X-ray excited and CL spectroscopies have established the luminescence of Gd^{3+}, Ce^{3+}, Eu^{2+}, Er^{3+}, Sm^{3+}, Pr^{3+}, Tb^{3+}, and Dy^{3+}, while PL spectroscopy has established Sm^{2+} (Tarashchan 1978; Baumer et al. 1997).

The natural anhydrite in our study consisted of five samples from a variety of geologic environments. Concentrations of potential luminescence impurities in one sample are presented in Table 4.9.

Table 4.9. Concentrations of rare-earth elements in anhydrite (ppm)

Pr	Sm	Eu	Nd	Dy	Tb	Er	Tm	Ho	Gd	Ce
0.3	0.6	0.3	1.7	0.7	0.2	0.4	0.1	0.2	0.8	2.3

By using laser-induced time-resolved spectroscopy we were able to detect the following emission centers: Mn^{2+}, Sm^{2+}, Sm^{3+}, Dy^{3+}, Eu^{2+} and Eu^{3+} (Figs. 4.17–4.18).

4.1.8 Apophyllite $Ca_4KF(Si_8O_{20})x8H_2O$

Apophyllite is an uncommon mineral, which is of interest largely because of its unusual atomic structure: this bears some relationship to that of the micas

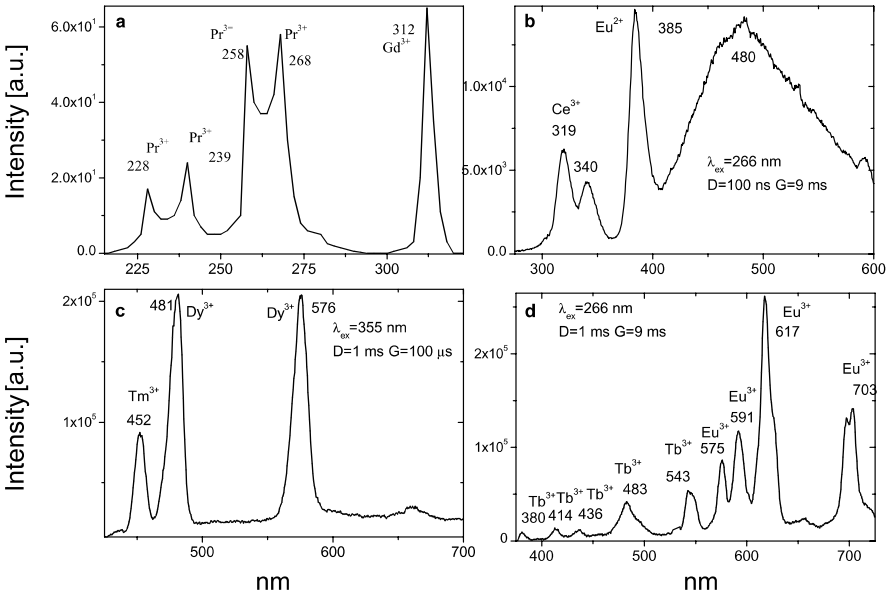

Fig. 4.17. a–d Laser-induced time-resolved luminescence spectra of anhydrite demonstrating Gd^{3+}, Ce^{3+}, Eu^{2+}, Eu^{3+}, Pr^{3+}, Tm^{3+}, Tb^{3+} and Dy^{3+} centers

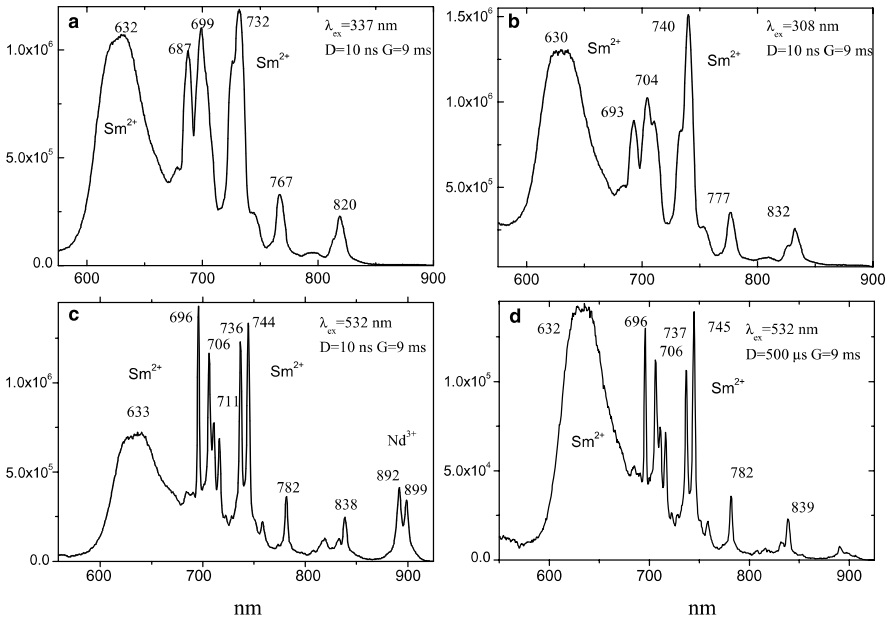

Fig. 4.18. a–d Laser-induced time-resolved luminescence spectra of anhydrite demonstrating Sm^{2+} centers

since a basic part of it is a sheet of composition Si_8O_{20}. Instead of forming an approximately hexagonal network, however, the (Si–O) tetrahedra are arranged in four-fold and eight-fold rings, and alternate rings of four tetrahedra point in opposite directions. Between the sheets of tetrahedra lie K, F, Ca ions and water molecules. The structure is characterized by an eight-fold tetragonal-prismatic potassium site and a seven-fold capped trigonal-prismatic calcium site.

Two different Mn^{2+} luminescence centers have been found in steady-state spectra of apophyllite: in the Ca position with orange luminescence peaking at 620 nm and in the K position with green emission peaking at 500 nm (Tarashchan 1978). The apophyllite in our study consisted of three samples from different environments. The laser-induced time-resolved technique enables us to detect the following emission centers: Ce^{3+}, Mn^{2+} with orange emission and possibly $(UO_2)^{2+}$ (Fig. 4.19).

4.1.9
Hardystonite $Ca_2ZnSi_2O_7$

Hardystonite is a calcium zinc silicate of the melilite group. The crystal structure is tetragonal ($P42_1m$) consisting of $[Zn_2Si_2O_7]$ sheets within which the nature of the bonding is dominantly covalent, with the adjacent sheets being held together by Ca^{2+} ions. The melilite group is composed of minerals of the general formula $X_2YZ_2O_7$ where X is Ca or Na, Y is Al or Mg and Z is Si. X is

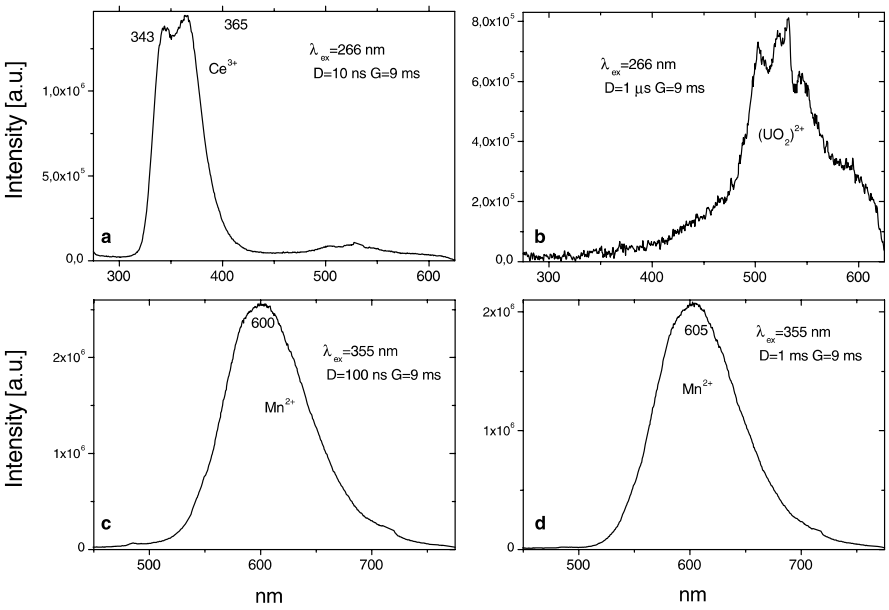

Fig. 4.19. a–d Laser-induced time-resolved luminescence spectra of apophyllite demonstrating Ce^{3+}, $Mn^{2+}$and $(UO_2)^{2+}$ centers

a large 8-coordinated site. Luminescence properties of hardystonite have been not studied. The natural hardystonite in our study consisted of three samples. Concentrations of potential luminescence impurities in one sample are presented in Table 4.10. The laser-induced time-resolved technique enables us to detect the following emission centers: Gd^{3+}, Ce^{3+}, Mn^{2+}, Pb^{2+}, Tb^{3+}, Tm^{3+} and Dy^{3+} (Fig. 4.20).

Table 4.10. Concentrations of rare-earth elements in hardystonite sample (ppm)

	Pr	Sm	Eu	Nd	Dy	Tb	Er	Tm	Ho	Gd	Ce	Yb
NJ	9.7	9.2	1.3	43.5	7.5	1.4	2.5	0.2	0.1	11	55	0.8

4.1.10 Esperite $Ca_3PbZn_4(SiO_4)_4$

Esperite is a calcium lead zinc-silicate mineral. The crystal structure is monoclinic-prismatic ($P21/m$) with a $B21/m$ group. Steady-state laser-induced luminescence of esperite was ascribed to Mn^{2+} in Zn and Ca positions, accompanied by Dy^{3+} and Sm^{3+} lines. Besides that reabsorption lines of Nd^{3+} and U^{4+} have been found (Gorobets and Rogojine 2001). The laser-induced time-resolved

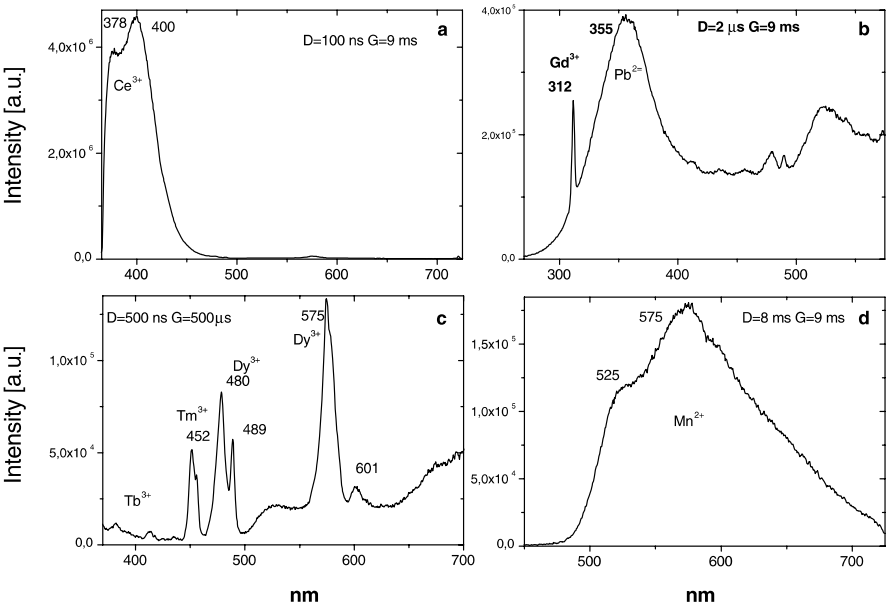

Fig. 4.20. **a–d** Laser-induced time-resolved luminescence spectra of hardystonite demonstrating Ce^{3+}, Pb^{2+}, Tm^{3+}, Dy^{3+} and Mn^{2+} centers

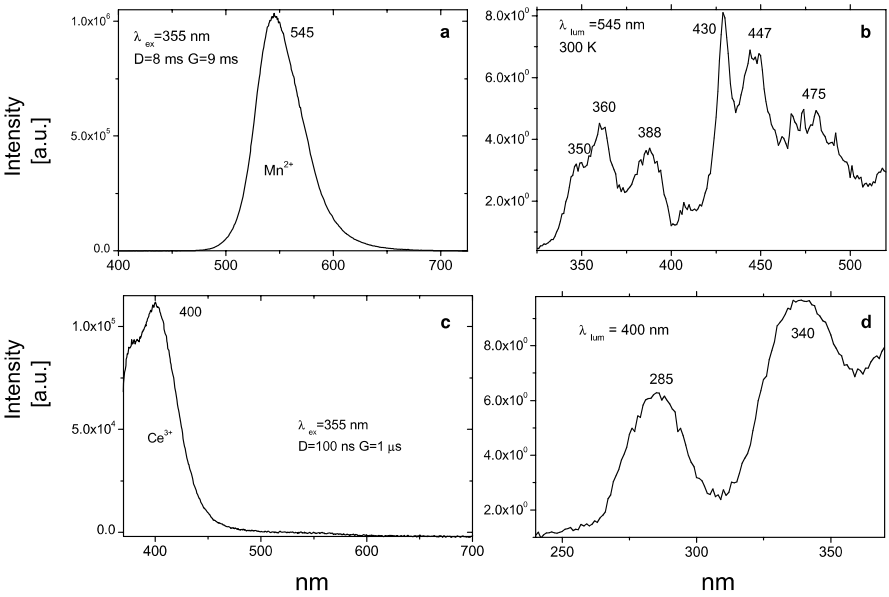

Fig. 4.21. **a, c** Laser-induced time-resolved luminescence spectra of esperite demonstrating Ce^{3+} and Mn^{2+} centers. **b, d** Excitation spectra of Mn^{2+} and Ce^{3+}

technique enables us to detect Ce^{3+} and a green band of Mn^{2+} evidently in a Zn position (Fig. 4.21).

4.1.11
Charoite $K_2NaCa_5(Si_{12}O_{30})Fx3H_2O$

The structure of charoite is monoclinic-prismatic (2/*m*) with space group *P**/4. Luminescence centers Ce^{3+}, Eu^{2+} and Mn^{2+} characterize the steady-state spectra of charoite (Gaft 1989; Gorobets and Rogojine 2001).

The natural charoite in our study consisted of one sample. The laser-induced time-resolved technique enables us to detect the Ce^3 and Eu^{2+} luminescence centers (Fig. 4.22).

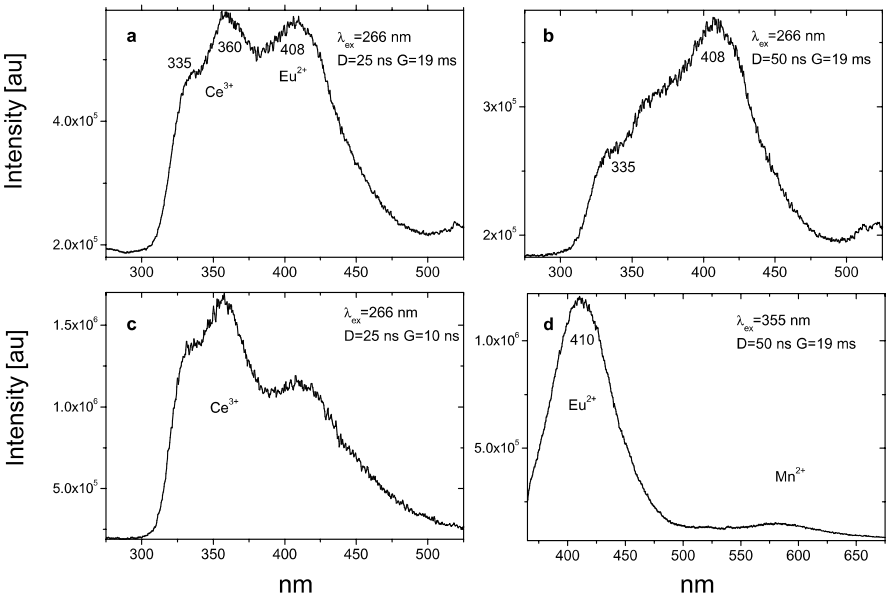

Fig. 4.22. **a–d** Laser-induced time-resolved luminescence spectra of charoite demonstrating Ce^{3+} and Eu^{2+} centers

4.1.12
Prehnite $Ca_2Al_2Si_3O_{10}(OH)_2$

Prehnite is sheet silicate with orthorhombic structure (*mm*2). Luminescence properties of prehnite have not been studied. The natural prehnite in our study consisted of two samples. The laser-induced time-resolved technique enables us to detect emission center Pb^{2+} (Fig. 4.23).

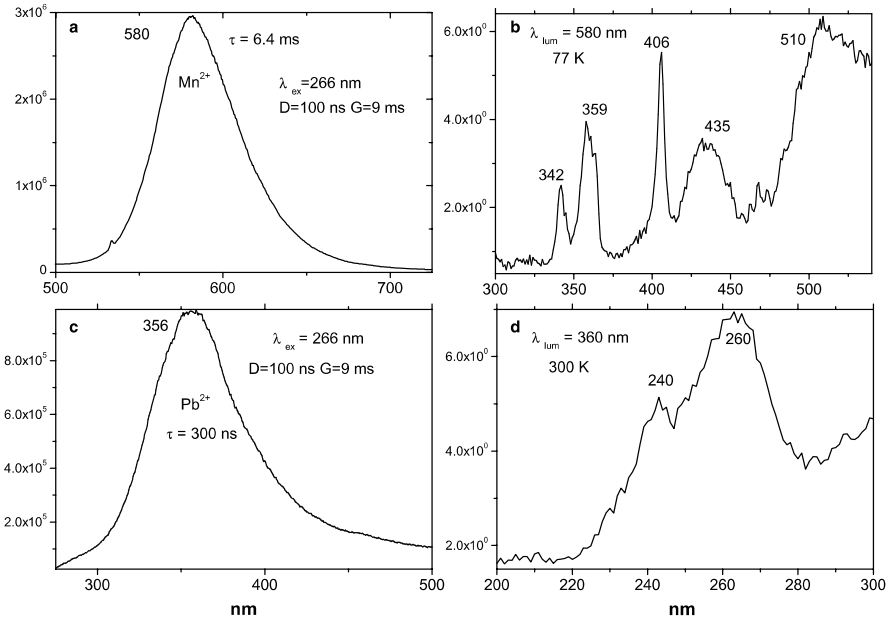

Fig. 4.23. **a, c** Laser-induced time-resolved luminescence spectra of Mn^{2+} in pectolite and Pb^{2+} in prehnite. **b, d** Excitation spectra of pectolite demonstrating Mn^{2+} and Pb^{2+}

4.1.13
Pectolite $NaCa_2Si_3O_8(OH)$

Pectolite is a hydrous pyroxenoid with a triclinic-pinacoidal structure and space group *P*-1. The structure of pectolite is based on single Si–O chains in a sequence of alternate single and double tetrahedral groups similar to that found in wollastonite. The Ca atoms are coordinated by oxygen octahedra sharing edges to form a lath-like strip, while the Na atoms have trigonal pyramidal coordination and these pyramids also share edges with those of the Ca octahedra. Luminescence center Mn^{2+} characterizes steady-state spectra of pectolite (Gorobets and Rogojine 2001). The natural pectolite in our study consisted of one sample. The laser-induced time-resolved technique enables us to detect a Mn^{2+} emission center (Fig. 4.23).

4.1.14
Pyrochlore $(Ca,Na)_2Nb_2O_6(OH,F)$

The structure of pyrochlore is considered to be an anion deficient derivative of the fluorite structure type. Ca atoms are in eight-fold coordination, while Nb atoms are in six-fold coordination. Steady-state luminescence spectra of pyrochlore revealed emission of REE, such as trivalent Dy and Nd (Gorobets and Rogojine 2001). The natural pyrochlore in our study consisted of four

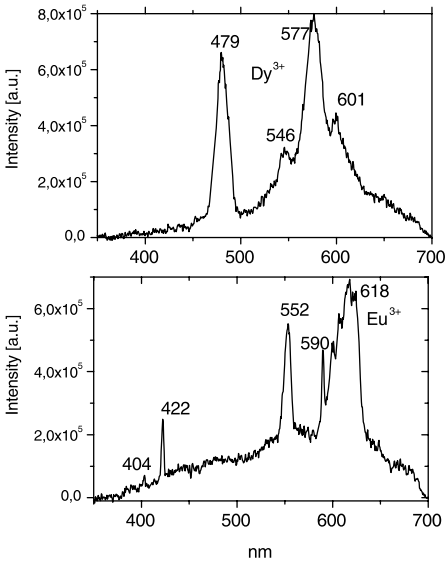

Fig. 4.24. Laser-induced time-resolved luminescence spectra of pyrochlore demonstrating Dy^{3+} and Eu^{3+} centers

samples. The laser-induced time-resolved technique enables us to detect Sm^{3+}, Dy^{3+}, Tb^{3+}, Eu^{3+} and Nd^{3+} emission centers (Fig. 4.24).

4.1.15
Leucophane $NaCaBe(Si_2O_6)F$

Leucophane is a relatively rare beryllium silicate. Of interest are the trace amounts of rare earth elements in its chemistry, especially cerium which substitutes for some calcium. Its true symmetry is triclinic, pedion class which is the lowest symmetry possible in a three dimensional system. The only symmetry element is translational shift as it lacks any mirrors, rotations, or even a center. The symmetry is noted by a **1.** Ce^{3+}, Eu^{2+}, Sm^{3+}, Dy^{3+}, Tb^{3+}, Nd^{3+} and Mn^{2+} centers characterize steady-state luminescence spectra of leucophane (Gorobets and Rogojine 2001). Time-resolved luminescence spectra contain additionally Eu^{3+} and Tm^{3+} centers (Fig. 4.25).

4.2
Lead (Pb^{2+}) bearing minerals

Minerals of leads are principally capable of intrinsic luminescence. The main substituting luminescence centers are TR^{2+} (Eu), TR^{3+} (Ce, Sm, Eu, Dy). Ionic radii of Pb^{2+} are 1.33 Å in 6-coordinated form and 1.43 Å in 8-coordinated form, while the ionic radius of Eu^{2+} is 1.31 Å and the ionic radii of TR^{3+} change from 1.00 Å to 1.13 Å.

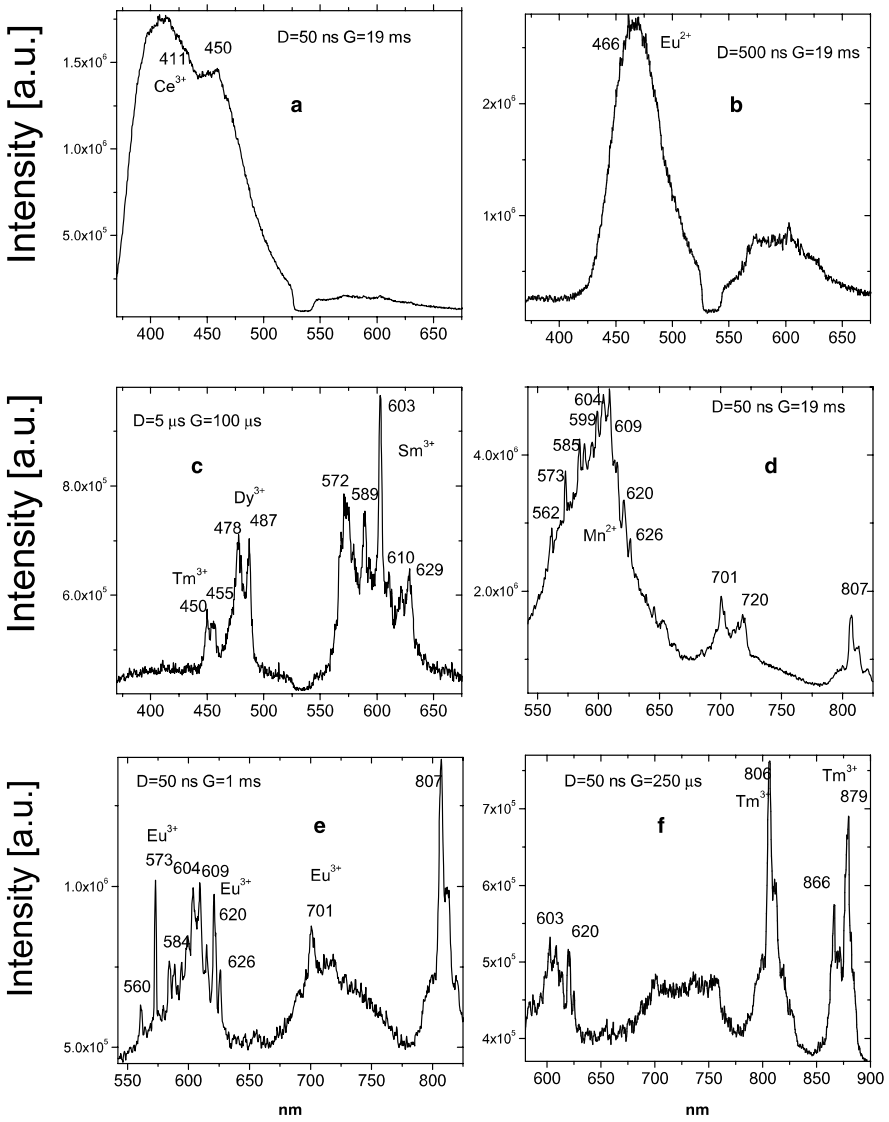

Fig. 4.25. **a–f** Laser-induced time-resolved luminescence spectra of leucophane under 355 nm (**a–c**) and 532 nm (**d–f**) excitations demonstrating Ce^{3+}, Eu^{2+}, Eu^{3+}, Tm^{3+}, Dy^{3+}, Sm^{3+} and Mn^{2+}

4.2.1 Pyromorphite $Pb_5(PO_4)_3Cl$

Pyromorphite belongs to the apatite group. This group is divided into two series, the apatite series and pyromorphite series. These minerals are isostructural, however the unit cell volume of pyromorphite is about one-fifth larger

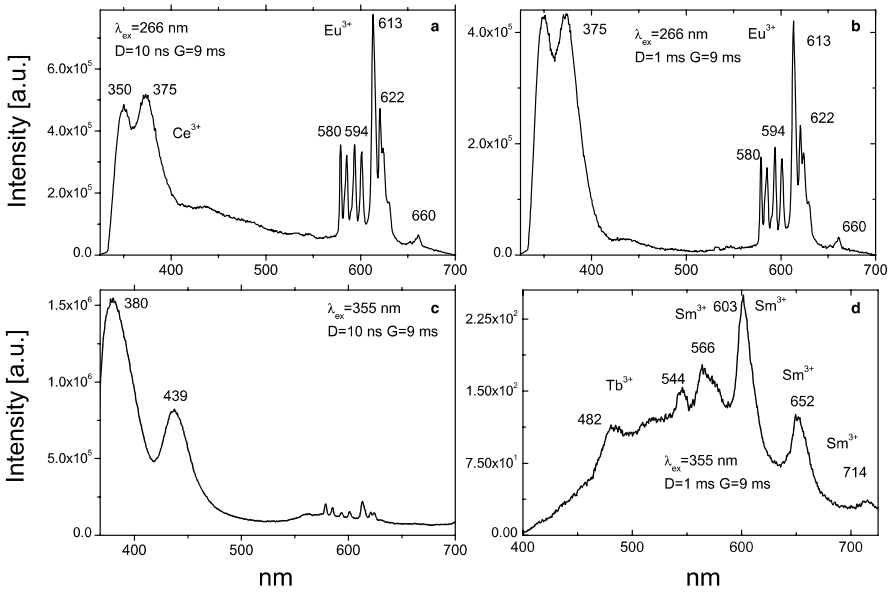

Fig. 4.26. **a–d** Laser-induced time-resolved luminescence spectra of pyromorphite demonstrating Ce^{3+}, Eu^{3+}, Tb^{3+}, Sm^{3+} and possibly Pb^{2+}centers

than that of apatite. Luminescence centers O_2^- (Tarashchan 1978) and evidently $(VO_4)^{3-}$ (Gaft 1984; Gaft 1989) characterize steady-state spectra of pyromorphite. The natural pyromorphite in our study consisted of two samples. The laser-induced time-resolved technique enables us to detect Ce^{3+}, Eu^{3+}, Sm^{3+} and Tb^{3+} emission centers (Fig. 4.26).

4.3 Tin (Sn^{4+}) Bearing Minerals

Minerals of tin are capable of intrinsic luminescence, possibly connected with defect centers containing Sn^{2+}. The ionic radius of Sn^{4+} is of 0.83 Å and the possible substituting luminescence center is Ti^{4+} with an ionic radius of 0.75 Å.

4.3.1 Cassiterite SnO_2

The structure of cassiterite resembles that of rutile TiO_2, each tin ion being surrounded by six oxygen ions approximately at the corners of a regular octahedron, and each oxygen having three tin ions around it forming a nearly equilateral triangle.

The considerable zonation was found in CL of cassiterite with respect to W and Ti. It was concluded that W is responsible for blue luminescence,

while Ti is responsible for yellow luminescence (Waychunas 1989). Steady-state photoluminescence of natural cassiterite and artificial SnO_2 was also studied. Under UV lamp excitation cassiterite samples are luminescent only at low temperatures, starting from 77 K. The luminescence center was found to be related to intrinsic centers, namely to Sn of diverse valence (Sn^{2+}, Sn^{3+}) (Gaft and Vorontzova 1982; Gaft et al. 1982). Under powerful UV laser excitation cassiterite has luminescence even at room temperature with a spectrum that is similar to those at 77 K with lamp excitation. The decay time of luminescence has two components, namely 100 ns and 280 ns (Gaft et al. 1988; Gaft 1989).

The natural cassiterite in our study consisted of six samples. The laser-induced time-resolved technique enables us to detect emission centers similar to those in the steady-state technique (Fig. 4.27).

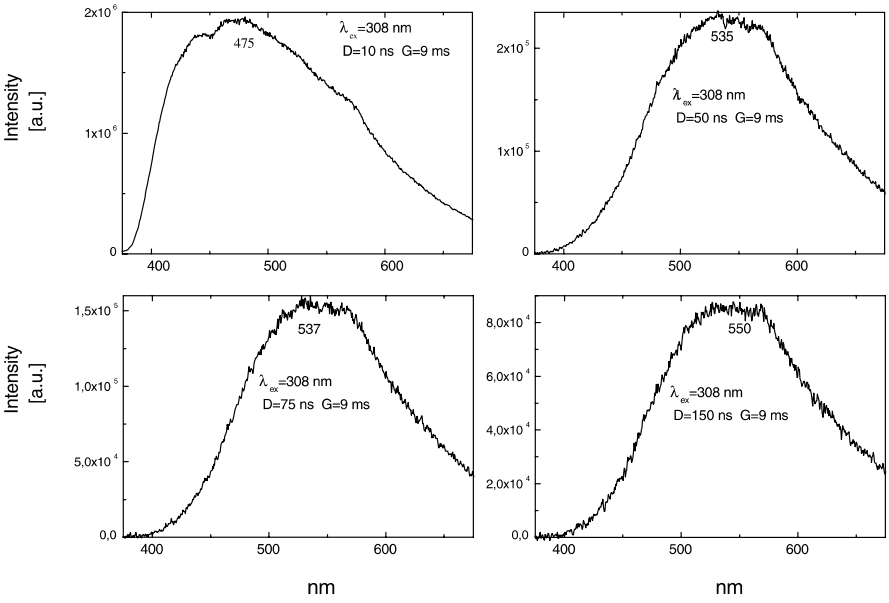

Fig. 4.27. Laser-induced time-resolved luminescence spectra of cassiterite demonstrating intrinsic, possibly Sn^{2+} centers

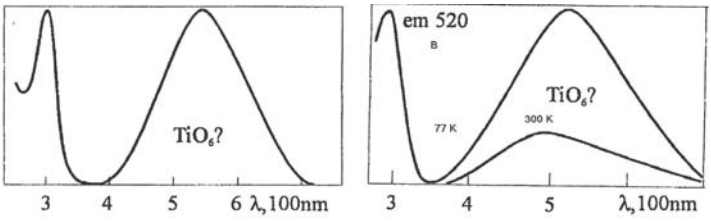

Fig. 4.28. a,b Luminescence (*right*) and excitation (*left*) spectra of malayaite (**a**) and sorensenite (**b**) (Gaft et al. 1982)

Other tin minerals with luminescence are malayaite $CaSn(SiO_5)$ and sorensenite $Na_4SnBe_2Si_6O_{18}x2H_2O$, where emission centers (Fig. 4.28) are evidently Ti impurities (Gaft et al. 1982).

4.4 Barium (Ba^{2+}) Bearing Minerals

Ionic radii of Ba^{2+} are of 1.49 Å in 6-coordinated form and 1.56 Å in 8-coordinated form. The main substituting luminescence centers are Bi^{3+} with an ionic radius of 1.49 Å and 1.56 Å in 6-coordinated and 8-coordinated forms, respectively, Ag^{+} with ionic radii of 1.29 Å and 1.42 Å in 6-coordinated and 8-coordinated forms, respectively, Cu^{+} with an ionic radius of 0.91 Å in 6-coordinated form, Eu^{2+} with an ionic radius of 1.31 Å, Ce^{3+} with an ionic radius of 1.15 Å and other TR^{3+}.

4.4.1 Barite $BaSO_4$

Barite is a barium sulfate, $BaSO_4$, with orthorhombic structure (2/*m*2/*m*2/*m*) where the sulfur is situated in tetrahedral coordination with oxygen, and barium in twelve-fold coordination with oxygen. The mineral barite is one of the first luminescent materials from which the famous "Bologna stone" was obtained. Nevertheless, up to today understanding of natural barite luminescence

Table 4.11. Concentrations of rare-earth elements in barite samples (ppm)

Origin	Ag	Bi	Cu	Ti	Fe	Mn
Spain	–	–	3.5	0.5	75	6.0
France 1	1.5	–	3.3	2.7	950	3.5
France 2	21	–	5.0	–	45	2.1
France 3	4	–	3.6	1.3	230	6.5
Romany	0.4	–	1.2	1.0	70	2.2
England	0.6	–	5.7	1.7	120	13.0

Origin	Al	Pb	Sn	U	Sr
Spain	20	1.0	–	0.2	1,180
France 1	5.0	62	–	0.1	760
France 2	120	1.5	–	–	685
France 3	60	0.8	–	0.2	590
Romany	–	1.0	1.5	–	10,300
England	200	9,500	–	2.0	390

is very scarce. It has been known for a long time that some specimens of barite are fluorescent under UV exposure and emit white, yellow, green or orange light. In steady-state luminescence spectra of barite different luminescence bands from the UV to the red part of the spectrum have been detected. However, only UO_2^{2+} and Eu^{2+} luminescence centers have been confidently identified (Tarashchan 1978; Gaft et al. 1985; Gaft 1989).

Barite that is colorless is pure, but radiation damage centers commonly cause color. For example, O^- (in some blue crystals), SO_3^- (in some honey-yellow and blue crystals), and SO_2^- (in yellow crystals) centers have been identified in barite.

The natural barite in our study consisted of twenty-five samples of different origin. Concentrations of potential luminescence impurities in several samples are presented in Table 4.11. For the correct interpretation of the luminescent bands, artificial barite standards have been investigated, as nominally pure, and activated. The laser-induced time-resolved technique enables us to detect Ag^+, Bi^{2+}, Bi^{3+}, Eu^{2+}, Ce^{3+}, Nd^{3+}, $(UO_2)^{2+}$ and several still not identified emission centers (Figs. 4.29–4.31).

4.5 Strontium (Sr^{2+}) Bearing Minerals

The ionic radius of Sr^{2+} is 1.32 Å in 6-coordinated form. The possible substituting elements are Eu^{2+} with an ionic radius of 1.31 Å and Ce^{3+} with an ionic radius of 1.15 Å.

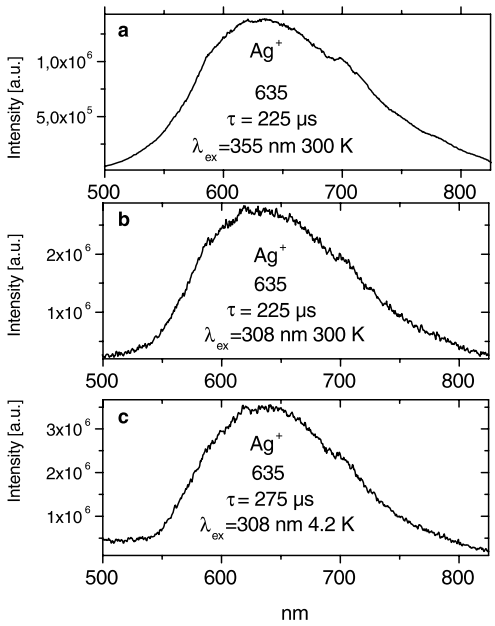

Fig. 4.29. **a–c** Laser-induced time-resolved luminescence spectra of barite with Ag^+ centers

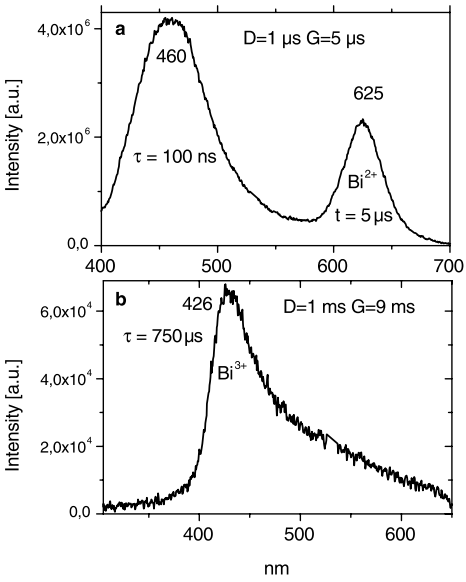

Fig. 4.30. **a**,**b** Laser-induced time-resolved luminescence spectra of barite with Bi^{2+} and Bi^{3+}

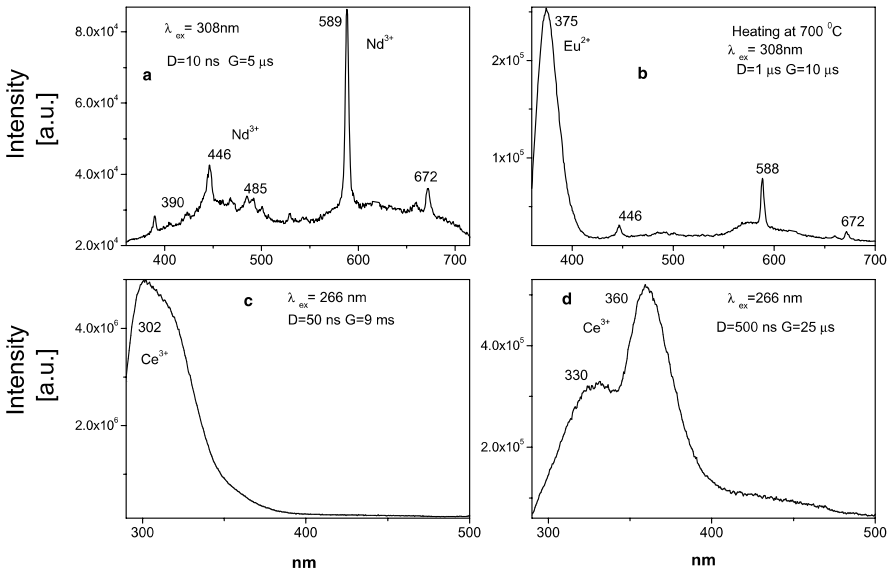

Fig. 4.31. **a**–**d** Laser-induced time-resolved luminescence spectra of barite demonstrating Eu^{2+}, Ce^{3+} and possibly Nd^{3+} centers

4.5.1 Celestine $SrSO_4$

The structure of celestine is similar to that of barites, with Sr taking the place of Ba.

Steady-state luminescence of celestine is characterized by broad bands, which are associated with adsorption of water-organic complexes (Tarashchan 1978).The natural celestine in our study consisted of five samples. The laser-induced time-resolved technique enables us to detect strong emission bands but their interpretation is not finished yet (Fig. 4.32).

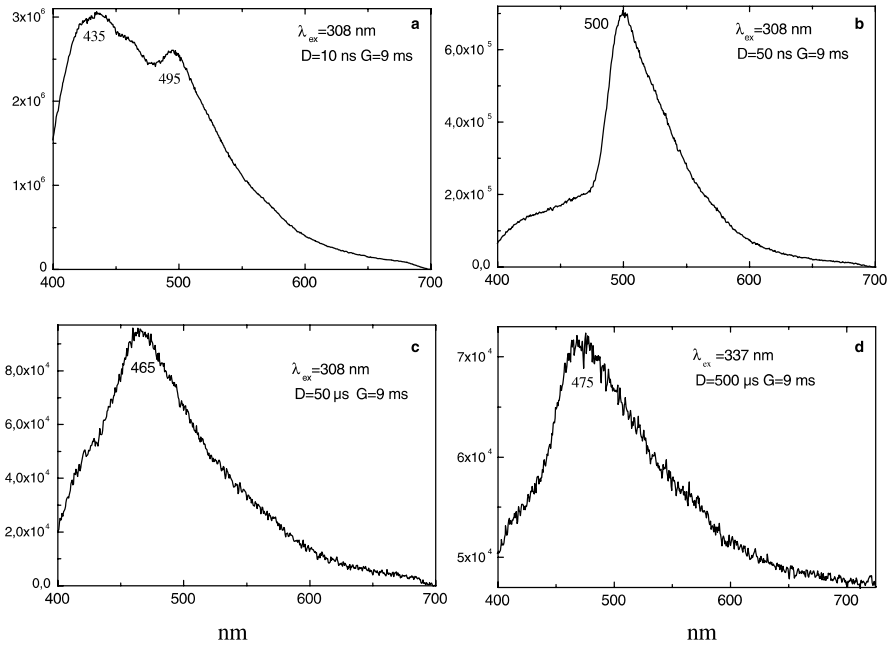

Fig. 4.32. a–d Laser-induced time-resolved luminescence spectra of celestine demonstrating possibly Pb^{2+} centers

4.6 Titanium (Ti^{4+}) Bearing Minerals

Minerals of Ti are capable of intrinsic luminescence, which is connected with $(TiO_6)^{8-}$ groups and a Ti^{3+} center. The ionic radius of Ti^{4+} is 0.75 Å in 6-coordinated form. The possible substituting element is Cr^{3+} with an ionic radius of 0.76 Å.

4.6.1 Titanite $CaTiSiO_5$

Titanite (formerly called "sphene") is an orthosilicate mineral with the chemical formula $CaTiOSiO_4$, where approximately 20% of the oxygens can be partially replaced by OH (hydroxyl) and F. Titanite has a monoclinic symmetry

with a space group $P2_1/a$. It has an optically positive character with $\alpha = 1.84-1.95$, $\beta = 1.87-2.034$, $\gamma = 1.943-2.11$, very high refractive indices (1.843 to 1.950) and extreme birefringence (0.100 to 0.192). The structure of titanite consists of chains of octahedral sites occupied by Ti^{4+}, cross-linked by isolated SiO_4 tetrahedra. Large cavities in this structure provide the seven-fold coordinated site occupied by Ca^{2+}.

Titanite may be a very interesting luminescent material. Potential luminescent centers include intrinsic TiO_6 and Ti^{3+} and different impurities such as trivalent and divalent rare-earth elements (REE), Pb^{2+} and Mn^{2+} substituting for Ca^{2+}, Cr^{3+} and Mn^{4+} substituting for Ti^{4+}, and Cr^{4+}, Cr^{5+} and Fe^{3+} substituting for Si^{4+}. Besides that, titanite can incorporate minor amounts of radioactive impurity components (particularly U and Th) that affect the crystal structure through α- and β-decay events. Thus radiation-induced luminescence centers are also possible. Nevertheless, steady-state luminescent spectroscopy of titanite under UV and X-ray excitations did not reveal characteristic bands and lines (Gaft 1989; Gorobets and Rogojine 2001) and only the ionoluminescence spectrum of titanite exhibits various narrow lines on the broadband background. According to their spectral positions those lines have been attributed to Sm^{3+}, Eu^{3+} and Nd^{3+} (Yang 1995).

The natural titanite in our study consisted of nine samples. Concentrations of potential luminescence impurities in one sample are presented in Table 4.12. The laser-induced time-resolved technique enables us to detect Sm^{3+}, Nd^{3+}, Tm^{3+}, Pr^{3+}, Er^{3+}, Eu^{3+} and Cr^{3+} emission centers (Figs. 4.33–4.34).

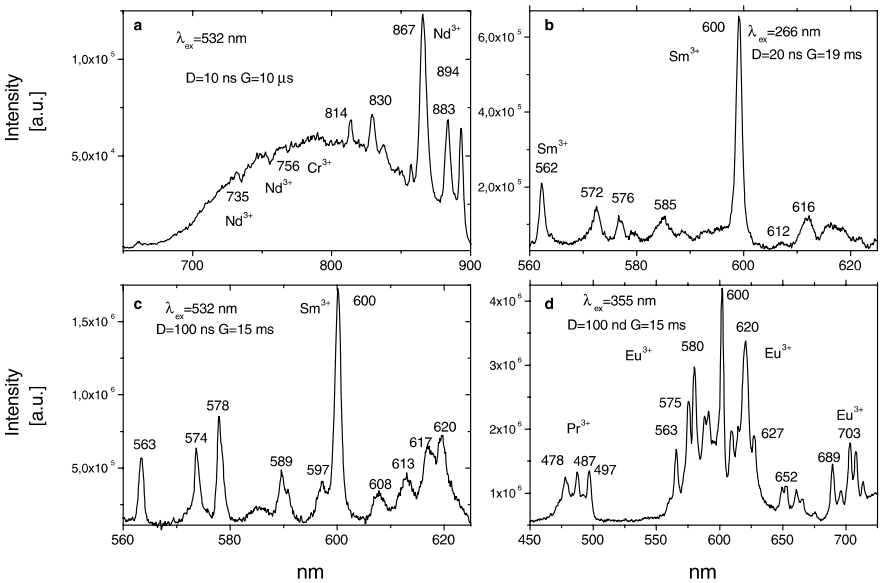

Fig. 4.33. **a–d** Laser-induced time-resolved luminescence spectra of titanite demonstrating Cr^{3+}, Eu^{3+} and Sm^{3+} centers

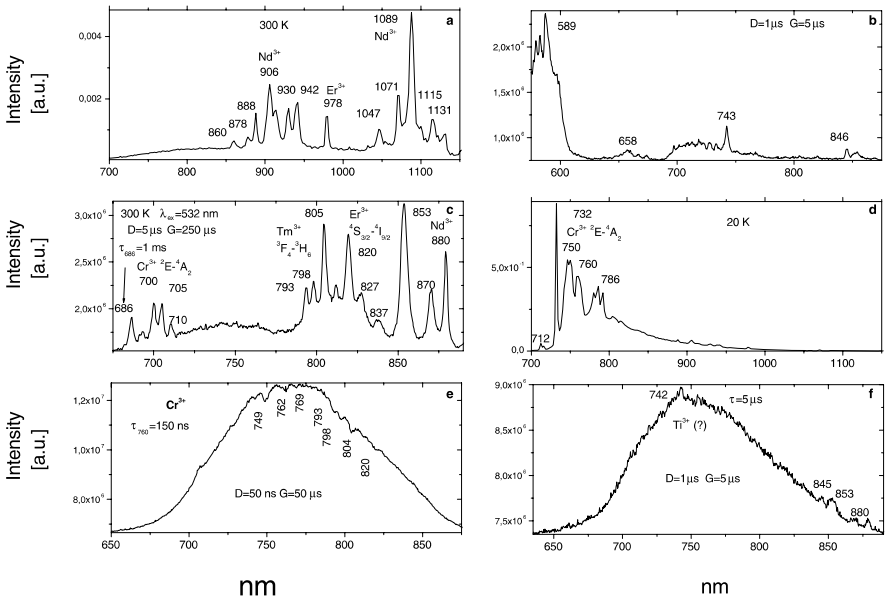

Fig. 4.34. **a–f** Laser-induced time-resolved luminescence spectra of titanite demonstrating Cr^{3+}, Nd^{3+}, Tm^{3+} and possibly Ti^{3+} centers

Table 4.12. Concentrations of rare-earth elements in titanite sample (ppm)

	Pr	Sm	Eu	Nd	Dy	Tb	Er	Tm	Ho	Gd	Ce
Green	90	210	275	555	290	50	165	22	60	280	390

4.6.2 Benitoite $BaTiSi_3O_9$

Benitoite belongs to the cyclosilicates subclass. It contains rings of linked SiO_4 tetrahedra. The tetrahedra are linked in the same manner as in the single-chain inosilicates, each SiO_4 group sharing two oxygens with adjoining tetrahedra on either side, giving the same overall formula $(SiO_3^{-2})_n$. However, instead of forming straight chains the tetrahedra are joined at angles, which result in the formation of the rings. The minimum number of tetrahedra to form a ring is three and a few three-member-ring minerals are known, the best known being benitoite. It is the only known mineral to crystallize in the bar $6m2$ class called the ditrigonal-dipiramidal symmetry class.

Benitoite is a rare, strongly dichroic, blue mineral used as a gemstone. In spite of much effort in its study, the origin of color in benitoite has not been definitively established. Because traces of Fe are found, ideas proposed include the Fe^{2+}–Ti^{4+} or the Fe^{2+}–Fe^{3+} inter-valance charge transfer. While most benitoite is colorless when viewed down the c-axis, there are a very small number of exceedingly rare stones, which are pink in this direction (Rossman 1988).

Benitoite is characterized by very intensive blue luminescence (White 1990). Laser-induced time-resolved technique enables us to detect three broad bands and one narrow line, connectet with TiO_6, Ti^{3+} and Cr^{3+} or Mn^{4+}, luminescence centers (Fig. 4.35).

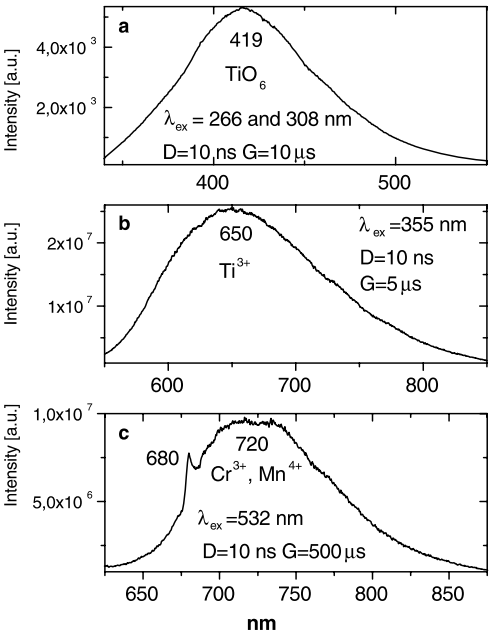

Fig. 4.35. Laser-induced time-resolved luminescence spectra of benitoite demonstrating TiO_6, Ti^{3+} and Cr^{3+} or Mn^{4+} centers

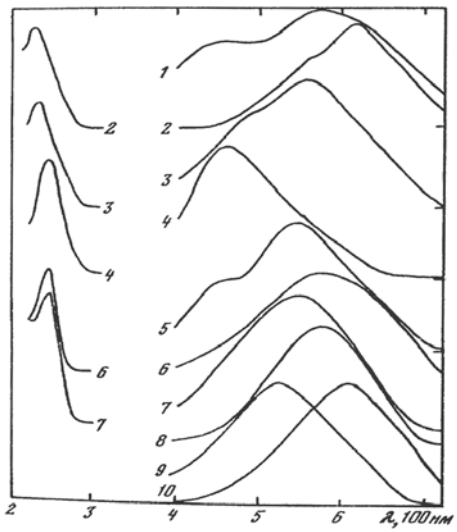

Fig. 4.36. Luminescence (right) and excitation (left) spectra of titanite (1), vuonnemite (2), epistolite (3), natisite (4), penkvilsite (5), Ti-silicate (6), vinogradovite (7), leucosphenite (8), Ti-carbonatesilicate (9), fersmanite (10) (Gaft et al. 1981)

4.6.3
Other Titanium Bearing Minerals

Groups of Ti bearing minerals have been studied by Gaft et al. (1981) and the broad bands in the blue-green part of the spectrum have been connected with individual TiO_6 luminescence centers and their clusters, while the yellow band was ascribed to a Ti^{3+} center (Fig. 4.36).

4.7
Zinc (Zn^{2+}) Bearing Minerals

Ionic radii of zinc are of 0.74 Å in 4-coordinated form and 0.88 Å in 6-coordinated form. The main substituting luminescence centers are Mn^{2+} and Pb^{2+}.

4.7.1
Hydrozincite $Zn_5(CO_3)_2(OH)_6$

Hydrozincite is anhydrous carbonates. The crystalline system is monoclinic-prismatic with the space group $C2/m$. The structure is composed of Zn in both octahedral and tetrahedral coordination, in the ratio 3 : 2. The octahedral Zn atoms form part of a *C*6 type sheet with holes. The octahedral Zn atoms occur above and below these holes. The natural hydrozincite in our study consisted of three samples. Concentrations of potential luminescent impurities are presented in Table 4.13. The laser-induced time-resolved technique enables us to detect Pb^{2+} center (Fig. 4.37).

Table 4.13. Concentrations of rare-earth elements and other potential luminescent impurities in hydrozincite samples (ppm)

	Pr	Sm	Eu	Nd	Dy	Tb	Tm	Ho	Gd	Ce	Pb	Mn
1	3.6	2	0.5	13.5	2.3	0.4	0.2	0.5	3	1	2,000	–
2	0.4	0.3	0.5	1.5	0.2	0.04	0.02	0.04	0.35	3.5	35	200
3	0.2	0.2	0.006	1	0.45	0.06	0.06	0.12	0.3	0.5	600	10

4.7.2
Willemite Zn_2SiO_4

Willemite is a trigonal silicate with well-known green luminescence. It is connected with an Mn^{2+} luminescence center (Tarashchan 1978). The natural willemite in our study consisted of three samples. The laser-induced time-resolved technique enables us to detect an Mn^{2+} emission center (Fig. 4.37).

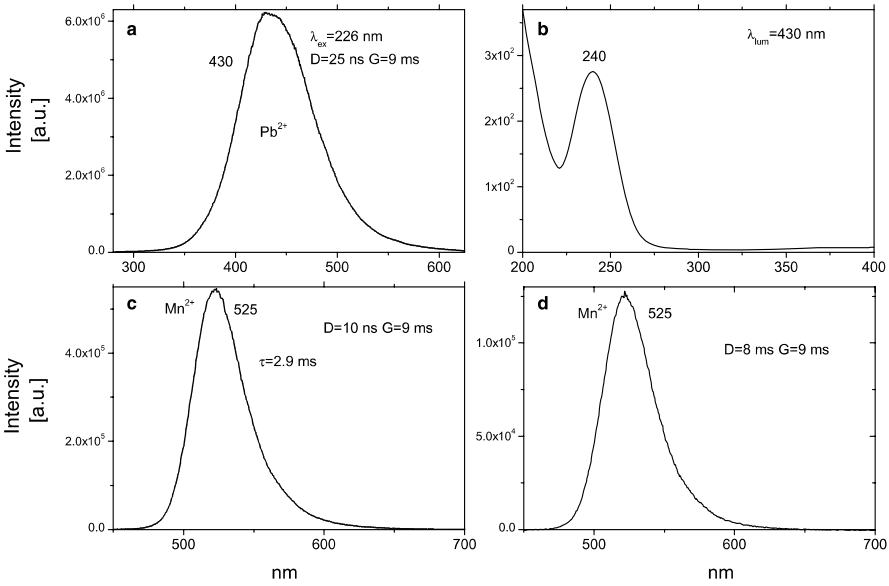

Fig. 4.37. **a**–**d** Laser-induced time-resolved luminescence and excitation spectra of hydrozincite (**a**, **b**) and luminescence of willemite (**c**, **d**) demonstrating Pb^{2+} and Mn^{2+} centers, respectively

4.8 Zirconium (Zr^{4+}) Bearing Minerals

Ionic radii of zirconium are of 0.73 Å in 4-coordinated form and 0.86 Å in 6-coordinated form. The possible substituting luminescence centers are Ti^{4+} with an ionic radius of 0.75 Å in 6-coordinated form, TR^{3+}, Cr^{5+}, Cr^{4+}, Mn^{2+}, and Fe^{3+}. Impurities of U and Th are also possible, which may radiatively decay with formation of radiation induced luminescence centers.

4.8.1 Zircon $ZrSiO_4$

Zircon, is a zirconium silicate, $ZrSiO_4$, with a tetragonal structure ($I4_1/amd$) where in the unit cell there are four SiO_4^{4-} and four ZrO_8^{12-} groups. In nature, zircon is an accessory mineral almost always found in igneous, sedimentary and metamorphic rocks. Zircon's crystal chemistry strongly favors the incorporation of REE in the Zr^{4+} site. The REE impurities become luminescent in a crystallographic environment of the lattice. This property, coupled with the ability to form waveguides in this material by the technique of ion implantation, makes zircon of interest as a potential host material for laser waveguide cavities. Thus spectroscopic analysis of zircon is needed to identify possible laser transitions.

Zircon may show a large variety of colors, depending on the content of transition metals and radiation-induced color centers. Reported colors range for crystalline to moderately radiation-damaged zircons from colorless to pale brown, olive, yellow, orange, green, and blue. The color in zircon comes from both uranium ions and radiation damage. U^{4+} enters the zircon structure because, like Zr^{4+}, it has a large ionic radius. U^{4+} substituting in zircon causes the blue color of heat-treated zircon. Over geologic time, the uranium undergoes radioactive decay and the resulting radiation damage centers cause a range of red-brown and amber colors. Heat treatment removes the radiation damage centers and restores the blue color with which zircon presumably originally crystallized. Green colors are associated with a mixture of the blue color from uranium and red-brown color from radiation damage centers. Colorless zircons have little uranium (Platonov et al. 1984). Chromium activated zircon exhibited bluish to greenish color, which was originally interpreted on the basis of local D_{2d} symmetry for Cr^{4+} substituting for Si^{4+} (Beletti et al. 1995). An alternative explanation was double substitution Cr^{3+}–Cr^{5+} within two Zr^{4+}–Si^{4+} neighbors of the zircon lattice (Gaft et al. 2000b). Synthetic zircon doped with vanadium exhibits a blue color, which was attributed to V^{4+} substituting for Zr^{4+}. The red color of zircon was attributed to Nb^{4+} substituting for Zr^{4+}.

X-ray fluorescence spectrometry and inductively coupled plasma analysis reveal the presence in the zircons of all existing REE. The steady-state luminescence in natural zircons is dominated by a broad emission arising from radiation-induced centers and narrow emission lines of Dy^{3+} (Trofimov 1962; Tarashchan 1978). These emissions obscure the spectra of other REE. The thermal treatment enables us to solve this problem in certain cases using the fact that the intensity of broad band luminescence quickly decreases after heating at 700–800 °C, while the intensities of the REE lines remain nearly constant (Shinno 1986; Shinno 1987). Even after heating the samples not all the REE can be identified by steady-state spectroscopy since the weaker luminescence lines of certain REE are obscured by the stronger luminescence of others. For example, luminescence of Pr^{3+} is difficult to detect because the lines of Sm^{3+}, Dy^{3+} and Nd^{3+} hide its radiative transitions. In turn, Tb^{3+} conceals the luminescence of Tm^{3+} and so on.

Besides REE, broad spectral bands characterize the luminescence of zircon. They are structureless down to 4.6 K, which makes difficult the correct interpretation of the nature of the luminescent centers. Different suppositions are made in previous studies and even the question about a yellow luminescence connection with intrinsic or impurity defect remains open. For example, the yellow band ("*C*-band") was ascribed to SiO_m^{n-}-defects (Votyakov et al. 1993; Krasnobayev et al. 1988) while the same emission ("band VII") was explained by impurity luminescence, namely by Yb^{2+} created by radioactive reduction of Yb^{3+} (Kempe et al. 2000).

It was proposed that yellow zircon luminescence is connected not with one, but with many centers, which have similar luminescence and excitation spectra, but different decay times and thermal stability (Gaft et al. 1986; Shinno 1987;

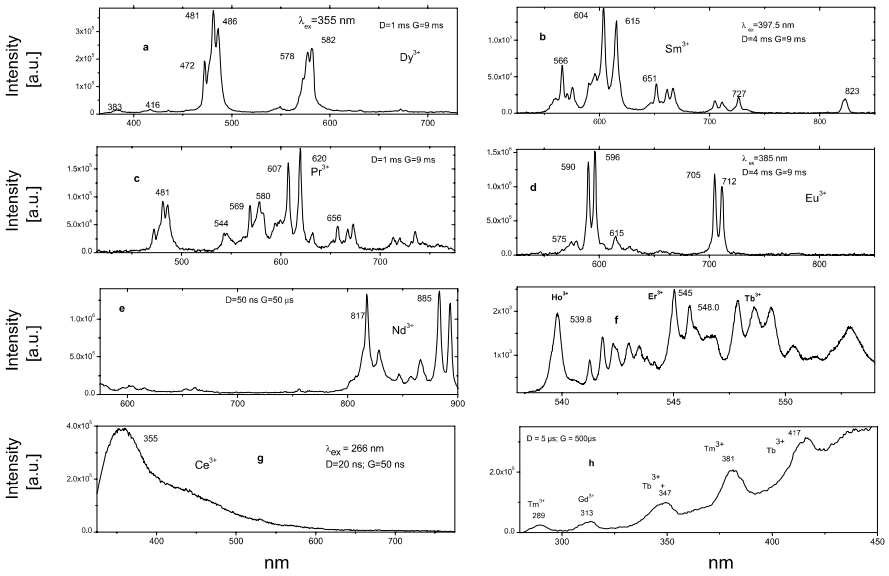

Fig. 4.38. **a–h** Laser-induced time-resolved luminescence spectra of zircon demonstrating Dy^{3+}, Sm^{3+}, Eu^{3+}, Pr^{3+}, Tm^{3+}, Er^{3+}, Ce^{3+} and Nd^{3+} centers

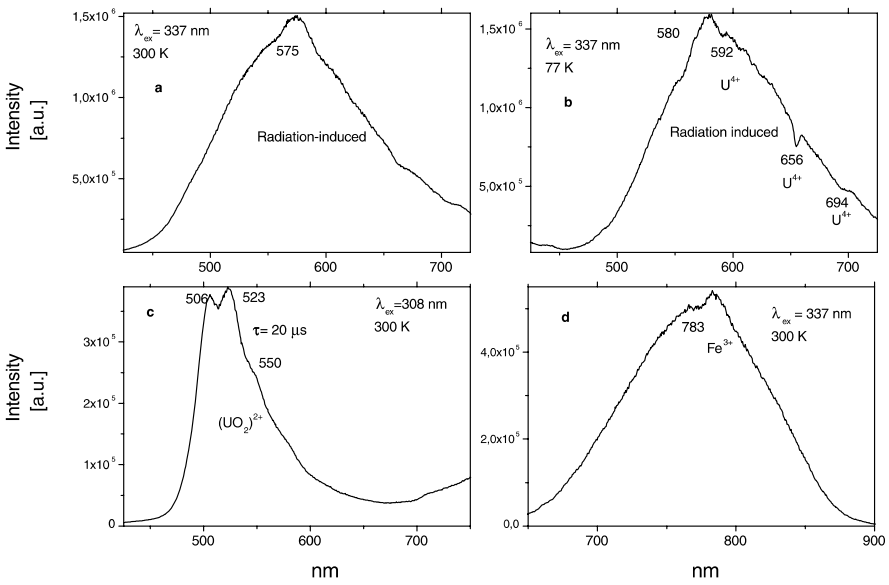

Fig. 4.39. **a–d** Laser-induced time-resolved luminescence spectra of zircon demonstrating intrinsic radiation induced, uranyl and Fe^{3+} center

Gaft 1992; Gaft et al. 2002b; Nasdala et al. 2003). For these reasons spectroscopic methods alone are not enough for the separation of the broad spectra into individual bands.

It is interesting that yellow zircon luminescence is very specific and different from other Zr-bearing minerals such as catapleite, keldyshite, vlasovite, khibinskite and others, which are usually characterized by blue luminescence evidently connected with titanium impurity, namely TiO_6 complexes (Gaft et al. 1981).

Approximately 50 natural zircons have been investigated together with synthesized analogs, as nominally pure and activated by potential luminogens. Concentrations of potential impurities in several zircxon samples are presented in Tables 4.14–4.15 The laser-induced time-resolved technique enables us to detect the following emission centers: radiation induced; trivalent rare-earth elements such as Gd^{3+}, Ce^{3+}, Tb^{3+}, Tm^{3+}, Er^{3+}, Ho^{3+}, Dy^{3+}, Eu^{3+}, Sm^{3+}, Yb^{3+} and Nd^{3+}; $(UO_2)^{2+}$; Fe^{3+} and Cr^{3+} (Figs. 4.38–4.40).

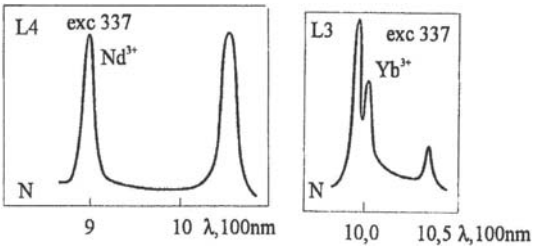

Fig. 4.40. Luminescence of zircon in IR demonstrating Nd^{3+} and Yb^{3+} centers (N – 77 K)

4.8.2 Baddeleyite ZrO_2

Baddeleyite has a monoclinic structure with space group $P21/c$. The Zr^{4+} ion has seven-fold coordination, while the idealized ZrO_7 polyhedron is close to tetrahedral orientation, where one angle in the structure is different significantly from the tetrahedral value. Natural baddeleyite is a raw material for zirconium. In industry ZrO_2, named usually zirconia, is important in areas such as surface chemistry, where its activity as a red ox material and its acid-based functions are important. As a ceramic material, zirconia can resist very high temperatures and its stabilized form, yttrium-stabilized zirconium, shows remarkable mechanical properties.

Baddeleyite is characterized by bright green-blue luminescence (Fig. 4.41) with a decay time of 0.7–2.0 μs under laser excitation (Gaft 1989). It was concluded that such an emission is connected with Ti impurity. Besides that, emission lines of trivalent Dy and Sm have been found in baddeleyite (Eremenko and Khrenov 1982).

Table 4.14. Concentrations of rare-earth elements (ppm) in several zircon samples

	Pr	Sm	Eu	Nd	Dy	Tb	Er	Tm	Ho	Gd	Ce	Yb
Kola	10	48	25	63	352	40	300	56	96	143	68	350
Norway	2.5	7	5	12	120	9	220	50	45	30	120	15
GQ	3	4	1.3	12	56	6	100	32	22	12	28	300
Ural	2.5	7.5	4	13	86	8	125	35	30	25	38	300

Table 4.15. Concentrations of potential luminescent impurities (ppm) in several zircon samples

	Mn	Fe	Ti	Mo	V	Nb	Ni	Pb	Ta	U
Australia	10	400	1,200	0.5	90	20	10	15	4	550
Norway	150	475	120	0.5	3	100	15	8	15	120
Canada	100	2,200	75	5	250	20	75	9	20	700
Kola	40	400	40	2	150	150	30	5	2.5	40

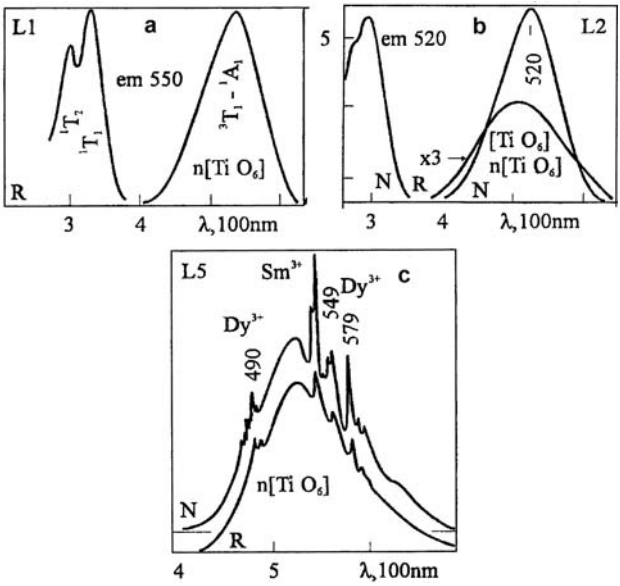

Fig. 4.41. **a–c** Laser-induced luminescence of baddeleyite (**a**, **b**) (Gaft 1980) and photoluminescence of baddeleyite with REE emission (**c**) (Eremenko and Khrenov 1982) (N – 77 K; R – 300 K)

4.9 Silicon (Si^{4+}) Bearing Minerals

The ionic radius of silicon in tetrahedral coordination is 0.4 Å. The main substituting luminescence center is $Fe^{3+}$with an ionic radius of 0.63 Å in tetrahedral coordination.

4.9.1 Wollastonite $CaSiO_3$

Wollastonite is calcium silicate with a triclinic crystal system (*P*21). It has infinite-chain structure, with three tetrahedra per unit cell arranged parallel to y, this repeat unit consists of a pair of tetrahedra joined apex to apex as in the [SiO_7] group, alternating with a single tetrahedron with one edge parallel to the chain direction. Steady-state luminescence of wollastonite has been previously studied and luminescence of Mn^{2+}, Fe^{3+} and supposedly Cr^{3+} has been proposed (Min'ko et al. 1978).

The natural wollastonite in our study consisted of three samples. The laser-induced time-resolved technique enables us to detect Mn^{2+}, Fe^{3+} and possibly Cr^{3+} emission centers (Fig. 4.42).

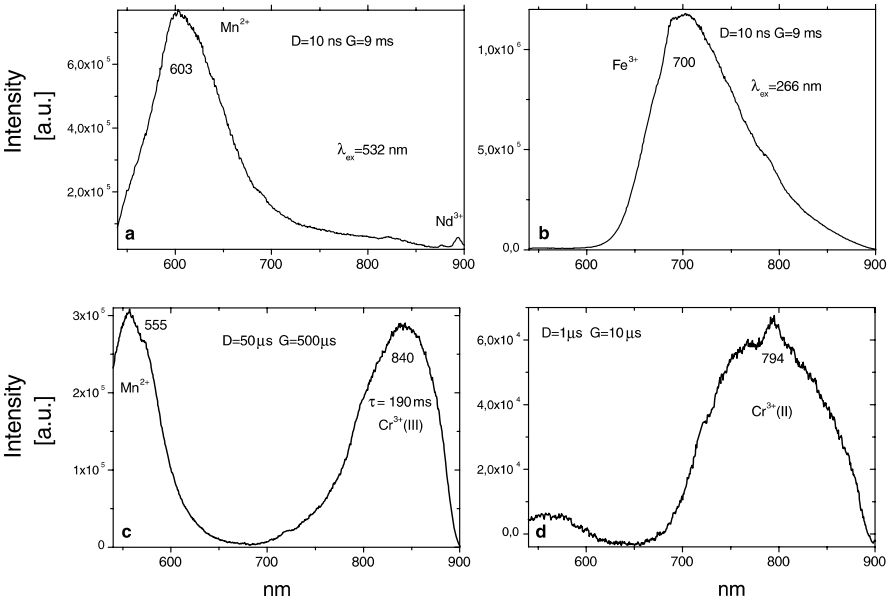

Fig. 4.42. **a–d** Laser-induced time-resolved luminescence spectra of wollastonite demonstrating Mn^{2+}, Fe^{3+} and possibly Cr^{3+} centers

4.9.2 Feldspars

Feldspars are mainly MT_4A_8 alumosilicates whose structures are composed of corner-sharing AlO_4 and SiO_4 tetrahedra (T sites) linked in an infinite three-dimensional array. Charge compensating cations (K^+, Na^+, Ca^{2+}, Ba^{2+}) occupy large, irregular cavities in the tetrahedral framework (M sites). Most natural feldspars occur in the K–Na–Ca ternary diagram – orthoclase-albite-anorthite). In general, feldspars have a disordered structure with respect to Al and Si at high temperatures and ordered structures at low temperatures. Monoclinic sanidine is the most disordered K-feldspar polymorph. If the rocks are annealed over geologic times at lower temperatures, Al migrates and monoclinic orthoclase and ordered triclinic microcline are formed. In K-feldspars large cations enter the M-sites, whereas the number of substituents in plagioclases is limited because of the smaller cations in the M site. Small cations are incorporated into the tetrahedral T sites. Some of these substituting elements in natural feldspars can act as luminescence centers.

The pale yellow color in feldspar is due to Fe^{3+} in a tetrahedral Si/Al site. This color is often masked by the pervasive turbidity of common feldspars. A smoky color, the result of radiation damage from the decay of K-40, is also common but often masked. The blue color in the amazonite variety of potassium feldspar (and pale-blue albite) is from the interaction of trace amounts of Pb^{2+} in the feldspar with ionizing radiation. Lead-containing feldspars with a higher

degree of Al/Si disorder than occurs in microcline become green from radiation damage. There are also rare varieties of plagioclase feldspar colored green and red from Cu ions (Platonov 1979).

Steady-state luminescence of feldspars is well studied. The following impurity centers have been found: Tl^{+}, Pb^{+}, Pb^{2+}, TR^{3+} (Ce, Dy, Sm, Tb, Nd), Eu^{2+}, Mn^{2+}, Fe^{3+}, Cr^{3+} (Tarashchan 1978; Walker 1985; Bakhtin and Moroshkin 1986; White et al. 1986; Kuznetsov and Tarashchan 1988; Waychunas 1989; Götse 2000; Correcher and Garcia-Guinea 2001; Gorobets and Rogojine 2001; Krbetschek et al. 2002).

The natural feldspars in our study consisted of twelve samples. Concentrations of rare-earth elements in one of them are presented in Table 4.16. The laser-induced time-resolved technique enables us to detect Pb^{2+}, Gd^{3+}, Ce^{3+}, Eu^{2+}, Eu^{3+}, Tb^{3+}, Er^{3+}, Dy^{3+}, Sm^{3+}, Nd^{3+}, Mn^{2+}, Fe^{3+} and possibly Cr^{3+} emission (Figs. 4.43–4.45).

Table 4.16. Concentrations of rare-earth elements (ppm) in feldspar samples

Pr	Sm	Eu	Nd	Dy	Tb	Er	Tm	Ho	Gd	Ce
5.0	9.0	0.3	30.0	11.0	1.9	6.4	0.8	3.4	14.0	32.0
1.1	3.3	1.4	7.0	4.0	0.8	1.8	0.3	0.6	4.5	6.2

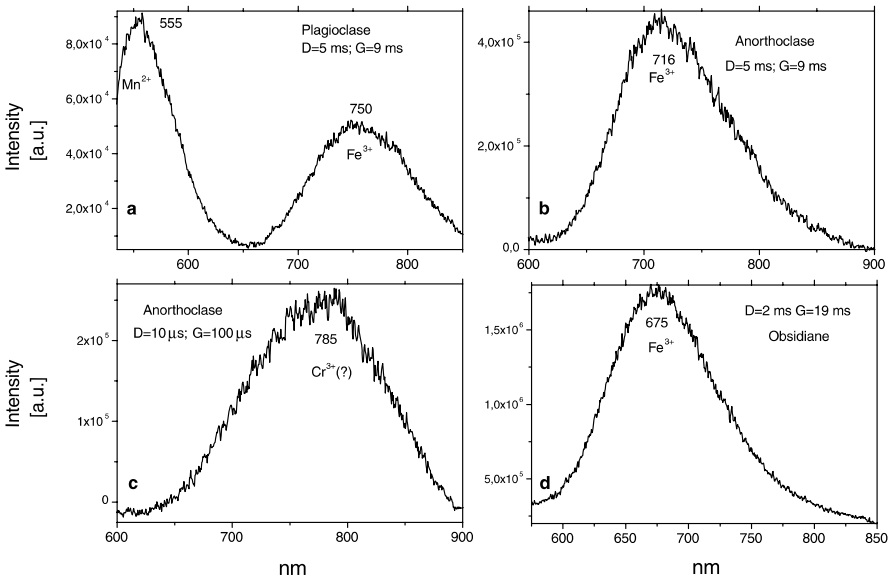

Fig. 4.43. a–d Laser-induced time-resolved luminescence spectra of feldspars demonstrating Mn^{2+}, Fe^{3+} and Cr^{3+} centers

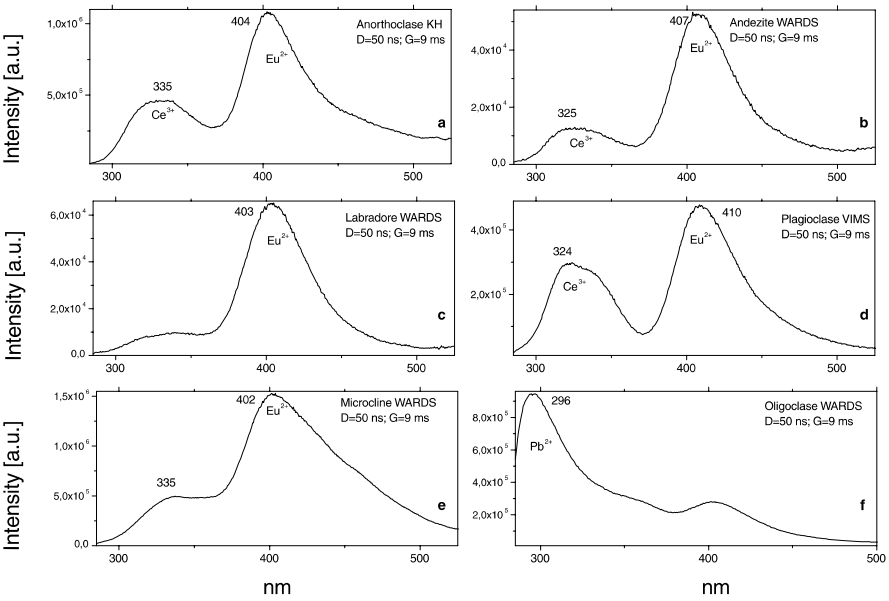

Fig. 4.44. **a–f** Laser-induced time-resolved luminescence spectra of feldspars demonstrating Ce^{3+}, Eu^{2+} and Pb^{2+} centers

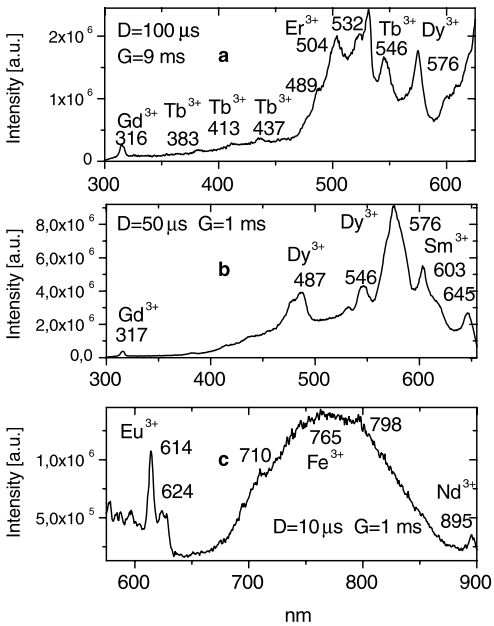

Fig. 4.45. **a–c** Laser-induced time-resolved luminescence spectra of feldspars demonstrating Gd^{3+}, Tb^{3+}, Er^{3+}, Dy^{3+}, Sm^{3+}, Eu^{3+}, Nd^{3+}, and Fe^{3+}

4.9.3
Obsidian SiO_2

Silica makes up 12.6 mass-% of the Earth's crust as crystalline and amorphous forms. It was found that both modifications show similar main luminescence bands, namely a blue one centered at 450 nm ascribed to Al^{3+} which substitutes for Si^{4+}, red centered at 650 nm linked with non-bridge O^*, and dark-red at 700–730 nm linked with Fe^{3+}. Time-resolved luminescence of hydrous volcanic glasses with different colors and different Fe, Mn, and H_2O contents were measured and interpreted (Zotov et al. 2002). The blue band with a short decay time of 40 ns was connected with $^4T_2(^4D)$–$^6A_1(^6S)$ and $^4A_1(^4G)$–$^6A_1(^6S)$ ligand field transitions of Fe^{3+}, the green band with a decay time of approximately 250 µs with a $^4T_1(^4G)$–$^6A_1(^6S)$ transition in tetrahedrally coordinated Mn^{2+}, while the red band with a much longer decay time of several ms with $^4T_1(4G)$–$^6A_1(^6S)$ transitions in tetrahedrally coordinated Fe^{3+}. We detected Fe^{3+} in the time-resolved luminescence spectrum of black obsidian glass (Fig. 4.43d).

4.10
Aluminum (Al^{3+}) Bearing Minerals

The ionic radius of aluminum in octahedral coordination is of 0.67 Å. The main substituting luminescence centers are Cr^{3+} with an ionic radius of 0.75 Å in octahedral coordination, Mn^{2+} and Mn^{4+} with ionic radii of 0.81 and 0.67 Å in octahedral coordination and V^{2+}, V^{3+} and V^{4+} with ionic radii of 0.93, 0.78 and 0.72 Å in octahedral coordination correspondingly.

4.10.1
Kyanite and Sillimanite $Al_2O[SiO_4]$

Kyanite has a structure in which the oxygen atoms are arranged in a slightly distorted close-packed cubic array. There are chains of Al–O octahedral and these chains are linked together by the remaining Si, Al and O ions, Si being coordinated by 4 oxygen ions, and Al by 6 oxygen ions. The Si lying between 4 oxygens thus gives a structure with independent SiO_4 tetrahedra. Four crystallographically different octahedral sites present in kyanite structure, with mean Al–O distances ranging from 1.896 to 1.919 Å. Steady-state luminescent properties of kyanite are connected with several Cr^{3+} centers (Tarashchan 1978; Platonov et al. 1998; Wojtovicz 1991), and possibly Ti^{3+} (Gaft 1989). The natural kyanite in our study consisted of three samples with Cr concentrations from 70 to 100 ppm. The laser-induced time-resolved technique enables us to detect three different Cr^{3+} emission centers (Fig. 4.46).

Sillimanite is polymorph of kyanite. It has an orthorhombic symmetry with a space group *Pbnm*. The structure contains edge-sharing, strictly centrosymmetric octahedra (Al sites) arranged in straight chains parallel to [001] and

alternating corner-sharing tetrahedra (Al and Si sites). The broadband luminescence with a relatively long decay time of 160 µs peaking at 790 nm was detected in sillimanite (Wojtowicz and Lempicki 1988). The emission has been ascribed to Cr impurities (Fig. 4.47).

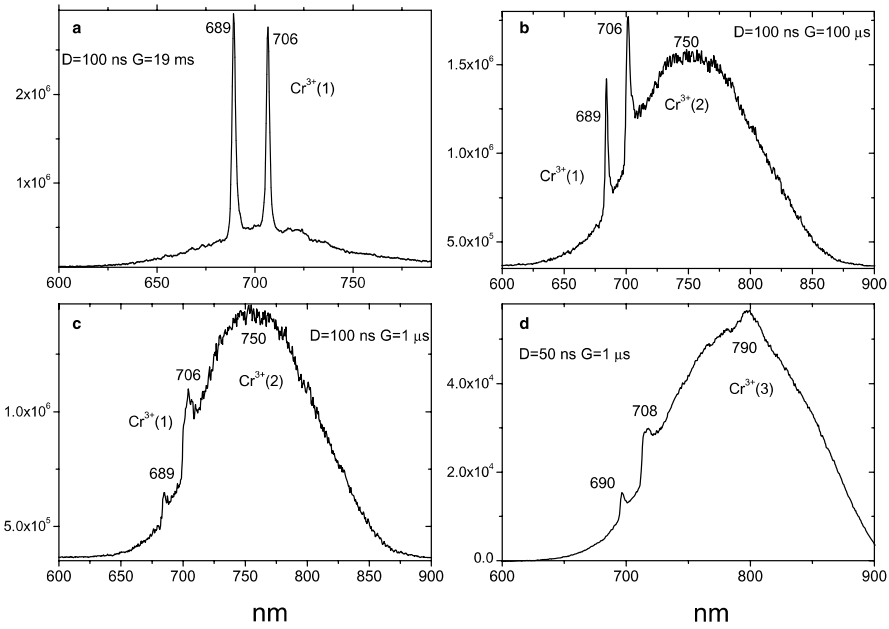

Fig. 4.46. **a–d** Laser-induced time-resolved luminescence spectra of kyanite demonstrating different Cr^{3+} centers

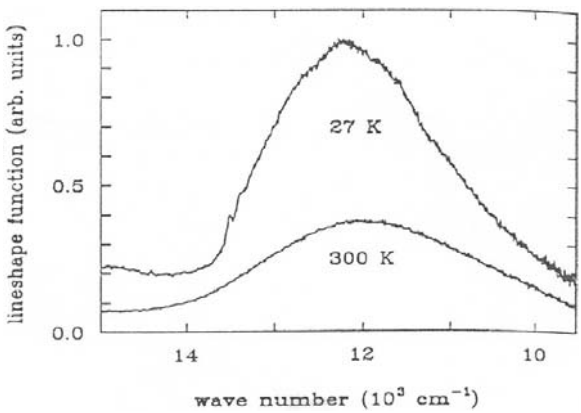

Fig. 4.47. Laser-induced luminescence spectrum of sillimanite (Wojtowicz and Lempicki 1988)

4.10.2
Topaz $Al_2SiO_4F_2$

A chain like structure of connected irregular octahedrons controls topaz structure. These octahedrons have Al in the middle surrounded by four O atoms. Above and below the Al are the (OH) or F ions. The chains of octahedrons are held together by individual Si tetrahedrons. The crystal system is orthorhombic (2/*m*2/*m*2/*m*).

The colors are clear, yellow, orange, red, blue and green, while the main color centers are radiation induced. Violet and violet-red colors in Cr-containing topaz are generated by two absorption bands in the visible part of the spectrum, which are connected with Cr^{3+} substituting for Al^{3+}. Yellow topaz besides Cr^{3+}

Table 4.17. Concentrations of Mn, Fe, Cr, V and Ti (ppm) in topaz samples

	Mn	V	Cr	Ti
Yellow	< 10	25	25	160
Yellow	< 10	20	55	130
Yellow	< 10	25	180	110
Yellow	< 10	30	60	90
Red	125	30	500	130

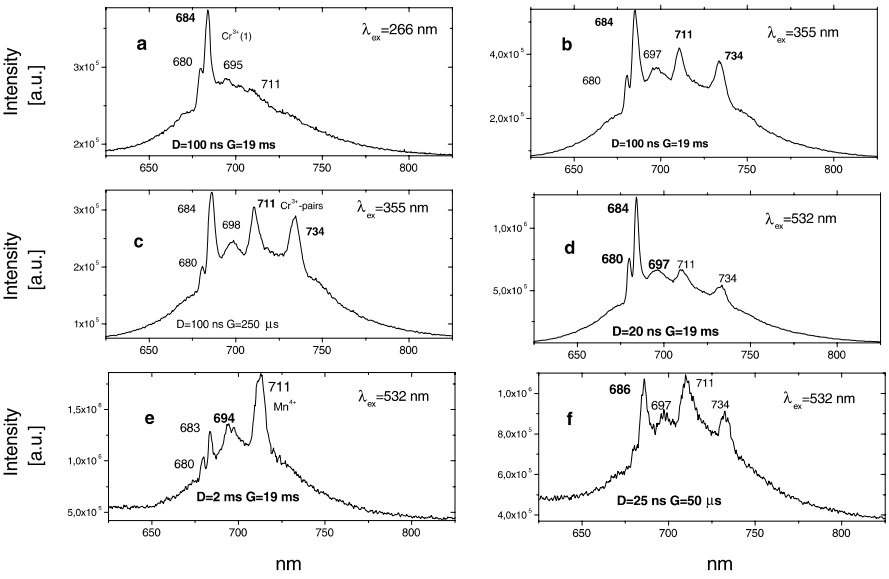

Fig. 4.48. **a**–**f** Laser-induced time-resolved luminescence spectra of topaz demonstrating different Cr^{3+} and possibly Mn^{4+} centers

contains a radiation-induced O^- hole-center (O^{2-} with a trapped hole) with a corresponding strong ultra-violet absorption. Orange-red topaz besides Cr^{3+} contains a F-center (F-vacancy with a trapped electron) with strong absorption in the violet part of the spectrum. The origin of the color in topaz without Cr is radiation induced. The yellow color is connected with absorption in the blue-violet part of the spectrum generated by the F-center. The red-brown color is connected with absorption in the blue part of the spectrum created by the combination of a F-center and O^--center. A blue color is connected with a broad absorption band in the red part of the spectrum generated by so-called R-centers (two F-vacancies with two trapped electrons) (Platonov et al. 1984; Schott et al. 2003).

Steady-state luminescence of topaz has been studied in (Tarashchan 1978). At 77 K narrow lines at 680, 696, 712 and 730 nm have been ascribed to single Cr^{3+} (R-lines) and Cr^{3+}-pairs. The presence of at least three different types of Cr^{3+} luminescence centers have been proposed, which most probably differ by ligand surroundings, such as O_4F_2, $O_4F(OH)$ and $O_4(OH)_2$. It was concluded based on R-emission line behavior as result of heating. Its fine structure is changed as result of annealing, namely in the spectrum of the sample annealed at 1,150 °C during 1.5 h the side two lines at 678 and 684 nm practically disappear, whereas the central line at 682.5 nm significantly increases (Taran et al. 2003).

The natural topaz in our study consisted of seven samples. Concentrations of several potential impurities (luminogens) are presented in Table 4.17. The laser-induced time-resolved technique enables us to detect three different Cr^{3+} and possibly Mn^{4+} and (TiO_4) emission centers (Figs. 4.48–4.49).

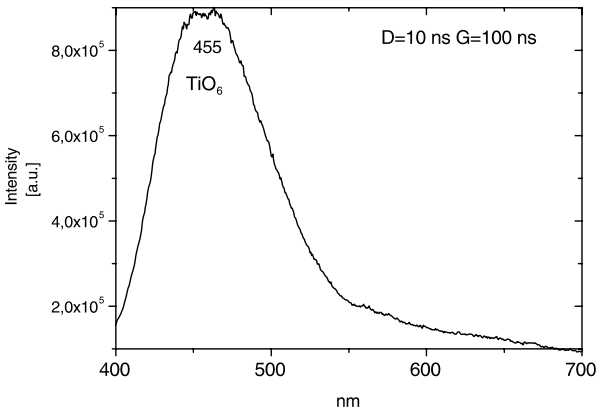

Fig. 4.49. Laser-induced time resolved luminescence spectra of topaz demonstrating possibly TiO_4 luminescence

4.10.3 Corundum Al_2O_3

Corundum has a trigonal structure. The oxygen ions are arranged in approximately hexagonal closed packing. Between the oxygen layers there are sites

for cations octahedrally coordinated by six oxygen ions, but in corundum only two-thirds of the available positions are filled. Groups of three oxygen ions form a common face of two neighboring octahedra and thus the groups are linked to a pair of Al ions.

The main colored varieties are ruby (red) and sapphire (blue). The corresponding color centers may present in different quantitative and qualitative proportions with resulting varieties of colors (up to 2,000 different tints). The main color center in ruby is an impurity of Cr (up to 4%). The ion Cr^{3+} generates two strong absorption bands in the visible part of the spectrum, which explain the red color. Different tints of red, which influence the commercial value strongly, are connected with impurities of Fe^{3+} and V^{3+}. Under UV excitation, ruby may exhibit the red luminescence of Cr^{3+}, which makes the red color of ruby stronger under sun illumination. The main color centers in sapphire are impurities of Fe and Ti. Strong absorption bands in the green-blue sapphires are connected with Fe^{2+} and Fe^{3+}. Usually the Fe absorption is relatively weak, but in sapphire the cations Fe^{2+} and Fe^{3+} are structurally paired and exchange interaction between ions provides mechanisms by which the intensity of absorption increases dramatically. Absorption bands of blue sapphire are connected with Ti^{4+}–Fe^{2+} and Fe^{2+}–Fe^{3+} structural pairs (Platonov et al. 1984).

Steady-state luminescent properties of natural corundum Al_2O_3 were carefully investigated. Strong well-known $^2E \rightarrow {}^4A_2$ lines of Cr^{3+} with a long decay time characterize their photoluminescence spectra. Besides that, much weaker narrow lines present, which are connected with Cr-pairs and more complicated complexes (so called *N*-lines) (Tarashchan 1978). A broad blue band of CL peaking at approximately 480 nm of undetermined origin (Ponahlo 2000) and a broad red band peaking at 690 nm preliminarily ascribed to Ti^{3+} (Gorobets and Rogojine 2001) have been also detected. The natural corundum in our study consisted of four samples. The laser-induced time-resolved technique enables us to detect Cr^{3+} and possibly Fe^{3+} emission centers (Fig. 4.50).

4.10.4 Spinel $MgAl_2O_4$

The spinel structure is a cubic close packing of anions bound together by interstitial cations. The lattice is a face-centered cubic, space group *Fd*3*m*, with eight $MgAl_2O_4$ formula units per face-centered cell. One of the peculiarities of spinel is the cation inversion responsible for its disordered structure. There are two cation positions in the spinel lattice, one tetrahedrally coordinated and one with octahedral coordination. Among them, two kinds of cations A^{2+} and B^{3+} are distributed. The so-called normal spinel is described by the formula $A^{\{4\}}B2^{\{6\}}O_4$, where A is in tetrahedral and B in octahedral coordination. In the diverse spinel, the divalent cations A are placed in the octahedral positions $B^{\{4\}}(AB)^{\{6\}}O_4$. Thus in a normal spinel, the Al^{3+} ions are in octahedral coordination with local symmetry D_{3d}, while the Mg^{2+} ions are in regular tetrahedral coordination, with point symmetry T_d.

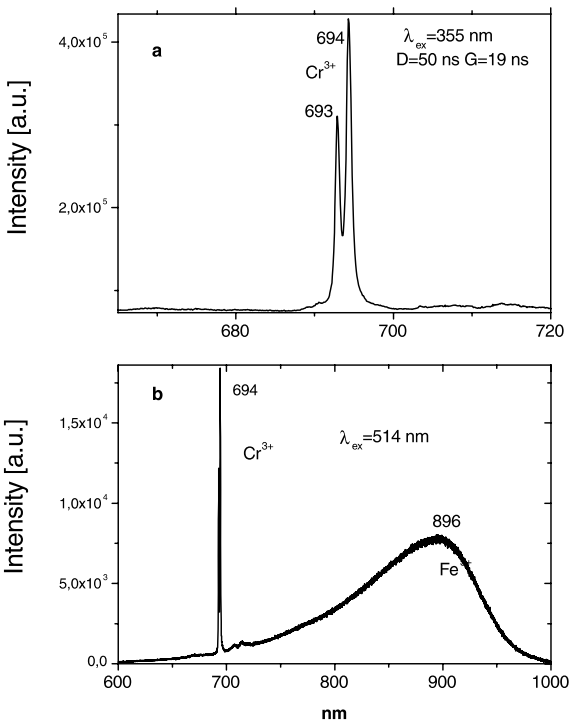

Fig. 4.50. Laser-induced time-resolved luminescence spectra of ruby (**a**) and steady-state spectra of sapphire (**b**) demonstrating Cr^{3+} and possibly Fe^{3+} centers

The colored varieties are red, pink-red, orange-red and violet-red. The main color centers are Cr^{3+}, Fe^{2+}, Co^{2+} and Fe^{3+}, which give all tints of color from violet to red. The mutual feature of pink and red spinel is two broad absorption bands in the visible part of the spectrum, which are connected with Cr^{3+} substituting for Al^{3+}. The set of the narrow absorption bands, which give the violet color are connected with a Fe^{2+} impurity substituting for Mg^{2+}. Absorption spectra of blue spinel is similar to those of the violet ones, but the absorption in the red and violet parts of the spectrum are higher. This is connected with the additional influence of Fe^{3+} and Co^{2+} substituting for Al^{3+} and Mg^{2+}, correspondingly. Though mostly clear, the coloring action of these impurities is seen in green and blue spinels (Platonov et al. 1984).

The emission of natural spinel exhibits a great deal of fine structure, which was ascribed to Cr^{3+} luminescence (Tarashchan 1978; Mohler and White 1995). The natural spinel in our study consisted of three samples. The laser-induced time-resolved technique enables us to detect Cr^{3+} and possibly Mn^{2+} emission centers (Fig. 4.51).

4.10.5 Beryl and Emerald $Be_3Al_2Si_6O_{18}$

The dominant features in the structure are the hexagonal rings of six Si–O tetrahedra, these rings forming hollow columns parallel to the z-axis. Within the

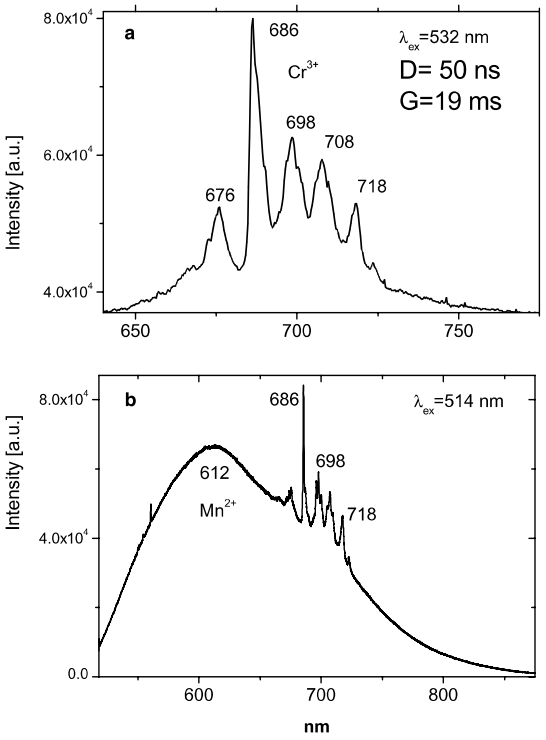

Fig. 4.51. Laser-induced time-resolved (**a**) and steady state (**b**) luminescence spectra of spinel demonstrating Cr^{3+} and possibly Mn^{2+} centers

rings two of the oxygen atoms in each SiO_4 group are shared by SiO_4 groups on either side, thus giving the meta-silicate ratio. Between the rings lie the Al and Be atoms, each Al coordinated with an octahedral group of six oxygen atoms, and each Be surrounded by four oxygen atoms on a distorted tetrahedron.

The main colored varieties are emerald (green), heliodor (yellow) and aquamarine (blue). The main color center in emerald is Cr^{3+} substituting for Al^{3+}, which generates two strong absorption bands in the visible part of the spectrum. Additional impurities which also influence the color are Fe^{2+} in two different structural positions: instead of Be and instead of Al. They generate absorption bands in the red and near IR parts of the spectrum and give the yellowish tints to the color. Green beryl is known which does not contain Cr^{3+}. The corresponding absorption bands are connected with V^{3+} substituting for Al^{3+} and the name emerald is controversial in this case. Two different color centers are known in heliodor, both connected with Fe^{3+} impurities, but in different structural positions: instead of Be^{2+} (yellow-green color) and instead of Al^{3+} (yellow-orange color). In both cases the corresponding absorption bands are connected with charge transfer electron transitions in the O^{2-}–Fe^{3+} centers. Three different color centers are known in aquamarine, all connected with Fe impurities. The first type of absorption bands is connected with electronic transitions inside Fe^{2+} substituting for Al^{3+}. The second color center

is connected with a double substitution: two Al^{3+} are substituted by Fe^{2+} on the place of Al^{3+} and Fe^{3+} in an interstitial position (between two positions of Al^{3+}). The corresponding absorption bands are connected with charge transfer electronic transitions between Fe^{2+} and Fe^{3+}. The last color center has the same nature as the previous one, but Fe^{3+} substitutes for the Al^{3+} position (Platonov et al. 1984).

The steady-state emission of beryl has been previously studied. The broad band at 720 nm is connected with Fe^{3+}, while the relatively narrow bands at 480 and 570 nm are ascribed to Mn^{2+} in tetrahedral and octahedral coordination, respectively. Cr^{3+} emission was connected with narrow *R*-lines at 680 and 682 nm (Tarashchan 1978; Kuznetsov and Tarashchan 1988).

The natural beryl and emerald in our study consisted of seven samples. The laser-induced time-resolved technique enables us to detect Cr^{3+}, Fe^{3+} and possibly Mn^{4+} emission centers (Figs. 4.52–4.53).

4.10.6 Chrysoberyl and Alexandrite $BeAl_2O_4$

The host crystal of chrysoberyl has a hexagonal-close-packed structure. The space group is orthorhombic *Pnma* with four molecules per unit cell. The Al^{3+} ions are octahedrally coordinated by the oxygen ions and occur in two not equivalent crystal field sites in the lattice. The Al^{3+} sites lying in the mirror-

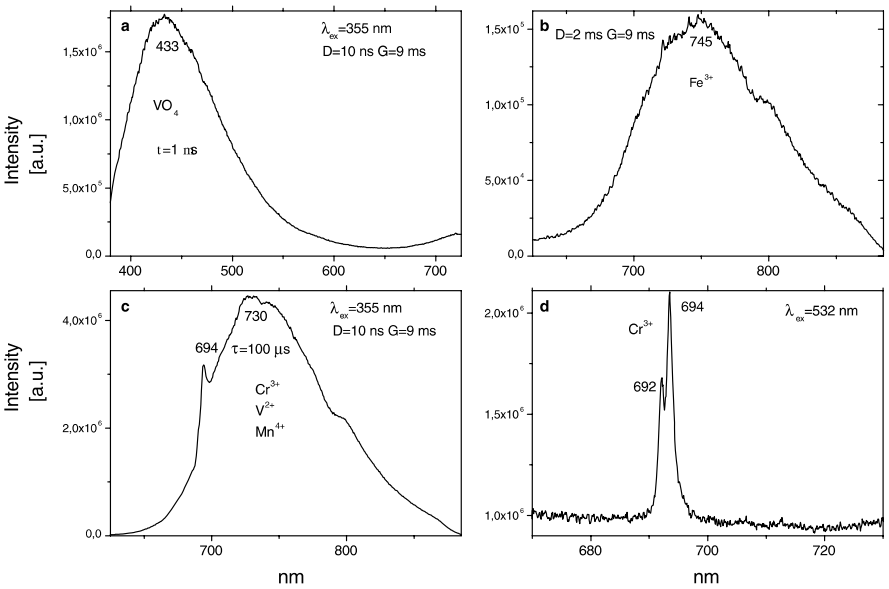

Fig. 4.52. **a–d** Laser-induced time-resolved luminescence spectra of beryl demonstrating different Cr^{3+}, Fe^{3+} and possibly Mg^{4+}, V^{2+} and VO_4 centers

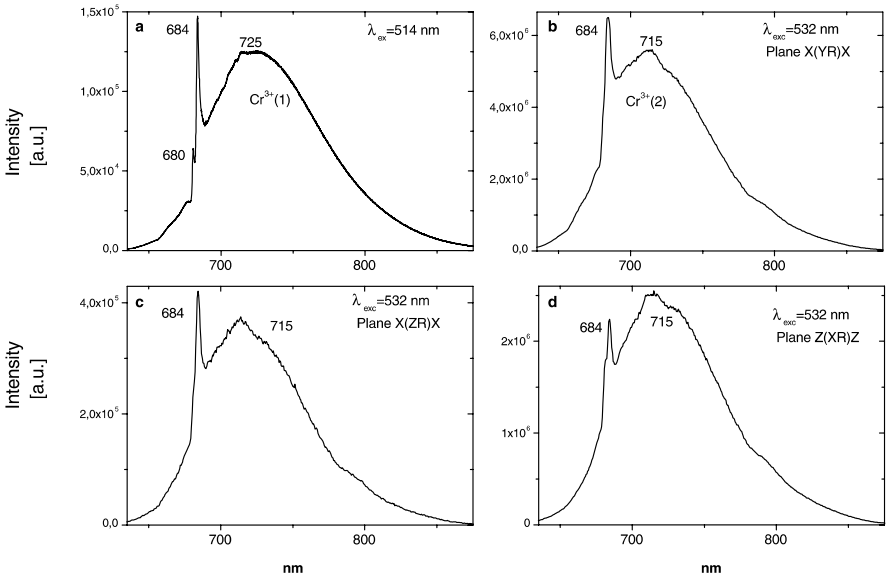

Fig. 4.53. **a–d** Laser-induced time-resolved luminescence spectra of emerald demonstrating Cr^{3+} center

symmetry planes of the lattice have the site symmetry of the C_s point group, while the other Al^{3+} sites possess inversion symmetry and belong to the C_i point group. The Cr^{3+} ions enter the crystal substitutionally for the Al^{3+} ions, 78% replacing Al^{3+} ions in the mirror sites and the rest going into the inversion sites. Alexandrite is a green variety of chrysoberyl. Its main feature is the so-called alexandrite effect, which is manifested as a change in the color of the crystal from bluish-green in sunlight to magenta-red on illumination by an incandescent lamp. It is assumed that responsible for all these effects are the centers, which are formed by the impurity Cr^{3+} (Powell et al. 1985).

Two types of Cr^{3+} luminescence centers have been found in steady-state natural alexandrite, characterized by *R*-lines at approximately 680 and 692 nm, accompanied by very many *N*-lines of Cr–Cr pairs (Tarashchan 1978). Those centers have been identified as connected with substitutions of Al^{3+} in different structural sites. It was found that natural alexandrites with very rare exceptions are characterized by very low CL intensities (Ponahlo 2000). Pulse CL study revealed that the spectrum consists of a relatively broad red band peaking at 685–695 nm, accompanied by narrow lines with the strongest one at 679 nm and the weaker ones at 650, 655, 664, 700, 707 and 716 nm. All lines and bands have been ascribed to several Cr^{3+} centers (Solomonov et al. 2002). The natural chrysoberyl and alexandrite in our study consisted of six samples. The laser-induced time-resolved technique enables us to detect two different Cr^{3+} and possibly Mn^{4+} and V^{2+} emission centers (Figs. 4.54–4.55).

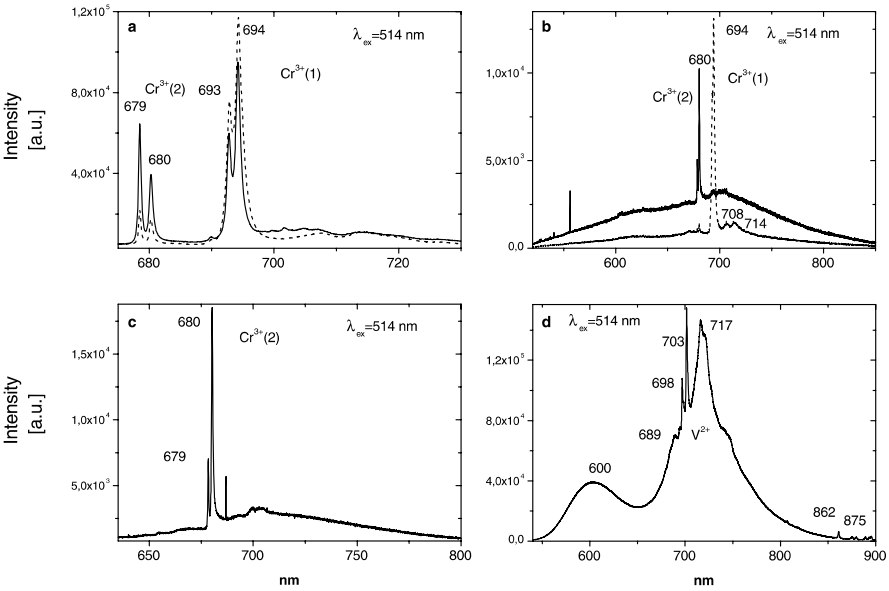

Fig. 4.54. Laser-induced steady-state luminescence spectra of alexandrite (**a–c**) and chrysoberyl (**d**) demonstrating different Cr^{3+} and possibly V^{2+} centers. Vertical polarisation – straight line, horizontal polarization – dash line

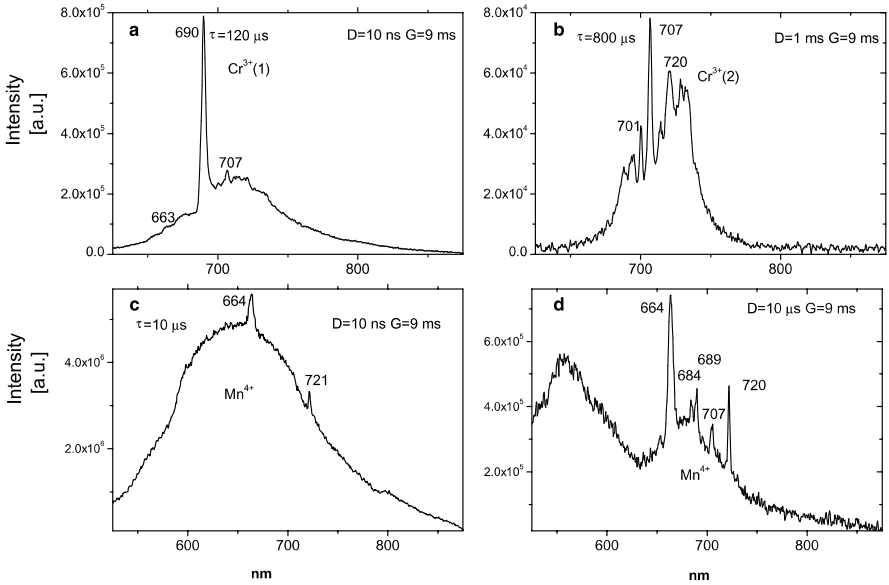

Fig. 4.55. a–d Laser-induced time-resolved luminescence spectra of alexandrite demonstrating Cr^{3+} and possibly Mn^{4+} centers

4.10.7
Garnet: Pyrope $Mg_3Al_2(SiO_4)_3$ and Grossular $Ca_3Al_2(SiO_4)_3$

The unit cell of garnet contains eight formula units. It's silicon-oxygen tetrahedra exist as independent groups linked to octahedral of the trivalent ions, while the divalent metal ions are situated in the interstices within the Si–Al network, each divalent ion being surrounded by eight oxygen atoms.

The main color center is Cr^{3+} substituting for Al^{3+}. It generates two absorption bands in the visible part of the spectrum with resulting red color. The larger intensity of the ultra-violet absorption, resulting in the red tint increasing, is connected with the presence of Fe^{3+} impurity. Besides that, the orange-red color of pyrope may be connected with Fe^{2+} and Ti^{4+} impurities. Rodolite has a complex pyrope-almandine composition and its red color is connected with a Fe^{2+} center. The main color centers in spessartite are Mn^{2+} and Fe^{2+}. Mn^{2+} generates absorption bands in the violet part of the spectrum with corresponding yellow and orange tints. The green color of grossular is mainly connected with Fe^{3+} impurity substituting for Al^{3+}. The orange color is connected with additional absorption in the violet part of the spectrum. The reason is the influence of Fe^{3+} impurities substituting for Si^{4+}. Another reason for the green color may be V^{3+} impurity with two absorption bands in the visible part of the spectrum (Platonov et al. 1984).

Steady-state photoluminescence spectra of natural garnet were connected with a Cr^{3+} broad emission band peaking at 880 nm (Tarashchan 1978). Two strong bands, one in the yellow, and the other in the red characterize CL spectra of natural hydrogrossular. The first band at 590 nm was ascribed to Mn^{2+} substituting for Ca^{2+}. The red one extends into the NIR and has narrow peaks at 689, 701 and 717 nm and was not interpreted (Ponahlo 2000).

The grossular is the very rare specie of the six common anhydrous minerals of the garnet group. Its luminescence has been connected with Cr^{3+} centers, which substitute for the Al^{3+} and occupy a site of the distorted octahedral symmetry, which in fact is trigonal C_{3i}. Trivalent chromium in grossular occupies a high crystal field position, the vibronic $^4T_{2g}$ level is found at energies higher than the ^2E_g state. The emission can occur from both levels at room and liquid helium temperatures. Based on optical absorption spectra, spectral field strength D_q and Racah parameters B and C have been calculated: $10D_q$ = 17,460 cm^{-1}, B = 670 cm^{-1} and C/B = 4.78. The luminescence spectra of Cr^{3+} in grossular at room temperature contain a strong broad band peaking at 720 nm and three sharp lines centered at 697, 700 and 701 nm. The decay times of both R-lines were found to be equal within the experimental error for the whole range of temperatures as expected in the case of two thermalized levels. This indicates that the nonradiative transitions between them are much faster than any other radiative transitions in the system (Czaja and Mazurakb 1994).

The natural garnet in our study consisted of ten samples with different colors. The laser-induced time-resolved technique enables us to detect trivalent rare-earth elements, Mn^{2+} and possibly Mn^{4+} emission centers (Figs. 4.56–4.57).

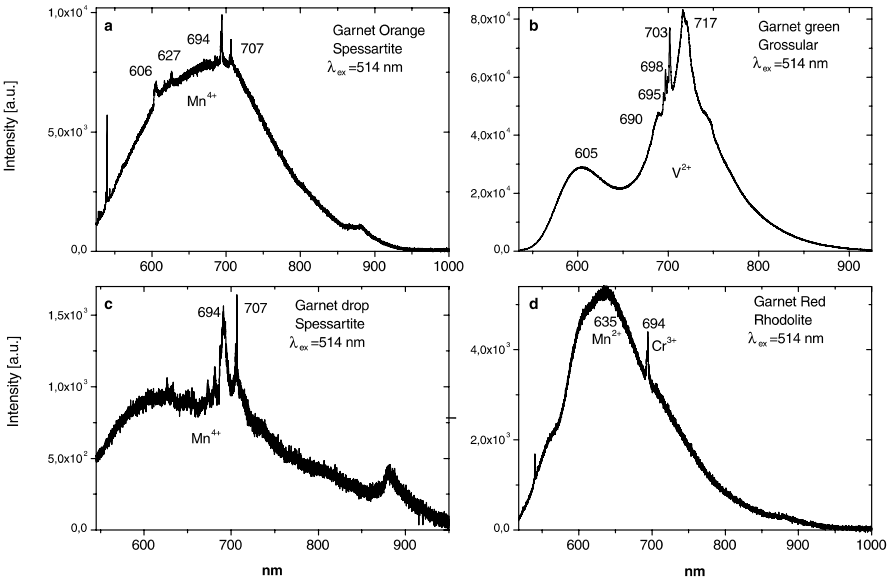

Fig. 4.56. a–d Laser-induced steady-state luminescence spectra of garnet demonstrating Cr^{3+}, Mn^{2+}, and possibly Mn^{4+} and V^{2+} centers

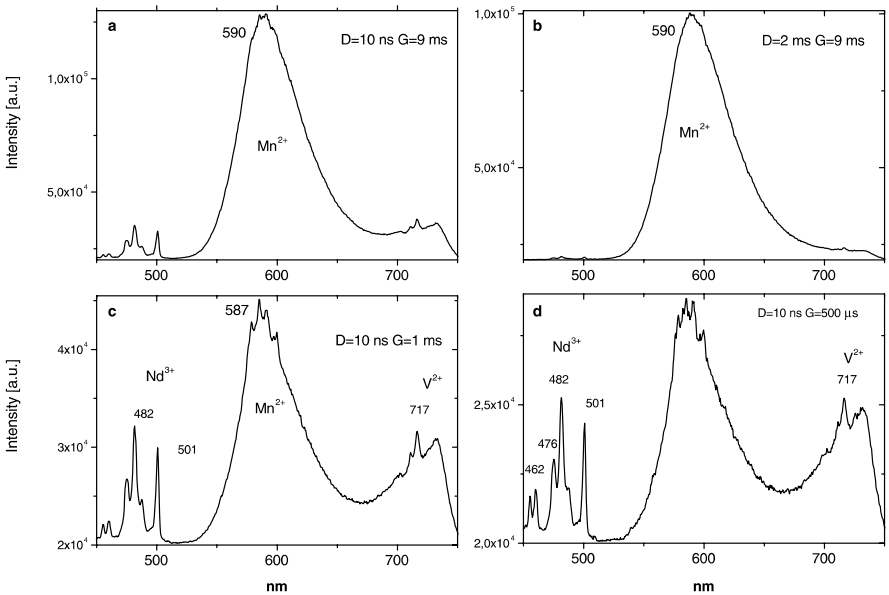

Fig. 4.57. a–d Laser-induced time-resolved luminescence spectra of garnet demonstrating Mn^{2+}, and possibly V^{2+} and Nd^{3+} centers

4.10.8
Tourmaline $(Na,Ca)(Mg,Al,Li)_3Al_6x(BO_3)_3Si_6O_{18}OH$

Tourmaline has a rhombohedral unit cell. The six silicon atoms are each surrounded tetrahedrally by four oxygen atoms, each tetrahedron sharing two of its oxygens with the neighboring tetrahedra to form a six-member ring of composition Si_6O_{18}: the Al ions are coordinated to six oxygen atoms in a very distorted octahedron.

Under lamp excitation tourmaline is practically non-luminescent, while under X-ray excitation it exhibits impurity luminescence from Fe^{3+} centered at 700–750 nm and Mn^{2+} centered at 560–570 nm (Kusnetsov and Tarashchan 1988). The natural tourmaline in our study consisted of four samples. The laser-induced time-resolved technique enables us to detect Cr^{3+} emission centers (Fig. 4.58).

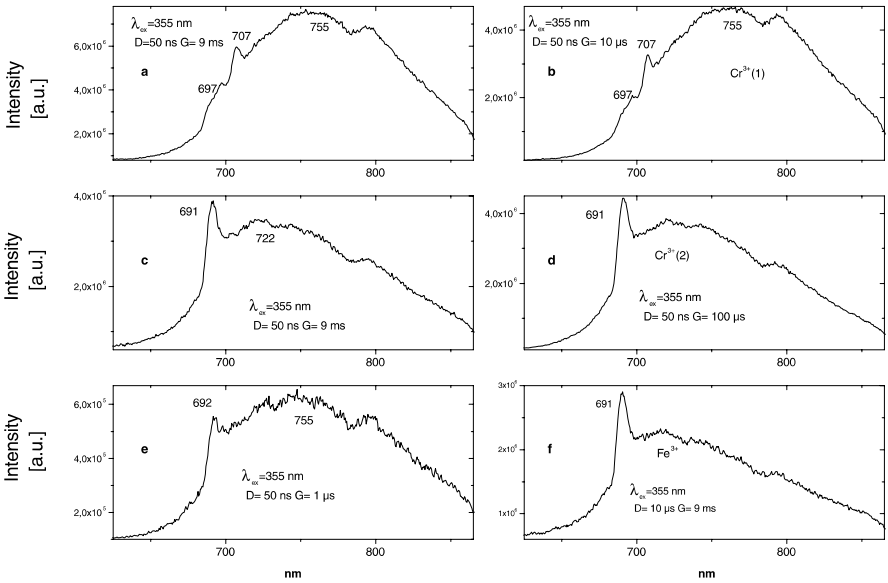

Fig. 4.58. **a–f** Laser-induced time-resolved luminescence spectra of tourmaline demonstrating Cr^{3+}, and Fe^{3+} centers

4.10.9
Epidote (Zoisite) $Ca_2AlAl_2O(OH)(Si_2O_7)(SiO_4)$

Epidote is the group name for a family of minerals of the general composition $Ca_2(Fe^{3+}, Al, Mn^{3+})Al_2O[SiO_4][Si_2O]–(OH)$. Epidote (octahedral Fe^{3+}) and clinozoisite (Al) represent the most common compositions among the epidote group. Zoisite is equivalent to clinozoisite, but it has a different crystalline system. Rare epidote-clinozoisites abundant in Cr, V, and Pb also exist. The

epidote structure consists of chains of octahedra (M sites) elongated parallel to the y crystallographic axis and cross-linked by the silicate groups SiO_4 and Si_2O_7. There are three distinct kinds of octahedra (M1, M2, and M3) arrayed along two types of chains. One chain type consists entirely of edge-sharing octahedra (M2), whereas the other contains M1 octahedra alternating with M3 octahedra along its length. The resulting framework structure contains large cavities (A sites) where the Ca^{2+} cations are housed in 9–10-fold coordination. Like the chains of octahedra, epidote crystals themselves are also elongated parallel to the y-axis. In typical epidote-clinozoisites, Fe^{3+} and Mn^{3+} substitute for Al principally in M3 sites; M2 sites house only A1. M1 sites are usually dominated by A1 but may contain Mn^{3+}. The explanation for the preference of these cations for the M3 site is twofold. First, both cations are larger than Al^{3+}, and the M3 octahedron is the largest in the structure. Second, the M3 sites are relatively distorted, and this characteristic may permit Mn^{3+} to gain additional stabilization energy here, over the other M sites.

The optical absorption and luminescence properties of zoisite have been studied (Koziarsca et al. 1994). It was found that the strong absorption bands around 750 and 585 nm are connected with transitions between the ground $^3T_1$ state and the first excited state $^3T_2$ of V^{3+} ions at Al(II) and Al(I) sites, respectively. The band peaking at 545 nm was associated with the transition from the $^3T_1$ ground state to the $^1A_1$ states for both of these crystallographic sites. The possible presence of V^{2+} ions was also proposed. The strong line at 709 nm in the low-temperature luminescence spectra has been assigned to transitions between the ground and the lower component of the first excited level ^2E (R_1-line) in the $3d^3$ shell. The line at 692 nm, observed in the luminescence at higher temperatures was associated with luminescence from the upper component (R_2 line) of the ^2E level. At room temperature the luminescence from ^2E level overlaps with a broad band of vibronic origin. The other line at 704 nm was also observed and connected to a vibronic origin. The decay time of those lines at room temperature was 260 µs. The possible ions with $3d^3$ shell were supposed as Cr^{3+} and V^{2+}. The weak low-temperature IR emission band was connected with V^{3+} luminescence. The natural zoisite in our study consisted of one sample. The laser-induced time-resolved technique enables us to detect Eu^{2+}, Dy^{3+}, Tb^{3+}, Sm^{3+} and possibly V^{2+} emission centers (Fig. 4.59).

4.10.10 Eosphorite $AlPO_4Mn(OH)_2H_2O$

Mineral eosphorite has been studied by Vergara et al. (1990). The crystal structure of eosphorite contains two kind of octahedra. One of these is composed of $MnO_4(OH)_2$ sharing opposite O–O edges and the other of $AlO_2(OH)_2(H_2O)_2$ sharing opposite H_2O corners. Absorption spectra are characterized by a number of bands, which have been associated with transitions of Mn^{2+}. All photoluminescence was connected with Cr^{3+} ions (Fig. 4.60).

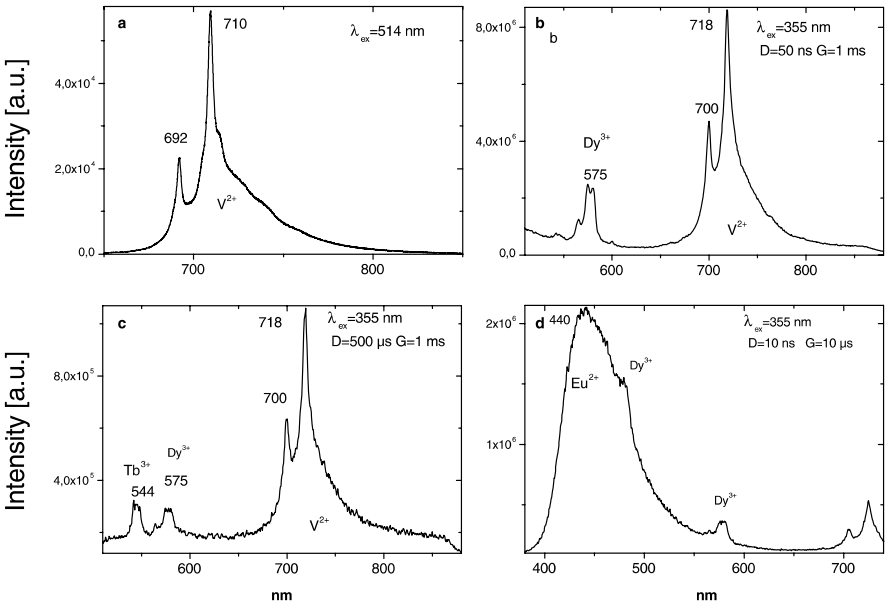

Fig. 4.59. Laser-induced steady-state (**a**) and time-resolved (**b–d**) luminescence spectra of zoisite demonstrating Cr^{3+}, Eu^{2+}, Tb^{3+}, Dy^{3+} and possibly V^{2+} centers

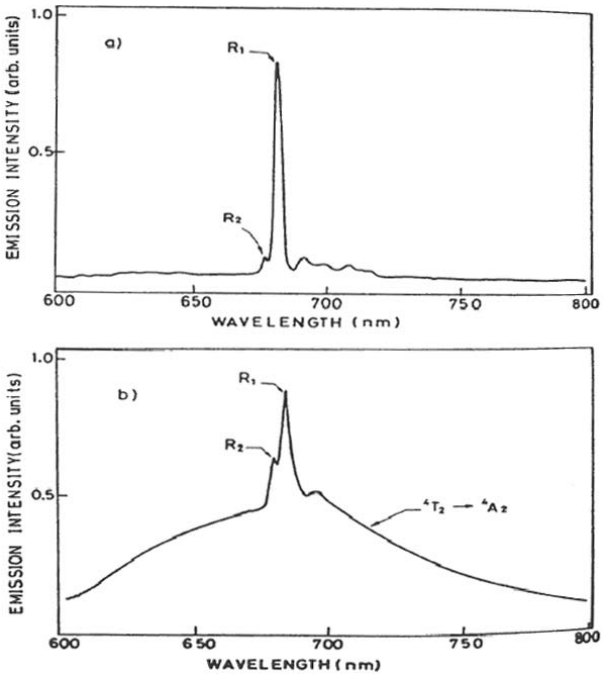

Fig. 4.60. Laser-induced luminescence spectra of eosphorite Vergara et al. (1990)

4.10.11 Spodumen $LiAlSi_2O_6$

Spodumen is a monoclinic pyroxene, space group $C_{2h}^6(C2/c)$, with two not equivalent metal cation sites M1 and M2. The aluminum occupies the smaller M1 site, which is approximately octahedral (actual symmetry C_2) with an average metal-oxygen distance of 1.92 A. The M2 site, occupied by Li, is also six-fold coordinated with an average metal-oxygen distance of 2.23 Å. Both Al and Li sites may be substitutionally replaced by ions of the transitional metals in various proportions. Both Mn^{2+} and Cr^{3+} centers have been identified in luminescence spectra by steady-state spectroscopy (Tarashchan 1978; Walker et al. 1997). At room and lower temperatures only one emission band of Mn^{2+} occurs and the excitation spectra taken for the different wavelengths of the luminescence bands are always the same. So it is very probable that Mn^{2+} ions in the spodumen matrix present only in one site. The calculated values of $10D_q$ and B are consistent with the occupation of larger M2(Li) weak-field site. Mn^{2+} is mainly in Li-sites rather than Al-sites.

The color of spodumen can vary from pale pink for the kunzite variety to a deep green for the hiddenite variety, but colorless crystals also exist. The green color of hiddenite is connected with Cr^{3+} substituting for Al^{3+}, while V^{3+} also takes part in optical absorption spectrum formation. The green-yellow color of spodumen is connected with Fe^{3+} in the M1 position and Fe^{2+} in the M2 position. Pink color of kunzite is connected with Mn^{3+} impurities in different structural positions M1 and M2 (Platonov et al. 1984).

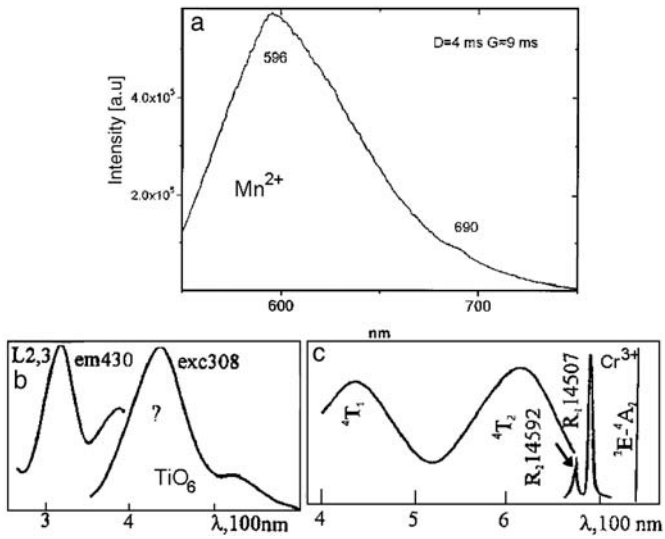

Fig. 4.61. Laser-induced time-resolved (**a**) and steady state (**b,c**; Gorobets and Rogojine 2001) spectra of spodumen demonstrating Mn^{2+}, Cr^{3+} and possibly TiO_6 centers

The natural spodumen in our study consisted of three samples. The laser-induced time-resolved technique enables us to detect Mn^{2+} and Cr^{3+} emission centers (Fig. 4.61).

4.10.12
Boehmite and Diaspor AlOOH

The structure of boehmite contains double sheets of octahedra with Al ions at their centers, and the sheets themselves are composed of chains of octahedra. In diaspor the oxygens are in a hexagonal close packed layer; those within the double octahedral layers in boehmite are in a cubic packing relationship. Luminescence center Cr^{3+} characterizes steady-state spectra (Solomonov et al. 1994; Shoval et al. 1999). The natural boehmite and diaspor in our study consisted of twelve samples. The laser-induced time-resolved technique enables us to detect Cr^{3+} emission centers (Figs. 4.62–4.63).

4.10.13
Chlorite $(Mg,Al,Fe)_{12}[(Si,Al)_8O_{20}](OH)_{16}$

The chlorites are a group of minerals with a layered structure, which in many respects resemble the micas. The monoclinic structure of chlorite is one of regularly alternating talc-like $Y_6Z_8O_{20}(OH)_4$ and brucite-like $Y_6(OH)_{12}$ sheets.

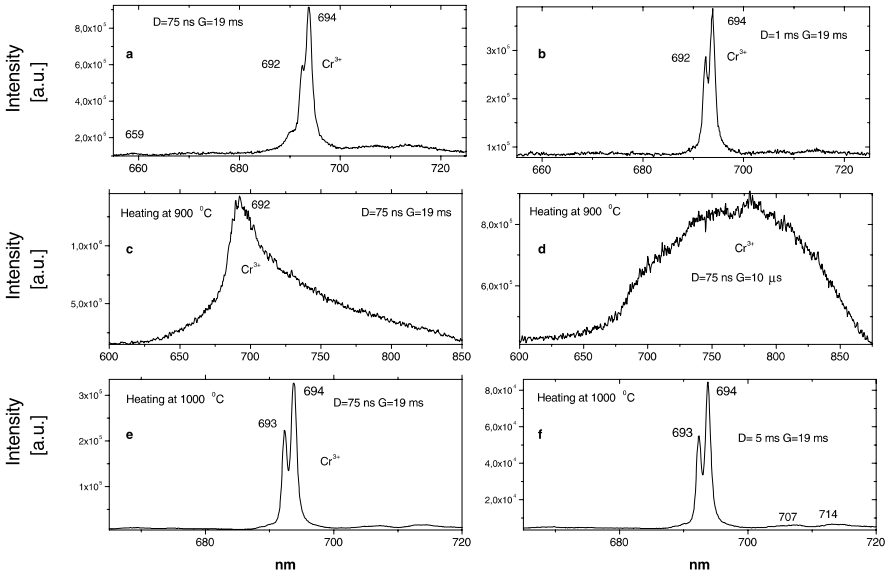

Fig. 4.62. a–f Laser-induced time-resolved luminescence spectra of diaspore demonstrating Cr^{3+} centers and its change with heating

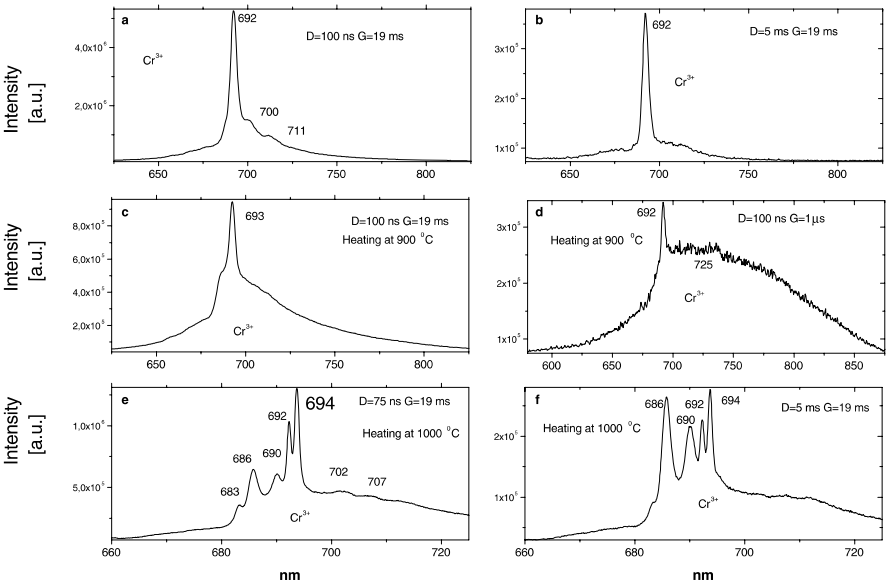

Fig. 4.63. a–f Laser-induced time-resolved luminescence spectra of boehmite demonstrating Cr^{3+} centers and its change with heating

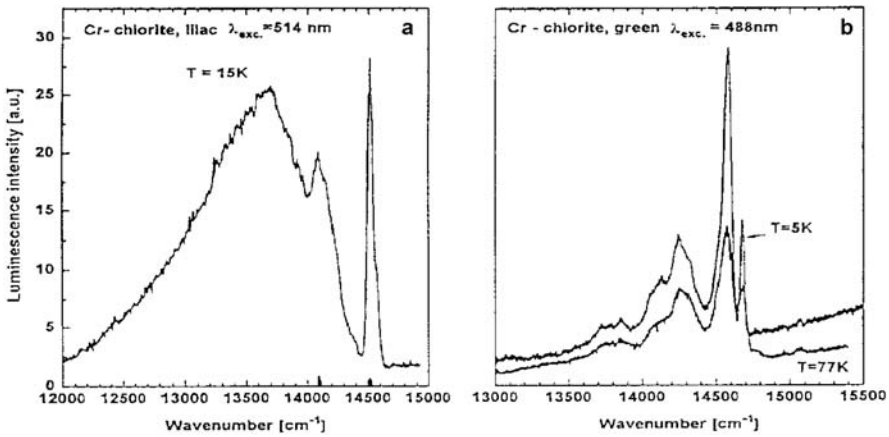

Fig. 4.64. Laser-induced luminescence of chlorite with Cr^{3+} emission (Czaja 1999)

For chromium containing lilac chlorite two types of luminescence were observed at 15 K: phosphorescence at 14,518 and 1,547 cm^{-1} with a decay time of 60 µs and a fluorescence band at about 13,850–13,500 cm^{-1} with a decay time of several microseconds. For green chlorite weak fluorescence at 13,900 cm^{-1} and phosphorescence at 14,320 and 14,665 cm^{-1} were observed at room tem-

perature. At low temperature phosphorescence lines at 14,580 and 14,676 cm^{-1} were observed on the short wave range of the vibronic band (Fig. 4.64). Such emission has been connected with Cr^{3+} present in different sites in the brucite-like layers (Czaja 1999). It is very interesting that iron ions (1.54 wt. %) did not quench Cr^{3+} emission. The same was detected in iron containing chlorites under X-ray excitation (Kusnetsov et al. 1991).

4.11 Sodium (Na^+) Bearing Minerals

The main substituting luminescence center is Mn^{2+} (ionic radius of Na^+ = 1.16 Å). It is interesting to note that Na bearing minerals are very often characterized by luminescence connected with S_2^- and O_2^- impurities.

4.11.1 Sodalite $Na_8[Al_6Si_6O_{24}]Cl_2$

The alumosilicates framework is formed by the linkage of SiO_4 and AlO_4 tetrahedra in approximately equal numbers, each corner oxygen being shared by two tetrahedra. In sodalite, cage-like cubo-octohedral units are formed bounded by six rings of four tetrahedra and eight rings of six tetrahedra, which are differently oriented. The six-member rings define a set of channels, which intersect to form large cavities. The cavities are occupied by chlorine

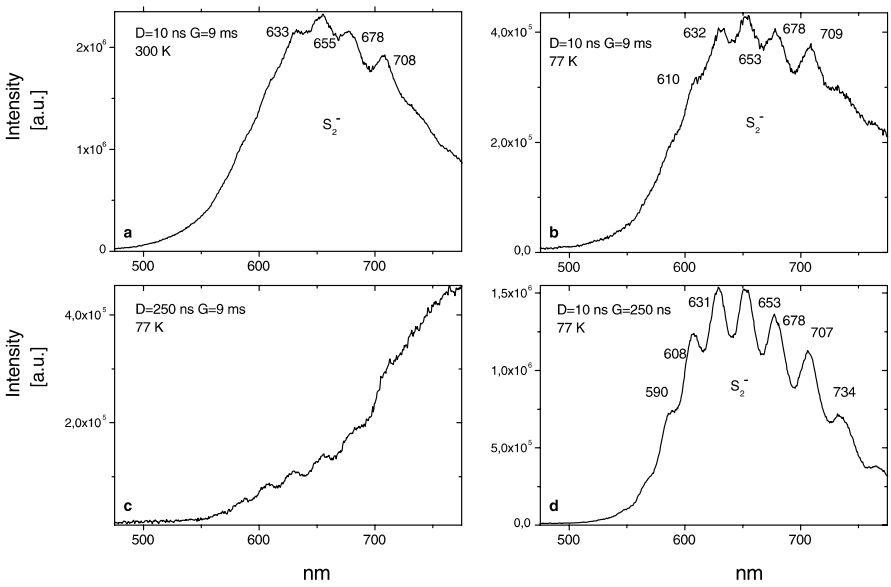

Fig. 4.65. a–d Laser-induced time-resolved luminescence of S_2^- in sodalite

ions and these are tetrahedrally coordinated by sodium ions. In sodalite the emission is related to the presence of molecular ions S_2^- with a unique emission profile. Similar emission was found also in hackmanite, scapolite and others (Tarashchan 1978).

The natural sodalite in our study consisted of two samples. The laser-induced time-resolved technique enables us to detect the S_2^- emission center (Fig. 4.65).

4.12 Silver (Ag^+) Minerals

Silver halides are capable of intrinsic luminescence.

4.12.1 Chlorargyrite AgCl and Embolite Ag(Cl,Br)

It was found by steady-state luminescence spectroscopy that silver halides, such as chlorargyrite and embolite, formed in oxidized zones of silver ores demonstrate luminescence at low temperatures. Such emissions were explained in a energy band scheme by donor-acceptor recombination. By analogy with synthetic AgCl and AgBr samples the determined bands have been connected in the energy bands scheme with a recombination of electrons with autolocalized holes and holes associated with metal-vacancy complexes. Under powerful laser excitation such luminescence was detected even at room temperature. The spectra (Fig. 4.66a–c) are evidently connected with the same luminescence centers (Gaft et al. 1989b). The laser-induced time-resolved luminescence spectrum of chlorargyrite demonstrates a relatively narrow green band with a short decay time of $\sim 2-3$ μs, which is especially strong in spectra with narrow gate (Fig. 4.66d).

4.13 Manganese (Mn^{2+}) Bearing Minerals

Minerals of manganese are capable of intrinsic luminescence.

4.13.1 Rhodonite $CaMn_4Si_5O_{15}$ and Rhodochrosite $MnCO_3$

It was established by steady-state luminescence spectroscopy that minerals of Mn, such as rhodonite, rhodochrosite, helvine, triplite, Mn-apatite, Mn-milarite and others, show dark red luminescence, mainly at 77 K, which is uncommon to impurity Mn^{2+}. The excitation center proved to be regular Mn^{2+}, while the emission center is Mn^{2+}, situated near some lattice defect (Gorobets et al. 1978; Gaft et al. 1981).

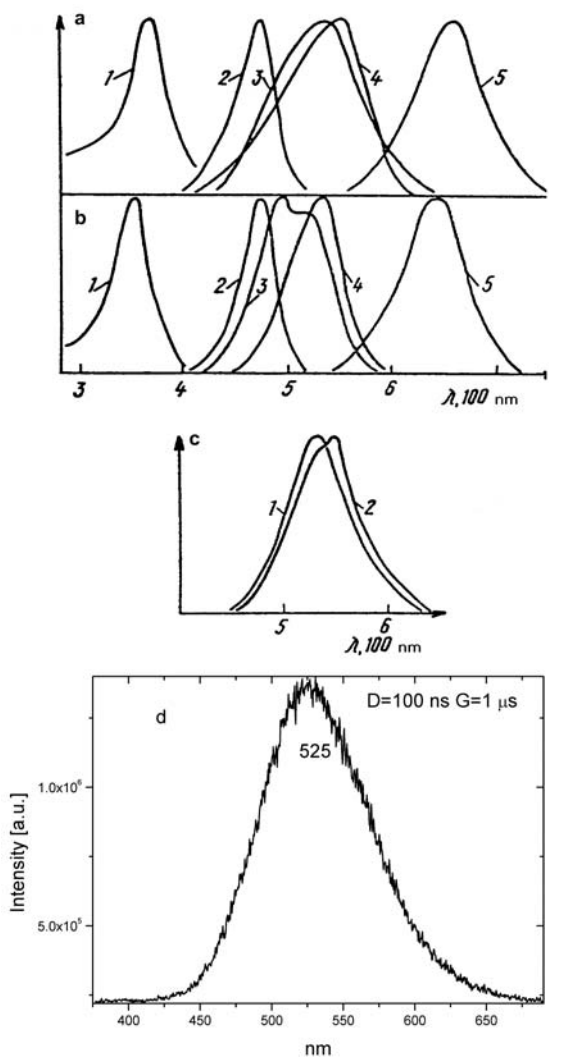

Fig. 4.66. Laser-induced excitation (1) and luminescence spectra of natural silver halides (2,3-cerargerite, 4-embolite, 5-bromargeritechlorargyrite and embolite): (**a**) *upper* – 300 K; (**b**) 77 K; (**c**) *middle* – time-resolved spectra with zero delay time (1) and delay time of 150 ns (2) (Gaft et al. 1989b). (**d**) *bottom* – laser-induced time-resolved luminescence spectrum of chlorargyrite under 355 nm excitation

The natural Mn minerals in our study consisted of four samples. The laser-induced time-resolved technique enables us to detect impurity and intrinsic luminescence of Mn^{2+} and Nd^{3+} (Fig. 4.67).

4.14 Uranium (U^{6+}) Bearing Minerals

Minerals of uranium are capable of intrinsic luminescence, which is connected with uranyl emission. It is well known that certain minerals, which contain

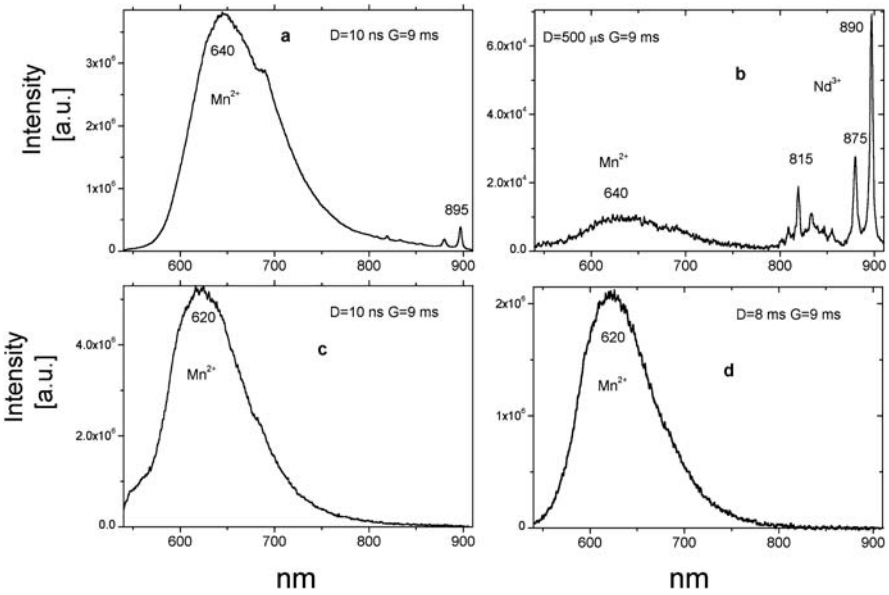

Fig. 4.67. **a–d** Laser-induced time-resolved luminescence spectra of rhodonite and rhodochrosite demonstrating Mn^{2+} and Nd^{3+} centers

uranium as the uranyl ion UO_2^{2+}, exhibit fluorescence with distinctive spectral and temporal characteristics. The photoluminescence of nearly 40 uranyl minerals was investigated at 300 and 77 K, mainly under UV lamps, but also under UV lasers excitation. The highly fluorescent uranyl ion may also be present in other geologic materials, such as siliceous matrices, calcites and barites (Gororbets and Sidorenko 1974; Tarashchan 1978; Kasdan et al. 1981; Gorobets and Rogojine 2001). This luminescence is effectively excited only by the short UV and its decay time is in the several hundreds of μs range. Three different models of uranyl ion interrelation with host mineral were proposed: surface films of uranyl-containing minerals; presence in the host matrices that are relatively transparent at the excitation and luminescence wavelength of UO_2^{2+}. Uranium mineralisation was the first object for luminescence LIDAR.

Representative time-resolved luminescence spectrum is given in Fig. 4.68.

4.15 Magnesium (Mg^{2+}) Bearing Minerals

Mn^{2+} is the mostly probable luminescence center suitable for substitution for Mg^{2+} in the natural process of crystallization because of their close ionic radii and charges. The next possible candidates are Cr^{3+} replacing Mg^{2+} and Cr^{4+} replacing Si^{4+}.

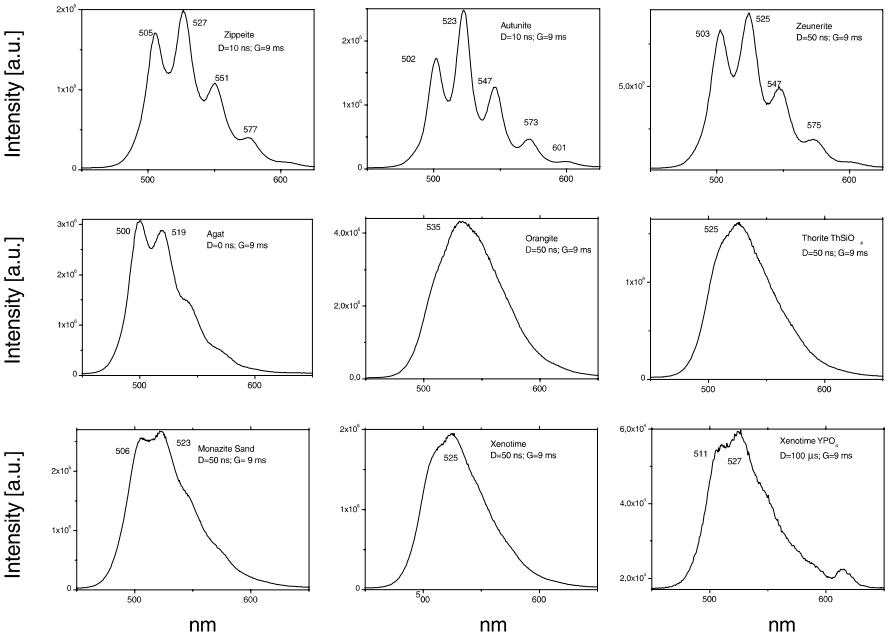

Fig. 4.68. Laser-induced time-resolved luminescence spectra of uranyl minerals

4.15.1
Forsterite Mg_2SiO_4

Forsterite belongs to the minerals of the olivine group, which all possess orthorhombic symmetry and a structure consisting of independent SiO_4 tetrahedra linked by divalent atoms in octahedral coordination. Forsterite has space group Pnma. The oxygens are arranged in approximately hexagonal packing and lie in sheets parallel with the (100) plane. The SiO_4 tetrahedra point alternatively either way in both the x and y direction; half the (Mg, Fe) atoms are located at centers of symmetry and half on reflection planes. Natural forsterite demonstrates luminescence of Mn^{2+} with a very long decay time of 12–15 ms and Fe^{3+} (Tarashchan 1978). Laser-induced time-resolved luminescence spectra demonstrate emission of Mn^{2+} with very long decay time (Fig. 4.69).

4.16
Rare-Earth Bearing Minerals

The mineral matrix is formed chiefly by La^{3+} or Ce^{3+}. The last one is widely regarded as the luminescence impurity center, but in rare-earth bearing minerals it is subjected to concentration quenching because of strong exchange

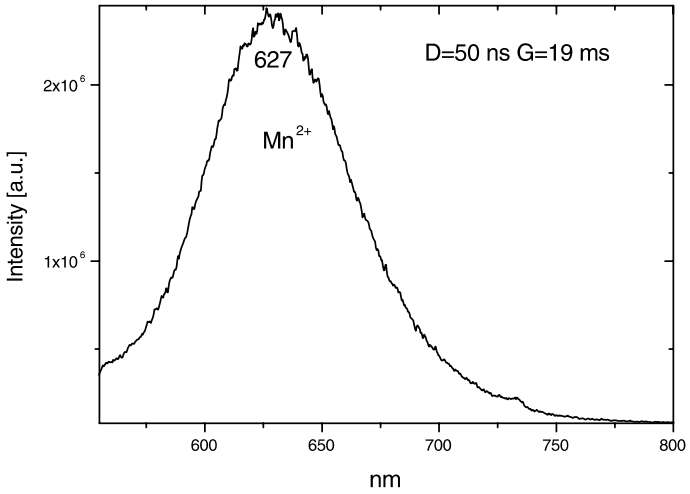

Fig. 4.69. Laser-induced time-resolved luminescence spectra of Mn^{2+} in forsterite

interaction of outer 5*d* orbitals of neighboring Ce^{3+} ions. Hereby its luminescence is not observed in REE minerals. From the other side, other trivalent REE can achieve some concentrations without quenching of luminescence, because outer electron shells, such as $5s^2$ and $5p^6$, shield their inner $4f$–$4f$ transitions.

4.16.1 Monazite (Ce,La)PO_4

The monazite structure consists of distorted PO_4 tetrahedra with each metal atom roughly equidistant from nine oxygen atoms. Minor amounts of other rare-earth elements may occur. Steady-state luminescence under X-ray excitation of monazite revealed emission of Gd^{3+}, Tb^{3+}, Dy^{3+} and Sm^{3+} (Gorobets and Rogojine 2001). Laser-induced time-resolved luminescence enables us to detect Sm^{3+}, Eu^{3+} and Nd^{3+} emission centers (Fig. 4.70).

4.16.2 Thorite $ThSiO_4$

Thorite and orangite (orange thorite) have a tetragonal structure and are isostructural with zircon. Steady-state spectra under X-ray and laser (337 nm) excitations are connected with REE^{3+}, namely Sm^{3+}, Tb^{3+}, Dy^{3+} and Eu^{3+}. Reabsorption lines of Nd^{3+} have been also detected (Gorobets and Rogojine 2001). Laser-induced time-resolved luminescence enables us to detect Eu^{3+} and uranyl emission centers (Fig. 4.70).

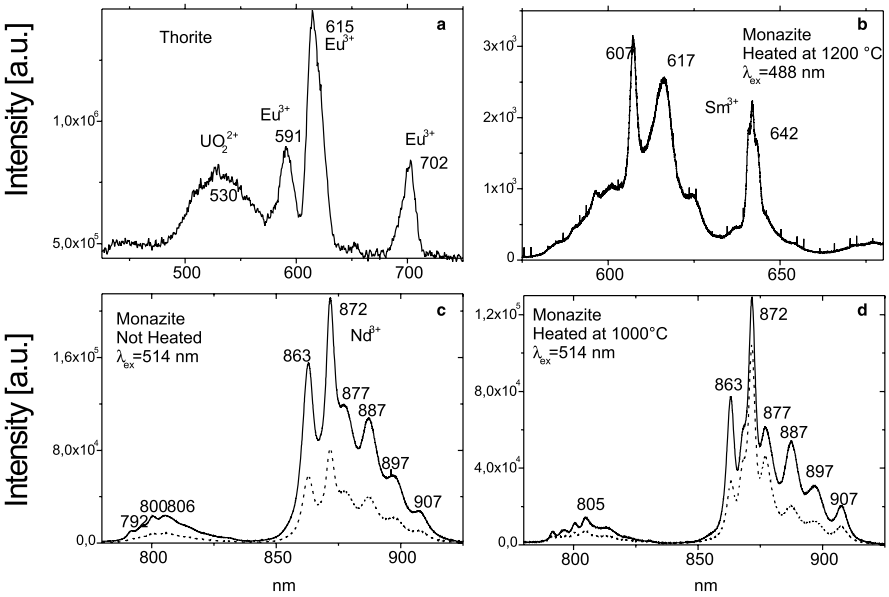

Fig. 4.70. Laser-induced steady-state luminescence spectra of thorite (**a**) and monazite (**b–d**) natural and heated demonstrating uranyl, Eu^{3+}, Sm^{3+} and Nd^{3+} centers. *Straight line*-vertical polarization, *dashed line*-horizontal polarization

4.17 Carbon Bearing Minerals

4.17.1 Diamond C

A unique situation exists in the case of diamonds, where the detailed spectroscopic descriptions of the centers are detected, but models are only proposed for a few of these. From more then 100 detected centers models are only determined for seven, mainly based on EPR interpretations. The model includes identification of the impurity, vacancy, interstitial atom, their aggregations and their crystallochemical position together with quantum-chemical and spectroscopic description.

The luminescence of diamonds is related to various defects in its structure. Almost always, luminescence centers in diamonds are related to N atoms. It is logical, because the atomic radii of C and N are nearly equal (approximately 0.77 Å). Luminescence spectroscopy has proven to be the most widely used method in studies of diamonds even in comparison with optical absorption, ESR, IR and Raman spectroscopies. Hundreds of spectra have been obtained, fluorescence characteristics enter into diamond quality gemological certificates, a wide range of electronic and laser applications are based on diamond optical properties in excited states; nitrogen center aggregation is controlled by the residence time of diamond in the mantle, distinction between natural

and synthetic, irradiated, and enhanced diamonds and identification of any particular diamond can be made by detailed luminescence studies; CL topography reflects growth parameters (Walker, 1979; Bokii et al. 1986; Plotnikova 1990; Tarashchan and Lupashko 1999; Collins 2000).

Determination of tint is the essential and the most intricate aspect in diamonds evaluation and may be useful for luminescence interpretation. The coloration of diamond is a reflection of its complex structural peculiarity. To describe a slight shade of color, one has to use a lot of physics, crystallography and analytical tools. The following types of diamond coloration are generally distinguished.

Colorless to yellowish: a common color of diamonds of gem quality given to the crystal by nitrogen impurity and certain types of nitrogen centers. Brown to yellow Australian (Argail) colors called Cognac and Champagne are due to dislocation related centers. In rare blue diamonds the color is connected with boron impurity. In green diamonds the color is radiation induced (resulting from either natural or artificial irradiation) and is connected with vacancies (vacancies formation is possible not only after irradiation, but during growth and as a result of certain transformations in the solid state). Rare Australian rose or purple colors are connected with dislocation related centers of a different nature compared with the centers of brown and yellow colors. Yellow color is where individual nitrogen atoms substitute for carbon. Black and ink violet colors are from epigenetic finely dispersed carbon. Certain raw diamonds acquire or change colors when subjected to radiation and further change color when heated. This dynamic is traced to the earlier part of the crystal's history.

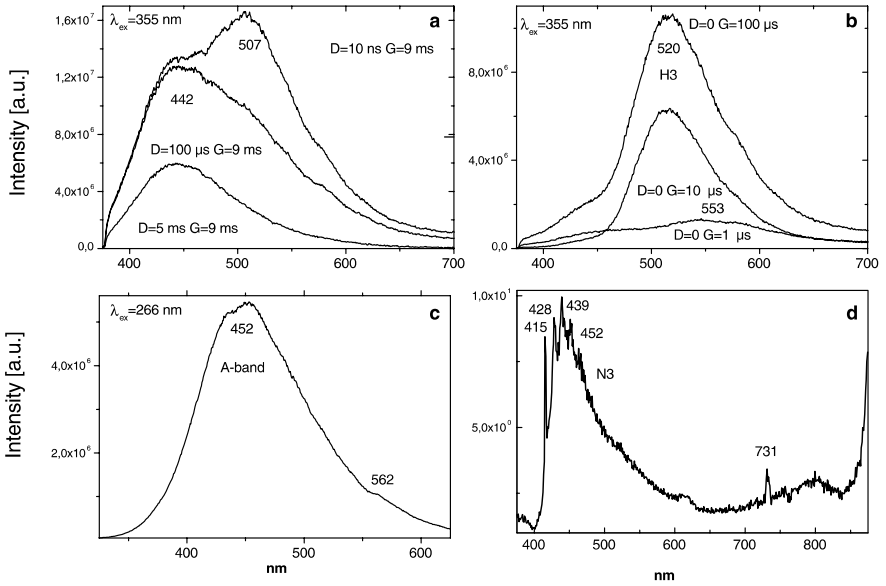

Fig. 4.71. a–d Laser-induced time-resolved luminescence spectra of diamonds demonstrating N3, A, and H3 centers

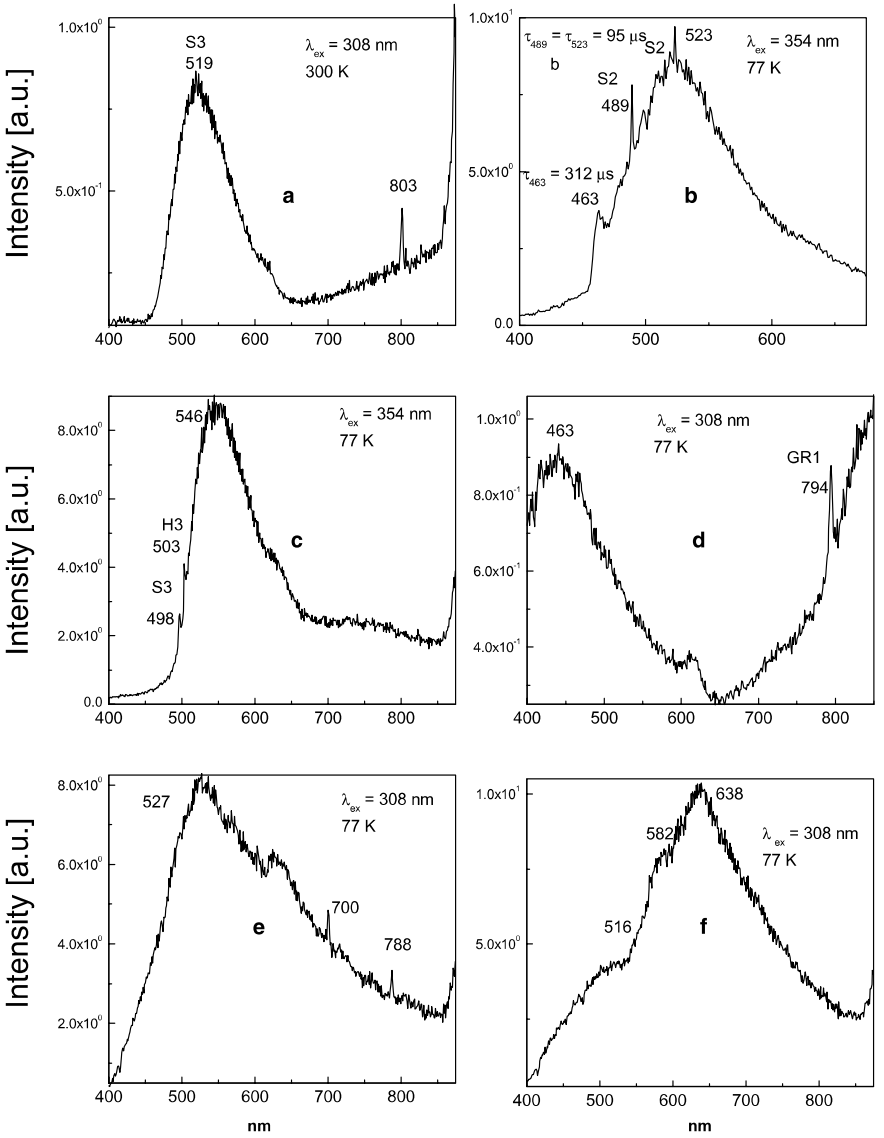

Fig. 4.72. a–f Laser-induced steady state luminescence spectra of diamonds demonstrating S3, S2, H3, GR1, 700, 788 and possibly 640 nm

As much as the diamonds colors are extraordinary their absorption spectra are monotonous. Their absorption curve bends slightly from IR to UV.

Ten specimens have been chosen from the collection of approximately 200 characteristic crystals taken from some thousands of Yakutian diamonds. Representative time-resolved luminescence spectra are given in Figs. 4.71–4.72.

CHAPTER 5

Interpretation of Luminescence Centers

The interpretation of luminescence in minerals begins with the characterization of the luminescence centers, including the identity of the ions involved, their locations in the crystal structure, their energetic interactions, and their modes of energy transfer with each other, with other ions in the structure, or with vibrational states.

5.1 Rare-Earth Elements (REE)

The geochemical rare-earth (RE) data provide major evidence to test, support, and constrain various theories and processes proposed for the origin of the major rock groups in the Earth. Our understanding of the various rock-forming processes and geochemical evolution of the Earth has been considerably aided by data provided by the geochemical studies of the rare-earth elements. Neutron-activation analysis, isotope dilution mass spectrometry, inductive coupled plasma spectrometry, optical emission spectrometry, and X-ray fluorescence spectrometry are used to determine the RE contents in geological materials. The naturally occurring members of the lanthanide series make up a significant class of activator ions in minerals. The most common oxidation state for lanthanide ions is trivalent, but several members are known to exist in the divalent state. The optical properties of rare earths in minerals may be analyzed in a manner similar to that of impurities in crystals.

5.1.1 The Classical Treatment of Optical Properties of Trivalent REE

The optical transitions typical of RE ions in glasses, crystals and solutions correspond mainly to intra f^N transitions of predominantly electric dipole character. For a free ion, electric dipole transitions between states of the same configuration are strictly parity forbidden and the observed spectra of glasses, crystals, or solutions result from non-centrosymmetric interactions that lead to a mixing of states of opposite parity. The full description of the various mechanisms of mixing is thoroughly discussed. One of the most important mechanisms responsible for the mixing is the coupling of states of opposite parity by way of the odd terms in the crystal field expansion of the perturbation

potential V, provided by the crystal environment about the ion of interest. The expansion is done in terms of spherical harmonics or tensor operators that transform like spherical harmonics. This can be formulated in a general equation:

$$V = \sum_{k,q,i} B_q^k \left(C_q^k\right)_i \tag{5.1}$$

where the summation involving i is over all the electrons in question, k is the rank of the tensoral operator C, q is the relevant component of that operator ($-k \leq q \leq k$) and B is the expansion coefficient. The first term in the expansion has $k = q = 0$ and is spherically symmetric. This term gives the shift of spectral bands to the longer wavelength, as its influence on the upper levels is stronger than it is on the lower, more shielded levels. When only f electrons are involved, the terms in the expansion with $k \leq 6$ are nonzero. In addition, all terms with odd k vanish; hence it is the even terms in the expansion that reflect the splitting. B can be regarded as the coefficient of expansion to be determined empirically from ΔE,the magnitude of the splitting. A comparison of the spectra of the REE and the transition metal ions reveals that the crystal field splitting is of about 100–300 cm^{-1} in the former compared to several thousands cm^{-1} in the latter. The number of levels into which a single level can be split is determined by the site symmetry.

The crystal field model may also provide a calculation scheme for the transition probabilities between levels perturbed by the crystal field. It is so called weak crystal field approximation. In this case the crystal field has little effect on the total Hamiltonian and it is regarded as a perturbation of the energy levels of the free ion. Judd and Ofelt, who showed that the odd terms in the crystal field expansion might connect the $4f$ configuration with the $5d$ and $5g$ configurations, made such calculations. The result of the calculation for the oscillator strength, due to a forced electric dipole transition between the two states makes it possible to calculate the intensities of the lines due to forced electric dipole transitions.

$$f_e = \sigma \sum_{\lambda,q} T\left(\lambda_1 q_1 \varrho\right) \left(l^N \alpha S L J J_z \left\| U_{q+\varrho}^{\lambda} \right\| l^N \alpha^1 S L^1 J^1 J_z^1\right)^2 \tag{5.2}$$

while for rare earth, $\lambda = 2, 4, 6$.

T_λ are components of a tensor operator, the explicit expression for them being

$$T_\lambda = \sum_{\varrho,q} \frac{8\pi^2 m c}{3 h e^2} \frac{\left(n^2+2\right)^2}{9} Y^2\left(\lambda, q, \varrho\right) \tag{5.3}$$

where n is the refractive index of the medium. Other constants have their usual

meaning and:

$$Y\left(\lambda_1 q_1 \varrho\right) = -\frac{2}{E_{\mathrm{av}}} \sum_k (-1)\, q + \varrho\left(2\lambda + 1\right) \tag{5.4}$$
$$x \begin{pmatrix} 1 & \lambda & k \\ \varrho & (-\varrho + q) & q \end{pmatrix} x \begin{pmatrix} l & l' & \lambda \\ 1 & k & k'' \end{pmatrix}$$
$$x \left\langle l \left\| C^{(1)} \right\| l' \right\rangle \left\langle l' \left\| C^k \right\| l \right\rangle B_q^k e \int R_{nl}\, r\, R_{n'l'}\, \mathrm{d}r$$

E_{av} is the average energy difference between the configuration l^N and the perturbing configuration $l^{N-1}\, l$ ($l = 5d$ or $5g$). The quantities B_q^k are the odd parity terms in the static crystal field expansion, where $k = 1, 3, 5$ and 7, q are the components of k and depend on the symmetry of the medium, ϱ refers to the expansion of the dipole moment and determines the polarization of the transition

- $\varrho = 0 : \sigma$ components of the transition
- $\varrho = \pm 1 : \pi$ component of the transition

$R_{nl}\, R_{n'l'}$ are the radial parts of the wave function in the l^N and l^{N-1} configuration, respectively.

In theoretical calculations of the oscillator strengths the free ion-reduced matrix elements U$\sim$ are used and the coefficients T_λ are treated as adjustable parameters. Later the parameters T_λ were exchanged by Ω_λ. All attempts to derive the value $B \sim$ from micro-crystalline parameters of the lattice using the electrostatic point charge approximation theory have been thus far, unsuccessful. This is probably due to the extreme sensitivity of $B \sim$ to the exact positions of the ions, the exact form on the radial part of the wave functions and to the percentage of covalence of the bond. It is clear that a molecular orbital treatment should be applied in such cases. The existence of the nephelauxetic effect clearly indicates the overlapping of the charge clouds of the central ion and its ligand as a result of participation of f-orbitals in the chemical bonding of rare earth complexes. The observation of hypersensitive transitions obeying the selection rule, $\Delta J = \pm 2$, emphasize the influence of the ligand on spectral levels of the rare earth ion.

5.1.2 Theory of Optical Transitions in Trivalent REE

The characteristic absorption and emission spectra of lanthanide compounds in the visible, near ultra-violet and infra-red is attributed to transitions between $4f$ levels due to the fact that they present a sharp line with oscillators strengths typically of the order of 10^{-6}. These transitions are electric dipole forbidden but became allowed as forced electric dipole transitions.

The forced electric dipole mechanism was treated in detail for the first time by Judd (1962) through the powerful technique of irreducible tensor operators. Two years later it was proposed by Jørgensen and Judd (1964) that an additional mechanism of $4f$–$4f$ transitions, originally referred to as the pseudo-quadrupolar mechanism due to inhomogeneities of the dielectric constant, could be as operative as, or, for some transitions, even more relevant than, the forced electric dipole one.

In the standard theory the integrated coefficient of spontaneous emission of a transition between two manifolds J and J' is given by

$$A_{JJ'} = \frac{4\,e^2\,\omega^3}{3\,\hbar\,c^3}\left[\frac{n\left(n^2+2\right)^2}{9}\,S_{\mathrm{ed}} + n^3\,S_{\mathrm{md}}\right] \tag{5.5}$$

where ω is a regular frequency of the transition, e is the electronic charge, c is the velocity of light, $\hbar$ is Planck's constant and n is the refractive index of the medium. The electric and magnetic dipole strengths, respectively, S_{ed} and S_{md} (in units of e^2), are given by

$$S_{\mathrm{ed}} = \frac{1}{(2J+1)}\sum_{\lambda=2,\,4,\,6}\Omega_\lambda\left\langle \alpha' J'\left\| U^{(\lambda)}\right\|\alpha J\right\rangle^2 \tag{5.6}$$

where the quantities Ω_λ are the Judd-Ofelt intensity parameters as described before

$$S_{\mathrm{md}} = \frac{\hbar^2}{4\,c\,m_e\,c^2}\left\langle \alpha' J'\,\|L+2\,S\|\,\alpha J\right\rangle^2\frac{1}{2J+1} \tag{5.7}$$

and m is the electron mass. The reduced matrix elements are evaluated in the intermediate coupling scheme, and the angular momentum operators L and S are in the units of $\hbar$. The corresponding expression for the oscillator strength may be obtained from the relation

$$P_{JJ'} = \frac{2J+1}{2J'+1}\,\frac{m\,c^2}{2\,\omega^2\,e^2\,n^2}\,A_{JJ'} \tag{5.8}$$

The intensity parameters Ω_λ depends on both the chemical environment and the lanthanide ion, and theoretically they are given by

$$\Omega_\lambda = (2\lambda+1)\sum_{t,p}\frac{\left|B_{\lambda\,t\,p}\right|^2}{2\,t+1} \tag{5.9}$$

where $B_{\lambda tp}$ depends on the radial wave function, and the odd crystal parameters and energy difference between the $4f$ and next excited configuration of the opposite parity.

Here we are discussing only the static model and omit the vibronic interaction.

$$B_{\lambda t\,p} = \frac{2}{\Delta E}\,\langle rt+1\rangle\,\theta\left(t,\lambda\right)\gamma_{\mathrm{p}}^{\mathrm{t}} - \left[\frac{\left(\lambda+1\right)\left(2\lambda+3\right)}{\left(2\lambda+1\right)}\right]^{1/2} \times \left\langle r^{\lambda}\right\rangle\left(1-\sigma_{\lambda}\right)\left\langle 3\left\|C^{(\lambda/}\right\|3\right\rangle\Gamma_{\mathrm{p}}^{\mathrm{t}}\,\delta_{t,\lambda+1} \tag{5.10}$$

where ΔE is the energy difference between the barycenters of the excited $4f^{N-1}\ 5d$ and ground $4f^{N}$ configurations, $\langle r^{\mathrm{x}}\rangle$ is a radial expectation value, $\theta(t,\lambda)$ is a numerical factor, σ_{λ} is a screening factor, $C^{(\lambda)}$ is a Racah tensor operator of rank λ and $\delta_{t,\lambda+1}$ is the Kronecker delta function. The first term in the right-hand-side of Eq. 5.9 corresponds to the forced electric dipole mechanism, as expressed by the average energy denominator method, and the second term corresponds to the dynamic coupling mechanism within the point dipole isotropic ligand polarizability approximation (not discussed here).

5.1.3 Relaxation Processes in Trivalent REE

The luminescence intensity of emission depends on a given level on the radiative and nonradiative probabilities. The quantum yield is expressed as follows:

$$Q\cdot Y = \frac{\sum Ar}{\sum Ar + Wnr} \tag{5.11}$$

where Ar are the radiative transition probabilities and Wnr are the nonradiative ones.

These include ion-ion energy transfer, which can give rise to concentration quenching and non-exponential decay and relaxation by multiphonon emission, which is usually essential for completing the overall scheme, and can affect the quantum efficiency. For low concentration of rare earth dopant ions the principle nonradiative decay mechanism is a multiphonon emission.

The *ab initio* calculation of the transition rate between two electronic states with the emission of p phonons involves a very complicated sum over phonon modes and intermediate states. Due to this complexity, these sums are extremely difficult to compute; however, it is just this complexity, which permits a very simple phenomenological theory to be used. There are an extremely large number of ways in which p phonons can be emitted and the sums over phonon modes and intermediate states are essentially a statistical average of matrix elements. In the phenomenological approach it is assumed that the ratio of the p-th and $(p-1)$-th processes will be given by a coupling constant characteristic of the matrix in which the rare earth is situated and not depending

on the rare-earth electronic states. For a given lattice at low temperature the spontaneous relaxation rate is given by

$$W(0) = B e^{\alpha \Delta E} \tag{5.12}$$

where B and α are characteristic of the host (α is negative). Thus, the graph of the spontaneous rate versus energy gap will be a straight line in a case when this approach is valid. Experimental data have shown that the approach is very good for a large variety of hosts. In this way, all multiphonon rates can be inferred from a few measured rates.

The dominant emission process is the one, which requires the least number of phonons to be emitted. The minimum number of phonons required for a transition between states separated by an energy gap ΔE is given by

$$p = \frac{\Delta E}{\hbar \omega_{\max}} \tag{5.13}$$

where $\hbar\omega_{\max}$ is the maximum energy of optical phonons. With increased temperature, stimulated emission of phonons by thermal phonons increases the relaxation rate W according to

$$W\left(T\right) = W\left(O\right)\left(1 + \bar{n}\left(\hbar\omega_{\max}\right)\right)^{\mathrm{P}} \tag{5.14}$$

where n is the average occupation number of phonons at energy $\hbar\omega_{\max}$.

The non-radiative relaxation in the rare earth ions are related to their excited state population and are governed by the energy difference between the emitting level and the next lower level, separated by the number of phonons of the host. In the weak-coupling case for the rare-earth ions the temperature dependence of the nonradiative rate is given by:

$$W\left(T\right) = \beta \exp\left[-\left(\Delta E - 2h\nu_{\max}\right)\alpha\right]\left(\left[\exp\left(h\nu/kT\right) - 1\right]^{-1} + 1\right)^{\mathrm{P}} \tag{5.15}$$

where $p = \Delta E/h\nu$, ΔE the energy difference between the levels involved, α and β constants, and $\nu_{\max}$ the highest available vibrational frequency of the surroundings of the rare-earth ion. For example, the Eu^{3+} may not only emit from $^5D_0$ (red), but also from $^5D_1$ (green) and $^5D_2$ (blue). The Tb^{3+} ion may not only emit from $^5D_4$ (green), but also from $^5D_3$ (blue). However, this depends critically upon the host lattice.

5.1.4 Energy Transfer to the Trivalent REE

As already mentioned the population density of the luminescent levels is generally weak because of the low transition probabilities. However there are other possibilities to increase the luminescence mainly by creating strongly absorbing species that will transfer the energy to the R.E. ion.

The two main ways of such excitation in minerals are:

1. Exciting closed shell transition metal complexes such as tungstates, molybdates, vanadates, titanites etc. This way of excitation and its transfer to the rare-earth elements has been known since the late fifties.
2. Energy transfer from strongly absorbing R.E. due to f–d, or charge transfer band.

The energy levels scheme of trivalent REE may be seen in Fig. 5.1 and excitation spectra in Fig. 5.2.

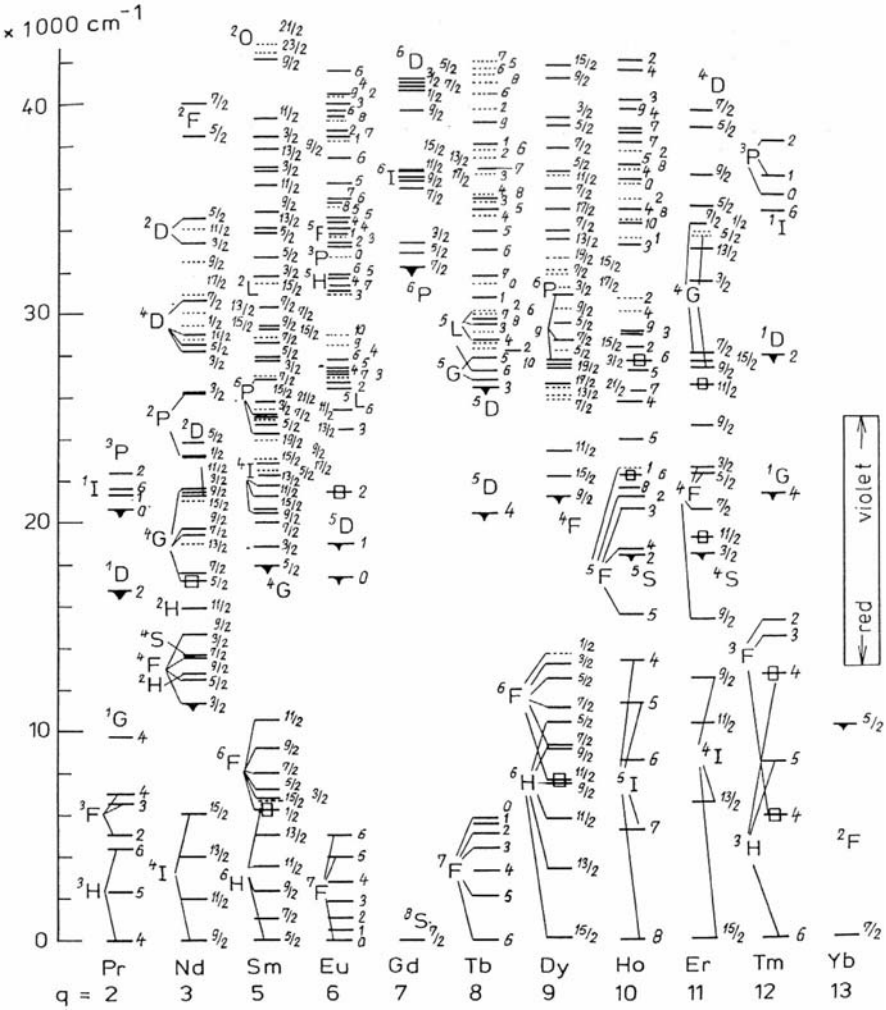

Fig. 5.1. Energy levels scheme of trivalent rare-earth elements

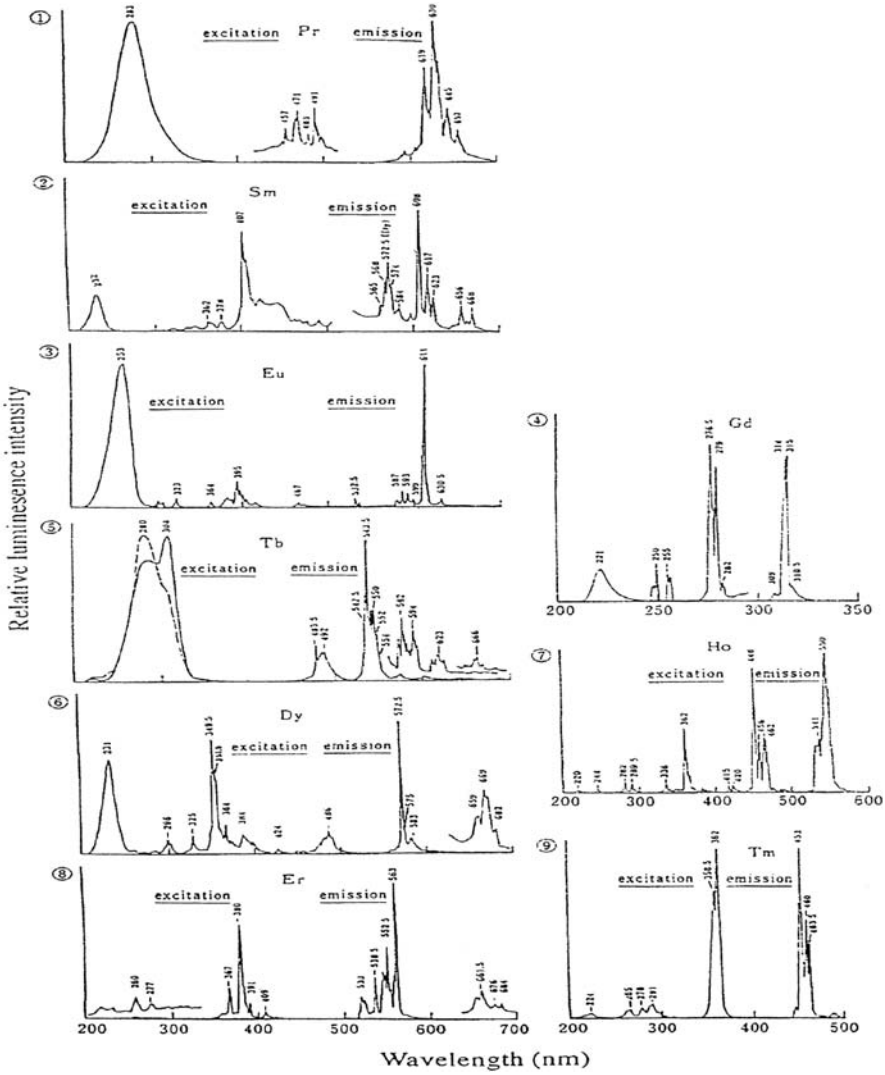

Fig. 5.2. Excitation spectra of trivalent REE (from Shinoya and Yen 1999)

5.1.5
The Treatment of Optical Properties of Divalent REE

Two specific features determine the similarity and difference of energy levels in di- and trivalent ions of rare-earth elements. First, isoelectronic configurations of TR^{2+} and TR^{3+} of the next elements in the periodic system determines a qualitatively similar pattern of terms and multiplet levels, namely for TR^{2+} the order of the $4f^k$-configuration levels and of excited $4f^{k-1}5d$-configuration levels

is the same as for trivalent ions isoelectronic to them. Second, the difference in the charge of the nuclei in isoelectronic TR^{2+} and TR^{3+} ions, on the one hand, in an essential but relatively small and approximately equal fall of energies of all levels derived from $4f^k$-configuration and, on the other hand, it brings about a sharp drop in the energy of levels derived from mixed $4f^{k-1}5d$-configurations. It is just this fall of the $4f^{k-1}5d$ levels that causes a sharp difference in the absorption and luminescence spectra of the TR^{2+} and TR^{3+} ions (Marfunin 1979).

Transitions onto the levels of mixed $4f^{k-1}5d$-configuration result in the appearance of broad intensive absorption bands. These specific features are due, first, to the fact that the said transitions occur between states with dissimilar electron configurations and, therefore, are parity-allowed. In these transitions

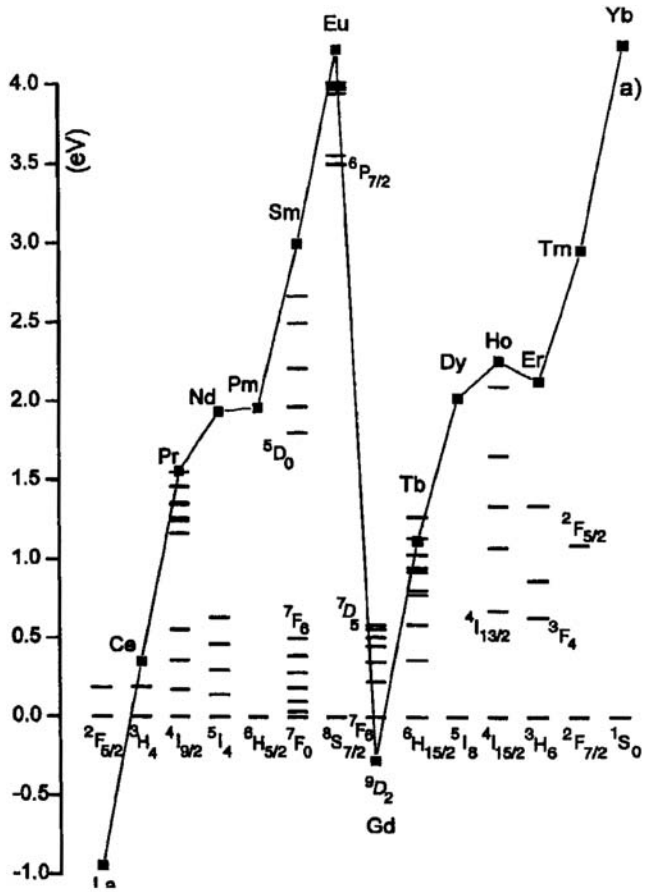

Fig. 5.3. The energy levels scheme of the free divalent lanthanides. The solid curve (*a*) connects the locations of the first $4f^{n-1}5d$ level (Dorenbos 2003)

the oscillator strength is by 3–4 orders higher than for the forbidden f–f transitions and characterized by much shorter emission lifetimes. Second, in these transitions d-electrons are involved, unshielded against interactions with the lattice, which makes for greater splitting by the crystal field, greater half-width of the lines and greater shifting of these bands in different crystals (Blasse and Grabmaier 1994).

A relative ratio between the $4f^k$ and $4f^{k-1}5d$-configuration levels energies specifies a sharply distinctive position of broad bands in the spectra of trivalent and divalent rare-earth ions. In the TR^{3+} spectra, with the exception of Ce^{3+}, broad bands fall into a relatively far UV region and they yield only line spectra in the visible and adjacent regions. In the TR^{2+} spectra broad bands fall into the visible and near-UV regions. Thus in the case of TR^{2+} the f–d and f–f transitions lie close to each other and overlap. Three individual cases are distinguished in the TR^{2+} luminescence spectra, namely broad bands due to d–f transitions, line IR spectra and a combination of bands and lines.

Emission of d–f type in the divalent lanthanides is usually quenched by multiphonon relaxation from the $5d$ level to levels of the $4f^n$ configuration. There are a few exceptions. When the red shift and Stokes shift place the $5d$ level of Sm^{2+} near to or below the $^5D_0$ state (Fig. 5.3) – df emission may occur. The same applies for Eu^{2+} when the level is shifted to near to or below $^6P_{7/2}$. When for Tm^{2+} the $5d$ level is not shifted too much towards the $^2F_{5/2}$ level, df emis-

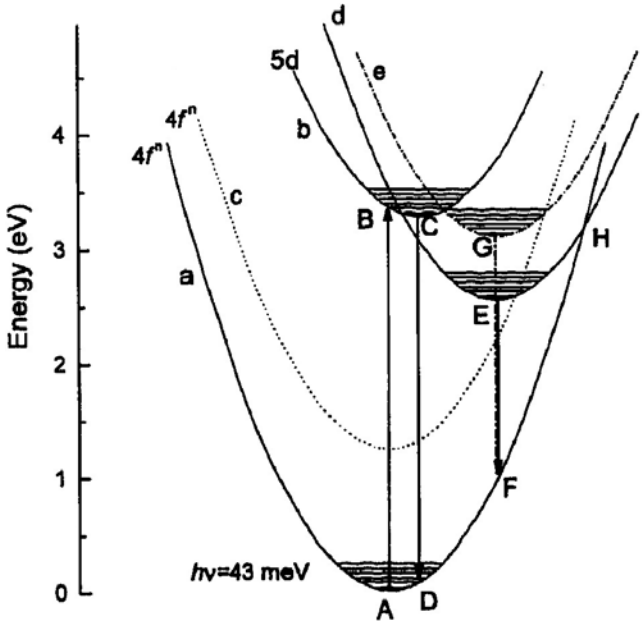

Fig. 5.4. The configuration diagram illustrating normal df emissions and anomalous emission (energy values realistic for SrF_2 and BaF_2, Dorenbos 2003)

sion can also be observed. Finally, for Yb^{2+} there is no multiphonon relaxation path and *df* emission cannot be quenched in that way. Figure 5.4 illustrates different emission mechanisms with a configuration coordinate diagram. Initially the system is in the $4f^n$ configuration state, indicated by point A on parabola a. After excitation to the 5*d* level, point B on parabola b is reached. Subsequent lattice relaxation brings the system to point C and several routes can be followed from here. The usual possibility is normal *df* emission (arrow CD) with a small Stokes shift. Nevertheless, for example, the system may relax to the impurity-trapped exciton state indicated by point E on parabola d. From here anomalous emission (arrow EF) takes place with high a Stokes-shifted emission band. Another possibility is relaxation to point G on parabola e with the following anomalous emission (arrow GF). Parabola c represents an excited state of the $4f^n$ configuration. Via the crossing point with parabola d, the anomalous emission is quenched and the excited $4f^n$ state becomes populated. The existence of the $^7F_6$ and $^2F_{5/2}$ levels in Sm^{2+} and Tm^{2+} is very likely the reason that anomalous emission has never been observed for these lanthanides. It has only been detected for Eu^{2+} and Yb^{2+}, precisely those lanthanides where excited $4f^n$ levels, that may quench anomalous emission, are absent (Dorenbos 2003).

5.2 Rare-Earth Elements Luminescence in Minerals

The promise of luminescent methodology is based on many types of information that can be derived from mineralogical samples. These include RE from Ce to Yb, identities down to the ppb range, the valence states of the RE, the nature of the sites at which RE reside and the ways of compensating the charge, and features related to the presence of other ions (donors, activators). All this information can be used to determine the chemical, thermal, and deformational history of the material.

5.2.1 Ce^{3+}

In minerals cerium can occur in a trivalent state, i.e. by losing its two 6*s* electrons and one of its 4*f* electrons. When cerium enters a solid, the expansion of the electron shells decreases the electrostatic interaction between the electrons resulting in a reduction of the energy of the excited states from their free ion values. This nephelauxetic shift increases with the degree of covalence of the cerium-anion bond. The spin–orbit interaction splits the 2*f* ground into two *J* states separated by $\sim 2{,}200\ cm^{-1}$. The $(2J + l)$-fold degeneracy of these states is reduced by the ligand field. Because the 4*f* electron is shielded from the ligand field by the closed 5*s* and 5*p* electron shells, the overall splitting of the 2*J* states is small, typically only a few hundred cm^{-1}. When the 4*f* electron is excited to the outer 5*d* state, however, it is subjected to the effect of the ligands.

Depending upon the site symmetry, the degeneracy of the 5*d* state is partially or completely removed. The overall splitting of the 5*d* manifold is typically in the order of 5,000 – 10,000 cm^{-1}.

Electric-dipole transitions between the 4*f* ground state and the 5*d* excited state of Ce^{3+} are parity and spin allowed and have a large oscillator strength and very short decay time. Contrary to a long lived emission of many $4f^q j$-levels of several lanthanides in glasses and crystals, corresponding to very low (10^{-6}) oscillator strength, Ce^{3+} is the only trivalent lanthanide which in the UV spectrum region shows high oscillator strength (0.01 to 0.1). Due to configurational admixing, normally forbidden transitions to the 6*s* state can also be observed in wide band gap materials. Optical excitation in the Ce-containing materials is normally performed in the range between 300 and 350 nm. The excitation arises from optical inter-shell Ridberg transitions between 4*s* and 5*d* levels.

5.2.1.1 Apatite

Two types of Ce^{3+} centers have been found in apatite by steady-state spectroscopy, connected with substitution in two different Ca sites (Tarashchan 1978). Both centers are well detected by time-resolved spectroscopy (Fig. 4.1a). The narrow UV band with two shoulders at 340 and 360 nm in apatite is connected with ^2D–$^2F_{3/2,\,5/2}$ electron transitions in Ce^{3+} in the higher symmetry Ca(I) position. The very short decay time of this band of 25 ns is typical for Ce^{3+}. An additional band peaking at 430 nm is also characterized by a short decay time, only slightly longer compared to the former one. It is considerably shifted to the long wavelength side from excitation bands, and two bands corresponding to transitions from the excited state to two levels of the ground multiplet are absent. This luminescence is connected with Ce^{3+} in the Ca(II) site. Since the 4*f* electron is shielded from the ligand field by the closed 5*s* and 5*p* electron shells, the overall splitting of the ^2F_J states is small. This is due to spin–orbit coupling, which may be lower in the Ca(II) position, leading to the absence of the double-band shape. When the 4*f* electron is excited to the outer 5*d* state, however, it experiences the full effect of the ligands. Depending upon the site symmetry, the degeneracy of the 5*d* state is partially or completely removed. The overall splitting of the 5*d* manifold is much larger in the Ca(II) site, which explains the larger Stokes shift. The longer decay time is consistent with the fact that for Ce^{3+} the decay time is longer if the emission is at longer wavelength (Blasse and Grabmaier 1994).

5.2.1.2 Barite and Anhydrite

A narrow band with a main shoulder at 302 nm with a very short decay time of $\approx$ 25 ns, and another with shoulders at 330 and 360 nm with a longer decay of $\approx$ 75 ns (Fig. 4.31c,d) in time-resolved spectra have spectral-kinetic

parameters suitable for Ce^{3+}. It is known that narrow bands near 300 nm are especially strong in $(Ba,Sr)SO_4$ (baritocelestine), while in barite they are situated at a longer wavelength (Gaft et al. 1985). The ionic radius of Ce^{3+} is 128 pm and a possible accommodation is isomorphic substitution for Ba^{2+} (156 pm) or Sr^{2+} (140 pm). Thus, two types of Ce^{3+} centers may be connected with Sr impurity, the presence of which in barite samples is confirmed by ICP analysis (450–720 ppm). Luminescence of Ce^{3+} in anhydrite is seen under excitation at 266 nm (Fig. 4.17b) and it disappears after a delay of 75–100 ns because of its short decay time (Gaft et al. 1985; Baumer et al. 1997).

5.2.1.3 Calcite

Two types of Ce^{3+} centers in calcite were detected by steady-state spectroscopy (Kasyanenko and Matveeva 1987). The first one has two bands at 340 and 370 nm and is connected with electron-hole pair Ce^{3+}–CO_3^{3-}. The second one has a maximum at 380 nm and was ascribed to a complex center with Ce^{3+} and OH^- or H_2O as charge compensators. Such a center becomes stronger after ionizing irradiation and disappears after thermal treatment. The typical example of Ce^{3+} luminescence in the time-resolved luminescence of calcite consists of a narrow band at 357 nm with very short decay time of 30 ns, which is very characteristic for Ce^{3+} (Fig. 4.13a). It was found that Ce^{3+} excitation bands occurs also in the Mn^{2+} excitation spectrum, demonstrating that energy transfer from Ce^{3+} to Mn^{2+} occurs (Blasse and Aguilar 1984).

5.2.1.4 Feldspars

Narrow bands at 320–335 nm with very short decay time of 20–30 ns may be confidently ascribed to Ce^{3+} luminescence (Fig. 4.44). In steady-state spectra different bands in this spectral range without decay time analyses, especially under X-ray and electron beam excitations may be mistakenly considered as Ce^{3+} emissions (Götze 2000).

5.2.1.5 Danburite and Datolite

Steady state luminescence of Ce^{3+} in danburite and datolite was found under X-ray and UV laser excitations (Gaft et al. 1979; Gaft 1989). The narrow band with two maxims at 346 and 367 nm in danburite (Fig. 4.15a), with a short decay time component of 30 ns is evidently connected with Ce^{3+}. After a long delay, the luminescence of Ce^{3+} becomes dominant (Fig. 4.15b), showing the presence of a long decay-time component. The change in the lifetime is unambiguously indicative of a resonance radiationless mechanism of the energy transfer. The

possible mechanism is Gd^{3+}–Ce^{3+} energy migration, because the emission of $Gd^{3+6}P_{7/2}$–$^8S_{7/2}$ in the UV region coincides with excitation of Ce^{3+}.

The narrow band with two maxims at 335 and 360 nm in time-resolved emission spectra of datolite (Fig. 4.16a), with a short decay time of 30 ns is connected with Ce^{3+}.

5.2.1.6 Pyromorphite

At λ_{ex} = 266 nm excitation, with a 10 ns delay and 9 ms gate (practically steady state), there is a UV band with two maxims at 350 and 375 nm in the emission spectrum (Fig. 4.26a). This band looks exactly like a Ce^{3+} center. However, its luminescence is not quenched after a delay of 100 ns, which would be typical for Ce^{3+}, or after a delay of 1 ms, when even luminescence of Eu^{3+} with forbidden f–f transitions starts to reduce its intensity (Fig. 4.26b). In addition, the intensity of the maximum at 375 nm decreases with increasing delay time more quickly than that at 350 nm, thus indicating a somewhat shorter decay time. This behavior is not consistent with the existence of two transitions from one excited state into split $2f$ ground states of Ce^{3+}, and rather confirms the presence of two different luminescence centers, or two excited states. At λ_{ex} = 355 nm excitation, the band with two maxims at 380 and 439 nm in the spectrum with 10 ns delay also resembles a Ce^{3+} (Fig. 4.26c). It has a short decay component of approximately 67 ns and a much longer one of several ms (Fig. 4.26d). The presence of a long component in the Ce^{3+} decay may be connected with energy migration from the long-lived centers, for example Pb^{2+} or Gd^{3+}.

5.2.1.7 Esperite

The narrow band with two maxims at 378 and 400 nm (Fig. 4.21c), with a decay time of 300 ns is evidently connected with Ce^{3+}, while the decay time is unusually long for this center. The excitation spectrum (Fig. 4.21d) exhibits a short-waved band at 280 nm, which may be connected with Pb^{2+} excitation with the following energy migration from Pb to Ce. It may be the reason for the relatively long decay component in Ce^{3+} luminescence.

5.2.1.8 Other Minerals

Luminescence of Ce^{3+} is clearly seen under excitation at 266 nm in apophyllite (Fig. 4.19a), charoite (Fig. 4.22a,c), fluorite (Fig. 4.10a), leucophane (Fig. 4.25a) and hardystonite (Fig. 4.20a).

5.2.2
Pr^{3+}

Luminescence of Pr^{3+} consists of many multiplets as follows: 480–500 ($^3P_0$–$^3H_4$), 650–670 ($^3P_0$–$^3F_2$), 750–770 ($^3P_0$–$^3F_4$), 610–630 ($^1D_2$–$^3H_6$), 400–410 ($^1S_0$–$^1I_6$), and UV ($5d$–$4f$) transitions. The emission color of Pr^{3+} depends strongly on the host mineral lattice. The radiative decay time of the $^3P_0$–^3H_j or ^3F_j emissions is approximately 10–5 μs, which is the shortest lifetime observed in $4f$–$4f$ transitions. The short decay time of Pr^{3+} is ascribed to the spin-allowed character of the transition. It also may be explained by nonradiative relaxation due to the presence of high frequency vibrations in the lattice. And another possible reason is that the $4f$ orbitals are probably more spread out in the lighter rare earths (with lower nuclear charge), facilitating the mixing with opposite-parity states (Blasse and Grabmaier 1994; Reisfeld and Jörgensen 1977).

The steady-state luminescence of Pr^{3+} in minerals was found only in scheelite, where the line near 480 nm has been ascribed to this center (Gorobets and Kudrina 1976) and possibly in fluorite (Krasilschikova et al. 1986). The luminescence of Pr^{3+} in minerals is difficult to detect because its radiative transitions are hidden by the stronger lines of Sm^{3+} in the orange range of 600–650 nm, Dy^{3+} in the blue range of 470–490 nm and Nd^{3+} in the near IR (870–900 nm). In order to extract the hidden Pr^{3+} lines time-resolved luminescence was applied. The fact was used that Pr^{3+} usually has a relatively short decay time compared to its competitors Dy^{3+}, Sm^{3+} and Nd^{3+}, especially from the $^3P_0$ level. In order to correct identification of Pr^{3+} lines in minerals several of them were synthesized and artificially activated by Pr (Fig. 5.5). Besides, comparison has been made with CL spectra of synthetic minerals artificially activated by Pr (Blank et al. 2000).

5.2.2.1
Magmatic Apatite

The presence of Pr in apatite samples, up to 424.4 ppm in the blue apatite sample, was confirmed by induced-coupled plasma analysis (Table 1.3). The luminescence spectrum of apatite with a broad gate width of 9 ms is shown in Fig. 4.2a where the delay time of 500 ns is used in order to quench the short-lived luminescence of Ce^{3+} and Eu^{2+}. The broad yellow band is connected with Mn^{2+} luminescence, while the narrow lines at 485 and 579 nm are usually ascribed to Dy^{3+} and the lines at 604 and 652 nm, to Sm^{3+}. Only those luminescence centers are detected by steady-state spectroscopy. Nevertheless, with a shorter gate width of 100 μs, when the relative contribution of the short lived centers is larger, the characteristic lines of Sm^{3+} at 652 nm and Dy^{3+} at 579 nm disappear while the lines at 485 and 607 nm remain (Fig. 4.2b). It is known that such luminescence is characteristic of Pr^{3+} in apatite, which was proved by the study of synthetic apatite artificially activated by Pr (Gaft et al. 1997a; Gaft

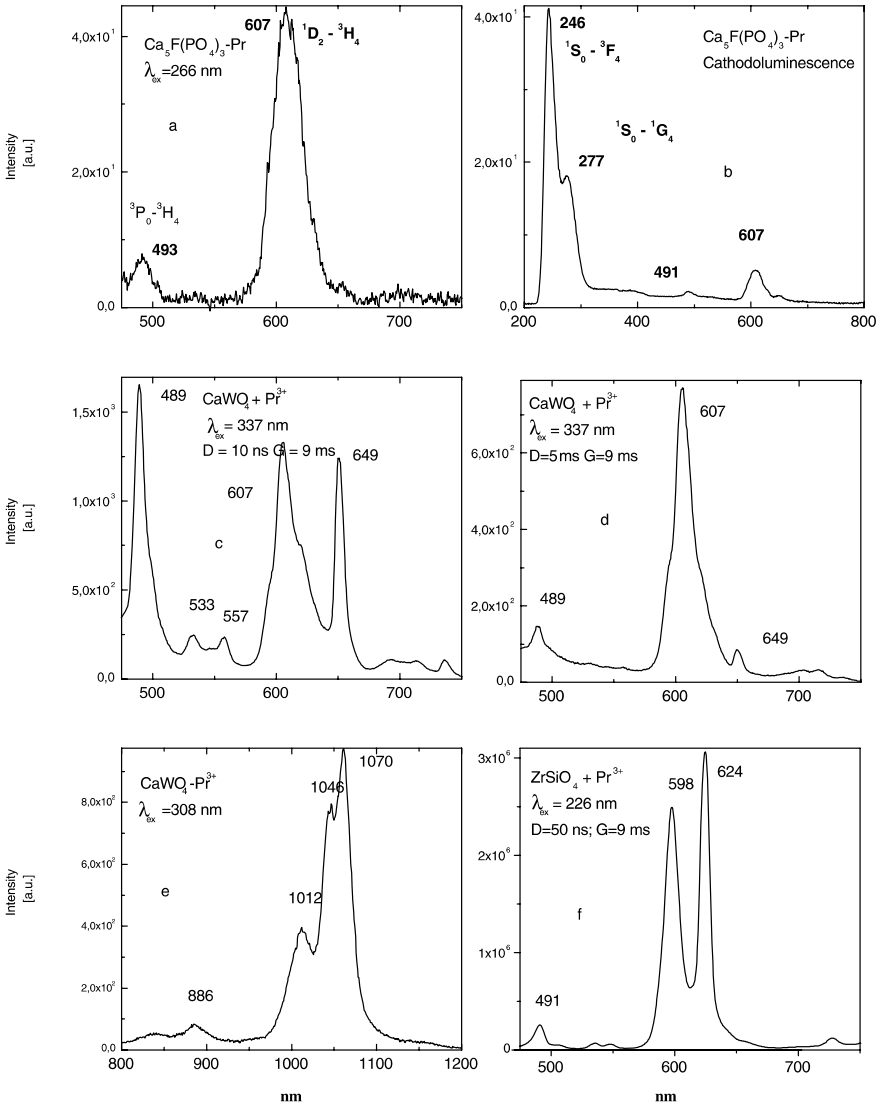

Fig. 5.5. a–f Laser-induced time-resolved luminescence spectra of synthesized apatite, zircon and scheelite artificially activated by Pr

et al. 1999a). The connection with Pr^{3+} was confirmed by strong emission at 485 and 607 nm under $\lambda_{ex} = 462$ nm, which is suitable for $^3H_4 \rightarrow {}^3P_0$ transition in Pr^{3+}. The lines at 485 and 607 nm have different decay times. After delay of 2 µs the first of the lines disappears indicating that they are connected with transitions from different levels. The line at 485 nm belongs to the $^3P_0 \rightarrow {}^3H_4$ transition. The short decay of the blue line is connected

with nonradiative relaxation between ^3P_J and $^1D_2$ levels due to the presence of high frequency vibrations of (PO_4)-groups in the apatite lattice at 1,040 cm^{-1}. The line at 607 nm belongs to the $^1D_2$ level, which is confirmed by its effective excitation at 570 nm, the energy of which is much lower then the energy of $^3P_0$ level.

The luminescence of Pr^{3+} described above is also detected under excitations, which do not coincide with transitions inside this center. It may be ascribed to energy transfer from Eu^{2+} or Ce^{3+}, which have luminescence in the blue range.

5.2.2.2 Sedimentary Apatite

In sedimentary apatites, which are formed in marine conditions at ambient temperature, after high temperature treatment a set of very intensive and narrow luminescence lines appears with strongest maxims at 594, 619, 626, 634 and 645 nm (Fig. 4.5a), these are related to REE^{3+} luminescence which was not observed in the unheated samples. The lines at 634 and 645 nm are characterized by a decay time of 0.5 ms and the line at 619 nm has a decay time of 0.1 ms. At 77 K new lines appear with maxims at 603, 651, 653 and 656 nm and decay times of 0.6 ms, and at 615 nm with a decay time of 0.2 ms. The spectral form and long decay times of the sharp lines are sure indicators that this luminescence is connected with f–f transitions in REE^{3+}. For the correct interpretation of the luminescent lines, artificial activation of natural francolite by different REE was accomplished by heating the corresponding mixtures at 1,200 K in air. It was found that all lines might be connected mainly with the luminescence of Pr^{3+} (Gaft et al. 1996a; Gaft et al. 1996b; Gaft et al. 1997a). The strongest lines at 619, 634 and 645 nm may be ascribed to the $^3P_0$–$^3F_2$ and $^1D_2$–^3H_j transitions in Pr^{3+}. The luminescence of REE^{3+} is well known in magmatic apatites, but the spectral positions of the lines are significantly different. In apatite the calcium ions are located in two crystallographically distinct sites, labeled Ca^{2+}(I) and Ca^{2+}(II). The luminescence of trivalent REE in magmatic apatites is due to their substitute in the Ca(I) position. The luminescence properties of magmatic apatites do not change after heating to temperatures up to 1,200 K, but after thermal activation with REE, they enter the Ca^{2+}(II) position and the luminescence spectra change (Gorobets 1968; Tarashchan and Marfunin 1969; Tarashchan 1978). The spectral properties of the trivalent REE which substitute for Ca II in magmatic apatite are very similar to those obtained from the apatite of fossil fish teeth after heating, indicating that luminescence of Pr^{3+} on the Ca II position takes place in this case. Luminescence of trivalent REE is more intensive when the site symmetry is lower and the parity inhibition is partially lifted. The Ca^{2+}(II) site in the apatite lattice has a lower symmetry then Ca^{2+}(I), and REE in site II may have parity forbidden electron transitions. This explains the great intensity of trivalent REE luminescence in heated sedimentary apatites.

Two possibilities exist which allow explanation of the different luminescence of the REE in magmatic and sedimentary apatites. It is possible that in sedimentary ones REE are incorporated in the Ca II position, but luminescence is not detected because of quenching by the components with high-energy phonons (water and organic matter). The latter are removed during heating with resulting luminescence. Nevertheless, francolite is different from the magmatic apatite due to crystallization at low temperature, while activation by REE results in luminescence in the Ca^{2+}(I) position. Thus another explanation may be needed. It is possible that francolite accommodates, at least partly, REE in concentrated form (e.g. free minerals), which is usually not suitable for registration by luminescence due to concentration quenching. As a result of high temperature heating, thermal diffusion of REE in the apatite lattice takes place. These changes initiate luminescence. The similarity with luminescence spectra of the francolite, which was artificially activated by the thermal diffusion of the REE, supports this interpretation.

It is interesting to note, that Pr^{3+} spectra obtained under $\lambda_{ex} = 308$ nm excitation do not resemble the shape and the lifetimes of those obtained under direct excitation to the Pr^{3+} levels. They exhibit the lines at 619, 634 and 645 nm with the same long decay time components of $\sim$ 750 µs (Fig. 4.5b). The excitation at 308 nm does not correspond for transitions inside Pr^{3+}. It was firstly supposed that an effective non-radiative energy transfer from the first excited state of uranyl to the levels ^3P_J ($J = 0, 1, 2$) and $^1I_6$ of Pr^{3+} may be responsible for the excitation, especially because the energy transfer between donor uranyl ion to Pr^{3+} was earlier demonstrated to take place in phosphate glasses (Reisfeld and Jörgensen 1977). Uranyl is present in natural sedimentary apatite and has strong green luminescence at 530 nm after heating (Fig. 4.5c). We studied artificial oxyapatite activated by Pr^{3+}, which does not contain uranyl impurity. In accordance with our model, this sample does not exhibit Pr^{3+} luminescence under excitation at 308 nm, while characteristic Pr^{3+} lines under 462 and 570 nm excitations exist. Nevertheless, the relatively short decay time of 100 µs for uranyl at negligible concentration of Pr^{3+} does not enable to explain the very long decay of Pr^{3+} of 650–750 µs. Besides that, excitation by UV longer then 308 nm with $\lambda = 337-360$ nm leads to strong uranyl luminescence but the lines of Pr^{3+} are absent (Fig. 4.5c).

The very long decay time of Pr^{3+} of 650–750 µs which is obtained only at 308 nm excitation in the presence of uranyl can be explained by energy transfer from excited uranyl ion to one of the ^3P states and followed by excited state absorption to $^1S_0$ level due to short UV laser excitation. The $^1S_0$ level serves as storage of an excited state of Pr^{3+}, which is slowly decaying to the lower lying $^3P_0$ level. As a result, a strong emission signal from ^3P_j is observed in the visible domain. Such a kind of photon-cascade emission with high quantum efficiency under V-UV excitation is well known for Pr^{3+} in oxide matrix.

The active participation of the $^1S_0$ level is indirectly accredited by the simultaneous observation of UV and visible emission in cathodoluminescence

and synchrotron excited spectra (Fig. 5.6) Excitation into the $4f5d$ and higher lying bands evidently decays to the $^1S_0$ level located at 46,300 cm^{-1} which exhibits luminescence in wide band-gap hosts due to radiative de-excitation to the lower lying levels of Pr^{3+}. The $^1S_0 \rightarrow {}^3F_4$ transition at 246 nm is especially strong in oxyapatite. In F-apatite only the line at 269 nm is present. It may be explained by the relatively long-waved absorption edge in fluorapatite, which is at about 300 nm (Morozov et al. 1970).

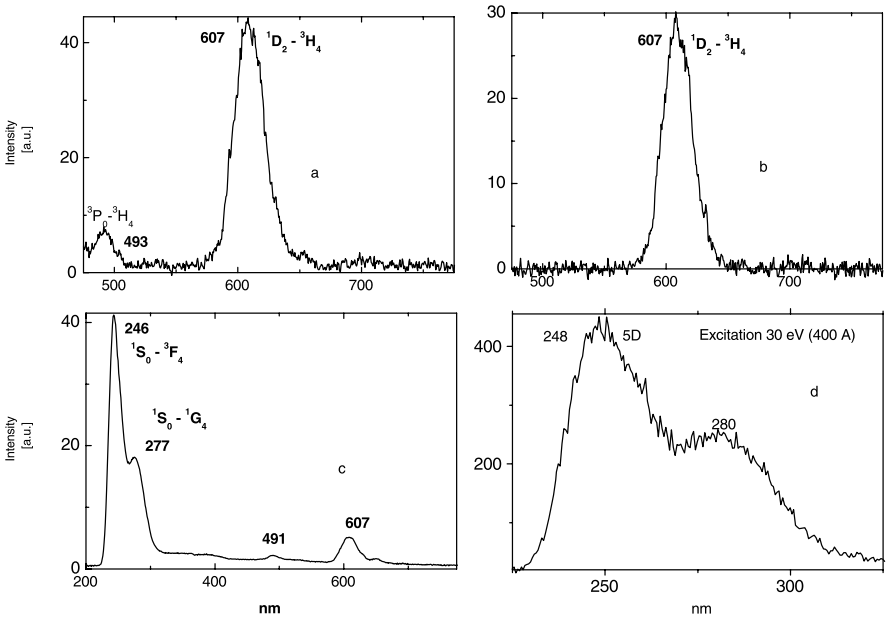

Fig. 5.6. a–d Cathodoluminescence and synchrotron excited spectra of Pr activated apatite

5.2.2.3 Scheelite

Luminescence spectrum of scheelite with a broad gate width of 9 ms is shown in Fig. 4.9d. The narrow lines at 490 and 572 nm are usually ascribed to Dy^{3+} and the lines at 607 and 647 nm to Sm^{3+}. Nevertheless, the relative intensity of the line at 607 nm compared to the line at 647 nm is lower at longer delay times (Fig. 4.9e,f). Besides that with a shorter gate width of 1 µs, when the relative contribution of the short lived centers is bigger, the characteristic lines of Sm^{3+} at 647 nm and Dy^{3+} at 575 nm disappear while the lines at 488 and 607 nm remain. Such luminescence is characteristic of Pr^{3+}, which was confirmed by a time-resolved luminescence study of scheelite artificially activated by Pr^{3+} and Sm^{3+} (Fig. 5.5). Unlike in apatite, the phenomenon exists not only under 308 nm, but also under 337 nm excitation due to the higher energy

of intrinsic WO_4 luminescence compared with UO_2. The active participation of blue intrinsic scheelite luminescence is confirmed by the reabsorption line at 448 nm (Gaft et al. 1999a), which corresponds to $^3H_4 \rightarrow {}^3P_2$ transition inside Pr^{3+}.

Luminescence of Pr^{3+} in the red and IR parts of the spectrum was also found (Fig. 5.5). According to the energy levels scheme of Pr^{3+} the following interpretation is possible: 840 nm – $^1D_2 \rightarrow {}^3F_2$, 886 nm – $^3P_1 \rightarrow {}^1G_4$ and 1,070 nm – $^1G_4 \rightarrow {}^3H_4$.

5.2.2.4 Anhydrite

Ultra-violet X-ray excited luminescence of Pr^{3+} was first observed in minerals in anhydrite, but have been mistakenly ascribed to transitions from $^6I_{7/2}$ and $^6D_{5/2}$ levels in Gd^{3+} (Gaft et al. 1985). According to CL spectra of anhydrite artificially activated by Pr^{3+} (Baumer et al. 1997; Blank et al. 2000) the emission lines at 228, 239, 258 and 268 nm (Fig. 4.17a) belong to Pr^{3+} and may be connected with $^1S_0 \rightarrow {}^3H_5$, $^1S_0 \rightarrow {}^3H_6$ and $^1S_0 \rightarrow {}^1G_4$ transitions. The lines of Pr^{3+} in the visible range are much weaker.

5.2.2.5 Zircon

Luminescence of Pr^{3+} in zircon is very difficult to detect under UV excitation even by time-resolved spectroscopy. The reason is that it has a relatively short decay time similar to those of radiation-induced centers. Visible excitation, which is not effective for broadband luminescence, allows the revealing of Pr^{3+} luminescence lines, using high-resolution steady-state spectroscopy. Under such experimental conditions each element has individual lines, enabling confident identification of the spectrum to be possible (Gaft et al. 2000a). Only if radiation-induced luminescence in zircon is relatively weak, the lines of Pr^{3+} may be detected by UV excitation (Fig. 4.38c).

5.2.2.6 Titanite

The group of visible lines at 478, 487, 497 and 613 nm (Fig. 4.33d) with a short decay time of 20 μs may be ascribed to the Pr^{3+} center. Because all lines have the same decay time it may be concluded that they belong to one $^3P_0$ excited state. In such a way, the triplet at 478, 487 and 497 nm belongs to the $^3P_0$–$^3H_4$ transition, the line at 613 nm to the $^3P_0$–$^3F_1$ transition.

5.2.3 Nd^{3+}

Nd^{3+} energy levels arise from the $4f^3$ electronic configuration. The $4f^2 5d$ higher lying states are almost always completely in the UV range. Some transitions among $4f^3$ levels of Nd^{3+} ion are spin-allowed, such as $^4I_{9/2}$–$^4F_{3/2}$, $^4F_{5/2}$, $^4F_{7/2}$, $^4F_{9/2}$, $^4G_{7/2}$ or $^4F_{3/2}$–$^4G_{7/2}$, $^4D_{3/2}$ and so on, but this is not valid for the remaining ones. Neodymium has been recognized as one of the most efficient rare-earth luminescence centers in minerals, while its emission has been found only in the IR part of the spectrum. Nevertheless it is well known that Nd^{3+} may also generate UV-visible luminescence in certain matrixes, for example in YAG-Nd (Marech et al. 1989; Balda et al. 2001). The Nd^{3+} UV and visible luminescence spectra consists of many narrow lines whose half-widths reach only several cm^{-1}. It was found that the Nd^{3+} UV and visible luminescence depend on the excitation wavelength. Most narrow luminescence lines together with slightly broader peaks were observed for λ_{ex} = 355 nm where there is strong Nd^{3+} absorption. Nearly 140 lines have been found under this excitation. The mostly important lines detected at room temperature are near 396, 401, 435, 461, 488, 500, 524, 550, 588, 609, 617, 620, 629, 638, 663, 712 nm. The measurements of luminescence decay times revealed that several various lifetimes are observed ranging from 3 to 300 µs. The observed Nd^{3+} UV and visible luminescence spectra were interpreted in the following way: the most intense lines originates from the UV lying Nd^{3+} level $^2F_{5/2}$: to $^4F_{5/2}$, $^2H_{9/2}$ (lines around 400 nm), to $^4F_{9/2}$ (lines around 435 nm), $^2H_{11/2}$ (lines in the range 450–464 nm), to $^4G_{5/2}$ (lines around 480 nm) and to $^2G_{7/2}$ (lines around 488 nm). In minerals such luminescence is mixed with other REE lines and not detected by steady-state spectroscopy.

5.2.3.1 Apatite

Neodymium in natural and artificial apatite is characterized by anomalous distribution of luminescence intensity in the groups at 1.06 and 1.3 µm. In each of these spectral groups there is one line whose intensity exceeds many times the intensity of the remaining lines of said group (Morozov et al. 1970). In laser-induced luminescence of natural apatites we also found somewhat different luminescence spectra (Fig. 4.3). Decay times of these lines are rather close and it is possible to suppose that all Nd^{3+} occupy the Ca(I) sites with different charge compensations.

5.2.3.2 Scheelite

Figure 4.8a represents scheelite luminescence in the near IR ranges of the spectrum. The usual characteristic lines of Nd^{3+} are detected in the spectral

range up to 1.6 µm. Strong reabsorption lines of Nd^{3+} are characteristic for the luminescence of many minerals, but were first detected in scheelite (Gorobets 1975).

Unusual behavior of the luminescence line at 417 nm has been detected by time-resolved spectroscopy. It is usually ascribed to Tb^{3+}, but sometimes in spectra with a narrow gate this line remains strong, while other lines of Tb^{3+} disappear (Fig. 4.8b,c). The supposition that those lines are connected with Nd^{3+} was confirmed by our study of $CaWO_4$:Nd, where, besides the known IR, the group of UV and violet lines with short decay times are detected, while in $CaWO_4$:Tb such lines are absent (Fig. 5.7).

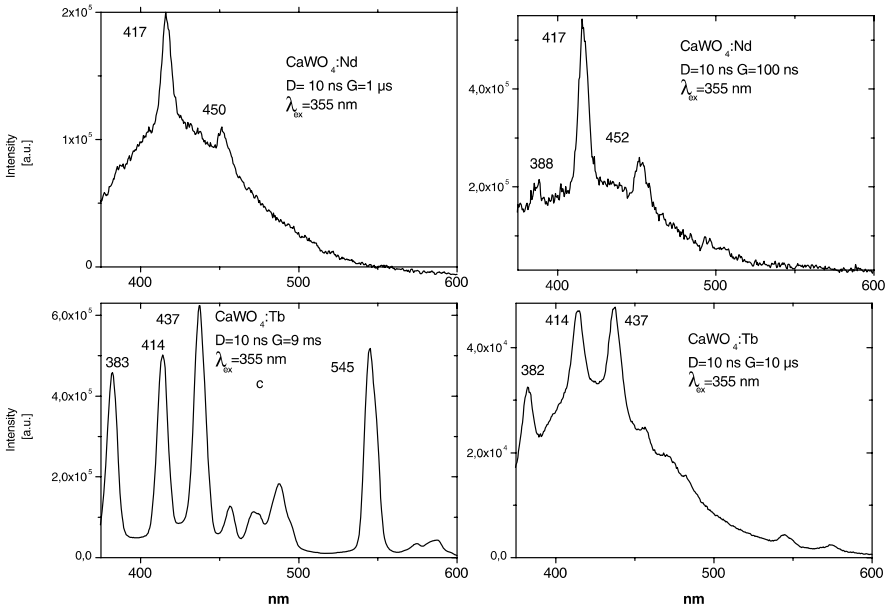

Fig. 5.7. **a–d** Laser-induced time-resolved luminescence spectra of synthetic $CaWO_4$ artificially activated by Nd and Tb

5.2.3.3 Garnet

Narrow lines at 462, 476, 482, 501 and 590 nm in the luminescence spectrum of the Ca-variety of garnet (grossular) with a relatively short decay time are not typical for "traditional" trivalent REE in minerals. Evidently they may be connected to visible emission of Nd^{3+} (Fig. 4.57c,d), but this has to be checked.

5.2.3.4 Fluorite

IR luminescence lines with relatively short decay times connected with Nd^{3+} are very strong in the fluorite emission spectrum (Fig. 4.11c,d). Besides that, UV and violet lines with a short decay time appear, which are ascribed to Nd^{3+} (Fig. 4.11a,b).

5.2.3.5 Barite

Figures 4.31a,b represent narrow luminescence lines detected in barite by time-resolved spectroscopy. Much weaker lines at 446 and 672 nm accompany the strongest one at 588 nm. They have a relatively short decay time of 5 μs and emphasized in the spectrum with short gate. Such a combination of spectral and kinetic properties is not suitable for any trivalent REE besides $^2P_{1/2} \rightarrow {}^4I_{9/2}$ (446 nm), $^4G_{7/2} \rightarrow {}^4I_{11/2}$ (588 nm) and $^4G_{7/2} \rightarrow {}^4I_{12/2}$ (672 nm) transitions in Nd^{3+}.

5.2.3.6 Titanite

Figures 4.34a,b demonstrate the emission lines of titanite, which according to their spectral positions may be confidently connected with Nd^{3+}. The luminescence spectrum in the 860–940 nm spectral range, corresponding to the $^4F_{3/2}$–$^4I_{9/2}$ transition, contains six peaks at 860, 878, 888, 906, 930 and 942 nm, while around 1,089 nm corresponding to $^4F_{3/2}$–$^4I_{11/2}$ transition it contains five peaks at 1,047, 1,071, 1,089, 1,115 and 1,131 nm. The decay time of IR luminescence of Nd^{3+} equal to approximately 30 μs in titanite is evidently the shortest one in the known systems activated by Nd^{3+}. The typical radiative lifetime of this level depends on the properties of the solid matrix and varies from approximately 100 μs to 600 μs (Kaminskii 1996). To explain the fast decay time of Nd^{3+} in titanite, the energy level quenching by the host matrix may be considered.

Another group of lines is detected in the titanite luminescence spectrum, which may be considered as connected with the Nd^{3+} emission. Those lines at 589, 658, 743 and 846 nm are especially strong in the luminescence spectra with a narrow gate excited by $\lambda_{ex} = 532$ nm (Fig. 4.34b). Such a combination of emission lines with relatively short decay times is very unusual for minerals and may not be easily connected to any rare-earth element traditional for luminescence in the visible range. If we were to consider the possible connection with the visible emission of Nd^{3+}, the detected lines correspond very well, for example, to electron transitions from $^2G_{7/2}$ level to $^4I_{9/2}$, $^4I_{11/2}$, $^4I_{13/2}$ and $^4I_{15/2}$ levels.

5.2.3.7
Zircon, Anhydrite, Calcite, Rhodonite, Feldspars

Infrared luminescence lines of Nd^{3+} are detected also near 817 and 885 nm in zircon (Fig. 4.38e), 892 and 899 nm in anhydrite (Fig. 4.18c), 817 and 889 nm in calcite (Fig. 4.13b), 815, 875 and 890 nm in rhodonite (Fig. 4.67b), and 895 nm in feldspars (Fig. 4.45c).

5.2.4
Sm^{3+}, Sm^{2+}

Trivalent samarium activated minerals usually display an intense luminescence spectrum with a distinct line structure in the red-orange part of the spectrum. The radiating term $^4G_{5/2}$ is separated from the nearest lower level $^6F_{11/2}$ by an energy interval of $\sim$ 7,500 cm^{-1}. This distance is too large compared to the energy of phonons capable to accomplish an effective non-radiative relaxation of excited levels and these processes do not significantly affect the nature of their spectra in minerals. Thus all detected lines of the Sm^{3+} luminescence take place from one excited level and usually are characterized by a long decay time.

An important feature of the electronic structure of Sm^{2+} is the low energy of the $4f^5$–$5d^1$ excited electronic configurations. As a result, the $4f^5$–$5d_1$ configurations interact significantly with the ^5D_j levels of the $4f$ ground configuration and exert a strong influence on the optical properties of Sm^{2+}. Sometimes the $4f^5 5d1$ level of Sm^{2+} is located below its $4f$ levels, for example, in fluorite, resulting in band luminescence due to the $5d$–$4f$ transition with a decay time of several μs. On the other hand in different hosts a line spectrum due to the $4f$–$4f^5 D_0$–$^7F_1$ transitions has been observed (Tarashchan 1978).

5.2.4.1
Apatite

In apatite two kinds of Sm^{3+} luminescence are detected connected with substitution in different Ca sites (Fig. 4.2c), while the substitution in the Ca(I) site is much more widespread. Artificial activation by Sm in vacuum is characterized by the lines at 465, 598 and 645 nm with a decay of $\sim$ 2 ms. After activation in air the lines at 607 and 654 nm appear with a different excitation spectrum and a shorter decay of $\sim$ 1.6 ms (Tarashchan 1978; Gaft et al. 1997a). It is possible to suppose that the first group of lines appearing in vacuum may be ascribed to substitution on Ca(I) while the second one appearing in the air – on the Ca(II) site. The splitting of the lines indicating the removal of the degeneracy is better seen in the case of activation in air. It is consistent with the lower symmetry of the Ca(II) site.

Sm^{2+} luminescence is detected only at low temperatures, where the strongest line at 734 nm, connected with the $^5D_0$–$^7F_2$ electron transition, is clearly

seen (Fig. 4.1d). Such an emission was found very rarely, but the presence of Sm^{2+} in natural apatite may be seen in an indirect way after oxidizing heating, where the luminescence intensity of Sm^{3+} becomes enhanced evidently as a result of Sm^{2+}–Sm^{3+} transformation.

5.2.4.2 Fluorite

The lines of Sm^{3+} connected with several types of centers are well studied in fluorite by steady-state luminescence spectroscopy (Tarashchan 1978; Krasilschikova et al. 1986). In time-resolved spectra it is mostly prominent after long delay times and is mainly characterized by the lines at 562, 595 and 651 nm (Fig. 4.10d).

Together with Sm^{3+} another group of lines is often detected with the main line at 685 nm, which also has a very long decay time of several ms (Fig. 4.10d). It is very close to the known resonance line of Sm^{2+}. Under low power UV lamp excitation, the luminescence of Sm^{2+} in fluorite is known only at low temperatures, starting from approximately 77 K, and is composed of narrow f–f transition lines and a broad band of $4f$–$5d$ transitions (Tarashchan 1978; Krasilschikova et al. 1986). Evidently, under strong laser excitation, luminescence of Sm^{2+} may be seen even at room temperature, where $4f$–$5d$ luminescence is usually quenched because of radiationless transition.

5.2.4.3 Anhydrite

The Sm^{2+} ion ($4f^6$) demonstrates $5d$–$4f$ broad emission together with intraconfigurational $4f^6$ line emission (Fig. 4.18). It is worth noting that, despite their different origins, the broad band and narrow lines have a similar decay time. The possible reason is a thermally stimulated electron exchange between the lower $4f$ and higher $5d$ excited states. It ceases at 77 K and the $5d$–$4f$ broad emission is absent. Using different excitations several types of Sm^{2+} are detected in anhydrite.

5.2.4.4 Titanite

The line at approximately 600 nm has a long decay time of 1 ms. It is the strongest one in the titanite luminescence spectrum under 266, 355 and 532 nm (Fig. 4.33b,c), but its relative intensity is much lower under 514 nm excitation (Gaft et al. 2003b). It appears that from all lines found in titanite luminescence spectra only two weaker ones at 563 and 646 nm have similar kinetic and excitation characteristics with the line at 600 nm. Such a combination of luminescence lines is very typical for Sm^{3+}. Thus the emission spectrum of Sm^{3+} in titanite exhibits three peaks corresponding to $^4G_{5/2}$–$^6H_{5/2}$, $^6H_{7/2}$

and $^6H_{9/2}$. The intensity of the $^4G_{5/2}$–$^6H_{7/2}$ transition is much stronger than the other emission transitions, which is in accordance with Sm^{3+} behavior in glasses (Javasankar and Babu 2000). The little difference in spectral position and half-width of the line at 600 nm under different excitations evidences that several Sm^{3+} centers may present. The presence of relatively high Sm concentration in titanite is confirmed by absorption spectrum and ICP data (Table 4.7).

5.2.4.5
Calcite, Feldspars, Hardystonite, Pyromorphite, Scheelite, Zircon, Baddeleyite

Narrow lines with long decay time characteristic for Sm^{3+} are also detected at 601, 614, 650 and 710 nm in calcite (Fig. 4.13b), at 603 and 645 nm in feldspars (Fig. 4.45b), 601 nm in hardystonite (Fig. 4.20c), 566, 603, 652 and 714 nm in pyromorphite (Fig. 4.26d), 601, 609 and 647 nm in scheelite (Fig. 4.9f), 566, 604, 615 and 651 nm in zircon (Fig. 4.38b), 549 nm in baddeleyite (Fig. 4.41) and 603 nm in leucophane (Fig. 4.25c).

5.2.5
Eu^{3+}, Eu^{2+}

Eu^{3+}

Trivalent europium is an excellent ionic probe for materials and its luminescence properties are extensively studied. Eu is one of the mostly informative elements in mineralogy, especially when the ratio Eu^{2+}/Eu^{3+} may be assessed. Both oxidation states are luminescent, but the lines of Eu^{3+} in minerals are usually very weak and concealed by other centers. By steady state luminescence spectroscopy its luminescence has been confidently detected only in scheelite and anhydrite (Tarashchan 1978; Gorobets and Rogojine 2001).

The energy levels of Eu^{3+} arise from the $4f^n$ configuration. In a configuration coordinate diagram these levels appear as parallel parabolas ($\Delta R = 0$), because the $4f$ electrons are well shielded by the $5s^2 5p^6$ outer shells and the crystal field influence is weak.The emissions arising from f–f transitions yield sharp lines in the spectra. Because the transitions occur between states of the same parity, the lifetime of the excited state is long. The emission in Eu^{3+} corresponds to transitions from the excited $^5D_0$ level to the ^7F_j ($J = 0, 1, 2, 3, 4, 5, 6$) levels of the $4f^6$ configuration. Because the $^5D_0$ level is not split by the crystal field (because $J = 0$), the splitting of the emission transition lines yields the crystal field splitting of the ^7F_j levels (Fig. 5.8). If Eu^{3+} occupies a crystal lattice site with inversion symmetry, optical transitions between levels of the $4f^n$ configuration are strictly forbidden as electric-dipole transitions (parity selection rule). They can only occur as the much weaker magnetic-dipole transitions which obey the selection rule $\Delta J = 0, \pm 1$ (but $J = 0$ is forbidden) or as vibronic electric-dipole transitions. If there is no inversion symmetry at the site of Eu^{3+}, the uneven crystal field components can mix opposite-parity states into

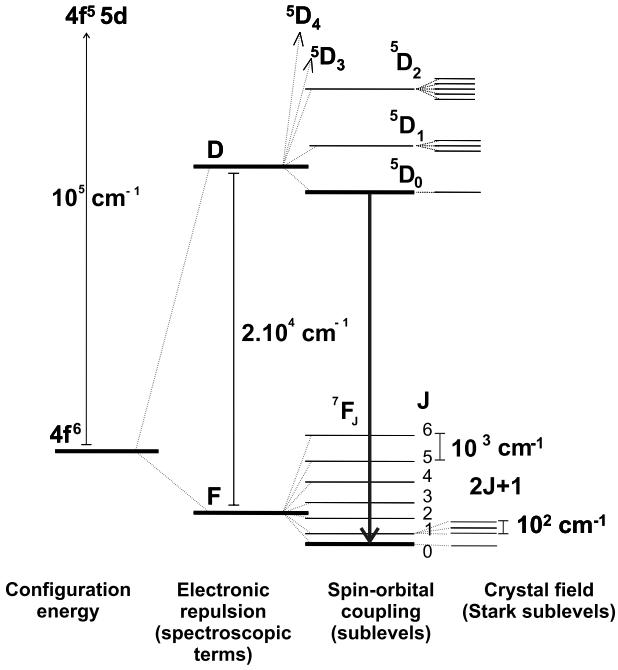

Fig. 5.8. Energy levels scheme of Eu^{3+}

$4f^n$-configurational levels. The electric dipole-transitions are now no longer strictly forbidden and appear as weak lines in the spectra, the so-called forced electric-dipole transitions. Some-transitions, viz. with $\Delta J = \pm 2, \pm 4$, are hypersensitive to this effect. Even for small deviations from inversion symmetry, they appear dominantly in the spectrum (Blasse and Grabmaier 1994; Reisfeld and Jörgensen 1977; Reisfeld 1973). Intensity ratio analysis of the ${}^5D_0 \rightarrow {}^7F_1$ and ${}^5D_0 \rightarrow {}^7F_2$ transition allows approaching the symmetry of the involved europium site. It is then possible to define the asymmetry ratio R:

$$R = \frac{I\left({}^5D_0 \rightarrow {}^7F_2\right)}{I\left({}^5D_0 \rightarrow {}^7F_1\right)} \tag{5.16}$$

The asymmetry ratio R follows the evolution of the ${}^5D_0 \rightarrow {}^7F_2$ transition especially sensible to the crystal field. Parameter R increases when the covalent bonds with the neighbors are reinforced and when the symmetry of the site decreases.

Crystal field theory enables us to define certain parameters in order to characterize and distinguish the different europium site configurations. Crystal field parameter calculation involves several steps:

1. Site selective excitation in the ${}^7F_1 \rightarrow {}^5D_0$ absorption band;
2. Deconvolution of the ${}^5D_0 \rightarrow {}^7F_1$ transition for each excitation;

3. Determination of the three contributions, which are the three states of the crystal field for each environment. The contributions are labeled from the highest energy to the lowest one: ε_0, ε_- and ε_+, respectively. The ε_0 line is the thinnest and the most sensible to the excitation energy;
4. Determination of the energy of the Stark sub-level triplet (one triplet per site);
5. Representation of the Stark sub-level position in energy (cm^{-1}) for each site according to the excitation energy (cm^{-1});
6. Calculation of the B_{20} and B_{22} crystal field parameters using the three following equations:

$$E\left(\varepsilon_0\right) = E\left({}^7F_1\right) + B_{20}/5 \tag{5.17}$$

$$E\left(\varepsilon_+\right) = E\left({}^7F_1\right) - \left(B_{20} + 6^{(1/2)} \cdot B_{22}\right)/10 \tag{5.18}$$

$$E\left(\varepsilon_-\right) = E\left({}^7F_1\right) - \left(B_{20} - 6^{(1/2)} \cdot B_{22}\right)/10 \tag{5.19}$$

where $E(\varepsilon_0)$, $E(\varepsilon_+)$, $E(\varepsilon_-)$ represent the energy in wave number (cm^{-1}) of the three composants and $E({}^7F_1)$ the barycenter of the ${}^7F_1$ multiplet. The B_{20} and B_{22} parameters characterized the spitting of the ${}^7F_1$ level, which depends of the neighbor cation surrounding the luminescent ion and thus the environment of the rare earth element.
7. Calculation of the standardized B_2 parameter as followed:

$$B_2 = \left((B_{20})^2 + 2(B_{22})^2\right)^{(1/2)} \tag{5.20}$$

8. Representation of the evolution of the B_2 parameter in function of the excitation energy (cm^{-1}).

Eu^{2+}

The absorption and emission spectra of divalent europium are due to electronic transitions between the $4f^7$ and $4f^6 5d^1$ electronic configurations (Fig. 5.9). An approximate energy level scheme was proposed (Blasse et al. 1968) for the electronic transitions in Eu^{2+} by using strong field formalism to describe the $5d$ levels and the weak field formalism to describe the $4f$ orbitals. The ground state of Eu^{2+} is ${}^8S_{7/2}$ because of the $4f^7$ electronic configuration. In the configuration $4f^6 5d^1$, one electron occupies a $5d$ orbital which is split into two orbital sets, t_{2g} and e_g, by a cubic crystal field. Thus the energy terms are ${}^2E_g$ and ${}^2T_{2g}$ in full cubic symmetry.

In the group of divalent RE luminescence centers Eu^{2+} is the most well known in minerals. It shows a $5d$–$4f$ emission, which varies usually from UV to blue. The host lattice dependence of the emission color of the Eu^{2+} is mainly

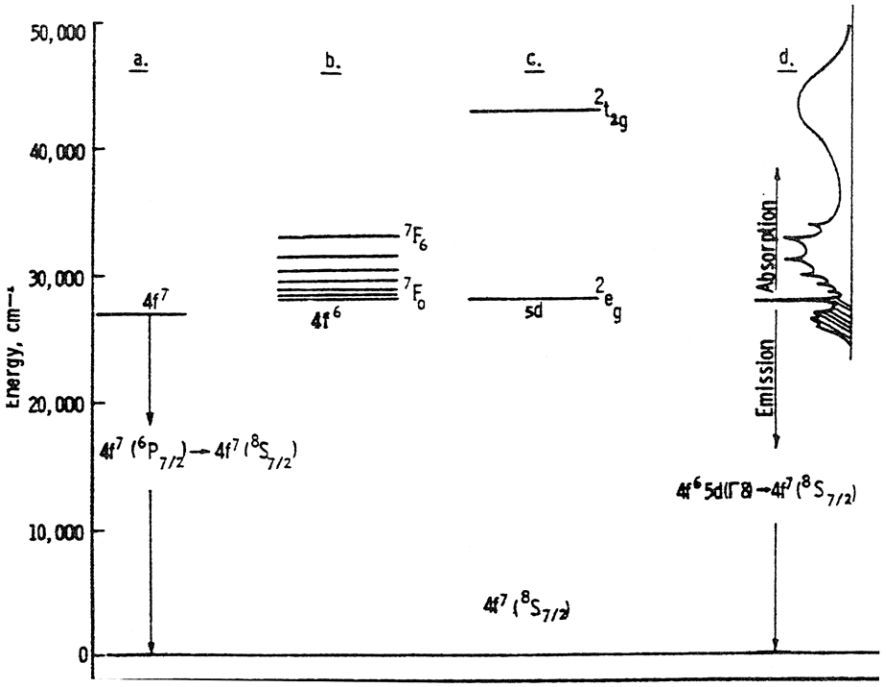

Fig. 5.9. Energy levels scheme of Eu^{2+}

connected with covalence (the nephelauxetic effect), which will reduce the energy difference between the 4*f* and 5*d* configurations, crystal field splitting of the 5*d* configuration and the Stokes shift (Blasse and Grabmaier 1994).

Nevertheless, in certain cases anomalous luminescence may be possible, identification of which may be based on the following aspects: an abnormally large Stokes shift and width of the emission band; a wavelength of emission that is not consistent with the wavelength anticipated from the properties of the compound; an anomalous decay time and thermal behavior (Dorenbos 2003). Such luminescence may be red, for example at 600 nm in BaF_2, with a decay time of about 600–800 ns. This is due to the fact that the emitting level contains spin octets and sextets, whereas the ground state level is an octet, so that the optical transition rate is slower because of spin selection rule (Dorenbos et al. 2003).

5.2.5.1 Apatite

5.2.5.1.1 Eu^{2+}

Divalent europium is detected in apatite as a shoulder of Ce^{3+} luminescence when studied by steady-state spectroscopy (Tarashchan and Marfunin 1969;

Gorobets 1968). The reason is that Eu^{2+} and Ce^{3+} emit in the same spectral range, but the Eu concentration in all investigated samples is very low compared to that of Ce. Besides that, since the $5d$–$4f$ transitions in Ce^{3+} is parity allowed and spin selection is not appropriate, the emission transition is a fully allowed one and luminescence intensity is very strong. Thus Ce^{3+} makes Eu^{2+} luminescence detection hardly possible (Fig. 4.1a). However, because Eu^{2+} has a much longer decay time, time-resolved spectroscopy enables the isolation of the Eu^{2+} luminescence in pure form. After a delay of 500 ns and with a gate width of 500 ns, the short-lived luminescence of Ce^{3+} is already quenched and the long-lived luminescence of other trivalent RE and Mn^{2+} is not detected yet. At such conditions the blue, relatively narrow band peaking at 450 nm appears with an intermediate decay time of $\sim$ 400 ns (Fig. 4.1b). Such an emission band is known in natural and in synthetic artificially activated apatite and is connected with Eu^{2+}. On excitation with UV, two types of lowest excited states are possible, namely ^6P_j (f–f) or $4f^6 5d$ (f–d), depending on the host matrix. The nature of Eu^{2+} emission, namely either an intraconfigurational (f–f) line or inter-configurational ($f - d$) band emission in a given host, is mainly decided by the effect of the ligand field on the Eu^{2+} energy levels. In the apatite case, the anions constituted by the PO_4^{3-} network produce a strong nephelauxetic effect and hence the $4f^6 5d$ level is the lowest excited state, leading to band emission. It was found that in calcium fluorapatite there is only one emission band. The emission maximum dependence on the halogen type confirms that this band can be assigned to the Ca(II) sites (Kottaisamy et al. 1994).

5.2.5.1.2
Eu^{3+}

After a delay of several μs, the luminescence of Eu^{2+} is already very weak, and narrow long-lived lines of trivalent RE dominate in the spectrum. The lines at 589, 617, 651, and 695 nm (Fig. 4.1c) have never been detected in natural apatite by steady-state spectroscopy. According to their spectral position they may be ascribed to Eu^{3+}, but they are different from known lines in synthetic apatites activated by Eu (Jagannathan and Kottaosamy 1995; Morozov et al. 1970; Piriou et al. 1987; Piriou et al. 2001; Voronko et al. 1991). In order to clarify this problem we studied artificially activated samples by laser-induced time-resolved luminescence spectroscopy.

Fluorapatite activated by Eu in air and in vacuum has been studied (Gaft et al. 1997b). Two main centers appear after activation in air both characterized by the abnormal relative intensity of the $^5D_0$–$^7F_0$ transition at 574 and 579 nm. Activation in a vacuum leads to prominent changes. New lines at 590, 618 and 700 nm appear which dominate at $\lambda_{ex} = 384$ nm (Fig. 5.10).

Thus different luminescence takes place after activation in air and in vacuum. As was already mentioned, in the apatite structure $Ca_5(PO_4)_3F$ there are two types of Ca site: Ca(I) with C_3 symmetry and Ca(II) with C_s sym-

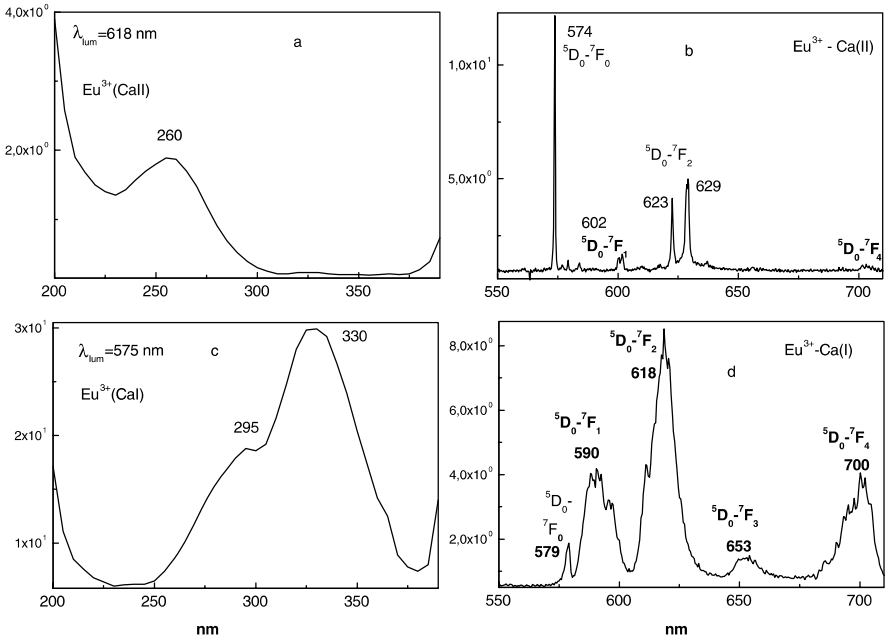

Fig. 5.10. **a–d** Laser-induced luminescence and excitation spectra of synthetic apatite artificially activated by Eu in vacuum (**a**) and in air (**b**)

metry. The $^5D_0$–$^7F_0$ transition has been reported to exist in cases where the site symmetry allows an electric dipole process: C_s, C_n, C_{nv}. This is consistent with the conclusion that the centers with the main line at 574 nm belongs to the Ca(II) site with C_s symmetry, while the asymmetry of the crystal field is lower for the center with the main line at 618 nm. The ratio between $^5D_0$–$^7F_0$ and $^5D_0$–$^7F_2$ which are forced electric dipoles to $^5D_0$–$^7F_1$ which is magnetic dipole tells us about the symmetry of the site in which Eu^{3+} is situated (Blasse and Grabmaier 1994; Reisfeld 1973). In fluor-apatite activated in air the ratio is higher meaning a lower symmetry Ca(II) site, while in natural fluorapatite or a synthetic one activated in a vacuum the ratio is lower indicating a high symmetry Ca(I) site. The decay of the corresponding transitions is longer for the center with the main line at 618 nm indicating the higher symmetry.

The excitation spectra of the line at 573 nm after activation in air and the line at 618 nm after activation in a vacuum are totally different (Fig. 5.10). The excitation bands of the line at 618 nm have the higher energies. They are connected with a charge transfer which occurs by an electron jumping from one of the highest filled molecular orbitals of the ligand to the partly filled shell of the central atom (Reisfeld 1973). The higher energy of the charge transfer bands indicates the larger Eu^{3+}–O^{2-} distance corresponding to the Ca(I) position. For the samples activated in a vacuum by Eu and Na it was indeed found that Eu^{3+}

luminescence in the higher symmetry Ca(I) position is the only one and corresponds exactly to Eu^{3+} luminescence in natural fluorapatite (Gaft et al. 1997b).

Under laser excitation, Eu^{3+}(I) is especially prominent under λ_{ex} = 266 nm and it is the main form of Eu^{3+} in natural apatites. Extremely rare, 337 and 355 nm excitations lead to the appearance of the new lines at 574, 623, 630 and 711 nm (Fig. 4.1d), which are similar to those received as a result of activation in air. Thus they are connected with Eu^{3+} in the low symmetry Ca(II) site. Because of the lower symmetry its luminescence has a relatively short decay time and is more prominent in the spectrum with a narrower gate width. This center is especially strong at liquid nitrogen temperature where the prominent $^5D_0$–$^7F_0$ line at 574 nm can bee seen, unhidden by Dy^{3+} luminescence.

5.2.5.2
Fluorite CaF_2

5.2.5.2.1
Eu^{2+}

The luminescence center of divalent europium in fluorite is well known (Haberland et al. 1934; Tarashchan 1978; Krasilschikova et al. 1986; Barbin et al. 1996). It is clearly seen in laser-induced time-resolved luminescence spectra with a decay time of 600–800 ns (Fig. 4.10a). In several samples the band with a spectrum similar to those of Eu^{2+} has a very long decay time and remains even after a delay of several ms. Principally it may be connected with energy migration from a UV emitting center with a long decay time, for example, Gd^{3+}.

5.2.5.2.2
Eu^{3+}

The luminescence of Eu^3 has not been detected in natural samples using steady-state spectroscopy, because it is obscured by the strong emission band of Eu^{2+} and other centers. Because the decay time of Eu^{2+} is in the range of 600–800 ns, it is already quenched after a delay of 10 µs and only the long-lived luminescence of RE^{3+} is detected. Two groups of lines appear which may be ascribed to Eu^{3+}. The first is especially strong under excitation of 266 nm with the main line at 573 nm (Fig. 4.10b). The second type is also especially strong under excitation of 266 nm with the main lines at 595, 622, 645 and 700 nm (Fig. 4.10c). Two types of RE luminescence centers are well known in synthetic artificially activated fluorite (Stepanov and Feofilov 1956). Eu^{3+} may be located in the CaF_2 lattice in several non-equivalent positions with cubical, tetragonal, trigonal and rhombic symmetries. Decay times of the first group of luminescence lines are extremely long, possibly indicating high symmetry cubic symmetry. Another group of Eu^{3+} lines with a shorter decay time is connected with a Eu^{3+} site of lower symmetry in the fluorite lattice. The Eu^{3+} line at 574 nm belongs to the $^5D_0$–$^7F_0$ transition which exists only in cases where the site symmetry allows an electric dipole process: C_s, C_n, C_{nv} (Reisfeld 1973).

5.2.5.3 Zircon

Time-resolved luminescence spectroscopy of zircon revealed luminescence lines, which may be confidentially ascribed to a Eu^{3+} center (Fig. 4.38d). Usually they are hidden by a broad band yellow emission of zircon and may be detected only with a long delay time using its much longer decay time compared to yellow luminescence.

In order to interpret those lines detected time-resolved luminescence of synthetic $ZrSiO_4$ activated by Eu was studied (Gaft et al. 2000c) (Fig. 5.11). Time-resolved luminescence spectroscopy enabled us to detect at least two Eu^{3+} centers with different decay times: a main line at 616 nm and much weaker lines at 593 and 702 nm with a relatively short decay time, and main lines at 596 and 707 nm and a weaker line at 616 nm with a long decay time. The shorter decay and the higher ratio of forced electric dipole $^5D_0$–$^7F_2$ to magnetic dipole $^5D_0$–$^7F_1$ transition indicate the lower local symmetry of the Eu-I center as it is normally observed. The relatively high intensity of the $^5D_0$–$^7F_2$ transition in Eu-I may be connected with the absence of inversion symmetry on the site. This is consistent with the behavior of hypersensitive transitions with $|\Delta J| = 2$ (Blasse and Grabmaier 1994). In the Eu-II center the magnetic dipole transition $^5D_0$–$^7F_1$ is dominant indicating a higher symmetry site. The determined difference in the excitation into charge transfer spectra

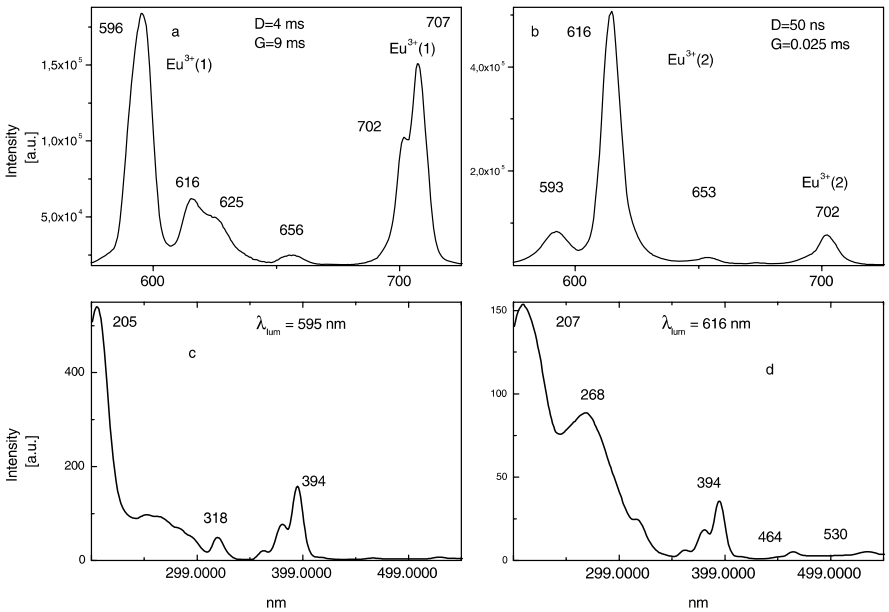

Fig. 5.11. Laser-induced time-resolved luminescence spectra of synthetic zircon artificially activated by Eu (**a**, **b**) and excitation spectra of different Eu^{3+} centers (**c**, **d**)

of the two emissions at 596 and 616 nm confirms the existence of two sites with different symmetry, one associated mainly with a single charge transfer band at 205 nm, another associated with two charge transfer bands at 207 and 268 nm. Charge transfer occurs by electron jumping from one of the highest filled molecular orbitals of the ligand to the partly filled shell of the central atom. The higher energy of the charge transfer bands indicates the larger Eu^{3+}–O^{2-} distance. The line at 596 nm belongs to the Eu-II center, which has only one type of the oxygen sites in coordination polyhedron having the highest symmetry and the longest decay of up to 1.8 ms. The line at 616 nm belongs to the Eu-I center, which has a big difference between the largest and the shortest Eu–O distances having the lowest symmetry and the shortest decay of 125 µs.

Zircon belongs to the tetragonal system and is a positive uniaxial. The typical form shows the $\{111\}$ and the $\{110\}$ planes. The two orientations selected for luminescence polarization study were the (110) plane, parallel to the basal section and the [100] row. In such cases the axis perpendicular to the (110) plane will be called X. The orientation notation is made according to the so-called Porto notation (Porto et al. 1956). The $X_1(ZX_2)X_1$ orientation means that the laser light entered parallel to the X_1 axis of the crystal and is polarized in the Z direction, while the emission is collected along the X_1 axis with X_2 polarization. By polarization spectroscopy with a high spectral resolution (less then 0.1 nm) six lines are observed for the ${}^5D_0$–${}^7F_1$ transition of the Eu-II center instead of the maximum three allowed for an unique site (Fig. 5.12). In Z(XX)Z geometry which corresponds to observation of σ-polarized luminescence we

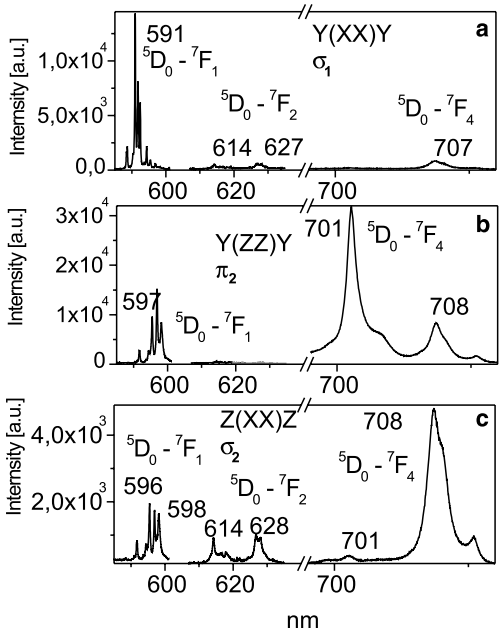

Fig. 5.12. **a–c** Laser-induced polarized spectra of synthetic zircon artificially activated by Eu

see a relatively strong $^5D_0$–$^7F_2$ line. It may be explained by a splitting scheme where $^5D_0$–$^7F_2$ transition has four lines with σ-polarization while the other three are forbidden both as electric and magnetic dipole transitions (Dicke 1968). In such cases the $^5D_0$–$^7F_1$ transition has two lines at 596 and 598 nm with π-polarization and one line at 597 nm with σ-polarization. The $^5D_0$–$^7F_4$ transition has four pure resolved lines at 708 nm with σ-polarization and three pure resolved lines at 701 nm with π-polarization while other lines are very weak. It is confirmed by observation in Y(ZZ)Y geometry which corresponds to observation of π-polarized luminescence where we see the strongest line at 597 nm in the $^5D_0$–$^7F_1$ transition and at 707 nm in the $^5D_0$–$^7F_4$ transition, while the $^5D_0$–$^7F_2$ transition is practically absent. It is important to note that the $^5D_0$–$^7F_4$ transition is the strongest one in such cases, which is first observed for Eu^{3+} luminescence. In the case of a Y(XX)Y geometry which also corresponds to observation of σ-polarized luminescence we see the three strongest lines of the $^5D_0$–$^7F_1$ transition at 591, 592 and 593 nm and much weaker lines of the $^5D_0$–$^7F_2$ transition at 614 and 627 nm and of the $^5D_0$–$^7F_4$ transition at 707 nm.

Thus at least three Eu^{3+} centers take place in zircon, which have been characterized in Table 5.1 by the main transitions, polarizations and decay times of each emitted level. These centers may be reasonably connected with Zr^{4+} cation substitution within a tetragonal $ZrSiO_4$ structure with space group $I4_1/amd$

Table 5.1. Different Eu^{3+} luminescence centers in artificially activated zircon

Center	λ (nm)	I	τ (μs)	Transition polarization	
Eu^{3+}–I	587, 593	20	125	$^5D_0$–$^7F_1$	
	616, 630	100	125	$^5D_0$–$^7F_2$	
	653	5	125	$^5D_0$–$^7F_3$	
	702	10	125	$^5D_0$–$^7F_4$	
Eu^{3+}–II	596, 598	15	1,600	$^5D_0$–$^7F_1$	π
	597	15	1,600	$^5D_0$–$^7F_1$	σ
	614, 628	10	1,600	$^5D_0$–$^7F_2$	σ
	653	1	1,600	$^5D_0$–$^7F_3$	σ
	701	100	1,600	$^5D_0$–$^7F_4$	σ
	708	100	1,600	$^5D_0$–$^7F_4$	π
Eu^{3+}–III	591, 593	100	1,800	$^5D_0$–$^7F_1$	π
	592	100	1,800	$^5D_0$–$^7F_1$	σ
	614, 628	5	1,800	$^5D_0$–$^7F_2$	σ
	653	1	1,800	$^5D_0$–$^7F_3$	σ
	701	10	1,800	$^5D_0$–$^7F_4$	σ
	707	10	1,800	$^5D_0$–$^7F_4$	π

for two main reasons: the ionic radius of Eu^{3+} is 0.99 Å while of Zr^{4+} is 0.79 Å compared with 0.42 Å of Si^{4+}, and in addition, the eight oxygen atoms coordinated to the Zr^{4+} cation, instead of four for Si^{4+}, which corresponds to the usual one for the Eu^{3+} ion. In fact the $ZrSiO_4$ unit cell contains four ZrO_8 groups, which are equivalent in the sense that they have the same geometry but different orientation. The possible reason for several Eu^{3+} centers could be the association with local charge compensation by way of electron-hole centers. The following schemes may be considered: i) Substitution of Eu^{3+} –Zr^{4+} leads to the formation of the hole center on the oxygen, as in the case of the substitution Y^{3+} –Zr^{4+} when O^- center SiO_4^{3-} forms (Marfunin 1979b); ii) Zr^{3+} centers are known in zircon at the expense of an adjacent oxygen vacancy or an interstitial alkali metal ion (Marfunin 1979a). It may be substituted by Eu^{3+} for two reasons: the ionic radius of Zr^{3+} has to be between 0.79 Å for Zr^{4+} and 0.109 Å for Zr^+, so even closer to the radius of Eu^{3+}, and in addition, it has the same charge.

5.2.5.4 Baddeleyite

Luminescence of Eu^{3+} has not been detected in natural samples yet, but is well studied in artificially activated ZrO_2 (Gutzov et al. 1998; Gedanken et al. 2000; Reisfeld et al. 2000). The main emission occurs between the $^5D_0$ level to the ^7F_j multiplet with a decay time of approximately 0.5 ms (Fig. 5.13). The luminescence intensity is relatively weak, but may be substantially increased by co-doping with nanoparticles of semiconductors, such as CdS. The origin of the

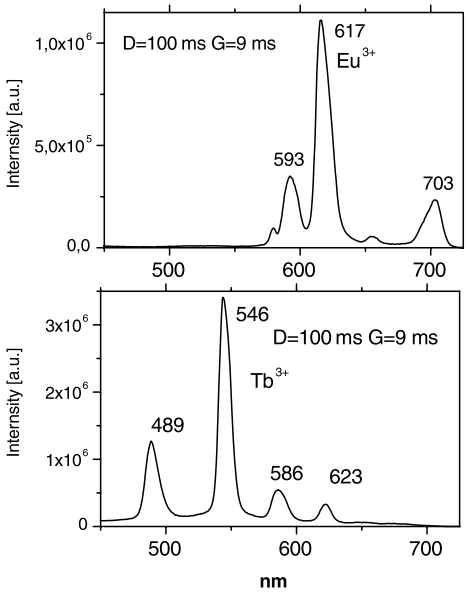

Fig. 5.13. Laser-induced time-resolved luminescence spectra of ZrO_2 activated by Eu^{3+} (**a**) and Tb^{3+} (**b**)

intensification could be explained by the following reasoning. CdS nanoparticles have intensive absorption bands, while the formation of electron-hole pairs is not followed by radiation at room temperature. The energy from non-radiative recombination can be transferred to the high lying energy levels of the Eu^{3+}. These excited levels once again non-radiatively decay to the long-lived $^5D_0$ level. Such a mechanism will increase the population of the emitting level, but not their emission probability to the ground level, which was confirmed by the unchanged decay time of Eu^{3+}.

5.2.5.5 Scheelite

Figures 5.14a,b represent luminescence spectra of scheelite enriched by Eu. Luminescence of Eu^{3+} is well known in steady-state spectra of scheelite (Tarashchan 1978; Gorobets and Kudrina 1980). In time-resolved spectroscopy its relative intensity is stronger after a long delay time, which is explained by the longest decay time of Eu^{3+} in scheelite compared to other REE.

The possible luminescence of Eu^{2+} in scheelite is a very interesting problem. It was not detected by steady-state luminescence spectroscopy. The possible reason is that the very strong intrinsic luminescence of scheelite is situated in the same spectral range, which covers the weaker emission of Eu^{2+}. We tried to solve this problem by the time-resolved method using different decay times for intrinsic and Eu^{2+} bands. Time-resolved spectroscopy

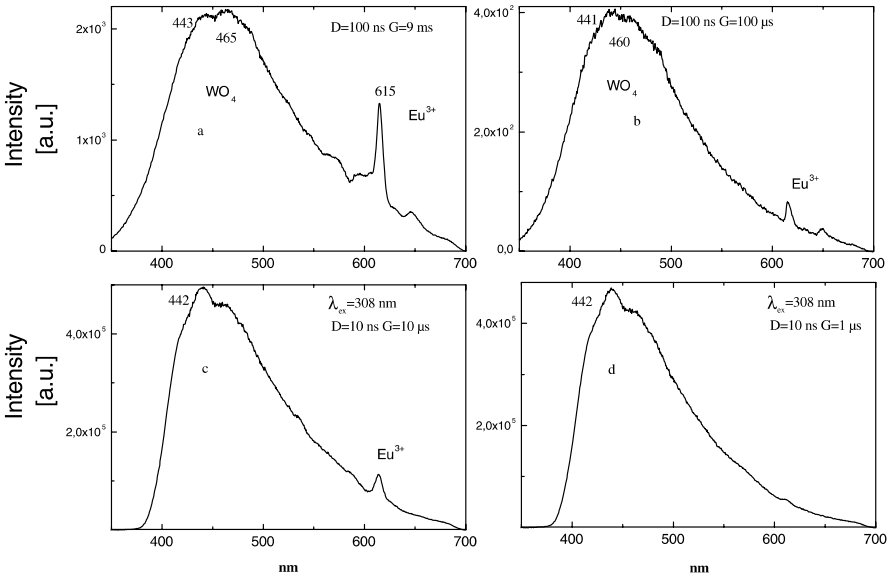

Fig. 5.14. **a–d** Laser-induced time-resolved luminescence spectra of scheelite with elevated concentration of Eu (**a**, **b**) and synthetic scheelite artificially activated by Eu (**c**, **d**)

of synthetic $CaWO_4$:Eu (Fig. 5.14c,d) revealed the blue band peaking in the same spectral region, but with a narrower bandwidth compared to intrinsic scheelite emission. Thus it may be supposed, that the blue emission consists of several luminescence bands and the participation of Eu^{2+} is principally possible.

5.2.5.6 Barite and Anhydrite

The spectral-kinetic parameters of the narrow band at 375 nm enable its confident identification as Eu^{2+} luminescence, which is confirmed by emission of synthetic $BaSO_4$ artificially activated by Eu (Fig. 5.15a). Such emission was also detected and interpreted by steady-state spectroscopy (Tarashchan 1978). It is interesting to note that very often such a band is absent in natural barite and appears only after heating in air at 600–700 °C (Fig. 4.31b). Such a transformation is reversible, at least partly. Under X-ray excitation the intensity of the UV band diminishes, and a new blue-green emission appears (Fig. 5.16). This shows some kind of transformation, which takes place in the barite lattice under these conditions. Several possibilities exist. It is possible that in barite the luminescence is quenched by the components with high-energy phonons. The water and organic matter may represent the latter. They are removed after

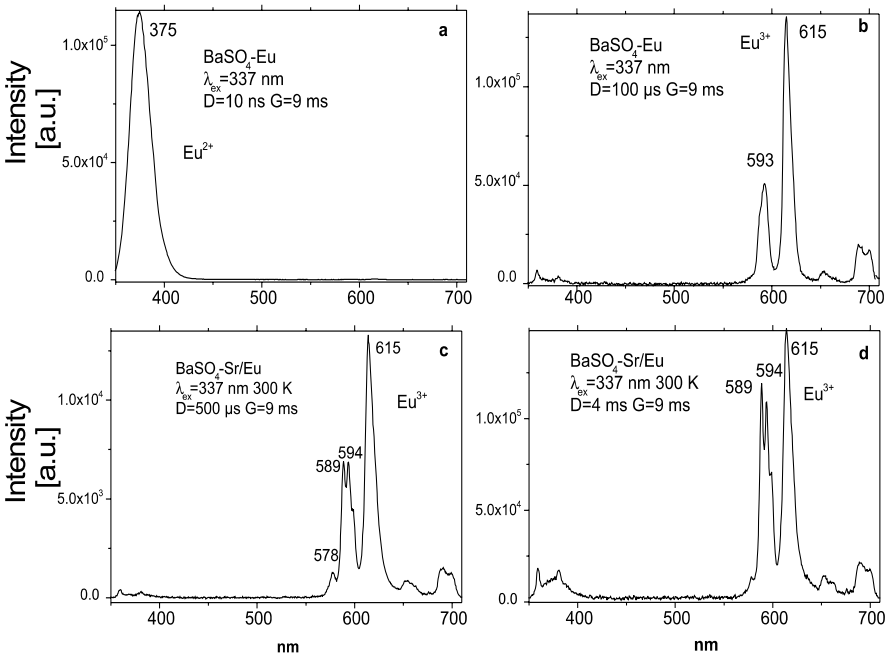

Fig. 5.15. a–d Laser-induced time-resolved luminescence spectra of $Ba(Sr)SO_4$:Eu

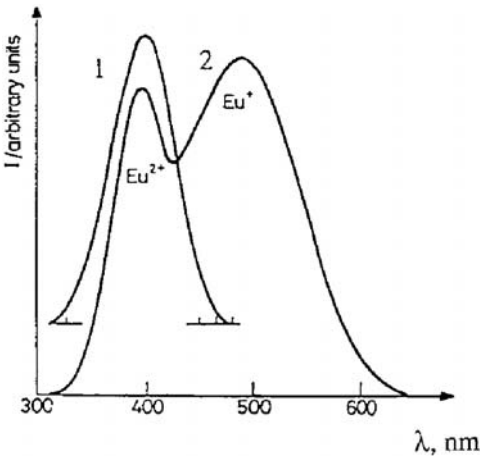

Fig. 5.16. Laser-induced luminescence of barite: 1 – after heating at 600 °C while violet luminescence of evidently Eu^{2+} appears; 2 – after X-ray irradiation of the heated sample where blue shoulder appears, supposedly connected with Eu^{+} (Gaft and Rudenkova 1993)

heating and luminescence becomes visible. Another possibility is that barite accommodates RE in concentrated adsorbed form, which is not suitable for detection by luminescence due to concentration quenching. As a result of high temperature heating, thermal diffusion of Eu in the lattice takes place with resulting luminescence. The isomorphic substitution in Eu^{2+} form is easy because its ionic radius (139 pm) is close to that of Ba^{2+} and Sr^{2+} (Gaft and Rudenkova 1993).

The other model is also principally possible. Europium initially enters the barite lattice as Eu^{+}, which oxidizes to Eu^{2+} at 700 °C. The relatively small difference between the Ba^{2+} and the Eu^{+} ionic radii (1.5 and 1.7 A) makes this substitution possible. The luminescence of Eu^{+} was still not observed in minerals, but is known in luminofors (Gorobets et al. 1968). Eu^{+} has $6s^1$ electron configuration and the mostly probable are electric-dipole electron transitions $6s^1$–$6p^1$, taking place between uneven $^7S_3$ $^9S_4$ and even $^7P_{2,3,4}$ $^9P_{3,4,5}$ terms. It usually generates the broadband luminescence in the UV-green part of the spectrum.

Luminescence of trivalent Eu was not detected in natural barite yet, but the possible emission may be seen on artificially activated $BaSO_4$ (Fig. 5.15). The Sr addition generates the appearance of an additional Eu^{3+} luminescence center compared with $BaSO_4$. The luminescence of Eu^{3+} and Eu^{2+} is well known in anhydrite (Tarashchan 1978; Gaft et al. 1985; Baumer et al. 1997). They are also found in time-resolved spectra under excitation at 266 nm (Fig. 4.17).

5.2.5.7 Calcite

Steady-state luminescence of Eu^{3+} was found in CL spectra (Haberman et al. 1996). Figure 4.13c represents laser-induced time-resolved luminescence of calcite under 266 nm. Luminescence lines of Eu^{3+} are seen. Hypersensitive

$^5D_0$–$^7F_2$ (618 nm) emission dominates Eu^{3+} luminescence, showing local coordination without inversion symmetry. Another type of Eu^{3+} is characterized by a strong $^5D_0$–$^7F_0$ line at 575 nm.

5.2.5.8 Danburite and Datolite

The narrow band at 437 nm with a decay time of 650 ns in the danburite luminescence spectrum belongs to Eu^{2+} luminescence (Fig. 4.15a), which was also detected by steady-state spectroscopy (Gaft et al. 1979). Besides that, under 308 nm excitation narrow lines appear at 580, 592, 611, 618, 655 and 692 nm (Fig. 4.15c) with a long decay time, which confidently may be ascribed to Eu^{3+}. Under 266 nm excitation another group of lines appear with the main line at 575 nm connected with a different type of Eu^{3+} (Fig. 4.15d).

The narrow band at 455 nm with a decay time of 750 ns in the datolite luminescence spectrum belongs to Eu^{2+} luminescence (Fig. 4.16b), which was also detected by steady-state spectroscopy (Gaft et al. 1979). Besides that, narrow lines appear in the orange part of the spectrum with the main one at 610 nm (Fig. 4.16c) with a long decay time, which confidently may be ascribed to Eu^{3+}.

5.2.5.9 Pyromorphite

Figure 4.26 demonstrates the time-resolved luminescence of pyromorphite under 355 and 266 nm laser excitations. Luminescence lines of Eu^{3+} are clearly seen in both cases.

5.2.5.10 Feldspars

Most of the natural alkali feldspars and plagioclases rarely contain more than a few ppm of Eu and its emission is often very difficult to detect, especially when superposed by strong emission of other activators. In natural samples the blue-violet Eu^{2+} activated luminescence is known by steady-state spectroscopy (Haberland and Köhler 1939; Moroshkin et al. 1987). Time-resolved spectroscopy enables us to detect separate narrow luminescence bands with decay times in the range of 600–800 ns, which confidently may be ascribed to Eu^{2+} (Fig. 4.44). In our study its emission maximum was changed from 403 nm in labrador to 410 nm in plagioclase. It has to be mentioned that very often, additional blue bands are detected, but with much longer decay times, which may be mistakenly interpreted as Eu^{2+} in steady-state spectra. Eu^{3+} luminescence was first detected in feldspars by laser-induced time-resolved spectroscopy. It was excited by green laser light at 532 nm and is characterized by the narrow lines at 614 and 624 nm (Fig. 4.45c) with a long decay time of 550 μs.

5.2.5.11 Charoite

The narrow band near 410 nm in the time-resolved luminescence spectra of charoite (Fig. 4.22) is connected with Eu^{2+} luminescence.

5.2.5.12 Titanite

Based on similar behavior under different excitations, decay times and synchronous change of intensities in different samples, we detected two groups of lines in titanite luminescence spectra, which are evidently connected with Eu^{3+} emission (Fig. 4.33). The first group contains the lines at 574, 589, 613, 620, 657, 662, 700 and 706 nm, while the second group the lines at 578, 590, 598, 608, 620, 649, 658, 701, 705 and 711 nm (Gaft et al. 2003b). All lines have long decay times of approximately 840 µs. Transition $^5D_0$–$^7F_0$ presents in both centers, which exists only in cases where the site symmetry allows an electric dipole process (Reisfeld 1973). The most probable substitution for Eu^{3+} in titanite structure is instead of Ca^{2+} with corresponding charge compensation. The relative intensities of magnetic dipole transition $^5D_0$–$^7F_1$ and electric dipole transition $^5D_0$–$^7F_2$, together with strong $^5D_0$–$^7F_0$ transition in titanite is very similar to Eu^{3+} emission in low symmetry sites in apatite structure, where Ca^{2+} has seven nearest neighbors, six oxygens and one fluor. Thus Eu^{3+} in titanite may substitute for seven-fold coordinated Ca^{2+} where F initially substitutes one of the oxygen atoms. In such case charge compensation may be achieved by opposite substitution of F^- by O^{2-}.

5.2.5.13 Zoisite

Narrow band peaking at 440 nm with decay time of approximately 1 µs is evidently connected with Eu^{2+} center substituting for Ca^{2+} (Fig. 4.59d).

5.2.5.14 Leucophane

Luminescence of Eu^{2+} and Eu^{3+} has been found in the X-ray excited luminescence spectra of synthetic leucophane activated by Eu (Prokofiev et al. 1982; Fig. 5.17), while in natural samples only Eu^{2+} was detected. Laser-induced time resolved luminescence under 532 nm excitation enables us to detect clear lines of Eu^{3+} with the strongest $^5D_0$–$^7F_0$ electron transition at 573 nm (Fig. 4.25).

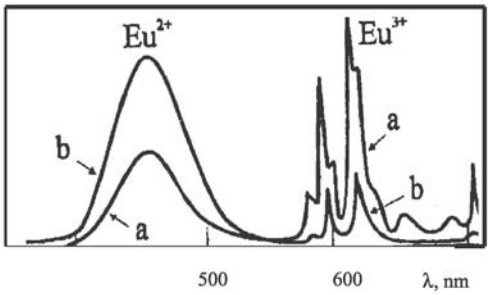

Fig. 5.17. Steady-state X-ray excited luminescence of artificial leucophane activated by Eu (a-2% and b-0.5% Eu_2O_3 in blend, respectively) (Prokofiev et al. 1982)

5.2.6 Gd^{3+}

In all minerals the gadolinium luminescence spectra are completely located in the UV part of the spectrum and consist of several lines at 310–315 nm, corresponding to transition $^6P_{7/2}$–$^8S_{7/2}$. The main line is characterized by a long decay time and is especially prominent in the spectra with a long delay. Gd^{3+} is known as a good sensitizer of the other rare-earth ions luminescence. It is detected in spectra of fluorite (Fig. 4.12a), zircon (Fig. 4.38h), anhydrite (Fig. 4.17a), and hardystonite (Fig. 4.20b).

5.2.7 Tb^{3+}

Luminescence spectra consisting of many lines due to ^5D_j–^7F_j transitions are observed for Tb^{3+}. The intensity of the emissions from $^5D_3$ decreases with increasing Tb^{3+} concentration due to cross-relaxation. Among the emission lines from the $^5D_4$ state, the $^5D_4$–$^7F_5$ emission line at approximately 550 nm is the strongest in nearly all host crystals when the Tb^{3+} concentration is high. The reason is that this transition has the largest probability for both electric-dipole and magnetic-dipole induced transitions. The Tb^{3+} emission has a broad excitation band in the region from 220 to 300 nm originating from the $4f^8$–$4f^7 5d^1$ transition. The intensity ratio of the emission from $^5D_3$ to that from $^5D_4$ depends not only on the Tb concentration, but also on the host material. Two additional factors have to be considered in order to determine the possible ratio of $^5D_3$ to $^5D_4$ intensity. One is the maximum energy of phonons that causes phonon-induced relaxation. If the maximum phonon energy is large, the ratio of $^5D_3$ to $^5D_4$ intensity becomes small. The other factor is the energy position of the $4f^7 5d^1$ level relative to $4f^8$ levels, which can be discussed in terms of the configurational coordinate model. If the minimum of the $4f^7 5d^1$ is low in energy and the Franc-Condon shift is

large, there is a possibility that an electron excited to the $4f^7 5d^1$ level can relax directly to the $^5D_4$, bypassing the $^5D_3$ and thus producing only $^5D_4$ luminescence.

In order to enable correct identification of Tb^{3+} lines in minerals several of them were synthesized and artificially activated by Pr (Fig. 5.18). Besides that,

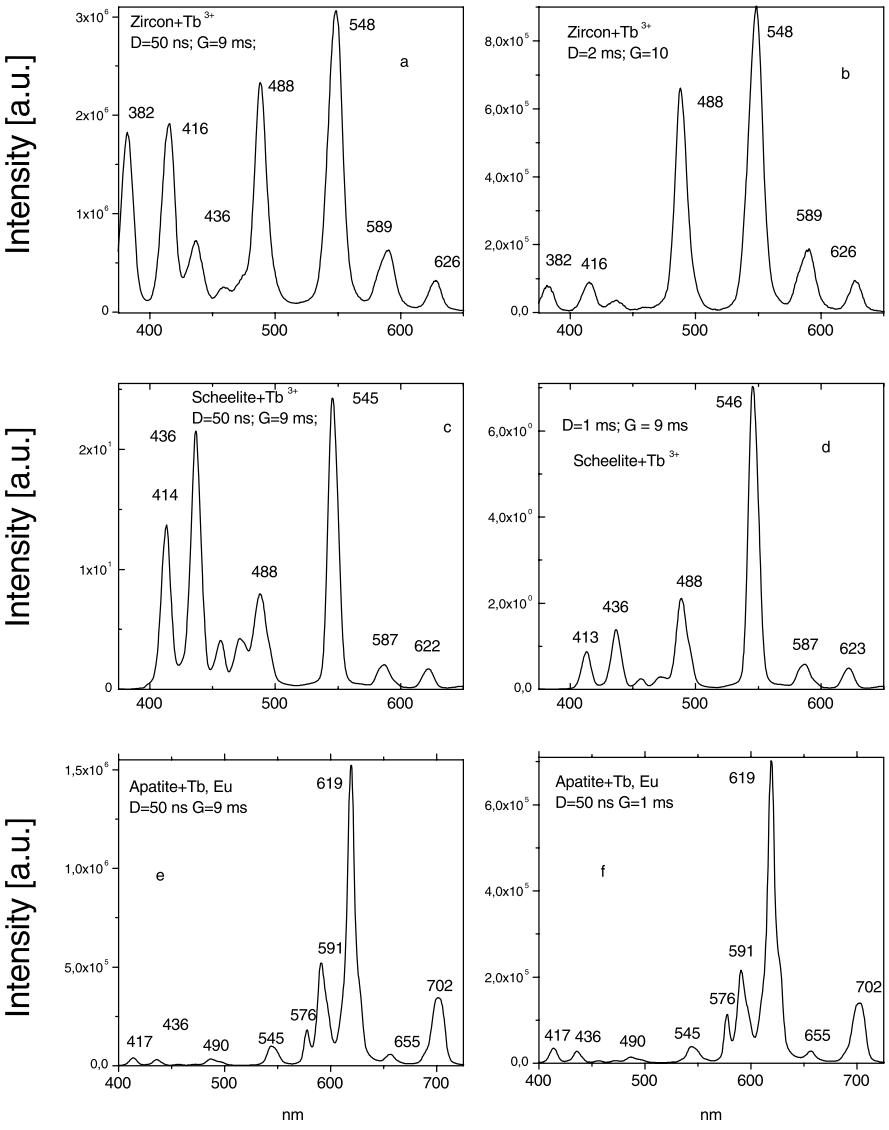

Fig. 5.18. **a–f** Laser-induced time-resolved luminescence spectra of synthetic zircon, apatite and scheelite artificially activated by Tb

comparison has been made with CL spectra of synthetic minerals artificially activated by Tb (Blank et al. 2000).

5.2.7.1 Apatite

Usually the strongest lines at 380, 414 and 436 nm of $^5D_3$–^7F_j transitions (Fig. 4.2d) are known in natural apatite, which represent Tb^{3+} luminescence in the Ca(I) position. The intensity of the 545 nm line ($^5D_4$–$^7F_2$) of Tb^{3+} is strongest in red apatite, as compared to the others (Fig. 4.1c). Evidently in this case Tb^{3+} is in the Ca(II) site. The abnormal intensity is not connected with unusually high Tb concentration (Table 4.4), but with lower symmetry of this site. Simultaneous activation by Tb and Eu (Fig. 5.18e,f) demonstrates that blue emission lines of Tb^{3+} have shorter decay times compared with green ones in accordance with different symmetries of Ca(I) and Ca(II) sites.

5.2.7.2 Scheelite

In Tb^{3+} the luminescent lines are connected with electron transitions from different excited levels: $^5D_3$ and $^5D_4$. The lines at 436 and 414 nm have $\tau = 375$ µs while the lines at 546 and 489 nm are characterized by a very long $\tau = 2.4$ ms. In the time-resolved spectra of natural samples with 337 nm excitations, the previously hidden lines at 416 and 439 nm enable sure identification of Tb^{3+} (Fig. 4.9e,f).

5.2.7.3 Anhydrite, Feldspars, Fluorite, Hardystonite, Zircon, Zoisite

The strongest lines of emission of Tb^{3+} in these minerals are in the UV-violet part of the spectrum at (Figs. 4.17d, 4.45a, 4.10c, 4.20c, 4.38a,4.59c).

5.2.8 Dy^{3+}

Dysprosium activated minerals have luminescence in the visible part of the spectrum. The spectra of Dy^{3+} in minerals are mainly characterized by narrow lines near 480 and 575 nm, accompanied by the weaker ones near 660 and 752 nm corresponding to transitions from level $^4F_{3/2}$ to the levels of multiplets ^6H_j and ^6F_j (Tarashchan 1978). Consequently, the spectra are not changed with delay time and excitation energy and all luminescence lines of Dy^{3+} are characterized by decay time. The best excitation at 350 nm is connected with $4f$–$4f$ $^6H_{15/2}$–$^4G_{7/2}$ transition. Such luminescence is detected in

apatite (Fig. 4.1c), scheelite (Fig. 4.9e), zircon (Fig. 4.38a) where they usually dominate in the spectrum, anhydrite (Fig. 4.17c), calcite (Fig. 4.13d), hardystonite (Fig. 4.20c), zoisite (Fig. 4.59b), and feldspars (Fig. 4.45b). Several types of Dy^{3+} centers may be discerned in time-resolved luminescence spectra of fluorite. The main bands are at 477 and 573 nm (Fig. 4.11). Under certain excitation and registration conditions it may be seen that narrow lines at 588, 673 and 765 nm appear (Fig. 4.12b), which are typical for Dy^{3+} in cubic symmetry (Tarashchan 1978).

5.2.9 Er^{3+}

The main feature is the green emission corresponding to transitions from state $^4S_{3/2}$ to the ground state $^4I_{15/2}$. At the same time, an intense luminescence may be detected at 1.5 µm, which is caused by resonance transitions $^4I_{3/2}$–$^4I_{15/2}$. The presence of green luminescence indicates that the de-activation of the high level accompanied by IR emission is not complete, but it results in a relatively short decay time of Er^{3+} green emission. Thus the luminescence of Er^{3+} is easier to detect in time-resolved spectra with a narrow gate. In order for correct identification of Er^{3+} lines in minerals several of them were synthesized and artificially activated by Er (Fig. 5.19) . Besides that, comparison has been made with CL spectra of synthetic minerals artificially activated by Er (Blank et al. 2000).

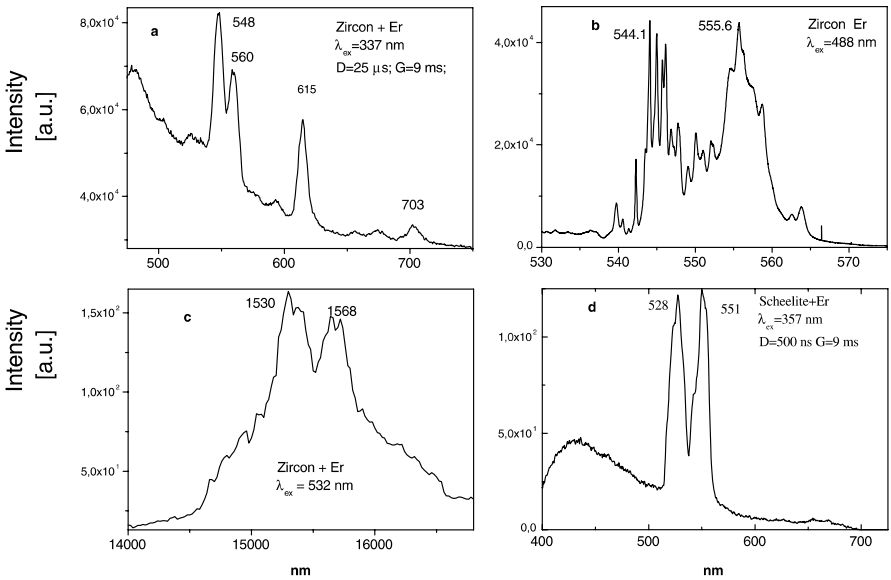

Fig. 5.19. a–d Laser-induced time-resolved (**a, d**) and steady-state (**b, c**) luminescence spectra of synthetic zircon and scheelite artificially activated by Er

5.2.9.1 Apatite

A relatively rare strong line appears in the luminescence spectrum of apatite near 544 nm (Fig. 4.2c). Spectrally it is similar to the line of Tb^{3+}, but it is characterized by a much shorter decay time and its intensity is not correlated with other lines of Tb^{3+}. By analogy with other hosts it is known that Er^{3+} and Ho^{3+} may generate luminescence in this spectral region. Artificial fluor-apatite activated by Er exhibits green and IR luminescence near 550 and 1,500–1,600 nm, respectively (Morozov et al. 1990). Cathodoluminescence spectra of artificial chlor-apatites activated by Er and Ho demonstrate green lines for both cases (Blank et al. 2000). We investigated Er and Ho activated chlor-apatite samples under argon laser excitation with $\lambda = 488$ nm and it was found that both Er and Ho are characterized by luminescence lines at 545 nm, but for Ho the strong lines present near 650–660 nm were not detected in natural fluor-apatites. IR luminescence allows detection of the band at 1,540 nm the intensity of which is correlated with the intensity of the lines at 545 nm (Gaft et al. 1997a). Thus the luminescence of Er^{3+} present in natural fluor-apatite corresponds to $^4S_{3/2}$–$^4I_{15/2}$ (545) and $^4I_{13/2}$–$^4I_{15/2}$ (1,540) electron transitions.

5.2.9.2 Scheelite

The lines of Er^{3+} are difficult to point out because they have short decay times, which are comparable with the decay of broad band luminescence of scheelite at the same spectral region. Using a dye laser with 357 nm emission solved this problem. It is effective for Er^{3+} but not suitable for the excitation of the WO_4-center (Fig. 4.8c). These lines of Er^{3+} are most clearly seen with a narrower gate width when the luminescence of short-lived centers dominates. Investigation of the time-resolved luminescence of synthetic $CaWO_4$:Er confirmed our interpretation (Fig. 5.19).

5.2.9.3 Zircon

Luminescence of Er^{3+} in the emission spectra of zircon is very difficult to detect under UV excitation even by time-resolved spectroscopy. The reason is that it has a relatively short decay time similar to those of zircon yellow luminescence, which usually is much stronger than Er^{3+} lines. Visible excitation, which is not effective for broad band luminescence, allows the revealing of Er^{3+} luminescence lines, using high-resolution steady-state spectroscopy (Fig. 4.38f).

5.2.9.4 Titanite

Three emission lines at 563, 853 and 978 nm (Figs. 4.33, 4.34) demonstrate correlated behavior and are evidently connected with one emission center. Such

an emission is characteristic for Er^{3+}. The main feature of Er^{3+} luminescence in titanite is connected with the $^4S_{3/2}$ excited state. It is responsible for green emission at approximately 550–560 nm corresponding to $^4S_{3/2}$–$^4I_{15/2}$ transition and for near IR emission at 850 nm corresponding to $^4S_{3/2}$–$^4I_{9/2}$ transition. The other important state is the $^4I_{11/2}$, which is upper level for the $^4I_{11/2}$–$^4I_{15/2}$ transition at about 980 nm.

5.2.10 Ho^{3+}

Holmium activated minerals display green luminescence from a resonant transition from state $^5S_2$ to the ground state $^5I_8$. Because Ho^{3+} has luminescent lines connected with electron transitions from the same excited level, the spectra are not changed with delay time and excitation energy. The high intensity of the green luminescence indicates that the de-activation of the high level $^5S_2$ accompanied by IR emission from the $^5I_7$ level is not complete, but it results in the relatively short decay time of the Ho^{3+} green emission. Thus the luminescence of Ho^{3+} is better to detect in narrow gate time-resolved spectra.

In order to enable correct identification of Ho^{3+} lines in minerals several of them were synthesized and artificially activated by Ho (Fig. 5.20). Besides that, comparison has been made with CL spectra of synthetic minerals artificially activated by Ho (Blank et al. 2000). Luminescence of Ho^{3+} was detected in time-

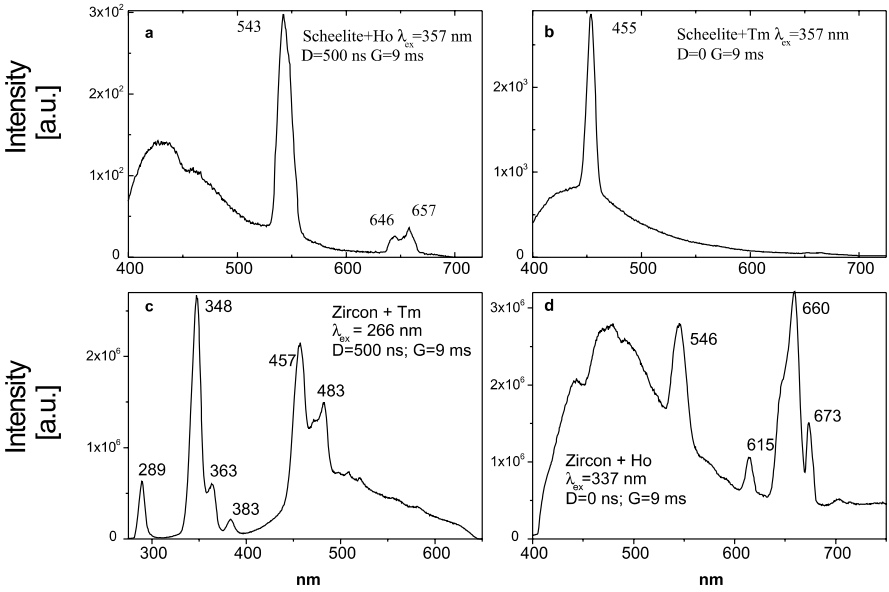

Fig. 5.20. **a–d** Laser-induced time-resolved luminescence spectra of synthetic zircon and scheelite artificially activated by Ho and Tm

resolved luminescence spectra of scheelite (Fig. 4.8d), fluorite (Fig. 4.12c), and zircon (Fig. 4.38f).

5.2.11 Tm^{3+}

Thulium displays in minerals an intense UV and blue visible luminescence with a line spectrum near 360 and 450 nm, correspondingly. They are connected with electron transitions from different excited levels $^1D_2$ and $^1D_4$ at 360–365 and 450–455 nm. The luminescence of Tm^{3+} is more easily detected in time-resolved spectra with a narrow gate, because it usually has a relatively short decay time. The UV line usually has a much shorter decay time compared with the blue line. Different decay times from these levels are evidently connected with nonradiative relaxation due to the presence of high frequency vibrations in the lattice. The best excitation is at 355 nm, which is connected with transition $^3H_6$–$^1D_2$.

In order to enable correct identification of Tm^{3+} lines in minerals several of them were synthesized and artificially activated by Tm (Fig. 5.20). Besides that, comparison has been made with CL spectra of synthetic minerals artificially activated by Tm (Gruber et al. 1997; Blank et al. 2000).

The luminescence of Tm^{3+} was detected in apatite (Fig. 4.2c,d), scheelite (Fig. 4.8d), fluorite (Fig. 4.11a,b), zircon (Fig. 4.38 h), anhydrite (Fig. 4.17c), calcite (Fig. 4.13d), and hardystonite (Fig. 4.20c).

Titanite has rather unusual luminescence of Tm^{3+} (Gaft et al. 2003b). The lines near 800 nm are very characteristic for its luminescence spectra under different excitations (Fig. 4.34). It is interesting to note that the lines at 796, 806 and 820 nm present also in optical absorption spectra of titanite (Fig. 5.21). Such absorption lines are usually ascribed to electron transitions to the $^4F_{5/2}$ level of Nd^{3+}. Thus in such cases it is logical to suppose that the emission lines at 800 nm have to be correlated with other Nd^{3+} luminescence, for example with IR emission from the $^4F_{3/2}$ level. Nevertheless, this is not the case. For example, with λ_{ex} = 488 nm excitation the lines at 800 nm are absent, while the IR emission of Nd^{3+} is very strong. The same situation is present in the ionoluminescence spectrum, where the lines near 800 nm are absent and the luminescence of Nd^{3+} presents (Yang 1995). Thus it is possible to suppose that the lines near 800 nm with a relatively short decay time of 60 μs belong to another luminescence center.

A possible candidate may be Tm^{3+}. For example, the doublets at 803 and 817 nm and at 796 and 813 nm are the strongest ones in cathodoluminescence spectra of fluorite and scheelite activated by Tm^{3+} (Blank et al. 2000). It is possible to suppose that the strong lines at 805 and 820 nm with a relatively short decay time of 60 μs in the titanite luminescence spectrum belong to Tm^{3+}. They appear under 532 nm excitation and are evidently connected with the $^1G_4$–$^3F_5$ electron transition. Similar emission of Tm^{3+} was also detected in the time-resolved luminescence spectra of leucophane (Fig. 4.25).

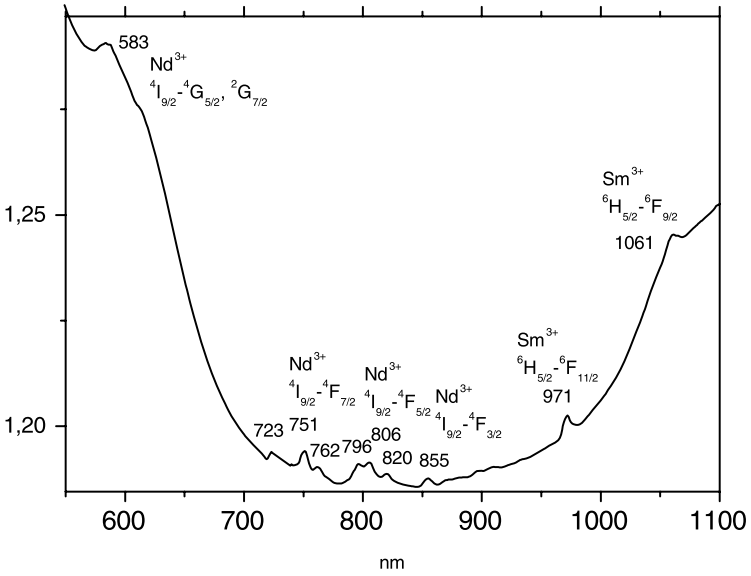

Fig. 5.21. Absorption spectrum of titanite

5.2.12 Yb^{3+}, Yb^{2+}

IR luminescence of Yb^{3+} in minerals has been detected in steady-state luminescence of fluorite (Tarashchan 1978) and zircon (Gaft et al. 1986). Time-resolved luminescence spectra of apatite (Fig. 4.3b) and scheelite (Fig. 4.8a) also exhibit such emission. Emission lines in natural apatite are very similar to those in Yb^{3+} doped artificial apatite (DeLoach et al. 1994). The excitation of Yb^{3+} is strongly affected by energy transfer from Nd ions, because the direct excitation of Yb^{3+} is difficult, since it requires a comparatively short-wavelength UV radiation.

The luminescence of Yb^{2+} in the near UV and visible is due to $4f^{14}$–$4f^{13}5d$ transitions. The energy level scheme of the $4f^{13}5d$ configuration of Yb^{2+} in crystals is complicated due to the simultaneous action of the crystal field and spin–orbit coupling on the free ion states. The lowest energetic excited states, arising from the $^3P_2$ free ion level, have $^3T_{2u}$ and ^3E_u symmetry. About 2,000–3,000 cm^{-1} above these levels there are $^3T_{1u}$ levels from the $^3H_5$ state. Only transitions between the ground state ($^1A_{1g}$) and states with T_{1u} symmetry are symmetry allowed.

It was found that, in the sequence: sulfates, phosphates, borates, silicates, aluminates, and simple oxides the probability of observing normal *df* emission decreases and the probability of observing anomalous emission or no emission at all increases. Normal *df* emission is only observed in the sulfates MSO_4 (M=Ca, Sr, Ba) and in the condensed borate SrB_4O_7. Anomalous emission

occurs in several phosphates and a few silicates, but not in the aluminates or CaO. In aluminates and simple oxides, even down to 4 K, no broad band Yb^{2+} emission has been reported. Most compounds for which normal *df* emission is observed contain large halogen ions. Anomalous emission is much more frequently observed when the small Yb^{2+} is the dopant than when Eu^{2+} is the dopant and normal *df* emission is never observed for Yb^{2+} on trivalent cation sites and always observed for Yb^{2+} on monovalent cation sites (Dorenbos 2003).

In minerals, luminescence of Yb^{2+} was found in the steady-state low temperature luminescence spectra of fluorite (Tarashchan 1978), danburite and datolite (Gaft and Gorobets 1979; Fig. 5.22). It is characterized by a broad band in the green part of the spectrum. The strong thermal quenching of Yb^{2+} is connected with its very small Stokes shift. It may be expected to find luminescence of Yb^{2+} in low temperature luminescence spectra of natural sulfates, because UV luminescence was detected in synthetic $CaSO_4$, $SrSO_4$ and $BaSO_4$ artificially activated by Yb^{2+}. The corresponding decay time was several ms at 20 K and the luminescence was quenched at approximately 200 K (Lizzo et al. 1994).

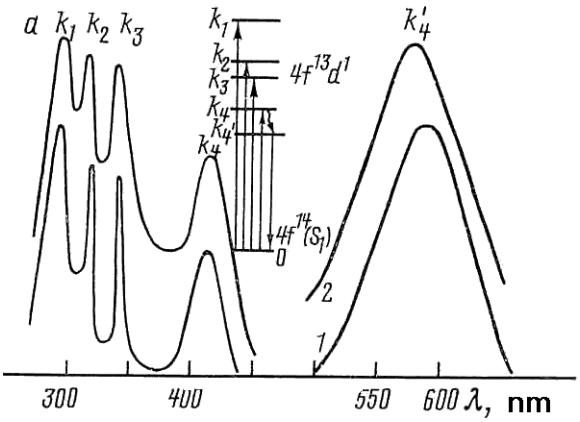

Fig. 5.22. Luminescence and excitation spectra of Yb^{2+} in danburite and datolite (Gaft and Gorobets 1979)

5.3 Transition Metal Elements

Transition metal ions have an incompletely filled *d*-shell, i.e. their electron configuration is d^n. The optically active electrons are thus bound to central potential as well as experiencing crystal field potential, and are not shielded by outer electrons. Most transition metal ions are multi-valent. Mainly the number of 3*d* electrons and the crystal field determine their optical properties. Thus the groups below have similar optical behavior:

Configuration	$3d^1$	$3d^2$	$3d^3$	$3d^4$	$3d^5$	$3d^6$	$3d^7$	$3d^8$	$3d^9$	$3d^{10}$
Ions									Cu^{2+}	Cu^+
							Ni^{3+}	Ni^{2+}		
							Co^{2+}			
						Co^{3+}				
					Fe^{3+}	Fe^{2+}				
	Mn^{6+}	Mn^{5+}	Mn^{4+}	Mn^{3+}	Mn^{2+}	Mn^+				
	Cr^{5+}	Cr^{4+}	Cr^{3+}	Cr^{2+}	Cr^+					
	V^{4+}	V^{3+}	V^{2+}							
	Ti^{3+}	Ti^{2+}								

5.3.1
$3d^3$ Elements

The elements with such an electronic configuration known as luminescent centers are Cr^{3+}, Mn^{4+} and V^{2+}. They are capable of substituting in a wide variety of metal oxide host systems. They are invariably oxygen-coordinated with six nearest neighbors, and may be in a pure octahedral or a distorted octahedral symmetry site. These luminescent centers exists in a d^3 configuration (Fig. 5.23), and the electronic repulsion, which results from placing three electrons in the same set of d-orbitals yields several states identified as "free

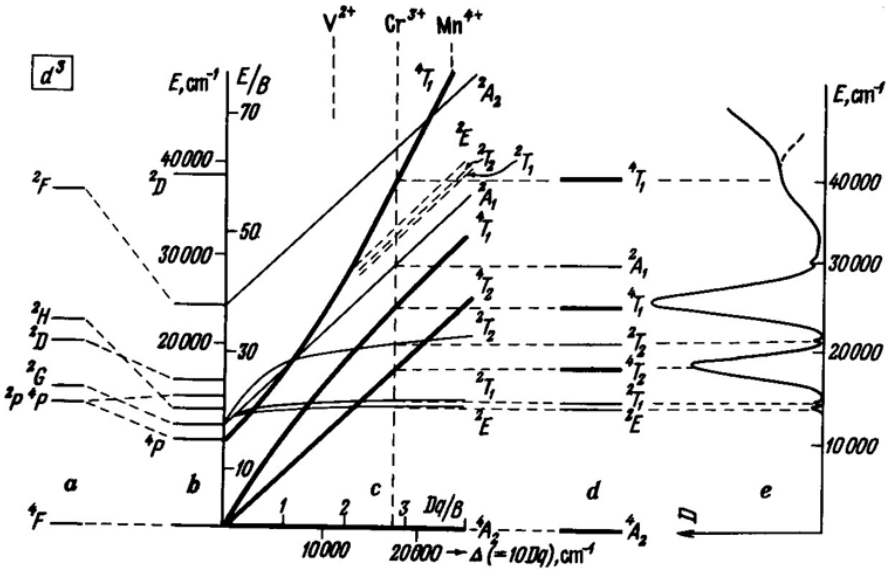

Fig. 5.23. Tanabe-Sugano diagram for d^3 elements

ion" energy levels. The placement of such ions in a crystal lattice produces a further splitting of the free ion levels. The exact energy spacing between the energy levels is therefore determined by the strength of the crystal field experienced by the luminescent center. Since different crystal field strengths are anticipated for each mineral host into which Cr^{3+} can be placed, it may be concluded that the luminescence may be a reliable indicator of the mineral structures properties.

The most important free ion states are ${}^4F$ ground level and excited ${}^2H$ level. In an octahedral field, the ${}^4F$ level splits into the ${}^4A_2$ ground state and the excited ${}^4T_2$ and ${}^4T_1$ states. The spin allowed transitions that could therefore be used to populate the excited states directly correspond to ${}^4A_2 \rightarrow {}^4T_2$ and ${}^4A_2 \rightarrow {}^4T_1$. Mostly Cr^{3+} appears in minerals as a trace constituent substituting for Al^{3+} in six-fold coordination. As such, the larger Cr^{3+} ion is placed in a site with small metal-ligand distances and where the crystal field is large, typically 1,650–1,750 cm^{-1}. As may be seen in Fig. 5.24, if the crystal field is sufficiently strong to make the doublet state the lowest energy excited state, there will be a red luminescence. Because the doublet state belongs to the same orbital configuration as the ground state, the Stokes shift and Condon offset will be small. As a result, the line width of emission is narrow and a considerable amount of phonon fine structure is observed even at room temperature. Such a transition is forbidden by symmetry and spin selection rules and the decay time is usually very long. Although the narrow line emission is essentially independent of the crystal field and thus of site size and symmetry, the energy of the double levels does depend on Racah parameters B and C, which are

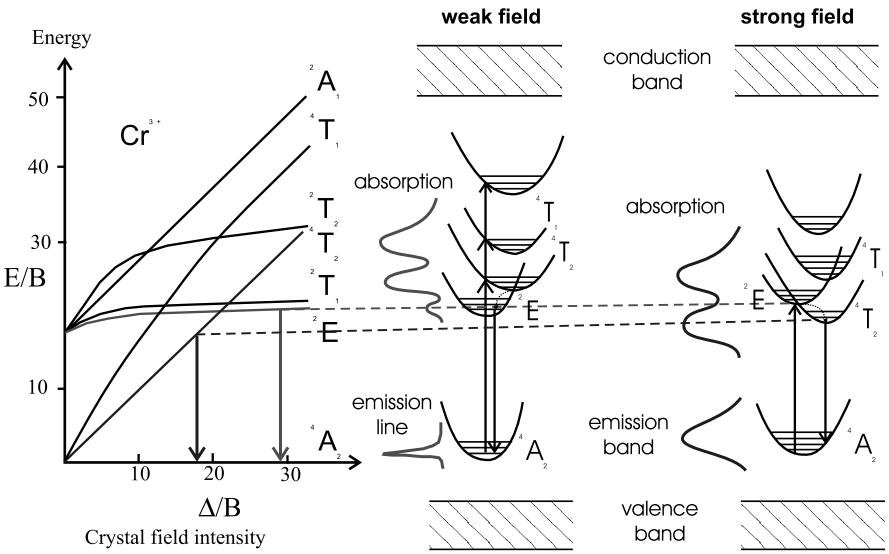

Fig. 5.24. Energy levels scheme of Cr^{3+} in different crystal fields

dependent on the covalency of the metal-ligand bond and thus there is some variability in the line emission from mineral to mineral.

At weaker crystal fields, a strong broad band quartet-quartet $^4T_2 \rightarrow {}^4A_2$ transition appears, which is only symmetry forbidden and has a much shorter decay time. Within the intermediate crystal field there is a complicating mixing between doublet and quartet states with complicated spectra, non-radiative transfer and the temperature dependence of luminescence. It was suggested, that spin–orbit interaction, coupling ^2E and $^4T_2$ states, was responsible for breaking of the selection rule forbidding the ^2E–$^4A_2$ transition. The admixture of the $^4T_2$ wave function into the ^2E wave function, which depends on the doublet-quartet energy separation, determines the radiative lifetime of the doublet, which, therefore, may change significantly with crystal field.

It has been empirically known that the energies of the lowest excited state of octahedrally coordinated $3d^3$ metals increase in the order $V^{2+} < Cr^{3+} < Mn^{4+}$. This tendency has been considered to originate from the difference in covalency, which reduced two-electron repulsion between the electrons occupying $3d$ orbitals. Recently this question was considered using first-principles electronic-structure calculation (Ishii et al. 2002). It was found the tendency was that the $3d$ levels went toward lower energy as the atomic number increased. The effective ligand field splitting increased as the atomic number increased. Distance dependent multiplet-energy diagrams for these elements have been obtained (Fig. 5.25). It is similar to traditional Tanabe-Sugano diagram, but is different in that they are specific to every metal. The ground state is $^4A_{2g}$ and excited states concerning spin-allowed transition are expressed as broken

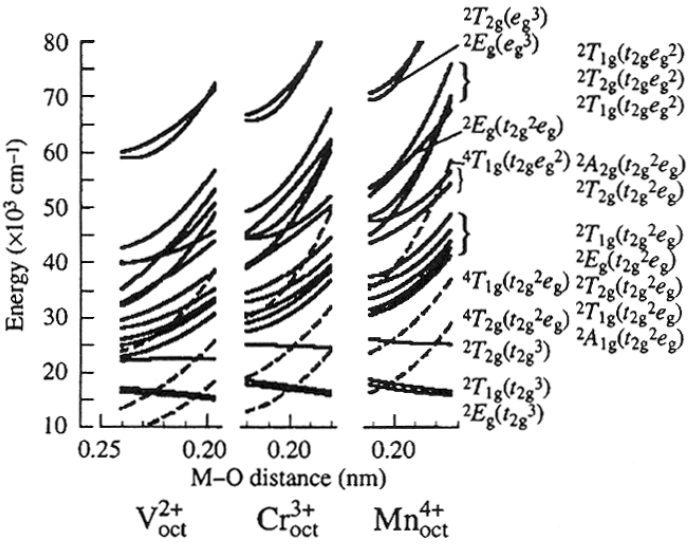

Fig. 5.25. Distance-dependent multiplet-energy diagram for Mn^{4+}, Cr^{3+} and V^{2+} (Ishii et al. 2002)

lines, while the states concerning spin-forbidden transitions are expressed as solid lines. It is clearly seen that the ^2E_g and $^4T_{2g}$ states of these centers in octahedral coordination are located close to each other indicating a possible dependence of the shape of emission on the M–O distance.

5.3.1.1 Cr^{3+}

Cr^{3+} is a very important ion because it is widely used in lasers (Reisfeld and Jörgensen 1977; Fabeni et al. 1991; Kaminskii 1996). The active ion lasers are based on the notion that a transition or rare-earth metal can be doped into inactive matrix, thus yielding isolated species where the metastable states are less prone to nonradiative decay. Some of the desired physical properties of matrices for active ion lasers are: hardness, low temperature dependent refractive index, high thermal conductivity and high transparencies. However, before it is possible to measure the above physical quantities, the crystal must be synthesized, and thus the matrix must fulfill some chemical requirements. Some of them are: that the matrix should melt congruently, that there should only be one ion in one geometry which has the same size as the dopant ion, that the diffusion rate of the dopant should be high in order to obtain a homogenous crystal, and that the material should form large single crystal without defects. These qualities are all found in natural gemstones, that is why materials like sapphire, garnet, alexandrite, etc. are used in many laser systems. Thus luminescence of Cr^{3+} in minerals may yield extremely important information and was carefully investigated, where studied minerals include corundum, spinel, kyanite, topaz, beryl, emerald, diopside, spodumen and jadeite. Nevertheless, strongly different decay times of different transitions in Cr^{3+} centers make time-resolved spectroscopy useful for a much better understanding of Cr^{3+} luminescence in minerals.

5.3.1.1.1 *Topaz*

Steady-state luminescence of topaz has been studied by Tarashchan (1978). At 77 K narrow lines at 680, 696, 712 and 730 nm have been ascribed to single Cr^{3+} (R-lines) and Cr^{3+}-pairs (N-lines). We studied two transparent, four yellow and one orange natural topaz. The two transparent precious stones have not been subjected to destructive chemical analyses. In other samples their Cr, Mn and V concentrations have been measured by ICP-AS method (Table 4.17). The absorption spectrum typical for Cr^{3+} has been detected only in red topaz with the highest Cr content of 500 ppm. The spectrum clearly revealed two broad bands typical of the octahedrally coordinated Cr^{3+} (Gaft et al. 2003a). The bands centered at 418 and 533 nm evidently correspond to the spin-allowed $^4A_{2g} \rightarrow {}^4T_{2g}$ and $^4A_{2g} \rightarrow {}^4T_{1g}$ transitions, respectively. The peak attributed to the spin-forbidden $^4A_{2g} \rightarrow {}^2E_g$ transition is located near 685 nm, while other very weak lines at 696 and 712 nm are also present.

Luminescence spectra at 300 K of all topaz samples contain strong narrow lines at approximately 680 and 684 nm and a weaker line at 695 nm together with a relatively broad band (half-width of 1,100 cm^{-1}) peaking near 680 nm. In the purest form such luminescence was detected in precious transparent topaz (Ural) where other luminescence lines are not detected (Fig. 4.48a). The temporal behavior of the lines and the band in time-resolved spectra is somewhat different, where the band has a shorter decay and dominates in the spectra with a narrow gate starting from 100 μs. Nevertheless, the difference between decay times of the lines and the band is substantially less compared to the sites with strong and low crystal fields. Such behavior may be explained by Cr^{3+} in intermediate crystal field sites for which the crystal field parameters lie in the crossing region of the $^4T_2$ and ^2E states. Within the intermediate crystal field there is a complicating mixing between doublet and quartet states with complicated spectra, non-radiative transfer and the temperature dependence of luminescence. In such a case emission from both $^4T_2$ and ^2E states may be expected. At 300 K the lower ^2E state acts as an energy reservoir for the $^4T_2$ state and thermal activation enables it to emit from both levels. Because the $^4T_2$ and ^2E states are in thermal equilibrium emission from both levels should occur with similar decay. At 77 K the thermal activation is impossible and the broad band at 680 nm disappears (Gaft et al. 2003a). Besides that, the R_1 narrow line at 680 nm is quenched at 20 K, which indicates thermal equilibrium at 300 K between the populations of the two Kramers doublets of the ^2E_g crystal-field split state. At 300 K decay time of the *R*-line at 684 nm is changed from 160 to 270 μs in different samples, while at 20 K with the absence of phonon-electron interaction its exponential decay of approximately 2.4 ms is the same in all samples and becomes suitable for this spin-forbidden transition.

The time-resolved spectra of topaz samples with elevated Cr contents, starting from 180 ppm, contain additional luminescence lines with different excitation and temporal behaviors. Luminescence spectra at 300 K of red topaz under λ_{ex} = 266 nm contains only lines and band typical for single Cr^{3+} luminescence. Under λ_{ex} = 355 nm the lines at 697, 711 and 734 nm appear, while their intensities in the spectra with the narrower gates are higher compared with the lines at 684 nm, which may be explained by their shorter decay times (Figs. 4.48b,c). It is well known that with the increase in Cr^{3+} concentration, additional luminescence lines begin to appear at the longer wavelength side of the *R*-lines. Those lines are attributed to magnetically coupled Cr^{3+} –Cr^{3+} pairs and clusters. The shorter decay time compared with single Cr^{3+} luminescence and the strongest luminescence under 355 nm excitation, which is exactly twice of the energy of the line at 711 nm, are also compatible with the pairs model.

5.3.1.1.2
Kyanite and Sillimanite

Steady-state luminescent properties of kyanite at room temperature are characterized by two narrow lines of Cr^{3+} at 688 nm and at 706 nm as well as by a broad band centered at 780 nm (Tarashchan 1978; Votyakov et al. 1993 ; Platonov et al.

1998). Kyanite evidently was the first mineral investigated by time-resolved luminescence technique (Wojtowicz, 1991). It was found that Cr^{3+} can substitute for any one of the four nearly octahedral Al sites with the average metal-ligand distance of about 1.91 Å. Three different emissions have been identified, originating from three different sites, while the fourth position is non-emitting. It was found that the strongly changing doublet-quartet coupling in different sites of kyanite manifests itself in doublet radiative lifetimes spanning the range of 100 – 3,000 μs.

Our results are rather similar to those of Wojtowicz (1991). Two narrow lines at 689 and 706 nm with long and slightly different decay times together with broad bands at 750 and 790 nm with short decay times characterized time resolved spectra of kyanite at 300 K (Fig. 4.46). Those data clearly indicate that we have emissions coming from the Cr^{3+} in three different sites: site *A* with a strong crystal field – doublet *R*-lines at 689 and 706 nm, site *B* with a weak crystal field – quartet broad band at 750 nm accompanied by only one doublet *R*-line at 704 nm which may be detected only at low temperatures, and site *C* with a weak crystal field – quartet broad band at 790 nm.

Very unusual properties have been found in luminescence of Cr^{3+} in sillimanite (Wojtowicz and Lempicki 1988). It is characterized by broadband luminescence peaking at about 790 nm (Fig. 4.47).

5.3.1.1.3
Wollastonite

Spectra with narrow gates where the centers with a short decay time are emphasized enables us to detect broad bands at 794 nm with a decay time of 5 μs and broad band at 840 nm with a decay time of 190 μs (Fig. 4.42). These bands may be ascribed to Cr^{3+} luminescence centers, in addition to Cr^{3+} with narrow *R*-lines at 720 nm, detected by steady-state spectroscopy (Min'ko et al. 1978). Wollastonite structure has three different types of six-coordinated calcium-oxygen groups, which enables the formation of several types of Cr^{3+} luminescence centers. Nevertheless, luminescence of Cr^{3+} as result of Ca^{2+} substitution has not been confidently found yet and another interpretation is also possible. For example, ions of V^{2+} may be considered, which have similar luminescence properties with Cr^{3+} and may substitute in Ca^{2+} sites.

5.3.1.1.4
Corundum

Chromium activated ruby was the first laser material and its luminescence properties are carefully studied. It is a classical example of Cr^{3+} in octahedral crystal field. Here Cr^{3+} substitutes the Al^{3+} ions, while such a possibility can be rationalized by an excellent chemical fit of Cr in place of Al. Ruby is a high crystal field material and thus the $^4T_{2g}$ state lies above the $^2E_{2g}$ level. Pumping is accomplished by a spin-allowed transition into the ^4T state, while emission occurs from the ^2E level without vibrational broadening and almost all excited

states can be converted into laser action. Both ^2E and $^4A_2$ states are split due to the trigonal crystal field and spin–orbit coupling. The splitting of the ^2E excited state is the reason for the 1.4 nm wavelength difference between the R_1 and R_2 lines. The splitting of the $^4A_2$ ground state is much less intensive and accounts for splitting of the R_1 line into two lines less than 0.02 nm apart, which is only observed in low temperature measurements. The two main Cr^{3+} lines are well known for their marked frequency shift with increasing pressure (Mao et al. 1986).

Time-resolved spectra demonstrate a doublet of *R*-lines with a very long decay time of several ms, accompanied by sidebands and *N*-lines (Fig. 4.50).

5.3.1.1.5
Emerald

Emerald, Cr^{3+} doped beryl, has a beryl structure with the Cr^{3+} impurity ions in highly distorted octahedron sites. The discovery of lasing action in emerald stimulated investigation of its luminescence properties. It was established that its tuning range is approximately 730–810 nm, while luminescence consists of a narrow line at 684 nm and a band peaking at 715 nm with similar decay times of 62 μs. The relative intensities of those line and band are different in σ- and π-polarized spectra (Fabeni et al. 1991).

Laser-induced time-resolved luminescence spectra of natural emeralds also demonstrate *R*-lines of Cr^{3+} at 680 and 684 nm accompanied by a narrow band peaking at 715 nm, which have similar decay times of approximately 55 μs (Fig. 4.53).

5.3.1.1.6
Garnet

Garnet activated by trivalent Cr^{3+} is a promising system for tunable laser applications and those systems have been well studied. Cr^{3+} replaces Al^{3+} in octahedral sites with a weak crystal field. The transition involved in laser action is $^4T_2$–$^4A_2$, a vibrationally broadened band. At room temperature it has a maximum in the 715–825 nm range with a decay time in the 100–250 μs range depending on ΔE between the ^2E and $^4T_2$ levels. When the ΔE is maximal, narrow lines also appear from the ^2E level. At low temperatures, when thermal activation of the $^4T_2$ level is difficult, *R*-lines luminescence becomes dominant with the main line at 687 nm (Monteil at al. 1988). We studied pyrope artificially activated by Cr and also found the two emission types described above (Fig. 5.26).

Laser-induced time-resolved luminescence spectra of natural garnet demonstrate broad red bands with a relatively short decay time which may be ascribed to Cr^{3+} emission in a weak crystal field (Fig. 4.56a).

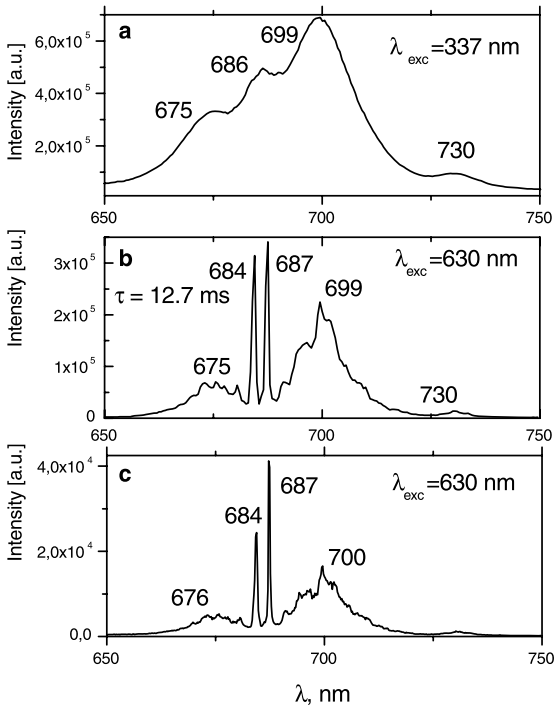

Fig. 5.26. **a–c** Laser-induced time-resolved luminescence spectra of pyrope activated by Cr^{3+}

5.3.1.1.7 Alexandrite

Alexandrite, the common name for Cr-doped chrysoberyl, is a laser material capable of continuously tunable laser output in the 700–800 nm region. It was established that alexandrite is an intermediate crystal field matrix, thus the non-phonon emitting ^2E state is coupled to the $^4T_2$ relaxed state and behaves as a storage level for the latter. The laser-emitted light is strongly polarized due to its biaxial structure and is characterized by a decay time of 260 µs (Fabeni et al. 1991; Schepler 1984; Suchoki et al. 2002). Two pairs of sharp *R*-lines are detected connected with Cr^{3+} in two different structural positions: the first near 680 nm with a decay time of approximately 330 µs is connected with mirror site fluorescence and the second at 690 nm with a much longer decay of approximately 44 ms is connected with inversion symmetry sites (Powell et al. 1985). The group of narrow lines between 640 and 660 nm was connected with an anti-Stokes vibronic sideband of the mirror site fluorescence.

Laser-induced time-resolved luminescence spectra of natural alexandrite revealed two narrow doublets, the first at 679 and 680 and the second at 693 and 694 (Fig. 4.54). They have strongly different polarizations and decay times and evidently may be connected with *R*-lines of Cr^{3+} in two different structural sites. Besides that a narrow line at 690 nm with a decay time of 120 µs is also found, which also may be connected with Cr^{3+} emission.

5.3.1.1.8
Boehmite, Diaspor

Time-resolved luminescence spectra of diaspor samples are demonstrated in Fig. 4.62 (Shoval et al. 2003). Two narrow lines at 694 and 692 nm, accompanied by a line at 690 nm and phonon repetitions at 707 and 714 nm characterize the time-resolved luminescence spectra of this sample After a long delay of several ms the relative intensity of the line at 692 nm becomes stronger, the evident reason is that this line has a longer decay time compared to the line at 694 nm. After heating at 900 °C, the spectra are pronouncedly changed. Now they contained a relatively broad line at 692 nm and a broad band peaking at 780 nm, which dominates the spectra with a narrow gate (Figs. 4.62c,d). Such behavior evidences that the broad band has very short decay time compared with the line at 692 nm. After heating at 1,000 °C, the spectra contain again two narrow lines at 694 and 692 nm in the time-resolved luminescence spectra (Figs. 4.62e,f). However, the lines are strong and their relative intensities in time-resolved spectra are not changed which evidence that they have similar decay times. It is clear that the luminescence of natural diaspor is connected with Cr^{3+} in a strong crystal field position. The lines in the luminescence spectra of diaspore treated at 900 °C are related to Cr^{3+} luminescence in the meta-phase. The broad asymmetric line peaking at 692 nm with a long decay time is evidently connected with inhomogeneously broadened *R*-lines of Cr^{3+} luminescence in octahedral sites with a strong crystal field and a very disordered environment. The broad band peaking at 780 nm with a much shorter decay time is attributed to Cr^{3+} luminescence in the weaker crystal fields, where a strong broadband quartet-quartet $^4T_2 \rightarrow {}^4A_2$ transition appears, which is only symmetry forbidden. These spectral types are similar to those of Al_2O_3 powders heated to temperatures from 400 to 1,000 °C (Pilonett et al. 2000). The lines in the luminescence spectra of diaspore treated at 1,000 °C are related to Cr^{3+} luminescence in corundum. These lines are typical for the $^2E \rightarrow {}^4A_2$ transitions of Cr^{3+} luminescence centers (*R*-lines) of Cr-corundum (ruby), which are characteristic for Cr^{3+} luminescence, which is substituting for Al^{3+} in octahedral symmetry. Both lines are long-lived and have the same decay times.

A narrow line at 692 nm with a very long decay time accompanied by phonon repetitions characterizes the time-resolved luminescence spectra of boehmite (Fig. 4.63). After heating at 900 °C, this emission remains but an additional broad band appears peaking at 725 nm with a short decay time, which dominates the spectrum with a narrow gate. After heating at 1,000 °C, lines at 683, 686 and 690 nm accompanied by lines at 692 and 694 nm are observed in the steady-state luminescence spectra. These two groups of lines appear with different decay times time-resolved luminescence spectra: at 683, 686 and 690 nm with a longer decay time and at 694 and 692 nm with a shorter decay time. Luminescence of natural boehmite is connected with Cr^{3+} in a strong crystal field position. The lines in the luminescence spectra of diaspore treated at 900 °C are related to Cr^{3+} luminescence in the meta-phase. The broad band peaking at 725 nm with a short decay time is evidently connected with Cr^{3+}

luminescence in a weak crystal field site. The lines at 683, 686 and 690 nm in the luminescence spectra of boehmite treated at 1,000 °C are related to Cr^{3+} luminescence in Al-spinel. The other lines at 692 and 694 nm are connected with the presence of corundum. Durville et al. (1985) related the splitting and the inhomogeneous broadening of the ^2E level in the spectra of Mg-spinel formed during heating of magneso-alumino silicate glass to wide distribution of the Cr^{3+} sites in the microcrystallites. They related the wide distribution to the well-known disordered distribution of Mg^{2+} and Al^{3+} in the Mg-spinel.

5.3.1.1.9
Zircon

Luminescence of Cr^{3+} was firstly detected in synthesized $ZrSiO_4$ artificially activated by Cr (Gaft et al. 2000b). This host has been chosen, first of all, by the presence of tetrahedrally coordinated Si^{4+}, which has been assumed to accept Cr^{4+} in silicate crystals without any charge compensation. A second reason is the presence of Zr^{4+} in triangular dodecahedron with four close oxygen atoms arranged according to a distorted tetrahedron. It was proposed that Cr^{4+} could replace either Si^{4+} or Zr^{4+} and the interpretation of absorption spectra led to the hypothesis of a replacement of Si^{4+} with Cr^{4+} (Beletti et al. 1995).

Luminescence spectra of $ZrSiO_4$: Cr at different temperatures under λ_{ex} = 532 nm demonstrate narrow lines and broad bands in the red-IR range. Cr^{3+} ions can be easily detected by a distinct ^2E–$^4A_2$ transition (R-line) at 694 nm (Fig. 5.27b). It appears above 150 K whereas at lower temperatures only $^4T_2$–$^4A_2$

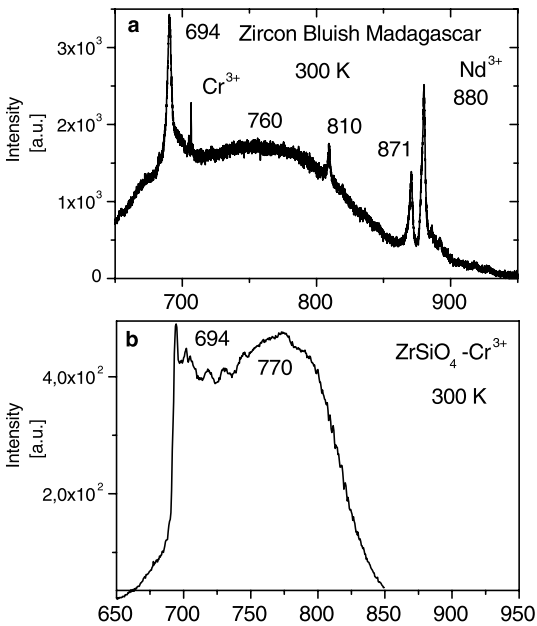

Fig. 5.27. Laser-induced time-resolved luminescence spectra of Cr^{3+} in natural zircon (**a**) and Cr^{3+} in artificial $ZrSiO_4$–Cr (**b**)

broadband emissions can be seen peaking at 775 nm. It indicates that the $^4T_2$ level is lower than ^2E and consequently the relatively low crystal field site symmetry takes place. The ^2E excited level has the same decay time of 3 – 5 μs as the broad band, which means that it is thermally occupied at temperatures higher than 150 K. It is worth mentioning that the $^4T_2$–$^4A_2$ band at low temperature demonstrates a vibrational structure indicating a tetragonally distorted excited state (Blasse and Grabmaier 1994). Beside that, the *R*-line of Cr^{3+} is strongly polarized and is detected with experimental geometry, which corresponds to observation of σ-polarized luminescence only. Under these observations and on the basic ideas that the ionic radius of Cr^{3+} in octahedral coordination (75.5 pm) is close to those of Zr^{4+} (73 pm), and that the Zr–O distances are close to Cr–O length in systems with Cr^{3+}, we can assume the presence of Cr^{3+} in the place of the Zr^{4+} ion. Recently the emission of Cr^{3+} has been found in a precious variety of natural zircon (Fig. 5.27a).

5.3.1.1.10
Titanite

The lines at 686 and 693 nm with a long decay time of approximately 1 ms in the titanite emission spectrum are not correlated with any other lines and bands (Fig. 4.34). Such lines are very typical for Cr^{3+} in a high field coordination and may be connected with such a center. The broad luminescence band appears peaking at 765, which may be ascribed to Cr^{3+} in a weak field coordination. The band at 765 nm has distinct dips at 749, 762, 793, 798, 804 and 820 nm. Comparison with the titanite absorption spectrum (Fig. 5.19) demonstrates that those lines exactly coincide with the absorption spectrum of Nd^{3+} (Bakhtin and Gorobets 1992). Cr^{3+} is a good energy sensitizer, because it has broad, allowed absorption bands with a broad emission spectrum, which overlaps the absorption bands of the lasing ion (Nd^{3+}, Ho^{3+}).

Thus radiative energy transfer to Nd^{3+} may explain "negative" lines. Such an emission-reabsorption type of the energy transfer implies emission of light by a single ion and its absorption and emission by the other ion. Both ions should be activators and have sufficiently strong absorption bands, while the luminescence emission band of one of them must be overlapped by the absorption band of the other. Radiative energy transfer may increase the laser efficiency of Nd^{3+} substantially. For example, amplification of the emission of Nd^{3+} as a result of coating a laser rod by organic dye was about 50% (Eyal 1988).

The decay time of the Cr^{3+} band of approximately 150 ns is very short for such emission. Radiative energy transfer may not explain it because in such a case the decay curves of each of the ions are independent of the presence of the other. Thus non-radiative energy transfer may also take part, probably via multipolar or exchange interactions. In such cases the process of luminescence is of an additive nature and the lifetime of the sensitizer from which the energy is transferred is determined, apart from the probability of emission and radiationless transitions, by the probability of the energy transfer to the ion activator.

The low concentrations of Cr and Nd in natural samples (200 and 555 ppm, correspondingly) make it difficult to understand the strong energy transfer between them. Thus it may be supposed that the distribution of donors and acceptors are not random and that the presence of a dopant in a particular site in the crystal will affect the probability of a second dopant (either identical or different) locating in nearby sites. It is a known situation in minerals where exchange-connected impurity pairs explain many peculiarities of mineral colors (Bakhtin and Gorobets 1992). In order to explain pair formation in laser materials the relative ionic radii of dopant and the host ion have been considered (Rotman and Hartman 1988). For a dopant to enter a lattice site, it is advantageous for the dopant to be approximately the same size as the host ion it is replacing. Failure to do so may severely limit its degree of substitution. To lower a crystal strain, the two dopants, which are considerably smaller and considerably larger than the ions they replace, have to collocate next to each other and form preferential pairs with enhanced energy transfer. In the titanite case such an approach is not working because ionic radii of Nd^{3+} and Cr^{3+} are practically similar to the ionic radii of Ca^{2+} and Ti^{4+}, respectively. In such a case the charge compensation consideration is evidently the most important, namely $Nd^{3+}+Cr^{3+} \rightarrow Ca^{2+}+Ti^{4+}$. A similar model was also proposed for titanite enriched by light rare-earth elements (up to 3.5 wt %). It was concluded that the following mechanism of substitution was consistent with compositional data: $[LREE]^{3+}+[Fe^{3+}] \rightarrow Ca^{2+}+Ti^{4+}$.

A drastic change takes place in the luminescence spectrum of titanite at low temperatures (Fig. 4.34d). At 77 K, Nd^{3+} luminescence intensity becomes lower and a narrow line appears at 732 nm with a long decay time of 2.5 ms accompanied by phonon repetitions. At an even lower temperature of 20 K such emission totally dominates the luminescence spectrum. Such behavior may be explained by Cr^{3+} in intermediate crystal field sites for which the crystal field parameters lie in the crossing region of the $^4T_2$ and ^2E states. Within the intermediate crystal field there is a complicating mixing between doublet and quartet states with complicated spectra, non-radiative transfer and the temperature dependence of luminescence. In such a case the emission from both $^4T_2$ and ^2E states may be expected. At 300 K the lower ^2E state acts as an energy reservoir for the $^4T_2$ state and thermal activation enables it to emit only from the $^4T_2$ level. At lower temperatures the thermal activation is impossible and the ^2E level becomes luminescent. It is worth noting, that the energy of the $^2E \rightarrow {}^4A_2$ bandwidth is rather low; at least in known minerals luminescence the spectral position of this so-called *R*-line is variable from 677 to 705 nm (Tarashchan 1978). Additionally, in $LiSc(WO_4)$:Cr crystals the $^2E \rightarrow {}^4A_2$ transition in high field Cr^{3+} sites is situated near 760 nm (Grinberg et al. 2002) and 778 nm in $BaCaTiO_3$–Cr crystals (Jastrabik et al. 2002). The energy of the ^2E level in the d^3 electron system, according to Tanabe-Sugano theory, increases a little with an increase of the strength of the crystal field. The high-pressure low-temperature Cr^{3+} luminescence experiments show, contrary to the prediction of the Tanabe-Sugano theory, that the energy of the ^2E level of Cr^{3+} ions

decreases slightly with an increase of the crystal field strength (Suchoki et al. 2002). It was explained by the nephelauxetic effect, i.e. decrease of interelectronic crystal field Racah's repulsion parameters B and C due to covalency of bonds between the central ion and ligands. Thus the red shift in Cr^{3+} luminescence may be attributed to greater covalency in titanite structure. Thus two different Cr^{3+} sites are detected in titanite structure in strong, and intermediate field sites. The energy transfer to Nd^{3+} evidently takes place only as a result of allowed broad $^4T_2$ emission, because any long time tail in Nd^{3+} decay is absent as expected if transfer will come from strong crystal field sites.

5.3.1.1.11
Spinel

An identification of the nature of Cr^{3+} luminescence in synthetic spinel by the line narrowing technique enabled to distinguish up to 25 different Cr^{3+} sites (Deren et al. 1996). Laser-induced time-resolved spectroscopy enables us to see typical for spinel emission of Cr^{3+}, while the different broadness of the spectral lines at different time windows demonstrates that different Cr^{3+} sites are present also in natural spinel (Fig. 4.51).

5.3.1.1.12
Fluorite

Luminescence of Cr^{3+} was not found in natural fluorite, but such emission has been found in fluoride hosts, including CaF_2, artificially activated by Cr (Payne et al. 1988). It was found that despite a big difference in ionic radii of Ca^{2+} and Cr^{3+} the last one forms the luminescence center, which is characterized at low temperature by a broad emission band peaking at approximately 920 nm.

5.3.1.2
Cr^{3+}*-pairs*

The most well known is the Cr^{3+}-pair in ruby with elevated Cr contents (Powell 1967). The satellite lines appear in absorption and luminescence spectra, which were interpreted by exchange pair coupling theory. Theoretical calculations based on the DV-ME method were made for the first and fourth nearest neighbor ion pairs (Ishii et al. 1999). The resulting scheme of ground and excited states correspond well to experimental data. The calculated results demonstrate that the first and fourth nearest neighbor ion pairs are anti-ferromagnetically and ferromagnetically coupled, respectively.

5.3.1.3
Mn^{4+}

In artificial phosphors the luminescence bands due to Mn^{4+} exist from 620 to 715 nm. The spectrum has a structure consisting of several broad lines

originating from transitions aided by lattice vibrations. Because the crystal field at the higher charged Mn^{4+} ion is stronger than for Cr^{3+} (Fig. 5.23), the emission is most probably connected with the ^2E–$^4A_2$ transition, but in many cases the origin of the emitting and ground states is doubtful (Buttler 1966; McNicol and Pott 1973; Stade et al. 1974; Bryknar et al. 2000).

5.3.1.3.1 Topaz

Time-resolved luminescence spectra of red topaz under $\lambda_{ex} = 532$ nm excitation are different from those under 355 nm excitation (Gaft et al. 2003a). The relative intensities of the lines at 697 and 711 nm are higher as in the spectra with narrower gates, and in the spectra with longer delays (Fig. 4.48d–f). The evident reason is that two different transitions with strongly different decay times take place both at 697 and 711 nm. At 20 K both those lines remain and the presence of at least two decay components for the line at 711 nm is evident (Fig. 5.28). The intensity of those "long lived" components is not correlated with Cr concentration. They are especially strong in the yellow sample with only 60 ppm of Cr, and even in transparent precious topaz, which was not analyzed for Cr, but evidently its content is low. In both samples the short-lived lines connected with Cr-pairs are absent, which may be seen in the spectrum with a narrow gate.

Such luminescence may not be connected with Cr^{3+} pairs because of their

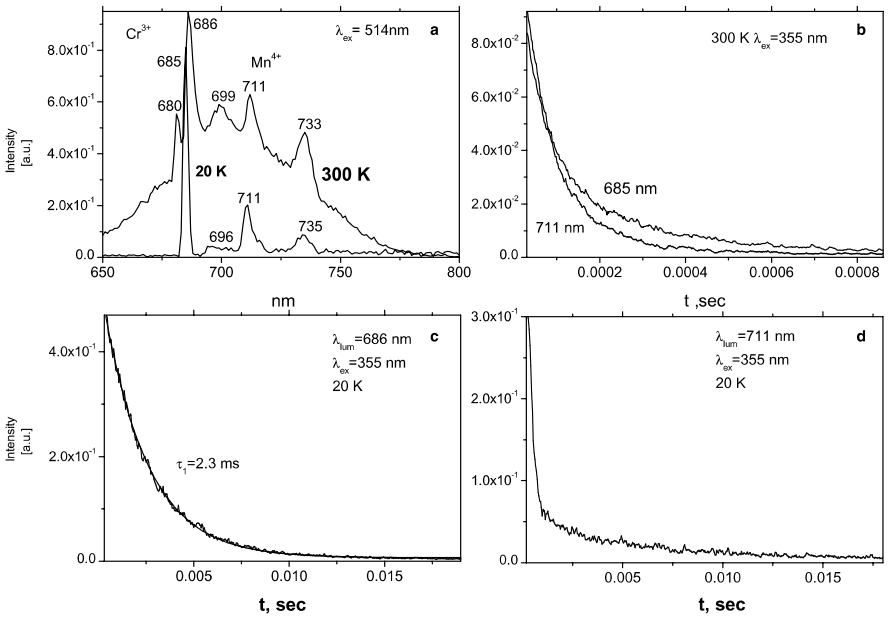

Fig. 5.28. **a–d** Laser-induced time-resolved luminescence spectra of topaz at different temperatures demonstrating different decays of Cr^{3+} and possibly Mn^{4+} centers

longer decay time compared with single Cr^{3+}. Principally it may be connected with the following: energy migration from a long-lived center on single Cr^{3+} centers; a single Cr^{3+} in a strong field position, luminescence center different from Cr^{3+}. To clarify this, we studied the influence of thermal treatment of topaz on its luminescence properties. After heating the yellow topaz with 180 ppm of Cr at the relatively low temperature of 200 °C, the yellow color disappears and the sample becomes transparent. The intensity of the line at 711 nm with a long decay strongly diminishes, which is clearly seen in the spectrum with long delay, while the line at 711 nm with a short decay remains (Fig. 5.29). Such behavior evidently excludes the possibility of single Cr^{3+} luminescence, because the trivalent state of Cr is the most stable in the topaz structure and oxidation at such low temperature is improbable.

From the other side, such a result enables us to consider the possible participation of other d^3 elements, such as Mn^{4+}, while such valence states are not stable and can appear and disappear as a result of irradiation and thermal treatment. Unfortunately, the sensitivity of Mn to the ICP-MS method is relatively low and it is confidently detected only in the red topaz. However, Mn was detected in several topaz samples, while it is not correlated with Mn^{2+}, found by EPR and another valence state was supposed (Schott et al. 2003). The ionic radius of Mn^{4+} of 0.67 Å is practically equal to the ionic radius of

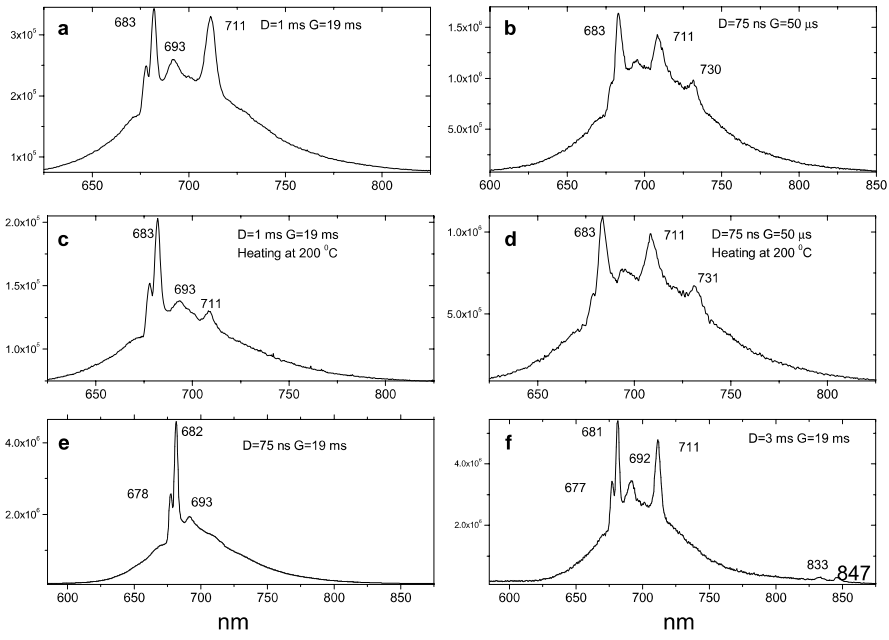

Fig. 5.29. **a–f** Laser-induced time-resolved luminescence spectra of topaz before (**a–c**) and after heating at 200 °C (**d–f**)

Al^{3+} (0.675 Å). Thus from crystallochemical positions the presence of Mn^{4+} in topaz structure is quite possible. Strong absorption bands due to Mn^{4+} corresponding to the spin-allowed transitions to ^4T levels in the visible to near-UV region generate the yellow color of the phosphors, which corresponds to the yellow color of topaz. Thus we propose that a connection may be considered between the long-lived lines at 697 and 711 nm and Mn^{4+} centers, which may be formed as a result of natural irradiation of topaz.

5.3.1.3.2
Garnet

The luminescence of Mn^{4+} in GGG at room temperature is characterized by a narrow band peaking at approximately 680 nm. At low temperatures the spectra consist of relatively sharp lines at 663 and 668 nm, which are related to two different sites for manganese ions, named *A* and *B*. The decay time of Mn^{4+} at the *B* site is much shorter compared to the *A* site, namely approximately 450 μs and 1,300 μs at low temperatures, correspondingly. At high temperatures decay times are much shorter and exhibit several-exponential behaviors (Brenier et al. 1992). The laser-induced time-resolved luminescence spectra of natural Mn-containing garnet (spessartite) revealed narrow lines at 606, 627, 694 and 707 nm on the background of the broad band peaking at 690 nm (Fig. 4.56). Such an emission may be preliminary ascribed to Mn^{4+} centers.

5.3.1.3.3
Eosphorite

Detected narrow red lines have been connected with Cr^{3+} (Fig. 4.60), but the sample contains 19.45 wt % of Mn and less than 5 ppm of Cr and it may be supposed that Mn^{4+} centers also participate in emission.

5.3.1.3.4
Beryl

The radio-luminescence of transition metal doped natural beryl has been studied (Chithambo et al. 1995). It was found that Mn containing samples gave intense red radio-luminescence with sharp emission lines, while the Mn activated beryl (morganite) emission is more than twice as bright as that from emerald. Such luminescence has been ascribed to Mn^{3+}, but it may be supposed that such emission is connected with Mn^{4+} luminescence. The laser-induced time-resolved luminescence spectra of natural morganite revealed a band peaking at 730 nm, which may be preliminary ascribed to the Mn^{4+} center (Fig. 4.52).

5.3.1.3.5
Corundum

Mn^{4+} sharp-line fluorescence at 672 and 676 nm in artificial Al_2O_3–Mn^{4+} (Fig. 5.30) are known (Geschwind et al. 1962; Fergusson 1970), but such emission has not been detected in natural corundum yet.

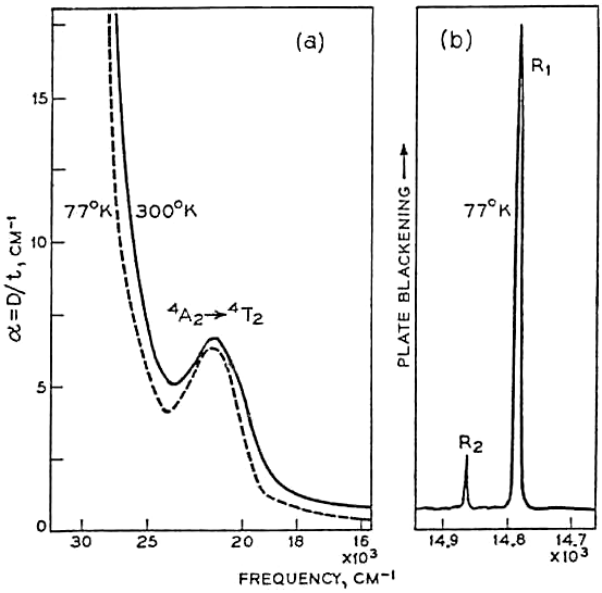

Fig. 5.30. **a,b** Luminescence of Al_2O_3:Mn^{4+} (Fergusson 1970)

5.3.1.3.6
Chrysoberyl

The broad band peaking at 660 nm with a decay time of 10 μs accompanied by several narrow lines with the strongest one at 664 nm, which are characterized by a longer decay time (Fig. 4.55) can be preliminary ascribed to Mn^{4+} centers.

5.3.1.3.7
Benitoite

Under 355 and 532 nm excitations at 300 K the certain benitoite samples exhibit red band peaking at 720 nm with half-width of ~ 125 nm accompanied by narrow line at 680 nm (Fig. 4.35c). Time resolved spectroscopy with different decays and gates revealed that both band and line behave in a similar way, namely they have similar decay time of ~ 170 μs. It may be supposed that band and line belong to the same luminescence center. The broad band disappears at low temperatures. The line is much stronger at lower temperatures, where two additional weak lines appear at 695 and 702 nm. Decay time at low temperature is very long reaching τ = 1.1 ms (Gaft et al. 2004b).

Combination of broad emission band and narrow line is typical for elements with d^3 electronic configuration, such as Cr^{3+}, Mn^{4+} and V^{2+}. Manganese participation is supported by chemical analyses of benitoite, where chromium was never mentioned as micro-impurity, while Mn is known with concentrations changing from 0.03 to 0.11% (Laurs et al. 1997). Such concentrations are quite enough for luminescence generation. Substitution in Mn^{2+}form substituting

for Ba^{2+} is doubtful because of the great difference in ionic radii, thus Mn^{4+} form is possible.

5.3.1.4 V^{2+}

Divalent vanadium belongs to $3d^3$ ions and is isoelectronic with Cr^{3+}. Hence all energy levels and spectral characteristics are similar. The difference between them lies in the lower crystal field strength for V^{2+} in comparison with Cr^{3+}.

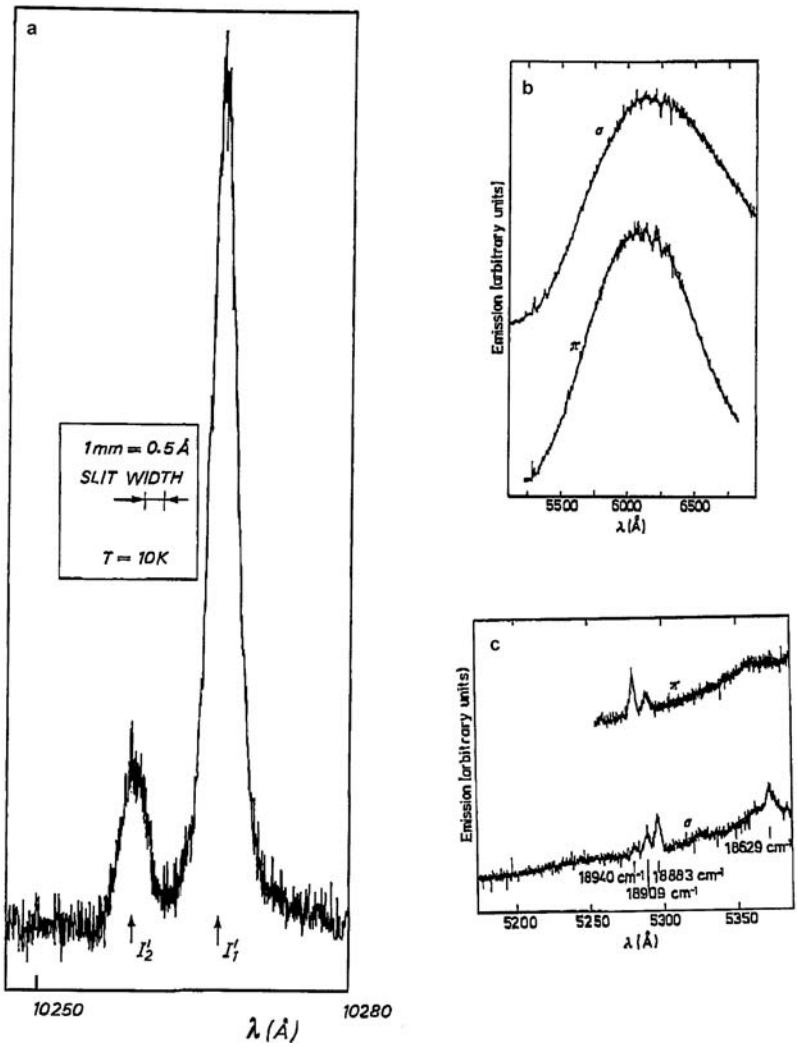

Fig. 5.31. Luminescence of Al_2O_3:V (Champagnon and Duval 1977)

Luminescence of V^{2+} is known in Al_2O_3–V (Fig. 5.31a) where it is characterized by linear luminescence from the ^2E levels as in Cr^{3+}, but shifted in the IR (855 and 856 nm) (Champagnon and Duval 1977).

5.3.1.4.1
Zoisite

As was already mentioned, the narrow lines at 692 and 710 nm in the luminescence spectrum of zoisite have been connected with d^3 element emission, while Cr^{3+} and V^{2+} were considered as the possible candidates (Koziarsca et al. 1994). Laser-induced time-resolved luminescence spectra of zoisite reveal the same lines (Fig. 4.59). We are inclined to connect these lines with V^{2+} for the reason that vanadium concentration in our sample is much higher than the chromium concentration.

5.3.1.4.2
Chrysoberyl

Luminescence similar to those in zoisite has been found in the laser-induced time-resolved spectrum of chrysoberyl (Fig. 4.54d). A relatively broad band accompanied by narrow lines at 698, 703 and 717 nm with a decay time of 150 µs, which are not connected with Cr^{3+} emission, may be preliminary ascribed to V^{2+} luminescence.

5.3.1.4.3
Grossular

Similar luminescence is detected also in grossular (Fig. 4.57). As it was already mentioned, the same emission has been found in the CL spectrum (Fig. 5.32)

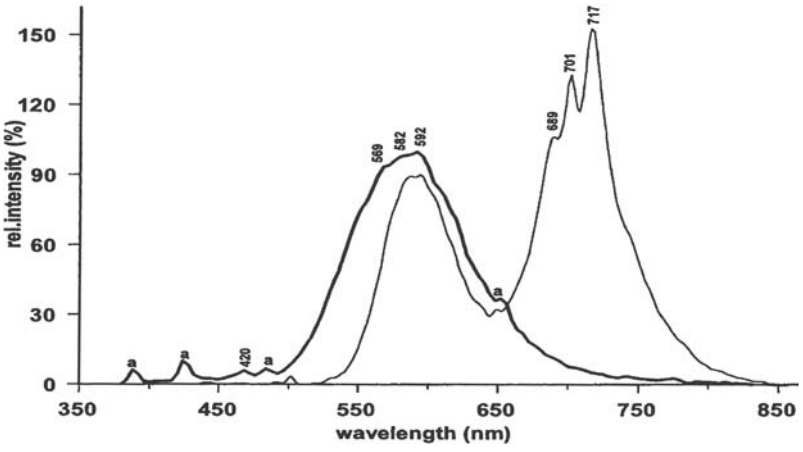

Fig. 5.32. Cathodoluminescence spectra of hydrogrossular (Ponahlo 2000)

of hydrogrossular (Ponahlo 2000). We think that its connection with V^{2+} luminescence may be supposed.

5.3.1.4.4
Beryl

The broad band peaking at 730 nm accompanied by a narrow doublet at 692 and 694 nm (Fig. 4.52) with a mutual decay time of 100 µs in the laser-induced time-resolved luminescence spectrum of beryl is not similar to the Cr^{3+} emission in emerald. Thus we suppose that such typical d^3 emission may be connected with the V^{2+} center.

5.3.2
$3d^2$ Elements

The elements with such an electronic configuration known as luminescent centers are Cr^{4+}, Mn^{5+}, V^{3+} and Ti^{2+} (Fig. 5.33). Within this model, the ground state is a spin triplet $^3A_2$ (e^2 electron configuration) and the first excited state is the triplet $^3T_2$ ($t^1 2e^1$ electron configuration). Above this state it is possible to see the singlet ^1E (t_2^2 electron configuration) roughly independent of the crystal field strength and also another triplet state labeled $^3T_1$. It is the analogy with the evolution of the two first $^4T_2$ and ^2E energy levels of Cr^{3+} ion with a crossing point (Scott et al. 1997).

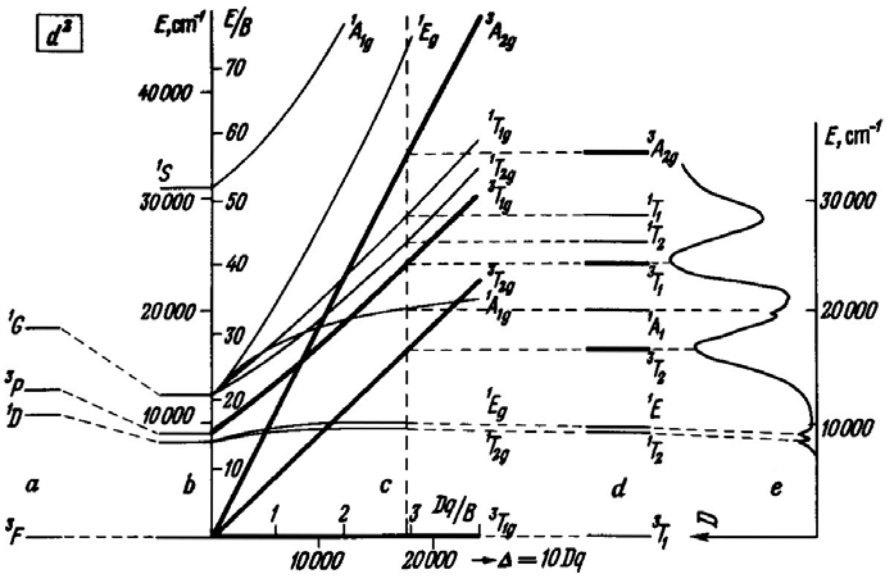

Fig. 5.33. Tanabe-Sugano diagram for d^2 ions

It has been empirically known that the energies of the lowest excited state of tetrahedrally coordinated $3d^2$ metals decrease in the order $Cr^{4+} < Mn^{5+} < Fe^{6+}$. As in the case of $3d^3$ elements, this tendency has been considered to originate from the difference in covalency, which reduced two-electron repulsion between the electrons occupying $3d$ orbitals. Recently this question was treated using first-principles electronic-structure calculation (Ishii et al. 2002). The same tendencies were found as for the $3d^3$ ions. Distance dependent multiplet-energy diagrams for these elements have been obtained (Fig. 5.34), which enable us to envisage the typical shapes of the possible emissions. As in

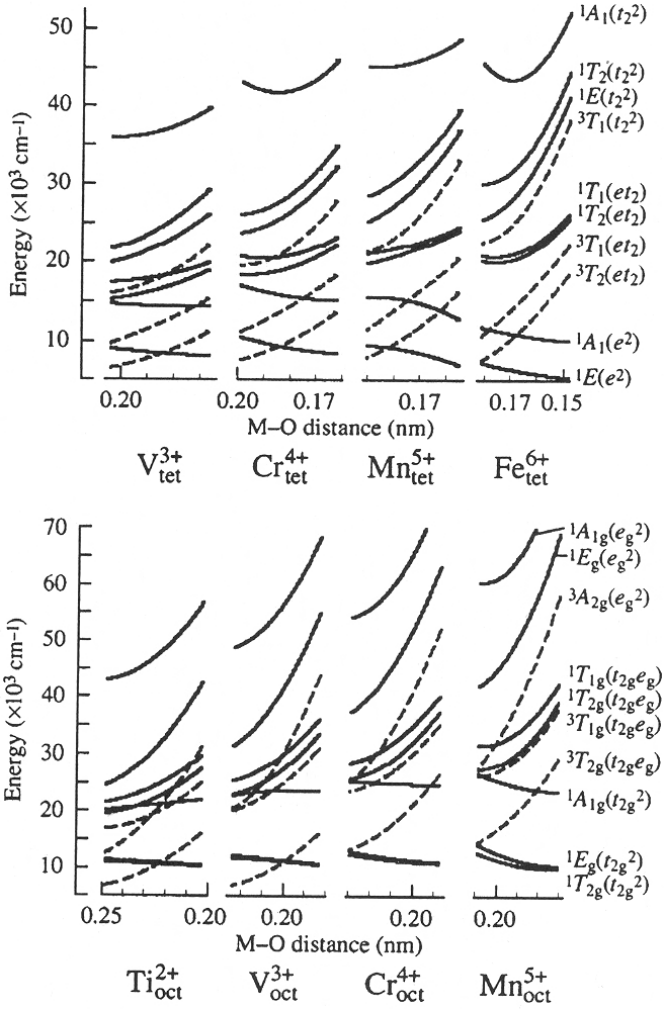

Fig. 5.34. Distance-dependent multiplet-energy diagram for Mn^{5+}, Cr^{4+}, Ti^{2+} and V^{3+} (Ishii et al. 2002)

the Tanabe-Sugano diagram, in the tetrahedrally coordinated $3d^2$ system, the positions of the ^1E state, corresponding to narrow line emission, and the $^3T_2$ state, corresponding to broad band emission, are responsible for the shape of the luminescence spectrum.

5.3.2.1 Cr^{4+}

The tetravalent chromium has attracted great interest in recent literature due to tenability over a large spectral range in both CW and pulsed operation of the forsterite ($Mg_2Si_2O_4$) laser. According to the energy levels scheme (Fig. 5.33), ^1E and $^3T_2$ states in a tetrahedral coordination of Cr^{4+} are located close to each other. This means that the shapes of the emission are sensitive to the M–O distances. In most cases of Cr^{4+}_{tet}, the lowest excited states have been considered as $^3T_2$, splitting under low symmetry, but some crystal fields led to the ^1E state as the lowest (Boulon 1997). Many of the solid- state laser materials with Cr^{4+} possess both tetrahedrally and octahedrally coordinated sites. Although the site for the dominant laser emission is the tetrahedrally coordinated one, the contribution of the octahedrally coordinated site is not negligible. The ^2E_g and $^4T_{2g}$ states of Cr^{3+}_{oct} will be typically located in the energy region overlapping with the lowest states of Cr^{4+}_{tet} (Fig. 5.34). Although the corresponding transitions are spin-forbidden ones with weak intensities, some confusing structures could be created in the near IR region.

Luminescence of Cr^{4+} has not been detected in minerals yet, but the first candidates are evidently forsterite and apatite (Fig. 5.35).

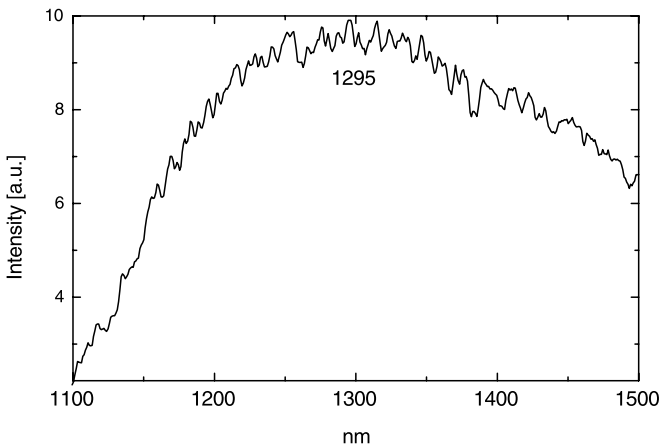

Fig. 5.35. Laser-induced luminescence of artificial apatite activated by Cr^{4+}

5.3.2.2 Mn^{5+}

The experimental data recorded for Mn^{5+} are consistent with the Tanabe-Sugano diagram by assuming the higher crystal field compared to Cr^{4+}, which leads to the higher energy of the emission with the occurrence of the singlet ^1E metastable state as a final state before emission and then longer a lifetime from this level (Boulon 1987).

5.3.2.2.1 *Magmatic Apatite*

In the IR spectra of blue and green-blue magmatic apatites the strong narrow band was detected (Fig. 4.3b). It was associated with tetrahedrally coordinated Mn^{5+} on the site of P^{5+} (Gaft et al. 1997a). Such an interpretation was firstly proposed by Kingsley et al. (1965) and confirmed by the study of artificial apatite activated by Mn^{5+} (Moncorge et al. 1994). According to the Tanabe-Sugano diagram the ground state is a spin triplet $^3A_2$ and the sequence of the energy levels of Mn^{5+} in natural apatite correspond to a strong field situation for which the first excited state is a singlet ^1E partially mixed with the higher $^3T_2$ state. The emitting state ^1E gives two sharp lines at 1,149 and 1,160 nm as result of splitting into two components. The situation in synthetic apatites corresponds to a lower field in which the first excited state is the triplet $^3T_2$ giving rise to broader emission bands (Fig. 5.36). Even with the existence of strong mixing between ^1E and $^3T_2$ excited states, the different origin of the narrow and broad bands is confirmed by their different decay times of 350 and 200 μs, respectively.

5.3.2.2.2 *Sedimentary Apatite*

Certain sedimentary apatites have a blue color after oxidizing heating at 700–800 °C. It appears that before heating they are characterized by luminescence of Mn^{2+} while after heating luminescence of Mn^{5+} appears. For example, mastodon ivory, also called odontolite or bone turquoise is one of the most fascinating imitations of turquoise mineral used in the Middles Ages as a semi-precious stone. The understanding of the mysterious turquoise-blue color formation induced by heat treatment in this material is the subject of much confusion. Former studies demonstrated that its chemical and structural composition corresponds to fluorapatite. Laser-induced time-resolved luminescence spectroscopy was used to determine the accommodation of the potential elements responsible for the color (Reinshe et al. 2001). It was proved that the color of odontolite can be ascribed to Mn^{5+} traces in the fluorapatite host matrix. These manganese traces are situated on the tetrahedral phosphorus sites. These usually unstable cations are stabilized by the apatite host matrix. The characteristic luminescence revealed that there is a thermal diffusion from Mn^{2+} in the calcium sites to the phosphorus sites accompanied by an oxidation into Mn^{5+}, which produces an intense blue color by an oxygen- Mn^{5+} charge transfer.

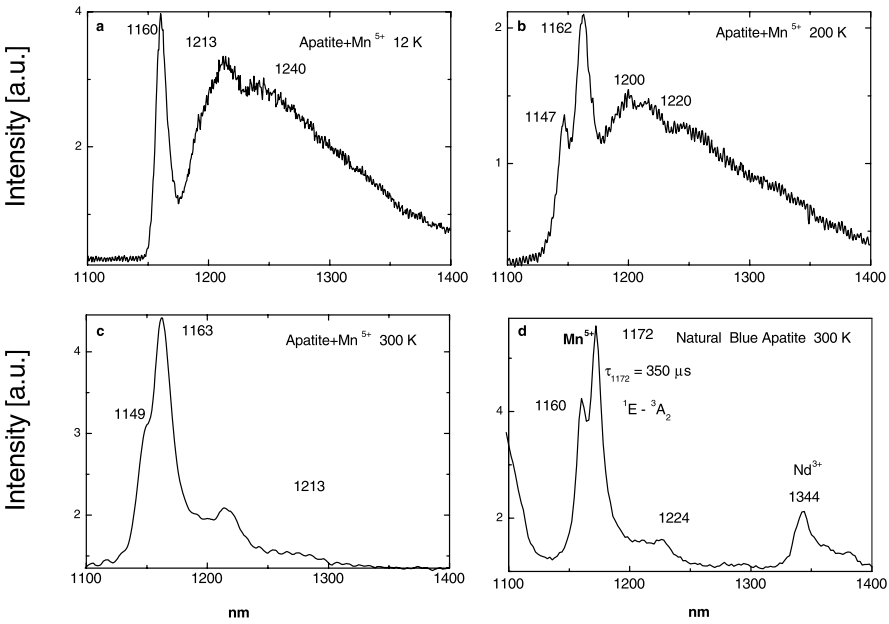

Fig. 5.36. **a–d** Laser-induced luminescence of Mn^{5+} in artificially activated (**a–c**) and natural blue (**d**) apatite

Besides apatite, luminescence of Mn^{5+} has been found in other phosphate related minerals, such as triplite (Ajo et al. 1997). It was proposed that the lattice distortion is smaller for the substituting Mn^{5+} ion than for the structural P^{5+}, which explains the occurrence of Mn^{5+} in several mineral phosphates, while the oxidizing state V is unusual for Mn in aqueous solutions.

5.3.2.3 V^{3+}

The energy levels diagram of V^{3+} is similar to that of Cr^{3+}, though these ions are not isoelectronic. Having a different number of electrons and hence different multiplicity, these ions have the same orbital ground state (^3F and ^4F) and one more state with the same multiplicity (^3P and ^4P) that leads to the three intense spin-allowed absorption bands with some weak narrow lines related to spin-forbidden transitions.

Luminescence of V^{3+} in minerals was proposed in tsavorite where the broad-band IR luminescence with a short decay time less than 1 µs was associated with this center (Mazurak and Czaja 1996). The luminescent level has been identified as a component of the $^3B_2$ ($^3T_{2g}$) energy level. At least two different V^{3+} sites are detected.

Luminescence of V^{3+} has been found in α-Al_2O_3 under argon laser excitation at 514.5 nm, which consists of two narrow IR lines with the strongest one at 1,026 nm, characterized by a decay time of 1.6 μs at 77 K (Champagnon and Duval 1979).

Connection of V^{3+} with 833 and 847 nm lines with long decay time in luminescence spectrum of topaz (Fig. 5.29e,f) is also possible (Gaft et al. 2003a).

5.3.2.4 Ti^{2+}

Ti^{2+} can be stabilized in halide lattices with broad-band luminescence, characterized by considerable thermal quenching. Thus the potential minimum of the $^3T_2$ excited state lies below the $^1E(T_2)$ minimum and is thus the emitting state. If Ti^{2+} is forced into a very tight site, such as in $MgCl_2$, the crystal field gets larger and $^1E(T_2)$ becomes the emitting level with sharp lines IR emission. Upon warming the $^3T_2$ state is gradually populated and the sharp-line spectrum changes to a broad-band spectrum and the luminescence lifetime drops by more than two orders of magnitude (Güdel et al. 1997).

5.3.3 $3d^1$ Elements

The elements with such electronic configuration known as luminescent centers are Cr^{5+}, Mn^{6+}, V^{4+} and Ti^{3+} (Fig. 5.37). The ^2E ground state has a single unpaired electron occupying the π antibonding set of *e*-orbitals. In the first

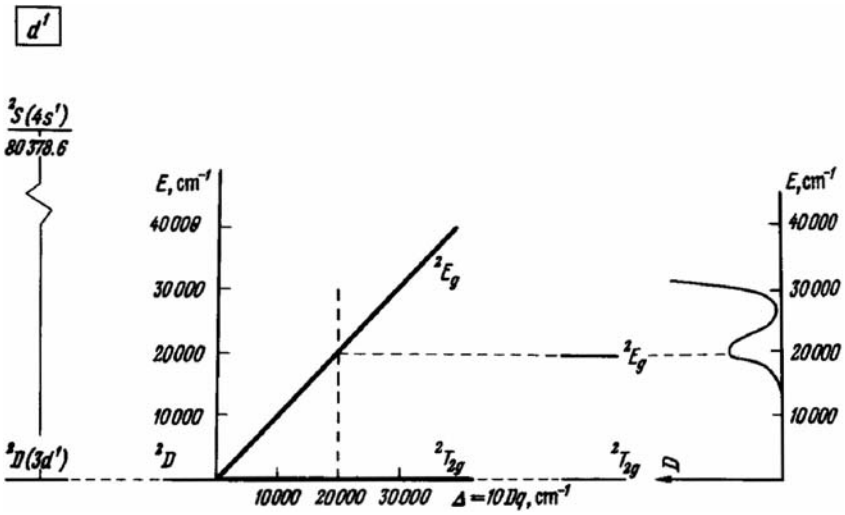

Fig. 5.37. Tanabe-Sugano diagram for d^1 ions

excited state this electron is promoted to the π and σ antibonding set of t_2-orbitals, giving rise to the $^2T_2$ ligand-field excited state. The ^2E–$^2T_2$ transition usually appears as a weak broad absorption band in the near-infrared region.

5.3.3.1 Cr^{5+}

5.3.3.1.1 *Zircon*

IR luminescence detected in $ZrSiO_4$–Cr has an excitation band peaking at 920 nm. Its luminescence spectrum at 300 K (Fig. 5.38) is characterized by a relatively unresolved broad band peaking at 1,200 nm. It is very similar to Cr^{4+} luminescence in silicates, especially in forsterite except for a very short decay time shorter than the time resolution of our detection system about 200 ns. It is not suitable for Cr^{4+} with a much longer decay in the µs range (Boulon 1997). Luminescence at lower temperatures is much more intensive and spectra are characterized by several strong narrow lines with very short decay which appear already at 100 K. Once again, it is rather unusual for Cr^{4+}.

Luminescence spectra at low temperature, together with very short decay times are rather characteristic for Cr^{5+} luminescence, which was not known until recently, and which is especially similar to the luminescence of CrO_4^{3-} doped YPO_4 with zircon structure (Brunold et al. 1997). At 15 K it also consists

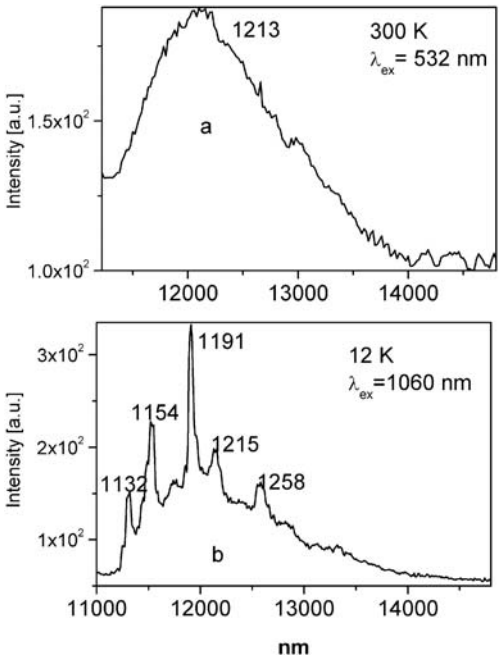

Fig. 5.38. **a–b** Laser-induced steady-state luminescence of $ZrSiO_4$:Cr^{5+}

of several narrow lines with a very short decay time of less than 20 ns. Thus we proposed the assignment of the luminescence spectrum to ^2E–$^2T_2$ allowed electric dipole transition or, more precisely, to $^2B_1$–$^2A_1$ components of D_{2d} symmetry in distorted tetrahedral SiO_4^{4-} groups (Gaft et al. 2000b). The origin of the spectrum in $ZrSiO_4$: Cr is situated at 8,881.00 cm^{-1} and built upon it progressions in two modes, $\nu_1 = 170-180\ cm^{-1}$ and $\nu_2 = 440-445\ cm^{-1}$ are observed. The last one is the same as in Cr^{5+} doped YPO_4 where it has been connected with the O–Cr–O bending mode (Hazenkamp and Gudel 1996). Nevertheless, IR and Raman spectra of pure zircon contain this band and thus it may be a lattice mode also. From the other side, the mode at 170–180 cm^{-1} is absent in vibrational spectra of pure zircon and may be connected with vibrational frequencies of the CrO_4^{3-} unit, which are between 270 and 830 cm^{-1}.

EPR spectra of $ZrSiO_4$: Cr contain a single line with $g_{\|} = 1.986$, $g_{\perp} = 1.956$ which is characterized by D_{2d} local symmetry ($K_m = 1$). The Cr^{5+} ion has spin $S = 1/2$ and with any symmetry of the crystal field, splitting in the magnetic field always leads to the appearance of a single line in the EPR spectrum. The possible connection of the line with Cr^{5+} is confirmed by its intensity correlation with Cr concentration in the melt. The ratio of the main values of g-tensor is characteristic for Cr^{5+} ($3d^1$ configuration) in tetrahedral coordination (Krasnobayev et al. 1988).

5.3.3.2
Mn^{6+}

5.3.3.2.1
Barite

Luminescence of Mn^{6+} was not detected in minerals yet, but is well known in phosphors. The first possibility will be barite (Fig. 5.39), because $BaSO_4$–Mn^{6+} has IR luminescence and is considered as a potential material for a tunable NIR laser (Brunold and Güdel 1997; Brunold et al. 1997).

5.3.3.3
Ti^{3+}

Ti^{3+} belongs to the d^1 configuration, which is the simplest one. The free ion has fivefold orbital degeneracy (^2D), which is split into two levels (^2E and $^2T_2$) in octahedral symmetry, which is quite common for transition metal ions. The only possible optical transition with excitation is from $^2T_2$ to ^2E. This transition is a forbidden one, since it occurs between levels of the d-shell. Therefore the parity does not changed. The parity selection rule may be relaxed by the coupling of the electronic transition with vibrations of suitable symmetry.

Ti^{3+} is able to create a tunable laser in a sapphire lattice (Fabeni et al. 1991). It substitutes the Al^{3+} ion of the host crystal in a trigonally distorted octahedral lattice site and is characterized by a strongly polarized band peaking at approximately 750 nm with a decay time of 3.1 μs (Fig. 5.40).

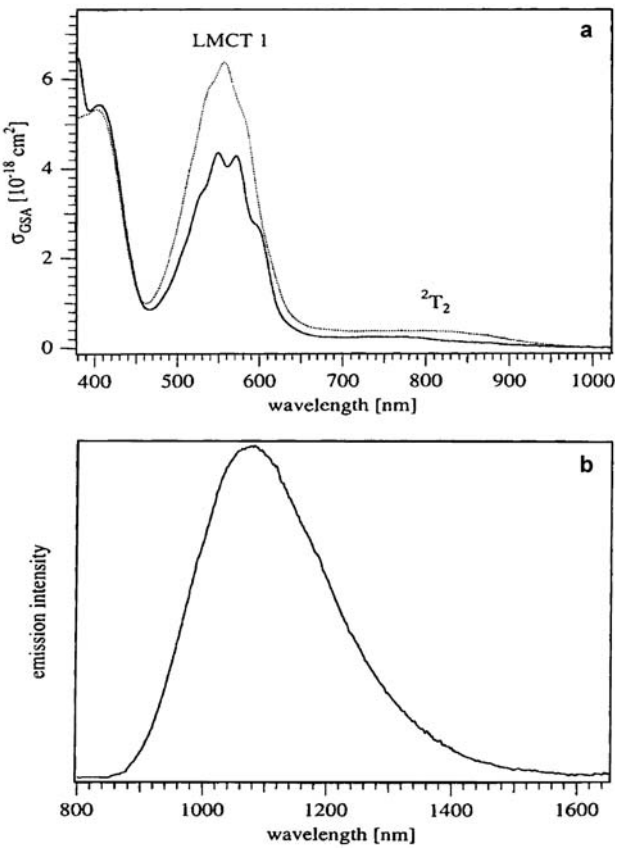

Fig. 5.39. Luminescence (**b**) and excitation (**a**) spectra of $BaSO_4$–Mn^{6+} (Brunold and Güdel 1997; Brunold et al. 1997)

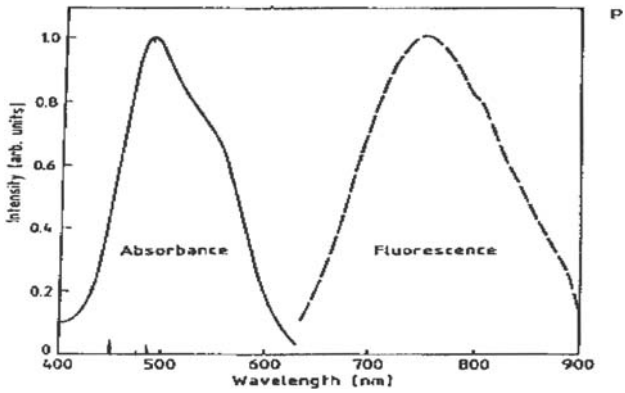

Fig. 5.40. Luminescence and absorbance of Ti^{3+} in artificial sapphire (Fabeni et al. 1991)

5.3.3.3.1 Benitoite

Luminescence of Ti^{3+} was not confidently detected in steady-state luminescence spectra of minerals. In Ti minerals studied by laser-induced time resolved

spectroscopy broad read band have been found with decay time of several μs: at 660 nm in benitoite (Fig. 4.35) and 750 nm in titanite (Fig. 4.34f).

At room temperature the benitoite band with a maximum at 660 nm has half-width of ∼ 135 nm and may be approximated by one Gaussian (Gaft et al. 2004b). One exponent with decay time of 1.1 μs approximates well its decay curve at room temperature in all spectral range of luminescence band. At lower temperatures up to 30 K this red luminescence intensity becomes approximately 10 times higher and the spectrum undergoes certain changes, namely its maximum shifts in long wave direction to 668 nm and the band becomes a little narrower with half-width of ∼ 105 nm. Such red emission is not excited by laser sources in the visible part of the spectrum, such as 488, 514 and 532 nm. Excitation spectrum at lower temperatures, when luminescence intensity becomes strong enough for UV lamp source, contains one asymmetric band peaking at ∼ 350 nm with half-width of ∼ 75 nm and the corresponding Stokes shift is approximately 13,000 cm^{-1}. It may be approximated by to Gaussian curves peaking at 28,130 cm^{-1} (355 nm) and 30,279 cm^{-1} (330 nm). Decay curve at lower temperatures remains mono-exponential, but decay time becomes substantially longer changing to ∼ 20 μs.

Comparison of this luminescence intensity in different samples reveals that any correlation is absent any impurity concentration. Thus it was supposed that the mostly probable luminescence center is Ti^{3+}, which presence is quite natural in Ti bearing benitoite. The wide occurrence of Ti^{3+} minor impurities in minerals was detected by EPR. Like the other d^1 ions (V^{4+}, Mo^{5+}), Ti^{3+} ions occur often in minerals as electron center (Marfunin 1979). It may be realized in benitoite, which does have some natural exposure to gamma rays in its natural setting. There could be radiation centers, such as, for example, Ti^{4+} + gamma ray + electron donor ⇐ Ti^{3+} + electron hole. Benitoite color does not change with gamma irradiation to quite high doses (Rossman 1997) but luminescence is much more sensitive compared to optical absorption and can occur from centers at such low concentration that they do not impact the color of a benitoite.

Figure 5.41 summarizes the temperature behavior of decay time and quantum efficiency of red benitoite luminescence at 660 nm in the forms $\ln(\tau)$ and $\ln(\eta)$ as a functions of 1/T. In such case the luminescence may be explained using simple scheme of two levels, namely excited and ground ones. The relative quantum yield (η) and decay time (τ) of the red emission may be described by simple Arhenius equations:

$$\eta = \frac{1}{1 + A_d/A_r \exp(-U/kT)} \tag{5.21}$$

$$\tau = \frac{1}{A_r + A_d \exp(-W/kT)} \tag{5.22}$$

where A_r and A_d are radiation and non-radiation transition probabilities between excited state and ground level and U is energetic barrier between them.

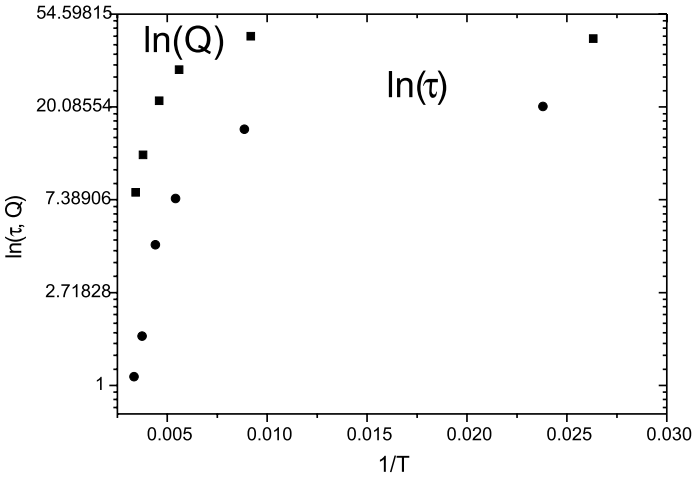

Fig. 5.41. Temperature dependence of quantum efficiency (Q) and decay time (τ) of red emission band of benitoite at 660 nm

The best fit to the experimental results is received when $A_r = 5.4 \times 10^4\ \mathrm{sec}^{-1}$, $A_d = 2.66 \times 10^7\ \mathrm{s}^{-1}$ and $U = 0.09$ eV. Two competing processes take place after excitation: emission with radiation probability A_r and non-radiative quenching due energetic barrier U with probability $A_d \exp(-U/kT)$. At low temperatures the first one dominates and quantum yield is relatively higher with long decay time. At elevated temperatures non-radiative mechanism dominates with the following quenching and decay time shortening.

Such behavior is quite compatible with Ti^{3+} luminescence center. In such case, excitation peaking at 355 nm is connected with $^2T_2 - {}^2E$ transition, while the splitting of the ^2E state is a reason of the two shoulders presence in excitation spectrum. At lower temperature the opposite transition generates intensive luminescence band peaking at 660 nm with decay time of 20 µs. Thermal quenching and drastically reducing decay time with increasing temperature result from non-radiative transition from excited to ground state.

The main difference between considered benitoite luminescence and Ti^{3+} emission in well studied Al_2O_3 and $Y_3Al_5O_{12}$ is strong short-waved shift of benitoite emission and especially excitation bands. For example, excitation and absorption maximum of Ti^{3+} in sapphire is at 550 nm, while in benitoite at 355 nm. Nevertheless, it is not so uncommon for Ti^{3+} in different matrixes. The optical absorption spectrum of Ti^{3+} in $YAlO_3$, where Ti^{3+} substitutes for Al^{3+} in sites with orthorhombic symmetry, is composed of two broad bands with peak wavelengths of 434 and 492 nm, the energy separation of which is due to splitting of the excited ^2E state (Yamaga et al. 1992). Such luminescence parameters are closer to those found in benitoite.

5.3.3.4 V^{4+}

Diagrams of V^{4+} levels splitting in crystal fields of different symmetry are identical with those for the isoelectronic Ti^{3+} ion. An emission spectrum attributed to V^{4+} was found in αAl_2O_3 in the visible region at low temperatures (Champagnon and Duval 1979). It consists of broad band peaking at 625 nm and narrow lines at approximately 528 and 529 nm (Fig. 5.31b,c).

Three slightly different octahedrally coordinated V^{4+} centers have been found in topaz by the EPR method (Schott et al. 2003), thus its participation in topaz luminescence is possible.

5.3.4 $3d^8$ Elements

5.3.4.1 Ni^{2+}

Center Ni^{2+} has the electronic configuration $3d^8$ (Fig. 5.42). Three luminescence bands in the near IR, red and green parts of the spectrum characterize Ni^{2+} in many synthetic luminofors (Blasse and Grabmier 1994). For example, a broad IR band peaking at 1,520 nm and connected with electron transition from the lowest excited state ${}^3T_{2g}$ has been found in enstatite artificially activated by Ni^{2+} (Moncorgé et al. 1999). Green luminescence is connected with ${}^1T_{2g}(D)$–${}^3A_{2g}(F)$ while the red one with ${}^1T_{2g}(D)$–${}^3T_{2g}(F)$ electron transition (Fig. 5.43). The emissions from the ${}^1T_{2g}$ state are not only observed at cryogenic temperatures but persist up to room temperature as, for example, in MgO (Mironova and Ulmanis 1988) and $KZnF_3$ (Grimm et al. 2003).

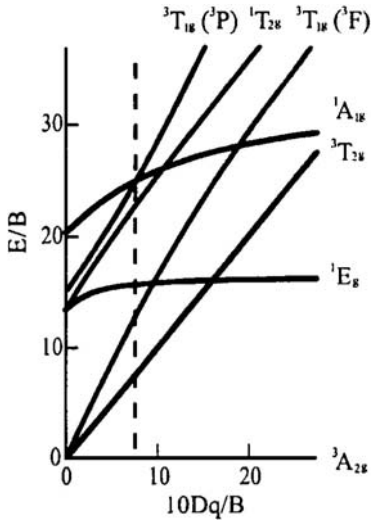

Fig. 5.42. Tanabe-Sugano diagram for the $3d^8$ coordination in an octahedral crystal field

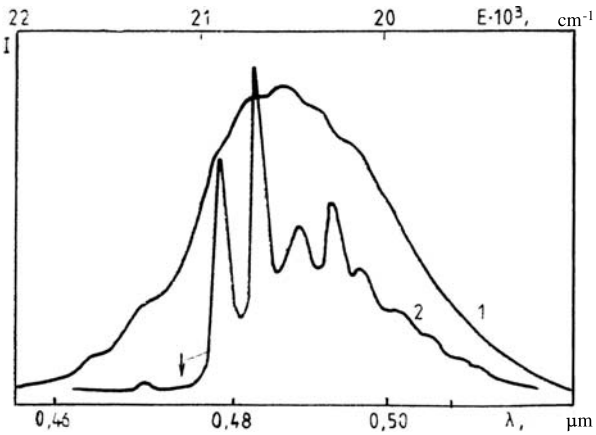

Fig. 5.43. Green luminescence of Ni^{2+} in MgO at room (1) and liquid helium (2) temperatures (Mironova and Ulmanis 1988)

The possibility of Ni^{2+} participation in minerals luminescence has not been seriously considered yet, but we are confident that it has to be done. The ionic radius of Ni^{2+} is 69 pm in tetrahedral coordination and 83 pm in the octahedral one. Thus it may substitute many cations with similar dimensions, such as Mg, Zn, Ca.

5.3.5 $3d^6$ Elements

5.3.5.1 Fe^{2+}

The ion Fe^{2+} has the electronic configuration $3d^6$. It is characterized by extremely strong absorption and is the strongest visible luminescence quencher in minerals, but it has an emission band in the IR part of the spectrum.

5.3.6 $3d^5$ Elements

5.3.6.1 Mn^{2+}

The $3d^5$ system manganese(II) with sextet (^6S) ground state is a well-known activator in many minerals (Tarashchan 1978; Gorobets and Rogojine 2001). Emission bands due to Mn^{2+} have been observed in practically all classes of minerals. It is responsible for green, yellow and orange-red luminescence. For the case of octahedrally coordinated Mn^{2+}, as in calcite, the position of the minimum of the configurational curves occurs at different Mn^{2+}–O distances for states, which are dependent on the crystal field strength, D_q, such as $^4T_1$ and $^4T_2$. For states whose energies are independent of D_q, the minimum occurs at the same interatomic distance as in the ground state, $^6A_1$ (states ^4E_g and $^4A_1$). The consequence of this is that there is a progressive

shift in the energy of the $^6A_1 \rightarrow {}^4T_1$ and $^6A_1 \rightarrow {}^4T_2$ transitions as D_q increases, producing band broadening and a shift toward longer wavelengths for both emission and absorption bands. It is easy to see (Fig. 5.44) that the curvature of the excited states leads to the width of the bands in the absorption spectrum. States not involved in bonding give rise to sharp absorption lines because they are only weakly coupled to the host, while strongly coupled ion states vary considerably in energy with interatomic distance and yield broad bands.

Changes in coordination, such as from octahedral to tetrahedral, produce a considerable change in D_q. The tetrahedral D_q value is smaller and the energy of all of the transitions in Mn^{2+} increases. This creates a shift toward short wavelengths. Octahedral Mn^{2+} coordination in calcite thus has a red-orange emission at 620 nm (Fig. 4.14a), while the analogous transition for Mn^{2+} in willemite yields yellow-green emission at 525 nm (Fig. 4.37c,d). Prominent changes in the color of the emission may also occur from a change in the emission state. The $^4T_1$ state is responsible for emission in calcite and willemite, but the $^4T_2$ state is responsible for the green luminescence of fluorite (500 nm) and anhydrite (505 nm) even though Mn^{2+} has larger coordination sites.

It was originally stated that $CaCO_3$ activated with manganese cannot be excited by UV radiation, but $CaCO_3$ activated with lead, thallium or cerium and manganese shows an orange-red manganese luminescence under UV irradiation at room temperature (Bolden 1952). Nevertheless, in many minerals luminescence of Mn^{2+} has been found with excitation spectra typical for this center without additional bands of Pb or Ce impurities.

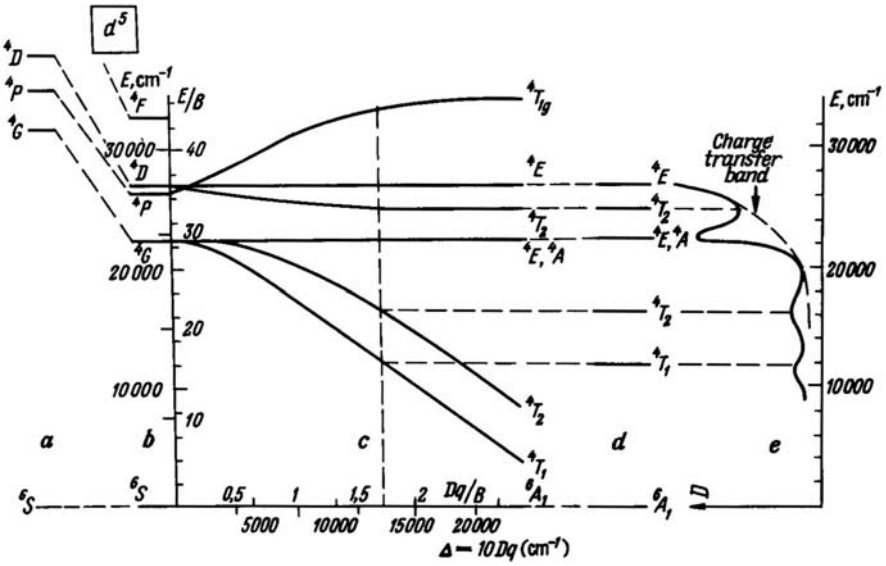

Fig. 5.44. Tanabe-Sugano diagram for d^5 elements

5.3.6.1.1
Apatite

The typical Mn^{2+} luminescence in natural apatite is connected with a band peaking at 569 nm (Fig. 4.1e) with a delay time of $\sim$ 5 ms. Various laser lines were used to excite the luminescence but the spectra were all very similar. All portions of the curve have the same decay time and the spectra were found to be identical for different delay times and gate widths. All of this suggests that we a dealing with a simple single-ion fluorescence. Red apatite has unusual for a natural sample luminescence of Eu^{3+} and Tb^{3+} in Ca(II) instead of Ca(I) sites. Luminescence of Mn^{2+} in this sample is also exceptional. Its spectrum is characterized by a maximum at 583 nm (Fig. 4.1f) and an extremely long decay time of $\sim$ 12 ms. By analogy with artificially activated apatite (Ryan et al. 1970) it is possible to suppose, that luminescence of Mn^{2+} in the Ca(I) position takes place in the red apatite. As in our case, the Mn(I) band is 10 nm shifted to the red part of the spectrum compared to the Mn(II) one (Fig. 5.45). The longer decay time is consistent with the higher symmetry of the Ca(I) site. From the other side, according to the Tanabe-Sugano diagram, the lower crystal field in the Ca(I) position has to lead to the luminescence band shift in the opposite direction. Nevertheless excitation spectra of Mn^{2+} (II) in natural and

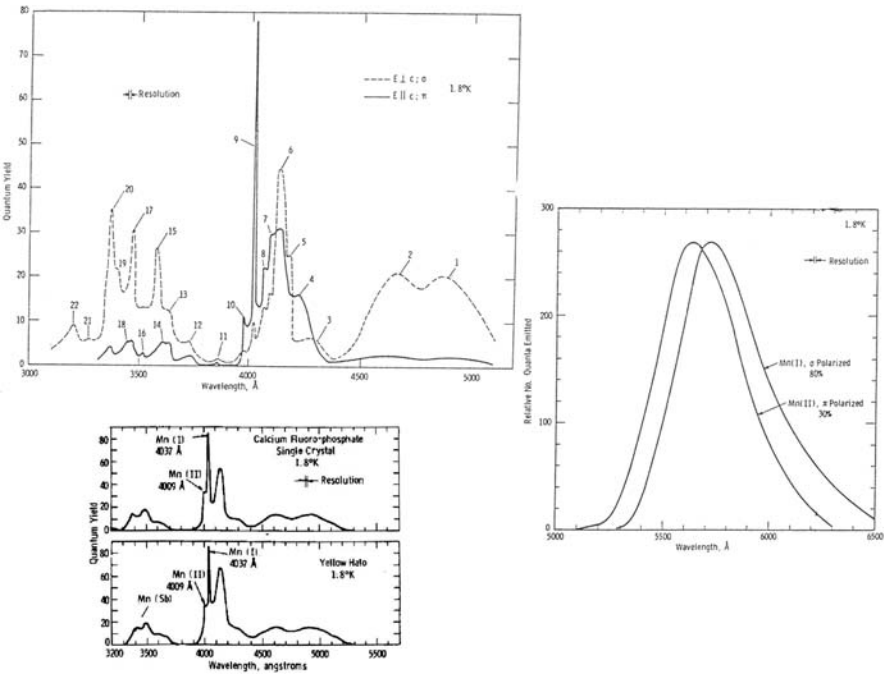

Fig. 5.45. Excitation and luminescence spectra of Mn^{2+} in Ca(I) and Ca(II) positions in artificially activated apatite (Ryan et al. 1970)

artificially activated apatite contain only the ${}^6A_1(S)$–${}^4T_2(G)$ band, implying that the luminescence is connected with the opposite ${}^4T_2(G)$–${}^6A_1(S)$ transition after relaxation. Such deactivation is due to electron-phonon interaction, which is very effective in apatite. The luminescence transition from the lower lying level leads to the lower photon energy even in the site with a lower crystal field strength.

The situation with Mn^{2+} center distribution between Ca(I) and Ca(II) positions in the apatite lattice is the opposite to this for REE^{3+}: in artificially activated apatite the Mn(I) center clearly dominates the fluorescence spectra (Ryan et al. 1970), while in the natural one only Mn(II) centers have been detected (Tarashchan 1978). In order to clarify the distribution in different Ca positions, luminescence spectra have been measured with different polarizations from one section or from prismatic and basal sections with the same analytical conditions. As was found earlier (Barbarand and Pagel 2001) the shapes of the spectra are usually the same for both crystallographic orientations, while the major difference in the spectra is their intensity, with the mean intensity for the basal section lower than for the prismatic face. Nevertheless, in certain cases polarization changes lead to different spectra (Fig. 5.46). In this case spectra are composed mainly of the Nd^{3+} and Mn^{2+} with relatively weak Eu^{3+} lines. The polarization change results in an inversion of the relative intensities of the luminescence bands: Mn^{2+}(I) emission dominates in one orientation and REE emission is practically not seen, but Mn^{2+}(II) in other orientations is much weaker compared to Mn^{2+}(I), while the

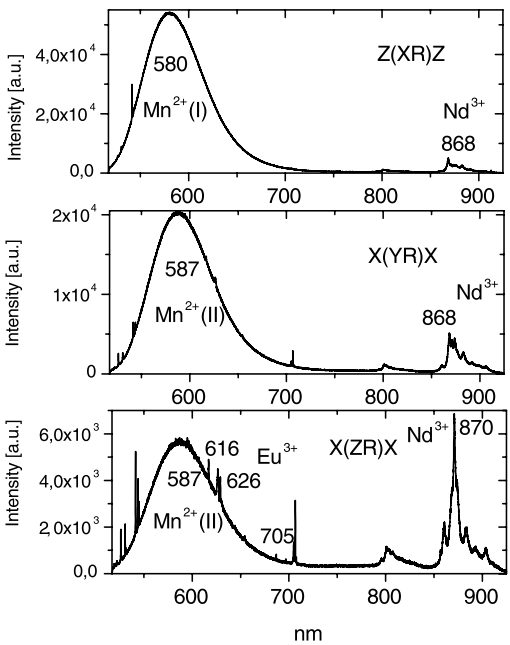

Fig. 5.46. Polarized laser-induced luminescence of different Mn^{2+} centers in apatite

REE are much stronger. The similar result was described for a CL study of apatite, where the Ce^{3+} band is significantly higher for the zone analyzed in a section perpendicular to the c-axis, but the Mn^{2+} band is significantly higher for the zone analyzed in a section parallel to the c-axis (Barbarand and Pagel 2001).

5.3.6.1.2
Feldspars

Luminescence of Mn^{2+} is well known in the steady-state luminescence spectra of feldspars (Tarashchan 1978; Waychunas 1989; White 1990; Götze 2000; Gorobets and Rogojine 2001). Its green luminescence is predominantly detected in plagioclases. In K-feldspars the Mn^{2+} emission is less common because of the difficulty of the Mn^{2+} – K^{+} substitution. Its band is also very well detected in laser-induced time-resolved spectra peaking at 550–560 nm (Fig. 4.43a). It is characterized by an extremely long decay time of 10–12 ms.

5.3.6.1.3
Hardystonite, Apophyllite and Esperite

Broad bands at 525 and 575 nm in the time-resolved luminescence spectra of hardystonite under 355 nm excitation (Fig. 4.20d) with very long decay time of several ms may be ascribed to strongly forbidden *d*–*d* transitions in the Mn^{2+} luminescence center. Two bands may be connected with isomorphous substitutions on Ca in Zn structural positions. The spectrum of a famous yellow-green esperite luminescence (Fig. 4.21a) consists of a narrow band peaking at 545 nm with a very long decay time of 9 ms. Such parameters together with the typical excitation spectrum (Fig. 4.21b) enable confident identification of the luminescence center as Mn^{2+}. The orange emission near 600 nm of apophyllite is also evidently connected with the Mn^{2+} center (Fig. 4.19c,d).

5.3.6.1.4
Garnet

The relatively broad band peaking at approximately 590 nm in grossular with a very long decay time of several ms (Fig. 4.57) can be confidently ascribed to the Mn^{2+} center substituting for Ca^{2+}.

5.3.6.1.5
Spinel

Artificially activated spinels of composition $Mg_{1-x}Al_2O_{4-x}$:Mn^{2+} were studied (Mohler et al. 1994). It was found that $MgAl_2O_4$:Mn^{2+} emits at 650 nm, while when $x = 0.05$ emission bands appear at 517 and 744 nm. They increase intensity and the 650 nm band disappears as x increases. The green emission is connected with Mn^{2+} in tetrahedral sites, while the red one evidently with Mn^{2+} in octahedral ones.

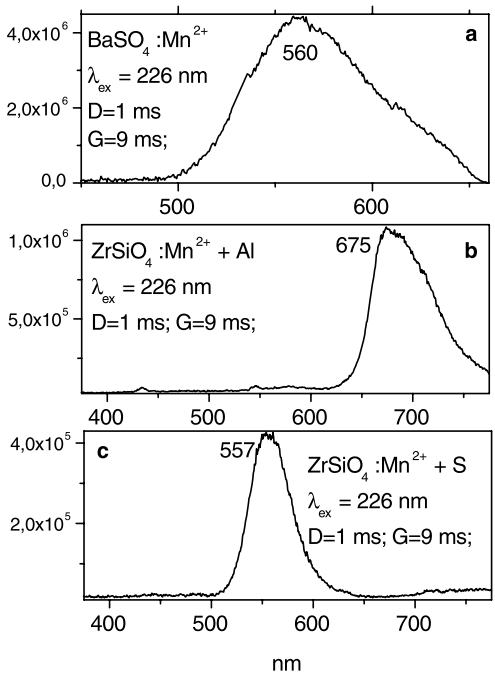

Fig. 5.47. **a–c** Laser-induced time-resolved luminescence of $ZrSiO_4$–Mn^{2+} and $BaSO_4$–Mn^{2+}

In natural spinels emission bands with maxims from 570 to 620 nm have been found interpreted as connected with Mn^{2+} in octahedral sites (Mironova et al. 1991). According to such an interpretation it is possible to ascribe the band at 612 nm to Mn^{2+} in octahedral positions (Fig. 4.51).

5.3.6.1.6
Zircon

Certain narrow luminescence bands with a long decay time detected in the time-resolved luminescence spectra of zircon may be principally connected with Mn^{2+} luminescence. In order to clarify this, artificially activated $ZrSiO_4$–Mn has been studied (Gaft et al. 2002b). The ionic radius of Mn^{2+} of 0.97 Å is close to that of Zr^{4+} (0.88 Å) and the corresponding substitution is possible with proper charge compensation. The presence of Mn impurities in quantities in zircons under investigation was confirmed by ICP analyses (Table 4.14). Intensive narrow bands with very long decay times were found with the spectral position strongly dependent on the co-activator (Fig. 5.47b,c). Principally, such differences may be connected with several kinds of Mn^{2+} centers with different local symmetry, for example, Mn^{2+}–Si^{4+} (tetrahedron) and Mn^{2+}–Zr^{4+} (octahedron) substitutions, but the small ionic radius of Si^{4+} of 0.4 Å makes such substitution very doubtful. At any case, such luminescence bands have never been detected in the luminescence spectra of natural zircon. It is

possible to suppose that zircon contains Mn not in the form of Mn^{2+}, but as Mn^{4+}, which is confirmed by EPR data (Votyakov et al. 1993).

5.3.6.1.7
Barite

Manganese impurities are always found in barite samples and Mn^{2+} participation in barite luminescence was considered as possible. In order to check this we studied synthetic $BaSO_4$ artificially activated by Mn^{2+}. Relatively weak green luminescence was found (Fig. 5.47a) with a very long decay time of several ms, but such emission has not been found yet in natural barite.

5.3.6.1.8
Other Minerals

Characteristic bands of Mn^{2+} well studied by steady-state luminescent spectroscopy (Tarashchan 1978; Gorobets and Rogojine 2001) have been found in time-resolved luminescence spectra of calcite (Fig. 4.14a), fluorite (Fig. 4.10d), datolite (Fig. 4.16d), wollastonite (two bands at 555 and 603 nm; Fig. 4.42a,c), and spodumen (Fig. 4.61a).

5.3.6.2
Mn^{2+} – *Clusters*

In such a case, the excitation does not stay on the same ion of Mn^{2+}, but can travel readily through the sub-lattice of in-resonance Mn^{2+} ions. The emission originates from Mn^{2+} ions associated with impurities and other defects. They occupy regular cation sites in the lattice and perturb the surrounding Mn^{2+} ions, lowering their energy levels relative to those of the unperturbed (intrinsic) Mn^{2+} ions. The diffusing excitons can now be trapped by the perturbed Mn^{2+} ions. At low temperatures the excitation cannot return to the exciton state; the excited, perturbed Mn^{2+} ions decay radiatively with a spectrum characteristic of the particular trap. Deeper traps are also present and are effective as quenching states, i.e. traps from which no emission occurs, but where the excitation is lost non-radiatively. At low temperatures the traps are effective, but at higher ones they begin to lose their trapped excitation energy by thermally activated back-transfer to the exciton level. From here deeper traps may trap the energy. Finally all the emitting traps are emptied and only the deep, non-emitting traps are operative. As a consequence the luminescence has been quenched. These quenching traps may be Ni or Fe ions. If the mineral contains two or three-dimensional chains Mn–O–Mn–O, excitation energy migrates over the lattice, which results in the following distinctions from luminescence properties of impurity Mn^{2+} in isostructural non-manganese minerals:

a) sharp drop in luminescence quenching temperature due to an enhanced probability of excitation energy to hit quenching centers,

b) long-wave shift of emission λ_{max}, because luminescence proceeds at local levels of Mn^{2+} near defects where the shift occurs either due to the electron-phonon interaction or due to a strong local crystalline field with the possible change of the radiation level of Mn^{2+}.

If there are only one-dimensional chains or the Mn ions are linked through two oxygen ions, the energy migration does not take place and the luminescence peculiarities mentioned above are not observed. The dependence of luminescence features on peculiarities of Mn mutual arrangement and not only on there spacing makes clear indication that the main mechanism of the energy transfer is the exchange one (Powell and Blasse 1980). Steady-state luminescence of Mn-clusters in natural minerals of manganese has been found at liquid nitrogen temperatures (Gorobets et al. 1980; Gaft et al. 1981) and interpreted in terms of minerals structure (Fig. 5.48).

Under powerful laser excitation with $\lambda = 532$ nm manganese minerals, such as rhodonite and rhodochrosite, exhibit orange-red luminescence even at room temperature. In rhodonite it is a band peaking at 620 nm with a half-width of 85–95 nm and a very long decay time of 5–6 ms (Fig. 4.67c,d). Such luminescence is typical for impurity Mn^{2+}. In rhodochrosite luminescence is more complicated. The luminescence band has a maximum near 640 nm and a half-width of 80–90 nm, which is typical for impurity Mn^{2+}, but a decay time of only 5–10 μs is very short for such a center and indicates strong energy migration (Fig. 4.67a,b).

Excitation spectra of Mn^{2+} enable us to calculate the crystal field force Δ and Raka parameters B and C. The relative position of the ground level ${}^6A_{1g}$ (S) and excited levels ${}^4A_{1g}$, ${}^4E_g(G)$ and ${}^4E_g(D)$ does not depend on Δ. Using the frequencies of electronic transitions from the ground level to those excited levels (k_3 and k_5), parameters B and C may be calculated based on formulas:

$$k_3 = 10B + 5C\,,$$
$$k_5 = 17B + 5C \qquad (5.23)$$

Resulting B and C are substituted for:

$$k_1 = -\Delta + 10B + 6C - 26B^2/\Delta\,,$$
$$k_2 = -\Delta + 18B + 6C - 26B^2/\Delta \qquad (5.24)$$

And two independent values of Δ are received.

5.3.6.3 Fe^{3+}

Luminescence of Fe^{3+} may be considered from the same positions as Mn^{2+} emission because it also has d^5 configuration. Nevertheless, because of the large value of crystal field, the emission is shifted into the deep red when Fe^{3+}

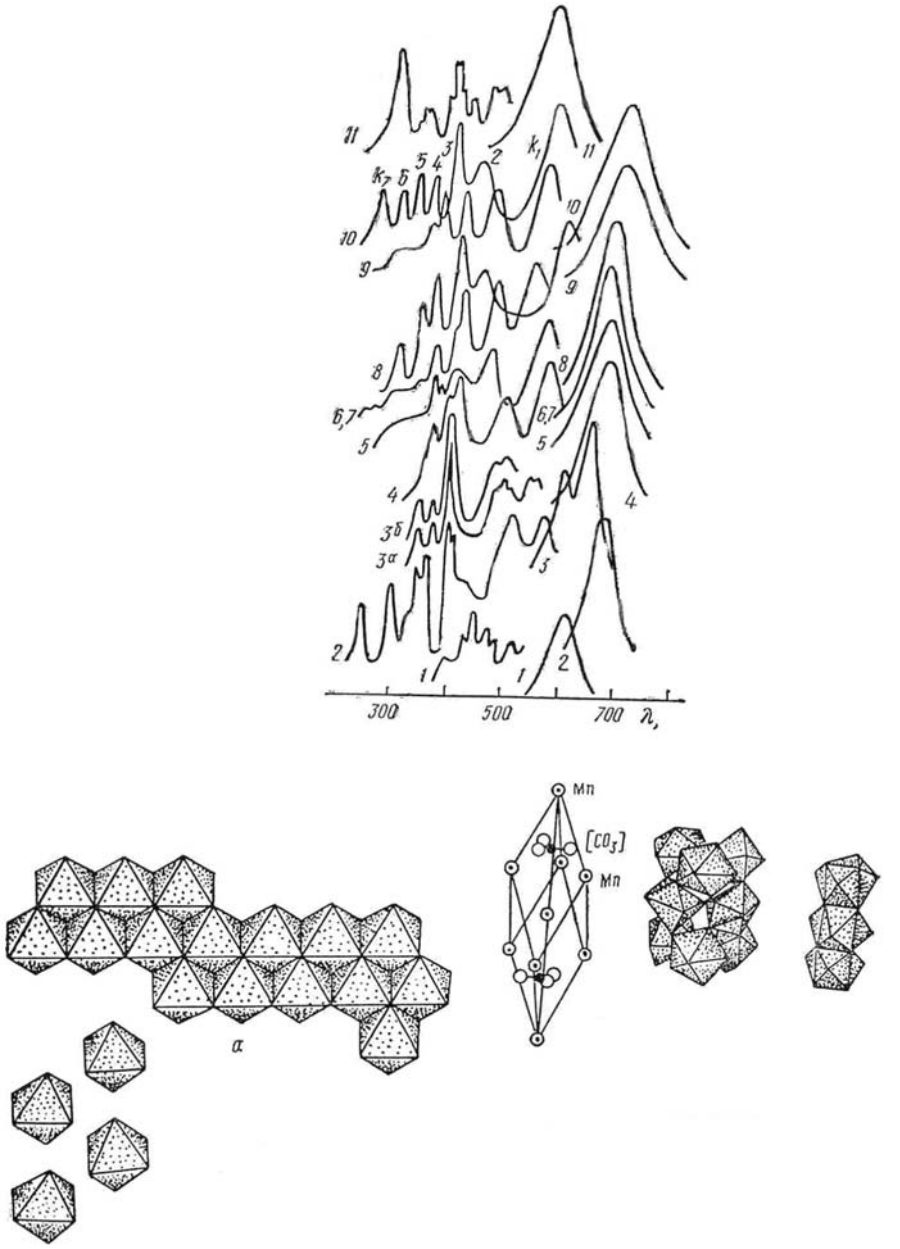

Fig. 5.48. Laser-induced luminescence of Mn bearing minerals (1-helvine; 2-severgenite; 3-Mn-milarite; 4-triplite; 5-rodonite; 6-rhodochrosite; 7-Mn-calcite; 8-Mn-curchatovite; 9- Mn-tantalite; 10-dgimboite; 11-Mn-apatite) and its connection with crystallochemical structure: *a*-rhodonite; *b*-rhodochrosite; *c*-Mn-apatite; *d*-carpholite ($MnAl_2(Si_2O_6)(OH)_4$ (Gaft et al. 1981)

is present on tetrahedral sites. Fe^{3+} in octahedral coordination is predicted to emit in the near IR at about 900 to 1,000 nm, but was not confidently observed in minerals. Steady-state luminescence of Fe^{3+} in minerals is mainly observed when it substitutes for Al^{3+} or Si^{4+} in tetrahedral sites in alumosilicates (Tarashchan 1978; White et al. 1986). It has luminescent transitions, which are forbidden and correspondingly the decay times are rather long. Zotov et al. (2002) studied the time-resolved luminescence of Fe^{3+} in volcanic glasses.

In the time-resolved luminescence, Fe^{3+} dominates spectra with long delay times. The examples may be seen in feldspars and obsidian (Fig. 4.43), wollastonite (Fig. 4.42b), zircon (Fig. 4.39d), and beryl (Fig. 4.52b).

5.4 s^2 Ions

In this case the filled *s* shell of a free ion gives rise to a $^1S_0$ ground state. The excited *sp* state gives a triplet $^3P_{0,1,2}$ for spins parallel and a singlet $^1P_1$ for spins antiparallel. In view of the selection rules, only the transitions between the singlets are allowed.

5.4.1 Bi^{3+}, Bi^{2+}

The luminescence of Bi^{3+} is quite diverse and depends strongly on the host lattice (Boulon 1987; Blasse and Grabmaier 1994; Blasse et al 1994). For the heavy $6s^2$ Bi^{3+} the transitions between the ground state and the $^3P_1$ state becomes additionally allowed by spin–orbit mixing of the $^3P_1$ and $^1P_1$ states. After excitation at low temperature, the system relaxes to the lowest excited state. Consequently, the emission at low temperatures can be ascribed to the forbidden transition $^3P_0$–$^1S_0$ and has a long decay time. Nevertheless, both $^3P_1$ and $^3P_0$ are emitting levels and they are very close so that at higher temperatures the luminescence from the $^3P_1$ level may appear with a similar spectrum, but shorter decay (Fig. 5.49).

Electron configuration of Bi^{2+} is $(6s)^2(6p)^1$, yielding a $^2P_{1/2}$ ground state and a crystal field split $^2P_{3/2}$ excited state (Hamstra et al. 1994). Because the emission is a 6*p* inter-configurational transition $^2P_{3/2}$–$^2P_{1/2}$, which is confirmed by the yellow excitation band presence, it is formally parity forbidden. Since the uneven crystal-field terms mix with the $(6s)^2(7s)^1$, $^2S_{1/2}$ and the $^2P_{3/2}$ and $^2P_{1/2}$ states, the parity selection rule becomes partly lifted. The excitation transition $^2P_{1/2}$–$^2S_{1/2}$ is the allowed one and it demands photons with higher energy.

5.4.1.1 Barite

Under short wave 266 nm excitation of barite two bands are detected: the intensive blue one peaking at 460 nm with a very short decay time of 100 ns

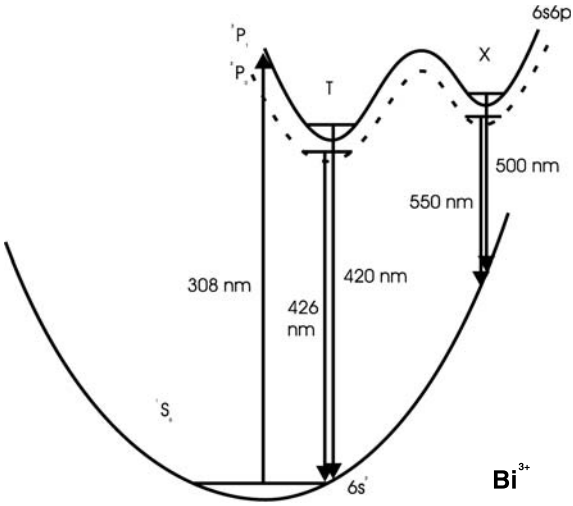

Fig. 5.49. Configurational coordinate diagram with emission and excitation transitions in Bi^{3+}

and the relatively weak narrow orange one peaking at 625 nm with a half-width of 30 nm and decay time of 5 μs (Fig. 4.30a). In order to present both bands in comparable magnitudes, the 1 μs delay is used to diminish the intensity of the short-lived blue emission. Such luminescence is not detected under longer UV laser lines.

It is interesting to note that the narrow orange band was first reported for synthetic $BaSO_4$:Bi in 1886 by Locoq de Buisbaudran. Half a century later this was confirmed and connected with Bi^{3+} luminescence (Kroger and Overbeek 1949). Another half a century later a new interpretation has been done and it was assumed that the luminescence center is Bi^{2+} (Hamstra et al. 1994). We also studied $BaSO_4$–Bi (Fig. 5.50) by the laser-induced time-resolved technique and under 266 nm excitation the narrow orange band, exactly similar to that in natural barite, has been found. Thus the connection of the narrow orange band in the luminescence spectrum of natural barite with Bi was confirmed. In an attempt to clarify its connection with Bi^{3+} or Bi^{2+} we used a step-like thermal treatment in air in order to stimulate Bi oxidation with possible change of valence state. In natural barite the narrow orange band totally disappeared after heating at 700 °C (Gaft et al. 2001a). Such behavior usually evidences that emission is connected with a luminescence center in the lowest valence state, namely Bi^{2+}.

Figure 4.30b represents luminescence spectra of natural barite after a long delay of 1 ms, when the emissions with a long decay time are emphasized and the narrow violet band at 426 appears. At liquid helium temperature this violet band becomes even narrower, shifts substantially in the short wavelength direction and its decay time of 3.1 ms becomes much longer (Gaft et al. 2001a). Such a band is absolutely similar to those detected in $BaSO_4$–Bi and ascribed to the Bi^{3+} luminescence center (Kroger and Overbeek 1949).

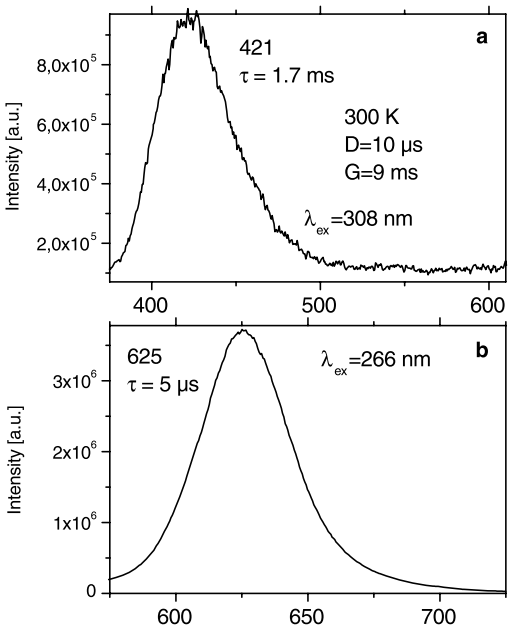

Fig. 5.50. **a,b** Laser-induced time-resolved luminescence spectra of $BaSO_4$:Bi

The only possible position for Bi^{3+} and Bi^{2+} in the barite lattice is in the Ba^{2+} site. The Ba ions in the structure of barite lie on the mirror planes and link the sulfate ions in such a way that twelve oxygen atoms coordinate each Ba. The exact ionic radius for Ba^{2+} in such coordination is unknown, but for coordination number 8 it is equal to 156 pm. Bi^{3+} in such a coordination has an ionic radius of 131 pm, which is very close. The exact ionic radius for Bi^{2+} is also unknown, but it has to be even bigger than for Bi^{3+}, which is compatible with the large ion Ba^{2+}, especially for isomorphous substitution, when the charge compensation is not needed. The large half-width of the Bi^{3+} luminescence band of 75 nm in barite is not surprising. It was observed that when Bi^{3+} is a substitute for the large ion the Stokes shift increases and very broad luminescence bands take place (Boulon 1987; Blasse and Grabmaier 1994). The large variation of Bi^{3+} luminescence is ascribed to the amount of space available for the Bi^{3+} ion in the lattice. The Bi^{3+} ion in the Ba position with coordination number 12 has enough space for relaxation after excitation with a resulting large Stokes shift and half-width. The magnitude of this shift depends on the details of vibrational relaxation in the excited and ground states, which, in turn depend on the interaction of the emitting ion with the adjacent coordination ions in the structure. The lower Stokes shift and half-width for Bi^{2+} indicate the weak interaction where configuration curves are essentially flat.

5.4.2 Pb^{2+}

All considerations above for Bi^{3+} are also relevant for Pb^{2+}, which also belongs to s^2 elements (or mercury like).

5.4.2.1 Calcite

Figure 4.14c demonstrates time-resolved luminescence spectra of calcite, Franklin, NJ, under 266 nm laser excitation. A very intensive UV band at 312 nm with a short decay time of 120 ns is detected. It may not be connected with Ce^{3+} emission, because its spectrum is situated at a substantially longer wavelength near 400 nm (Fig. 4.14e). The excitation spectrum of the band at 312 nm consists of one band at 240 nm (Gaft et al. 2003a).

Tarashchan (1978) already ascribed the UV luminescence band at 325 nm with an excitation band at 237 nm in pink calcite to Pb^{2+}. A decay time of 120 ns measured in our sample is consistent with such interpretation. Such a UV band was unique in the calcite collection at our disposal and ICP-MS analyses of its impurities have been done (Table 4.7). It was found that Pb concentration in Franklin, NJ calcite of 450 ppm is approximately 50 times higher than in pink calcite, taken for comparison sake, while its Ce content is more than 10 times lower. Those data confirm the connection of the UV band at 325 nm with the Pb^{2+} luminescence center.

The only possible position for Pb^{2+} in calcite structure is instead of Ca^{2+} with a coordination number of 6, where ionic radii of Ca^{2+} and Pb^{2+} are 114 and 133 pm.

5.4.2.2 Hardystonite

Luminescence spectra of hardystonite under 266 nm laser excitation reveal an extremely strong, rather narrow UV band at 355 nm, with a very short decay time of $\sim$ 25 ns (Fig. 4.20b). Usually such bands in minerals are attributed to Ce^{3+} luminescence. However as another band was already confidently ascribed to this center (Fig. 4.20a) assignment appears problematic. In principle it is possible that several different Ce^{3+} centers occur in a structure, which are formed, for example, as a result of substitutions on Ca and Zn positions or because of different types of charge compensations. The first possibility may be excluded based on the large differences in ionic radii of Ce^{3+} (115 ppm) and Zn^{2+} in tetrahedral coordination (74 ppm), while the second possibility may be taken into consideration.

In order to check this, the excitation spectra of both UV bands have been determined (Gaft et al. 2002a). It was found that the UV band ascribed to Ce^{3+} according to its luminescence and decay, has an excitation spectrum which is typi-

cal for this center, while the excitation spectrum of the UV band at 355 nm is different, containing one excitation band with a large Stokes shift of ~11,000 cm^{-1}. Thus it may be suspected that the UV band at 355 nm is connected not with Ce^{3+} in a different structural position, but with a different luminescence center.

The luminescence of Pb^{2+} in synthetic $Ca_2ZnSi_2O_7$ has been reported (Butler 1980). The emission and excitation peaks occur at 251 and 347 nm, respectively with a Stokes shift of 10,000 cm^{-1}. It is very close to luminescence and excitation bands detected in natural samples. In order to prove the possible relation of the UV luminescence band at 355 nm to Pb^{2+} in natural hardystonite, its decay time as a function of temperature has been studied. These decay curves are very specific for mercury-like ions, where the emission at low temperatures is ascribed to the forbidden transition $^3P_0$–$^1S_0$ and has a long decay time. Nevertheless, both $^3P_1$ and $^3P_0$ are very close emitting levels so that at higher temperatures the luminescence from $^3P_1$ level may appear with a similar spectrum, but with shorter decay (Boulon 1987; Blasse and Grabmaier 1994). In contrast, the decay times of the broad emissions of Ce^{3+} or Eu^{2+} are not temperature-dependent. At room temperature the decay time of the UV band in hardystonite at 355 nm is very short (~ 25 ns). Nevertheless, with decreasing temperature a very long decay component of approximately 150 µs appears while the luminescence spectrum remains practically the same (Fig. 5.51). This

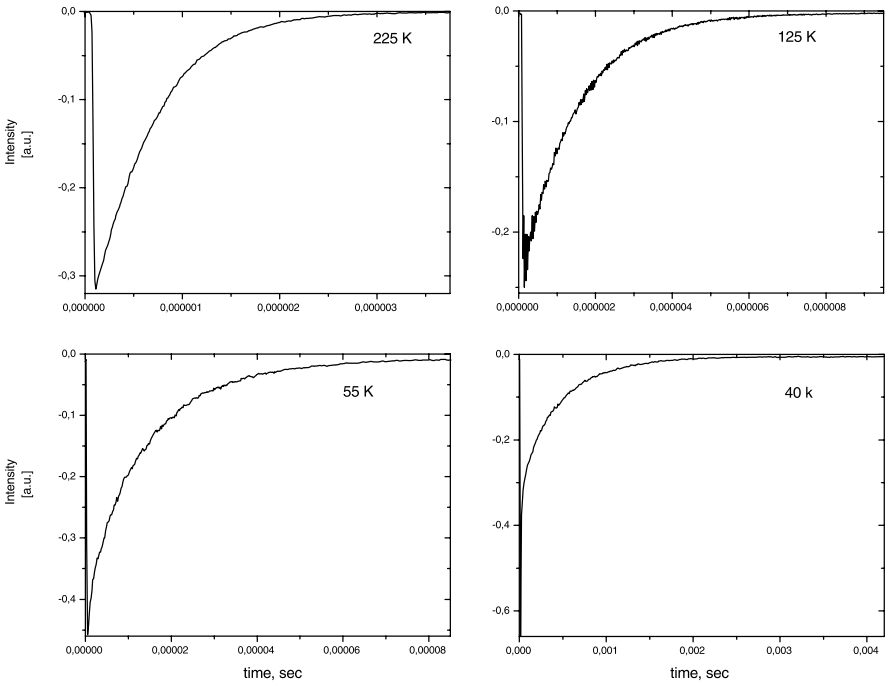

Fig. 5.51. Decay time of Pb^{2+} in hardystonite as a function of temperature

typical behavior is strong evidence that the emission band of hardystonite at 355 nm is caused by Pb^{2+}.

ICP analyses of the hardystonite sample in our study confirms a very high Pb content of 5,000 ppm, while the Ce concentration of 55 ppm is two orders of magnitude lower. This elevated Pb concentration may be the reason for a extremely short decay time at room temperature because of energy migration, with a corresponding decrease in decay time. The most likely position for Pb^{2+} in the hardystonite structure is at the Ca^{2+} site. The four-coordinated Zn site is less probable. Moreover, the difference between the ionic radii of Zn^{2+} and Pb^{2+} is quite large.

5.4.2.3 Hydrozincite

Figure 4.37a represents the time-resolved luminescence spectrum of a hydrozincite under 266 nm laser excitation. A relatively broad band is detected at 430 nm, which is responsible for the well-known blue hydrozincite luminescence. Its spectral position and decay time of approximately 700 ns are typical for Eu^{2+} luminescence. However, the excitation spectrum of this band consists of one narrow band at 240 nm (Fig. 4.37b), which does not correspond to an Eu^{2+} excitation spectrum. Two bands usually characterize the latter with relatively small Stokes shifts of 30 – 50 nm caused by crystal field splitting of the $4f^6 5d$-levels. Moreover, the measured Eu concentrations in the hydrozincite samples under investigation are very low (less than 0.5 ppm) and they do not correlate with the intensity of the blue luminescence, i.e. the band at 430 nm.

Three hydrozincite samples with different blue luminescence intensities were analyzed by ICP-MS. The first one with the strongest emission has 2,000 ppm of Pb, the second with weaker luminescence has 600 ppm, while the last one, practically without emission, has only 35 ppm. Such strong correlation supports interpretation of a Pb^{2+} luminescence center as responsible for the hydrozincite blue emission. In contrast, the Eu concentrations (another candidate for a luminescence center) are very low and do not correlate with the intensities of the blue luminescence.

In order to confirm the observed correlation of blue luminescence of hydrozincite with Pb^{2+}, artificial analogs of the mineral have been synthesized, activated by different amounts of Pb. It was found that the blue emission intensity increases with the Pb content, up to approximately 2,000 ppm, while a decrease of luminescence at higher Pb concentrations is evidently connected with concentration quenching (Gaft et al. 2002a). The only possible position for Pb^{2+} in the hydrozincite structure is the site of Zn^{2+}. Evidently, Pb^{2+} substitutes for Zn^{2+} in octahedral coordination where the crystal field splitting is especially strong, and this may be the reason for the long-wave Stokes shift of Pb^{2+} luminescence. Another reason may be the presence of hydroxyl groups, which strongly increase the crystal field splitting.

5.4.2.4 Barite, Anhydrite and Celestine

Luminescence of Pb^{2+} in synthetic alkaline earth sulfates is well known (Folkerts et al. 1995). In this study, $CaSO_4$:Pb^{2+} shows an emission band with a maximum at 235 nm at 300 K, while the excitation maximum is at 220 nm. The decay curve of the emission is single exponential with a decay time of 570 μs at 4.2 K. The emission spectrum of $BaSO_4$:Pb^{2+} demonstrates a broad band peaking at 340 nm with an excitation maximum at 220 nm, while in $SrSO_4$:Pb^{2+} the luminescence band has a maximum at 380 nm. In natural barite and anhydrite samples we detected several narrow UV bands, which may be connected with Pb^{2+} emission, but for confident conclusion additional study is needed. In any case, Pb^{2+} participation in natural sulfates luminescence has to be taken into consideration.

5.4.2.5 Minerals of Pb

5.4.2.5.1 Pyromorphite

As was described earlier, evidently Ce^{3+} emission in pyromorphite is characterized by a very long decay component, which is not typical for this luminescence center. The possible reason may be energy migration from Pb ions, which are the major elements in these minerals. It is well known that Pb^{2+} is a very effective sensitizer for many luminescence centers in minerals, including Mn^{2+} and REE (Marfunin 1979). The excitation spectrum of Ce^{3+} luminescence in esperite revealed a UV band at 280 nm, which is not typical for Ce^{3+} luminescence and is possibly connected with Pb^{2+} excitation with energy migration.

Besides that, narrow luminescence bands with long decay components in pyromorphite luminescence spectra may be in principal connected with Pb^{2+} emission. The main problem with the luminescence of elements with high concentration is the concentration quenching. Nevertheless, it was found that the concentration quenching of Mn^{2+} luminescence in Mn-apatite is nearly absent (Gaft et al. 1981). It was explained by the absence of energy migration by exchange mechanism in the apatite structure. Thus, the concentration quenching may be also negligible for Pb^{2+} in pyromorphite. A similar case is $PbSO_4$ where the luminescence of Pb^{2+} was found despite its high concentration. The simultaneous presence of two emission bands connected with Pb^{2+} is well known. For example, in $SrSO_4$:Pb^{2+} the emission spectrum shows an intense broad band with two maxima at 285 and 380 nm. It has been proposed that this luminescence originates from two different excited states: the shorter wavelength emission is assigned to the ^3P–S_0 transition, while the longer wavelength band is attributed to emission from an as yet unidentified D-level (Folkerts et al. 1995).

For example, narrow bands in pyromorphite luminescence spectra at 380 and 439 nm (Fig. 4.26) may be connected with Pb^{2+} emission. Two structurally

different Pb sites in pyromorphite structure may cause the two bands in the luminescence spectrum. For comparison, it was already mentioned that the luminescence of all impurity centers is drastically different at Ca(I) and Ca(II) positions in the isostructural mineral apatite because the crystal field strength of the Ca(I) position of the apatite structure is unusually strong. As a consequence, in pyromorphite it may generate a strong splitting of the ^3P excited level for the Pb(I) site with a strong separation between the $^3P_0$ and $^3P_1$ levels. Thus, the forbidden luminescence transition $^3P_0$–$^1S_0$ takes place with a long decay time. On the other hand, in the Pb(II) position the splitting is less, and an allowed $^3P_1$–$^1S_0$ transition takes place.

5.4.2.5.2 Cerussite

Cerussite is characterized by several broad luminescence bands in the green-yellow part of the spectrum with different decay times (Fig. 5.52). Those bands are not confidently interpreted yet and only recently the idea of Ag^+ or Cu^+ participation has been proposed based on their close radii with Pb^{2+} (Gorobets and Rogojine 2001). We think that such interpretation is principally logical and has to be checked, but the possible participation of intrinsic lead also may be considered.

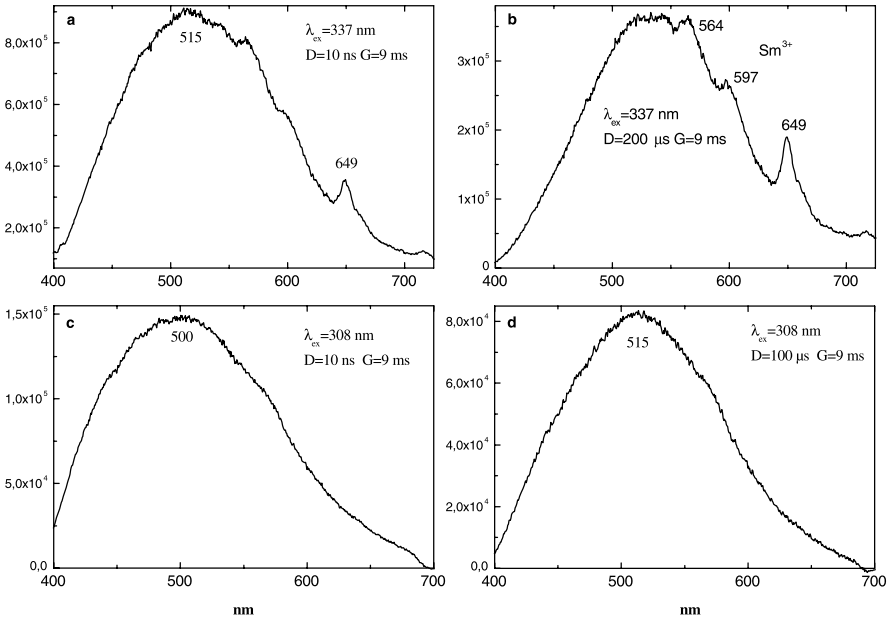

Fig. 5.52. a–d Laser-induced time-resolved luminescence spectra of cerussite

5.4.3
Pb^+

Luminescence of monovalent Pb was proposed for explanation of an IR luminescence band peaking at 860 nm in the emission spectrum of feldspars (Kusnetsov and Tarashchan 1988).

5.4.4
Tl^+

All considerations above for Bi^{3+} and Pb^{2+} are also relevant for Tl^+, which also belongs to the s^2 elements (or mercury like). In minerals its UV luminescence peaking at 290 nm was found in microcline, where the isomorphous substitution of K^+ for Tl^+ takes place (Kusnetsov and Tarashchan 1988).

5.4.5
Sn^{2+}

Center Sn^{2+} belongs to the $5s^2$ configuration. As an impurity in artificial phosphors it is mainly responsible for narrow luminescence bands from the UV to the red part of the spectrum. Besides that intrinsic luminescence of tin compounds is also known (Donker et al. 1989).

5.4.5.1
Cassiterite

Based on considerable zonation, which was found in CL spectra of cassiterite with respect to W and Ti impurities it was concluded that W is responsible for blue luminescence, while Ti for the yellow one (Hall and Ribber 1971). Luminescence of synthetic nominally pure SnO_2 have been studied (Agekyan et al. 1981) and it was concluded that the green-yellow broadband emission is connected with electron- hole pair formation under UV excitation with the following recombination. Nevertheless, in natural monocrystals of cassiterite it was found that as luminescence and excitation bands are strongly polarized in the direction perpendicular to the C_4 axes (Gaft and Vorontzova 1982). Evidently that is not complied with a recombination mechanism, because electron-hole pair formation does not depend on light polarization. It was also found that luminescence spectra under 250 nm excitation, where photon energy is larger than the energy gap of cassiterite, and 312 nm excitation, where photon energy is less than the energy gap, are different, namely green and yellow-orange bands, respectively (Fig. 5.53). It may be explained by different luminescence mechanisms, recombination in the first case and inner in the second.

In order to find the impurity responsible for the yellow emission, artificial SnO_2 have been studied activated by different impurities such as Ti, Nb, Ta, W, Fe (Gaft et al. 1982). From crystallochemical positions such ions are capable of substituting for Sn^{4+}. Nevertheless, the correlation of luminescence with

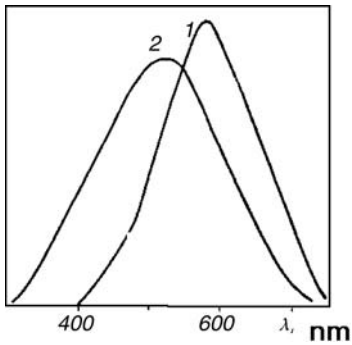

Fig. 5.53. Photoluminescence spectra of cassiterite under different excitations: 1–312 nm; 2–200 and 250 nm

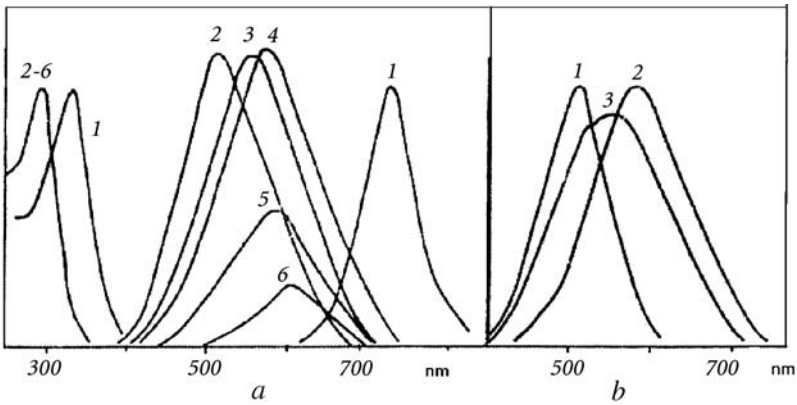

Fig. 5.54. **a,b** Photoluminescence and excitation spectra of pure SnO_2: **a** – at different temperatures: 1–4.6 K; 2–77 K; 3–120 K, 4–140 K; 5–180 K; 6–200 K; **b** – after thermal treatment and ionizing irradiation (all spectra at 77 K): 1 – original SnO_2; 2-heating in air at 1,500 °C during 3 h; 3-X-ray irradiation during 3 h of the sample heated at 1,500 °C

any impurity was not found. On the other hand, in nominally pure super pure SnO_2 all luminescence bands have been found, which were detected in natural cassiterite (Fig. 5.54). Thus it was concluded that luminescence is connected to intrinsic, namely to Sn of diverse valence, possibly Sn^{2+}. Studer and Blasser (1981) arrived at the same conclusion concerning the intrinsic nature of SnO_2 luminescence.

5.4.5.2 Barite

We studied laser-induced time-resolved luminescence of synthetic $BaSO_4$ artificially activated by Sn and found several intensive UV and blue bands evidently connected with Sn^{2+} emission (Fig. 5.55). Similar bands have been also found in natural barite laser-induced luminescence spectra and we think that their connection with an Sn center is quite possible.

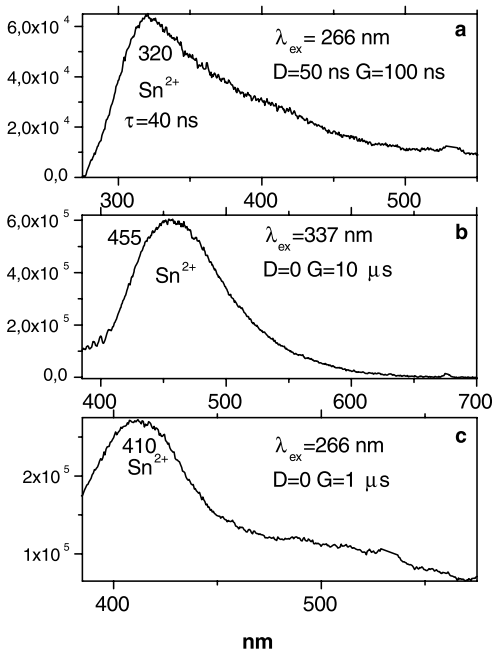

Fig. 5.55. **a–c** Laser-induced time-resolved luminescence spectra of $BaSO_4$–Sn

5.4.6 Sb^{3+}

This luminescence center is not detected in minerals yet, but is well known in synthetic phosphors, for example in halophosphates, which are closely related to hydroxyapatite (Blasse and Grabmaier 1994). The Sb^{3+} doped calcium halophosphate is a very efficient blue-emitting phosphor under short wave 254 excitation (Fig. 5.56). When the halophosphate host lattice contains not only Sb^{3+}, but also Mn^{2+}, part of the energy absorbed by the Sb^{3+} ions is transferred to Mn^{2+}, which shows an orange emission. By carefully adjusting the

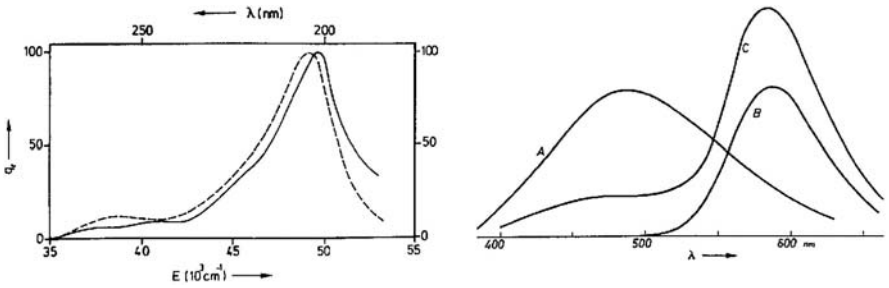

Fig. 5.56. Emission and excitation spectra of calcium halophosphates: *A*-Sb^{3+} emission; *B*-Mn^{2+} emission; *C*-warm-white halophosphate (Blasse and Grabmaier 1994)

ratio of the Sb^{3+} and Mn^{2+} concentrations, a white emitting phosphor can be obtained.

Another example is the luminescence of Sb^{3+} in YPO_4 with tetragonal zircon structure (Oomen et al. 1988). The emission consists of two bands, one in the UV region and one in the visible part of the spectrum. The intensity ratio of these bands is strongly temperature dependent (Fig. 5.57).

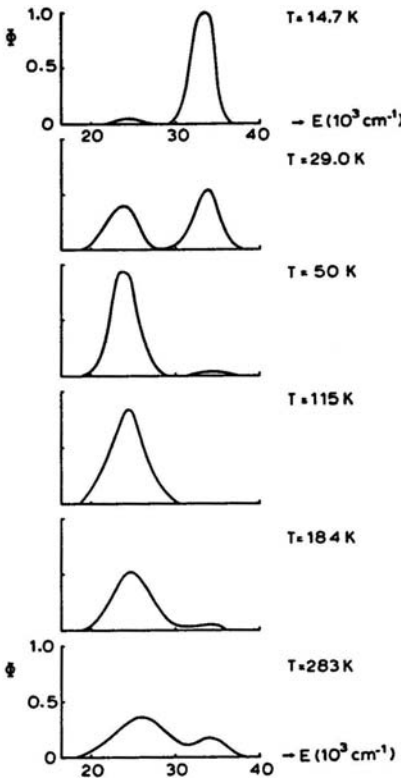

Fig. 5.57. Luminescence spectrum of YPO_4–Sb^{3+} (Oomen et al. 1988)

5.5 d^{10}-Ions

5.5.1 Ag^+

Complexes with monovalent d^{10} ions often show efficient luminescence at room temperature. The emission transition has been assigned to a d^9s–d^{10} transition, a ligand-to-metal charge-transfer transition, or a metal-to-ligand charge transfer transition, depending on the ligands (Boulon 1987). For the sulfur ligands a ligand-metal character is proposed as evident (Blasse and Grabmaier 1994). As in the case of Bi^3, the presence of several luminescence

bands with strongly different decay times may be preliminary connected with excited state splitting.

5.5.1.1 Barite

Figure 4.29 represents a typical laser-induced luminescence spectra recorded from natural barite with orange luminescence. At room temperature under 308, 337 and 355 nm excitations orange luminescence consists of a very broad band peaking at 635 nm with a half-width of approximately $\Delta = 150$ nm (Fig. 4.29a). At lower temperatures up to liquid helium the spectrum is very similar and only the half-width of $\Delta = 130$ nm becomes a little narrower (Fig. 4.29b). At all temperatures the spectra are not dependent on delay times and gate widths. The possible conclusion is that only one luminescence center is responsible for this orange band. The decay time of luminescence is approximately 225 µs at 300 K and 275 µs at 4.2 K.

Let us first discuss why the orange luminescence cannot be assigned to some obvious reasons. The host itself may be excluded, because pure barite is not luminescent. The usual luminescence center in minerals, which are responsible for broad orange bands with relatively long decay time, is Mn^{2+}. This possibility may be excluded also for the following reasons. ICP data reveals Mn impurity presence (Table 4.11), but the correlation between Mn concentration and orange luminescence intensity is absent. For example, two samples with the strongest orange luminescence have 3.5 and 400 ppm of Mn. Nevertheless, we prepared and studied synthetic barite artificially activated by Mn. As a result only an extremely weak green band with a very long decay time of 1 ms is seen, which is not detected yet in natural samples (Fig. 5.47a). According to EPR data ionic impurities of 4-fold coordinated Mn^{5+} were detected in barite (Greenblat 1980), while luminescence of Mn^{6+} in $BaSO_4$–Mn has been found (Brunold and Güdel 1997). It is possible to suppose that they are the main form of Mn in natural barite.

The possibility of Cr^{3+} emission may be excluded because octahedral coordination is absent in barite structure. Luminescence of Fe^{3+} is crystallographically possible because tetrahedral surrounding presents in barite structure but Fe^{3+} –S^{6+} substitution is very difficult to suppose. The iron presence in ICP data is evidently connected with micro-impurities of iron minerals, which is usual for natural barite. Other ions, such as Ti^{3+} and Ni^{2+} with possible red luminescence, have ionic radii of 81 and 83 pm, respectively, which are small compared to the 156 ppm of Ba^{2+}. ICP data confirm the absence of Ni in barite, while the minor quantities of Ti may be connected to Ti^{4+}.

In order to check the possibility of d^{10}-ions luminescence in the barite lattice, activation by Ag was accomplished (Gaft et al. 2001a). The main reason was that in all natural barite samples the Ag and Cu impurities have been determined by ICP analysis (Table 4.11). Besides that, weak orange luminescence on the tail of the strong UV band was detected in $BaSO_4$:Ag under X-ray excitation (Prokic 1979).

In $BaSO_4$:Ag (Fig. 5.58) three bands have been detected: red, green and UV. The red one peaking at 650 nm at room temperature has a half-width of 150 nm and decay time of 75 μs and its spectrum is similar to the broad orange band in natural barite. The decay time of this band in artificially activated barite is shorter compared to the natural one, which may be connected with higher Ag content with resulting concentration quenching. Ag^+ is very big ion with ionic radius of 142 pm for coordination number 8, which is close to those of Ba^{2+}.

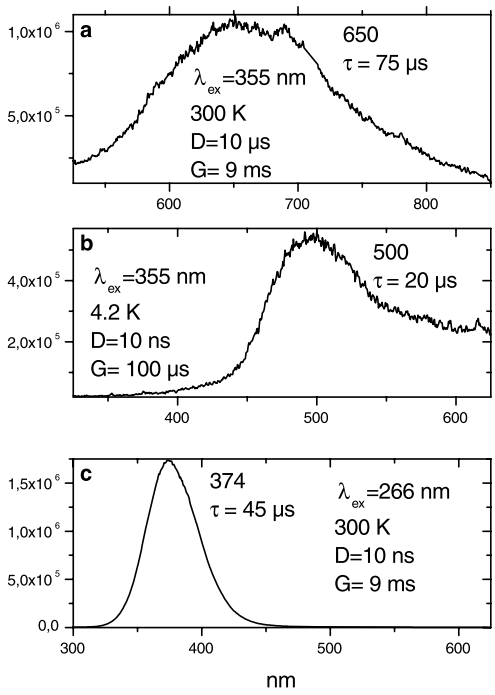

Fig. 5.58. **a–c** Laser-induced time-resolved luminescence of $BaSO_4$–Ag

5.5.1.2
Ag *Minerals – Chlorargyrite, Bromargerite and Embolite*

In this case emission is not connected with electron transitions inside the Ag^+ ion and may be interpreted in the energy band scheme (Gaft et al. 1989b). Under UV lamp excitation at 300 K those minerals do not exhibit luminescence but at the lower temperature of 77 K a very strong emission appears with a blue-green color for chlorargyrite, yellow-green for embolite and yellow-orange for embolite. The excitation spectra for all luminescence bands are similar and consist of one narrow UV band peaking at 350 nm. Under laser excitation luminescence appears even at 300 K (Fig. 4.66a) with a decay time of 200–250 ns. At 77 K the emission intensity becomes much stronger and the decay time substantially longer, approximately 3–6 μs. Time-resolved spectra

demonstrate that there is a minimum of two luminescence bands present with different decay times (Fig. 4.66b).

An interpretation was done based on investigation of synthetic silver halogenides (Vacek 1969; Vacek 1971). The blue emission band in AgCl is intrinsic and connected with electron-hole recombination. At temperatures higher than 77 K holes start to migrate and may be recaptured on the deeper traps and once again recombine with electrons. This process explains the luminescence color change at temperatures between 77 and 300 K. The orange emission of AgBr was connected with the Mn^{2+} impurity, while the yellow-green one with I impurity (Helder and Junod 1976). As for natural silver halogenides, under powerful laser excitation synthetic AgCl is also detected at 300 K, which is possibly connected with the higher density of excited states and the higher probability of luminescent transition.

5.5.2
Cu^+

Copper in minerals luminescence is usually considered only as an effective quencher. Nevertheless, it is well known that a bright blue luminescence is emitted from Cu^+ ions in inorganic solids by UV light irradiation. It was found that these materials have potential application to tunable lasers. For example, in $CaO–P_2O_5$ glasses Cu^+ is characterized by a luminescence band at 440 nm with a half-width of 100 nm and an excitation maximum at 260 nm. The decay time of luminescence is approximately 25 μs (Tanaka et al. 1994). Red fluorescence possibly connected with the Cu^+ pair is also known (Moine et al. 1991).

5.5.2.1
Barite

In $BaSO_4$:Cu two bands are detected: red and violet (Fig. 5.59). The red one peaking at 740 nm at room temperature has a half-width of 150 nm and decay time of 350 μs. The violet band peaking at 410 nm has at room temperature a half-width of 35 nm and decay time of 7 μs. At lower temperatures both bands disappear and the new IR one is detected. Such deep red luminescence in natural barite has been described earlier (Gaft et al. 1985) while the possible connection with Cu was not considered.

5.6
d^0 Complex Ions

Complexes of transition metal ions with a formally empty *d* shell often show intense broadband emission with a large Stokes shift of 10,000–20,000 cm^{-1}. The most important examples for minerals are VO_4^{3-}, WO_4^{2-}, MoO_4^{2-} and TiO_6^{8-}. Atomic orbitals *s*, *p*, *d* of the central atom and *p* orbitals of oxygen form molecular orbitals of the complexes (Fig. 5.60). The excited state is considered to

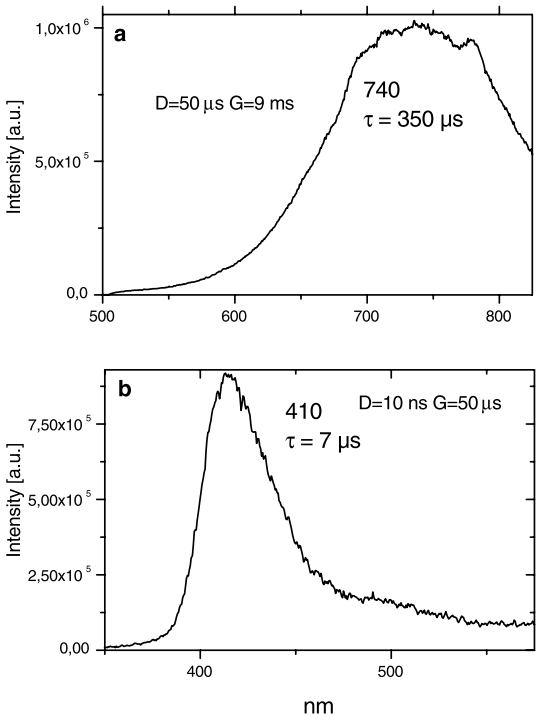

Fig. 5.59. a,b Laser-induced time-resolved luminescence spectra of $BaSO_4$:Cu

be a charge-transfer state, i.e. electronic charge has moved from the oxygen ligands to the central metal ion (Blasse 1980; Blasse and Grabmaier 1994). The real amount of charge transfer is usually small, but a considerable amount of electronic reorganization occurs, in which electrons are promoted from bonding orbitals in the ground state to antibonding orbitals in the excited state. The value of ΔR is large, the Stokes shift is large, and the spectral bands broad. Especially the complexes with the lighter metal ions show long decay times of their emission. The spin–orbit interaction is strong in WO_4^{2-} because of the high atomic number of W and the emission lifetimes decrease correspondingly. The lifetime of the blue emission of the WO_4^{2-} ion is as short as 10 µs, which is 10 times shorter than that of the MoO_4^{2-} and 100 times shorter than that of the VO_4^{3-} ion.

5.6.1 Scheelite – WO_4

The most important mineral example is natural scheelite. Scheelite emits a bright blue emission in a broad band centered at 425 nm (Fig. 4.9) with a decay time of several µs. Calcium tungstate $CaWO_4$ has long been known as a practical phosphor, and has been carefully studied. The intrinsic blue luminescence center is the WO_4^{2-} complex ion in which the central W metal ion is

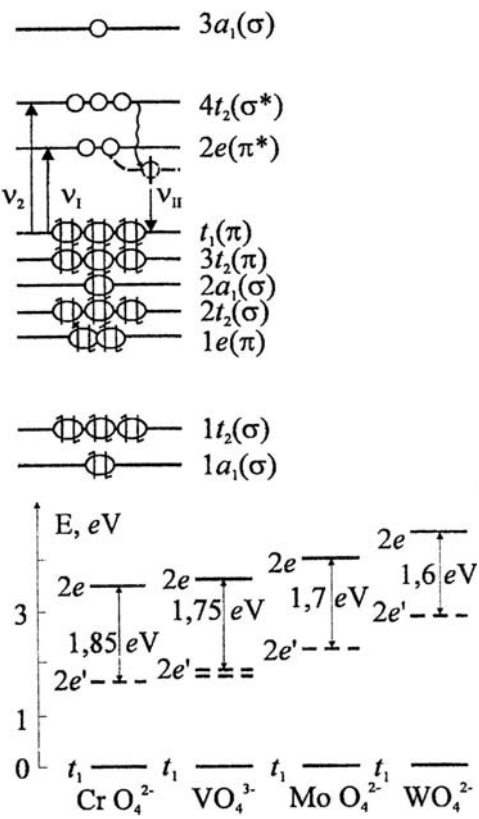

Fig. 5.60. Energy levels scheme in tetrahedral molecular ions CrO_4, VO_4, MoO_4, WO_4 (Tarashchan 1978)

coordinated by four O^{2-} ions in tetrahedral symmetry. It is widely accepted to use T_d symmetry to classify the terms and tentatively interpret the experimental data, while all of the modern work on tetroxo ions recognizes the fact that its symmetry is not maintained. Since the ground states $1t_2$, $1a_1$, $1e$, $2t_2$, $2a_1$, $3t_2$ and t_1 one electron molecular orbitals are occupied, the WO_4^{2-} molecular complex can be excited via the t_1–$2e$ transition to the following molecular terms: $^3T_1$, $^3T_2$, $^1T_1$ and $^1T_2$ resulting from the $(t_1^5, 2e)$ configuration. The lower lying triplet is believed to be responsible for luminescence (Fig. 5.60). Other analogous T_d complex is molybdate MoO_4^{2-}, which is considered to be responsible for the green luminescence in scheelite (Tarashchan 1978), but activation by Pb also generates a very strong green emission (Blasse 1997).

5.6.2
Pyromorphite – VO_4

Pyromorphite usually has an orange to yellow UV excited luminescence characterized by a broadband peaking at 580 nm (Fig. 4.26). It was earlier supposed

that such luminescence is connected with the $(VO_4)^{3-}$ emission center (Gaft 1984), but the possible role of Ag^+ also may be considered (Gorobets and Rogojine 2001).

5.6.3
Beryl – VO_4

The blue emission band in the beryl luminescence spectrum with a short decay time of 1 µs (Fig. 4.52a) can be connected with the $(VO_4)^{4-}$ complex, especially because a similar emission has been found in the radioluminescence spectrum of beryl with an elevated concentration of vanadium (Chithambo et al. 1995).

5.6.4
Benitoite – TiO_6

The luminescence of many titanium minerals was studied by steady-state luminescence spectroscopy and it was proposed that the blue luminescence bands mutual for these minerals is connected with TiO_6 complex luminescence (Gaft et al. 1981a; White 1990; Fig. 4.36). Figure 4.35 represents spectral properties of the blue emission from benitoite at 300 K. Under short and middle-wave UV laser excitation, such as at 266 and 308 nm, respectively, an intensive broad blue emission band peaking at approximately 420 nm with half-width of $\sim$ 80 nm is detected. Spectra with different excitations, delays and gates revealed that this band consists of only one component. The decay rate may be approximated by a mono-exponential curve with decay time of 2.6 µs. The excitation spectrum of the blue luminescence consists of a narrow band with half-width of 40 nm peaking at 290 nm and accompanied by the shoulder at 245 nm. At lower temperatures the luminescence efficiency becomes higher, while the spectral form is basically the same. At temperatures higher than room temperature the efficiency decreases and at 465 K is nearly quenched, while the band shape remains practically the same. Additional bands or shoulders do not appear at higher temperatures range. Decay curves at all temperatures remain monoexponential, but the decay time becomes substantially longer with reduced temperature, from 1.1 ms at 40 K to 200 ns at 465 K (Gaft et al. 2004a).

According to our experience all benitoite samples have intensive blue emissions under short wave and middle wave UV, and we have never seen or heard of any that did not. On the other hand, efficient luminescence has been observed from the TiO_4^{4-}, TiO_6^{8-} and even TiO_5^{6-} complexes. In addition, bazirite $BaZrSi_3O_9$ with the benitoite structure demonstrates luminescence of zirconate complexes ZrO_6^{8-} (Blasse 1980). The blue luminescence of impurity Ti^{4+} centers has been found in synthetic $BaSnSi_3O_9$–Ti^{4+} and $BaZrSi_3O_9$–Ti^{4+} with the benitoite structure (Konijenendijk 1981). We thus have strong evidences in favor of an intrinsic model for the blue luminescence in benitoite, connected with the TiO_6 octahedra. Hence we have tried to determine if the spectroscopic experimental data may be explained based on such a model (Gaft et al. 2004).

Figure 5.61 summarizes the temperature behavior of decay time τ and quantum efficiency η of the blue luminescence from benitoite in the forms $\ln(\tau)$ and $\ln(\eta)$ as a function of reciprocal temperature $1/T$. Figure 5.62.a demonstrates a suitable energy levels scheme. After excitation the metastable level 1 is populated due to nonradiative fast transition from excited level. Between levels 1 and 2 the equilibrium population is established due to nonradiative transition. The relative quantum yield of the blue emission may be described by simple Arrhenius equation:

$$\eta = \frac{1}{C\exp(-U/kT)} \tag{5.25}$$

where C is constant and U is energetic barrier between two closely spaced emitting excited states and excited level. The best fit to the experimental results is obtained when $U = 0.145$ eV or 1,150 cm^1. The decay time is determined by the equation:

$$\tau = \eta\frac{1 + \exp(-W/kT)}{A_1 + A2\exp() - W/kT} \tag{5.26}$$

where A_1 and A_2 are radiation transition probabilities between the ground state and the first and second excited emitting states, respectively, and W is the energy difference between the first and the second excited emitting states. The best fit with experimental data is obtained for $W = 0.06$ eV or 460 cm^{-1}.

Such an energy levels scheme is compatible with the TiO_6 complex. Figure 5.62.b represents a typical energy levels scheme for empty shell octahedral molecular complex centers. A molecular orbital calculation leads to e^* and t_1 states for the lowest unoccupied molecular orbital and the highest occupied molecular orbital, respectively. By taking the e-t_1 transition into account, the excited electronic states of $t_1^5 e$ electron configuration are found to consist of ${}^3T_{1u} \leq {}^3T_{2u} < {}^1T_{1u} < {}^1T_{2u}$ in order of increasing energy, with the ground state being a ${}^1A_{1g}$ state (Blasse, 1980).

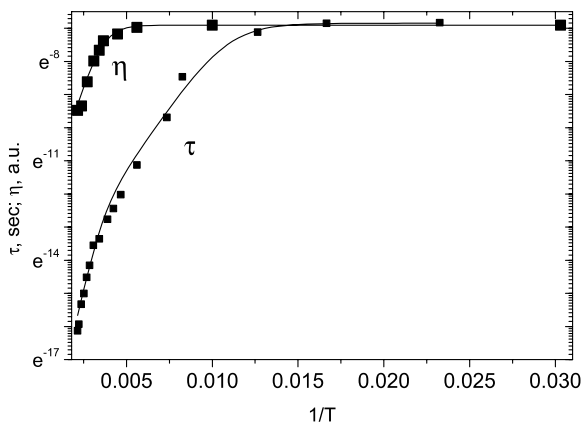

Fig. 5.61. Decay time and quantum yield of blue emission as a function of temperature: *dots* are experimental data and *solid lines* are best fit curves

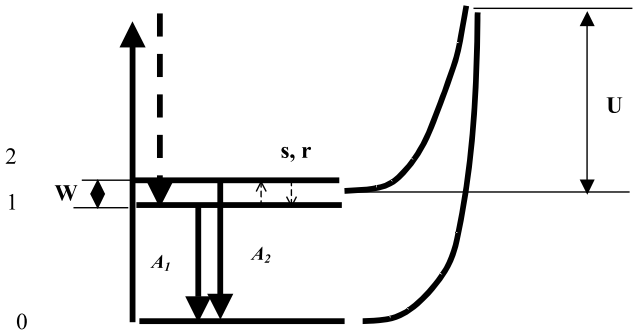

Fig. 5.62.a. Calculated energy levels cheme for blue benitoite luminescence

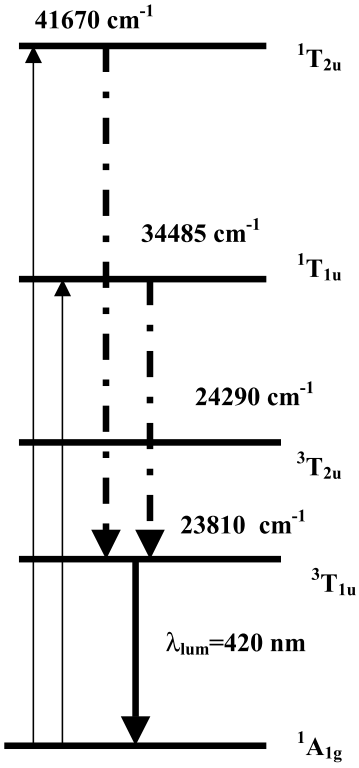

Fig. 5.62.b. Energy levels scheme for TiO_6 luminescence center in benitoite

Thus the excitation band at 240 nm may be assigned to the allowed $^1A_{1g} - {}^1T_{2u}$ transition, and the weaker band at 290 nm assigned to the formally forbidden $^1A_{1g} - {}^1T_{1u}$ transition. Because of very long decay time, the emission at low temperatures must originate from the parent $^3T_{1u}$ triplet states, because the $^3T_{1u}$ state is the only level which produces a sublevel from which a transition to the $^1A_{1g}$ ground state remains spin and orbitally forbidden. The presence

of a higher level with higher radiation probability may be connected with the splitting of the emitting ${}^3T_{1u}$ levels into levels of A_{1u}, E_u, T_{1u} and T_{2u} symmetry due to spin orbit coupling. The $T_{1u} - A_{1g}$ transition is allowed, while the others forbidden (Blasse, 1980). One of the latter levels can act as an optical trap, which explains the temperature dependence of the decay time. In view of the small energy difference between the ${}^3T_{1u}$ and ${}^3T_{2u}$ levels, the ${}^3T_{2u}$ level may also play a role in the luminescence process at high temperatures.

5.7 Molecular Centers

5.7.1 Uranyl $(UO_2)^{2+}$

Uranyl is formed due to σ and π bonds of $5f$, $6d$, $7s$ electrons of the uranium atom and $2p$ electrons of two oxygen atoms. Molecular orbitals of uranyl are formed by the interaction of atomic orbitals of uranium and oxygen with the same type of symmetry and close energy levels. Bonding orbitals $1\sigma_u$, $1\sigma_g$, $1\pi_u$, $1\pi_g$ are filled with electrons with antiparallel spin directions. Nonbonding orbitals $1\sigma_g^*$, $1\sigma_u^*$, $1\pi_g^*$, $1\pi_u^*$ and so on are empty and form excitation levels. The ground state of uranyl is $1\sum_g^+$, which is a singlet with summary spin 0 and a center of symmetry. The excited state of uranyl is split. It has levels of different symmetry types A_{2g}, E_{2g}, A_{1g} and so on. These levels are split, in their turn, due to electron=phonon interaction forming a system of vibrational sublevels owing to vibration of oxygen atoms in uranyl. Absorption of photon by uranyl results in electron transition from the upper filled orbital $1\pi_g^4$ to one of excited levels of empty orbitals $1\delta_u$ and $1\varphi_u$ with vibrational sublevels. Electron transition in the opposite direction results in the emission of photon. Its energy is about $k_0 \approx 2 \times 10^{-4}\ \mathrm{cm}^{-1}$. This is a zero-phonon electron transition. Its peak is accompanied by a series of electron-phonon lines (Fig. 5.63). A feature distinguishing the molecular excitation and luminescence spectra of UO_2^{2+} is the fact that they arise from the transitions between electron-vibrational levels, i.e., the levels of electronic states split into sublevels whose spacing equals the vibrational frequency of the molecule (Marfunin 1979b). The color of luminescence of uranyl in different minerals is variable from a green-blue to orange-red and the mean frequency interval alters from 840–880 to 680 cm^{-1}, correspondingly. The UO_2^{2+} always exhibits comparably long decay times in the range of 60–600 µs (de Neufille et al. 1981; Gaft 1989). Some of them fluoresce strongly at 300 K, some relatively weakly and others do not fluoresce at all. The emission of some of the weakly fluorescent uranyl minerals is dramatically increased by cooling to 77 K. The differences in the luminescence parameters are connected with the energy migration probability between the uranyls which, in turn, depends on the mineral structure, the connection type between various uranyl units and the chemical nature of ligands which interact with uranyl (Gorobets and Sidorenko 1974; Sidorenko et al. 1986; Gorobets and Rogojine 2001).

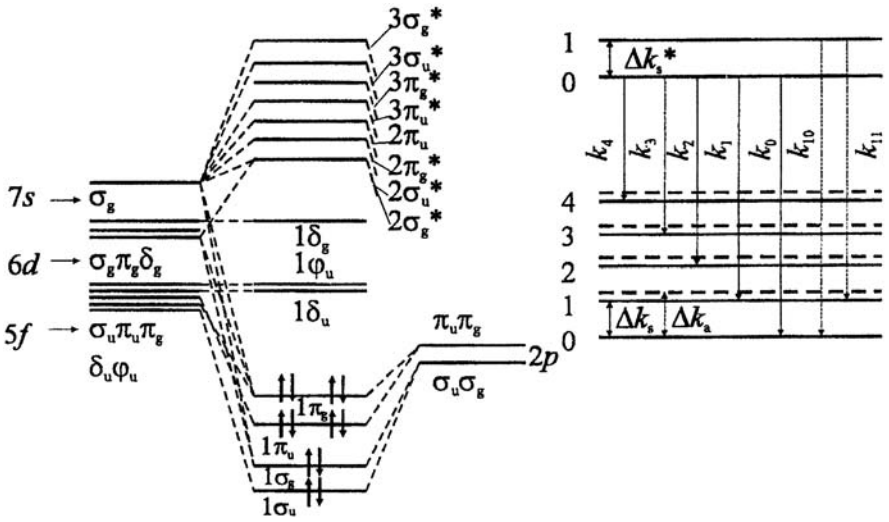

Fig. 5.63. Molecular orbitals scheme of UO_2 (Marfunin 1979b)

5.7.1.1 Apatite

Sedimentary carbonate-fluor-apatite $Ca_5(PO_4,CO_3)_3F$ is not luminescent under X-rays, and under UV lamp excitation it is characterized by broad structureless bands which are very similar to those encountered in many sedimentary minerals. It was concluded that this luminescence is due to different kinds of water-organic complexes (Tarashchan 1978). For this reason the luminescence properties of the sedimentary apatites is much less informative compared to magmatic apatite and attracted not much attention.

Carbonate-fluor-apatite accommodates large quantities of trace elements, mainly uranium, which are potential luminescence centers. It has been proposed that uranium may occur in phosphorites in the following forms: as a separate uraninite phase; as an adsorbed or structurally incorporated uranyl ion; as a dominantly U^{4+} replacement for Ca^{2+}, to be structurally incorporated appreciably as both U^{4+} and U^{6+} (Altshuller 1980).

The steady-state luminescence of water-organic complexes is strong and conceals the weaker characteristic luminescence of uranium containing centers, which can be detected by the difference in decay times only. The reason is that the decay time of water-organic complexes is characterized by two time intervals: less then 30 ns and more then 10 ms. Since the uranium centers have decay times in the microseconds range, it is possible to detect them by time-resolved spectroscopy. In the time-delayed laser-induced spectroscopy, the luminescence spectra are recorded at a fixed moment after a laser pulse. These spectra may be different from the integrated steady-state ones since after a certain time short luminescence will be practically absent.

Thermal treatment has great influence on luminescence spectra. Certain cations may change valence and accommodation form during heating, with transformation from a nonluminescent form to a luminescent form.

Spectra of the laser-induced luminescence of apatites with the long decay time (more then 1 μs) consist of several sets of relatively narrow bands in the green part of the spectrum, which are characterized by the clear vibrational structure (Panczer et al. 1998). The first type contains at 300 K the characteristic set of maxima at 484, 504, 526, and 546 nm. At 77 K the intensity only slightly increases, the spectrum is nearly the same, but the structure is more pronounced (Fig. 4.4c). The luminescent decay measured at 526 and 504 nm may be represented by the exponential fitting with the main decay component of 350 μs. The second type contains at 300 K the set of bands at 467, 486, 505, 526 and 547 nm (Fig. 4.4b). At 77 K the intensity is much stronger, the band at 467 nm disappears and the other bands are narrower. The quenching of the emission monitored at 526 nm at 300 K may be represented by the exponential fitting with the main decay component of 200 μs. The third type contains at 300 K the bands at 508 and 524 nm which are the strongest at 77 K (Fig. 4.4a). The quenching of the emission monitored at 524 nm at 300 K may be represented by the exponential fitting with the main decay component of 300 μs.

Luminescent properties under UV excitation of the sedimentary phosphorites are strongly changed after the oxidizing thermal treatment. Thermal annealing at temperatures of up to 600 °C did not cause spectral changes, but above that temperature drastic alteration took place. The spectra at 300 K are characterized by a very strong structureless band with a maximum at 527 nm. The decay curve has the main component of $\sim$ 110 μs. At 77 K the spectrum is strongly changed with the intensive narrow line at 522 nm (Fig. 4.4d). The decay is substantially slower with the main component of $\sim$ 280 μs.

The spectral-kinetic parameters of the green laser-induced luminescence of the sedimentary apatites allow its association with UO_2^{2+} emission. The spectra presented in Fig. 4.4b,c are typical for uranyl minerals and it is possible to suppose that we are dealing with a separate uranyl mineral phase on the apatite surface. Comparison with known uranyl minerals laser-induced luminescence shows that minerals andersonite $Na_2Ca(UO_2)(CO_3)_3 \times 6H_2O$ and liebigite $Na_2(UO_2)(CO_3)3 \times 10H_2O$ have the most similar spectral-kinetic parameters, but this identification is ambiguous.

The spectra of the green laser-induced luminescence represented in Fig. 4.4a, together with their decay time, also allows its association with UO_2^{2+}. These luminescence spectra strongly differ from the spectral parameters of all known uranyl minerals. For this reason it is not possible to connect this type of green luminescence with finely dissipated uranyl phases. On the other hand, this luminescence is very similar in such different host minerals as sedimentary apatites, opalites, chalcedony, chert, quartz and barites. Luminescence independence from the minerals structure evidences that it may be connected with uranyl adsorption on the minerals surface, supposedly in the form of $(UO_2 \times nH_2O)^{2+}$.

When the samples are heated the emission spectra are much less structured, more intensive and short-lived. It is known (Reisfeld and Jörgensen 1977) that uranyl, which is a linear triatomic molecule, can form complexes with ligands in the equatorial plane. When OH-group or F are the complexing species, the bond is very weak since there is no significant overlap of the molecular orbital of the ligands with those of the uranyl. As a result, a well resolved spectrum is obtained, resembling gaseous molecules, resulting from the electron transitions from the oxygen to the 5*f* orbitals of the uranium. The spectra become much less resolved with stronger ligands occupying the ecvatorial plane. When water molecules are evolved at elevated temperatures, the OH groups disappear and, probably, P-ligands become strongly bounded with uranyl orbitals in the ecvatorial plane. The spectrum becomes less distinct, the intensity increases because of the less pronounced presence of a center of inversion which makes the parity-forbidden transitions in uranyl more allowed and correspondingly this is followed by shortening of the decay time.

Spectral parameters of the structured green luminescence (Fig. 4.4d) are absolutely similar to those of U^{6+} luminescence in fluorite after thermal treatment (Tarashchan 1978). Principally, during the calcination of the sedimentary phosphates new mineralogical phases, including fluorite, may be formed. Taking these data into account, it is possible to conclude that after thermal treatment uranium is concentrated in the fluorite lattice in the form of U^{6+}.

It is interesting to note that in magmatic apatites the luminescence of uranium containing centers have not been discovered before or after oxidizing heating. Thus it is reasonable to suppose that uranium is present mainly in the U^{4+} form. The U^{4+} with an ionic radius of 0.97 Å may be located in the apatite structure instead of Ca^{2+} with the ionic radius of 0.99 Å. The most likely way for achieving the excess charge compensation is the Na^{+} for Ca^{2+} structural substitutions.

5.7.1.2 Minerals of Uranyl

The luminescence of uranyl minerals is connected with uranyl emission. Energy migration plays a very important role and its behavior was well analyzed by Gorobets and Rogojine (2001). In carbonates there is no energy transfer between $(UO_2)^{2+}$ and they therefore give a bright blue-green emission at 300 K with a maximum decay time of approximately 600 μs, narrow spectral lines and a large vibration constant of 820–840 cm^{-1}. In sulfates, phosphates and arsenates, uranyl ions are bound more strongly and their luminescence is green with decay times, vibration constants and temperatures of quenching a little lower. In silicates, vanadates, molybdates and hydroxides of uranyl strong exchange interaction and energy transfer takes place. In this case, the luminescence decay time falls to approximately 100 μs and vibration constant decreases to 750–680 cm^{-1}. Yellow, orange and red luminescence of these minerals can be observed at low temperatures.

5.7.1.3
U^{4+}

The reabsorption lines of U^{4+} have been found in zircon (Gaft et al. 1986) luminescence spectra. The strongest reabsorption lines at 592 and 656 nm are (Fig. 4.39b) clearly seen, which are totally identical to absorption lines of U^{4+} in zircon (Platonov et al. 1989).

5.7.2
O_2^-, S_2^- and F-Centers

A distinctive feature of the O_2^- and S_2^- luminescence spectra in minerals is a quasi-linear vibrational structure of the broad luminescence band (Tarashchan 1978). The O_2^- and S_2^- molecular ions are isoelectronic. From the molecular orbital diagram describing their electron structure the emission transition $^2\Sigma_g - ^2\Pi_{3/2}$ is determined. When observing luminescence spectra at 77 K, a fine structure associated with the frequency of intra-molecular vibrations of O_2^- and S_2^- is detected. This frequency depends on the type of the molecular ion, on inter-nuclear distance and upon the particular position of the molecular ion in the structures. For S_2^- the maximum of the emission band lies within the range of 600–700 nm with a mean vibration frequency of 500–600 cm^{-1}, while for O_2^- the respective maximum is 450–550 nm with a frequency in the 800–1,200 cm^{-1} range.

Time-resolved luminescence spectroscopy of sodalite evidences that the vibration structure has a very short decay time and disappears after a delay of 250 ns. Such structure is superimposed on the very broad IR band (Fig. 4.65).

5.8
Radiation-Induced Centers

5.8.1
Zircon

Figure 4.39a represents the luminescence band detected in all investigated natural zircons. It has an excitation band peaking at 310 nm. The broad yellow band at 575 nm with a decay time of 25–35 μs represents "classical" zircon luminescence. The picture is not principally changed with different delay times and gate width. After heating the sample up to 700 °C the luminescence intensity is nearly the same, but after that it is strongly reduced and at 800 °C the yellow luminescence disappears. Luminescence spectra at 77 and 4.2 K are not substantially different.

As was already mentioned, the origin of this band was ambiguous. In order to clarify this we studied the irradiation influence on laser-induced time-resolved luminescence of the following samples (Gaft et al. 2003b):

- $ZrSiO_4$ activated by Eu with characteristic narrow Eu^{3+} lines and irradiated by different doses of thermal neutrons;

- $ZrSiO_4$ activated by Ca and P practically without luminescence and internally irradiated by alpha particles;
- Natural zircons heated at 800 °C during one hour when natural yellow broadband luminescence nearly totally disappears and irradiated by different doses of alpha particles.

Non-irradiated $ZrSiO_4$–Eu is characterized by strong orange luminescence (Fig. 5.64a). After n-irradiation a broad yellow luminescence band appears, which is much stronger then the original Eu^{3+} emission. Such yellow luminescence is proportionally stronger with increasing irradiation time (Fig. 5.64b,c). Strong broadband yellow luminescence appears also after alpha-irradiation in $ZrSiO_4$–Ca/P and in natural zircon after heating at 800 °C, which were not luminescent before irradiation. Investigation made at 300 and 77 K with different laser excitations, delays and gates proved that despite of a very broad half-width and apparently asymmetric form, luminescence consists of only one band. Both for alpha and neutron irradiations, such induced luminescence is stable with time and in our study it has been detected several years after irradiation. The spectral shape of this radiation-induced luminescence is very close to that of natural zircon samples. Its decay time is of approximately 30–35 μs and the intensity remains stable under the heating up to 700 °C, which is characteristic for natural samples. Thus according to our knowledge it may be unequivocally concluded that the "classical" yellow luminescence band in natural zircon with λ_{max} = 575 nm, half-width Δ = 160 nm, decay time of

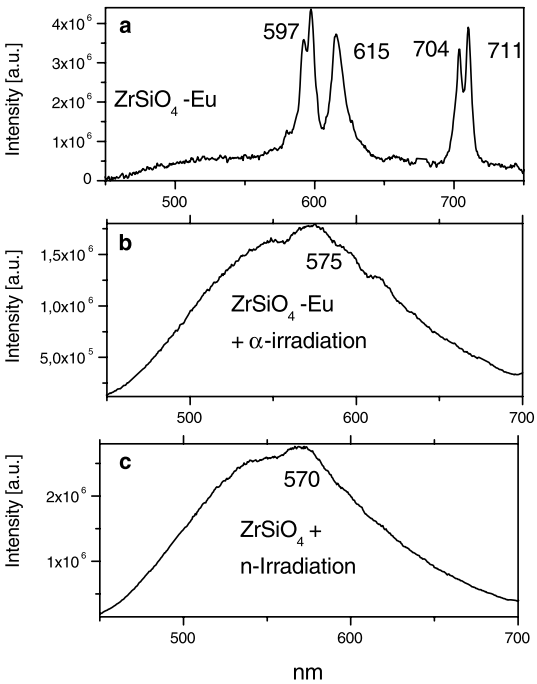

Fig. 5.64. a–c Laser-induced time-resolved luminescence spectra of $ZrSiO_4$–Eu^{3+} (**a**) irradiated by α-particles and neutrons

$\tau = 30-35$ µs and thermally stable up to approximately 700 °C is connected with radiation induced centers. In minerals, the source of irradiation may be connected with the radioactive decay of U and Th impurities.

For the interpretation of such centers it is important to note that yellow luminescence is connected only with neutron and alpha irradiations and not generated by higher doses of X-rays, beta and gamma irradiations. Thus corresponding centers have to be specific only for neutron and alpha treatment. According to EPR data (Hayashi et al. 1990) the neutron irradiation produces four typical signals in $ZrSiO_4$ with $g = 2.000$, 2.001, 2.003 and 2.008, while gamma-ray irradiation produces only the first two signals. The last one is completely extinguished already eight months after irradiation, while the signal with $g = 2.003$ remains. Laser-induced luminescence in our study is detected even 10 years after irradiation and it is possible to suppose that it is connected with the radiation-induced center with $g = 2.003$. Such values of g-factor corresponds to SiO_m^{n-} structural defects. Thermal stability of SiO_m^{n-} defects have been studied by EPR and compared with those of integrated yellow zircon luminescence. It was found that any correlation is absent (Gaft et al. 1986). Thermal stability of the radiation-induced part of yellow luminescence is correlated with those of SiO_m^{n-} structural defects (Fig. 5.65), but SiO_m^{n-} defects are easily reproduced by X-ray irradiation after heating, while yellow luminescence is not. Thus the exact type of the yellow luminescence center needs further clarification.

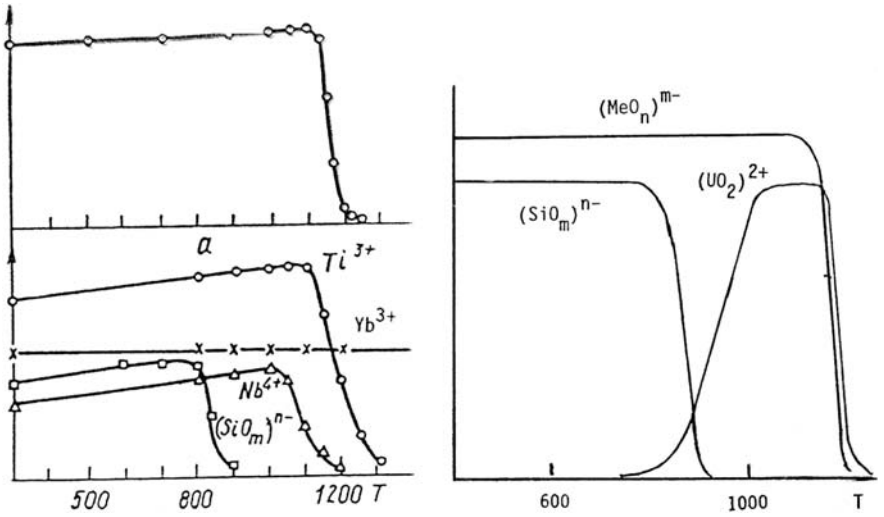

Fig. 5.65. Comparison of radiation-induced luminescence and EPR of different centers as a function of the heating temperature. *Left*: integrated yellow luminescence (*upper*) and EPR of Ti^{3+}, Yb^{3+}, Nb^{4+} and SiO_m^{n-} (*lower*). *Right*: yellow luminescence bands of different origin with different thermal stability (Gaft et al. 1986)

5.8.2 Calcite

The violet emission of the radiation-induced center $(CO_3)^{3-}$ is well known in steady-state luminescence spectra of calcite (Tarashchan 1978; Kasyanenko, Matveeva 1987). The problem is that Ce^{3+} also has emission in the UV part of the spectrum. In time-resolved luminescence spectroscopy it is possible to differentiate between these two centers because of the longer decay time of the radiation-induced center. Its luminescence peaking at 405 nm becomes dominant after a delay time of 100–200 ns while emission of Ce^{3+} is already quenched (Fig. 4.14f).

Another evidently radiation-induced band occurs in the orange part of spectrum. Under long waved UV and visible excitations the band peaking at 600 nm is detected with half-width of 95 nm (Fig. 5.66a). Excitation spectrum of this emission contains for maxima peaking at 345, 360 and 410 nm (Fig. 5.66b). The band is evidently not symmetrical with shoulder at 625 nm, but such form remains in all time-resolved spectra with different delays and gates and does not resolved to several emission bands. This band can be detected with extremely narrow gate width, which is a strong evidence that its decay time is very short, approximately 10–12 ns, which is on the border of our experimental system ability. At 40 K the band becomes extremely intensive, while its spectrum and decay time remain practically the same.

Such short-lived orange emission is thermally very unstable and after heating the sample at 180–220 °C this band disappears. Such behavior is compatible with radiation-induced thermally not stable centers. This model is confirmed

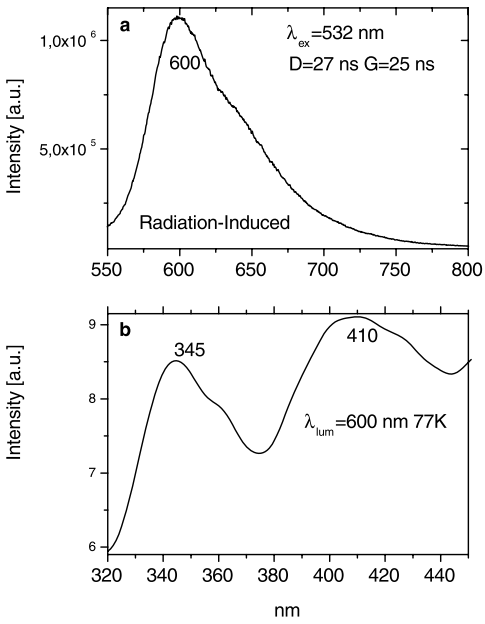

Fig. 5.66. Laser-induced time-resolved luminescence spectrum (**a**) and excitation spectrum (**b**) of radiation induced center in calcite

by the fact that such orange luminescence is especially strong in the red colored parts of calcite, which also disappears with the heating synchronous with the orange luminescence. Color centers generating such red tint have been interpreted as radiation-induced centers (Platonov, 1978).

5.8.3 Topaz

Color centers in topaz can be produced by irradiation with fast neutrons and gamma-rays (Platonov et al. 1989). It was found that luminescence bands are connected with such color centers, which may be detected by steady state and time-resolved spectroscopy (Marques et al. 2000). The detected luminescence bands have been connected with both impurities and structural changes.

5.8.4 Interstellar Matter

Simulated interstellar matter, such as forsterite, enstatite and magnesite, has been irradiated by gamma-rays and fast neutrons and their induced spectra have been investigated. For the forsterite and magnesite after irradiation the spectra exhibit rather intensive peaks at approximately 650 and 660 nm, respectively. Besides that, forsterite demonstrates several narrow lines the strongest one at 610 nm (Koike et al. 2002).

5.9 Reabsorption Lines of Oxygen and Water

5.9.1 Apatite-Luminescence Spectroscopy

The laser-induced time-delayed (more then 1 μs) luminescence spectra of magmatic and sedimentary apatites contain several "negative" lines at the red part of the visible spectrum (Fig. 4.6). The correlation analyses reveal that this group is subdivided into two (Gaft et al. 1997c): the strongest line at 760 nm accompanied by the weaker line at 687 nm; a doublet at 720 nm accompanied by a triplet at 823 nm. The following results allow us to conclude that these lines are not connected with noise or artifacts: the spectral features are "negative", thus they may not be connected with second order lines or incidental sources of light; the spectrum is presented without any smoothing or other mathematical treatment.

It is clearly seen that negative lines are much stronger then the noise. Besides that, the negative lines are always situated at the same places. The invariability of the spectral positions provides the evidence that they are not connected with fluctuations of the laser pulses and detection system. Thus it may be concluded that we a dealing with a reabsorption mechanism. The optical absorption spectra of natural apatites in the range 600–900 nm contain several lines and bands connected with Nd^{3+}, Pr^{3+}, Mn^{5+}, SO_3^- (Gorobets 1975;

Gilinskaya and Mashkovtsev 1994) but they do not coincide with the negative lines detected in our study. The optical spectroscopy data connected with other minerals and solids have been also checked, but all attempts were unsuccessful (Platonov 1979).

Nevertheless, these absorption lines though not previously mentioned in solids are well known to absorb the visible light in the atmosphere (Measures 1985). The strongest absorption lines of molecular oxygen are named as the *A*-band, or 760 nm, and *B*-band, or 687 nm. The 760 nm band is extremely famous in the field of astronomy, because its presence in the atmosphere is used as a test of photosynthetic activity on a distant planet. The strongest absorption lines of water in the visible range consist of a doublet at 718 and 729 nm and a triplet at 818, 823 and 829 nm, which exactly coincide with reabsorption lines in apatite. These is a striking identity between the reabsorption spectrum of the apatite and absorption spectrum of the atmosphere determined with high spectral resolution and signal to noise ratio (Kuze and Chance 1994). Not only the strong lines, but also the weak ones are the same. Even the splitting of the *A*-band is similar in both cases. It consists of the narrower and more intensive line situated at 760 nm and the broader and less intensive one situated at 763 nm.

The absorption of molecular oxygen and water in the air is very weak. It is explained by the energy levels scheme (Fig. 5.67) of molecular oxygen and water (Wallace and Hunten 1968; Castellan 1993). The corresponding electron transitions to excited states, which give rise to absorption bands of molecular oxygen and water, are forbidden on the bases of spin and symmetry. The low transition probability is reflected in the long radiative lifetime of 7 seconds from the $^1E_g^+$ state of molecular oxygen. Why in such cases is the absorption in apatite relatively strong? One possible explanation is that this forbiddenness, strictly observed in the spectra of free molecules, is less stringent inside crystals where forbidden transitions often occur owing to interaction with heavy metal impurities, such as U, Fe, Mn, which are responsible for spin–orbit coupling relaxing to some extent the forbiddenness of the spin-forbidden transitions. It is worthwhile to note that the long lifetimes are in the limit of the zero pressure and may be considerably modified even by perturbations from surrounding gases.

The next interesting problem is why reabsorption lines disappear at liquid nitrogen temperature? In the emission-reabsorption process both centers behave as independent systems, and do not interact directly. Thus energy migration is not temperature dependent. The possible explanation is that at liquid nitrogen temperature (77 K) the oxygen and water exist not as gas and liquid, but as liquid and solid, correspondingly. It is known that in the spectra of condensed or compressed oxygen there are bands that are not due to transitions of isolated O_2 molecules. They are attributed to transitions in molecular complexes, perhaps short-lived collision complexes. The strongest band near 633 nm is attributed to the (0–0) transition associated with simultaneous excitation of two $3E_g^-$ oxygen molecules to the $1\Delta_g$ state (Ogryzlo 1965). We do not see such lines at 77 K. Another possibility that the interaction between molecular oxygen and water may be decreased at lower temperature and electron transitions remain strictly forbidden.

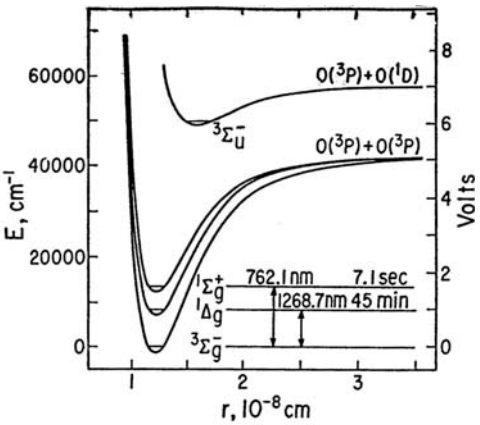

Fig. 5.67. Energy levels scheme of molecular oxygen and water

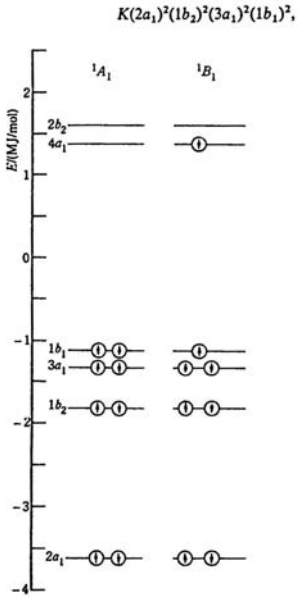

Thus it is possible to conclude that the optical active centers in apatite, which are responsible for the reabsorption lines, are molecular oxygen and water. Apatite structure is characterized by the existence of channels, running along the C-axis of the hexagonal structure. It has been proposed that the space existing in the channels of non-stoichiometric apatites may be available for molecular trapping. The most evident example is given by oxygen containing apatites. It has been shown, in the case of phosphor-calcium apatites, that they occupy all the available space of the channels and their maximum amount is

approximately 0.5 molecular percents. Water has been suggested to exist in vacancies of the channels. However quantitative data are scarce because of the difficulty to distinguish molecules inside the crystal and molecules adsorbed on its surface (Rey 1991).

Besides that, investigation of Eu^{3+} luminescence in different kinds of artificial apatites leads to an analogous conclusion. It is apparent that the charge compensating species for the trivalent rare-earth elements occupying the divalent calcium may appear in the form of halogen being replaced by oxygen. However, the profound dependence of the Eu^{3+} spectra on the type of halogen ion involved in apatites makes us conclude that the halogen in the second type of calcium position remains intact. Hence, it is suggested that the charge compensating species, namely free oxygen, should occur as an interstitial in the vicinity of the Eu^{3+} center (Jagannathan and Kottaisamy 1991).

Thus the spectroscopic conclusion is in accordance with the crystallochemistry of apatite, namely with possible accommodation of molecular oxygen and water in different ways: by structural incorporation and by adsorption.

5.9.2
Apatite – Photoacoustic Spectrophotometry

Such unusual phenomena as reabsorption lines of molecular oxygen and water require a confirmation by an additional independent technique. The best method is to try to detect the corresponding absorption lines by UV-visible spectroscopy. The problem is that sedimentary apatite samples are in the form of non-transparent powder, which is not suitable for optical spectroscopy. The photoacoustic spectroscopy (PAS), which allows measurement of absorption spectra of powdered opaque samples, has been chosen for this purpose (Gaft et al. 1998b). PAS works as follows: light from a broad wavelength source is chopped by a rotating sector. The light, after monochromator, is directed into a gas tight cell, which contains the sample. A miniature microphone is connected to the cell. In the absence of photophysical or photochemical reactions, the light degrades to heat. This heat flows to the surface, and causes a heating and cooling of the gas in immediate contact with the sample. The acoustic wave thus produced is then detected with a miniature microphone. The microphone is an exceptionally sensitive instrument and can detect acoustic waves of very little power. The signal from the microphone is detected using a phase sensitive detector. This form of detection can detect a signal at a specific frequency 100 dB below the noise level. The resulting signal is that of the emission of the light modified by the transfer characteristics of the spectrometer and the absorption of the sample. In order to obtain the true spectrum one obtains the ratio of this signal to that of carbon black powder, which is assumed to be uniformly absorbing (Rosenzweig 1990).

It was found that the absorption spectrum of the apatite is characterized by the bands at 775 and 850 nm, which are close to reabsorption bands in the same sample and according to absorption in atmosphere may be connected with molecular oxygen and water, correspondingly (Fig. 5.68).

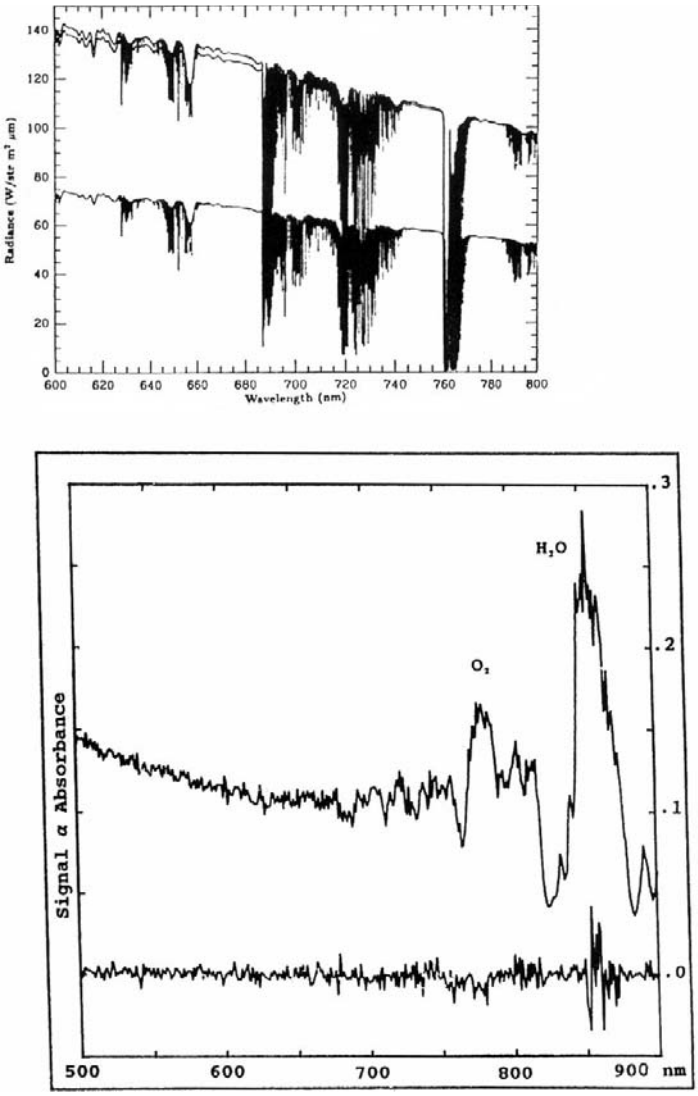

Fig. 5.68. **a, b** Absorption lines of molecular oxygen and water in the air (**a**) and photoacoustic spectra of apatite (**b**)

5.9.3 Diamond

Reabsorption lines of molecular oxygen and water have been detected in the time-resolved luminescence spectra of certain diamonds.

5.10 Luminescence Centers in Diamonds

The perfect diamond crystal consists of perfectly regular array of carbon atoms, every atom being symmetrically surrounded by four others, and forming an electron-pair bond with each one. Energy of about 5.5 eV is required to remove an electron from one of these bonds and the crystal is therefore transparent for ultra-violet wavelengths greater than 225 nm. For shorter wavelengths it will absorb strongly. No crystal is perfect and the deviation from perfection results in the optically active defects so common in diamonds. Several defects have a strong absorption in the UV and visible parts of the spectrum and are responsible for different kinds of luminescence. The defects may be chemical or structural, or a combination of both. It has to be noted that in the diamonds luminescence spectra very narrow intensive lines of purely electronic zero-phonon transitions are distinguished together with broad bands with maxima, which extend into the long wavelengths direction and represent a superimposition of the phonon vibrational replicas of the electron transitions. Because of the fact that the vibration energy at different points of the Brillouin zone is dissimilar, and also owing to the formation of di- and tri-phonon repetitions upon addition of similar and different phonons, 10–15 overlapping lines appear, which form a broad band perceived as blue, green, yellow, orange and red emission. At a lower temperature the sharp lines dominate in the spectrum, but at room temperature conditions they are drastically quenched and the broad relatively structureless bands prevail. We concentrated on the room temperature luminescence, which is especially important for diamond sorting.

5.10.1 N3

The N3 optical center is one of the best known in steady-state luminescence spectra diamond. It is connected with three substitutional nitrogen atoms bounded to a common carbon atom or a vacancy, the ground state being a $^2A_1$ level and the excited state where luminescence originates a ^2E state (C_{3v} point group). The zero-phonon line occurs at 2.985 eV and absorption and emission spectra show very closely a mirror relationship (Bokii et al. 1986). The N3 prompt luminescence decay is exponential and equal to 40 ns. Time-resolved luminescence spectroscopy enables us to detect that the N3 center has some metastable levels between the emitting and ground state. One of the decay paths of these metastable levels is delayed N3 luminescence, which occurs above 170 K. Besides this, time-resolved spectroscopy enables us to detect another center with zero-phonon lines with energy very similar to the N3 center (Pereira and Santos 1993; Pereira and Santos 1994). Under steady-state conditions there is some superposition of luminescence and excitation spectra of N3 and this center and they cannot be spectroscopically separated. By time-resolved spectroscopy the centers were separated and the second one, named 2.96 eV was connected with the Al impurity.

Our study of time-resolved luminescence of diamonds revealed similar behavior (Panczer et al. 2000). Short-decay spectra usually contain N3 luminescence centers (Fig. 4.71d; 5.69a,b) with decay time of $\tau = 30-40$ ns. Despite such extremely short decay, sometimes the long-delay spectra of the same samples are characterized by zero-phonon lines, which are very close in energy to those in N3 centers. At 77 K $\lambda_{ex} = 308$ nm excitation decay curve may be adjusted to a sum of two exponents of $\tau_1 = 4.2$ µs and $\tau_2 = 38.7$ µs (Fig. 5.69c), while at 300 K only the shorter component remains. Under $\lambda_{ex} = 384$ nm excitation an even longer decay component of $\tau_3 = 870$ µs may appear (Fig. 5.69d). The first type of long leaved luminescence may be ascribed to the 2.96 eV center, while the second type of delayed N3 luminescence is ascribed to the presence of two metastable states identified as quartet levels at the N3 center.

N3 is the only luminescence center with an appreciable fine structure at 300, while its zero-phonon line at 415 nm is characterized by different intensities down to practically total disappearance (Fig. 5.70b; Gaft 1994). The decrease of zero-phonon line intensity is accompanied by an increase of the 360 nm line in the excitation spectrum (Fig. 5.70a). The cause may be the N3 clusters formation of N3 centers with the ensuing concentration quenching resulting from energy migration. The transfer is of the emission-reabsorption type, namely, emission by one luminescence center and its reabsorption and emission by the other center. This is explained by the similarity of the energies of emission and reabsorption. The following model is possible: a feature distinguishing the N3

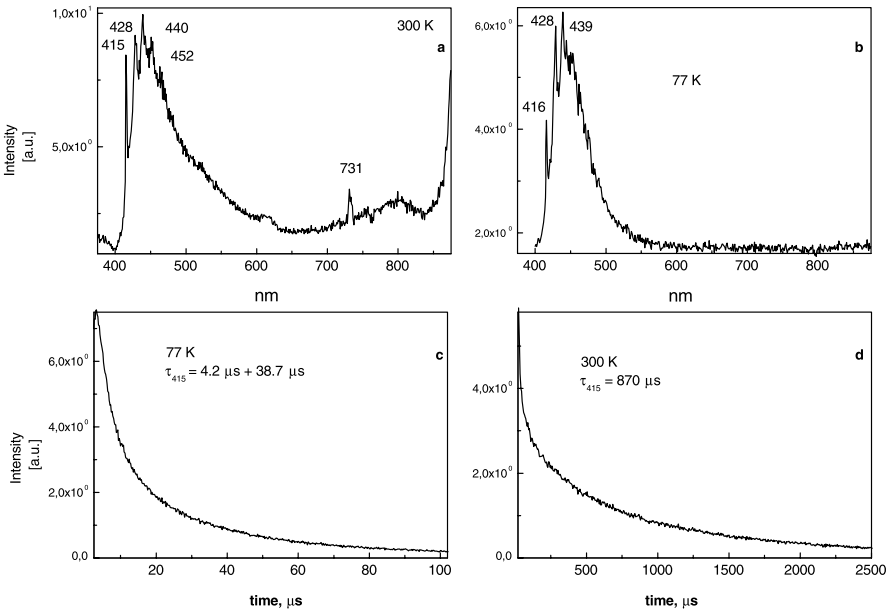

Fig. 5.69. **a–d** Laser-induced time resolved luminescence of N3 center in diamond (**a, b**) and decay times (**c, d**)

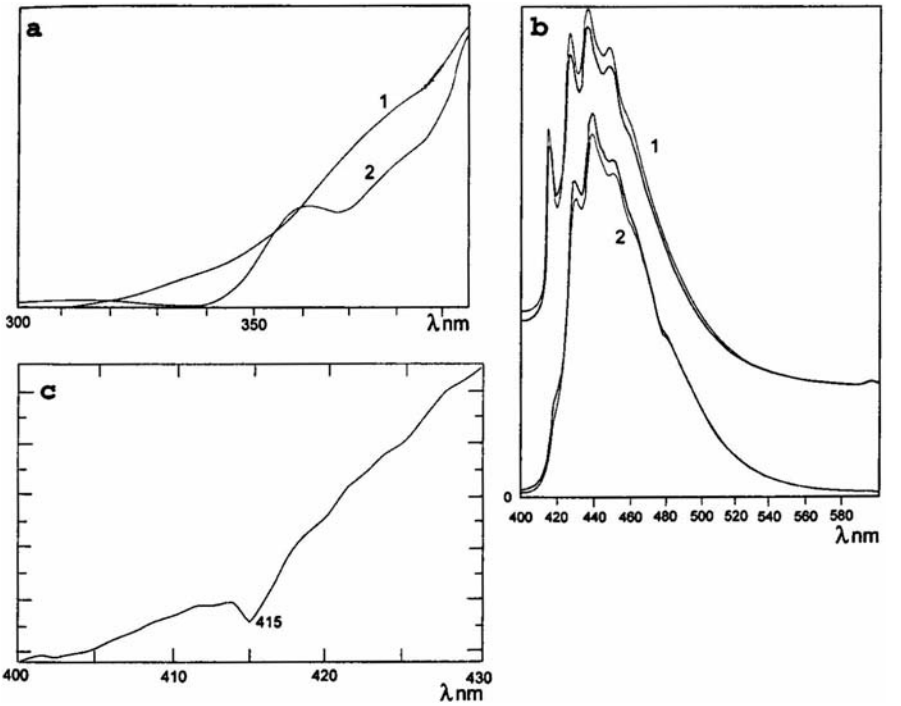

Fig. 5.70. **a–c** Reabsorption of the 415 nm line in diamond luminescence spectrum

center is that its absorption is similar to its excitation and presents a mirror reflection of its photoluminescence. The line at 415 nm is present in the emission and in the absorption spectra being subjected to the concentration quenching. This is confirmed by the fact that this process is particularly prominent in yellowish diamonds, which are characterized by elevated N3 contents. A strong reabsorption line at 415 nm in these diamonds is clearly seen in the spectrum, which was received with a time delay of 1 microsecond, when N3 luminescence is no longer detected because of its short decay time (Fig. 5.70c).

5.10.2 H3, H4, S2, S1 and S3

The H3 center is connected with a pair of nitrogen atoms, which captures one vacancy, while the H4 center is principally the same but with a slightly different configuration. Defect S2 is believed to be due to a combination of two vacancies and one nitrogen atom, while S3 is connected with a combination of several nitrogen atoms and a vacancy and S1 with a vacancy-nitrogen pair.

The H3 center is well known in the steady-state luminescence spectra of diamonds. It belongs to the C_{2v} point group, the ground state being $^1A_1$ level and the excited state from which luminescence takes place a $^1B_1$. Both emis-

sion and absorption spectra present a zero-phonon line at 2.463 eV. The decay time of the H3 luminescence is of 15–20 ns (Bokii et al. 1986; Davies 1994). Time-resolved luminescence spectroscopy also revealed a delayed luminescence spectrally identical to the fast one, but with a temperature dependent decay time of the order of a few ms. Results were interpreted as due to reversible non-radiative transitions from the emitting $^1B_1$ excited level to triplet levels (Pereira and Monteiro 1990; Pereira and Monteiro 1991).

In our study we found that H3, H4, S2 and S3 centers are characterized by relatively broad bands with λ_{max} at 520–545 nm, sometimes accompanied by very weak zero-phonon lines at 489 and 523 nm (S2), 498 (S3) and 503 (H3) nm. It is very difficult to distinguish between the centers of this group, especially when they present together. Under pulse laser excitation the decay time differences enable more definite recognition. Different decay components in the green part of the spectrum allow us to establish the presence of H3 (12 μs) and S3 (126 and 213 μs) centers. These broad bands are sometimes accompanied by narrow lines of GR1 center at 794 nm and by system at 700 and 788 nm (Bokii et al. 1986; Davies 1994). The relatively broad line at 463 nm with a decay time of 312 μs appears which is not described in the literature (Fig. 4.72).

5.10.3 *A*-Band

This luminescence band is believed to be due to segregation of defects B1, which is a relatively large spheroid of aggregates of nitrogen and is characterized by strong N9 (236 and 230.8 nm) and weak N10 (240 and 248 nm) absorption systems. It gives white-blue luminescence (Fig. 4.71) excited by UV shorter that 240 nm with practically structureless broadband. Its luminescence decay is characterized by three components, mainly 25 ns, 100 μs and 3 ms.

5.11 Unidentified Luminescence Centers

5.11.1 Apatite

The luminescence spectrum of the Canada apatite contains the yellow band, which is similar to Mn^{2+} emission in the Ca(II) site (Fig. 5.71). Nevertheless, this band has short decay time, which is not suitable for strictly forbidden *d*–*d* transitions in Mn^{2+}. It dominates in the time-resolved spectrum with a delay of 10 μs and gate of 100 μs when the shorter-lived centers are quenched, while the longer-lived ones are not detected. A change in the lifetime may be indicative of the energy transfer from Mn^{2+} by a radiationless mechanism. A condition necessary for this mechanism is coincidence or a close distance between energy level pairs of the ion sensitizer and the ion activator. Here, the process of luminescence is of an additive nature and a longer duration and greater quantum yield of the activator luminescence accompany a reduced

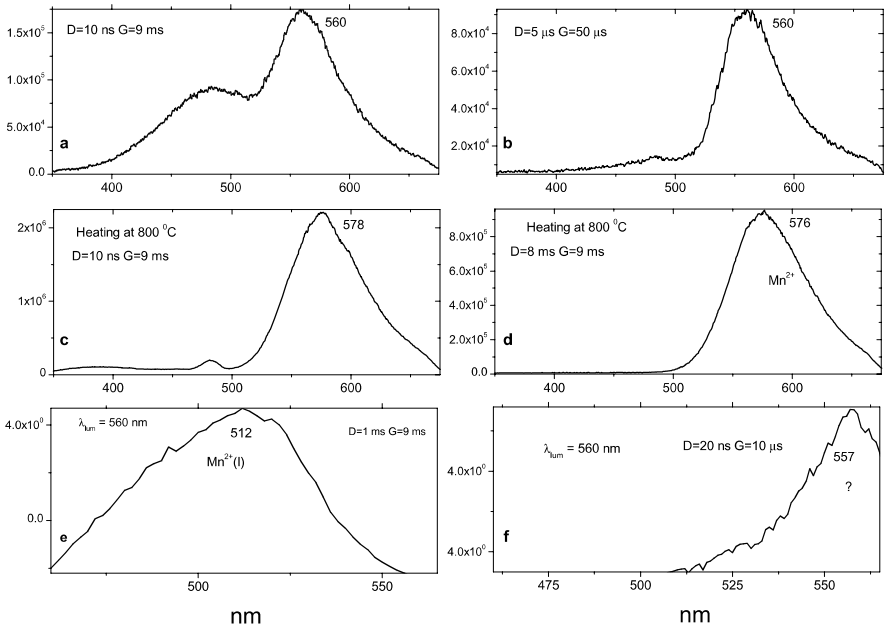

Fig. 5.71. **a–f** Unidentified emission center in apatite laser-induced time-resolved luminescence spectra of apatite. **a** Steady-state luminescence spectrum; **b** Time-resolved spectrum with narrow gate where yellow band with short decay time dominates; **c–d** Time-resolved spectra after heating at 800 °C; **e–f** Excitation bands of Mn^{2+} and short-lived yellow band, correspondingly

duration and decreased quantum yield of the luminescence of the sensitizer. The energy transfer explained the absence of Mn^{2+} luminescence in natural apatite, where its presence is ascertained from the EPR spectra, from levels $^4T_2$ and $^4T_1$ of Mn^{2+} to REE (Marfunin 1979b). In all samples where short-lived luminescence of Mn^{2+} is detected, the lines at 651 and 605 nm are unusually strong. They are well known in artificially activated apatite and belong to Sm^{3+} in the Ca(II) site (Morozov et al. 1970). In natural apatite such luminescence is extremely rare and was previously detected in Canada and yellow apatites only. Thus it is possible to suppose that energy migration from Mn^{2+} to the $^4G_{5/2}$ level of Sm^{3+} takes place. That these lines excitation is the result of energy migration from Mn^{2+} is confirmed by their unusually long decay time of 2 ms.

Nevertheless, such interpretation contradicts with the fact, that after heating at 800 °C the short-lived yellow band disappeared and a usual long-lived Mn^{2+} luminescence appears (Fig. 5.71d). Thus short-lived emission may be not connected with the Mn^{2+} center, but with another center, which transforms to Mn^{2+} as result of oxidizing heating. To check this possibility time-resolved excitation spectrum of the yellow band with a short decay time was determined, because it is very characteristic for Mn^{2+}. It was found that the excitation spec-

trum consists of one main broad band with an extremely low Stocks shift and is absolutely different from those for Mn^{2+} (Fig. 5.71e–f). The exact nature of the luminescence center needs further clarification, while one of the possibilities may be Mn^{+} luminescence, which transforms to Mn^{2+} after oxidizing heating at 800 °C. The Mn^{+} ion has $3d_6$ configuration and the only one known luminescence center with such a configuration is Fe^{2+} with an IR emission band. Nevertheless, it is known that the optical properties of d^{5+n} ions are similar to those of d^n configuration. Thus Mn^{+} is similar to such ions as Ti^{3+}, Cr^{5+}, Mn^{6+} and V^{4+} with IR and red emission bands.

Certain similarity may be seen between this luminescence and short-lived orange emission in calcite, which has been ascribed to radiation-induced center (Fig. 5.67). It is possible that natural irradiation may be a reason of orange luminescence in apatite also.

5.11.2 Zircon

Several luminescence bands are usually obscured by stronger emissions and may be detected only by time-resolved spectroscopy. These are: emission with $\lambda_{max} = 480$ nm, $\Delta = 70-80$ nm and $\tau = 300-325$ µs, emission with $\lambda_{max} = 515$ nm, $\Delta = 90-100$ nm and $\tau = 500-520$ µs, emission with $\lambda_{max} =$

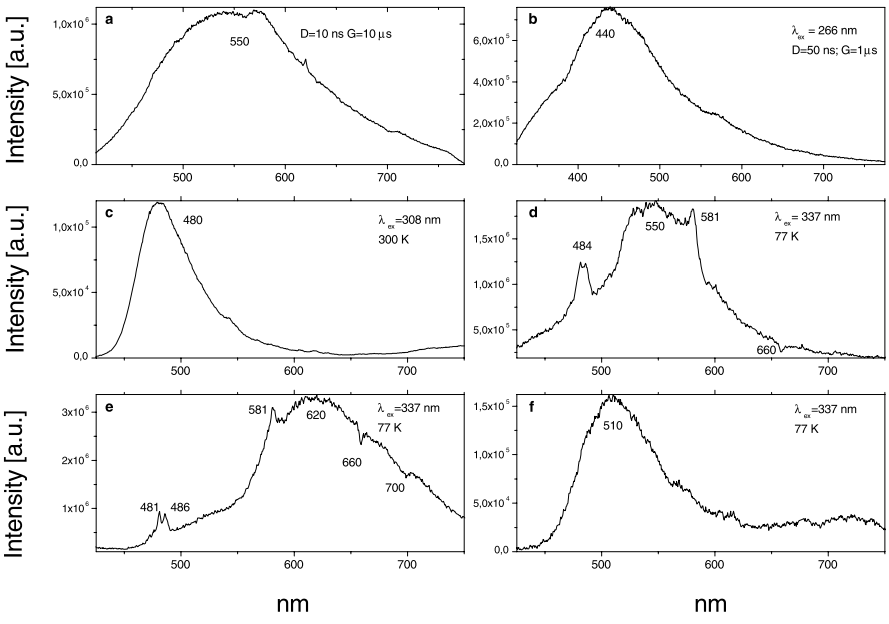

Fig. 5.72. **a–f** Unidentified emission centers in laser-induced time-resolved luminescence spectra of zircon

550 nm, Δ = 110−125 nm and τ = 8−10 µs, emission with λ_{max} = 620 nm, Δ = 110−125 nm and τ = 8−10 µs, emission with λ_{max} = 560 nm, Δ = 110−125 nm and τ = 3−5 µs, and emission with λ_{max} = 440 nm, Δ = 80−105 nm and τ = 1−3 µs (Fig. 5.72a–f). To identify the exact nature of those impurities, $ZrSiO_4$ artificially activated by potential activators, such as Mn, Cr, Ti, Co, Ni, Pb, Sb, have been studied (Gaft et al. 2002b). Nevertheless, the bands similar to those detected in natural zircon are not found and the nature of the corresponding luminescence centers needs further investigation.

5.11.3 Barite

The luminescence of all natural barite is influenced strongly by thermal treatment. After heating at 600 °C vibrational structure appears in some samples even at room temperature with mean frequency intervals of about 880 cm^{-1} and decay time of 10 µs. At 77 K this center is hidden by strong uranyl luminescence. A narrow yellow band peaking at 575 nm is also detected. After heating at 700 °C, in the luminescence spectrum at 77 K two bands are present, the first similar to those at 300 K and the second one with much a longer decay of 250 µs and vibrational structure. At 4.2 K three vibrational structures are detected by time-resolved spectroscopy: blue with decay time of 5 µs, green with decay

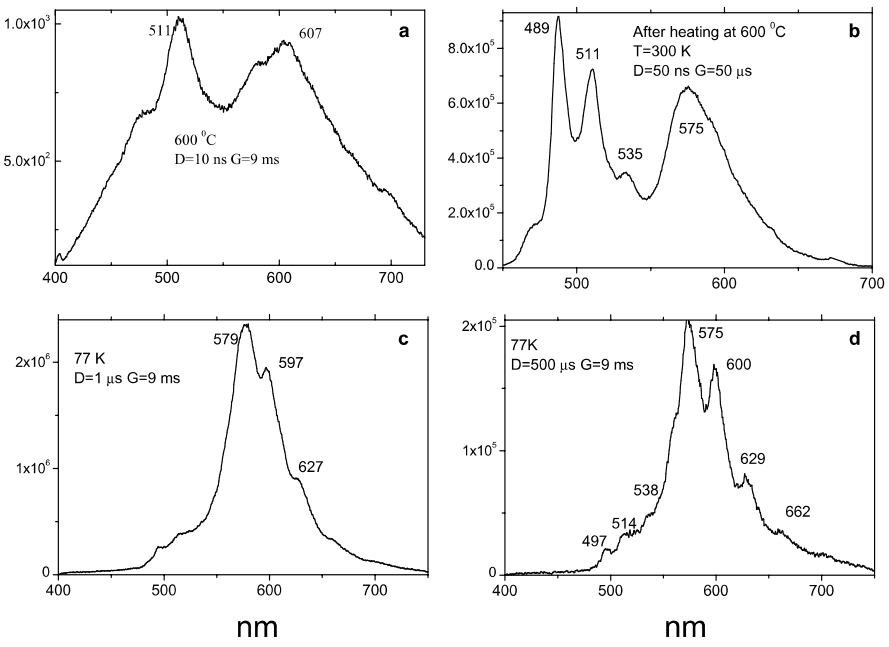

Fig. 5.73. **a–d** Unidentified emission centers in laser-induced time-resolved luminescence spectra of barite

time of 650 µs and red with decay time of 225 µs (Figs. 5.73, 5.74). In all cases the mean frequency vibrations are close to each other 820–850 cm^{-1}.

Three types of vibrational spectra are considered now in minerals: electron-hole centers O_2^- for the blue region and S_2^- for orange-red, together with UO_2^{2+} for green. O_2^- and S_2^- centers have been proposed earlier to explain the vibration bands in natural sulfates (Tarashchan 1978). Nevertheless, we checked the S_2^- luminescence in several minerals and it was found that it is characterized by a short decay of several ns, which is much shorter than in our case. The uranyl possibility for the green lines may be also excluded because the U content of 0.12 ppm in the corresponding sample is low.

Once again, Bi presents other possibility. It is known that the vibrational structure occurs in the emission and excitation spectra of Bi, which was observed if it replaces relatively small ions and the pressure on Bi^{3+} is large. Vibrational structures for Bi^{2+} in the orange part of the spectrum and for Bi^{3+} in the blue are known (Blasse and Grabmier 1994). According to the three-level scheme, the short-lived higher temperature band may be connected with $^3P_1$–$^1S_0$ transitions, while the longer-lived low-temperature one with $^3P_0$–$^1S_0$ transitions. The different luminescence centers of Bi in natural barite may be connected with its substitution for Sr^{2+} and Ca^{2+} impurities, the presence of which is established by ICP data. Substantially different luminescence of s^2 ions, such as Pb^{2+} and S^{2+}, in $CaSO_4$, $BaSO_4$ and $SrSO_4$ is well known. It is explained

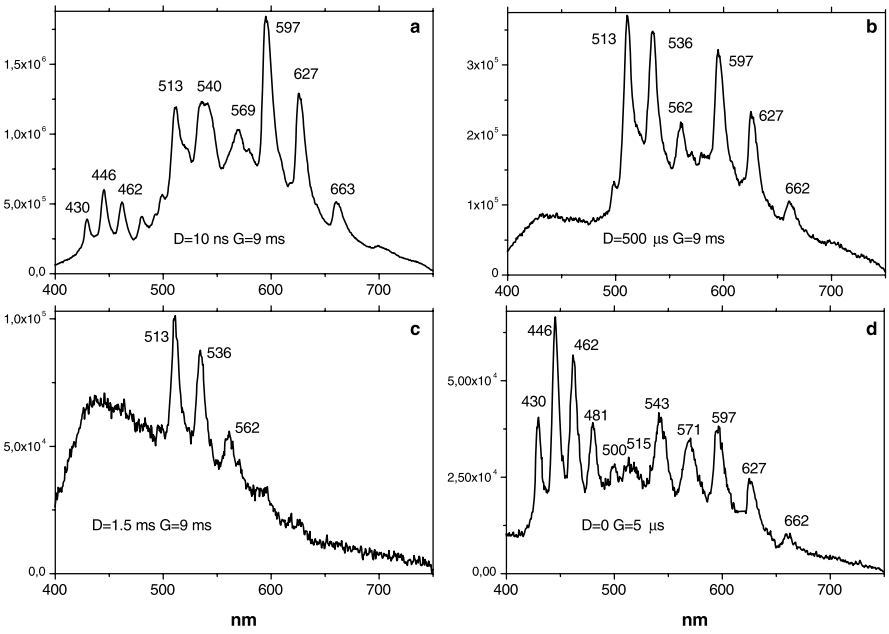

Fig. 5.74. **a–d** Unidentified emission centers in laser-induced time-resolved luminescence spectra of barite

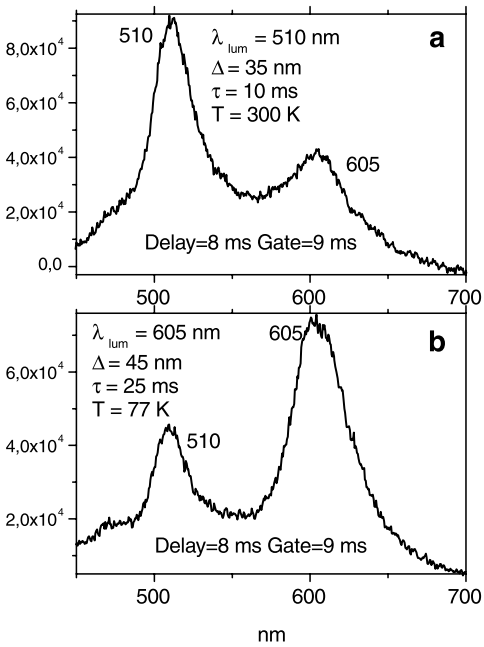

Fig. 5.75. **a,b** Unidentified emission centers in laser-induced time-resolved luminescence spectra of barite

by the fact, that Ca and Sr have much smaller ionic radii than Ba^2. Besides that, Ca in the anhydrite structure has 8 nearest neighbors and not 12, as in barite.

Other bands appear after heating with long decays. After a delay of 1 ms when the centers with a long decay are exaggerated the narrow green band appears peaking at 510 nm with a half-width of $\approx$ 35 nm and decay of 10 ms, while an additional band is also detected at 605 nm with a half-width of $\approx$ 70 nm (Fig. 5.75).

At 77 K the relative intensity of the band at 605 nm with an even longer decay time of 25 ms is much stronger. Such bands are usually connected with Mn^{2+}, but Mn^{2+} in barite has different luminescence. Mn^{2+} in anhydrite $CaSO_4$ is characterized by a narrow band peaking at 505 nm. Thus such a band in barite may be connected with Ca impurity and "anhydrite type" local structure.

5.11.4 Calcite

Under short-waved UV lamp excitation (254 nm) visually observed luminescence of calcite is violet-blue with very long phosphorescence time of several seconds. Under long-waved UV lamp excitation (365 nm) calcite exhibits visually the same violet-blue luminescence as under 254 nm excitation, but long phosphorescence is not detected. Under short laser excitations, such as 266 and 355 nm, at 300 K calcite demonstrates intensive UV-violet emission band peaking at 415 nm with half-width of $\sim$ 55 nm (Fig. 5.76a). Excitation spectrum of this band is composed of short waved tail in the spectral range less

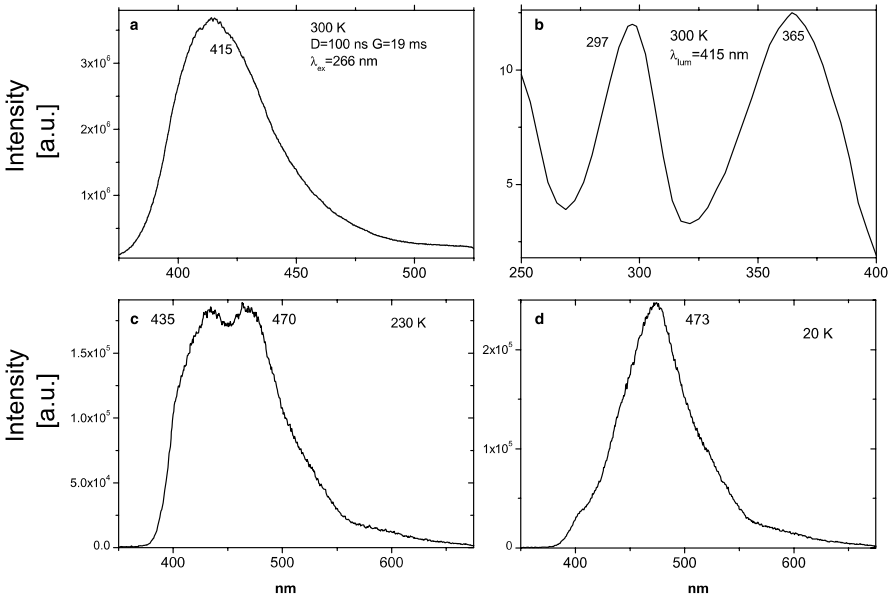

Fig. 5.76. Blue emission (**a**) and excitation (**b**) spectra of calcite at 300 K and luminescence spectra at lower temperatures (**c**–**d**)

than 250 nm and two UV bands peaking at 297 and 365 nm (Fig. 5.76b). Decay time is very long and may be approximated by the sum of two exponents of 1.9 and 19 ms. At lower temperatures luminescence spectrum changes dramatically. Down to approximately 250 K, the spectrum remains practically the same, while emission intensity is higher. After that, the second band appears (Fig. 5.76c), which at 200 K is situated at 473 nm and totally dominates the spectrum while the band at 425 nm disappears (Fig. 5.76d). Decay times of both bands in this temperatures interval remains in several ms diapason. At even lower temperatures down to 20 K, the band maximum remains the same, intensity becomes substantially stronger and decay time is extremely short, namely less than 25 ns, which is a lower limit of our measuring system. Besides that long phosphorescence is detected with decay time of several seconds. As it already mentioned, luminescence behavior when emission spectra and decay time strongly dependant on temperature is very typical for s^2 ions, such as Bi^{3+} and Pb^{2+}. Similar behavior with calcite luminescence under consideration may exhibit Sb^{3+} emission center. Additional research needed in order to clarify this problem.

CHAPTER 6

Applications of Laser-Induced Time-Resolved Spectroscopic Techniques

In any practical application in the mineralogy field the main task is composition analyses. There is no single detection technique that can by itself provide a 100% probability of different minerals detection combined with a low false alarm rate. We suggest the system approach, which combines different laser-based technologies having orthogonal detection and identification capabilities. In such a way the strength of one technique may compensate for the weaknesses of the others, and the vulnerability of one detection device could be compensated for by another detection device. Clever combination of the detection techniques may achieve detection probabilities and false alarm rates that are more acceptable than those of systems based on one method only.

The same equipment, which is used for time-resolved luminescence application is suitable for other laser-based spectroscopies. Thus several spectroscopic methods may be applied simultaneously. The most important techniques, which may be used together with time-resolved luminescence, are laser-induced breakdown spectroscopy, Raman spectroscopy and Second Harmonics Generation spectroscopy.

6.1 Time-Resolved Laser-Induced Breakdown Spectroscopy (LIBS)

6.1.1 Theory and Technique

Laser Induced Breakdown Spectroscopy (LIBS) has been developed for applications requiring the elemental analysis of materials, where the use of conventional analytical methods is not possible. A general and simplified LIBS process may be presented as follows (Kompitas et al. 2000). When a short duration laser pulse of sufficient energy density is focused onto the surface of a target, the surface temperature instantly increases to above the vaporization temperature. This violent photon-material interaction could include single- or multi-photon absorption, dielectric breakdown, and other still unknown mechanisms. Compared with the rate of energy delivery from the laser pulse, the energy dissipation through vaporization is relatively slow. As a result, before the surface layer vaporizes, the underlying layer of material reaches critical temperatures and pressures, and forces the surface to explode. Within

the same laser pulse, usually a few nanoseconds, the ablated material continues to absorb energy from the laser beam and forms luminous plasma. In the laser-induced plasma atoms, ions, molecules, and clusters exist, in their different energy states. The temperature of the plasma is in the range of $10^4 - 10^5$ K, and the electron number density is in the order of $10^{15} - 10^{19}$ cm^{-3}. The plasma finally starts to decay through radiative, quenching, and electron-ion recombination processes, within microseconds up to milliseconds. Consequently, the formation of clusters through condensation and collision, and the thermal and concentration diffusion of species into ambient gas stop the plasma.

The plasma light is analyzed to determine the elemental composition of the sample. Plasma emission can be divided into two time domains. The first one is characterized by a broad emission originating from the *Bremsstrahlung* of the free electrons and electron-ion recombination and it has a duration of a few hundred nanoseconds. Weak lines show up on the strong continuum and they are mostly identified as ionic lines of the plume constituents. The second time domain is characterized by an emission spectrum, where narrow atomic lines dominate corresponding to the elements present in the plume and the line strength is proportional to the atomic concentration. This time regime lasts for several microseconds, where in its early stage ionic lines are strong, while the atomic lines dominate later on. From the temporal behavior of plasma, it is clear that the identification has to be done by time-resolved spectroscopy, that is, the delay and the gate in respect to the laser pulse have to be optimized to maximize the informative line spectrum and avoid the early part of the signal, corresponding to the strong unstructured continuum.

Spatially resolved spectroscopy is used to measure the emission from plasma at its different positions, because the appearance and spectral characteristics of the plasma are quite different depending on the target species as well as the position (Xu et al. 1997).

The characteristics of a laser, such as energy, wavelength, pulse duration, beam quality, and mode quality, together with the properties of the target material, affect the production and characteristics of the plasma. The laser wavelength plays an especially important role in LIBS. It was found that the lines are narrower when excited with UV than with the IR wavelength. This may be explained by a lower temperature achieved by the plasma, in consistence with the λ^2 dependence of the laser photon absorption by the free plasma electrons, namely fewer ions are produced and the electric fields are correspondingly lower. Besides that, the number of lines is sometimes reduced when UV light is used. In particular, those lines are missing that originate from ionic species. This could speak for a thermal process again which is more pronounced for the IR wavelength than for the UV. But sometimes, additional lines have been observed, when the sample was irradiated with the UV light. This implies that some multi-photon excitation/ionization mechanism, in particular in the initial stage of the plasma formation, may play a role. The UV photons have high energy and three of them can directly ionize a large number of atoms encountered in minerals. Besides that, the difference in characteristic emission times between UV and IR excitations takes place (Ciucci et al. 1996). It depends

on initial plasma temperature while upon IR excitation it is usually higher with longer plasma continuum emission decay times.

The vast majority of LIBS experiments have been received using Q-switched Nd-YAG lasers for various reasons: they are extremely reliable; pulse energies between a few mJ and several hundred mJ can be easily realized; their beam quality is usually rather good and beam divergence is small, and thus very small focal spot sizes can be realized; choice of useful wavelengths can be provided by a single laser. The main disadvantage is relatively long laser pulses, such as 5–10 ns. When the laser pulse is so "long", a significant amount of the later part of the energy pulse goes into heating the plasma formed during the earlier part of the pulse through multiphoton ionization processes as well as through cascade ionization. The resulting plasma is formed from the minerals as well as the surrounding air molecules. The plasma thus formed is very highly ionized which results in large amounts of continuum emission, especially at short time scales. The air molecules also contribute to the broad emission background observed in the LIBS spectrum when nanosecond laser pulses are used to produce the breakdown. Time-resolved spectra enable us to solve the background problem, but at the cost of reduced intensity of emission lines, thus limiting the use of the LIBS when attempting to detect ion species at low concentrations. To overcome this problem it was proposed to use a femtosecond laser with lower energies than nanosecond pulses (Alexander 1998). Lasers generating ultra short light pulses from about 5 femtoseconds (fs) are now available for carrying out femtosecond LIBS. Recent technological advances in ultra fast technologies have resulted in the generation of light packets consisting of only a few cycles of the electric and magnetic fields. When using a diffraction limited parabolic mirror for focusing and moderate pulse energies of 1 μJ, peak intensities at the focal spot of over 10^{15} W/cm^2 can be achieved. The corresponding amplitude of the electric field at these intensities approaches 10^9 V/cm^2. These field strengths are high enough to trigger optical field ionization. Hence, detachment of the first electron is completed at substantially higher field strength and the optical-field ionization rate becomes comparable to the laser field oscillation frequency. The released electrons gain unprecedented kinetic energies (up to and beyond the keV level) during the first field oscillation cycle following their detachment, and a substantial fraction of the ionization occurs during one cycle of light. In comparison, long pulsed laser systems containing many field oscillation cycles depletes the atomic ground state. The above linear and nonlinear processes result in very precise thresholds for plasma formation since femtosecond interactions produce their own source of free electrons to initiate the plasma formation process. Longer nanosecond pulses produce breakdown at less defined thresholds. Because of the unique breakdown threshold offered by the femtosecond laser, it is possible to produce very small damage sites. Furthermore, less energy is transmitted to the air and surrounding materials. The plasma is produced that consists essentially of sample material without being contaminated by air plasma formation. Thus, the background emission is reduced and there is no need to wait for the plasma to cool down over time before detecting the spectral lines of the sample. Because there is no

need to wait for cooling before spectral measurements, lower detection limits are possible.

6.1.2 Quantitative Elemental Analysis

Generally, LIBS as an analytical technique, has many advantages. The analyses process is fast, for no sample preparation is needed. Furthermore, LIBS is good for analyses of both non-conducting and conducting samples, regardless of their physical states, i.e. solids, liquids or gases. The capability for simultaneous multi-element determination, localized microanalysis, and surface analysis is also appealing. Finally, with the advent of miniaturized lasers, field-portable instrumentation is possible. Remote analysis is also possible by transporting the laser beam through the fiber optic cable or by focusing the laser beam on the sample. Many authors assessed the potential of LIBS as a method to conduct remote, quantitative analysis, with the highest sensitivity and reproducibility possible. The analytical ability of LIBS is based on a few basic principles. The quantitative analysis of the spectral emission from a laser-produced plasma relies on the assumption that the plasma plume can mainly be characterized using a single variable parameter, i.e. plasma temperature. It has often been argued that one of the most important requirements for quantitative analysis is the so-called condition of local thermal equilibrium (LTE). The condition of LTE means that rather than having to rely on the system reaching full thermal equilibrium, it is sufficient to characterize a localized section of the plasma for a particular observation time. Assuming that LTE has been established, and its electron temperature T_e can hence characterize the appropriate section of the plasma, the relative elemental concentrations may be deduced from the intensities of the appropriate spectral lines. The relationship between observed line intensities and concentration of the trace element, denoted by subscript t, and a major constituent, denoted by subscript m, is given by:

$$\frac{I_t}{I_m} = \frac{N_t g_t A_t Z_m \lambda_m}{N_m g_m A_m Z_t \lambda_t} \exp\left[-\left(E_m - E_t\right) / k T_e\right] \tag{6.1}$$

Here I stands for the intensity of the spectral lines; N is the atom number density in cm^{-3}; Z is the partition function; E and g are the energies and degeneracy's of the upper levels, respectively; and A and λ are the Einstein coefficient and wavelength, respectively, for the observed transitions. When changing the concentration N_t relative to that N_m the line intensities I_t and I_m will likewise change, and according to (6.1) one should obtain a "calibration curve" with constant slope (Davies et al. 1995; Ciucci et al. 1999; Hou and Jones 2000).

The way to improve LIBS analytical abilities is double pulse LIBS. It is conducted by using two pulses from the same laser source operated at a single wavelength. By utilizing a modified commercial laser, a proper external trigger circuit allows us to extract two laser pulses with adjustable delay from the same flash-lamp emission, and a relative time delay variable from a few to several tenths of microseconds. The experimental results show that such a technique

increases significantly the intensity of spectral lines in the emission spectrum from near-surface plasma. This enables a significant increase in the sensitivity of this technique when applied to remote analysis. Another possible advantage of the double pulse technique is also related to the cleaning action produced by the first laser pulse, which can have positive effects in applications where samples with dust and coatings are not cleaned (Noll et al. 2003; Sabsabi et al. 2003).

6.1.3 LIBS in Geosciences

One of the key goals of the mining industry is to develop technologies for superior exploration and resource characterization through real time measurements of ore quality. This enables reduction of out-of-seam dilution, significantly reducing mineral processing and energy costs. Presently, most surface mining operations must rely on laboratory-based analysis to monitor the extraction process. This requires samples to be collected, transported to the instrument, analyzed, recorded, and data transmitted back to the pit location. This process is slow, subject to numerous errors, and does not support real time management of the extraction process. The best existing option for in-situ analysis is based on X-ray fluorescence. However, these instruments cannot measure light elements effectively, contain radioactive sources that must be regulated, and lack the detection limits necessary for many operations. Consequently, operations are forced to rely on centralized analysis laboratories. LIBS may be an ideal analytical method for real time quantitative analysis of inorganic elements in solids and liquids and requires no sample preparation.

Currently LIBS is used in different fields ranging from material analyses to cultural heritage study and environmental protection, including automated quantitative analysis of phosphate ores (Rusak et al. 1997; Rosenwasser et al. 2001). The major drawback of LIBS in industrial quantitative applications is related to the stability of the spectroscopic plasma signals, which undergo considerable fluctuations that originate from the very nature of the method. The laser intensity fluctuates within 1–5% and the scattered light depends on the local matrix effects and on physical and chemical characteristics. The geometrical parameters also vary during the measurement, due to the surface crater formation. Sample humidity variation as well as the atmospheric composition and even the samples color also contribute to the observed signal fluctuations (Xu et al. 1997). Many models and techniques have been developed in order to overcome such problems. Usually, calibration curves are needed for the quantitative determination of the elements. They emerge from a number of reference samples with known elemental composition, but a limit is set to the applicability of the method, because a similar composition for the unknown sample is also required. This can be good for laboratory measurements, where reference and unknown samples can be embedded in the same matrix, but is a severe restriction for field experiments (Kompitsas et al. 2001). Thus, field experiments are limited to a semi-quantitative analysis in the case of highly variable or unknown rock compositions. By applying the spectra normalization and plasma modeling, after first generating calibration curves for each

element and for a given experimental set-up, concentration measurements of unknown samples independently of their matrix composition, could be determined with an error lower than 40% and for some elements even within of 20% (Barbini et al. 1999).

6.2 Gated Raman Spectroscopy

6.2.1 Theory and Technique

When radiation passes through a transparent medium, the species present scatter a fraction of the beam in all directions. In 1928, the Indian physicist C. Raman discovered that the wavelength of a small fraction of the radiation scattered by certain molecules differs from that of the incident beam. Furthermore, the shifts in wavelength depend upon the chemical structure of the molecules responsible for scattering. Raman spectra are obtained by irradiating a sample with a powerful laser source of monochromatic radiation. During irradiation, the spectrum of the scattered radiation is measured. At the very most, the intensities of Raman lines are 10^{-6} of the intensity of Rayleigh diffusion line and as a consequence, their detection and measurement are difficult. The scattered radiation is of three types: namely Stokes, anti-Stokes, and Rayleigh. The last, whose wavelength is exactly that of the excitation source, is significantly more intense than either of the other two types. The Raman peaks appearing at lower energies relative to the excitation energy resembles the Stokes shift found in luminescence and it is the reason for their name. Shifts toward higher energies are termed anti-Stokes and those lines are generally much weaker than the corresponding Stokes lines, but fluorescence may interfere with the observation of Stokes shift but not always with that of anti-Stokes, which therefore may be more useful, despite their lower intensity. It is important to note that the patterns of the shifts on the two sides are identical. The magnitude of Raman shifts is independent of the wavelength of excitation and shift pattern is independent of the type of laser.

The Raman effect can be described in terms of transitions between vibrational energy levels. When an energetic photon strikes a molecule in its ground state, it may raise the molecule to a higher virtual state. Since this is not a stable energy state for the molecule, two things can occur. Most probably the molecule returns to its ground vibrational state and emits a photon with the same energy and frequency as the exciting photon. This is called Rayleigh scattering. However, some of the excited molecules will not return to the ground state, but to some excited vibrational state. Such a molecule emits a photon, which has a lower energy than the exciting photon, the energy difference being equal to the difference between the initial and final vibrational states. This is Raman scattering, Stokes type. If a molecule, which is in the first excited vibrational state, absorbs the photon then the molecule is again raised to some high, non-stable energy state. Most probably, this molecule then returns to the

ground state, and doing so, emits a photon, which has a higher energy than the exciting photon. The difference in energy between the exciting photon and the emitted photon is equal to the energy difference between the two excited vibrational states of the molecule. This is Raman scattering, anti-Stokes type. The relative populations of the two energy states are such that Stokes Raman is much favored over anti-Stokes. Rayleigh scattering has considerably higher probability of occurring than does Raman scattering because the most probable event reemission by the return of these molecules to the ground state.

The physical origin of Raman scattering may be viewed from a simple classical perspective in which the electric field associated with the incident light interacts with the vibrating crystal. In particular, this interaction occurs through the polarizability of the material: that is, its ability to produce an induced dipole in an electric field. It is the oscillations in the polarizability produced by vibrations, which cause Raman scattering: if a vibrational motion produces a change in the polarizability of a material, then the vibration is Raman active. Notably, while the induced dipole is a vector, the polarizability is a second rank tensor, and it is the symmetric properties of this tensor, which allow the prediction of which families of modes will be active when observed along different crystallographic directions.

The wave model of Raman scattering may be shortly presented in the following way. A beam of radiation having the frequency ν_{ex} is incident upon a mineral. The electric field E of this radiation can be described by the equation:

$$E = E_0 \cos\left(\omega t\right) = E_0 \cos\left(2\pi \nu_{ex} t\right) . \tag{6.2}$$

When the electric field of the radiation interacts with the electron cloud of the mineral bond, it induces a dipole moment m in that bond that is given by

$$m = \alpha E = \alpha E_0 \cos\left(2\pi \nu_{ex} t\right) , \tag{6.3}$$

where α is the polarizability tensor of the bond. In order to be Raman active, the polarizability of the bond, which is a measure of the deformability in an electric field, must vary as a function of the distance between nuclei according to the equation:

$$\alpha = \alpha_0 + \left(r - r_{eq}\right)\left(\frac{\partial \alpha}{\partial r}\right) , \tag{6.4}$$

where α_0 is the polarizability of the bond at the equilibrium distance r_{eq}. The change in internuclear separation varies with the frequency of the vibration ν_v and is given by:

$$r - r_{eq} = r_m \cos\left(2\pi \nu_{ex} t\right) , \tag{6.5}$$

where r_m is the maximum internuclear separation relative to the equilibrium. Thus

$$\alpha = \alpha_0 + r_m \cos\left(2\pi \nu_{ex} t\right)\left(\frac{\partial \alpha}{\partial r}\right) . \tag{6.6}$$

Extending the equation of polarizability with that of the internuclear separation, and by substituting the initial equation of the dipole moment, one obtains an expression for the induced dipole moment m:

$$m = \alpha E_0 \cos\left(2\pi \nu_{ex} t\right) + E_0 r_m \cos\left(2\pi \nu_v t\right) \cos\left(2\pi \nu_{ex} t\right) \left(\frac{\partial \alpha}{\partial r}\right) . \quad (6.7)$$

Recalling from trigonometry that $\cos x \cos y = [\cos(x+y) + \cos(x-y)]/2$ and applying it to the previous equation, gives:

$$m = \alpha E_0 \cos\left(2\pi \nu_{ex} t\right) + \left(E_0/2\right) r_m \left(\frac{\partial \alpha}{\partial r}\right) \cos\left[2\pi t \left(\nu_{ex} - \nu_v\right)\right] + \left(E_0/2\right) r_m \left(\frac{\partial \alpha}{\partial r}\right) \cos\left[2\pi t \left(\nu_{ex} + \nu_v\right)\right] \quad (6.8)$$

The first term of the last equation represents Rayleigh scattering, which occurs at the excitation frequency ν_{ex}. The second and the third terms correspond to the Stokes and anti-Stokes frequencies of $(\nu_{ex} - \nu_v)$ and $(\nu_{ex} + \nu_v)$. Here, the excitation frequency has been modulated by the vibration frequency of the bond. It is important to note that Raman scattering requires that the polarizability of a bond varies as a function of distance, that is $(\partial\alpha/\partial r)$ must be greater than zero if a Raman line is to appear.

The theory of the Raman scattering shows that the phenomenon results from the same type of vibrational changes that are associated with infrared (IR) absorption. Thus, the difference in wavelength between the incident and scattered radiation corresponds to wavelengths in the mid-infrared region. Indeed, the Raman scattering spectrum and IR spectrum for given specie often resemble one another quite closely. There are, however, enough differences between the kinds of groups that are IR active and those that are Raman active. It is not surprising when it is considered that the basic mechanisms, although dependent upon the same vibrational modes, arise from processes that are mechanically different. IR absorption requires that a vibrational mode of the molecule have a change in dipole or charge distribution associated with it. Only then can radiation of the same frequency interact with the molecule and promote it to an excited vibrational state. In contrast, scattering involves a momentary distortion of the electron distribution around a bond in a molecule, followed by reemission of the radiation as the bond returns to it ground state. In its distorted form, the molecule is temporarily polarized, namely develops momentarily an induced dipole, which disappears upon relaxation and reemission.

A Raman spectrum is a plot of light intensity versus photon energy. In the vibrational spectroscopy it is usual to express the photon energy by the wavenumbers, defined as $\nu = 1/\lambda$. In the Raman spectroscopy the use of absolute wavenumbers would be impractical, because the wavelength and, with that, the absolute wavenumber of each obtained Raman bands must always depend on the wavenumber of the incident light ν_0. However, only the

wavenumber shift, which corresponds to the atomic vibration in the sample, is of analytical interest. It has therefore, become usual to express Raman shifts using relative wavenumber, i.e., the wavenumber difference between incident and scattered light, $\nu_1 = \nu_0 - \nu$. By definition, the Rayleigh line is set at zero Raman shift and Stokes Raman bands have positive and anti-Stokes Raman bands have negative relative wavenumbers.

Thus each band in a Raman spectrum represents the interaction of the incident light with a certain atomic vibrations. Atomic vibrations, in turn, are controlled by the sizes, valences and masses of the atomic species of which the sample is composed, the bond forces between these atoms, and the symmetry of their arrangement in the crystal structure. These factors affect not only the frequencies of atomic vibrations and the observed Raman shifts, respectively, but also the number of observed Raman bands, their relative intensities, their widths and their polarization. Therefore, Raman spectra are highly specific for a certain type of sample and can be used for the identification and structural characterization of unknowns.

For many minerals, the types of vibrational modes may be divided into two categories: internal and lattice modes. Internal modes are vibrations, which can be associated with those of a molecular unit, shifted and split by interaction with the crystalline environment in which the molecular unit is bonded. Such internal modes are typically associated with the most strongly bonded units in a crystal, and thus with the highest frequency vibrations. Lattice modes comprise both a range of comparatively low-frequency vibrations not readily describable in terms of molecular units, and so called external modes. External modes are those, which involve motions of a molecular unit against its surrounding lattice. Figure 6.1 shows representative frequencies of different functional, or molecular-like groupings, in mineral spectra (Williams 1995). The reliable assignment of observed bands to certain vibrations in the sample is a challenging task. The general approach for Raman spectra of minerals interpretation was recently examined by Nasdala (2004).

The transition of Raman spectroscopy from a time-consuming, experts-only method to a standard analytical technique was propelled by several technological advances in the field of optics and electronics. The key factor is the laser light source. Optical fiber probes for remote monitoring applications have become available. Furthermore, volume holographic instruments greatly facilitate measurements and notch filters efficiently eliminate the contribution of Rayleigh scattered light. Holographic gratings serve to disperse the Raman scattered light on the detector, namely multichannel ICCD detectors, which allow us to sample the entire dispersed spectrum simultaneously.

The most serious problem associated with conventional Raman spectroscopy is the minuteness of the effect. Even in the most favorable cases, only on the order of 10^{-6} of the incident intensity is converted into signal. With the development of lasers and the improvements in detection sensitivity, Raman spectroscopy has made considerable progress in recent years. Still, the lack of sensitivity has restricted Raman use. Nevertheless, the magnitude of the Raman effect can be greatly increased using nonlinear Raman processes. If

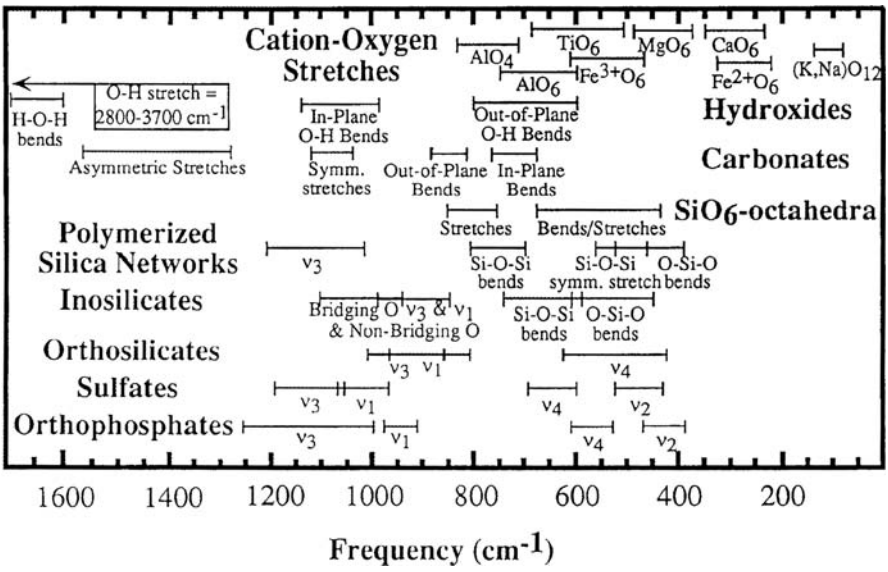

Fig. 6.1. Approximate frequency range of common vibrations of silicates, oxides and other functional groups within minerals (Williams 1995)

a laser beam of sufficiently high power excites the sample, two incident laser photons may be combined within the sample through non-linear optical mixing. As a consequence of this, weak Rayleigh scattering is observed at twice the incident frequency in addition to the normal Rayleigh line at the incident laser frequency. This frequency-doubled photon can also interact with the vibrational modes of the sample, and a hyper-Raman spectrum appears. The interest in hyper-Raman spectroscopy is that the selection rules are different to those for normal Raman scattering. If the laser power is even more, stimulated Raman scattering is observed instead of the hyper-Raman effect. In this way, there is extremely efficient conversion of the incident laser beam to Raman-shifted radiation, while the conversion efficiency may be up to 50%. The radiation with shifted frequency can act as the excitation frequencies for further vibrational modes and to give further Raman shift (Dubessi et al. 1994).

Surface Enhanced Raman Scattering (SERS) is a phenomenon whereby the Raman intensity is increased by as much as million fold due to the presence of nano-size silver particles on the surface to be analyzed. Enhancement of Raman scattering cross-section of molecules adsorbed on rough metal surfaces has been attributed to two major effects. The main and foremost contribution to SERS comes from the enhancement of electromagnetic (EM) fields close to the surface through interaction with surface plasmon excitations. The local EM field depends on the microscopic shape of the metallic surface, such as the presence of a sharp edge. Calculations suggest that protrusions on the surface of a colloidal particle as well as "cavities" formed between adjacent particles in an aggregate, lead to a giant enhancement of the local field, up to a factor of 10^{11}.

The second and smaller contribution to the enhancement of Raman scattering is a specific interaction of the adsorbed molecule with the metal surface. In some instances, this molecular chemisorption effect leads to formation of a charge-transfer interaction, whereby an electron is transferred from molecule into the empty levels on the metal surface or from occupied surface levels to the molecule. SERS is typically performed by depositing nanoparticles of silver, gold, or other suitable SERS metals on a substrate such as rough glass and then adding a solution of the molecule to be analyzed on the substrate. Adapting this technique to in situ analysis requires depositing the silver particles directly on the material to be analyzed, i.e. inverted SERS arrangement (Sridhar et al. 2002).

6.2.2 Raman and Luminescence

It is well known that a molecular process closely related to Raman spectroscopy is luminescence. Its quantum yield can be as high as unity, depending on the system. For minerals that exhibit even weak luminescence, the Raman scattering will be completely obscured. The usual approach to avoid luminescence is to change the laser wavelength to avoid electronic excitation, but it is not always possible to find an effective wavelength. Sometimes this necessitates using a near-IR laser and an interferometer detector (Fourier Transform Raman Spectroscopy). However, NIR excited Raman spectroscopy is inherently insensitive, giving relatively low signal/noise ratio. The reason is that the intensity of the Raman signal is nearly proportional to the intensity of the incident laser light and inversely proportional to the fourth power of the laser wavelength, namely $I_{\text{Raman}} \sim 1/\lambda^4$. Besides that, a number of minerals still fluoresce strongly under NIR laser excitation. At first sight such dependence on wavelength is a compelling argument to utilize short UV wavelengths, but they usually induced very intensive luminescence in minerals. Nevertheless, for non-luminescent minerals UV Raman may be very effective.

An alternative approach is Shifted-Subtracted Raman Spectroscopy (SSRS). The simple way is to subtract broad luminescence background using fitting procedure and to leave sharp Raman bands behind. Unfortunately random variations in the pixel-to-pixel sensitivity may be larger than the actual Raman signals. However, every spectrum recorded with a given detector under the same experimental conditions will have the same irregularity in response. Thus, sets of spectra are recorded at two slightly shifted, usually for 1 nm, excitations (it may be done using dye or OPO laser). In such a way luminescence spectrum remains the same, while the Raman lines are shifted. The pairs of shifted spectra are then subtracted and Raman spectrum becomes visible (Bell et al. 2002).

Another possible solution that has been under development for three decades is to use a pulsed laser and time-resolved detection to allow the Raman photons to be discriminated from the broad luminescence background. The Raman interaction time is virtually instantaneous (less than 1 picosecond), whereas luminescence emission is statistically relatively slow, with minimum hundreds of picoseconds elapsing between electronic excitation and radiative decay. If we illuminate a sample with a very short ($\cong$ 1 ps) laser pulse, all of the Raman

photons will be generated within $\cong$ 1 ps, whereas most of the luminescence photons will be emitted at much longer times. If the detection system is gated so as to detect only those photons scattered or emitted during the laser pulse, we will collect all of the Raman photons but reject the majority of the luminescence. Two rather different time-resolved approaches have been most effective in yielding high quality Raman data from highly luminescent materials. The first used a streak-camera to provide time-resolved Raman data ($\cong$ 10 ps resolution), which gave an estimated improvement of 280 for a fluorophore with a decay time of 4 ns. The second method used a Kerr gate with 3 ps full width at half maximum, which achieved three orders of magnitude suppression of the background from a fluorophore with a decay time of 2 ns, and produced excellent Raman signals that were completely obscured in the not gated spectra (Everal et al. 2000/2001).

6.2.3 Raman in Geosciences

In the geosciences Raman spectroscopy has traditionally been a laboratory tool for structural analysis of minerals. Recent developments in instrumentation make possible the use of Raman spectroscopy as a tool for routine identification of minerals in field situations. The following advantages characterize Raman analysis of minerals: no sample preparation; in situ real time measurement; non-destructive and non-intrusive sampling; samples may be transparent or opaque; spectra are well resolved and with high information content.

In the physics of minerals field, picosecond lasers are still very exotic, but even nanosecond lasers may be very effective in certain cases. The sensitivity is limited by time duration of the excitation source, the minimum time window accessible with the detection electronics, the luminescence lifetime, and the quantum yield of the mineral in question. The longer the luminescence lifetime, the better the separation of the Raman and fluorescence signals will be. The mostly effective nanosecond gating is for luminescence centers with very long decay times, such as transition metals and trivalent rare-earth elements. For example, the steady-state Raman spectrum of calcite with Mn impurity is characterized only by broadband emission of Mn^{2+}, while the weak Raman line is practically invisible (Fig. 6.2a). However, using time-resolved spectroscopy with a very narrow gate of several ns enables us to suppress the long-lived luminescence of Mn^{2+} and to detect the previously hidden Raman lines (Fig. 6.2b). Time-resolved spectroscopy enables us to differentiate between narrow lines of trivalent rare-earth elements and Raman lines. Steady-state laser-induced spectra of rhodonite demonstrate under λ_{ex} = 532 nm several lines typical for REE^{3+} (Fig. 6.2c), while with narrow gate width of 10 ns several of those lines remain, which is impossible for REE^{3+} with their long decay times (Fig. 6.2d). Thus in the steady state spectrum combination of Tb^{3+} (544 nm) and Dy^{3+} (578 nm) and Raman lines at 670, 990 and 1,085 cm^{-1} take place.

An experimental setup with a notch filter enables us to detect Raman spectra of many minerals from 5–10 m, starting from a Raman shift of approximately

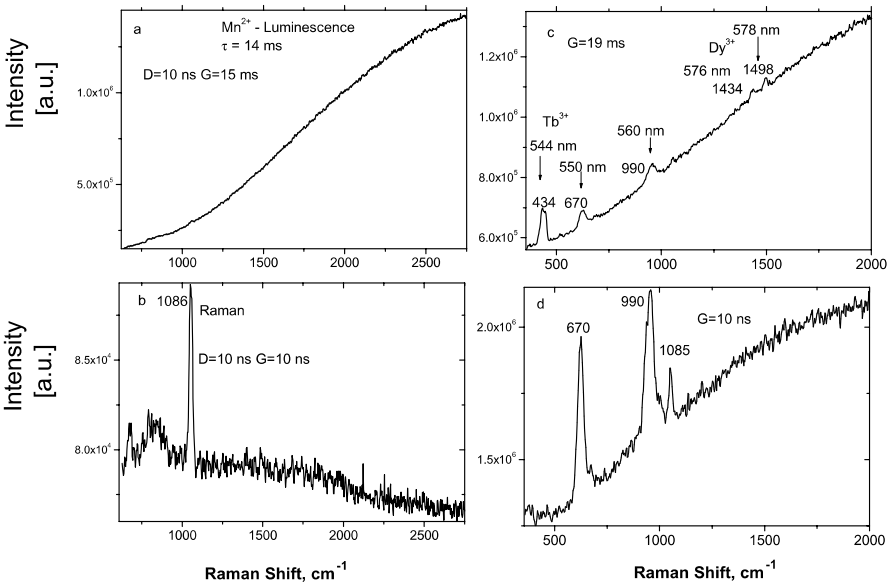

Fig. 6.2. a–d Time-resolved Raman spectrum of calcite with strong Mn^{2+} (**a**, **b**) and rhodonite with trivalent REE luminescence (**c**, **d**)

350 cm^{-1}. Several gated Raman spectra (Fig. 6.3) of minerals received in such a way demonstrate a quality quite satisfactory for identification needs. Thus, pulsed or time-resolved Raman spectroscopy offers two important benefits: (1) discrimination against unwanted ambient light, and (2) discrimination against long-lived emission from the sample. Advances in solid state lasers, gated intensified CCD detectors, small high-throughput spectrographs, and high performance holographic laser line rejection filters have made it possible to develop a high sensitive, compact and lightweight Raman system for remote analyses of minerals with visible laser excitation.

6.3
Second Harmonic Generation (SHG)

Another property of short-pulse lasers that has found wide application is their production of high peak powers. If one considers two independent light beams, which intersect at some point in space, it is a common experience that they pass through each other as if the other did not exist. This is a linear process and is observed in everyday life. However, if the light intensity is sufficiently great then non-linear coupling will occur, altering the properties of each beam. Second harmonic generation is one of many effects resulting from non-linear coupling between optical beams. The term "non-linear optics" is used to describe optical processes in which materials react nonlinearly to the electric field of the light incident on them. The result is that new frequencies

Fig. 6.3. Raman spectra of several minerals received using notch filter

can be produced and light beams can interact with each other when mixed together (Fig. 6.4).

In second harmonic generation, light of angular frequency ω pass through a crystal and generates a beam of angular frequency 2ω. With conventional light sources the electric polarization induced in the medium depends linearly on the electric field:

$$P = \varepsilon_0 \chi E \tag{6.9}$$

where χ is the susceptibility (tensor). Hence, if a beam of angular frequency ω is passing through the medium, a polarization oscillating at ω is produced

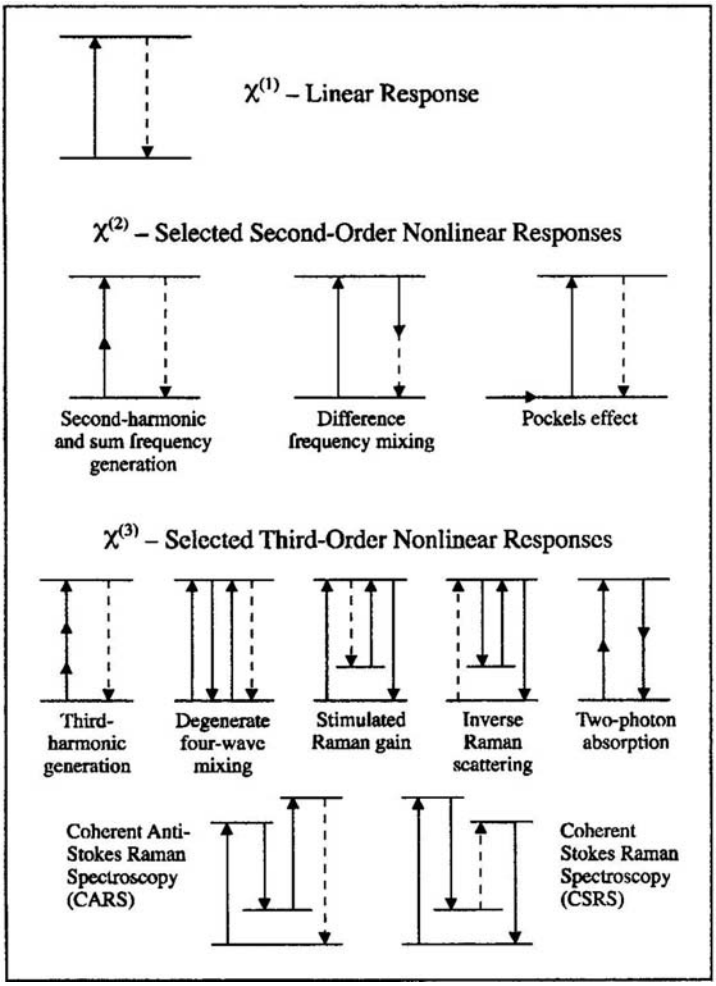

Fig. 6.4. Schematic representation of non-linear optics (Blanchard 2001)

which acts a source for the further propagation at ω of the original wave. This is only an approximation and at high intensities (as can be produced by lasers) the polarization is a non-linear function of electric field and hence the term non-linear optics. The polarization can be represented by an expansion in terms of the electric field:

$$\begin{aligned} P &= \varepsilon_0 \chi^{(1)} E + \varepsilon_0 \chi^{(2)} E^2 + \varepsilon_0 \chi^{(3)} E^3 + \ldots \\ &= \varepsilon_0 \left[\chi^{(1)} + \chi^{(2)} E + \chi^{(3)} E^2 + \ldots \right] E \end{aligned} \tag{6.10}$$

With a non-linear susceptibility, the polarization is composed of non-linear terms such as $\varepsilon_0 \chi^{(2)} E^2$, $\varepsilon_0 \chi^{(3)} E^3$ as well as the linear term $\varepsilon_0 \chi^{(1)} E$. It is clear that these elements in the polarization may be oscillating at 2ω and 3ω respectively, giving rise to harmonics of the original frequency ω. Because the higher order terms in the susceptibility are small compared with the first term, non-linear optical effects were not observed until after the invention of the laser in 1960.

To look at things slightly more generally, consider two beams of light incident on a crystal with a finite $\chi^{(2)}$, ignoring higher terms in the susceptibility. Define two electromagnetic fields:

$$\begin{aligned} E &= \frac{1}{2} E \exp\left\{ \mathrm{i} \left(\omega t - k z \right) \right\} + c.c. \\ E' &= \frac{1}{2} E' \exp\left\{ \mathrm{i} \left(\omega' t - k' z \right) \right\} + c.c. \end{aligned} \tag{6.11}$$

The magnitude of the total electric field due to their superposition is $E_{\mathrm{TOT}} = E + E'$ which gives a polarization of:

$$P = \varepsilon_0 \chi^{(1)} E_{\mathrm{TOT}} + \varepsilon_0 \chi^{(2)} E_{\mathrm{TOT}}^2 \tag{6.12}$$

The first term will only contribute frequencies of ω and ω' but the second term will generate the frequencies contained in E_{TOT}^2.

$$E_{\mathrm{TOT}} = \frac{1}{2} \left[E \exp\left\{ \mathrm{i} \left(\omega t - k z \right) \right\} + E' \exp\left\{ \mathrm{i} \left(\omega' t - k' z \right) \right\} \right] + c.c. \tag{6.13}$$

$$\begin{aligned} E_{\mathrm{TOT}}^2 = \frac{1}{4} \Big[& E^2 \exp\left\{ \mathrm{i} \left(2\omega t - 2kz \right) \right\} + E'^2 \exp\left\{ \mathrm{i} \left(2\omega' t - 2k' z \right) \right\} \\ & + 2EE' \exp\left\{ \mathrm{i} \left(\left(\omega + \omega' \right) t - \left(k + k' \right) z \right) \right\} \\ & + 2E^* E' \exp\left\{ \mathrm{i} \left(\left(\omega' - \omega \right) t - \left(k' - k \right) z \right) \right\} \\ & + 2EE^* + 2E'E'^* \Big] + c.c. \end{aligned} \tag{6.14}$$

Examination of E_{TOT}^2 term by term shows that there exists the possibility of generating the second harmonics of the two original angular frequencies ω and ω', the sum frequency $\omega + \omega'$, the difference frequency $\omega - \omega'$, and

DC electric fields. DC generation is known as optical rectification. The actual phenomena that will be observed depend on the experimental conditions and whether or not phase matching has been achieved. Three-wave mixing processes in which two beams interact to generate a third beam require the mixing medium to have a non-zero $\chi^{(2)}$. In an isotropic medium, reversal of the electric field will produce the same electric polarization as before reversal but in the opposite direction. An electric field of E_1 gives an electric polarization P_1:

$$P_1 = \varepsilon_0 \chi^{(1)} E_1 + \varepsilon_0 \chi^{(2)} E_1^2 + \varepsilon_0 \chi^{(3)} E_1^3 + \ldots \tag{6.15}$$

Reversal of the electric field such that $E_2 = -E_1$ gives an electric polarization P_2

$$\begin{aligned} P_2 &= \varepsilon_0 \chi^{(1)} E_2 + \varepsilon_0 \chi^{(2)} E_2^2 + \varepsilon_0 \chi^{(3)} E^3 + \ldots \\ &= -\varepsilon_0 \chi^{(1)} E_1 + \varepsilon_0 \chi^{(2)} E_1^2 - \varepsilon_0 \chi^{(3)} E_1^3 + \ldots \end{aligned} \tag{6.16}$$

Comparison of these two polarizations shows that $P_2 \neq P_1$. Hence, in an isotropic medium such as a gas or a liquid $\chi^{(2)} = 0$ and second order phenomena are not observable. Thus, only anisotropic media such as certain crystals are suitable for three-wave mixing processes. A consequence of a crystal being anisotropic is that it exhibits birefringence. However, the crystal birefringence enables phase matching to be achieved resulting in efficient generation of the new wave.

The second harmonic power I_2 is related to the crystal length ℓ and the mismatch parameter Δk ($\Delta k = k_1 - k_2$, where k_1 is the fundamental wave number and k_2 is the second harmonic wave number) in the following way:

$$\overline{I}_2 \propto \ell^2 \operatorname{sinc}^2 \left\{ \frac{1}{2} \Delta k \ell \right\} \tag{6.17}$$

If $\Delta k \neq 0$ then $\overline{I}_2$ is proportional to $\operatorname{sinc}^2 \left\{ \frac{1}{2} \Delta k \ell \right\}$ and it oscillates between zero and a certain maximum as the distance through the crystal is increased. However, if $\Delta k \Rightarrow 0$, $\operatorname{sinc}^2 \left\{ \frac{1}{2} \Delta k \ell \right\} \Rightarrow 1$ and $\overline{I}_2$ is proportional to ℓ^2 and the second harmonic intensity grows rapidly with increasing distance through the crystal. Phase matching is said to occur when $\Delta k = 0$ because then the refractive indices at the fundamental and second harmonic frequencies are equal or as the name implies, the phase velocities are equal. Under these conditions $\lambda_2 = \frac{1}{2}\lambda$ takes place. When $\Delta k \neq 0$, the second harmonic waves generated at different points along the path of the beam do not reinforce each other, as they are not traveling at the same speed as the fundamental wave. Thus, chaotic interference occurs and the second harmonic wave does not succeed in growing in intensity.

One common use of SHG is to convert the output of a fixed-frequency laser into a different spectral region. For example, the Nd-YAG laser operates in the near IR at a wavelength of 1,064 nm, while SHG is routinely used to convert the wavelength of the radiation to 532 nm. For $\chi^{(2)}$ processes, the conversion efficiency can be up to 30% for phase-matched case with a nanosecond laser pulse.

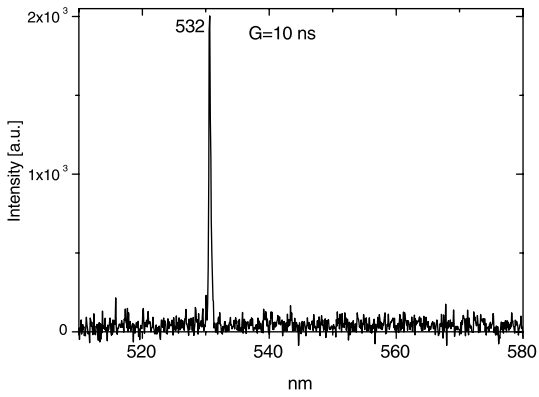

Fig. 6.5. Second harmonic generation by natural quartz under 1,064 nm irradiation

The study of nonlinear optical characteristics of minerals began in 1961 when Franken and his collaborators first observed how the red beam of the ruby laser with the $\lambda_1 = 694$ nm partly transformed to UV with the $\lambda_2 = \lambda_1/2$ after its passage through quartz crystal. Certain minerals besides quartz may be a non-linear medium. Prior to the invention of the lasers, the field of experimental nonlinear optics was virtually nonexistent, but growth in this area of spectroscopy has been dramatic, with a variety of nonlinear optical phenomena finding use daily. Using coherent spectroscopy and the method of Kurtz the space symmetry groups for 50 mineral species have been refined. A laser method for the rapid determination of the concentration of quartz and other non-centrosymmetric minerals in powder samples and thin sections was developed. The property of the quartz very effectively to convert IR laser irradiation at 1,064 nm to green light at 532 nm (Fig. 6.5) was used in the area of mineral separation, for example, in order to remove minerals of the feldspar group, which do not double the frequency of the laser radiation, from quartz-feldspar raw material. Quartz, which contains gas-liquid inclusions and quartz, which does not, differ both in the intensity of the SH and in the angular distribution of the intensity. This phenomenon may be used in quartz separation. Certain perspectives were gained for the gold-containing ores, i.e. those in which gold associates with quartz (Meisner 1984; Meisner and Kuz'min 1986; Meisner 1994).

CHAPTER 7

Minerals Prospecting

7.1 Earth Surface

7.1.1 Geology Applications

Powerful lasers as excitation sources make possible the use of luminescence for remote sensing. The basis of electromagnetic remote sensing is the recording by sensors placed on board aircraft or satellites of analogical or digital data, proportional to the intensity of an electromagnetic beam, reflected, emitted, or backscattered from the surface of the Earth. Where the source of the illuminating beam is the Sun, remote sensing is said to be passive. Remote-detection systems of Solar-Stimulated Luminescence are also known using Fraunhofer line discriminator. Fraunhofer lines (423, 486, 518, 589, 656, 687 and 760 nm) are bands of reduced intensity in the solar spectrum caused by the selective absorption of light by gaseous elements in the solar atmosphere. The sampling of these gaps in the smooth continuum, when compared with the direct solar emission, allows the determination of luminescence response.

Luminescence Lidar (Light Detection and Ranging) is an active instrument, which sends out coherent waves to the object concerned. A fraction of the transmitted energy is transformed by the objects and sends back to the sensor. Lidar instruments measure both the traveling time interval between sensor/object/sensor as well as the difference between emitted and returning energy, providing information on the exact position of the objects and on the material the objects are made of. Spectral selectivity was achieved usually with the aid of narrow band interference filters.

Within the past two decades environmental issues have drawn to attention the ease with which the biosphere can be perturbed. Lidar is playing an ever increasing role in studying and solving the different kinds of environmental problems. This method is ideally suited for detecting, identifying and mapping the oil spills and other kinds of pollutants, partly because of their own luminescence properties and partly because of "quenching" of the pure water luminescence. The last method may be used for surveying the total organic loading of natural bodies of water, which is very important because high contents of organic materials in the water can render the water harmful to man and the aquatic ecosystems (Measures 1984; Goldberg and Weiner 1989). Totally

ecologically pure luminescent tracers may be used to study water movement and drifts balance for natural bodies of water. Based on this, it is possible to recommend the placements of new hydrotechnical industrial enterprises, recreation zones and protection measures (Shteinman et al. 1997).

If the purpose of the given mission is to simply detect the presence of a specific target, such as a mineral, then the fluorescence return signal recorded within some pre-selected spectral window may be satisfactory. If, however, the mineral is to be distinguished from a similar background, then detection of fluorescence within one or even two spectral intervals may be inadequate. Indeed, from a luminescence point of view, emission intensity is very difficult to use, requiring a thorough knowledge of the overlap between the laser beam and the area of observation, the transmission losses, and the instrument calibration. In addition, the nature of the medium under investigation has to be well known, including the laser penetration depth and the scattering coefficient, which maybe controlled by the background. It is clear that the amplitude of the return signal is only a relative parameter possessing rather limited information.

In a remote sensing method operating under daylight conditions, the first principal limitations to detection of the faint fluorescence emission is imposed by the effects of solar radiation reflected from the mineral surfaces. The steady components of the solar radiation can be blocked electronically, but any fast-changing variations in reflected light and the electronic noise intrinsic to the PMP generated by the solar radiation will determine the minimum detectable change in intensity that can be ascribed to fluorescence. The second principal limitation is the presence of other unwanted luminescent components on the surface. Two main fields of laser-induced luminescence background of different nature can be revealed on the Earth's surface during minerals prospecting: the organic field consists of vegetation and inanimate organic substances disseminated in rocks (Fig. 7.1) and barren host rocks. This luminescence background is very strong, covers all the visible range and in many cases prevents target detection and identification by the steady-state laser induced luminescence method.

In the first attempts to overcome the background problem using decay time, the variation of the fluorescence decay time as a function of wavelength across the entire emission profile for a variety of materials have been used (Measures 1985). For a variety of rocks and minerals, it was proved that this information represents a new kind of signature, the so called fluorescence decay spectrum, that possesses considerable discrimination power, being able to characterize the irradiated material with far superior precision than the normal luminescence spectrum (Fig. 7.2).

In the following steps, decay times of different backgrounds, such as organic matter and host rocks, have been compared with decay times of industrial minerals (Seigel and Robbins 1982; Seigel and Robbins 1985). It was found that the decay time of complex organic molecules is characterized by two components of $\tau_1 \leq 20$ ns and $\tau_2 \approx 8-10$ ms, while barren host rocks with luminescence mainly connected with long-lived Fe^{3+} and Mn^{2+} have a decay time of several ms. Thus the intermediate vacant decay time range exists, which is a good "window" for targets detection and identification.

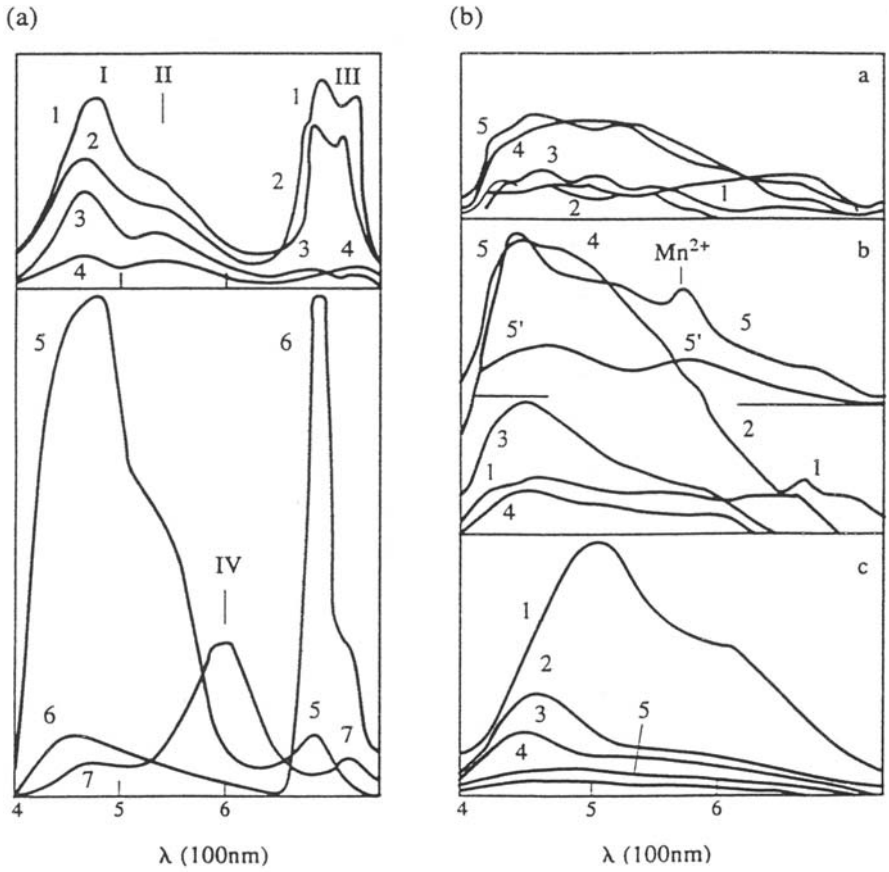

Fig. 7.1. Laser-induced luminescence spectra of foliage background (from Gorobets and Rogojine 2001)

According to accumulated experience, the discovered luminescence in this selective window may be related to certain ore bodies, such as uranium, wolfram, molybdenum, zinc, boron, and phosphorus bearing minerals. Another case is the so-called pathfinder minerals such as calcite, apatite, barite, and fluorite. These minerals presence may be related to the processes of differentiation of some ore forming elements and their accumulation in local structural and geomorphological traps. The accumulation of luminescent substances in separate sites of the Earth's crust is the result of the concentration of rare and ore elements. The ore elements give mineralogical and geochemical anomalies that can be used in searching for ore bodies. Such anomalies may form luminescent haloes in and around ore bodies, which have been mapped in the several mineral deposits (Kupriyanova and Moroshkin 1987; Gorobets and Walker 1994; Gorobets et al. 1995; Bushev and Portnov 2000; Portnov et al.

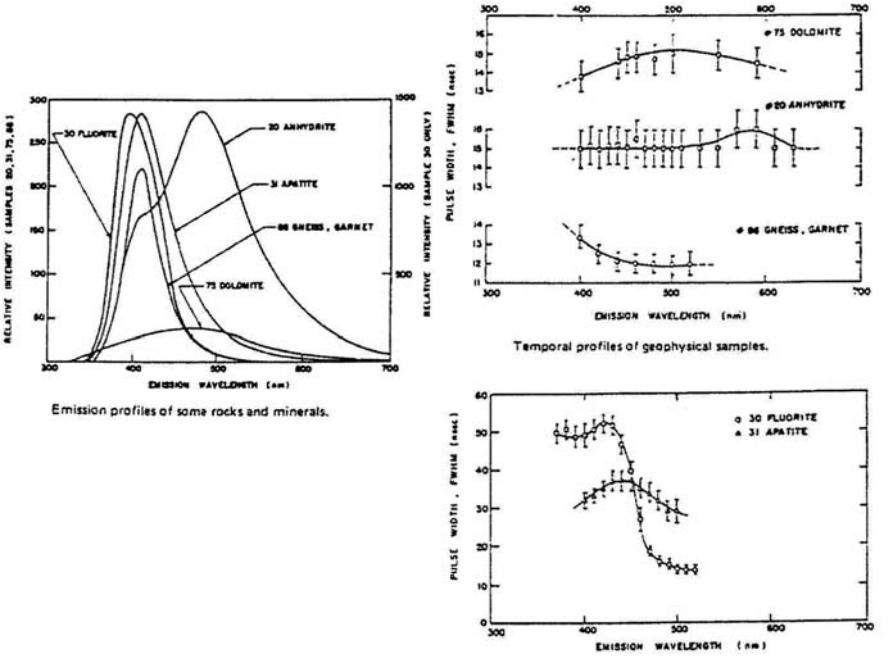

Fig. 7.2. Temporal profile of luminescence of minerals (Measures 1985)

2001). For example, the luminescent characteristics of calcite, apatite, zircon, barite and fluorite show the considerable influence of kimberlite on their country rocks. The luminescent haloes stretch up to some hundred meters and even to 1–1.5 km outside kimberlite bodies. Haloes around kimberlite-like pipes due to mechanical scattering of minerals were also detected with the aid of sand analysis. The most informative was the non-magnetic fraction smaller than 0.25 mm. The occurrence of apatite of "mantle" type with a bluish-violet glow of Ce^{3+} and Eu^{2+} within haloes surrounding some magnetic anomalies significantly increase the probability that a source of mantle fluids is located under them. Besides, luminescence haloes of mica pegmatite veins, connected with albite-oligoclase with a violet-blue glow and microcline with a violet glow of Eu^{2+}, haloes in ruby-bearing skarn, connected mainly with calcite with a red emission of Mn^{2+}, haloes of emerald-bearing bodies, mainly connected with apatite of "mantle" type and plagioclase with a blue emission of Eu^{2+}, haloes of mountain crystal veins, related to calcite with a red emission of Mn^{2+}, apatite, microcline and albite, and haloes of gold-bearing ore deposits, mainly related to outcrops of apatite, fluorite, calcite, scheelite and molybdoscheelite, have been described (Portnov et al. 2001). The luminescence of Eu^{3+} in scheelite may be served as an ore guide. It is particularly strong in the luminescence spectra of scheelite from gold-bearing quartz veins (Gorobets and Kudrina 1976; Uspensky et al. 1998).

An air-borne method of exploration for ore deposits has been realized with the help of luminescence Lidar. Lidar embodies a high power UV laser and a coaxial telescope detection system installed aboard a helicopter. The laser yields pulses having a peak power of 0.4–0.5 mJ, a time delay of 1 μs, gate width of 1 ms, repetition rate of 30–50 Hz, and a wavelength varying from 275 up to 400 nm. The laser "footprint" is about 400–500 cm^2 and the distance between the closest footprints about 1 m. The air-borne survey is carried out from an altitude of 50–75 m. Sensitivity is 0.2–0.5% by exposed area for most minerals (Seigel and Robbins 1982; Seigel and Robbins 1985).

Relatively recently, AIS Sommer GmbH of Germany delivered a laser-induced fluorescence (LIF) analyzer for quality control in minerals and mineral processing (Broicher 2000). The LIF analyzer includes two light detector systems with three photomultipliers each, which evaluate three spectral bands in two time windows each. It was done in the Kiruna phosphorous iron ore mine, Sweden. The limitation of LIF analysis is that its accuracy depends on the complexity of the composition of the ore and the concentration and fluorescence properties of the critical minerals in relation to all the other minerals present. The phosphorous iron ore in Kiruna is ideal for LIF analyzes, because its iron minerals are practically non-luminescent, while magmatic apatite is strongly fluorescent with intensive emissions of Ce^{3+} and Eu^{2+}.

7.1.2 Anti-Terror Applications

Another aspect of minerals and rocks laser-induced luminescence became important recently, especially in Israel. Terrorists have intensively used roadside bombs, while the plastic covers simulating local rocks have been used for camouflage of explosive materials. The possibilities of the luminescence method have been checked for the remote detection and identification of such camouflage materials. The luminescence properties of the colored plastics have been investigated in comparison with the corresponding properties of the dolomite rocks, which are imitated.

The steady-state luminescence spectra of three different plastics are characterized by blue luminescence with $\lambda_{max} = 445-465$ nm, while much broader luminescence band with yellow color characterizes the dolomite rocks. These spectra are different, but not enough to differentiate between them from big distance. The decay properties have been also checked in order to improve the selective feature. It was found that luminescence intensity of rocks in the blue part of the spectrum is drastically diminished after specific delay time, while the decrease of intensity in the yellow part of the spectrum is mush more moderate. Luminescence intensity of all plastics also diminishes after such delay, nevertheless remaining mush stronger then intensity of rocks luminescence in the blue part of the spectrum. The comparison of plastic and rock time-resolved spectra in specific time window clearly demonstrate that they are absolutely different, which made confident discrimination possible (Fig. 7.3).

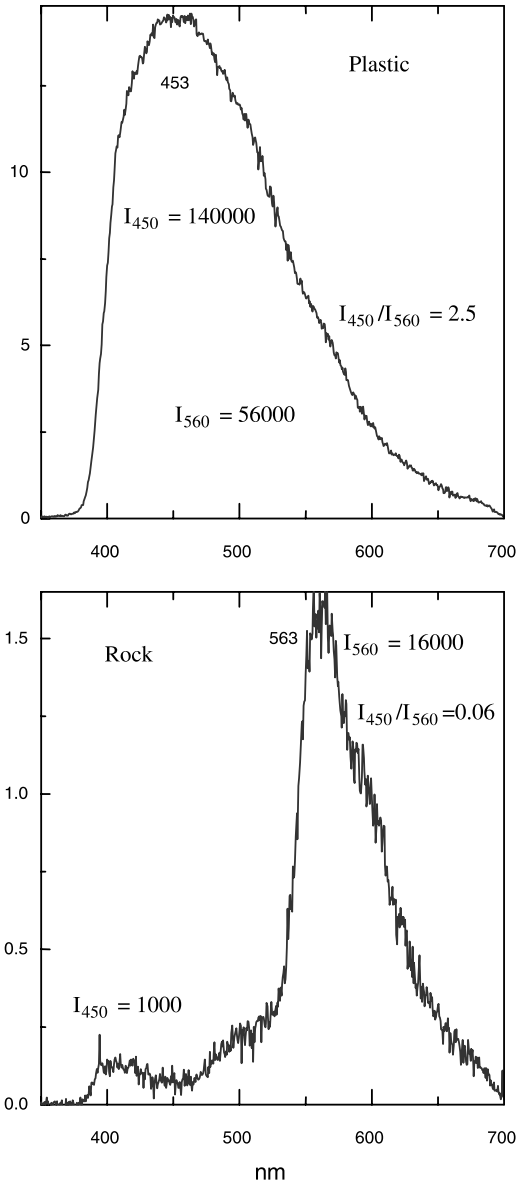

Fig. 7.3. **a**,**b** Laser-induced time-resolved luminescence spectra of plastic used for road-side bombs covering (**a**) and dolomite rock (**b**)

7.2 Earth Subsurface

The traditional subsurface rock characterization technique includes collection of field samples and subsequent analysis in the laboratory for both mineralogical and chemical data. A borehole or penetrometer sampler initially collects

the samples. These traditional techniques are characterized by relatively long time periods from sample extraction and preparation to laboratory analysis. Laser based spectroscopies enable us to employ the new techniques for both elemental and mineralogical determination by real-time, remote in-situ monitoring using a cone penetrometer unit with luminescence, Raman and LIBS equipments. Such systems are extensively used for environmental control of soil and groundwater contamination (Miziolek and Cespedes 1996).

7.3 Other Planets

7.3.1 LIBS System

NASA initiated programs for solar system exploration with the task of characterization of the different planets surfaces. The aim is a robotic ground investigation of the moon and other planets surfaces. Planetary rovers have provided and will continue to provide the mobility needed to explore terrains using remote sensing, conduct in-situ analyses of samples, and enable the detailed measurements needed to complement orbital observations (Golombek et al. 1997). One of the aims of the mission is to gather geological data, which may allow scientists to derive the location and quantity of minerals for future mining and space construction operations. The major elements of interest include: aluminum, calcium, magnesium, hydrogen, iron, oxygen, potassium, silicon, thorium, and titanium. In order to determine the elemental composition of the rocks, including hydrogen and oxygen, an elemental spectrometer is required.

The LIBS was recommended because of its speed of analyses, ability to analyze concentrated samples at a distance, versatility, and small mass and power consumption. Other instruments with similar capabilities, such as various particle spectrometers, require close contact and long analyses periods, and target larger sampling areas. Additionally, detection thresholds are typically higher and some critical elements, such as hydrogen, are often undetectable. The LIBS technique works well at pressures from one bar down to vacuum. As a function of decreasing pressure, the emission intensity rises strongly, reaching a peak roughly 10 times stronger at approximately 100 Torr pressure, before dropping off slowly, equaling terrestrial atmospheric intensity at 0.1 Torr and dropping slightly further in complete vacuum. For example, for Martian atmospheric pressures between 4 and 8 Torr, intensities are several times greater than observed at terrestrial atmospheric pressure. In simulated Martian atmosphere, using a very compact 35 mJ Nd-YAG laser at 19 m distance, detection limits for nearly all elements were found to be in the range of 2–700 ppm. The LIBS field instrument consists of two sections: the sensor head, which was mounted on the rover mast, and the body, mounted inside the body of the rover. The compact flash lamp-pumped Nd-YAG laser produces pulses of 10 ns duration and 85 mJ energy at 1,064 nm. The first LIBS results were qualitative in nature,

aimed at elucidating the mineralogy without giving exact elemental compositions. The instrument has a working range of 2–6 m (Wiens et al. 2001; Cremers et al. 2003).

7.3.2 Raman System

Raman spectroscopy, while typically used as a micro-analytical tool, can be conducted remotely. Performance of remote Raman analysis have been recently explored and realized for experiments on the surface of Mars (Sharma et al. 2001; Sharma et al. 2003). Raman spectroscopy is a powerful technique for mineralogical analysis, where the sharpness of spectral features of minerals allows for much less ambiguous detection, especially in the presence of mixtures. Visible, near-infrared, thermal, reflectance and in many cases emission spectroscopy of minerals all suffer from broad overlapping spectral features, which complicates interpretation of their spectra. On the other hand, Raman spectra of minerals exhibit sharp and largely non-overlapping features that are much more easily identified and assigned to various mineral species.

CW lasers based Raman remote sensing has been studied and the conclusion was that the high ambient light background during the day and long-lived fluorescence are significant problems with this method. However, utilizing a pulsed laser system and gated receiver overcome those limitations. A remote Raman system was constructed, utilizing a small pulsed Nd:YAG laser and 5-inch telescope coupled to a spectrograph with an optical fiber and gated intensified detector. The performance of such a pulsed-Raman system demonstrated the possibility to receive high quality Raman spectra of carbonates, silicates, hydrous silicates and sulfate minerals at distances from 10 to 66 meters. The quality of the data is sufficient to unambiguously determine the anionic groups present within minerals and in most cases further constrain the mineral composition.

The object of the other project was to investigate the feasibility of inverted SERS for analyzing small concentrations of organic molecules mixed with rock materials in the Mars soil. Chlorophyll, used as an analog of a biomarker molecule that could be present in small concentrations on Martian soil, yielded Raman spectra at concentrations as low as 78 femtomoles. Such a technique was also effective in detecting small concentrations of a powdered mineral mixed with a large concentration of another mineral, for example powdered pyrite mixed with silica powder. Minerals such as zeolites, where ion-exchange reactions occur between sodium and silver, also showed enhanced Raman scattering.

7.3.3 Combination of LIBS and Raman Systems

A minerals analysis at a distance of 10 m has been done with a modified Raman system to collect LIBS data, thus obtaining quantitative values for cation

composition in investigated samples. By analyzing the cation information collected in the LIBS experiment alongside the anion information provided by gated Raman scattering, a more complete image of the mineral's structure and composition can be obtained. The remote LIBS and Raman data on selected minerals clearly demonstrates that a development of a combined LIBS/Raman instrument will be very useful for planetary applications (Bishop et al. 2002; Hugh et al. 2002; Sharma et. al. 2003).

CHAPTER 8

Minerals Radiometric Sorting

In many mineral-processing installations it is of critical importance to provide an efficient mineral purification. Complicated processing steps involving grinding to very fine particle sizes carry it out. It is necessary to grind the particles in order to liberate the impurities from a mineral. However, purification of the coarse feed particles before grinding can provide significant benefit in overall energy efficiency and the final product purity. When the particles representing impurities can be separated before grinding they do not contaminate the feed stream for further processing and additionally they are not unnecessarily ground. This can be achieved by radiometric sorting carried out before the grinding stage when the particles have a size in a range of several centimeters.

Mineral sorting is a physical process in which particles are separated on the basis of their mineralogical composition. None of the minerals in the material treated undergoes any chemical change. The objective of any mineral-beneficiation process is to split the material being treated into two or more process streams. The intention is that valuable minerals are diverted into one stream, usually called the concentrate stream, while non-valuable minerals present are diverted into a second stream, which is called the tailings stream. At the same time as little as possible of the valuable minerals should be lost to the tailing stream. Sometimes when the mineral separations are difficult, a third stream, known as a middling stream, is produced.

Because the basis for mineral beneficiation is the physical separation of particles of different mineralogical composition, the success of such a particle separation as a means of separating one type of mineral from another depends on two prerequisites:

1. The most fundamental prerequisite is that the mineral to be beneficiated should, for the most part, be physically disengaged or liberated from the gangue, and
2. There should be sufficient differences in the physical properties of particles of different mineralogical compositions at the attained degree of liberation.

Provided that the physical properties of the minerals contained in the particulate ore are significantly different, the particles of distinct mineralogical compositions can be separated physically to achieve a mineral separation. Particles that consist predominantly of valuable mineral(s) will report to the concentrate under the influence of the exploited physical force, but will dilute

that concentrate with the valueless mineral(s) with which they are physically locked. Particles that consist predominantly of gangue minerals will report to the tailings, and the contained value-bearing minerals will be lost. What is needed to make good mineral separations is good mineral liberation, i.e. the proportion of multi-mineral particles should be minimized. If the degree of liberation in the run-of-mine material is insufficient, a higher degree of liberation is achieved by a size-reduction process (crushing and grinding), which reduces the particles into smaller fragments. In addition, each mineral beneficiation process requires an optimum size range for efficient processing; therefore, sizing operations are also required prior to mineral beneficiation operations. Two types of sizing operations are recognized, namely screening and classification. The former uses rigid surfaces that are uniformly perforated with apertures, and the surface acts as a go-no-go gauge so that particles are separated into oversize and undersize streams. Classification is based on the fact that particles of the same shape and density but of different sizes settle in a fluid (water, air) at different rates.

Ore sorting has long been used in mineral processing operations, and was first instituted as hand sorting according to a humanly perceived difference in the ore. Minerals applications today generally require automated sorting methods to cope with a high tonnage throughput in an economic fashion, and large mechanical sorters have been developed to meet this need. There are significant opportunities for the use of such technology in many minerals processing operations, but to date, industry applications have been limited to a few niche processing areas such as for diamonds, magnesite, talc and uranium ores.

The modern automated sorters (Fig. 8.1) are machines which examine feed lumps on an individual basis, compare the measured properties of each lump with predetermined criteria, and then separate the lumps, using an applied force, into different products according to the measured properties. A sorter treating −120 + 60 mm material typically treats 85–100 t/h and a unit treating −60 + 30 mm material – 30–40 t/h. Ore types treated by sorters around the world include different types of rocks (Mokrousov and Lileev 1979; Salter and Wyatt 1991; Cutmore and Eberhard 2001). These sorters were installed for one of the following duties: pre-concentration of plant feed, intermediate product production, finished product production. The main benefits are as follows:

- A pre-concentration plant reduces the main treatment plant's head-feed and can remove waste rocks for a fraction of the cost of treating the material through the complete process operation. In addition, the main plant may be fed at its optimum feed rate with a consistent grade of material thereby increasing overall plant economic performance. Besides that, very often the reject grade from a sorting plant is lower than the final tailings grade from the overall process without sorting thereby increasing overall economic recovery.
- If some distance separates the plants and the pre-concentration plant is situated nearer to the ore hoisting shaft or open pit then ore transport costs can be reduced significantly.

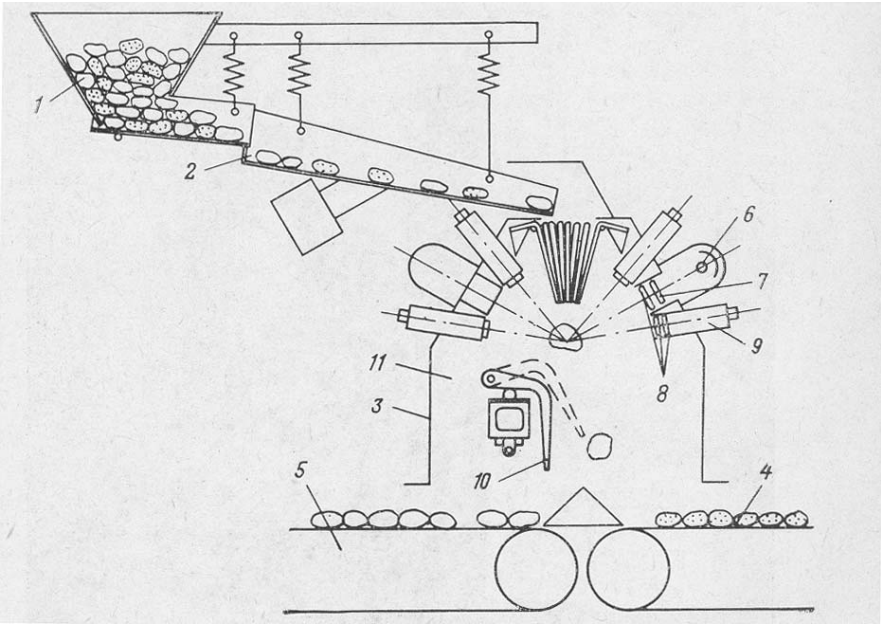

Fig. 8.1. Schematic representation of luminescent sorter: 1-funnel; 2-vibrational feeder; 3-frame; 4-conveyer for concentrate; 5-conveyer for waste; 6-luminescence excitation source; 7-collecting optics; 8-optical filter; 9-detector; 10-air valve (Moskrousov and Lileev 1979)

- The application of sorting can increase the life of the mine by increasing reserves to include in-situ and stockpiled previously below cut-off grade material. It also decreases the need for selective mining and often allows the previously stockpiled low grade or waste rock to be processed economically.
- The application of sorting can remove lumps with elevated concentrations of harmful components.
- Because of rich deposit exhaustion and the necessity to draw the low grade ores into production the volume of excavated rocks grows sharply and the velocity of waste accumulation constantly increases. Huge quantities of the mining industry waste not only fill the vaster territories of the Earth's surface but also influence very badly the ecological situation. But the ecological damage from this waste may be reduced due to additional products, which could be extracted here, because approximately 20–30% of useful minerals now are thrown away to the tailing dumps.

At the present time luminescent sorters are mainly used for the processing of diamonds, but also for the scheelite, fluorite and others types of ores (Mokrousov and Lileev 1979; Salter and Wyatt 1991; Gorobets et al. 1997a). The sources of luminescence excitation in these sorters are X-ray tubes and UV lamps, where the first is more powerful and the second is more selective. The UV impulse lasers employment as excitation sources enables us to combine the

very high power and extreme selectivity with the opportunity to use it for the discrimination of not only spectral, but also kinetic parameters of luminescence. Besides, other laser based spectroscopic techniques may be used with the same equipment. In the case of sorting the method must be much more effective than in remote sensing, since the distance from the excitation source to the sample is less, background from the daylight is absent and lumps of rock are washed and uniformly oriented. Despite of all this, this kind of sorting is not yet used. The main reason is the extreme complexity of natural raw materials and the absence of systematic investigations of mineral laser-induced spectroscopies.

8.1 Laseroluminescent Sorting

According to spectral-kinetic parameters, the optimal conditions of luminescence excitation and detection, so called selection window (SW) parameters, were calculated in the following way. At optimal for the useful component excitation, the luminescence spectra, decay time and intensity were determined for this mineral and for the host rock. After that, on the personal computer was calculated the proportion between useful and background signals for the full spectral region for each 50 ns after laser impulse. For calculation the spectral band was simulated by the normal distribution and the decay curve by the mono-exponential function. The useful intensity was multiplied by the weight coefficient, which corresponds to the concentration at which this component must be detected.

Relations between luminescence intensity in the corresponding SW and useful components concentration in the lumps were examined statically on an individual basis. For this task pilot equipment was developed, working in a polychromator regime with decay time registration in each spectral channel. Part of the channels monitors the luminescence of useful component and the remaining part detects the background. Personal computer analyses all information and calculates the contribution of background to the information about the mineral of importance. This pilot allows us to make one-source or two-sources excitation, to detect luminescence immediately after laser pulse or after a definite time and to account for the matrix effect, when the optical parameters of host rock influence on the luminescence intensity (Gaft et al. 1989c).

The main problem for luminescent sorting is the absence of natural luminescence in the case of very many industrially important minerals. In such cases artificially induced luminescence may be used. White (1984), for example, described such an approach to the differentiation of samples. Here the natural luminescence of accept and reject fractions is similar. The basis of separation of magnesium-bearing ore particles is obtained by first conditioning the exposed magnesium-rich mineral with a surface coupling agent of hydroxquinoline, then irradiating the conditioned ore to excite and induce fluorescence and then effecting separation of the magnesium-rich minerals from the lean ore

particles by detection of the difference of the intensity of the fluorescence. This method detects ores having high magnesium contents on the surfaces of the pebbles. Such an approach was also proposed for beneficiation of the precious metal ores (Gaft et al. 1991a; Gaft et al. 1991b).

8.2 LIBS Sorting

The available sensing technologies include nuclear, optical, electrical, magnetic, acoustic, thermal, and various others specific to the ore. Mostly the properties are used, which are indirectly connected with mineralogical composition of accepted and rejected minerals. The only method, which directly determines the major elements of separated minerals is the XRF technique. Nevertheless it is not suitable for the light elements, usually with an atomic number less than 20. If the energy of characteristic emission is less than 5 keV, the interference is very strong because of air absorption and water on the minerals surface. Besides, in many cases the XRF method is not selective enough, because many elements present with characteristic emission similar to those of valuable components (Table 8.1).

LIBS presently is mainly used for quantitative and semi-quantitative analyses. Much less attention has been paid to the potential of LIBS for qualitative analysis, which may be effectively used in radiometric sorting of minerals. In this sense we do not need to determine a detailed chemical composition of the minerals, but rather the aim is to find the specific lines, which enable us to identify the corresponding mineral. LIBS mineral sorting is in its early stages, but the prospects are very good. We developed the corresponding database of time-resolved LIBS under 1,064, 532, 355 and 266 nm laser excitations for the spectral range from 200 to 900 nm.

The main minerals in our library are apatite, calcite, fluorite, dolomite, borosilicates, zircon, scheelite, quartz, feldspars, micas, oxides of Mn, Fe, Ti, Al, Pb, native gold, silver (Table 8.2). The temporal history of the plasma was obtained by recording the emission features at predetermined delay times for the gated intensifier, while the intensities of the lines were obtained by integration of the peak area. To determine the temporal behavior of element related emissions, plasma emission spectra of mostly important elements were recorded at different delay times. Such information is very helpful in order to obtain a good compromise between the signal/noise ratio and the emission intensity of the selected lines. It is clear that the proper time delay is related to the energy of the laser, its wavelength, the target characteristics and the surrounding atmosphere (Sabsadi and Cielo 1995). Our results are mainly agreed with known temporal behavior of emissions from different species in the air: ions appear at early times ($< 2\,\mu s$), followed by neutral atoms (2 to 10 μs), and then simple molecules ($> 10\,\mu s$) (Radziemski et al. 1983).

The data from Table 8.2 evidence that practically in all cases it is possible to find the emission lines, which enable us to differentiate between accepted and rejected elements. Based on the minerals LIBS library, a method

Table 8.1. Characteristic association of metals in rocks (Ostapenko 1990)

Range of XRF spectrum	Element	Interfering element I	II	III
High energy	W	Fe, Cu, Zn, Mo, Sn, As	Pb, Bi	
	Pb	Fe, Cu, Zn, Sb, Ba, Sn	W	Bi
	Hg	Fe, Sb, Ba, As	W	Pb
	Bi	Fe, Mo, Sn, Zn	W	Pb
Average energy	Ba	Fe, Pb	Sb, Sn	Cs
	Cs	Fe		Ba
	Sb	Fe, Cu, Zn, Hg, Pb, As	Ba	Sn
	Zn	Fe, Cu, As, Zn, W, Pb	Mo, Ba	Sb
	Mo	Fe, Cu, W, Pb, Zn, As	Sn, Cs, Ba	
Low energy	Zr	Fe, Ti		
	Rb	Li, Be, Cs, Ta		
	As	Fe, Sn, Sb	Cu, Zn	Hg, Pb
	Zn	Fe, Mo, Sb, Sn, Ba	Fe, As, Pb	Cu
	Cu	Mo, Sb, Sn, Ba	Fe, As, Pb	Ni, Zn
	N		Fe	Co, Cu
	Fe		Ti	
	Cr		Fe	
	Pb	Fe, Cu, Sn, Sb	W, Hg, As	Bi
	W	Mo, Sn	Pb, As, Fe	Cu, Zn

has been developed for real time detection and content evaluation of minerals or trace concentrations of elements in minerals as they are conveyed on a moving belt, using the intensity ratios of the emission lines characteristic for specific elements or minerals. Because associated minerals always have different chemical compositions, namely major or minor elements, the relative intensities, defined by their characteristic spectral lines, enables all phases to be consistently identifiable and assessed within a short time span which is consistent with both LIBS and the moving belt system (Gaft and Nagli 2004).

Three main methods of pebbles irradiation and survey are used in radiometric sorting: a) integral where irradiation and survey zone is bigger than the pebble with maximal dimensions, namely simultaneous analyses of the whole sample; b) scanning with narrow aperture where irradiation and survey zone have a strip form perpendicular to pebbles movement trajectory, namely passive scanning using pebbles movement; c) point scanning where irradiation and survey zone is much smaller than pebbles dimensions, where at each time interval a small part of pebbles surface is analyzed, while an active scanning is accomplished in direction perpendicular to pebbles movement.

Table 8.2. LIBS lines of different elements important for mineral sorting

Element	λ_{emis}
Ag I	328.1, 338.3, 405.5, 418.5, 421.0, 478.7, 487.4, 520.9, 546.6, 567.7
Al II	308.2, 309.3, 394.4, 396.2, 515.0, 560.0, 618.0
Au I	242.8, 267.8, 311.1, 389.8, 406.5, 461.2, 479.5, 596.8, 627.8
B I	249.6
Ba II	413.6, 455.4, 493.4, 614.2, 650.0
Ca I	422.7, 430.0, 445.0, 527.0, 558.0, 617.0, 656.0, 672.0,
Ca II	317.0, 370.0, 373.0, 393.3, 396.7, 644.0
Cr I	298.6, 301.8, 358.0, 359.5, 425.5, 427.5, 429.0, 520.9
Cr II	268.1, 283.5, 360.5
Cu I	324.8, 327.4, 510.6, 515.3, 521.8
F I	532.0, 603.8, 604.5
Fe I	274.0, 358.0, 374.0. 382.0
K I	766.5, 769.9
Li I	610.0, 670.8
Mg I	285.2, 383.8, 518.3
Mg II	279.5, 280.2
MnI	403.3
Mn II	257.6, 259.5, 279.7, 293.3, 403.3
NaI	589.00, 589.6
O I	615.0, 777.5, 822.0, 845.0
P	253.4, 255.3 4,000
PbI	280.2, 357.2, 363.9, 368.3, 405.8, 423.5
Si I	250.7, 263.1, 288.3, 391
Si II	386.0, 413.0, 504.0, 576.0, 634.0, 637.0, 657.0
Sn I	270.6, 284.0, 286.3, 301.1, 303.4
TiII	308.0, 317.0, 323.0, 334.0
Zn II	213.9, 330.3, 334.5, 412.0, 429.0, 471.0, 481.0, 636.0
Zr II	268.1, 339.2, 347.8, 350.0, 360.2

It is evident that LIBS sorting may not be accomplished by integral irradiation, because it is based upon plasma analyses generated on relatively small area by focused laser beam. Nevertheless, if each pebble is composed of only one mineral, one laser pulse will be representative enough in order to determine the pebble composition. For uniformly embedded ores the situation is different and 2–5% of the pebble area has to be covered for the confident identification of useful mineral. Non-uniformly disseminated ores demand even more detailed scanning, which has to be determined individually for

each specific case. Lets consider parameters of laser and detector, which may be suitable for such cases. The following sorting conditions are selected as the mostly representative: the pebbles size of −20 + 40 mm and movement velocity in irradiation zone of 1 m/s. In such case the maximum sample area is 1,600 mm^2 and 30–80 mm^2 has to be scanned for uniformly disseminated ores during 40 ms when the pebble will be under laser beam. According to our experience, one laser pulse at 1,064 nm with energy of 5 mJ and duration of 8 ns generates plasma from the area of 0.2 mm^2. Contemporary Nd-YAG lasers, for example Quanta-Ray PRO-290, may generate 1,000 mJ/pulse with frequency rate of 50 Hz. In such case approximately $0.2 \times 200 = 40\ mm^2$ may be sampled during one pulse. Working with 50 Hz frequencies, one pebble will be analyzed twice and 80 mm^2 sampling may be achieved, which is compatible with practical demands.

8.3 Combination of Sorting Techniques

Luminescence and LIBS techniques may be used simultaneously with the same basic equipment. This property may be effectively used in minerals sorting. Besides that, other methods such as Raman and SHG may be effective.

8.3.1 Diamonds

Diamond bearing host rocks are crushed, then the diamonds are separated form the lighter minerals by gravimetric methods such as rotating pans. This produces a heavy mineral concentrate. One of two things is done with the concentrate. The concentrate is blended with water and passed over a grease table to catch the diamonds. The diamonds will adhere to the grease whereas most of the remaining minerals do not. In another option, the concentrate is passed in a dry state through an X-ray sorting machine, which identifies the diamonds by the X-ray induced fluorescence.

8.3.1.1 Luminescence Sorting

Diamond luminescence was studied mainly with the two following aims: to carry out a fundamental investigation of its physical properties and to determine the optimal conditions for luminescent sorting of diamond bearing rocks. For the first task, diamond photoluminescence was studied at liquid nitrogen temperature at which luminescence centers are marked by characteristic zero-phonon lines and are much more informative then at room temperature. For the second task, were diamond is one of the first minerals for which luminescence sorting was used, luminescence properties should be studied at 300 K. In the first stages it was established that X-ray luminescence of the *A*-band

always characterizes natural diamonds, while certain diamonds are without photoluminescence under UV lamps excitation. Thus it was concluded that sorting under X-ray excitation is better and such separators are used now in the diamonds industry. This conclusion was not changed after the first experiments with nitrogen lasers, which were relatively weak in order to achieve the needed recovery.

It is important to note that the modern X-ray diamond sorters use pulsed excitation. According to statistical analyses, 2 kg of rock contains one diamond crystal and 10^8 particles of other minerals including 10^6 particles of minerals with luminescence under X-ray excitation. The most abundant luminescent minerals are plagioclase, zircon and calcite. The luminescence of diamond is selected, first, by spectroscopic filtration, which is very good to "kill" the yellow zircon luminescence, and, second, using the temporal behavior of diamond emission under X-ray pulse excitation. The diamond is characterized by two decay components of the *A*-band, short of 100 ns and long of 3–10 ms, while plagioclase has decay time of 10 µs and calcite of 40 ms. During X-ray pulse with a 10 ms duration, plagioclase reaches its excited state on 100%, while for calcite this parameter is only of 1–2% and for diamond of 10–15%. Detection is accomplished in time-delayed mode, where it is started 10 ms later after the end of X-ray pulse. During this time the plagioclase emission is totally quenched, while the calcite signal remains on the 1–2% level. Diamond signal becomes twice lower, but it is well above the noise and may be electronically treated.

At the present time new deposits have been discovered which contain diamonds without luminescence under X-ray excitation. Sometimes the portion, which is unrecoverable in X-ray luminescent sorters, is big enough to warrant the development of a new sorting method. The luminescence spectra were investigated under excimer (193, 222, 248 and 308 nm), nitrogen (337 nm) and dye laser (340–360 nm) excitations (Fig. 8.2).

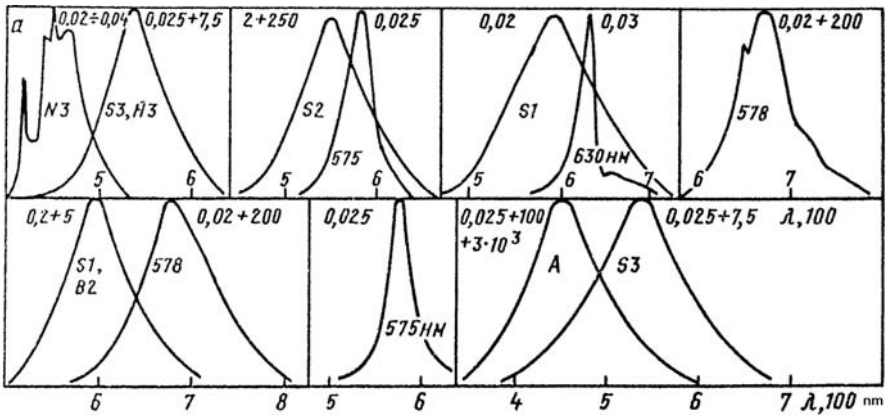

Fig. 8.2. Laser-induced luminescence spectra of diamonds at 300 K

It was found that for such diamonds the UV excitation by powerful UV lasers is very effective. The best way is to use the luminescence excitation by two lasers with different wavelength – the excimer laser with the line at 222 nm which excites the *A*-band, and the nitrogen laser which excites mainly *S*3 and "578 nm" centers. The *A*-band is present in approximately 95% of investigated diamonds, but with a big intensity variation. Practically all the diamonds with the weak *A*-luminescence are characterized by strong luminescence under nitrogen laser excitation. Detection is carrying out at two spectral-kinetic selective windows – between 420 and 480 nm with a time delay of 3–9 ms and between 450 and 650 nm with a time delay of 1–20 μs. Comparative investigation yielded the following results: in 12% of the sampling laser excitation is much more effective and may be used even for recovering diamonds from the wastes of X-ray sorters; in 85% of the sampling laser excitation is better and allows for higher feeding rates and recovery efficiency; in 3% of the sampling the diamonds were not luminescent under both kinds of excitation (Gaft 1989; Gaft et al. 1990; Gaft 1993).

8.3.1.2
Raman Extracting

Diamond is crystallized in cubic form (O_h^7) with tetrahedral coordination of C–C bonds around each carbon atom. The mononuclear nature of the diamond crystal lattice combined with its high symmetry determines the simplicity of the vibrational spectrum. Diamond does not have IR active vibrations, while its Raman spectrum is characterized by one fundamental vibration at 1,332 cm^{-1}. It was found that in kimberlite diamonds of gem quality this Raman band is very strong and narrow. In defect varieties the spectral position does not change, but the band is slightly broader (Reshetnyak and Ezerskii 1990).

Recently a new two-stage method of extracting diamonds was proposed, which is based on the use of laser radiation (Gudaev et al. 1997; Gudaev et al. 1999). In the first stage, Rayleigh scattering is used for initial beneficiation of the rock. The final extraction is performed on the basis of Raman scattering. In the first stage, all transparent objects are extracted from the rock regardless of the scattering features of the surface and volume. In the second stage, diamonds are extracted from the beneficiated rock, using the characteristic Raman signal of diamond. The advantages of the technology proposed are a significant decrease in the cost of detection devices and their dimensions, improved ecological safety, and possible extraction of high-quality diamonds that are not detected by the X-ray luminescence method.

8.3.2
Industrial Minerals

Industrial minerals are natural minerals and rocks used as raw materials or functional additives in a wide range of manufacturing and other industries.

The characteristics of the minerals sold depend upon the physico-chemical characteristics of the ore body from which they are extracted. Processing of the minerals before sale can be simple (mainly crushing, grinding and classifying), but may also be very sophisticated for the most expensive mineral types.

8.3.2.1 Calcium Carbonates

Industrial calcium carbonate ($CaCO_3$) is mainly produced by extraction/milling of natural ore. Suitable ore-bodies include chalk, limestone, marble, and travertine. Sufficiently pure ore-bodies are selected to allow direct exploitation. The main applications include paper, paints, plastics, pharmaceuticals, etc. Luminescence and LIBS (Fig. 8.3) sorting may be used for calcium carbonate ore radiometric sorting.

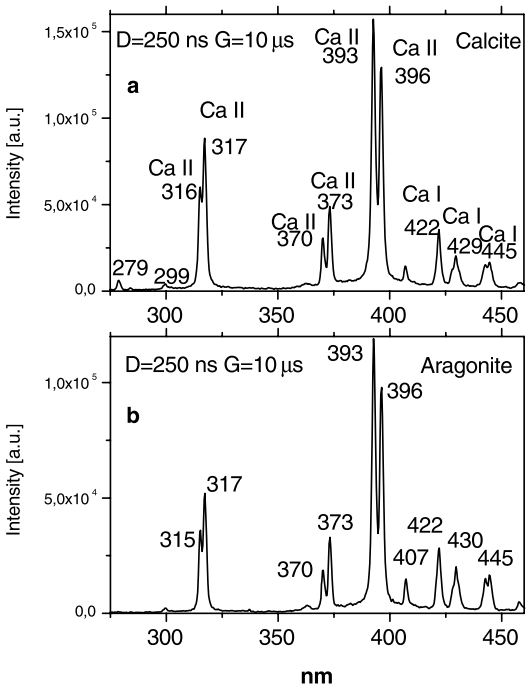

Fig. 8.3. a–b LIBS spectra of calcite and aragonite

8.3.2.2 Datolite and Danburite

Borates and borosilicates are used in hundreds of products and processes in ways that touch the lives of almost everyone. Major uses include glass production, detergents, agriculture, enamels, and ceramic glazes. Apart from

the industrial aspect, boron is an essential micronutrient, integral to a plant's life cycle and, as becomes increasingly obvious, essential to animal life as well.

8.3.2.2.1
Luminescence Sorting

Datolite and danburite have been sorted by neutron separation (Mokrousov and Lileev 1979). These minerals are characterized by strong UV-violet luminescence under laser excitation, which may enable us to sort them from the quartz host rock. Because the decay time of organic matter on quartz and Ce^{3+} in datolite are very close, the differencies in excitation and emission spectra may be used. A pilot unit was constructed and transported to the plant (Dalnegorskoe deposit, Russia) and sorting in a static regime was tested for the ore preconcentration and for the reprocessing of the coarse waste from heavy media separation (Gaft 1993). All sorting products were analyzed on useful (B) and harmful (Ca, Fe) elements. It was found (Table 8.3) that for datolite ore with lump sizes −50 + 30 mm it is possible to receive technological concentrate and waste product. The technological products after luminescent sorting are better then after heavy media separation, which is used in the factory. Besides, 30% from the old waste may be ex-

Table 8.3. Results of datolite $CaB(SiO_4)(OH)$ ore laseroluminescent sorting

Products before and after sorting	Yield	Concentration			Recovering
		B_2O_3	$CaCO_3$	Fe_2O_3	B_2O_3
1. **Before**					
Ore (−120 + 70) mm	100	8.4	17.6	4.1	
After					
Middling product	69.6	11.1	14.3	3.0	92.0
Coarse waste	30.4	2.4	25.0	6.5	8.0
2. **Before**					
Ore (−50 + 30) mm	100	7.64	9.9	4.6	78.8
After					
Concentrate	43.0	14.0	7.4	2.2	6.1
Middling product	9.0	5.2	12.0	7.0	15.1
Coarse waste	48.0	2.4	11.8	6.3	
3. Products of liquid separation (−50 + 30)					
Before					
Waste	100	4.3	32.0	2.04	
After					
Middling product	30	10.6	22.2	2.25	74
Coarse waste	70	1.6	36.0	1.95	26

tracted with the average concentration of useful component more then in the excavated ore.

8.3.2.2.2
LIBS Sorting

It is possible to suppose that LIBS sorting may be better than the luminescent one. It is clearly seen that the corresponding spectra of borosilicates, quartz and calcite are totally different (Fig. 8.4), which make radiometric sorting easy and confident.

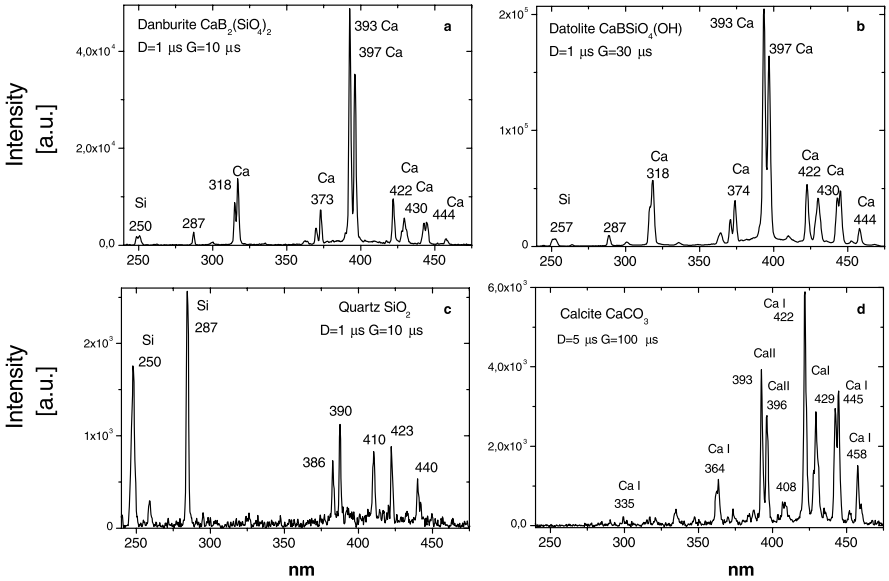

Fig. 8.4. **a–d** Time-resolved LIBS of datolite and danburite and gangue quartz and calcite

8.3.2.3
Microcline and Plagioclase

Feldspar is by far the most abundant group of minerals in the Earth's crust, forming about 60% of terrestrial rocks. The classification of a wide range of rocks is based on their feldspar content. Most frequently, commercial feldspar is mined from pegmatite, feldspathic sands or aplite deposits. For some applications, the ore has to undergo processing in order to remove some accessory minerals, such as quartz, mica, while in other cases their presence is advantageous. The two main properties that make feldspar useful for industry are its alkali and aluminum content. Main applications include the ceramic and glass industries.

8.3.2.3.1
Luminescence Sorting

For separation between microcline and plagioclase X-ray excited luminescence is used (Gorobets et al. 1997). The main problem is that their emission spectra are very close. Under laser excitation these minerals also demonstrate blue emissions connected with Eu^{2+}, which have close spectral and kinetic parameters. Nevertheless, the differences in excitation spectra (Fig. 8.5) enable effective sorting.

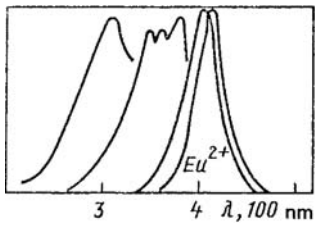

Fig. 8.5. Excitation and luminescence spectra of microcline and plagioclase

8.3.2.3.2
LIBS Sorting

Because the main reason of microcline-plagioclase sorting is to control the Na/K ratio, LIBS may be excellent separation technology. The analytical lines of Na and K are very strong and specific in order to promise confident identification (Fig. 8.6).

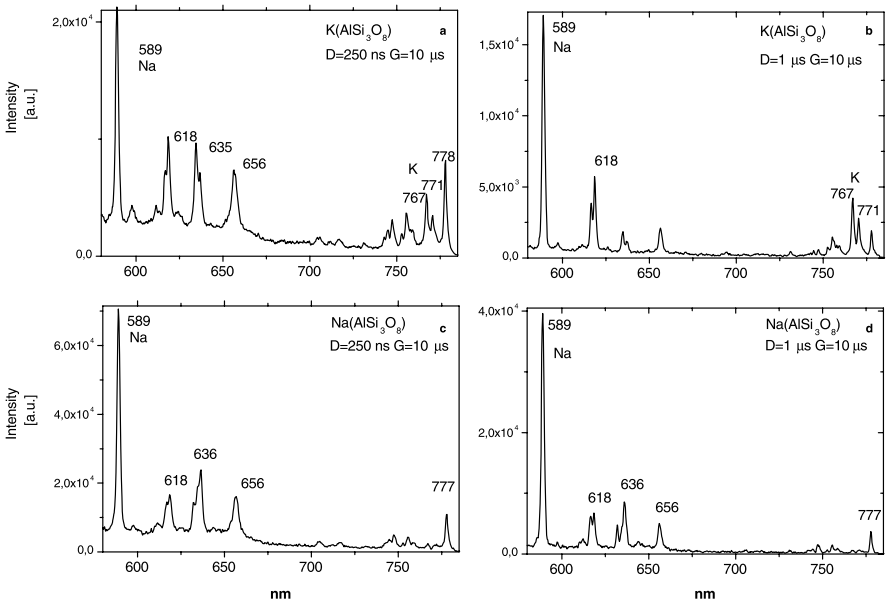

Fig. 8.6. Time-resolved LIBS of microcline and plagioclase

8.3.2.4 Silica

Crystalline silica is the name of a group of minerals composed of silicon and oxygen. The term crystalline refers to the fact that the silicon and oxygen atoms are arranged in a three-dimensional repeating pattern. The main minerals included in this group are: quartz, cristobalite and tridymite. Quartz is the most common of them and, after feldspar, is the second most abundant mineral on the Earth's surface. Crystalline silica, basically in the form of quartz, has been mined for thousands of years. It is really one of the building blocks of ancient and current civilizations, being also vital for modern technologies. Main applications include glass production, foundry, ceramics, building materials, etc. Crystalline silica has also acquired a fundamental place in the emerging information society, as the source of silicon.

The mostly difficult problems in quartz sorting are quartz-feldspar ores and differentiation of vein quartz into transparent and milky varieties. In the first case LIBS separation may be effective using Al emission lines present in feldspar, which are absent in quartz (Fig. 8.7).

For the second task second harmonic generation by quartz has been proposed. The first procedure is to determine the relative intensity of SH compared with etalon, where the ratio of SH intensities is used for sorting. In the second procedure the laser source is working with a very high repetition rate and the number of pulses with SH intensity above a certain level is used as the separation criterion. Sorting using non-linear optics may be very effective, because

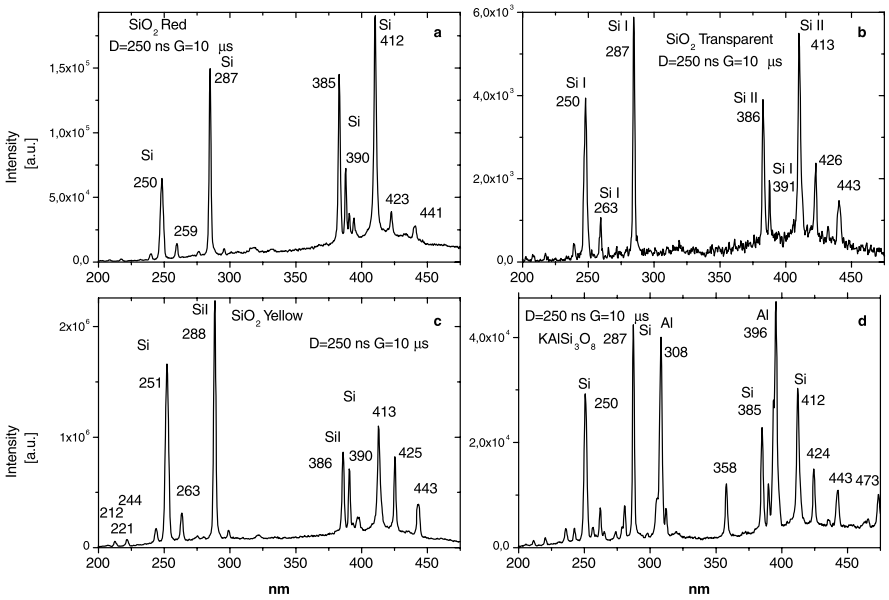

Fig. 8.7. LIBS of quartz and feldspar

the number of minerals with SH generation ability is relatively low, while only nepheline is abundant (Meisner 1994).

8.3.2.5 Fluorite

Fluorine for industrial use is almost exclusively obtained from fluorite. There are many possible fluorite-ore types. It occurs as fissure-fill and manto-replaced types, and in pegmatites, residual/eluvial deposits, carbonates and phosphate deposits. It is a gangue mineral in many base metal deposits, but due to stringent trace metal requirements often can't be economically beneficiated to a saleable product. Most fluorite ores are selectively mined, and ore from some minor vein deposits is then upgraded to a saleable product by sorting.

8.3.2.5.1 Luminescence Sorting

Fluorite is used as a flux in steel making and in the smelting of ores. Luminescence sorting of fluorite is a well-known technique, which is based on the strong blue luminescence of Eu^{2+}.

8.3.2.5.2 LIBS sorting

The LIBS technique may be extremely useful for sorting of fluorite ores. Figure 8.8 clearly demonstrates the opportunities of time-resolved LIBS in comparison with the steady-state method in the case of fluorite-carbonate ores. Fluorite and calcite both has Ca as a major element and its emission lines dominate in the steady-state spectra making sorting impossible. After a delay of several μs the intensity of Ca lines is strongly diminished and a F line with a longer decay becomes visible in the fluorite spectrum.

8.3.2.6 Barite and Gypsum

Barite belongs to the bulk minerals and is very rarely used as a source of metallic barium, but it is used in drilling fluids, paints, glass and as a filler in paper products. Conventional open pit methods and processes usually selectively extract barite by crushing and pulverizing. High-grade ores may not require any further concentration prior to sale. For lower grade ores luminescence sorting based on the UV band at 350 nm under X-ray excitation may produce a coarse-grained concentrate (Gorobets et al. 1997). As the drilling industry will not accept barite containing galena and other sulfides, or siderite, a saleable concentrate cannot usually be made from the barite gangue in base metal deposits. It may be proposed that LIBS and Raman methods may be effectively used for radiometric sorting of barite because of strong and characteristic emission lines of Ba and the strong Raman bands of barite (Fig. 8.9).

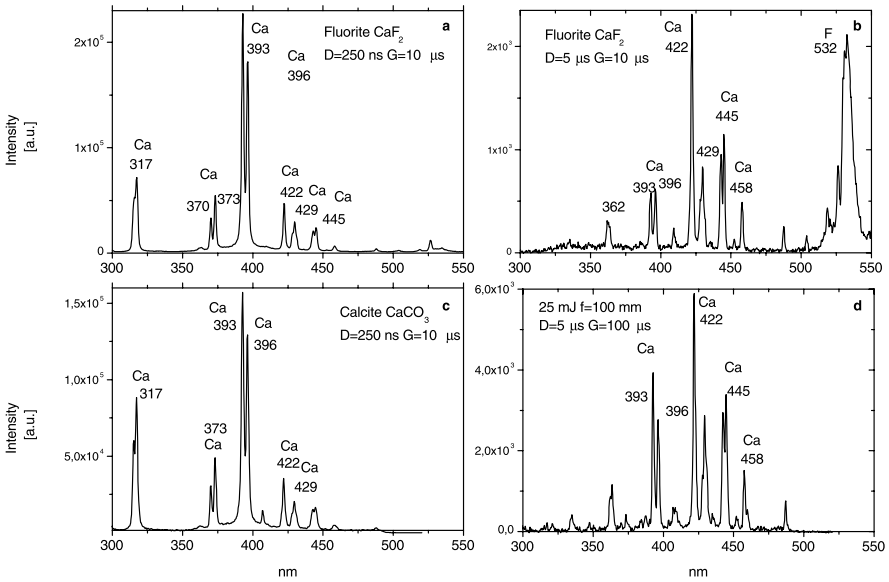

Fig. 8.8. Time-resolved LIBS of fluorite and calcite

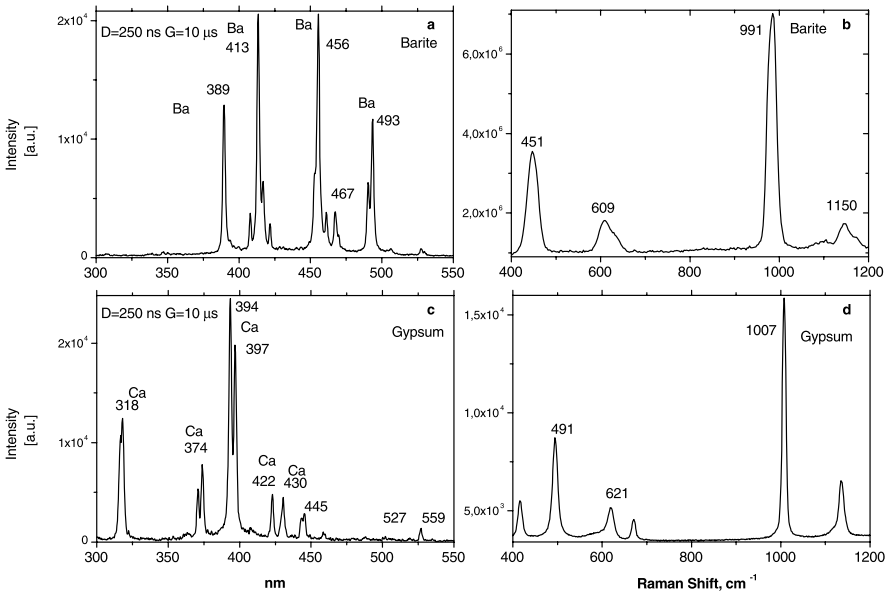

Fig. 8.9. Breakdown (**a, c**) and Raman (**b, d**) spectra of barite and gypsum

Most gypsum $CaSO_4 \times 2H_2O$ is used in building construction, to make plasterboard or as a setting retardant in Portland cement, but there is also substantial usage in developed countries as a soil conditioner. Gypsum sorting may be made using its strong and characteristic Raman signal (Fig. 8.9).

8.3.2.7 Bauxite and Kaolinite

Practically all world production of newly smelted aluminum was made from bauxite. The term bauxite is used for naturally occurring mixtures of aluminum monohydrate (boehmite or diaspore) and trihydrate gibbsite $Al(OH)_3$, including impurities which are typically clay minerals, free silica, iron hydroxides and titania. The luminescence of boehmite and diaspore and LIBS (Fig. 8.10) may be used for the detection, sorting and commercial value evaluation of Al minerals.

Another Al-bearing rock, kaolin, is a purified white plastic clay primarily composed of kaolinite $Al_2Si_2O_5(OH)_4$ in association with small quantities of other minerals such as feldspar, mica and quartz. It is made up of a loose aggregation of randomly oriented stacks of kaolinite flakes. Kaolin deposits are formed through the alteration, or kaolinisation of feldspar-rich rocks such as granite or gneiss by hydrothermal and/or weathering processes. The mineralogical and chemical composition of the kaolin depends on the nature of the parent rock and the type and degree of alteration. Kaolin's main applications include paper, in which it performs both filling and coating functions, and ceramics. In this latter application, it can account for as much as 60% of the recipe. LIBS of Al may be used for kaolinite sorting (Fig. 8.10).

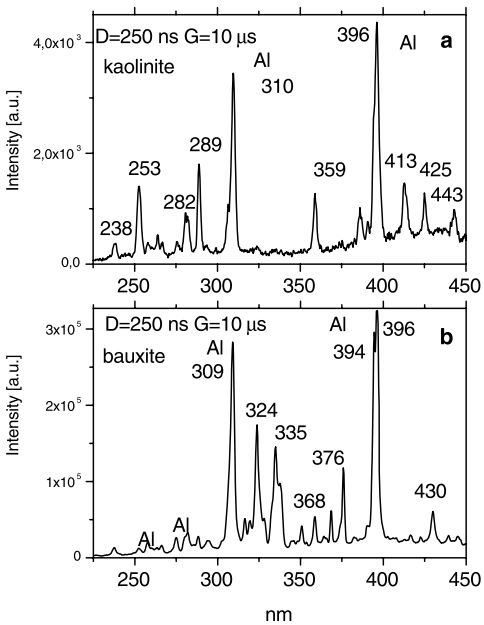

Fig. 8.10. LIBS of Al bearing minerals bauxite and kaolinite

8.3.2.8
Magnesium and Manganese Ores

The low specific gravity of this metal makes it invaluable for use in lightweight alloys used in aircraft and aerospace equipment. Magnesium is produced through the processing of its magnesite and dolomite ores, or by precipitation from natural brines. At the present time Mg containing minerals, such as magnesite $MgCO_3$, dolomite, talc $Mg_3Si_4O_{10}(OH)_2$, limestone and smectite are usually optically separated based on laser beam reflectance. LIBS sorting may be extremely effective in this case because Mg emission lines are exceptionally strong and characteristic, especially at 384 and 518 nm (Fig. 8.11).

About 90% of manganese ore is used in steel smelting. Although there are more than 300 manganiferous minerals, the common ore minerals are largely mixtures of manganese oxides and hydrated oxides. The usual field terms are psilomelane for a hard massive mixture of oxide minerals, pyrolusite for a soft black earthy mixture, and wad for impure, brown earthy oxides and hydrated oxides. LIBS sorting may be effective in this case (Fig. 8.11).

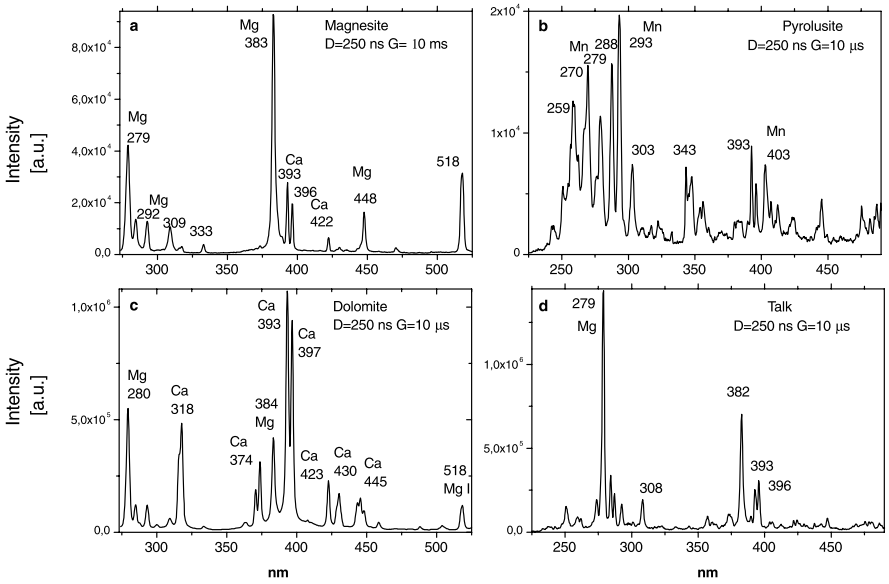

Fig. 8.11. LIBS of magnesium and manganese bearing minerals

8.3.2.9
Chromite

The only significant chromium ore mineral is chromite, a member of the spinel group, with the formula $(Fe,Mg)O(Fe,Al,Cr)_2O_3$. The important ore variables are Cr_2O_3 content, Cr:Fe ratio, SiO_2 content, amount and ratio of Al_2O_3 and

MgO, and sulfur and phosphorus content. In some operations high-grade ore is selectively mined, hand sorted and screened, and sold as lump and fines. More commonly the high-grade lump material is removed by hand, and the reminder is crushed and ground before beneficiation. LIBS may be used for chromite sorting and Mg, Al, Si contents evaluation (Fig. 8.12).

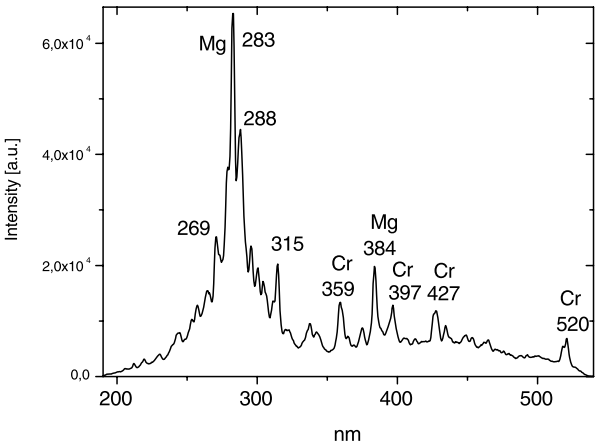

Fig. 8.12. LIBS of chromite

8.3.2.10 Phosphate with High Dolomite Content

Among the deleterious materials (Fe_2O_3, Al_2O_3, CaO, MgO) in phosphate rock, dolomite is the most troublesome. Dolomite causes higher consumption of sulfuric acids, reduces filtration capacity, and lowers the P_2O_5 recovery in fertilizer manufacturing. Therefore the MgO content is a very important index in evaluating the quality of the phosphate concentrate. In Florida, the MgO in the final phosphate concentrate is usually required to be less than 1%.

Phosphate rock is one of the basic materials for fertilizers. USA phosphate production represents approximately one third of the World's total, while about 70% of the US production comes from Florida. With the depletion of the low-dolomite, easy-to-process Bone Valley siliceous phosphate deposits, phosphate mining moves further south and southeast, and the phosphate matrix becomes leaner in grade and high in dolomite. The phosphate deposits in the Southern Extension will be low in P_2O_5 and high in the dolomite impurity, and may be divided into two zones. The upper zone may be processed using current technology, while the lower one is highly contaminated by dolomite. Geological and mineralogical data show that about 50% of the phosphate resource would be wasted if the lower zone is bypassed in mining, and about 13% of the resource would be lost if the dolomite pebble in the lower zone is discarded (Gao et al. 2002).

The high dolomite zones have been bypassed during mining operation because there is no technology available to process the high dolomite pebble economically. It has been well recognized that the development of a technically and economically feasible beneficiation technology to process dolomite pebbles is very important in order to improve the recovery of phosphate value, extend Florida phosphate reserves and prolong the life of the Florida phosphate industry.

This makes it more critical to control the quality of the pebble product, particularly the MgO content. Current practices require either stockpiling of pebble product until quality control data from sampling becomes available, or making the shipping or discarding decision based on visual observations of rock as it is being produced. Obviously, this practice can result in the shipping of undesirable products to the chemical plant or the discarding of acceptable pebbles. A reliable instantaneous analytical method is the ultimate solution to this problem.

At present, gravitation separation and photometric sorting are mainly used for the treatment of phosphates with high dolomite concentration (Salter and Wyatt 1991). However, their effectiveness in many cases is limited due to minimal density and reflectance differences between dolomite containing lumps and phosphate rock.

8.3.2.10.1
Luminescence Sorting

X-ray excited steady-state luminescence has been checked as a distinctive feature for the phosphorites, Karatau (Gorobets et al. 1997a). Sedimentary apatite (francolite) is not luminescent under X-ray excitation and red Mn^{2+} luminescence of dolomite was employed. As a result, concentration of MgO in the accepted fraction was lowered from 5.0% to 2.4%. The use of this method is limited because in many cases the X-ray luminescence of dolomite is very low or non-existent. Besides that, other minerals without luminescence come together with the accepted phosphate fraction, including siliceous shale, which is harmful for the following deep beneficiation. Thus new methods have to be developed for detection and content evaluation of dolomite in Florida phosphates on moving belt conveyors.

Our study of sedimentary apatite from Israel proved that laser-induced time-resolved luminescence is a perspective tool for evaluation of sedimentary phosphate ores with high dolomite content (Gaft et al. 1993b). The idea was based on the fact that natural apatite contains several characteristic luminescence centers, which enables us to differentiate it from dolomite. The most widespread characteristic luminescence center in sedimentary apatite is uranyl $(UO_2)^{2+}$ with a typical vibrational green band luminescence under nitrogen laser excitation (Fig. 8.13a,b). Nevertheless, it appears that such luminescence is absent in phosphate rock samples from Florida, evidently because of extremely low uranium concentration (Fig. 8.13c,d). In order to find potential luminescence centers, ICP-MS analyses of Florida phosphates was accomplished. From discovered REE, theoretically Dy^{3+} is the best candidate

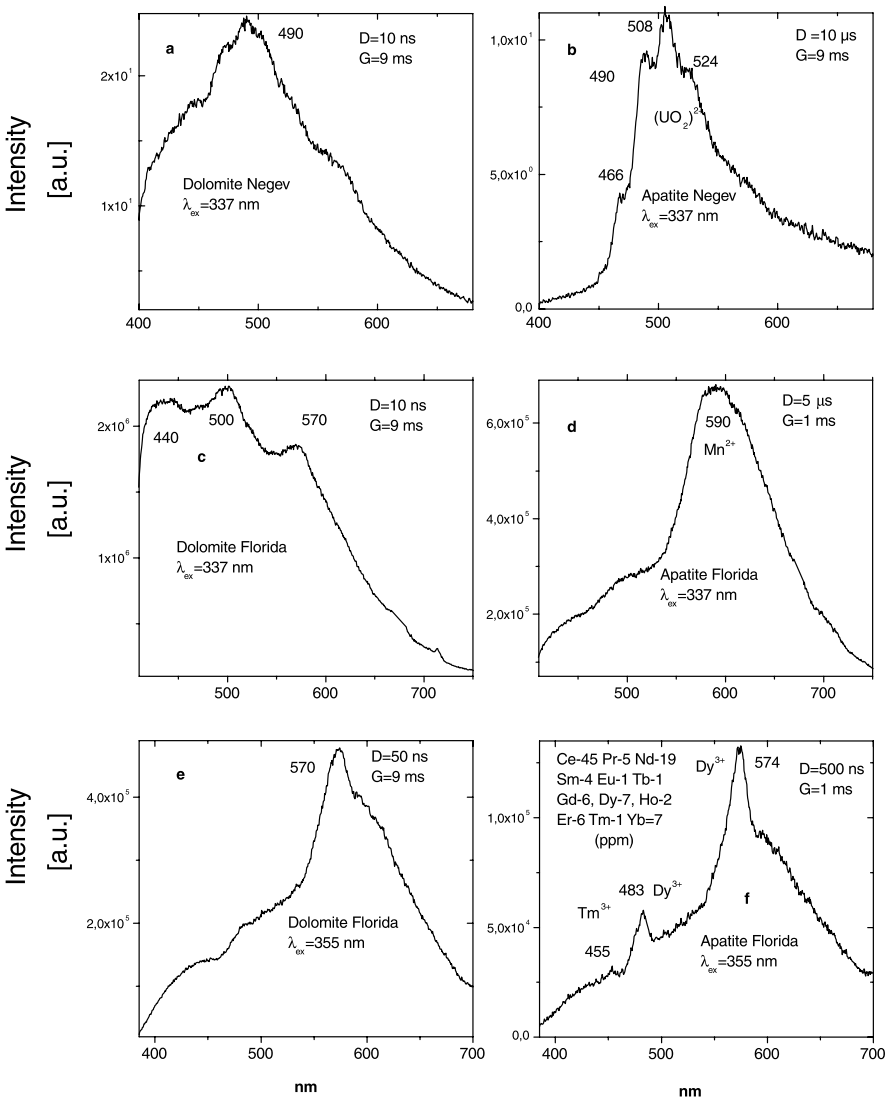

Fig. 8.13. Laser-induced time-resolved luminescence spectra of dolomite and apatite

because of the favorable combination of concentration, quantum efficiency, and spectral and temporal characteristics. Narrow lines of Dy^{3+} with a long decay time of 500–600 µs appear under $\lambda_{ex} = 355$ nm in Florida apatites, while they have never been detected in Florida dolomite (Fig. 8.13e,f). The reason is that dolomite is a very bad matrix for luminescence centers formation, even if it has suitable concentrations of corresponding impurities.

In the second stage, more than 200 samples of randomly chosen Florida phosphate rock samples have been analyzed for Dy^{3+} luminescence. The results prove the assertion, that Dy^{3+} lines are a good distinguishing feature between apatite and dolomite. They are not detected in a single dolomite and it allows 100% detection of dolomite pebbles. The problem is that Dy^{3+} luminescence intensity is strongly varying from apatite to apatite and in certain samples it was not confidently detected under existing experimental conditions. The average content of apatite with confident Dy^{3+} luminescence is slightly less that 70%. To improve the distinguishing feature efficiency, the optimal excitation has to be chosen. It is well known that Dy^{3+} has very narrow excitation bands. In order to determine the best excitation source of Dy^{3+}, the excitation time-resolved spectroscopy have been accomplished. For this task the tunable dye laser pumped by excimer XeCl (308 nm) was used. The selected dye enables the tuning in the 345–365 nm spectral range, which corresponds to the $^4F_{9/2}$ excited state of Dy^{3+} responsible for the luminescence lines at 480 and 573 nm. It was found that the optimal excitation for Dy^{3+} in apatite is at 351 nm, which enables us to increase Dy^{3+} luminescence by 25–30% compared to λ_{ex} = 355 nm. Besides being the optimal excitation for Dy^{3+}, the excitation at 351 nm exactly corresponds to the emission wavelength of the XeF laser.

Another way to improve sensitivity is computerized spectra analysis. All spectra measurements are accompanied by background and noise, thus all individuals or group parameters need the preliminary data processing for the background estimation and for the smoothing of the raw spectrum data. The principal problem of the background modeling is to find a suitable analytical function to model the background behavior. We developed the corresponding algorithm, which together with the optimal excitation at 351 nm enables the confident identification of approximately 85% of apatite samples based on Dy^{3+} time-resolved luminescence. Nevertheless, the remaining 15% will be counted as dolomite and removed from the following beneficiation. At the same time it is important to emphasize that according to XRD data, the remaining apatite without clear Dy^{3+} emission very often contain elevated quartz and calcite contents. It is well known that quartz has strong laser-induced luminescence, which may conceal the Dy^{3+} lines. Thus it is possible that using Dy^{3+} luminescence as distinguishing feature, we will be able to reject the portion of quartz and calcite before grinding, which is good for flotation efficiency.

8.3.2.10.2
LIBS Sorting

This methodology was previously successfully used for express on-line analyses of phosphate ores. The commercial TRACER^{TM} 2100 Laser Element Analyzer, a laser-induced breakdown spectroscopy instrument, was utilized for rapid analyses of phosphate ores at the mine site (Rosenwasser et al. 2001). Excellent calibrations were achieved for P and Mg with correlation coefficients significantly above 0.98. The instrument demonstrated strong potential of the LIBS for use in on-site, real-time or grading. LIBS apparatus was developed for ap-

plications in the phosphate industry (Smith et al. 2000). This includes rapid elemental analysis of P, Mg, Si and Fe in materials taken from various stages of phosphate mining and processing using a rapid, off-line measurement approach. A compact LIBS spectrometer was developed and evaluated in both the laboratory and in an industrial setting. The samples were dry fine powders deposited on an adhesive tape. Nevertheless, such equipment is developed for chemical analysis with an analysis time of several minutes per sample and is not suitable for radiometric sorting. The attempt was made to develop a LIBS analyzer for routine, rapid pseudo-on-line and real-on-line performance with the desire to apply LIBS to on-line slurry characterization. Nevertheless it was concluded that on-line quantitative chemical analysis in phosphate slurries does not appear to be practical at this time using LIBS. The reasons are the amount of water in the slurry and the large sizes of the particles analyzed (Winefordner 2000).

In order to use LIBS for real-time evaluation of dolomite content on the moving belt apatite and dolomite have to be confidently identified by LIBS with one laser pulse. Figure 8.14 demonstrates the typical breakdown spectra of Florida apatite and dolomite under 355 nm Nd-YAG excitation with an energy pulse of 15 mJ. Dolomite (Ca, Mg)$(CO_3)_2$ contains Mg as a major element and does not contain P and F, and phosphate $Ca_5(PO_4)_3(F,O)$:$Ca_5(PO_4)_3CO_3$ contains as major elements P and F, and does not contain Mg, which gives a good opportunity to differentiate between them by LIBS. According to expectation, it is clearly seen that the line at 604 nm, which is connected with F and P, belongs only to apatite, while the line at 518 nm, which are connected with Mg,

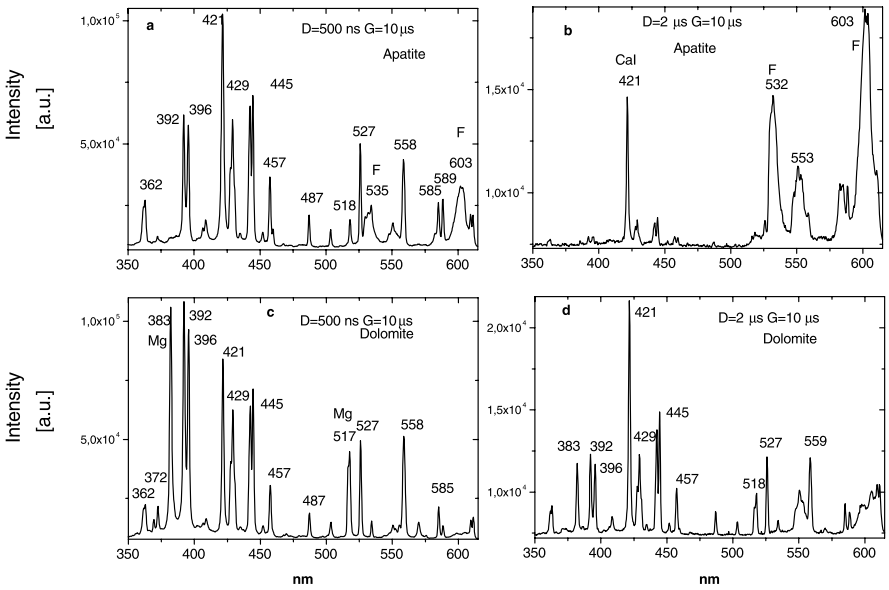

Fig. 8.14. Time-resolved LIBS of Florida dolomite and apatite under $\lambda_{ex} = 355$ nm

belongs only to dolomite. Thus LIBS enables confident dolomite and apatite identification.

To check the possibility of LIBS on preliminary unknown samples, 160 pebbles were randomly selected on the moving belt of the Four Corners Mine. They have been analyzed in conditions, similar to those on the moving belt, namely from the distance of 1 m using only one laser pulse (351 nm of excimer XeF laser). Three samples taken from the belt with time intervals of approximately 10 minutes were divided for two products each, named as "bad" (dolomite) and "good" (apatite). All products were subjected to chemical analyses in IMS-Phosphates analytical laboratory. The results are presented in Table 8.4. It is clearly seen, that the "bad" fraction contains mainly dolomite with the mean $MgO/P_2O_5 = 0.7$, while the "good" fraction is mainly apatite with the mean $MgO/P_2O_5 = 0.015$, namely nearly 50 times lower. Besides that, the dolomite products contain elevated concentrations of Fe_2O_3, Al_2O_3 and insoluble residue compared to apatite products (by 1.5, 2.5 and 4.7 times, respectively). Consequently, removing of the rock with elevated dolomite content enables us to lower together with Mg concentration, other harmful impurities also.

Table 8.4. Chemical analyses of apatite and dolomite fractions after LIBS separation

	No pebbles	MgO	P_2O_5	BPL	F	Fe_2O_3	Al_2O_3	Insoluble
Reject	20	2.2	3.5	7.6	0.4	1.1	2.2	70.4
Accept	31	0.5	28.6	62.5	3.6	0.7	1.1	12.9
Reject	18	2.5	5.9	12.9	0.5	1.1	3.8	63.9
Accept	33	0.4	28.1	61.42	3.3	0.8	0.8	13.3
Reject	13	4.6	4.5	9.81	0.3	1.3	2.0	56.5
Accept	45	0.3	27.4	59.80	3.4	0.8	1.4	14.2

8.3.2.10.3
LIBS Module Prototype

It is important to select the best laser source. For practical applications the first harmonic of Nd-YAG (1,064 nm) is preferential, because such a laser is powerful and exists in ruggedized industrial versions. It was found that the spectra are principally the same as under $\lambda_{ex} = 355$ nm (Fig. 8.15), but the characteristic line of F^- is much weaker and clearly seen only after a delay time of several microseconds when the overall intensity is already low. The characteristic line of P at 254 nm is very weak and the strongest lines in the spectra belong to Ca ions.

LIBS analyses under $\lambda_{ex} = 1{,}064$ nm enables us to conclude that the most efficient discriminative feature between dolomite and phosphate is the ratio between the MgI emission at 383 nm and the CaII emission at 393–397 nm after a relatively short delay of 500 ns. At such conditions the apatite intensity ratio $(I_{394.3}/I_{384.5}) = 30.2$, while for dolomite $(I_{394.3}/I_{384.5}) = 1.1$, namely this ratio

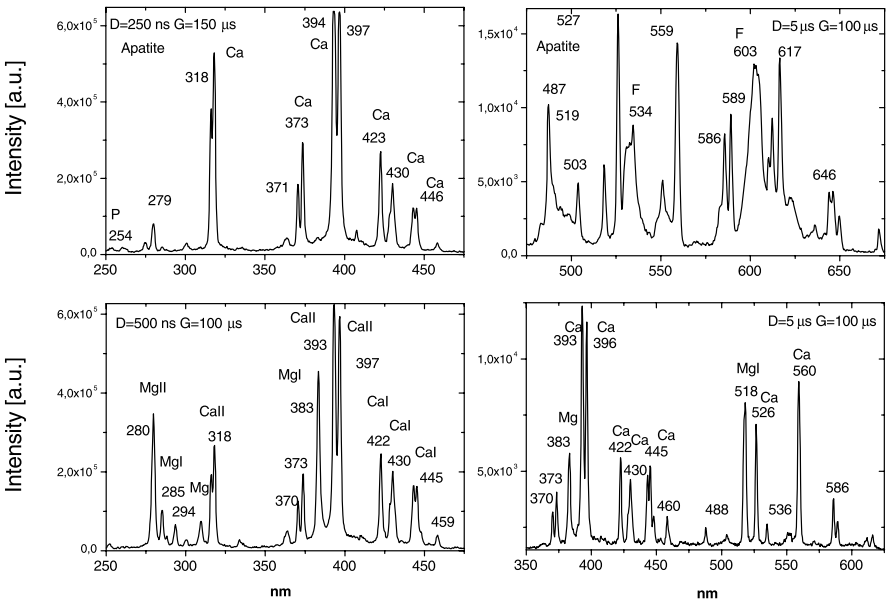

Fig. 8.15. Time-resolved LIBS of Florida dolomite and apatite under λ_{ex} = 1,064 nm

is 27 times higher in apatite compared to dolomite. At steady state conditions this ratio is more than twice lower (approximately 10), but nevertheless it is still very high.

Prototype LIBS sorting system is firstly developed by International Technologies Lasers (ITL) Company. In present modification, the system accomplishes evaluation of conveyed rocks composition. Beta site test was successfully accomplished at 2004 on Four Corners Mine, Florida.

8.3.3 Base Metals

The base metals are those that are either found with copper or alloyed with copper and now include all the copper, lead, zinc, arsenic and tin ores. Tin works as a much better metal to alloy with copper than arsenic in making bronze – but its much rarer. Zinc actually wasn't known to the ancients as it either was completely oxidized and went right up the furnace chimneys or reacted with copper to make brass directly in the furnace. The very large "gray area" in minerals applications would appear to be in sorting many base metal ores that require less proven or completely new sensing techniques for sorting. The perceived industry benefits have not been sufficient to support well-tested developments in this area. There are a large number of published articles on the development of sensing techniques for sorting base metals, a lower number on industry demonstrations of developed technologies (particularly in Russia), and very few on commercial operations using these technologies.

One explanation for this rather poor record over a period of at least 20 years is that there are entrenched misconceptions in regard to the economic viability of sorting. A recent renewal of interest in new mineral sorting applications would seem to indicate that this view may be changing on the basis of demonstrated operational experience with modern sorters over the past decade.

8.3.3.1
Cassiterite

8.3.3.1.1
Luminescent Sorting

In its oldest use tin was alloyed with copper and zinc to make bronze. Tin is still valuable today in alloys and coatings for steel. Cassiterite, a tin oxide, is the only important ore mineral. Under powerful laser excitation cassiterite very often is characterized by intensive luminescence (Fig. 4.27). The emission band consists of the main band at 560 nm with a decay time of 200–250 ns, the weaker band at 650 nm with a decay time of approximately 300 ns and the weak band peaking at 450 nm with a very short decay time of 50 ns. Using the shortwave part of the excitation band the blue emission becomes relatively stronger, while under the longwave part the red emission dominates. The main background luminescence in the cassiterite case is connected with the sorption of organic materials, but its extremely short decay of less than 20 ns enables effective sorting using a delay of approximately 75 ns and a gate of 1–5 µs.

8.3.3.1.2
LIBS Sorting

Tin has many intensive lines in the breakdown spectrum, the strongest ones at 284, 286, and 303 nm (Fig. 8.16).

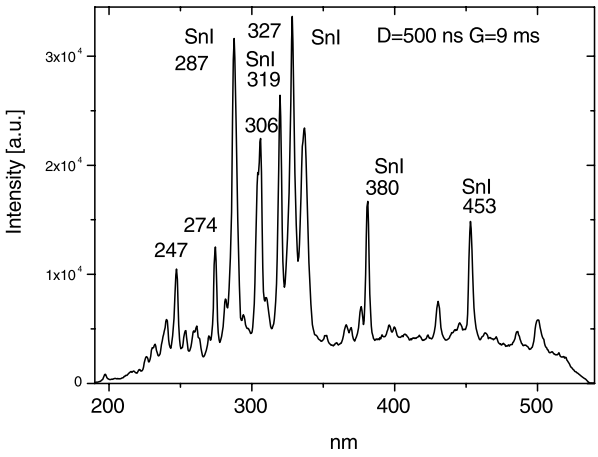

Fig. 8.16. Time-resolved LIBS of cassiterite

8.3.3.2
Lead, Copper, Zinc Containing Minerals

8.3.3.2.1
LIBS Sorting

These minerals have never been mentioned as potential targets for luminescent sorting because of the absence of natural emission even under laser excitation. LIBS may be an excellent opportunity, because all those elements have strong and characteristic lines. Figure 8.17 present examples of malachite (Cu), galena (Pb), and sphalerite (Zn) breakdown spectra.

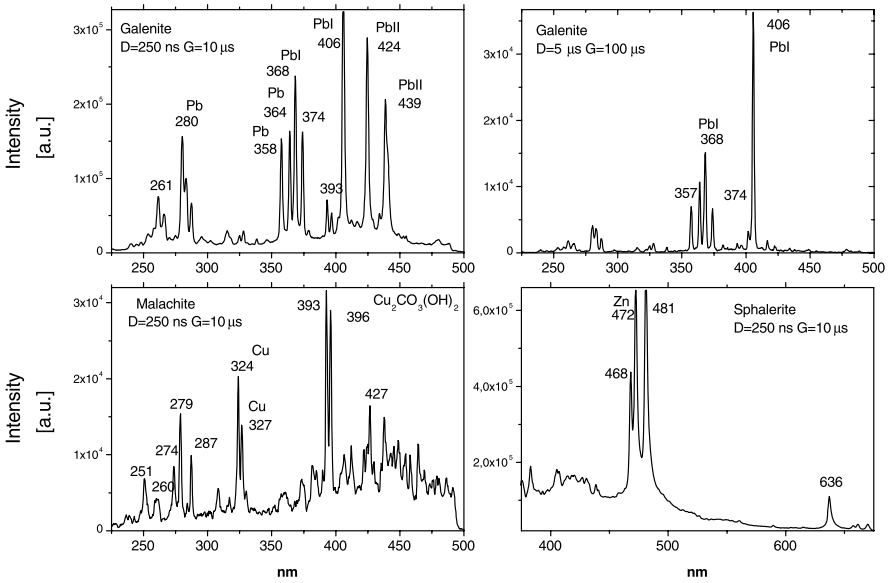

Fig. 8.17. Breakdown spectra of several base metals bearing minerals

8.3.4
Non-Ferrous Metals

8.3.4.1
Scheelite

Tungsten is mainly used in lamp filaments and steel-alloy cutting tools. Scheelite and wolframite are the major ores of tungsten. At the present time even deposits with very low tungsten concentrations (down to 0.1%) are considered as industrial. Scheelite was the second (after diamond) mineral which was sorted using X-ray excited luminescence enabling to select the pebbles with elevated W contents. Using this method it was possible to sort the tails with 0.03% of WO_3 and to select the product with 0.12% of WO_3.

Nevertheless, in certain cases such sorting may be difficult. For example, fluorite, apatite and calcite under X-ray excitation also have luminescence in the selective windows used for scheelite separation (Gaft et al. 1989). Laser-induced time-resolved luminescence may be much more effective, using different excitation spectra and decay times of corresponding minerals. Luminescence and excitation spectra demonstrate that excitation at 240 nm is optimal for scheelite, while Mn^{2+}, Ce^{3+} and Eu^{2+} in barren rock are substantially deminished. The strong difference in decay times enables us to lower the background further, because the delay of approximately 1 μs enables us to quench the short lived Ce^{3+}, Eu^{2+} and organic matter, while the gate of 20 μs licvidates the long lived Mn^{2+} background. On the other hand, in such a time window the scheelite emission with a decay time of 5–6 μs will be strong.

8.3.4.2 Zircon and Baddeleyite

The most important zirconium minerals are zircon and baddeleyite, often associated with rutile and ilmenite deposits. Zircon and baddeleyite are characterized by strong luminescence under powerful laser excitation. The main background emission is connected with organic matter sorption and sometimes with fluorite. Excitation and emission spectra of zircon and baddeleyite (Figs.· 4.39, 4.41) together with their decay times demonstrate that a delay time of 200 ns and gate of 10–50 μs combined with excitation near 300 nm enable us to remove the background signal drastically.

8.3.4.3 Eucryptite and Spodumen

8.3.4.3.1 Luminescent Sorting

These minerals have been successfully separated by X-ray excited luminescence, but the serious problem was the orange emission of carbonate host rocks (Gorobets et al. 1997a). Eucryptite is characterized by intensive red emission at 780 nm of Fe^{3+} (Prokofiev et al. 1979) with a very long decay time of 4–5 ms. Because Mn^{2+} emission in carbonates has also a long decay, the main effect may be in using the differences in excitation and emission spectra. Spodumen under laser excitation is often characterized by blue emission with a decay time of 50–60 μs (Fig. 4.61) and such relatively long decay enables effective sorting on the background of short-lived fluorite luminescence.

8.3.4.3.2 LIBS Sorting

It may be proposed that the LIBS method may be used for on-line real-time Li bearing minerals identification because of strong and characteristic lines of Li emission at 671 and 610 nm (Fig. 8.18).

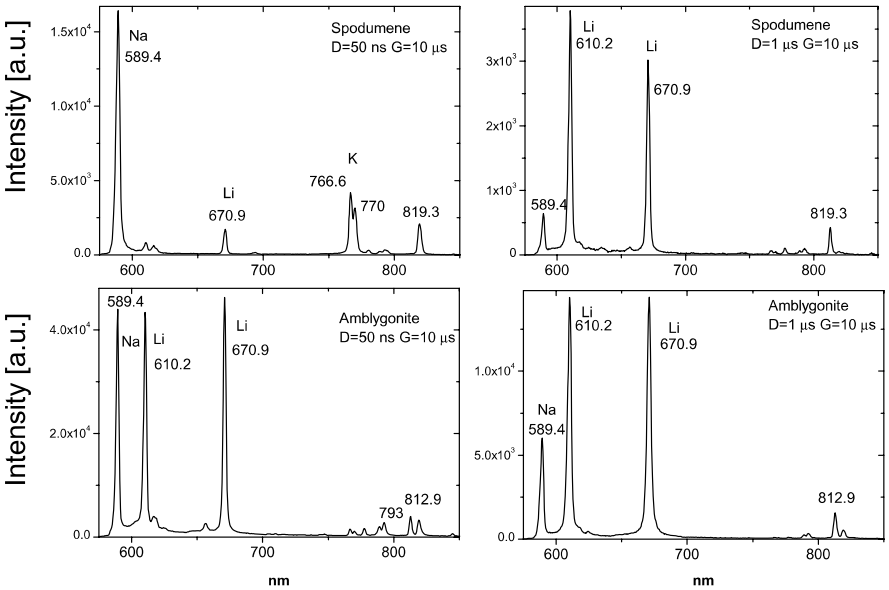

Fig. 8.18. Breakdown spectra of several Li bearing minerals

8.3.5 Precious Metals

8.3.5.1 Gold Bearing Minerals

Gold is used extensively in the manufacture of electronics, in medicine, and as the World's monetary standard. This valuable metal is often found in nature in the native form, usually associated with quartz or pyrite. When deposits containing gold are eroded, the heavy gold may become concentrated in placer deposits in the gravel of stream beds. Only rarely is visible gold found in good ore. It does occur as a compound with tellurium in minerals such as sylvanite and calaverite. On average, only five parts per million of every ton of ore mined are actually gold. It is, for example, necessary to separate the precious metal from the more than 100 million tons of ore milled each year in South Africa. This is carried out in the mine's gold plant. Initially, ore hoisted from the mine is broken into smaller pieces by a primary crusher; secondary crushers break it down further, followed by a milling stage to produce a fine rock dust. At this point most of the tiny particles of gold contained in the ore have been exposed. A cyanide solution chemically dissolves away the exposed gold particles and the resultant liquid follows one of two routes to recover the gold now held in solution. Gold bearing ores are now sorted by photometric and radioactive or X-ray fluorescence methods. The first one is used for gold containing quartz, while the accompanying rocks have a dark color. The second method detects the certain elements, which are correlated with Au (Mokrousov and Lileev 1979).

All these methods use selective features, which are not directly connected with gold contents.

8.3.5.1.1
Artificially Induced Luminescence Sorting

Luminescent sorting of gold containing ores was never used because native gold and its minerals are not luminescent. In order to overcome this problem, the methods of artificial luminescence creation on the surface of gold bearing minerals have been developed (Gaft et al. 1991a). Different kinds of the chemical and physical treatments induce strong yellow luminescence (Fig. 8.19) on the surface of gold minerals, while home rock remains non-luminescent. This gives an opportunity to discriminate and to separate gold bearing lumps. Laser excitation plays a decisive role hear, because in the case of extremely thin luminescent layers which are formed on the surface, X-rays and UV lamps are not effective excitation sources. Laser-induced luminescence for the first time gives the opportunity of gold ore sorting according to the direct separation feature. The best types in the gold case are conglomeratic, vein and stockwork deposits: mainly quartz, quartz-pyrite-chalcopyrite, quartz-silicate, barite and quartz-arsenopyrite compositions; low oxidized and with low and middle sulfides concentrations; with mainly gravitational and coarse Au (size more than 60–70 micron); emulsion Au in sulfides with content in mineral $\sim$ 0.01 wt % (Moroshkin et al. 1993).

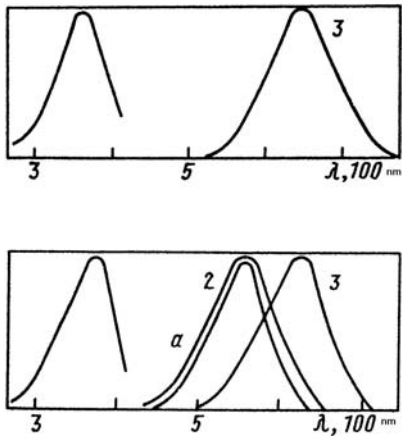

Fig. 8.19. Artificially induced luminescence on Au (*upper*) and Ag bearing minerals (1 – silver and argentenite; 2 – galenite) (Gaft et al. 1989c)

8.3.5.1.2
LIBS Sorting

Gold has many intensive lines in the breakdown spectrum. In gold containing quartz the characteristic Au lines appear after a relatively long delay, the strongest one at 312 nm (Fig. 8.20). Gold concentrations in certain types of ore are quite within the range of LIBS sensitivity. For example, quartz-sulfide

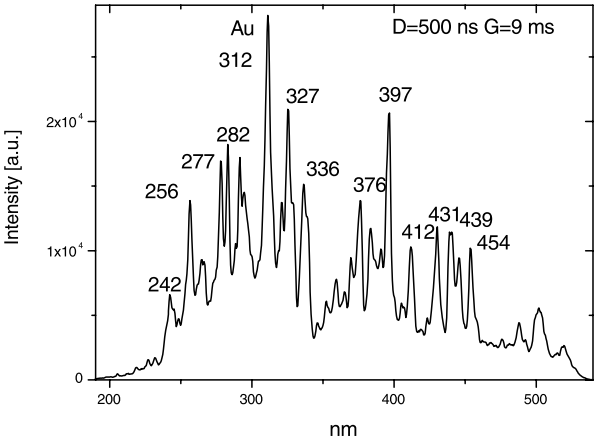

Fig. 8.20. LIBS of gold containing ore

veins of the *Berezovsk* deposit (Ural, Russia) contain 90–95 vol. % of quartz, 5–10 vol. % of sulfides and 18–20 ppm of Au. Massive sulfide ores of giant VMS (volcanogenic massive sulfide) Cu–Zn–Au–Ag deposits predominate with a subordinate amount of disseminated ores (commonly 5–15 vol. %). Gold is relatively uniformly distributed in massive sulfide ores (average values for the deposits 0.5–1.5 ppm), but local enrichments occur (up to 10–12 ppm of Au) (Prokin et al. 1999).

8.3.5.2 Silver Bearing Minerals

8.3.5.2.1 Natural Luminescence Sorting

Man has used this metal for centuries. It sometimes is found in native silver, but is more commonly found combined with sulfur as argentenite. Most of the World's supply of silver is obtained as a by-product when other metals such as lead, zinc, and copper are processed. Silver is used in photography, in medicines, and in coins.

Natural silver halogenides, which are secondary ores for silver production, are characterized by intensive luminescence under powerful laser excitation (Fig. 4.67). The main source of the background luminescence is the sorption of organic matter. The relatively long decay time of their luminescence may enable us to lower the short-lived background emission by several orders of magnitude.

8.3.5.2.2 Artificially Induced Luminescence Sorting

Native silver and argentenite are not luminescent in their natural form, but as in the case of gold, it is possible to induce the artificial emission (Fig. 8.19).

8.3.5.2.3
LIBS Sorting

Silver has many intensive lines in the breakdown spectrum, the strongest ones at 328 and 338 nm in the UV part of the spectrum and at 520 and 546 nm in the visible (Fig. 8.21), which it may be potentially used in radiometric sorting. Silver is relatively uniformly distributed in massive sulfide ores (average values for the deposits 10–50 ppm), but local enrichments occur (up to 150–300 ppm of Ag) (Prokin et al. 1999).

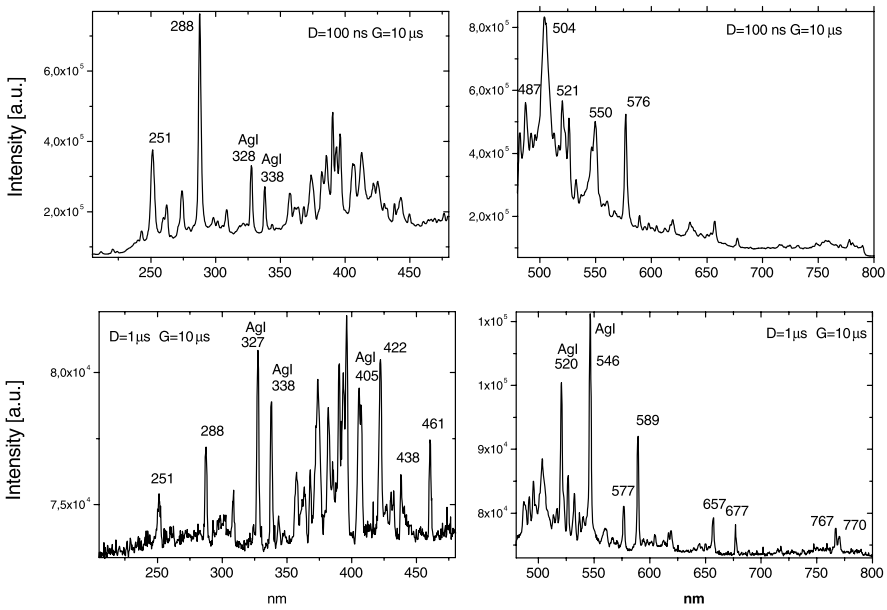

Fig. 8.21. LIBS spectra of Ag containing minerals

8.3.6
Fuel Minerals

There is an ongoing need within the international coal mining and utilization industry to better characterize coal and combustion products. Areas of particular interest include: improved coal characterization; the need for quantitative data on mineral distribution for better understanding of combustion behavior; and a generic analysis method for various environmental waste issues surrounding the industry, including coal dust analysis. Both coal particulates and unbroken coal, can be measured by LIBS, which makes the technique attractive to mine geologists, combustion engineers, waste and environmental scientists alike. The method can discriminate the elements that belong to most common ash-forming minerals in coal including: quartz, illite, kaolinite, calcite, ankerite, siderite, apatite, chamosite, gypsum, pyrite, and iron oxides. It

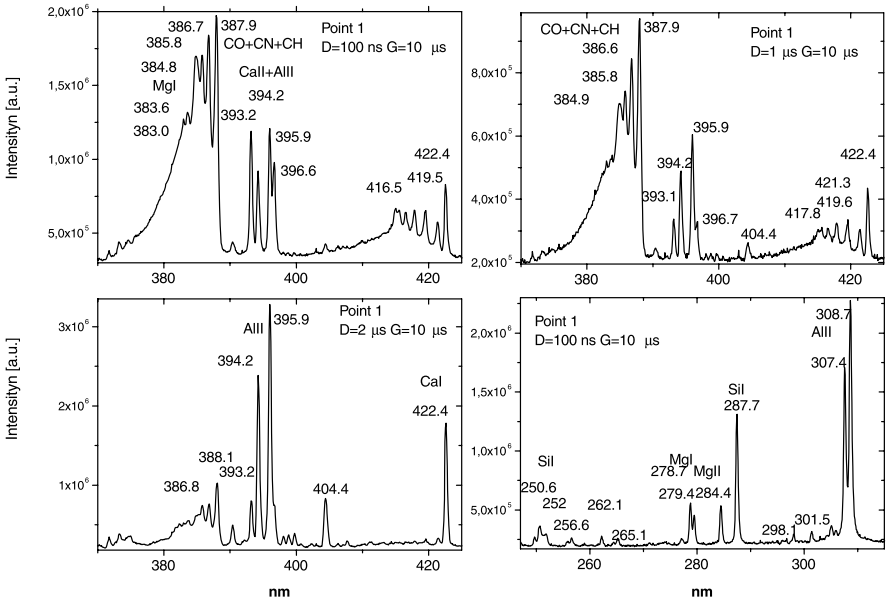

Fig. 8.22. LIBS of graphite

also may be useful in order to quantify the amount of organically bound sulfur within coals.

The breakdown spectra of graphite may be very different for pieces from the same deposit. Spectra with higher resolution enable us to detect impurities of Ca, Al, Mg and Si (Fig. 8.22).

CHAPTER 9

Identification of Minerals

9.1
Luminescent Minerals

Identification of minerals is not a trivial question when dealing with natural objects. Luminescent minerals received from different mineralogists, museums and collectors are often not correctly identified. It is a potential source of serious errors, because the presence of a certain luminescence center in one mineral may be trivial, while its luminescence in another mineral may represent a certain interest. For example, emission of Mn^{2+} is common in calcite, but its absence in scheelite is an interesting problem. Thus, when you find the band

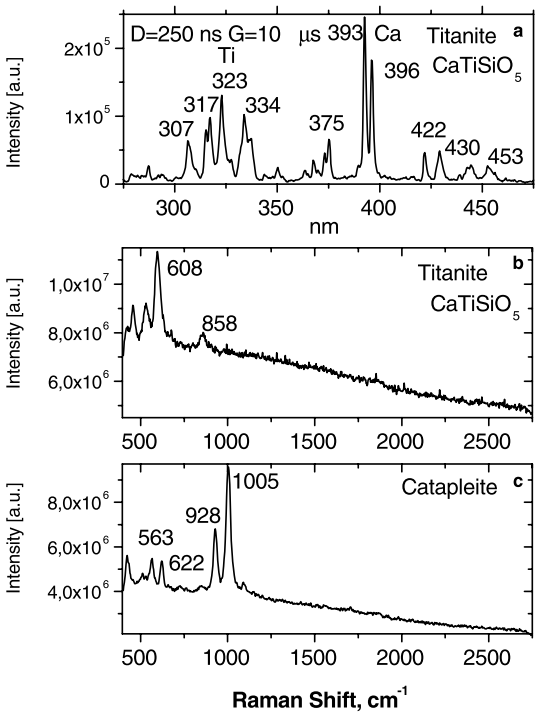

Fig. 9.1. **a–c** Raman and breakdown spectra of titanite and catapleite

suitable for Mn^{2+} in the mineral named scheelite you want to be sure that the mineral identification is correct. In such case express Raman or breakdown spectra may solve the problem. Two short examples are presented below.

Working with titanite, one sample has been found with luminescent behavior strongly different from the others. Suspicion was raised that its identification is not correct. In order to check it, LIBS and Raman data have been received from the same area where luminescence spectra were determined. Figure 9.1a demonstrates that breakdown spectra of titanite are really characterized by the group of UV lines at 300 nm of Ti and by many lines of Ca, the strongest ones at 393 and 396 nm. Nevertheless, such lines are absent in the LIBS of the "suspicious" sample, where only a strong line of Na presents at 589 nm and its Raman spectrum (Fig. 9.1c) is totally different from those of titanite (Fig. 9.1b). Subsequent EDX and XRD analyses enabled us to identify this mineral as catapleite.

Another example is a mineral named nasonite , which was not "suspicious" because of its luminescent properties, but gave unexpected results after routine LIBS checking (Fig. 9.2a), where the characteristic lines of Pb were absent, while the emission lines of Ca and Na were very strong. The Raman spectrum (Fig. 9.2b) was also different from those of nasonite. Subsequent analyses by EDX and XRD methods revealed that it is a mixture of two minerals: prehnite and pectolite.

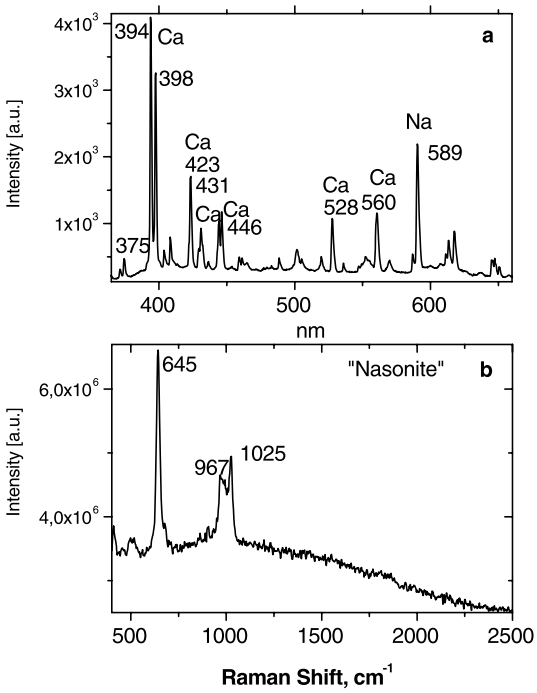

Fig. 9.2. **a–b** Raman and breakdown spectra of supposedly nasonite sample

9.2 Gemology

Gemology is the study of gemstones. At the heart of gemology is gem identification. For example, some rubies and garnets are impossible to tell apart from each other by observation, but their values are considerably different. A precise and accurate means to tell them apart is absolutely necessary. When dealing with whole crystals, the ruby and garnet are easy to distinguish, but most of the material that gets cut into gems isn't found in whole crystals, but in broken pieces. Using the techniques of mineralogy, they are easily distinguished from each other. Scratch tests will determine its hardness. Other useful tests are the reaction to acids and the flame of a blowtorch. These are categorized as destructive tests and are obviously inappropriate for cut gems.

A method needed to be devised where cut gems could be identified without damage. To this end scientists began to first identify the measurable physical and optical properties of the gems. Next they devised instruments to measure these properties. That is not to say that it doesn't require substantial education to identify gems. It is a large and complex subject that is continuing to increase in complexity as new gems are discovered and new ones are created in the laboratory.

Simulants or imitations are anything that is posing as something else. For example, a white topaz posing as a diamond is an imitation. With the continued development of crystal growth technology, various synthetic and imitation gem materials are increasingly encountered in the jewelry industry. For example, synthetic cubic zirconia, and synthetic moissanite (SiC–6H) have a very similar appearance to diamonds, and are used as imitation diamonds. Because of their very different chemical and physical properties, it is relatively simple to determine the imitation. Raman spectroscopy and LIBS may be useful for express gemstone identification, combining in-situ chemical and structural analysis (Table 9.1, Fig. 9.3).

"Synthetic" gem refers to materials that duplicate their natural counterparts. Emerald, sapphires and spinel are common synthetics (Armstrong et al. 2000a). One of the most critical areas of innovation and challenge involves alexandrite. This material is a beryllium aluminum oxide that typically exhibits a red to green color change as lighting environments are altered. This rare variety of chrysoberyl occurs in numerous places around the world, including Russia, Sri Lanka, Africa, Brazil, and India. Some laboratory-grown alexandrites have become so similar to their natural counterparts that there is a confidence crisis in the marketplace. Synthetic or laboratory-grown materials duplicate natural gems in physical, optical, and chemical terms. Indeed, synthetic materials grown under controlled laboratory conditions can exhibit higher overall quality than their natural counterparts. The significant advantage of gemstone synthesis is consistently higher yields of fine quality material, which is a stark contrast to the relatively finite percentages of higher-quality gems that emerge from the production of mines around the world. As a result, gem synthesis consistently produces larger quantities of fine and uniform gem material at a fraction of the cost of comparable natural alternatives.

Table 9.1. Luminescence, Raman and LIBS parameters of several gem stones

Mineral	Laser-based spectroscopy		
	Luminescence	Raman (cm^{-1})	LIBS (nm)
Diamond	N3, S2, S3, S4, A	1,332	C (248, 406, 427)
Spinel	Cr^{3+}	407, 665, 766	Mg (280, 383, 518) Al (309, 394, 396)
Topaz	Cr^{3+}	407, 459, 553, 843, 925	Al (309, 394, 396) Si (251, 287, 507)
Danburite	Eu^{2+}, Yb^{2+} (77 K)	611	Ca (393, 396, 422) B (251)
Forsterite	Mn^{2+}	824, 855	Mg (280, 383, 518) Si (251, 287, 507)
Fluorite	Eu^{2+}, Yb^{2+} (77 K)	323	Ca (393, 396, 422) F (603) K (766, 770)
Corundum	Cr^{3+}	418, 750, 812	Al (308, 394, 396)
Scapolite	S^{2-}	459, 538, 771	Ca (393, 396, 422) Na (589) K (766, 770) Al (309, 394, 396) Si (251, 287, 507)
Apophyllite	Mn^{2+}	432, 583, 663, 1,061	Ca (393, 396, 422) Si (251, 287, 507) F (603) K (766, 770)
Rhodonite	Mn^{2+}	671, 975, 999	Mn (258, 280, 293) Si (251, 287, 507)
Rhodochrosite	Mn^{2+}	1,086	Mn (258, 280, 293)
Cassiterite	Sn^{2+}	475, 632, 776	Sn (271, 284, 301)
Datolite	Ce^{3+}, Eu^{2+}, Yb^{2+} (77 K)	597, 697, 918, 987, 1,082, 1,175	Ca (393, 396, 422) B (251)
Scheelite	WO_4, MoO_4	798, 911, 1,010, 1,076, 1,305	Ca (393, 396, 422) W (295, 401, 407)
Emerald	Cr^{3+}	398, 686, 1,012, 1,069	Al (309, 394, 396) Si (252, 252) Mg (280, 383)
Alexandrite	Cr^{3+}	932	Be (318) Al (309, 394, 396) Si (252, 252)
Garnet	Cr^{3+}	344–376, 871–927	Al (309, 394, 396) Si (252, 252) Mg (280, 383)

Table 9.1. (continued)

Mineral	Laser-based spectroscopy		
	Luminescence	Raman (cm^{-1})	LIBS (nm)
Apatite	Ce^{3+}, Eu^{2+}, Sm^{3+}, Mn^{2+}	432, 584, 965	Ca (393, 396, 422) F (603)
Kyanite	Cr^{3+}	441, 490, 896, 957	Al (308, 394, 396) Si (251, 287, 507)
Benitoite	Ti^{4+}, Ti^{3+}	535, 577, 932	Ba (413, 456, 493) Ti (307, 317, 323, 334) Si (252, 252)
Charoite	Ce^{3+}, Eu^{2+}	640, 677, 1,141	Ca (393, 396, 422) Si (251, 287, 507) Na (589) F (603) K (766, 770)
Zircon	$(MeO_m)^{n-}$, Dy^{3+}, Fe^{3+}	974, 1,008	Zr (268, 339, 348)
Tourmaline	Mn^{2+}, Cr^{3+}, Fe^{3+}	375, 413, 643, 716	Al (308, 394, 396) Si (251, 287, 507) Mg (280, 383)
Titanite	Sm^{3+}, Cr^{3+}, Ti^{3+}	465, 611, 861	Ca (393, 396, 422) Ti (307, 317, 323, 334)

While natural and man-made materials can share the same physical and optical properties, there are still considerably differences, the main one being rarity. A natural gem takes considerable time to form and is usually millions of years old. Plus, many feel they have aesthetic qualities not found in mass-produced materials. While natural and man-made materials appear nearly identical, their values vary considerably. For this reason it is important to be able to distinguish between the two.

As crystallization techniques continue to improve, the technical challenges facing gem-testing laboratories will increase dramatically. However, regardless of the similarities between natural and laboratory grown products, the telltale differences between these growth environments can be entrapped in the chemical and physical natures of each material. Whether laboratory-grown or natural, each growth system leaves its indelible fingerprint on the final product. As the technical differences diminish between the natural and laboratory-grown gemstones, the degree of laboratory sophistication necessary to nondestructively distinguish between these materials must increase significantly. Technical superiority is essential to maintain the long-term stability of the gemstone market and the credibility of laboratory testing facilities (Armstrong et al. 2000b).

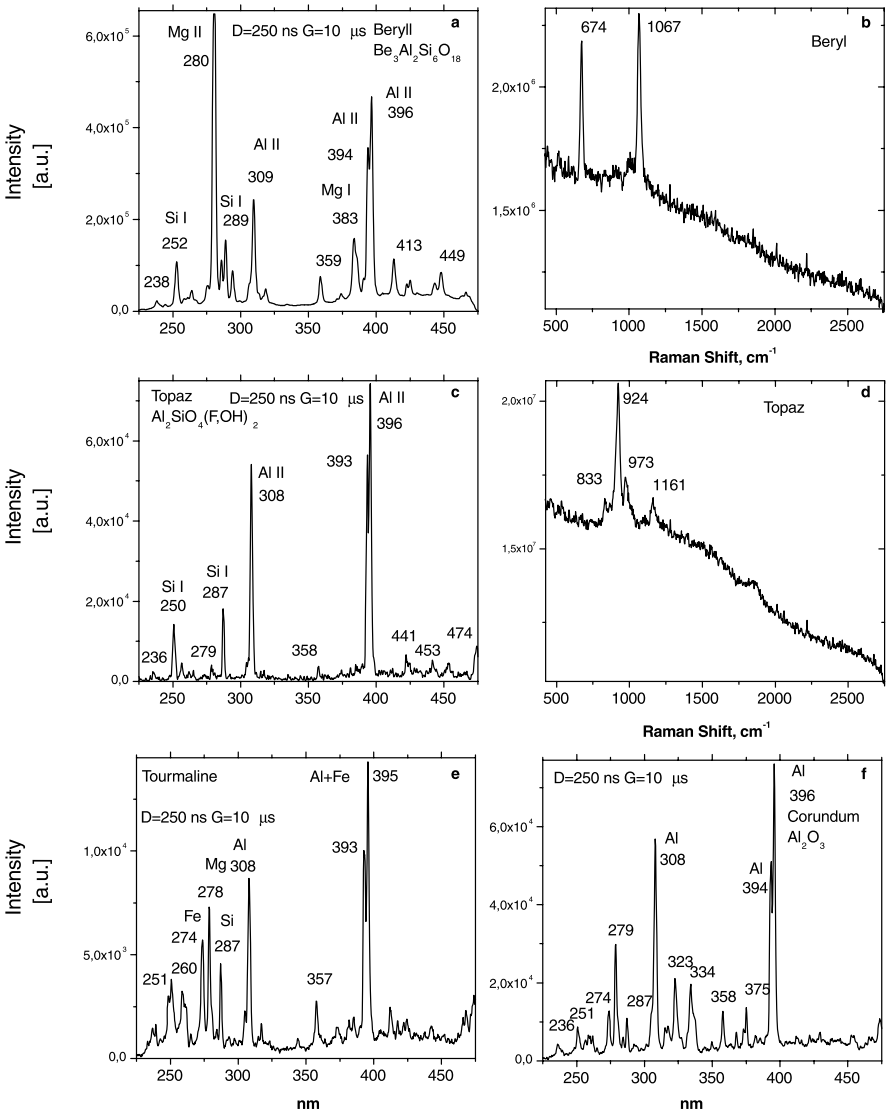

Fig. 9.3. **a–f** Raman spectra and LIBS of several precious stones

Because chemical and structural properties of natural and artificial gems are very similar in this case, the possibilities of Raman and LIBS methods are rather limited. It was found that another laser-based techniques could be very effective for rapid spectroscopic discrimination between natural and synthetic emeralds, rubies, and alexandrite (Armstrong et al. 2000a,b). The first one is DRIFTS (Diffuse Reflectance Fourier Transformed Infra-Red Spectroscopy)

and the second one is NIR (Near Infra-Red) Spectroscopy. In some cases it was even possible to discriminate between gems made by different synthetic processes. Once again, there is a significant benefit to having two independent methods available.

Luminescence properties may be very effective. The main two differences are the following (Gorobets et al. 2004).

1. Luminescence intensity with very rare exceptions is much higher in artificial gemstones compared to natural counterparts. It may be explained by the fact that the activator contents are usually higher in laboratory made gems, while the quenching center concentrations are lower.
2. Fine and super-fine structure of luminescence lines of Cr^{3+} and TR^{3+} are narrower in artificial gems. The reason is that in natural precious stones many optically active centers are usually present, while in artificial ones only one or two occur.

Luminescence appears to be effective for differentiation between the artificial and natural diamonds. For example, fluorescent characteristics are used in diamonds quality gemological certificates, for distinction between natural and synthetic, irradiated and enhanced gem diamonds. Most type IIa (and rare type IaB) diamonds transmit short-wave ultraviolet (SWUV) light while most of the diamonds (type Ia) do not transmit SWUV. As well, recording of the sample's photoluminescence spectrum at 77 K provides an excellent way to identified high pressure-high temperature treated (HTHP) diamond (GE POL, General Electric). Emission peaks at 637 and 575 nm under continuous 514 nm Ar laser excitation indicates the presence of a small amount of N–V centers (single nitrogen linked to a carbon vacancy) in the gemstone. While most but not all natural, i.e. non-treated colorless IIa diamonds also show an N–V (637 nm) and the N–V0 (575 nm) feature, the peak height ratio 637/575 is considered indicative for treatment identification (Fisher and Spits 2000). Diamonds with high ratios > 2.8 are HTHP treated, whereas diamonds with low ratios < 1.6 are natural (Chalain et al. 2000).

Lindblom et al. (2003, 2004) recently studied differentiation of natural and synthetic gem-quality diamonds by luminescence properties. It was found that time-resolved luminescence spectra of natural and synthetic diamonds display clear mutual differences. The spectra of natural diamonds revealed emission bands caused by complex nitrogen-vacancy aggregates whereas the bands of synthetic diamonds reflect simple nitrogen-vacancy aggregates and nickel-containing defects. The deep-UV excited time-resolved luminescence spectra of natural diamonds showed fast-decaying donor-acceptor pair recombination bands at around 410 nm. With longer delay and gates the broad band shifted to 435 nm. All synthetic diamonds display luminescence from nickel-related defects centered at 480 and 530 nm at 300 and 77 K, respectively, and all synthetic diamonds had a sharp luminescence bands at 694 nm caused by the Cr^{3+} ion impurity in corundum inclusions.

In addition, in the jewels industry there is needed to be able to quickly identify any particular diamond and to be able to distinguish it from the

others. For example, since the appearance of diamonds living the polishing factory have no resemblance to diamonds that entered it, the opportunity exists for the polished gems to be switched for less valuable ones (Curtis 1989; Yifrach and Neta 1992). The combination of luminescence properties (spectra of luminescence and excitation, decay time and intensity of luminescence) at 300 K together with suitable program for data treatment allows for a reliable identification of specific diamonds and distinguishing them from others. Time-resolved spectroscopy is especially effective, because 50–70% of diamonds have strong blue luminescence, which hinders the discrimination, and to distinguish between N3 and N3-like centers is extremely important. Besides that, after 1 μs delay the N3 is quenched and more individual bands with longer decay appear.

Another problem is that various processes, such as irradiation, heating, filling of open fractures or cavities, and coating, are also used to treat low quality gem materials to improve their color, appearance, or durability. Typical examples of heat-treated gemstones include sapphire (corundum) and citrine (quartz). Irradiation with gamma rays, X-rays, electrons, or neutrons is used to alter the color of specimens of diamond, topaz, and quartz. Both diamonds and emeralds can have surface reaching openings filled with various substances to improve their clarity. NIR spectroscopy can be used to detect gems that have been treated with organic clarifying agents. In some cases, the clarifying agent can be identified. NIR seemed to be most effective for aggregates and opaque gems such as turquoise and, potentially, jade and chalcedony (Armstrong et al. 1999). Small amounts of oils and resins used to fill cracks and fissures in emeralds and rubies could be detected by DRIFTS (Armstrong et al. 2000b).

Using a combination of IR, UV/VIS reflection and Raman spectroscopies, thermally treated corundum and zircon and radioactively irradiated topaz and spodumen may be identified (Tretyakova and Tretaykova 1996).

9.3 Micro Photoluminescence

Based on the principle of the Raman microscope, a regular transmission and reflex ion optical microscope has been modified to unable tunable pulsed laser injection as well as fluorescence collecting via an optic fiber up to a intensified CCD camera allowing time resolved records. For this purpose, all optics was replaced to support high-energy laser pulses. Such equipment allows the following (Panczer et al. 2003a; Panczer et al. 2003b):

- micro identification of the zone of interest in heterogeneous samples under white polarized light or UV illumination;
- a spatial resolution inferior to 5 μm of the analyzed zone, an monochromatic pulsed excitation (from 266–650 nm) and 3) and a time-resolved spectral analysis of the emission signal. It allows also in situ microanalyses at low and high temperature (Linkham type furnace −196 to 1,500 °C) as well as high pressure (sapphire or diamond anvil cells).

CHAPTER 10

Waste Storage Geomaterials

In the framework of nuclear waste, and especially long-lived high-level radioactive wastes disposal, multiple barriers matrices such as waste package, man-made barriers and geological barrier are studied (Ewing 2001). Therefore specific doped vitreous and crystalline phases are elaborated and their capacity to trap fission products (FP) and minor actinides, to resist dissolution and auto-irradiation is evaluated. At present, the uranium and plutonium are extracted from the general waste flow during spent-fuel reprocessing, the ultimate waste (C type), consisting of minor actinides (Np, Am and Cm) and fission products FP (Tc, I, Cs and Zr), is currently vitrified by incorporation in molten glass. Vitrification remains the most suitable process for all the high-level waste. As a matter of fact, the amorphous structure of glass allows the accommodation of a wide range of elements. Because of the similarity in their chemical features and electronic configuration, REE have been chosen for the simulate minor actinides. Their luminescent properties allow recognize

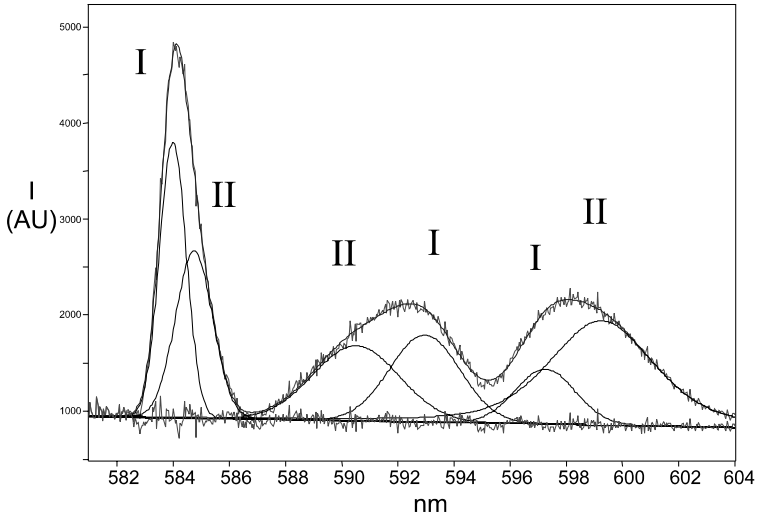

Fig. 10.1. Deconvolution of the $^5D_0 \rightarrow {}^7F_1$ transition of Eu^{3+} revealing two kinds of sites in Eu-doped complex nuclear borosilicate glass (577 nm excitation, 14 K)

whether the elements are incorporated in the bulk of the matrix, or adsorbed on the surface where they can be subjected to leaching out.

Figure 10.1 presents the emission lines of the $^5D_0 \rightarrow {}^7F_1$ transition revealing two kinds of environment in Eu^{3+}-doped complex nuclear borosilicate glass. These are attributed to (1) a borate environment and (2) a silicate one, by comparison of the ligand field parameters B_2 with referenced glassy matrices (Ollier et al. 2002).

Furthermore, specific mineral matrices for use in conditioning separated radio nuclides are also elaborated and studied on the basis of mineral structures, known in nature for their selective-insertion capabilities with respect to certain radio nuclides and their stability over time. Among those phases, hollandite, zirconolite, apatite and monazite are particularly studied.

Hollandite structure is derived from the quadratic rutile TiO_2 one with the general formula $A_2B_8O_{16}$. In nature, there is a whole range of minerals that crystallize in this structure. The difference between them lies in the chemical elements inserted as a substitute for titanium Ti in the B-site: hollandite (Mn totally substituted for Ti), priderite (Fe^{3+}), henrymeyerite (Fe^{2+}), redledgeite (Cr), ankangite (Cr, V). FP can be fixed in $BaCs_{0.1}Al_{1.5}Ti_{6.5}O_{16}$, with the A-site occupied by Ba^{2+} and Cs^+ while Al^{3+}, Ti^{3+} and Ti^{4+} are located in the B-site. Zirconolite structure $Ca^{2+}Zr_x^{4+}Ti_{(3-x)}^{4+}O_7$ with $0.8 < x < 1.35$, is able to accommodate lanthanides, hafnium Hf and tri- and tetravalent actinides by insertion into the calcium Ca and zirconium Zr sites as was shown in nature. Charge compensations are ensured by substituting trivalent cations (Al^{3+}, Ti^{3+}) in the titanium Ti^{4+} site.

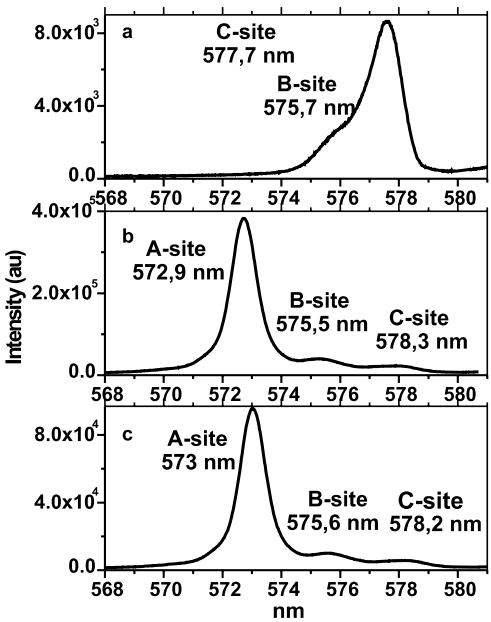

Fig. 10.2. **a–c** Emission of the $^5D_0 \rightarrow {}^7F_0$ of Eu^{3+}-doped britholithes $Ca_2La_8(SiO_4)_6O_2$(1), $Ca_{4,79}La_{4,89}(SiO_4)_{3,12}(PO_4)_{2,88}O_x$(2), $Ca_{8,06}La_{2,11}(PO_4)_6O_x$(3). The A, B and C-sites correspond to the Ca(II), Ca(I)+La(I) and La(II) sites

Phospho-silicate britholites, $Ca_9Nd(PO_4)_5(SiO_4)F_2$, with an apatite structure present high chemical durability, thermal stability and withstand radiation damage, are therefore considered as good candidates for actinide retention. Figures 10.2 and 10.3 show how the $^5D_0 \rightarrow {}^7F_0$ transition in trivalent europium-doped britholites along the phosphate-silicate solid solution allows us to distinguish different sites identified as Ca(II), Ca(I)+La(I) and La(II) sites (El Ouenzerfi et al. 2001). Phospho- and phospho-vanadate apatites are also considered to trap fission products ($Ca_8NdCs(PO_4)_6F_2$; $Pb_{10}(VO_4)_{4.8}(PO_4)_{1.2}I_2$).

Monazite, a rare earth orthophosphate $LaCePO_4$, has in nature the ability to incorporate large amounts of U and Th which leads at some point to the $CaTh(PO_4)_2$ brabantite phase. It remains crystalline despite high α-decay doses even in the case of very old crystals (over 2 billion years). Cathodoluminescence allowed estimation of the degree of auto irradiation received by natural monazite (Nasdala et al. 2002). Photoluminescence was used as well on

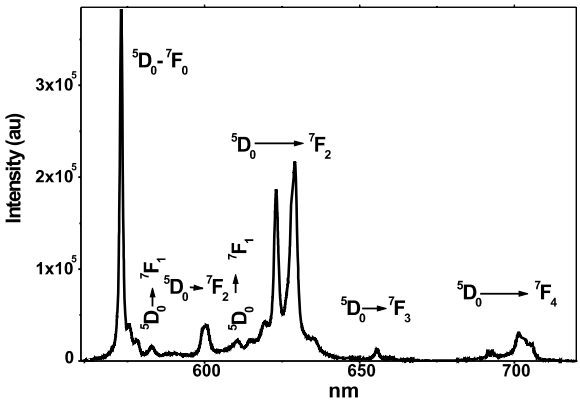

Fig. 10.3. Emission of the Eu^{3+}-doped (2 wt %) britholithe

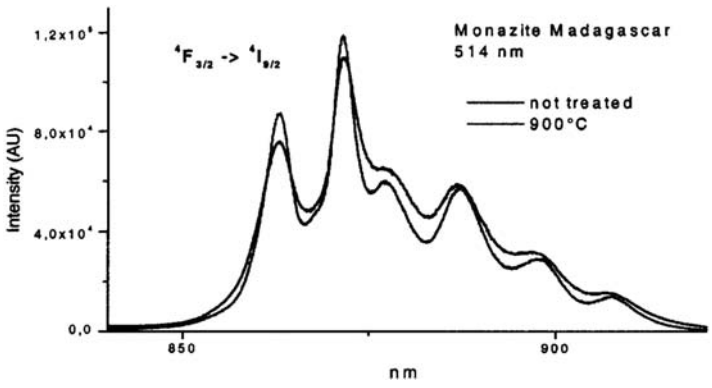

Fig. 10.4. Emission spectra of Nd^{3+} ($^4F_{3/2} \rightarrow {}^4I_{9/2}$ transition) of natural monazite from Madagascar before and after treatment at 900 °C

Table 10.1. Comparison of full-width at half-maximum (nm) of two Nd emission lines with Th concentration of different natural monazites and determination of equivalent annealing fictive temperature (Madagascar sample considered as reference material). (nd: not determined) (age: Schärer and Deutsch 1990; Paquette et al. 1994; Seydoux-Guillaume et al. 2002b; Schärer et al. 1994)

Monazites	Madagascar (reference)	Norway	Canada	Brazil
Age (Ma)	545	nd	1,928	474
Th (wt. %)	13.25	nd	9.03–10. 33	6.92
FWHM 3 (nm)	4.6(1)	4.4(5)	4.4(3)	3.9(4)
fictive T (°C)	25	160	178	670
FWHM 1 (nm)	6.1(1)	5.7(9)	5.5(1)	5.4(2)
fictive T (°C)	25	211	400	460

Monazites	China	Alps Trimouns	Alps Lauzière
Age (Ma)	24	nd	nd
Th (wt. %)	5.74–15. 60	nd	nd
FWHM 3 (nm)	3.4(7)–3. 6(9)	2.3(5)	2.1(5)
fictive T (°C)	921–1140	$\gg$ 1,200	$\gg$ 1,200
FWHM 1 (nm)	4.5(6)–5. 1(6)	3.2(3)	2.9(3)
fictive T (°C)	680–1025	$\gg$ 1,200	$\gg$ 1,200

natural monazites from different ages and different Th and U content, to follow thermal healing of radiation-induced defects. The full-width at half-maximum (FWHM) of Nd emission lines which indicates the degree of disorder, appears to decrease linearly with the treatment temperature (Fig. 10.4). The data collected from different natural monazites are compared in Table 10.1. While the Madagascar monazite presents the largest FWHM (6.1 nm) and can be considered as having undergone the strongest metamictization, the modern alpine monazite is the most perfectly ordered sample (FWHM 2.1 nm). The evolution trend with temperature of the Madagascar sample, which present before annealing the largest FWHM, is used to estimate the equivalent annealing fictive temperature of the other samples. The degree of disorder appears to be proportional to the thorium content and not to the age of the samples (Schärer and Deutsch 1990; Paquette et al. 1994; Schärer et al. 1994; Seydoux-Guillaume et al. 2002b).

CHAPTER 11

Luminescent Bio-Minerals

Hydroxyapatite $Ca_5(PO_4)_3OH$ is the main mineral constituent of bones and teeth. The chemical composition of biological apatite is somewhat different from the above given formula. They are usually defined as non-stoichiometric apatites. This nonstoichiometry is caused by the presence of different ions in very small or in trace amounts. Foreign ions might have an effect on the chemical or physical properties of hydroxyapatite. Trace ions might affect the mineralisation process or the dissolution of biological minerals, teeth and bones. The effect of trace ions is also important in the investigation of hydroxyapatite as a bone implant or as coating material for Ti or other implants. In this cases trace ions might influence the stability of the implant, the chemical interaction at the bone and the implant interface or mechanical properties. Whether foreign ions can substitute Ca^{2+} in one of its crystallographical sites in the hydroxyapatite lattice ions is a principal question in the preparation of mineral with foreign ions. The size of the ions, their chemical properties and the preparation conditions are among the most important factors in this respect.

La^{3+} is of interest in its relationship to biological hydroxyapatite because of their inhibitory effect on the demineralization of dental enamel. The form of La^{3+} was not clear, namely surface adsorption or lattice incorporation. In an attempt to clarify it, laser-induced luminescence has been used (Mayer et al. 1999). La^{3+} is not luminescent, Gd-containing samples were prepared and studied. Figure 11.1 demonstrates Gd luminescence spectra with 266 nm laser excitation before and after heating at 800 °C. It is clearly seen that luminescence intensity is drastically stronger after thermal treatment. Thus precipitated samples must be heated to 800 °C to enable Gd^{3+} to replace Ca^{2+} and become luminescent and its incorporation form is surface adsorption.

Another example is LIBS application for real-time identification of carious teeth (Samek et al. 2003). In the dental practice, usually more healthy tissue is removed than ultimately necessary. Carious and healthy tooth material can be identified through the decrease of matrix elements Ca and P in hydroxyapatite and/or the increase of non-matrix elements, typically Li, Sr, Ba, Na, Mg, Zn and C, using pattern recognition algorithms. A fiber-based LIBS assembly was successfully used for this task. As for the case of phosphate ores evaluation, the efforts aimed at normalizing the spectrum collection conditions and procedures, so that the spectra are sufficiently reproducible for precise quantitative

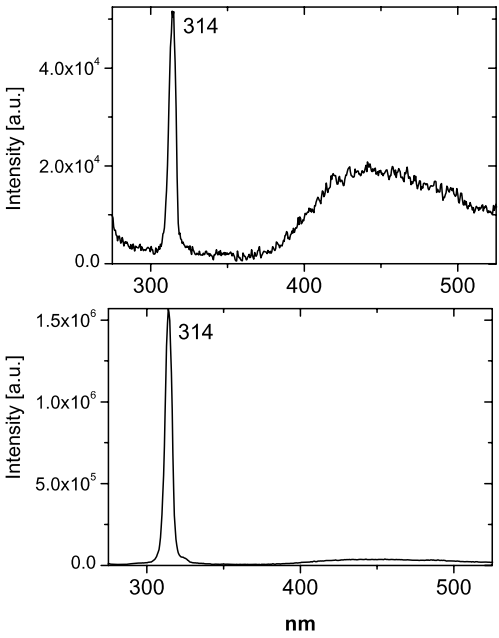

Fig. 11.1. Laser-induced luminescence of Gd^{3+} in precipitated hydroxyapatite before and after heating at 800 °C

analysis, down to detection of a few ppm, are not required. The combination of LIBS and discrimination analysis is a useful tool for real time *in vivo*/*in vitro* caries identification during the drilling process when luminous short laser pulses create plasma.

Conclusions

In the proposed book there is an emphasis on luminescence lifetime, which is a measure of the transition probability and non-radiative relaxation from the emitting level. Luminescence in minerals is observed over a time interval of nanoseconds to milliseconds. It is therefore a characteristic and a unique property and no two luminescence emissions will have exactly the same decay time. The best way for a combination of the spectral and temporal nature of the emission can be determined by time-resolved spectra. Such techniques can often separate overlapping features, which have different origins and therefore different luminescence lifetimes. The method involves recording the intensity in a specific time "window" at a given delay after the excitation pulse where both delay and gate width have to be carefully chosen. The added value of the method is the energetic selectivity of a laser beam, which enables us to combine time-resolved spectroscopy with powerful individual excitation. The book deals mainly with the theoretical approach, experimental results and their interpretation of laser-induced time-resolved spectroscopy of minerals in the wide spectral range from 250 to 2,000 nm, which enables us to reveal new luminescence previously hidden by more intensive centers. Artificial activation by potential luminescence centers has been accomplished in many cases, which makes sure identification possible. The mostly striking example is the mineral apatite, which has been extremely well studied by many scientists using practically all known varieties of steady-state luminescence spectroscopy: photoluminescence with lamp and laser excitations, X-ray excited luminescence, cathodoluminescence, ionoluminescence and thermoluminescence. Nevertheless, time-resolved spectroscopy revealed that approximately 50% of the luminescence information remained hidden. The most important new information is connected with luminescence of trivalent rare-earth elements in minerals, such as Eu^{3+}, Pr^{3+}, Ho^{3+}, Tm^{3+}, Er^{3+}, and Nd^{3+} (Table 12.1).

Luminescence information on transition elements is substantially improved. Besides well known Mn^{2+} centers, emission of Mn^{5+} was found and Mn^{4+} proposed as a possible participant in minerals luminescence. Luminescence characteristics of Mn^{6+}, Cr^{5+}, Ti^{3+}, V^{2+}, V^{3+}, Ni^{+}, Sb^{3+} are presented and their possible role in minerals luminescence is considered. Luminescence of Pb^{2+}, Bi^{3+}, Bi^{2+}, Ag^{+}, Cu^{+} has been found. Reabsorption lines of molecular H_2O and O_2 in apatite and diamond have been identified.

Table 12.1. REE luminescence centers detected in minerals

Center	λ_{lum}	λ_{ex}	τ (μs)	Transition	Minerals
Ce^{3+}	360–400	308	0.02	$5d^1$–$4f^1$ ($^2F_{5/2}$)	Apatite, barite, anhydrite, calcite, feldspars, danburite, datolite, esperite, apophyllite, charoite, fluorite, hardystonite
Pr^{3+}	228			$^1S_0$–$^3H_5$	Apatite, scheelite,
	239			$^1S_0$–$^3H_6$	zircon, anhydrite,
	268			$^1S_0$–$^1G_4$	zircon, titanite
	480			$^1D_2$–$^3H_6$	
	480		10	$^3P_0$–$^3H_4$	
	600	460	100	$^1D_2$–$^3H_6$	
	650		20	$^3P_0$–$^3F_2$	
	858			$^3P_0$–$^1G_4$	
Nd^{3+}	890			$^4F_{3/2}$–$^4I_{9/2}$	Apatite, scheelite,
	1,070	360	300	$^4F_{3/2}$–$^4I_{11/2}$	fluorite, barite,
	1,340			$^4F_{3/2}$–$^4I_{13/2}$	titanite, zircon,
	395	355	10–30	$^2F_{5/2}$–$^4F_{5/2}$	anhydrite, calcite,
	416			$^2F_{5/2}$–$^4F_{9/2}$	rhodonite,
	446			$^2P_{1/2}$–$^4I_{9/2}$	feldspars
	588			$^4G_{7/2}$–$^4I_{11/2}$	
	672			$^4G_{7/2}$–$^4I_{12/2}$	
	743			$^4G_{7/2}$–$^4I_{13/2}$	
	846			$^4G_{7/2}$–$^4I_{15/2}$	
Sm^{3+}	565			$^4G_{5/2}$–$^6H_{5/2}$	Apatite, zircon,
	599	308	2,250	$^4G_{5/2}$–$^6H_{7/2}$	scheelite, monazite,
	645			$^4G_{5/2}$–$^6H_{9/2}$	fluorite, anhydrite, titanite, zircon, hardystonite, pyromorphite
Sm^{2+}	630			$5d$–$4f$	Anhydrite, fluorite,
	688			$^7D_0$–$^7F_0$	apatite
	700			$^7D_0$–$^7F_1$	
	734			$^7D_0$–$^7F_2$	

Table 12.1. (continued)

Center	λ_{lum}	λ_{ex}	τ (μs)	Transition	Minerals
Eu^{3+} (I)	579			$^5D_0$–$^7F_0$	Apatite, zircon,
	590			$^5D_0$–$^7F_1$	scheelite,
	618	384	1,800	$^5D_0$–$^7F_2$	danburite, datolite,
	653			$^5D_0$–$^7F_3$	fluorite, anhydrite,
	700			$^5D_0$–$^7F_4$	calcite, xenotime, orangite, titanite
Eu^{3+}	574			$^5D_0$–$^7F_0$	
(II)	601			$^5D_0$–$^7F_1$	
	630	266		$^5D_0$–$^7F_2$	
	711			$^5D_0$–$^7F_4$	
Eu^{2+}	390–450	377	0.6–0.8	$4f5d$–$4f$	Fluorite, apatite, barite, danburite, feldspars, anhydrite, zoisite, charoite
Gd^{3+}	312	266	2,000	$^6P_{7/2}$–$^8S_{7/2}$	Fluorite, zircon, anhydrite, hardystonite
Tb^{3+}	380			$^5D_3$–$^7F_6$	Apatite, scheelite,
	415	308	600	$^5D_3$–$^7F_5$	zircon, calcite,
	437			$^5D_3$–$^7F_4$	fluorite, zoisite,
	545		2,400	$^5D_4$–$^7F_5$	monazite, feldspars, calcite
Dy^{3+}	480			$^4F_{9/2}$–$^6H_{15/2}$	Apatite, scheelite,
	575		720	$^4F_{9/2}$–$^6H_{13/2}$	zircon, calcite,
	663	354		$^4F_{9/2}$–$^6H_{11/2}$	fluorite, zoisite,
	750			$^4F_{9/2}$–$^6H_{9/2}$	monazite, titanite
Er^{3+}	545	308	23	$^4S_{3/2}$–$^4I_{15/2}$	Apatite, fluorite,
	854	532		$^4S_{3/2}$–$^4I_{9/2}$	scheelite, zircon,
	978	532		$^4I_{11/2}$–$^4I_{15/2}$	feldspars, titanite
	1,540		2,100	$^4I_{13/2}$–$^4I_{15/2}$	
Tm^{3+}	364			$^1D_2$–$^3H_6$	Apatite, scheelite,
	452	360	17	$^1D_2$–$^3H_4$	zircon, calcite,
	796			$^1G_4$–$^3F_5$	fluorite, anhydrite, aragonite, hardystonite

Table 12.1. (continued)

Center	λ_{lum}	λ_{ex}	τ (μs)	Transition	Minerals
Yb^{3+}	993	308	3,100	$^2F_{5/2}$–$^2F_{7/2}$	Apatite, scheelite, zircon
Ho^{3+}	540	360	5	$^5S_2$–$^5I_8$	Zircon, scheelite, fluorite

The possibilities of time-resolved laser based spectroscopies have been demonstrated, combining such techniques as luminescence, Raman, breakdown and second-harmonic generation. Radiometric sorting of minerals using LIBS was patented and apparatus for evaluation of phosphate rocks with elevated dolomite content has been developed and constructed.

References

Agekyan V, Shiryapov I, Oreshnikova L (1974) FTT 16:2473–2475 (in Russian)
Airken S, Kusachi I, Yamashita N (2003) Phys and Chem of Miner 30:478–485
Ajo D, Favaro M, Pozza G, Barba M, Callejas P (1997) J Material Sci 32:4217–4220
Alexander D (1998) US Patent, 5,847,825
Altshuller Z (1980) Int Cong Phosphorous Compounds, pp. 605–634
Armstrong D, Wang X, Beesley C, Rabinovitz R (1999) Amer Labor October: 41–45
Armstrong D, Wang X, Beesley C, Rabinovitz R (2000a) Amer Labor June:26-34
Armstrong D, Wang X, Beesley C (2000b) Analyt Let 33:111-123
Bakhtin A, Moroshkin V (1986) Geochemistry 10:1514–1515 (in Russian)
Bakhtin A, Gorobets B (1992) Kazan University Publishing (in Russian)
Balda R, Sanz M, Mendioroz A, Fernandez J, Griscom L, Adam J (2001) Phys Rev B 64:144101–1 – 144101–8
Barbarand J, Pagel M (2001) American Mineralogist 86:473–485
Barbin V, Jouart J-P, d'Almedia T (1996) Chem Geol 130:77–86
Barbini R, Colao F, Fantoni R, Pulucci A, Capitelli T (1999) Appl Phys A 69: 174–178
Baumer A, Blanc Ph, Cesbron F, Ohnenstetter D. (1997) Chemical Geology 138:73–80
Beletti A, Borromei R, Oleari L (1995) Inorganic Chimica Acta 235:349–362
Bell S, Bourguignon E, Grady A, Villaumire J, Dennis A (2002) Spectroscopy Europe 14/6:17-20
Bethe G (1929) Ann Physics 3:133-151
Bishop J, Lane M, Murad E (2002) Mars Spectral Workshop II
Blanchard G (2001) Focal Point 55:110A–118A
Blanc Ph, Baumer A, Cesbron F, Ohnenstetter D, Panczer G, Remond G (2000) Cathodoluminescence in Geosciences. Springer, Berlin Heidelberg New York, pp. 127–160
Blasse G, Wanmaker J, Vrigt J, Bril A (1968) Philips Res Rpts 23:201–209
Blasse G (1980) Structure and Bonding 42:1–41
Blasse G, Aguilar M (1984) J Lumin 29:239–241
Blasse G, Meijerink A, Nomes M, Zuidema J (1994) J Phys Chem Solids 55: 171–174
Blasse G, Grabmaier B (1994) Luminescent materials. Springer, Berlin Heidelberg New York

Blasse G (1997) J Luminescence 72–74:129–135
Bokii G, Bezrykov G, Kliyev Yu, Naletov A, Nepsha V (1986) Nauka, Moscow
Bolden P (1952) Philips Research Reports 7:197
Boulon G (1987) In: DiBartolo B (ed) Spectroscopy of solid-state laser-type materials. Plenum Press, NY, pp. 223–266
Boulon G (1997) In: DiBartolo B (ed) Spectroscopy and dynamics of Collective Excitations in Solids. Plenum Press, NY
Brenier A, Suchocki A, Pedrini C, Boulon G, Made C (1992) Phys Rev B 46:3219–3227
Brittain H (1990) In: Derry D (ed) Instrumental Surface Analysis of Geological Materials. Wiley-VCH, Weinheim
Broicher H (2000) Mining Engineering, September, pp. 73–77
Brugger J, Bettiol A, Costa S, Lahaye Y, Baterman R, Lambert D, Jamieson D (2000) Miner Mag 64:891–903
Brunold T, Güdel H (1997) J Opt Soc Am B 14:2373–2377
Brunold T, Hazenkamp M, Güdel H (1997) J Luminescence 72–74:164–165
Bryknar Z, Trepakov V, Potucek Z, Jastrabík (2000) J of Lum 87–89:605–607
Bushev A, Portnov A (2000) Izvestia VUZov, Geologia I Razvedka 2:40–42 (In Russian)
Buttler K (1966) Proc of the International Conference on Luminescence, pp 1313–1329
Butler K. (1980) University Park, Pennsylvania State University Press, 117 pp
Castellan G (1993) Physical Chemistry, Addison-Wesley Publ. Comp. 646
Chalain J-P, Fritsch E, Hanni HA (2000) J Gemm 27:73–78
Champagnon B, Duval E (1977) Journal De Physique 38:L-299–L-301
Champagnon B, Duval E (1979) J Phys C: Solid state Phys 12:L-425–L-429
Chithambo M, Raymond S, Calderon T, Townsend P (1995) J African Earth Sciences 20:53–60.
Cuicci A, Palleschi V, Rastelli S, Barbini R, Colao F, Fantoni R, Palucci A, Ribezzo S (1996) Applied Physics B 63:185–190
Cuicci A, Corsi M, Palleschi V, Rastelli S, Salvetti A, Tognoni E (1999) Appl Spectrosc 53:960–965
Collins A (2000) Diam Rel Mater 9:417–423
Correcher V, Garcia-Guinea J (2001) J Luminescence 93:303–312
Cremers D, Wiens R, Arp Z, Harris R, Maurice S (2003) Lunar and Planetary Science XXXIV
Curtis A (1989) Method UK Patent Application, N 8901759.4
Cutmore N, Eberhard M www.min-eng.com/protected/me02ex
Czaja M, Mazurakb Z (1994) Optical Materials 3:95–98
Czaja M (1999) Excited States of Transition Elements, Duszniki Zdroj, Poland, Abstracts, Polish Academy of Science, PO9
Davies G (1994) Properties and Growth of Diamonds. Gordon Davies, King's College, London
Davies C, Telle H, Montgomery D, Corbett R (1995) Spectrochimica Acta Part B 50:1059–1075
DeLoach L, Payne S, Kway W, Tassano J, Dixit S, Krupke W (1994) J Luminescence 62:85–94

DeNeufville J, Kasdan A, Chimenti R (1981) Applied Optics 20:1279–1296
Deren P, Malinowski M, Strek (1996) J Luminescence 68:91–103
Dicke J (1968) Spectra and energy levels in crystals. Interscience publishers, NY
Donker H, Smit W, Blasse G (1988) Phys Stat Sol (b) 148:413–419
Donker H, Smit W, Blasse G (1989) J Electrochem Soc 136:3130–3135
Dorenbos P (2003) J Physics: Condensed Matter 15:2645–2665
Dubessy J, Orlov R, McMillan P (1994) In: Marfunin A (ed) Advanced Mineralogy 2, Methods and Instrumentation. Springer, Berlin Heidelberg New York, pp 138–146
Durville F, Champagnon B, Duval E, Boulon G (1985) J Phys Chem Sol 46: 701–707
El Ouenzerfi R, Panczer G, Goutaudier C, Cohen-Adad MT, Boulon G, Trabelsi-Ayedi M, Kbir-Ariguib N (2001) Optical Materials 16:301–310
Eremenko G, Khrenov A (1982) Mineralogical Mag, V4, N1, pp 93–95 (in Russian)
Ewing R (2001) The Canadian Mineralogist 39:697–715
Eyal M (1988) SPIE 1182:140–150
Fabeni P, Pazzi G, Salvini L (1991) J Physics and Chemistry of Solids 52(1): 299–317
Fergusson J (1970) Prog Inorg Chem 12:159–294
Figgis B (1966) Wiley, NY
Folkerts H, Hamstra M, Blasse, G (1995) Chem Phys Lett 246:135–138
Gaft M, Gorobets B, Malinko S (1979) Docl Acad Nauk SSSR 244(5):171–174
Gaft M, Gorobets B (1979) Jurnal Prikl Spectr 6(31):987–990
Gaft M, Gorobets B, Barsukova N (1980) Zapiski Vses Miner Ob-va 4:493–497 (in Russian)
Gaft M, Gorobets B, Homyakov A (1981a) Docl Acad Nauk SSSR 263(3):1234–1237
Gaft M, Gorobets B, Naumova I, Mironova N, Grinvald G (1981b) Miner Journal N3:80–90 (in Russian)
Gaft M, Vorontsova V (1982) Miner Journal 4(5):75–78 (in Russian)
Gaft M, Gorobets B, Marshukova N, Pavlovskii F (1982) Docl Acad Nauk SSSR 266(1):217–220
Gaft M (1984) Miner Journal 4:83–86 (in Russian)
Gaft M, Bershov L, Krasnaya A, Yaskolko V (1985) Phys Chem Miner 11:255–260
Gaft M, Rassulov V, Zukova V, Rakov L (1986) Miner Journal 8(3):74–78 (in Russian)
Gaft M, Gorobets B, Marshukova N, Pavlovskii A (1988) Docl Acad Nauk SSSR 299(1):176–179
Gaft M (1989) Luminescence of minerals under laser excitation, Ministry of Geology, Moscow (in Russian)
Gaft M, Bershov L, Rassulov V (1989a) In: Intern Geol Cong Mineral, pp 118–123
Gaft M, Scorobogatova N, Rassulov V, Moroshkin V (1989b) Miner Journal 11:58–64 (in Russian)

Gaft M, Rassulov V, Litvinzev E, Evdokimenko E, Moroshkin V, Chernyak A, Shalashilina T (1989c) SSSR Ministry of Geology, ISSN 0130–0822, Moscow (in Russian)
Gaft M, Evdokimenko E, Moroshkin V (1991a) SSSR Certificate N 1566556 (in Russian)
Gaft M, Moroshkin V, Evdokimenko E (1991b) SSSR Certificate N 1584206 (in Russian)
Gaft M (1992) J Therm Anal 40:67–78
Gaft M (1993) Water Science and Technology 27(7–8):547–556
Gaft M, Pregerson B, Rabinovitz J (1993) Reviews in Chemical Engineering 9:267–281
Gaft M (1993) Seminar Franco-Israelinne, Abstracts, Lyon, Relation Internationales, 70–71
Gaft M, Rudenkova I (1993) J Therm Anal 42:187–195
Gaft M (1994) IMA, 16th General meeting, Italy, pp 131–132
Gaft M, Reisfeld R, Panczer G, Shoval S, Garapon C, Boulon G, Strek W (1996a) Acta Phys Polonica A 90:267–274
Gaft M, Shoval S, Panczer G, Nathan Y, Champagnon B, Garapon C (1996b) Palaeography, Palaeoclimatology, Palaeoecology 126:187–193
Gaft M, Reisfeld R, Panczer G, Boulon G, Shoval S, Champagnon B (1997a) Optical Materials 8:149–156
Gaft M, Reisfeld R, Panczer G, Shoval S, Champagnon B, Boulon G (1997b) J Luminescence 72–74:572–574
Gaft M, Reisfeld R, Panczer G, Champagnon B (1997c) Optical Materials 8(1–2):143–149
Gaft M, Reisfeld R, Panczer G, Blank Ph, Boulon G (1998a) Spectrochim Acta Part (A) 54:2163–2175
Gaft M, Trabjerg I, Reisfeld R, Panczer G (1998b) Spectrochim Acta Part(A) 54:1721–1724
Gaft M, Reisfeld R, Panczer G, Uspensky E, Varrel B, Boulon G (1999a) Optical Materials 13:71–79
Gaft M, Panczer G, Uspensky E, Reisfeld R (1999b) Mineral Mag 63:199–210
Gaft M, Panczer G, Reisfeld R, Shinno I (2000a) J Alloys and Compounds 300–301:267–274
Gaft M, Boulon G, Panczer G, Guyot Y, Reisfeld R, Votyakov S, Bulka G (2000b) J Luminescence 87–88:1118–1121
Gaft M, Panczer G, Reisfeld R, Shinno I (2000c) J Luminescence 87–89:1032–1035
Gaft M, Reisfeld R, Panczer G, Boulon G (2001a) Optical Materials 16(1–2): 279–290
Gaft M, Reisfeld R, Panczer G, Segal I (2001b) Journal of Alloys and Compounds 323–324:842–848
Gaft M, Panczer G, Reisfeld R, Uspensky E (2001c) Physics and Chemistry of Minerals 28:347–363
Gaft M, Seigel H, Panczer G, Reisfeld R (2002a) Eur J Mineralogy 14:1041–1048
Gaft M, Panczer G, Reisfeld R, Shinno I, Ioffe O, Segal I (2002b) Mineralogy and Petrology 76:235–246

Gaft M, Nagli L, Panczer G, Reisfeld R (2002c) In: Zhang P, El-Shall H, Somasundran P, Stana R (eds) Beneficiation of Phosphates, Fundamentals and Technology. SME, pp 145–152
Gaft M, Nagli L, Reisfeld R, Panczer G, Brestel M (2003a) J Luminescence 102–103:349–356
Gaft M, Nagli L, Reisfeld R, Panczer G (2003b) J Optical Materials 24:231–241
Gaft M, Nagli L (2004) US Patent 6,753,957 B1
Gaft M, Nagli L, Waychuas G (2004a) Physics and Chemistry of Minerals 31: 365–373
Gaft M, Nagli L, Waychunas G (2004b) Mitteilungen der Österreichischen Mineralogischen Geselleschaft, B149, 34
Galanin M (1996) Cambridge International Science Publishing
Gao Z, Zheng S, Gu Z (2002) In: Zhang P, El-Shall H, Somasundran P, Stana R (eds) Beneficiation of Phosphates, Fundamentals and Technology SME, pp 247–259
Gedanken A, Reisfeld R, Sominski E, Palchik O, Kolturin Yu, Panczer G, Gaft M, Minti H (2000) J Phys Chem B 104:7057–7065
Geschwind S, Kisluk P, Klein M, Remeika J, Wood D (1962) Phys Rev 126:1684–1686
Gilinskaya L, Mashkovtsev R (1994) Abstracts, IMA, 16th General Meeting, Pisa, Italy, p 145
Gilinskaya L, Mashkovtsev R (1995) J Struct Chem 36:89–101 (in Russian)
Goldberg M, Weiner E (1989) In: Luminescence applications in biological, chemical, environmental, and hydrological sciences. ACS Symposium Series, Denver, pp 1–22
Golombek M, Cook R, Economou T, Folkner W, Haldemann A, Kallemeyn P, Knudsen J, Manning R, Moore H, Parker T (1997) Science 278:1743–1748
Gorobets B (1968a) Optica i spectroscopiyay 25:292–294 (in Russian)
Gorobets B, Novozhilov A, Samoilovich M (1968b) Soviet Phisics – Doklady 13:519–521 (in Russian)
Gorobets B, Sidorenko G (1974) Atomic Energy 36:6–13
Gorobets B (1975) Zapiski of Vsesousn. Mineral. Ob-va 3:357–359 (in Russian)
Gorobets B, Kudrina M (1976) Constitution and properties of Minerals, Kiev, Naukova Dumka 10:82–88 (in Russian)
Gorobets B, Gaft M, Laverova L (1978) Jorn Pricladn Spectrosk 28:1100–1102
Gorobets B, Walker G (1994) In: Marfunin A (ed) Advanced Mineralogy 2, Methods and Instrumentation. Springer, Berlin Heidelberg New York, pp 138–146
Gorobets B, Portnov A, Rogojine A (1995) Radiation Measurements 24:485–491
Gorobets B, Litvintsev E, Rogojine A (1997a) Proc of the 5th Int Cong on Applied Mineralogy and Mineral Industry, Warsaw, Poland, pp 229–233
Gorobets B, Rogojine A, Portnov A (1997b) Proc of the 5th Int Cong on Applied Mineralogy and Mineral Industry, Warsaw, Poland, pp 229–233
Gorobets B, Rogojine A (2001) Luminescence Spectra of Minerals. Handbook, RPC VIMS, Moscow
Gororbets B, Kononov O, Rogojine A, Kvitko T (2003) Vestnik Gemmologii, 3(10):38–56 (in Russian)

Götze J (2000) Technische Universität Bergakademie Freiberg
Greenblatt M (1980) J Chem Education 57:546–551
Grimm J, Wenger O, Güdel H (2003) J Luminescence 102–103:380–385
Grinberg M, Barzovska J, Shen Y, Bray K, Hanuza J (2002) International Conference on Luminescence and Optical Spectroscopy of Condensed Matter, Budapest, Hungary, Abstracts, p 31
Gruber J, Wright A, Seltzer M, Zandi B, Merkle L, Hutchinson J, Morrison C, Allik T, Chai B (1997) J Appl Phys 83:1009–1016
Gudaev O, Kanaev I, Novomlintsev A, Surovtsev N, Termyaev A (1997) Physicotechnical problems of mining, N5
Gudaev O, Kanaev I, Shlyufman E (1999) Laser method of separation of diamonds from the ore. Detect and Systems 3:19–23
Gutzov S, Bredol M, Wasgestian F (1998) J Phys Chem Solids 59:69–74
Güdel H, Brunold T, Hazenkamp M, Herren M, Oetliker U, Schenker R (1997) Electrochemical Society Proceedings 29:225–23
Haberland H, Karlik B, Przibram K (1934) Sitzber. Akad Wiss Wien, Abt Iia 143:151–161 (in German)
Haberland H, Köhler A (1939) Naturwissenschaften 27:275–281 (in German)
Haberman D, Neuser R, Richter D (1996) Sed Geol 101:1–7
Hall M, Ribber P (1971) American Mineralogist 56:31–45
Hamstra M, Follkerts H, Blasse G (1994) J Mater Chem 4:1349–1350
Hazenkamp M, Güdel H (1996) J Luminescence 69:235–238
Hayashi M, Shinno I, Taguchi S, Sugihara S (1990) J Min Pet Econ Geol 85:27–33
Helder H, Junod P (1976) Soc Photogr Scient and Eng 20:50–52
Hou X, Jones B (2000) Microchemical J 66:115–145
Hugh W, Hubble H, Ghosh M, Sharma S, Horton K, Lucey P, Angel M, Wiens R (2002) Lunar and Planetary Science XXXIII
Ishii T, Ogasava K, Tanaka A, Adachi H (1999) Materials Transactions, JIM 40:416–419
Ishii T, Ogasava K, Adachi H (2002) J Chemical Physics, 116:471–479
Jagannathan R, Kottaisamy M (1995) J Phys: Condens Matter 7:8453–8457
Jastrablk L, Kudyk B, Kapphan S, Trepakov V, Pankrath R (2002) Int Conf on Luminescence and Optical Spectroscopy of Condensed Matter, Budapest, Hungary, Abstracts, 84 pp
Javasankar C, Babu P (2000) J Alloys and Compounds 307:82–93
Jørgensen C, Judd B (1964) Mol Physics 8
Judd B (1962) Phys Rev 127:750
Kaminskii AA (1996) CRC Press, Boca Raton, Florida
Kasdan A, Chimenti R, de Neufville J (1981) Appl Optics 20:1279–1307
Kasyanenko E, Matveeva O (1987) J Prikladn Spectroscop 46:943–949
Kempe U, Torsten G, Nasdala L (2000) In: Pagel M, Barbin V, Ohnenstetter D (eds) Cathodoluminescence in Geosciences. Springer, Berlin Heidenberg New York, pp 425–457
Kemper U, Plötze M, Brachmann A, Böttcher R (2002) Miner Petrol 76:213–234
Kingsley J, Prener J, Segall B (1965) Phys Rev 137:A189–A202
Koike K, Mnakagava M, Koike C, Okada, Chichara H (2002) Astronomy Astrophysics 2:35–41

Kompitsas M, Roubani-Kalantzopoulou F, Bassiotis I, Diamantopoulou A, Giannoudakos A (2000) Proceedings of EARSeL-SIG-Workshop LIDAR 1:130–138
Konijnendijk W (1981) Inorg Nucl Chem Lett 17:129–132
Kottaisamy M, Jagannathan R, Jeyagopal P, Rao R, Narayanan R (1994) J Phys (D):Appl Phys 27:2210–2215
Koziarsca B, Godlewski M, Suchoki A, Czaja M, Mazurak Z (1994) Physical Rev B50:12997–12300
Krasilschikova O, Tarashchan A, Platonov A (1986) Naukova Dumka, Kiev
Krbetschek M, Götze J, Irmer G, Rieser U, Trautmann T (2002) Miner Petrol 76:167–177
Krasnobaev A, Votyakov S, Krohalev V (1988) Nauka
Kroger F, Overbeek J (1949) Trans Electrochem Soc 96:132
Kupriyanova I, Moroshkin V (1987) Izvestia ANSSSR (Ser Geol) 9:84–90 (in Russian)
Kuze A, Chance K (1994) J Geoph Research 99:481–496
Kusnetsov G, Tarashchan A (1988) Naukova Dumka, Kiev (in Russian)
Kusnetsov G, Silaev V, Lupashko T, Melnikov V (1991) Zap Vses Miner Ob-va 4:70–77 (in Russian)
Lakowicz J (2000) N-Y-Boston, Kluwer, Dordrecht
Laurs B, Rohtert W, Gray M (1997) Geams&Gemology:166–187
Lindblom J, Hösla J, Papunen H, Häkkïen H, Mutaten J (2003) Optical Materials 24:243–253
Lindblom J, Hölsä J, Papunen H, Häkkänen H (2004) Amer Mineral (in Press)
Lizzo S, Mejernic A, Blasse G (1994) J Luminescence 59:185–194
Locoq de Buisbaudran (1986) CRA Sci Paris 103:629
Mao H, Xu J, Bell P (1986) J Geophys Res 91:4673–4676
Marech J, Jacquier B, Pedrini C, Boulon G (1989) Materials Chemistry and Physics 21:237–259
Marfunin A (1979a) Springer, Berlin Heidelberg New York
Marfunin A (1979b) Springer, Berlin Heidelberg New York
Marfunin A, Gaft M, Panczer G, Shigley J (1998) In: Advanced Mineralogy 3. Springer, Berlin Heidelberg New York, part 6.2, pp 400–432
Marques C, Santos L, Falcão A, Silva R, Alves E (2000) J Luminescence 87–89:583–585
Martin P, Chevarier A, Chevaruier N, Panczer G (1996) The French-Israeli Workshop on Apatites and Lasers, Jerusalem
Martin P, Carlot G, Chevarier A, Den-Auwer C, Panczer G (1999a) J Nuclear Materials 275:268–278
Martin P, Chevarier A, Panczer G (1999b) J Nuclear Materials, 278:202–206
Mazurak Z, Czaja M (1996) J Luminescence 65:335–340
Mayer I, Layani J, Givan A, Gaft M, Blanc P (1999) J Inorg Biochem 73:221–226
McClure D (1990) Laser Technologies in Luminescence Spectroscopy. Dinh V, Eastwood (eds), STP 1066:21–36
McNicol B, Pott G (1973) J Luminescence 6:320–334
Measures R, Houston W (1974) Optical Engineering 13:494–501
Measures R (1985) Wiley, New York

Meisner L (1984) Zapiski Vses. Miner Ob-va 6:731–736 (in Russian)
Meisner L, Kuz'min V (1986) Separaziya rud 5:22–25 (in Russian)
Meisner L (1994) In: Marfunin A (ed) Composition, Structure and Properties of Mineral Matte, pp 496–497
Mineeva R, Speranskii A, Bao Y, Bershov L, Ryabchikov I, Chukichev M (2000) Geochem Int 38:323–330
Minko O, Bahtin A, Shepelev Yu (1978). Abstracts of USSR Conference, Tallinn, pp 81–83 (in Russian)
Mironova N, Riekstinya D, Skvortzova V, Smirnov A (1991) Abstracts: Luminescence in Geology, Ekaterinburg, Russia, p 68 (in Russian)
Mironova N, Ulmanis U (1988) Riga, Zinatne (in Russian)
Miziolek A, Cespedes E (1996) Optics and Photonics News, September, pp 39–41
Mohler R, White W (1994) Material Res Bull 29:1109–1116
Mohler R, White W (1995) J Electrochemical Society 142:3923–3927
Moine B, Pedrini C, Duloisy E, Boutinaud P, Parent C, Flem G (1991) J De Physique IV 1:C7–289–C7–292
Mokrousov V, Lileev V (1979) Nedra
Moncorgé R, Manaa H, Boulon G (1994) Optical Materials 4:139–144
Moncorgé R, Bettinelli M, Gyot Y, Cavalli E, Capabiano J, Girard S (1999) J Phys: Condens Matter 11:6831–6841
Monteil A, Boulon G, Garapon C (1989) French-Israeli Workshop on Solid State Materials, SPIE 1182:162–182
Morozov A, Morozova L, Trefilov A, Feofilov P (1970) Opt Spectrosc 29:590–596
Moroshkin V, Gorobets B, Bushev A (1987) Izvestiya Acad Nauk SSSR (Geol) 10:87–91 (in Russian)
Moroshkin V, Evdokimenko E, Gaft M, Rassulov V, Rudenkova I (1993) Ministry of Geology of Russia, Moscow, pp 1–8
Nasdala L, Lengauer C, Hanchar J, Kronz A, Wirth R, Blanc P, Kennedy A, Seydoux-Guillaume A (2002) Chem Geol 191:121–140
Nasdala L, Zhang M, Kempe U, Panczer G, Gaft M, Andrut M, Plötze M (2003) In: Hanchar J, Hoskin P (eds) Zircon/Rev Mineral Geochem, vol 53. Mineral Soc Am, Washington, DC
Nasdala L, Götze J, Hanchar J, Gaft M, Krbetschek M (2004) In: Biran A, Lubowitzky E (eds) EMU Notes in Mineralogy, Spectroscopic Methods in Mineralogy vol 6, Chapter 2, pp 43-91
Nasdala L, Smith D, Kaindll R, Ziemann M (2004) In: Biran A, Lubowitzky E (eds) EMU Notes in Mineralogy, Spectroscopic Methods in Mineralogy vol 6, Chapter 7, pp 281–343
Noll R, Sattmann R, Sturm V, Winkelmann S (2003) Books of Abstracts, EMSLIBSII, Greece, p 10
Ofelt G (1962) J Chem Phys 37 511
Ogryzlo E (1965) J Chem Educ 42:647–652
Ollier N, Panczer G, Champagnon B, Boulon G, Jollivet P (2002) J Luminescence 94–95:197–201
Oomen E, Smit W, Blasse G (1988) Phys Rev B 37:18–26
Ostapenko M (1990) Moscow, Nedra (in Russian)

Paquette JL, Nedelec A, Moine B, Rakotondrazafi M (1994) R J Geology 102: 523–538
Panczer G, Gaft M, Reisfeld R, Shoval S, Boulon G, Champagnon B (1998) J Alloys and Compounds 275–277:269–272
Panczer G, Gaft M, Marfunin A (2000) Cathodoluminescence in Geosciences. Springer, Berlin Heidelberg New York, pp 359–373
Panczer G (2001) La photoluminescence resolue en temps, nouvel outil pour la mineralogy. Habilitation Thesis, Universite Claude Bernard, Lyon (in French)
Panczer G, Ollier N, Champagnon B, Gaft M (2003a) Geophysical Research Abstracts, 5:14145, European Geophysical Society
Panczer G, Ollier N, Champagnon B, Gaft M, Boudeulle M, Moine B (2003b) Optical Materials
Payne S, Chase L, Krupke F (1988) J Luminescence 40–41:305–306
Payne S, DeLoach L, Smith L, Kway W, Tassno J, Krupper W, Chai B, Loutts G (1994) J Appl Phys 76:497–503.hosts. J of Luminescence 40–41:305–306
Pedone V, Cercone K, Burrus R (1990) Chem Geol 88:183–190
Peixoto J, Oort A (1993) Physics of Climate, American Institute of Physics 93
Pereira E, Monteiro T (1990) J Luminescence 45:443–446
Pereira E, Monteiro T (1991) J Luminescence 48–49:814–818
Pereira E, Santos L (1993) Physica B 185:222–227
Pereira E, Santos L (1994) Diamond and Related Materials 4:26–32
Pillonnet A, Garapon C, Champeaux C, Bovier C, Jaffrezic H, Mugnier J (2000) J Luminescence 87–89:1087–1089
Piriou B, Fahmi D, Dexter J (1987) J Luminescence 39:97–102
Piriou B, Elfakir A, Quarton M (2001) J Luminescence 93:17–26
Platonov A (1979) Naukova dumka, Kiev (in Russian)
Platonov A, Taran M, Balizkii B (1984) Nedra, Moscow (in Russian)
Platonov A, Tarashchan A, Langer K, Andurut M, Partzsch G, Matsyuk S (1998) Phys Chem Minerals 25:203–212
Plotnikova S (1990) In: Kvaskov V (ed) Diamonds in Electronic Technology. Energoatomizdat, Moscow (in Russian)
Ponahlo J (2000) In: Pagel M, Barbin V, Ohenstetter D (eds) Cathodoluminescence in Geosciences. Springer, Berlin Heidelberg New York pp 479–500
Portnov A, Gorobets B (1969) Dokl Akad Nauk SSSR Seriya Geolog 184:199–202
Portnov A, Gorobets B, Rogojine A, Bushev A, Kvitko T (2001) Per Mineral 70:85–100
Porto S, Giordmaine J, Damen T (1956) Phys Rev 147:607–614
Powell R (1967) Phys Rev 155:296–308
Powell R, Blasse G (1980) Structure and Bonding 42:43–85
Powell R, Gang Xu, Quarles G (1985) Phys Rev B 32:2788–2797
Pringsheim P, Vogel M (1946) Interscience Publishers, NY
Prokic M (1979) J Phys Chem Sol 40:405
Prokofiev I, Gorobets B, Gaft M, Lurie Yu (1982) Mineralogich. Sbornik, Lvov State University, Vyshchaya Shkola 36:76–79 (in Russian)
Prokofiev I, Gorobets B, Shuriga T, Rub A, Lugovskoy G, Ryabtsev V (1979). Izvestia AN SSSR (Geol) 3:88–94 (in Russian)

Radziemski L, Loree T, Creams D, Hoffman N (1983) Anal Chem 55:1246–1253
Rassulov V, Rogojine A, Gorobets B, Gaft M (1988) Zapiski Vses Miner Ob-va 4:474–479 (in Russian)
Reiche I, Vignand C, Champagnon B, Panczer G, Bronder C, Morin G, Sole V, Charlet L, Menu M (2001) American Mineralogist 86:1519–1524
Reisfeld R, Jörgensen K (1977) Springer, Berlin Heidelberg New York
Reisfeld R (1991) In: Di Bartolo B, Chen X (eds) Proceedings of Advanced Study Institute on Advances in Nonradiative Processes in Solids. Plenum, NATO ASI Series (B) Physics 249:397–425
Reisfeld R (1973) Structure and Bonding 13:53–98
Reisfeld R, Gaft M, Boulon G, Panczer G, Jørgensen C (1996) J Luminescence 9:343–351
Reisfeld R, Gaft M, Saridarov Ts, Panczer G, Zelner M (2000) Material Lett 45:154–156
Rey C (1991) Phosphorus Res Bull 1:1–35
Rogojine A, Gorobets B, Ryabenko S (1982) Mineralogical Mag 4:45–52 (in Russian)
Rosenwasser S, Asimellis G, Bromley B, Hazlett R, Martin J, Pearce T, Zigler A (2001) Spectrochimica Acta 56B:707–723
Rosenzweig A (1990) Kriger, Florida
Rossman G (1988) Rev Mineral 18:207–254
Rotman S, Hartman F (1988) SPIE 1182:151–161
Rusak D, Castle B, Smith B, Wineford J (1997) Critical Rev Anal Chem 27: 257–290
Ryan F, Ohlmann R, Murphy J, Mazelsky R, Wagner G, Warren R (1970) Phys Rev B 2:2341–2352
Sabsabi M, Cielo P (1995) Apll Spectr 49:499–507
Sabsabi M, Detalle V, St-Onge L, Hamel A, Heon R (2003) Books of Abstracts, EMSLIBSII, Greece, 10 pp
Salter J, Wyatt N (1991) In: Proceedings of the XXVIIth Int Mineral Processing Symp 5:183–193
Samek O, Telle H, Beddows D (2003) BMC Oral Health, V1, BioMed Central
Schärer U, Deutsch A (1990) Cosmochim Acta 54:3435–3447
Schärer U, Zhang LS, Tapponnier P (1994) Earth Planet Sci Lett 126:379–397
Schepler K (1984) J Appl Physics 56:1314–1318
Schott S, Rager H, Schurmann K, Taran M (2003) Eur J Miner 15:701–706
Scott M, Han T, Gallagher H, Henderon B (1997) J Luminescence 72–74:260–262
Seigel H, Robbins J (1982) UK Patent Application, GB 2089029
Seigel H, Robbins J (1985) ITC J 3:162–168
Seydoux-Guillaume AM, Paquette JL, Wiedenbeck M, Montel JM, Heinrich W (2002a) Chem Geol 191:165–181
Seydoux-Guillaume AM, Wirth R, Nasdala L, Gottschalk M, Montel JM, Heinrich W (2002b) Phys Chem Minerals 29:240–253
Sharma S, Angel M, Ghosh M, Hubble H, Lucey P (2001) In Lunar and Planetary Science XXXII
Sharma S, Lucey P, Ghosh M, Hubble H, Horton K (2003) Spectrochimica Acta A59:2391–2407

Shinno I (1986) J Japan Assoc Miner Pet Econ Geol 81:433–445
Shinno I (1987) Mineralogical J 21:119–130
Shionoya S, Yen W (1999) CRC Press, Boca Raton, Florida
Shoval S, Champagnon B, Panczer G, Gaft M, Boudelle M (1999) Proceedings, Semaine Franco-Israelline, Universite Claude Bernard, Lyon, France
Shoval S, Gaft M, Panczer G (2003) J Thermal Anal Calorimetry 71:699–706
Shteinman B, Berman T, Inbar M, Gaft M (1997) Israel J Earth Sci 46:107–113
Sidorenko G, Gorobets B, Dubinchuk V (1986) Energoatomizdat, Moscow
Smith B, Gornushkin I, Winefordner J, Anzano J, Ruiz-Medina A, Nasajpour H (2000) LIBS 2000, Books of Abstracts, Tirrenia, p 6
Solomonov V, Osipov V, Mikhailov S (1993) Zhurnal Prikladnoi Spectroscopii 59:107–113
Solomonov V, Michailov S, Osipov V, Avdonin V, Vasilevskaya M, Yakshin V (1994) Zapiski Vses. Miner Obs 6:39–50 (in Russian)
Solomonov V, Mikhailov S, Osipov V, Lipchak A, Avdonin V, Vasilevskaya M (1996) J Gemm 25:299–305
Solomonov V, Mikhailov S, Lipchak A, Kozlov Yu (2002) J Appl Spectroscopy 69:423–429
Srivastava A (1998) J Luminescence 78:239–243
Stade J, Hahn D, Dittmann R (1974) J Luminescence 8:318–325
Stepanov I, Feofilov P (1956) Docl Acad Nauk SSSR 108:615–618
Studer F, Blasse G (1981) J Sol State Chem 39:195–198
Suchocki A, Gilliland G, Powell R, Bowen J (1987) J Luminescence 37:29–37
Suchoki A, Biernacki A, Arizmendi L (2002) Int Conf on Luminescence and Optical Spectroscopy of Condensed Matter, Budapest, Hungary, Abstracts, 35 pp
Tanaka K, Yano T, Shibata S, Yamane M, Inoe S (1994) J Non-Crystal Solids 178:9–14
Taran M, Tarashchan A, Rager H, Schott S, Schürmann K, Iwanuch W (2003) Phys Chem Minerals 30:546–555
Tarashchan A, Marfunin A (1969) Izvestia AN SSSR (Geol) 3:102–108 (in Russian)
Tarashchan A, Serebrennikov A, Platonov A (1973) Konstituziya I Svoistva Mineralov 7:106–111 (in Russian)
Tarashchan A (1978) Luminescence of minerals. Naukova Dumka, Kiev (in Russian)
Tarashchan A, Waychunas G (1995) In: Marfunin A (ed) Advanced Mineralogy 2, Methods and Instrumentation. Springer, Berlin Heidelberg New York, pp 124–135
Tarashchan A, Lupashko T (1999) Mineralog J 21:39–44 (in Russian)
Townsend P, Rowlands A (2000) In: Pagel M, Barbin V, Blanc P, Ohnenstetter D (eds) Cathodoluminescence in Geosciences. Springer, Berlin Heidelberg New York, pp 41–58
Tretyakova Yu, Tretyakova L (1996) Acta Mineralogica-Petrographica 37: 124–129
Trofimov A (1962) Geochemistry 11:972–975 (in Russian)
Uebbing J, Brust J, Sdorra W, Leis F, Niewear K (1991) Appl Spectr 45:1419–1426

Uspensky E, Novgorodova M, Mineeva R, Speransskii A, Bershov L, Gaft M (1989) Docl Acad Nauk SSSR 304:55–59
Uspensky E, Aleshin P (1993) International Geology Rev 35:1037–1051
Uspensky E, Brugger J, Graeseer S (1998) Schweiz Mineral Petrogr Mitt 78: 31–54
Vacek K (1969) Czech J Phys B19:771–775
Vacek K (1971) Czech J Phys B21:303–308
Vergara I, Sole J, Hoyos M, Calderon T (1990) Solid State Communications 76:289–292
Vikentiev I, Vikentieva O www.min-eng.com/protected/app03ex
Voronko K, Maksimova G, Sobol A (1991) Opt Spectrosc (USSR) 70:203–206
Votyakov S, Krasnobaev A, Krohalev V (1993) Nauka, Ekaterinburg, pp 233 (in Russian)
Walker G (1985) In: Berry F, Vaughan D (eds) Chemical bonding and spectroscopy in minerals chemistry. University of Birmingham
Walker G, Jaer A, Sherlock R, Glynn T, Czaja M, Mazurak Z (1997) J Luminescence 72–74:278–280
Walker G (2000) In: Pagel M, Barbin V, Blanc P, Ohnenstetter D (eds) Cathodoluminescence in Geosciences. Springer, Berlin Heidelberg New York, pp 23–40
Walker J (1979) Rep Progr Phys 42:1605–1659
Wallace L, Hunten D (1968) J Geophys Res 73:4813–4817
Waychunas G (1989) In: Hawthorne (ed) Spectroscopic Methods in Mineralogy and Geology. Rev Mineral Mineral Soc Am, pp 638–698
Waychunas G (2002) In: Kohn M, Rakovan J, Hughes J (eds) Reviews in Mineralogy and Geochemistry. Phosphates: Geochemical, Geobiological and Material Importance 48
White W (1984) US Patent 4,423814
White W, Matsumura M, Linnehan D, Fukukawa T, Chandrasekhar B (1986) American Mineralogist 71:1415–1419
White W (1990) In: Coyne L, McKeever W, Blake D (eds) Spectroscopic characterization of minerals and their surfaces. American Chemical Society, Washington, DC
Wiens R, Maurice S, Cremers D, Chevrees S (2003) Lunar and Planetary Science XXXIV:1646–1647
Winefordner J (2000) Florida Institute of Phosphate Research (FIPR), Publication N 04–057–169
Wojtowicz A, Lempicki (1988) Phys Rev B 39:8695–8701
Wojtowicz A (1991) J Luminescence 50:221–230
Xu L, Bulatov V, Gridin V, Schechter I (1997) Anal Chem 69:2103–2108
Yacobi C, Holt D (1990) Plenum, New York
Yamaga M, Yosida T, Henderson B, O'Donnel K, Date M (1992) J Phys: Condens Matter 4:7285–7294
Yang C (1995) Department of Nuclear Physics, Lund Institute of Technology, Lund, Sweden
Yifrach A, Neta U (1992) US Patent, 5,118,181
Zotov N, Yanev Y, Piriou B (2002) Phys Chem Minerals 29:291–299

Index

A

B

C

D

E

F

G

H

J

K

L

M

N

O

P

Q

R

S

T

U

W

X

Z